Sanichiro Yoshida · Luciano Lamberti
Cesar Sciammarella   *Editors*

Advancement of Optical Methods in Experimental Mechanics, Volume 3

Proceedings of the 2016 Annual Conference on Experimental and Applied Mechanics

SEM

Springer

Conference Proceedings of the Society for Experimental Mechanics Series

Series Editor

Kristin B. Zimmerman, Ph.D.
Society for Experimental Mechanics
Bethel, CT, USA

Sanichiro Yoshida • Luciano Lamberti • Cesar Sciammarella
Editors

Advancement of Optical Methods in Experimental Mechanics, Volume 3

Proceedings of the 2016 Annual Conference on Experimental and Applied Mechanics

Editors
Sanichiro Yoshida
Department of Chemistry and Physics
Southeastern Louisiana University
Hammond, LA, USA

Cesar Sciammarella
General Stress Optics
Chicago, IL, USA

Research Professor, Emeritus
Department of Mechanical, Materials
    and Aerospace Engineering
Illinois Institute of Technology
Chicago, IL, USA

Luciano Lamberti
Dipartimento di Meccanica,
    Matematica e Management
Politecnico di Bari
Bari, Italy

Preface

Advancement of Optical Methods in Experimental Mechanics represents one of ten volumes of technical papers presented at the SEM 2016 Annual Conference & Exposition on Experimental and Applied Mechanics organized by the Society for Experimental Mechanics and held in Orlando, FL, on June 6–9, 2016. The complete Proceedings also includes volumes on: *Dynamic Behavior of Materials*; *Challenges in Mechanics of Time-Dependent Materials*; *Experimental and Applied Mechanics*; *Micro- and Nanomechanics*; *Mechanics of Biological Systems and Materials*; *Mechanics of Composite & Multifunctional Materials*; *Fracture*, *Fatigue*, *Failure and Damage Evolution*; *Residual Stress*, *Thermomechanics & Infrared Imaging*, *Hybrid Techniques and Inverse Problems*; and *Joining Technologies for Composites and Dissimilar Materials*.

Each collection presents early findings from experimental and computational investigations on an important area within Experimental Mechanics, Optical Methods being one of these areas.

With the advancement in imaging instrumentation, lighting resources, computational power and data storage, optical methods have gained wide applications across the experimental mechanics society during the past decades. These methods have been applied for measurements over a wide range of spatial domain and temporal resolution. Optical methods have utilized a full range of wavelengths from X-ray to visible lights and infrared. They have been developed not only to make two-dimensional and three-dimensional deformation measurements on the surface but also to make volumetric measurements throughout the interior of a material body.

Hammond, LA   Sanichiro Yoshida
Bari, Italy   Luciano Lamberti
Chicago, IL   Cesar A. Sciammarella

Contents

Contributors

Fadi Abu-Farha Clemson University—International Center for Automotive Research, Greenville, SC, USA

Josh Anton Mechanical and Aerospace Engineering Department, University of Florida, Gainesville, FL, USA

Shuichi Arikawa Department of Mechanical Engineering Informatics, Meiji University, Kawasaki, Kanagawa, Japan

A. Baldi Dipartimento di Ingegneria Meccanica, Chimica e dei Materiali, Università degli Studi di Cagliari, Cagliari, Italy

F. Barlat GIFT, POSTECH, Pohang, Gyeongbuk, South Korea

Sally Bartelmo Department of Civil and Environmental Engineering, University of South Carolina, Columbia, SC, USA

K. Bertoldi School of Engineering and Applied Science, Harvard University, Cambridge, MA, USA

Sven Bossuyt Department of Mechanical Engineering, Aalto University, Aalto, Finland

Robin Bouclier Institut de Mathématiques de Toulouse, CNRS UMR 5219, INSA Toulouse, Université de Toulouse, Toulouse, France

Juan Caicedo Department of Civil and Environmental Engineering, University of South Carolina, Columbia, SC, USA

Jason Cantrell Mechanical and Aerospace Engineering Department, University of Florida, Gainesville, FL, USA

C. Casavola Dipartimento di Meccanica, Matematica e Management, Politecnico di Bari, Bari, Italy

A. Charbal LMT, ENS Cachan/CNRS/University of Paris-Saclay, Cachan, France

CEA, DEN-SRMA, Université of Paris-Saclay, Gif sur Yvette, France

Terry Yuan-Fang Chen Department of Mechanical Engineering, National Cheng Kung University, Tainan, Taiwan, ROC

Ran Chen State Key Laboratory of Material Processing and Die and Mould Technology, Huazhong University of Science and Technology, Wuhan, China

Po-Yu Chen Department of Power Mechanical Engineering, National Tsing Hua University, Hsinchu, Taiwan, Republic of China

G. Chiappini Dipartimento di Ingegneria Industriale e Scienze Matematiche, Università Politecnica delle Marche, Ancona, Italy

S. Chinzei Kobe Steel, LTD, Kobe, Hyogo, Japan

Phani Madhavi Ch Department of Applied Mechanics, Indian Institute of Technology Madras, Chennai, India

P.C. Collins Materials Science and Engineering, Iowa State University, Ames, IA, USA

L. Cortese Faculty of Science and Technology—Free University of Bozen, Bolzano, Italy

David Damiani Bartram Trail High School, Saint Johns, FL, USA

F. Davis Engineering Materials Group, Faculty of Engineering and the Environment, University of Southampton, Southampton, UK

Luke DiSandro Mechanical and Aerospace Engineering Department, University of Florida, Gainesville, FL, USA

S. Dreuilhe Engineering Materials Group, Faculty of Engineering and the Environment, University of Southampton, Southampton, UK

J.-E. Dufour LMT, ENS Cachan/CNRS/University of Paris Saclay, Cachan, France

Antti Forsström Department of Mechanical Engineering, Aalto University, Aalto, Finland

L. Francesconi Dipartimento di Ingegneria Meccanica, Chimica e dei Materiali, Università degli Studi di Cagliari, Cagliari, Italy

Motoharu Fujigaki Graduate School of Engineering, University of Fukui, Fukui, Japan

Yasuhisa Fujimoto Mitsubishi Electric Corporation Advanced Technology Research and Development Center, Amagasaki, Hyogo, Japan

Y. Fukami National Institute of Advanced Industrial Science and Technology (AIST), Tsukuba, Japan

Department of Mechanical Engineering, Tokyo University of Science, Chiba, Japan

Cosme Furlong Center for Holographic Studies and Laser Micro-mechaTronics (CHSLT), Worcester, MA, USA

Mechanical Engineering Department, Worcester Polytechnic Institute, Worcester, MA, USA

M.G.D. Geers Department of Mechanical Engineering, Eindhoven University of Technology, Eindhoven, The Netherlands

K. Genovese School of Engineering, University of Basilicata, Potenza, Italy

Paul J. Gloeckner Cummins Technical Center, Cummins Inc., Columbus, IN, USA

Manuel Grewer Lavision GmbH, Göttingen, Germany

Rishi Gurnani College of Engineering, University of California at Berkeley, Berkeley, CA, USA

Juuso Heikkinen Department of Mechanical Engineering, University of British Columbia, Vancouver, Canada

F. Hild LMT, ENS Cachan/CNRS/University of Paris-Saclay, Cachan, France

J.P.M. Hoefnagels Department of Mechanical Engineering, Eindhoven University of Technology, Eindhoven, The Netherlands

G.M. Hommer Mechanical Engineering Department, Colorado School of Mines, Golden, CO, USA

Chi-Hung Hwang ITRC, NARLabs, Hsinchu, Taiwan, ROC

Peter Ifju Mechanical and Aerospace Engineering Department, University of Florida, Gainesville, FL, USA

Alex Jerez Mechanical and Aerospace Engineering Department, University of Florida, Gainesville, FL, USA

D. Kanazawa Department of Mechanical Engineering, Aoyama Gakuin University, Sagamihara, Kanagawa, Japan

Pasi Karppinen ProtoRhino, Helsinki, Finland

Jordan E. Kelleher Cummins Technical Center, Cummins Inc., Columbus, IN, USA

Addis Kidane Department of Mechanical Engineering, University of South Carolina, Columbia, SC, USA

J.-H. Kim GIFT, POSTECH, Pohang, Gyeongbuk, South Korea

S.M. Kleinendorst Department of Mechanical Engineering, Eindhoven University of Technology, Eindhoven, The Netherlands

Behrad Koohbor Department of Mechanical Engineering, University of South Carolina, Columbia, SC, USA

Ramesh Krishnamurthi Department of Applied Mechanics, Indian Institute of Technology Madras, Chennai, India

Calvin Kroese Mechanical and Aerospace Engineering Department, University of Florida, Gainesville, FL, USA

L. Lamberti Dipartimento Meccanica, Matematica e Management, Politecnico di Bari, Bari, Italy

Albert Lasprilla Department of Civil and Environmental Engineering, University of South Carolina, Columbia, SC, USA

D.-H. Leem GIFT, POSTECH, Pohang, Gyeongbuk, South Korea

Ning Li Department of Mechanical Engineering, University of South Carolina, Columbia, SC, USA

Zhongwei Li State Key Laboratory of Material Processing and Die and Mould Technology, Huazhong University of Science and Technology, Wuhan, China

Meng Liu State Key Laboratory of Material Processing and Die and Mould Technology, Huazhong University of Science and Technology, Wuhan, China

Marek Lomnitz Dantec Dynamics GmbH, Ulm, Germany

Eduardo Lozano Colorado School of Mines, Golden, CO, USA

Ren-Shaung Lu Department of Mechanical Engineering, National Cheng Kung University, Tainan, Taiwan, ROC

Steven Mates National Institute of Standards and Technology, Gaithersburg, MD, USA

L.M. Mattucci Dipartimento di Ingegneria Industriale e Scienze Matematiche, Università Politecnica delle Marche, Ancona, Italy

M. El Mehtedi Dipartimento di Ingegneria Industriale e Scienze Matematiche, Università Politecnica delle Marche, Ancona, Italy

Chengyun Miao Department of Mechanical Engineering, Auburn University, Auburn, AL, USA

Manabu Murata Department of Mechanical Engineering, Aoyama Gakuin University, Sagamihara, Kanagawa, Japan

Yorinobu Murata Faculty of Systems Engineering, Wakayama University, Wakayama, Japan

M. Murata Department of Mechanical Engineering, Aoyama Gakuin University, Sagamihara-shi, Kanagawa, Japan

Kimmo Mustonen ProtoRhino, Helsinki, Finland

Department of Physics, University of Vienna, Vienna, Austria

J. Naito Kobe Steel, LTD, Kobe, Hyogo, Japan

F. Nalli Faculty of Science and Technology—Free University of Bozen, Bolzano, Italy

Erika Nieczkoski Colorado School of Mines, Golden, CO, USA

S. Ogihara Department of Mechanical Engineering, Tokyo University of Science, Chiba, Japan

Yohei Omoto Mitsubishi Electric Corporation Advanced Technology Research and Development Center, Amagasaki, Hyogo, Japan

H. Ono Department of Chemistry and Physics, Southeastern Louisiana University, Hammond, LA, USA

Department of Engineering, Niigata University, Niigata-shi, Niigata, Japan

G. Pappalettera Dipartimento di Meccanica, Matematica e Management, Politecnico di Bari, Bari, Italy

C. Pappalettera Dipartimento di Meccanica, Matematica e Management, Politecnico di Bari, Bari, Italy

J.S. Park Materials Physics and Engineering X-ray Science Division, Advanced Photon Source, Argonne National Laboratory, Lemont, IL, USA

Jean-Charles Passieux Université de Toulouse, Institut Clément Ader (INSA, ISAE, Mines Albi, UPS), CNRS UMR 5312, Toulouse, France

Jean-Noël Périé Université de Toulouse, Institut Clément Ader (INSA, ISAE, Mines Albi, UPS), CNRS UMR 5312, Toulouse, France

Vilem Petr Colorado School of Mines, Golden, CO, USA

Jean-Emmanuel Pierré Université de Toulouse, Institut Clément Ader (INSA, ISAE, Mines Albi, UPS), CNRS UMR 5312, Toulouse, France

F. Pierron Engineering Materials Group, Faculty of Engineering and the Environment, University of Southampton, Southampton, UK

A.L. Pilchak Air Force Research Laboratory, Wright-Patterson AFB, Ohio, OH, USA

M. Poncelet LMT, ENS Cachan/CNRS/University of Paris Saclay, Cachan, France

Sreehari Rajan Department of Mechanical Engineering, University of South Carolina, Columbia, SC, USA

Vivek Ramakrishnan Department of Applied Mechanics, Indian Institute of Technology Madras, Chennai, India

Payam Razavi Center for Holographic Studies and Laser Micro-mechaTronics (CHSLT), Worcester, MA, USA

Mechanical Engineering Department, Worcester Polytechnic Institute, Worcester, MA, USA

S. Ri Research Institute for Measurement and Analytical Instrumentation, National Institute of Advanced Industrial Science and Technology (AIST), Tsukuba, Japan

Dimtris Rizos Department of Civil and Environmental Engineering, University of South Carolina, Columbia, SC, USA

Sean Rohde Mechanical and Aerospace Engineering Department, University of Florida, Gainesville, FL, USA

M. Rossi Università Politecnica delle Marche, Ancona, Italy

S. Roux LMT, ENS Cachan/CNRS/University of Paris-Saclay, Cachan, France

A.P. Ruybalid Department of Mechanical Engineering, Eindhoven University of Technology, Eindhoven, The Netherlands

T. Sasaki Department of Engineering, Niigata University, Niigata-shi, Niigata, Japan

M. Sasso Dipartimento di Ingegneria Industriale e Scienze Matematiche, Università Politecnica delle Marche, Ancona, Italy

Gary S. Schajer Department of Mechanical Engineering, University of British Columbia, Vancouver, Canada

Hubert Schreier Correlated Solutions Inc., Irmo, SC, USA

C.A. Sciammarella Department of Mechanical, Materials and Aerospace Engineering, Illinois Institute of Technology, Chicago, IL, USA

R. Seghir Engineering and the Environment, University of Southampton, Southampton, UK

Yusheng Shi State Key Laboratory of Material Processing and Die and Mould Technology, Huazhong University of Science and Technology, Wuhan, China

Thorsten Siebert Dantec Dynamics GmbH, Ulm, Germany

Clive R. Siviour Department of Engineering Science, University of Oxford, Oxford, UK

O. van der Sluis Department of Mechanical Engineering, Eindhoven University of Technology, Eindhoven, The Netherlands

Karsten Splitthof Dantec Dynamics GmbH, Ulm, Germany

A.P. Stebner Mechanical Engineering Department, Colorado School of Mines, Golden, CO, USA

Douglas Steinbach Mechanical and Aerospace Engineering Department, University of Florida, Gainesville, FL, USA

Michael A. Sutton Department of Mechanical Engineering, University of South Carolina, Columbia, SC, USA

Y. Takashita Department of Mechanical Engineering, Tokyo University of Science, Chiba, Japan

M. Taylor Department of Mechanical Engineering, Santa Clara University, Santa Clara, CA, USA

Hareesh V. Tippur Department of Mechanical Engineering, Auburn University, Auburn, AL, USA

Daiki Tomita Graduate School of Systems Engineering, Wakayama University, Wakayama, Japan

James D. Trolinger MetroLaser, Inc., Laguna Hills, CA, USA

K. Ushijima Department of Mechanical Engineering, Tokyo University of Science, Tokyo, Japan

M. Usui Department of Engineering, Niigata University, Niigata-shi, Niigata, Japan

Guillermo Valeri Department of Mechanical Engineering, University of South Carolina, Columbia, SC, USA

C.V. Verhoosel Department of Mechanical Engineering, Eindhoven University of Technology, Eindhoven, The Netherlands

L. Vincent CEA, DEN-SRMA, Université of Paris-Saclay, Gif sur Yvette, France

Shou Hsueh Wang Department of Power Mechanical Engineering, National Tsing Hua University, Hsinchu, Taiwan, ROC

Q. Wang Research Institute for Measurement and Analytical Instrumentation, National Institute of Advanced Industrial Science and Technology, Tsukuba, Ibaraki, Japan

Wei-Chung Wang Department of Power Mechanical Engineering, National Tsing Hua University, Hsinchu, Taiwan, ROC

Bernhard Wieneke Lavision GmbH, Göttingen, Germany

Yen-Ting Wu Department of Power Mechanical Engineering, National Tsing Hua University, Hsinchu, Taiwan, Republic of China

Satoru Yoneyama Department of Mechanical Engineering, Aoyama Gakuin University, Sagamihara-shi, Kanagawa, Japan

Sung-ho Yoon Department of Engineering Science, University of Oxford, Oxford, UK

S. Yoshida Department of Chemistry and Physics, Southeastern Louisiana University, Hammond, LA, USA

Andie Young Mechanical and Aerospace Engineering Department, University of Florida, Gainesville, FL, USA

Xing Zhao Department of Mechanical Engineering, University of South Carolina, Columbia, SC, USA

Kai Zhong State Key Laboratory of Material Processing and Die and Mould Technology, Huazhong University of Science and Technology, Wuhan, China

Chapter 1
A General Mathematical Model to Retrieve Displacement Information from Fringe Patterns

C.A. Sciammarella and L. Lamberti

Abstract The extraction of the displacement field and its derivatives from fringe patterns entails the following steps: (1) information inscription; (2) data recovery; (3) data processing; (4) data analysis. Phase information is a powerful representation of the information contained in a signal. In a previous work, the above mentioned steps were formulated and discussed for a 1D signal, indicating that the extension to 2-D was a non trivial process. Proceeding along the same line of thought when one moves from the one dimension to two dimensions it is necessary to consider a 3D abstract space to generate the additional dimension that can handle the analysis of 2D signals and simultaneously extend the Hilbert transform to 2D. In this study the basic theory developed in the preceding reference is further elaborated to produce a version of the monogenic function yielding the necessary answers to the previously described processes. The monogenic signal, a 3D vector in a Cartesian complex space, is graphically represented by a Poincare sphere which provides a generalization of the Hilbert transform to a 2D version of what is called the generalized Hilbert transform or Riesz transform. These theoretical derivations are supported by the actual application of the theory and corresponding algorithms to 2D fringe patterns and by comparing the obtained results with known results.

Keywords 2D signals • Displacement and strain determination • Generalized Hilbert (Riesz) transform • Poincare sphere

1.1 Introduction

In [1], the present authors developed a one dimensional mathematical model of fringe patterns analysis based on the general Theory of Signal Analysis. This paper now deals with a generalization of the one dimension model derivations to 2-D. The extension to a higher dimension requires the review of some basic concepts of image signal analysis. To simplify the derivations we will consider the signal analysis on plane surfaces. The extension to general surfaces in the space requires further developments that cannot be covered on a single paper.

The information to be decoded is recorded as level of gray in a 2D sensor through a device composed of optical and electronic circuits commanded by software, a measure of the light intensity of the imaged field. At this point the details of the process of data generation will set aside and the paper will concentrate in the process of information extraction. The recorded levels of gray must be converted into data that provide displacement fields and the displacement derivatives in the case of deformed bodies or geometrical parameters and their derivatives. In [1], it is shown that data conversion in one dimension requires the description of gray levels in terms of 2D complex functions (analytical functions) that lead to the introduction of the concept of phasor:

$$\overrightarrow{\mathbf{I_{sp}}}(x) = I_{sp}(x)e^{2\pi j \phi(x)} \tag{1.1}$$

The symbol $\Rightarrow$ indicates a vector in the complex plane. A phasor in the complex plane is characterized by two separate pieces of information: amplitude related to the light intensity at the considered point and a phase representing the optical path followed by the recorded wave front from a selected reference point where the phase is assumed to be zero. The classical definition of phase in optics is,

_____

C.A. Sciammarella

Department of Mechanical, Materials and Aerospace Engineering, Illinois Institute of Technology, 10 SW 32nd St., Chicago, IL 60616, USA

L. Lamberti (✉)

Dipartimento Meccanica, Matematica e Management, Politecnico di Bari, Viale Japigia 182, Bari 70126, Italy
e-mail: luciano.lamberti@poliba.it

$$\boldsymbol{\phi}(x) = \frac{2\pi\boldsymbol{\delta}(x)}{p} \tag{1.2}$$

where $\boldsymbol{\delta}(x)$ is the optical path and p is pitch of the sinusoidal function, unit of measure utilized to evaluate a path length and convert distances into an angle.

The optical path length of the light arriving at an image is given by,

$$\boldsymbol{\delta}(x) = \int\limits_0^{S_0} n(x)\,dx \tag{1.3}$$

where n(x) is the index of refraction of the medium along the path followed by the light from a certain reference point to another point following a trajectory.

A question than can arise is: Why to begin with the review of the phase concept? The answer to this question is found in [2]: the phase concept is a fundamental tool to develop a consistent theory of image analysis. There is another important aspect to the concept of phase, the definition of local phase implicit in Eq. (1.1) and the more general concept of global phase expressed by Eq. (1.3). The phase concept is associated with the notion of vector. When one introduces the definition of local phase or phase at a point for a 1D signal, one introduces an additional dimension to the mathematical model required to associate one dimensional functions with the phase concept. This additional dimension corresponds not to the actual space but to the complex plane. It is a fundamental concept in the Gabor's analytic signal theory [3], basic starting point of many developments in Signal Analysis and in Optics. A complementary development to the analytic signal theory in one dimension is the Hilbert transform [4] that converts cosines into sines and is a unitary transform that changes the phase of the signal of $\pi/2$, leaving the signal amplitude unchanged. The Hilbert transform takes the original signal, a level of gray or intensity in some scale, and associates the gray level with an analytical function:

$$\mathbf{I_{sp}}(x) = I_p(x) + I_q(x)\mathbf{j} \tag{1.4}$$

where the symbol $\mathbf{j}$ is the imaginary versor, $I_p(x)$ is the recorded signal (in-phase signal) and $I_q(x)$ is the in-quadrature signal that provides the phase,

$$\boldsymbol{\phi}(x) = arctg\,\frac{I_q(x)}{I_p(x)} \tag{1.5}$$

and

$$\left\|\overset{\Rightarrow}{\mathbf{I_{sp}}}(x)\right\| = \sqrt{I_p^2 + I_q^2} \tag{1.6}$$

where the double bar symbol indicates the modulus of the vector in the complex plane.

A fundamental property of the Hilbert transform is to provide a definition of local phase concept that is ancillary to the definition provided by Eq. (1.3) but applies to a single point of the gray level continuum of a one-dimensional signal provided that the gray levels are smooth functions with smooth derivatives in $\mathbf{R}^2$ that symbolizes the 2D continuum. The preceding conditions are ideal conditions that are not satisfied by actual signals. Recorded signals are inherently stochastic, hence in actual applications it is necessary to apply to the recorded gray levels smoothing procedures to approximate with certain error the theoretical ideal continuum signal. One should keep in mind these two separated aspects of the local phase definition, the theory behind this definition that is a consequence of the continuum theory and the procedures needed to implement applications of the mathematical model to actual experimental signals. In the literature of analysis of actual optical signals there is a very extensive treatment of the subject of separating stochastic and deterministic information. In this section and following sections the emphasis is on the continuum model, the stochastic aspect will be introduced later on in the paper. This is a very important simplification for the subject matter of the paper, fringe pattern information retrieval. Later on we will indicate the impact of the assumption of continuity in the handling of actual stochastic signals.

The aim of the current paper is to extend the derivations presented in the framework of a one dimensional model continuum model, [1], to a two dimensional continuum case.

1.2 Two Dimensional Sinusoidal Functions

The next step in this process is to define the properties of two dimensional sinusoidal functions, a generalization of one dimensional sinusoidal functions utilized in the one dimensional continuum [1]. Figure 1.1a shows a two dimensional sinusoidal signal, it has an amplitude and a period p as is the case in one dimension but has an additional degree of freedom, the local orientation. Figure 1.1b illustrates the 2D sinusoid as a signal in 2-D. The yellow line shows a line of equal intensity (phase); the normal **n** provides the orientation of the signal, angle θ, and the vector **r** identifies a point of phase φ in the uniform field of the 2D sinusoidal signal. As shown by Eq. (1.2), the phase is computed with respect to a selected point O (center of coordinates) and is evaluated—Eq. (1.3)—as an angle that provides the number of cycles of the unit of measure p, a rational number n. The red line corresponds to points of equal number of cycles, since as the orientation of the vector **r** changes, it also changes the projected pitch p that is the unit measure to convert distances into angles. Comparing a 2D signal with a 1D sinusoidal signal, as mentioned before, there is an additional degree of freedom, the angle θ (see Fig. 1.1b).

The considerations that follow are very important because the information that we want to retrieve is connected with a model, the continuum mechanics of solids that has its basis on the differential geometry approach to the continuum deformation with specific requirements for the signal and its successive derivatives. What this last sentence means is: specific requirements are imposed on the signal and its derivatives.

The information that we want to obtain is a tensorial field that requires in the case of orthogonal Cartesian Coordinates a family of two orthogonal carrier fringes illustrated in Fig. 1.2. The vertical fringes and the horizontal fringes are represented in the frequency plane of the Fourier Transform (FT) by power spectrum dots whose coordinates are for example of the form $(f_x, f_y) = (10, 0)$ for the x-axis, and the coordinates of the point in the negative frequencies are $(f_x, f_y) = (-10, 0)$, that is a reflection with respect to the vertical axis. In analogous fashion, for the horizontal fringes we have $(f_x, f_y) = (0, 10)$ and for the negative frequency $(f_x, f_y) = (0, -10)$. In Fig. 1.2, the system of coordinates is selected as a left-handed system according with the usual practice in image analysis literature as opposed to Fig. 1.1 where a right-handed reference system is used.
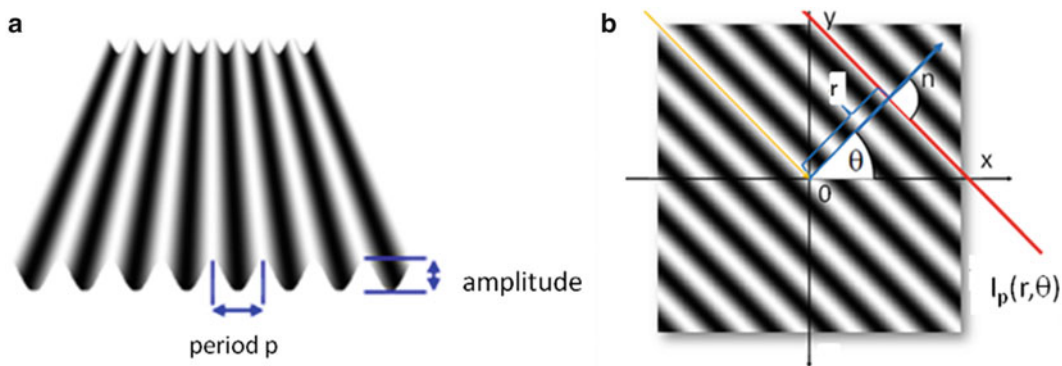
Fig. 1.1 (**a**) 2D sinusoidal signal; (**b**) additional parameter θ to define a two dimensional signal
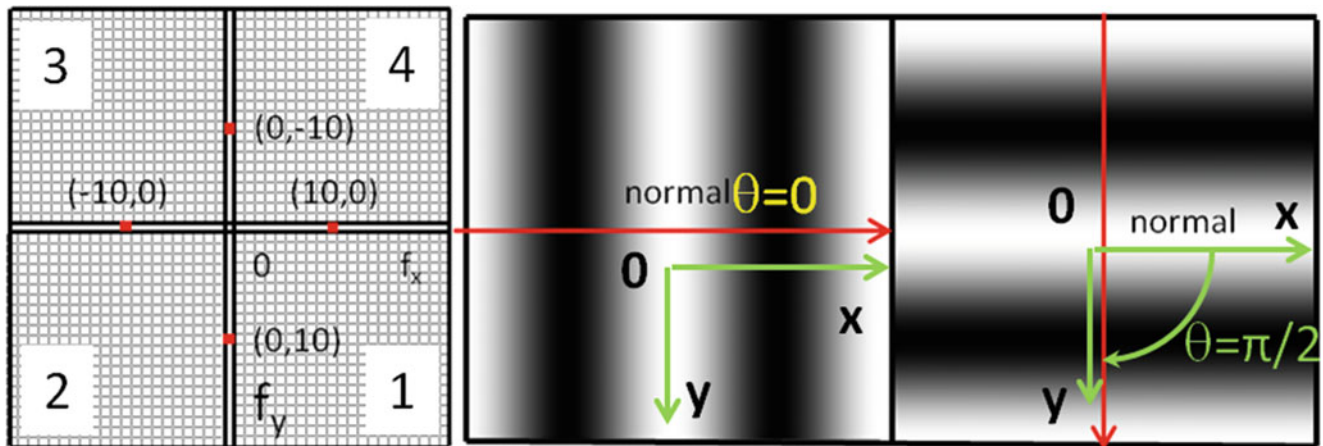
Fig. 1.2 Representation of a 2D cosinusoidal even signal when $\theta = 0$ and $\theta = \pi/2$ and the corresponding representation in the frequency plane represented by a sensor with square pixels

If we return to the concept of phase defined in Eq. (1.3) and compute the phase of a point defined by the vector $\mathbf{r} = x\mathbf{i} + y\mathbf{j}$ in the direction of the normal $\mathbf{n}$ (Fig. 1.1b) it follows

$$\boldsymbol{\phi}(\mathbf{r}, \boldsymbol{\theta}) = \frac{2\boldsymbol{\pi}\|\mathbf{r}\|}{p} \tag{1.7}$$

where the double bar indicate the modulus of the vector in agreement with Eq. (1.3).

To understand the developments that follow, it is necessary to come back to the concept of local phase that can be introduced [1] via the Hilbert transform. The concept of local phase is a fundamental step in the whole process described in this paper and will be dealt with later on in the paper since it involves the transition between the ideal continuum and the actual recorded stochastic signals.

The extension of local phase to 2D sinusoidal signals includes an additional degree of freedom, the angle θ indicated in Fig. 1.1b. The concept of phase requires a 2D vectorial field since it is associated with a vectorial function. The information captured by a sensor is given by levels of gray, a scalar quantity. This scalar function in the case of a 1D signal is connected to a 2D scalar potential in the complex plane that will be called $\dot{V}$; the symbol • indicates that the scalar potential is associated with a given point of coordinate x in the one dimensional continuum $\mathcal{L}^1$, that has a certain reference zero point from where the coordinate x is computed. In Eq. (1.4), the complex notation of [4] is utilized to represent an analytical function, for a more general approach in view to the extension to 3-D. A complex plane defined by the versors $\vec{\mathbf{i}}$ and $\vec{\mathbf{j}}$ is introduced, thus avoiding the utilization of quaternions that are the extension of the complex notation beyond 2-D.

Returning to the complex plane required to introduce the concept of local phase, the gradient of the scalar potential is given by

$$grad \ \dot{V} = \mathbf{G}_2 = \frac{\partial \dot{V}}{\partial x_c} \vec{\mathbf{i}} + \frac{\partial \dot{V}}{\partial y_c} \vec{\mathbf{j}} \tag{1.8}$$

where: $\vec{\mathbf{i}}$ and $\vec{\mathbf{j}}$ are the versors in the complex plane (introducing different symbols from $\mathbf{i}$ and $\mathbf{j}$ that represent the versors in the physical space); x_c and y_c are the coordinates in the complex plane; the subscript "2" indicates 2D gradient vector in the complex space. The sinusoidal signal is represented by gray levels defined by a function of the form,

$$\dot{V}^e = I_p \cos\left(\frac{2\pi}{p}x + \phi_0\right) \tag{1.9}$$

The upper script "e" expresses the fact that the selected function is a cosine, an even function. It is possible to see that the local phase depends on the selection of the phase at the reference point.

Computing the dot product of the ∇ operator with the vector $\mathbf{G}_2$, the divergence of the field is obtained as:

$$\nabla \bullet \mathbf{G}_2 = \frac{\partial^2 \dot{V}}{\partial x_c{}^2} + \frac{\partial^2 \dot{V}}{\partial y_c{}^2} \tag{1.10}$$

Calling $\dot{V}_{xc} = \frac{\partial \dot{V}}{\partial x_c}$ and $\dot{V}_{yc} = \frac{\partial \dot{V}}{\partial y_c}$, and computing the vector product "$\times$" of the ∇ operator with the $\mathbf{G}_2$ vector, it follows:

$$\nabla \times \mathbf{G}_2 = \left(\frac{\partial \dot{V}_{yc}}{\partial x_c} - \frac{\partial \dot{V}_{xc}}{\partial y_c}\right) \vec{\vec{\mathbf{k}}} \tag{1.11}$$

Since the field is a scalar field, the divergence of the field is zero and the rotor is also zero. Two equations can be derived:

$$\frac{\partial^2 \dot{V}}{\partial x_c{}^2} + \frac{\partial^2 \dot{V}}{\partial y_c{}^2} = 0 \tag{1.12}$$

$$\frac{\partial \dot{V}_{yc}}{\partial x_c} - \frac{\partial \dot{V}_{xc}}{\partial y_c} = 0 \tag{1.13}$$

These equations mean that the potential function in the complex plane must satisfy the Cauchy-Riemann equations,

$$\frac{\partial \dot{V}_{xc}}{\partial x_c} = -\frac{\partial \dot{V}_{yc}}{\partial y_c} \tag{1.14}$$

$$\frac{\partial \dot{V}_{xc}}{\partial y_c} = \frac{\partial \dot{V}y_c}{\partial x_c} \tag{1.15}$$

Equation (1.12) implies that the gray level potential $\dot{V}$ to define a local phase must be a solution of Laplace's equation in the complex plane. The solutions of the Laplace's equation are part of the theory of potentials; these solutions are known to be harmonic functions. The field is conservative and the vectorial field is the gradient of a potential scalar field.

The meaning of Eqs. (1.14) and (1.15) is that, in order to define a local phase, successive derivatives of gray levels must satisfy the above conditions. Furthermore, considering the full complex field, these equations are the conditions for $\dot{V}(\boldsymbol{\rho}_c) \cdot d\boldsymbol{\rho}_c$, where $\boldsymbol{\rho}_c = x_c \vec{\mathbf{i}} + y_c \vec{\mathbf{j}}$ is a given direction in the complex plane, to be an exact differential or, in other words, that is a potential such that the integral of the field is independent of the pathway followed. This conclusion leads to the complex function,

$$z(x) = \dot{V^e}(x) + \vec{j}\,\dot{V^o}(x) \tag{1.16}$$

where $\dot{V^o}(x)$ represents the odd component of the signal.

Through Eq. (1.16) one gets the connection between the Hilbert transform, holomorphic functions and the levels of gray as a potential function leading to the definition of a local phase. For example, if $\dot{V^e}$ is of the form given by Eq. (1.8), through the Hilbert transform we will obtain,

$$\dot{V^o}(x) = I_q \sin\left(\frac{2\pi}{p}x + \phi_0\right) \tag{1.17}$$

Each one of these derivatives can be computed from the information recorded in the image sensor. For each point of the $\mathcal{L}^1$ domain, one can plot the gray levels as $\dot{V}(x)$. From Eq. (1.8) $\frac{\partial \dot{V}}{\partial x_c} \equiv \frac{\partial \dot{V}(x)}{\partial x}$ and $\frac{\partial \dot{V}(x_c)}{\partial y_c} \equiv \frac{\partial \dot{V}(x)}{\partial y}$ can be obtained and, finally, complementary derivatives are obtained from Eqs. (1.13) and (1.14). In summary, to represent the deformation of a continuous field the derivatives must satisfy the above relationships for a one dimensional signal. However, recorded signals will be contaminated by different signals that we designate as noise. Whatever processes that are applied to the signal to remove noise they must get successive derivatives satisfying the above conditions.

All previous developments correspond to gray levels in one dimension. To introduce the definition of local phase for the 2D sinusoidal signal shown in Fig. 1.1 it is necessary to resort to a 3D complex space. Figure 1.1 showed a 2D cosinusoidal function which has the same parameters as a 1D signal but also additional parameter, the orientation θ. The normal $\mathbf{n}$ to the fringe trajectory shown in Fig. 1.1 provides the orientation of the signal at a given point of the physical space and the angle θ defines the orientation of the segment of curve with respect to a selected reference system. Some notations that will be useful in the developments that follow are now introduced. The unit normal to fringes in a point of a sinusoidal signal (Fig. 1.1b) is,

$$\mathbf{n} = x\cos\theta\mathbf{i} + y\sin\theta\mathbf{j} \tag{1.18}$$

The above relationship is converted into cycles per unit length by multiplying Eq. (1.18) by $2\pi/p$. Introducing the concept of wave vector for the sinusoidal signal, it can be written:

$$\mathbf{k} = \frac{2\pi}{p}\cos\theta\mathbf{i} + \frac{2\pi}{p}\sin\theta\mathbf{j} = k_x\mathbf{i} + k_y\mathbf{j} \tag{1.19}$$

The wave vector is an alternative way to define the orientation of a segment of a sinusoidal signal in 2-D and relates it to the projections of the trajectory into the reference axis x–y. From Eq. (1.19), the local value of θ is given by

$$\theta(k) = arctg\frac{k_y}{\sqrt{k_x^2 + k_y^2}} \tag{1.20}$$

At every given point of a cosinusoidal fringe field defined by the position vector $\mathbf{r} = x\mathbf{i} + y\mathbf{j}$ there is a phasor represented by Eq. (1.1) and the local orientation of the signal defined by the angle θ.

The addition of one more parameter, the angle θ requires to extend the definition of the gray levels as a potential scalar function $\dot{V}^r$ in a 2D space, where $\mathbf{r} = x\mathbf{i} + y\mathbf{j}$ is an upper script that indicates that the potential corresponds to a point in $\mathscr{R}^2$, the 2D continuum.

Following the same steps applied in two dimensions and recalling that levels of gray are scalar quantities,

$$grad\,\dot{V}^r = \mathbf{G}_3(\mathbf{r}) = \frac{\partial \dot{V}^r}{\partial x_c}\vec{\mathbf{i}} + \frac{\partial \dot{V}^r}{\partial y_c}\vec{\mathbf{j}} + \frac{\partial \dot{V}^r}{\partial z_c}\vec{\mathbf{k}} \tag{1.21}$$

where the versors $\vec{\mathbf{i}}$, $\vec{\mathbf{j}}$ and $\vec{\mathbf{k}}$ indicate a Cartesian coordinates system in a 3D complex space, the subscript "3" indicates that one is dealing with a 3D vector in the complex space.

The divergence of the field is determined as:

$$\nabla \bullet G_3(\mathbf{r}) = \frac{\partial^2 \dot{V}^r}{\partial x_c^2} + \frac{\partial^2 \dot{V}^r}{\partial y_c^2} + \frac{\partial^2 \dot{V}^r}{\partial z_c^2} \tag{1.22}$$

Calling $\dot{V}_{x_c}^r = \frac{\partial \dot{V}^r}{\partial x_c}$, $\dot{V}_{y_c}^r = \frac{\partial \dot{V}^r}{\partial y_c}$, $\dot{V}_{zc}^r = \frac{\partial \dot{V}^r}{\partial z_c}$, and computing the vectorial product of the ∇ operator with the vector $G_3(r)$, it follows:

$$\nabla \times \mathbf{G}_3(\mathbf{r}) = \left(\frac{\partial \dot{V}_{zc}^r}{\partial y_c} - \frac{\partial \dot{V}_{yc}^r}{\partial z_c}\right)\vec{\mathbf{i}} + \left(\frac{\partial \dot{V}_{xc}^r}{\partial z_c} - \frac{\partial \dot{V}_{zc}^r}{\partial x_c}\right)\vec{\mathbf{j}} + \left(\frac{\partial \dot{V}_{yc}^r}{\partial x_c} - \frac{\partial \dot{V}_{xc}^r}{y_c}\right)\vec{\mathbf{k}} \tag{1.23}$$

Since we are dealing with a scalar potential, the divergence is zero. Hence, it can be written:

$$\frac{\partial^2 \dot{V}^r}{\partial x_c^2} + \frac{\partial^2 \dot{V}^r}{\partial y_c^2} + \frac{\partial^2 \dot{V}^r}{\partial z_c^2} = 0 \tag{1.24}$$

Equation (1.24) indicates that the potential $\dot{V}^r$ satisfies the Laplace's equation in the complex 3D space. The meaning of this equation is the same as for two dimensions. The fact that the rotor is zero implies,

$$\frac{\partial \dot{V}_{xc}^r}{\partial y_c} = \frac{\partial \dot{V}_{yc}^r}{\partial z_c} = \frac{\partial^2 \dot{V}^r}{\partial y_c \partial z_c} \tag{1.25}$$

$$\frac{\partial \dot{V}_{xc}^r}{\partial z_c} = \frac{\partial \dot{V}_{zc}^r}{\partial x_c} = \frac{\partial^2 \dot{V}}{\partial x_c \partial z_c} \tag{1.26}$$

$$\frac{\partial \dot{V}_{yc}^r}{\partial x_c} = \frac{\partial \dot{V}_{xc}^r}{\partial y_c} = \frac{\partial^2 \dot{V}^r}{\partial x_c \partial y_c} \tag{1.27}$$

Equations (1.26)–(1.28) are the conditions for the existence of a scalar potential in the 3D complex space and are equivalent to the Cauchy-Riemann conditions in the two dimensional case.

The above derivations indicate that the information contained in a 2D cosinusoidal fringe pattern is described mathematically by a conservative 3D vectorial field in the complex space. Similarly with the one dimensional case the derivatives that appear in the preceding developments can be computed in the 2D real space as recorded in the sensor. The difference with the one dimensional case is now that the information is in the form of a Monge's type surface where the gray level is of the form,

$$\dot{V^r}(z_c) = F(x_c, y_c) \tag{1.28}$$

where F(x_c, y_c) indicates a 2D function.

From Eq. (1.28), it is possible to get all the derivatives that appear in the preceding developments of the 3D complex field proceeding in a similar way to that utilized in the one dimensional case.

Since we are dealing with Continuum Mechanics problems operating on tensorial entities, a family of orthogonal cosinusoidal signals must be defined in Cartesian coordinates as shown in Fig. 1.2. The orthogonal modulated fringe patterns project the displacement vectors in two orthogonal directions. These projections are not independent from each other since they are tied together by the compatibility conditions of the continuum and involve also the Eqs. (1.25)–(1.27) that both systems of fringes must satisfy at the same points of the image.

Conclusions similar to the one dimensional case can be obtained: the successive derivatives of the gray levels must satisfy the above conditions to define a scalar potential. Hence, the passage from the actual signals to the continuum signals requires operations that must enforce the above conditions as close as it may be feasible. This conclusion is very important because the change of the orientation of the fringes is related to the curvature of the fringes, the larger is the local change of orientation the more important is the effect of the orientation on the derivatives of the gray levels function.

1.3 The Monogenic 2D Signal

The extension of the one dimension approach of signal analysis to multiple dimensions has been the object of a large number of papers (see, for example, [5–8] and the references cited therein). This study will apply the complex Riesz transform presented in the preceding publications. In these four publications are introduced the required arguments to create a transform equivalent of the Hilbert transform in a multidimensional space. To achieve this purpose, the concept of monogenic function is introduced. The original derivation of the monogenic signal concept has its foundations on the algebra of quaternions that is connected to Lie algebra isomorphisms. In this paper, a variation of the original arguments is introduced. The derivations fit the mappings originally developed by Poincare and that for the particular field considered in this study, a 2D flat field, are graphically represented by a Poincare sphere [8] that it is utilized in the field of birefringent optics and in photoelasticity to define the different forms of polarization.

The relationship of Poincare sphere and the concept of phase of the components of polarized light has been the object of several publications (see, for example, [9–11]). The connection between the preceding applications of the Poincare sphere and the phase concept and the current version introduced in this paper is a subject of a great deal of interest but is beyond the purpose of this paper. The motivation in the current version follows from the isomorphism pointed out in [12]. It has been shown that in order to introduce the concept of phase in one dimensional signals, it is necessary to resort to a 2D vectorial field, similarly for 2D signals it is necessary to introduce a vector field in the 3D complex space. The 3D phasor representing the gray levels in 2D has an amplitude that corresponds to the intensity of the signal, a phase that corresponds to the optical path information, and introduces a new variable that corresponds to the orientation of the 2D sinusoid in the physical plane defined by the normal **n** Eq. (1.18), a function of the angle θ defined in Fig. 1.1.

Figure 1.3 illustrates the Poincare sphere notation. The vector amplitude is defined by the following components: (a) the components of the gray levels I_x, I_y associated with the versors $\vec{\vec{i}}$ and $\vec{\vec{j}}$, respectively; (b) to these two components it is added a third component I_q, corresponding to the versor $\vec{\vec{k}}$.

The complex amplitude vector in the complex space is given by,

$$I_{sp} = I_x \vec{\vec{i}} + I_y \vec{\vec{j}} + I_q \vec{\vec{k}} \tag{1.29}$$

and corresponds to the radius of a Poincare sphere shown in Fig. 1.3a. This sphere represents the local phase and amplitude at a point in the 2D continuum of gray levels. In the coordinate plane $\vec{\vec{i}}$, $\vec{\vec{j}}$, sphere equator, Eq. (1.29) becomes:

$$I_p = I_x \vec{\vec{i}} + I_y \vec{\vec{j}} \tag{1.30}$$

From Fig. 1.3, it follows:

$$I_x = \|\mathbf{I}_p\| \cos \theta \tag{1.31}$$
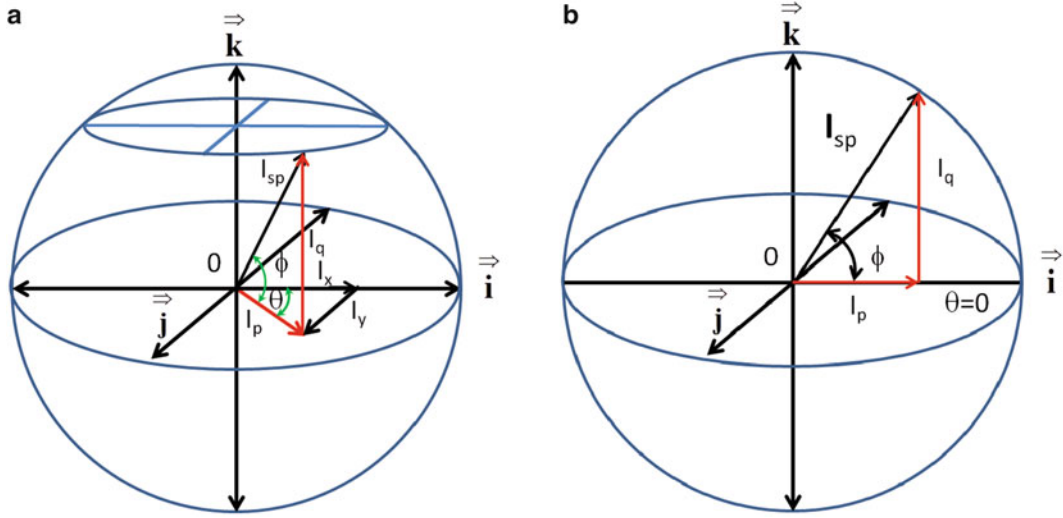
Fig. 1.3 (**a**) Poincare sphere of the levels of gray representing light intensities; (**b**) Poincare sphere of the levels of gray for $\theta = 0$

$$I_y = \left\| \mathbf{I}_p \right\| \sin \theta \tag{1.32}$$

Figure 1.3b shows that the following relationship applies:

$$\tan \phi = \frac{I_q}{I_p} \tag{1.33}$$

There are two in-quadrature quantities I_p and I_q and a phase ϕ that defines a local phase for a signal of orientation θ in the 2D space. The above derived equations lead to the following relationships between the intensities, defining I_{sp} as the modulus of the vector $\mathbf{I}_{sp}$.

$$I_x = I_{sp} \cos \phi \cos \theta \tag{1.34}$$

$$I_y = I_{sp} \cos \phi \sin \theta \tag{1.35}$$

$$I_q = I_{sp} \sin \phi \tag{1.36}$$

Finally, the monogenic signal can be represented by,

$$\mathbf{M}_s^r = I_{sp} \left[\cos \phi \cos \theta \, \overrightarrow{\mathbf{i}} + \cos \phi \sin \theta \, \overrightarrow{\mathbf{j}} + \sin \phi \, \overrightarrow{\mathbf{k}} \right] \tag{1.37}$$

The upper script indicates that it corresponds to a point **r** of the 2D continuum.

The angle θ defines the longitude of the point under consideration referred to the $\overrightarrow{\mathbf{i}} - \overrightarrow{\mathbf{k}}$ plane in the complex space. The angle ϕ is the latitude of the point with respect to the equatorial plane and provides the local phase associated with the actual signal.

The above derived relationships from local gray levels at a given point of a 2D image provide local orientation and the local phase. If a sinusoidal signal is such that the normal $\mathbf{n} \equiv \mathbf{i}$, then $\theta = 0$ and the corresponding representation in the Poincare sphere is shown in Fig. 1.3b. It can be seen from Fig. 1.2, for the vertical fringes that measure horizontal displacements the angle of the normal is $\theta = 0$. This case is depicted by the Poincare sphere of Fig. 1.3b.

An alternative space can be considered replacing the light intensities by the frequencies. Defining the energy of the vector $\mathbf{I}_{sp}$ in the frequency space as

$$I_{sp}^2 = I_x^2 + I_y^2 + I_q^2 \tag{1.38}$$

and taking into consideration the FT energy theorem, the following equation holds true in the frequency space:

$$f_{sp} = \sqrt{f_x^2 + f_y^2 + f_q^2} \tag{1.39}$$

The Poincare sphere in the intensity space depicted in Fig. 1.3a can be transformed into the Poincare sphere of the frequency space by replacing intensities by the corresponding frequencies. All the derivations made for the 3D complex space that are related to the intensities are valid also for the frequencies.

1.4   The Riesz Transform

All the quantities that define the Poincare sphere can be obtained directly by applying the generalized Hilbert transform or Riesz transform defined in [5–7]. The Riesz transform can be computed in the physical space or in the frequency space defined by the analytic function theory [4].

Equation (1.37) provides the monogenic vector corresponding to a given point of the $\mathscr{R}^2$ gray levels continuum represented graphically by a Poincare sphere in a 3D complex space. The monogenic function vector I_{sp} has three components I_x, I_y and I_q, and its position in space is defined by two angles, θ and ϕ, a total of five unknown quantities. These quantities are related by Eqs. (1.34)–(1.36). Since of these three equations only two are independent, only three quantities (i.e. I_x, I_y and I_q) must be determined while I_p is the level of gray captured by the sensor.

The Riesz transform of gray levels of an image in the spatial domain associates with each point of the continuum two orthogonal convolution kernels (Chap. 4 of [7]):

$$h_x(r) = \frac{x}{2\pi(x^2 + y^2)^{\frac{3}{2}}} \tag{1.40}$$

$$h_y(r) = \frac{y}{2\pi(x^2 + y^2)^{\frac{3}{2}}} \tag{1.41}$$

where $\mathbf{r} = x\mathbf{i} + y\mathbf{j}$. These kernels yield:

$$I_x(r) = \frac{x}{2\pi(x^2 + y^2)^{\frac{3}{2}}} ** I_p(r) \tag{1.42}$$

$$I_y(r) = \frac{y}{2\pi(x^2 + y^2)^{\frac{3}{2}}} ** I_p(r) \tag{1.43}$$

In the above equations, $I_p(r)$ is the gray level at $\mathbf{r}$ while the ** symbol [13] denotes a 2D convolution in physical space. These kernels satisfy the following relationships with the corresponding quantities in the frequency space:

$$h_x(\mathbf{r}) \rightarrow H_{f_x}(\mathbf{f}_r) = \frac{f_x}{\sqrt{f_x^2 + f_y^2}} \tag{1.44}$$

$$h_y(\mathbf{r}) \rightarrow H_{f_y}(\mathbf{f}_r) = \frac{f_y}{\sqrt{f_x^2 + f_y^2}} \tag{1.45}$$

where the symbols H_{f_x} and H_{f_y} indicate Hilbert transform in 2-D as it is called in [7]. The generic denomination multidimensional Hilbert transform is used in place of the Riesz transform and the frequency space corresponds to the analytic frequency space [4].

It should be noted that the operators H_{f_x} and H_{f_y} of Eqs. (1.44) and (1.45) define the $\cos\theta$ and $\sin\theta$ terms in the frequency plane, consistently with Eqs. (1.34) and (1.35). Then

$$\theta(r) = arctg \frac{I_y(r)}{I_x(r)} \tag{1.46}$$

The orientation of the signal is known through the angle θ.

Rotating the coordinate axis by the amount θ and calling the rotated coordinate x′,

$$I_q\left(x'\right) = \frac{1}{\pi} PV \int_{-\infty}^{\infty} \frac{I_p(\eta)}{x' - \eta} d\eta = \frac{1}{\pi}\left(I_p\left(x'\right) * \frac{1}{x'}\right) \tag{1.47}$$

where PV indicates the principal value and η is the dummy variable of integration.

Equations (1.44)–(1.47) allow obtaining the monogenic function vector Eq. (1.37). All the above introduced computations are performed in the physical space. These computations can also be performed in the analytical functions frequency space [4].

1.5 Retrieval of the Monogenic Vector

First we will recall some properties of the FT that are of interest in the current analysis and shed light on the relationship between the FT and the Riesz transform. Both of these two transforms provide signals in-quadrature by utilizing different algorithms that however are closely related to each other since theoretically the outputs must be the same. In practice, due to the numerical processes involved obtained results may differ.

The windowed FT provides the signals in-quadrature in 2-D. Let us recall some basic steps of the process of computing in-quadrature signals. The FT has symmetry properties,

$$\widetilde{F}\left(f_x, f_y\right) = \widetilde{F}^*\left(-f_x, -f_y\right) \tag{1.48}$$

$$\widetilde{F}\left(-f_x, f_y\right) = \widetilde{F}^*\left(f_x, -f_y\right) \tag{1.49}$$

Furthermore it also satisfies the condition of separable functions,

$$\widetilde{F}\left(f_x, f_y\right) = \widetilde{F}_1\left(f_x\right)\widetilde{F}_2\left(f_y\right) \tag{1.50}$$

In Fig. 1.4, a fringe pattern is plotted and its corresponding FT in the frequency space. It is possible see that the fringe pattern in the third quadrant of angle θ′ = 180 + θ corresponds the same components (−5, −6) as to a fringe pattern of angle θ(5, 6) but with signs changed. It satisfies Eq. (1.48), the components in the third quadrant are complex conjugates of the

Fig. 1.4 Symmetry conditions of the FT in the frequency space (**a**) for a 2D pattern (**b**)
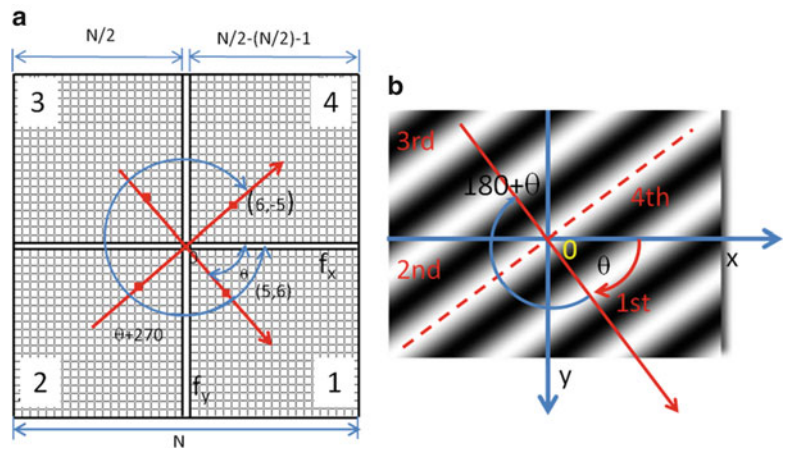
components in the first quadrant. Similar conclusion can be reached if we have a system of fringes in the second quadrant, that is the dashed red line represents the normal to the pattern with components $(-6, 5)$ and the corresponding system of fringes in the fourth quadrant $(6, -5)$ satisfying Eq. (1.49).

The FT components are complex numbers $(a_{ij} + jb_{ij})$ that can be arranged in a square matrix where "i" indicates the rows and "j" the columns. The carrier orientation is given by the angle θ of the normal to the carrier direction. In the case of a vertical carrier, it holds $\theta = 0$; in the case of a horizontal carrier, it holds $\theta = \pi/2$. In general, θ goes from 0 to $\boldsymbol{\theta} \Rightarrow \pm\boldsymbol{\pi}$. Because the signal satisfies Eq. (1.50) the computation can be carried separately along rows and columns.

Because of the symmetry conditions there are only $N^2/2$ independent components to obtain the FT. There are additional components that are real, the term a_{oo} that corresponds to $f_o = 0$ (the background term is a constant), and the terms corresponding to the Nyquist frequency $f = N/2$. Then, the number of independent coefficients to compute is $N^2/2$ and two real coefficients a_{oo} and the Nyquist frequency $f_{N/2}$.

The Riesz transform is an alternative to the FT computational method to obtain the in-quadrature signals and, as pointed out before theoretically, the final output must be the same independently of the computation path followed. First it must be realized that the background term is eliminated from the computation in the Hilbert transform since it is a singularity at the origin of coordinates of the frequency space.

Figure 1.5 represents the actual physical space and the corresponding analytical function frequency space (notice the difference between the frequency space of the FT and the frequency space of the analytic functions). Physical space quadrants 1 and 3 are represented in the frequency analytical space by the lower half space $f_x, f_y > 0$, while quadrants 2 and 4 are represented by the $f_x > 0, f_y < 0$ upper half space. The corresponding coefficients of the Riesz transform are complex quantities $Z(f_x, f_y) = (a_{ij} + jb_{ij})$; their magnitude is twice in magnitude of the coefficients in the FT transform because of the single side transform as illustrated in Fig. 1.5. The total number of independent coefficients is then $N^2/2$, because of the Nyquist transform symmetry that is the coefficients of the upper half space are the complex conjugated of the lower half space. Similarly to the FT property of separability stated by Eq. (1.50), coefficients can be computed by rows and columns. The angle θ goes from 0 to $\boldsymbol{\theta} \Rightarrow \pm\boldsymbol{\pi}$ and can be computed by means of Eqs. (1.44) and (1.45). The monogenic signal as defined in this paper allows us to compute all the parameters that define a 2D sinusoidal signal.

Figure 1.6 shows all the coefficients that it is necessary to compute in the frequency space to obtain the phase ϕ of a sinusoidal signal in the frequency space utilizing the monogenic signal concept. The above presented derivations emphasize the fact that the same objective can be reached by utilizing the FT.

There are many theoretical reasons for introducing the concept of analytic signals, or in other words, for eliminating the negative frequencies of the real and imaginary components of the spectrum of real signals. From the practical point of view, it has been pointed out that the negative spectrum has in essence the same information than the positive parts due to the conjugate symmetry previously mentioned. The elimination of the negative frequencies has also an impact in the efficiency signal processing by reducing the required bandwidth.

Fig. 1.5 (**a**) Frequency space for the analytical function; (**b**) physical space

Fig. 1.6 Table of coefficients in the half space assuming that the image has 1024×1024 pixels. The columns outlined in *red* will correspond to the coefficients of the zero order that are not present in the Riesz transform

1.6 Generalized Hilbert Transform for Signal Phase Retrieval

The phase shifter or Hilbert filter is an ideal symbolic operator capable of leaving signal amplitudes unchanged and introducing phase shifts of $\pi/2$. The ideal operator can be approximated in different ways. In the preceding section, it is outlined an approach in the frequency space of analytic signals with one sided spectrum. The operations can be carried out in the physical space or in the frequency space. In both cases, the Hilbert transformers are special class of filters. The difference between alternative filters can be quantified by the operational efficiency minimizing the number of operations required and minimizing phase and amplitude errors resulting from numerical operations. There are two basic types of filters: (a) infinite impulse response filters (IIR filters) whose response does not become zero, pass a certain point but continues indefinitely; (b) finite impulse filters whose response becomes zero at certain point. FIR filters are preferred filters for Hilbert transform operations, for a comprehensive discussion in this topic see [14, 15].

For reasons that will be explained further on in the manuscript we are interested in a shifted frequency modulated function that is in a function whose spectrum is shifted of a certain amount in the frequency space. We have a real function of the form (Fig. 1.1),

$$I(x) = I_p \cos \phi(x) = \frac{I_p}{2}\left[e^{j\phi(x)} + e^{-j\phi(x)}\right] \tag{1.51}$$

The corresponding in-quadrature signal is

$$\hat{I}(x) = I_q \sin \phi(x) = \frac{I_q}{2j}\left[e^{j\phi(x)} - e^{-j\phi(x)}\right] \tag{1.52}$$

The shifted modulated analytic function is defined as [4]:

$$z_m(x) = \frac{I_p}{2}\left[e^{j\phi(x)} + e^{-j\phi(x)}\right]e^{-j2\pi f_0 x} + j\frac{I_q}{2}\left[e^{j\phi(x)} - e^{-j\phi(x)}\right]e^{-j2\pi f_0 x} \tag{1.53}$$

Fig. 1.7 Process to generate the single side frequency modulated bandpass signal that provides shifted signals in-quadrature
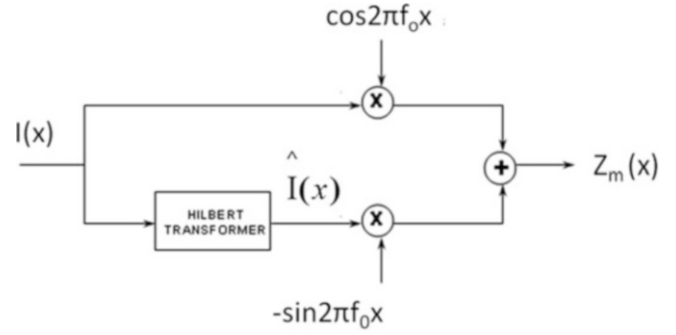
This expression yields,

$$z_m(x) = \frac{I_p}{2} \cos[\phi(x) - 2\pi f_0 x] + j\frac{I_q}{2} \sin[\phi(x) + 2\pi f_0 x] \tag{1.54}$$

Calling

$$P(x) = \frac{I_p}{2} \cos[\phi(x) - 2\pi f_0 x] \tag{1.55}$$

$$Q(x) = \frac{I_q}{2} \sin[\phi(x) + 2\pi f_0 x] \tag{1.56}$$

The function P(x) is the in-phase component while the Q(x) function is the in-quadrature component of the frequency modulated function $z_m(x)$.

$$z_m(x) = P(x) + jQ(x) \tag{1.57}$$

The net effect is to displace the frequency spectrum of the frequency f_o in the positive sense. Each component of the input experiences a shift that is proportional to its frequency and the overall final effect is to produce a translation of the FT of the original signal frequency spectrum by the frequency f_o. In order to implement the single band frequency modulation previously described and illustrated in the flow chart of Fig. 1.7, it is necessary to compute the Hilbert transform of I(*x*) (Eq. (1.51)). Afterwards, both I(*x*) and Î(*x*) must be modulated to obtain P(x) and Q(X), that is the signals in-quadrature but shifted to the frequency f_o. Algorithms that approximate the Hilbert Transformer, such as the Parks-McClellan FIR filter design technique, have been developed and can be found in MATLAB Signal Processing Toolbox™.

1.7 Transition from the Continuum to Actual Signals

To this point the continuum aspect of fringe pattern analysis has been dealt with in some detail. It has been pointed out the importance of phase in image analysis and certainly the fundamental role that it plays on fringe pattern studies. The two different concepts of phase, global and local have been introduced. The next step is to deal with the local phase and add to the continuum approach the statistical tools that are required to bridge the gap between the continuum model and the actual signals that are captured. The impact of local phase analysis in fringe pattern is in itself a huge topic. It is a well known fact that the FT is a powerful tool in global phase analysis but does not provide details of the local phase structure. A similar conclusion can be arrived for the analytical frequency space.

Reasoning in the FT frequency space, consider a 2D signal with energy [4],

$$E = \iint_\infty \|f(x, y)\|^2 dx dy \tag{1.58}$$

Assume that the values of its Fourier Transform (FT) are limited to a region A on the FT plane and in the physical plane the corresponding values of the function f(x, y) are limited to a region B. We further assume that the product A × B is also a small quantity. It is possible to define the energy ratio,

$$\boldsymbol{\alpha} = \iint_B \frac{\|f(x,y)\|^2 dxdy}{E} \tag{1.59}$$

Under the above assumption, f(x, y) is a slowly varying function in B. Then, it can be written in the local coordinate system,

$$\boldsymbol{\alpha} = \iint_B \frac{\|f(x,y)\|^2 dxdy}{E} \approx \frac{\|f(0,0)\|^2 B_0}{E} \tag{1.60}$$

where B_o is the considered local area. The optimum condition will be to maximize ||f(0, 0)/E||. This problem is related to the classical problem in signal analysis of the localization of a signal in space and in frequency. There is a limit to the resolution that can be achieved. The Heisenberg Uncertainty Principle of the FT puts a limit to the resolution in a rectangular local area,

$$\Delta_x \Delta_f \geq \frac{1}{4\pi} \tag{1.61}$$

where Δ_x is the uncertainty in the spatial coordinates and Δ_f is the uncertainty in the frequency value of the signal. An answer to the optimization of the approximated energy ratio defined in Eq. (1.60) [4] is to multiply f(x, y) by a window function. It is well known that the lower limit of Eq. (1.61) is obtained when the window function is a Gaussian function.

In the present case, the sensor gives $I_p(x, y)$ and it is necessary to locally smooth this function by introducing a band pass filter that will render the approximated energy ratio defined in Eq. (1.60) optimum. Hence, in the previously derived equations the recorded $I_p(x, y)$ can be replaced by:

$$I_p^b(x,y) = I_p * * g(x,y) \tag{1.62}$$

where the upper script b indicates a band pass filtered version of the recorded signal and g(x, y) is a selected band pass filter. In [7], a Poisson's and conjugate Poisson's kernels filters are utilized. However, there are many other alternative filters that can be utilized depending on the noise present in the analyzed signals. The derivation of the optimization of Eq. (1.60) suggests a Gaussian smoothing filter to be used for Eq. (1.51): in [7], Gaussian filters are introduced.

At this point one must go back to the derivations made in Sect. 1.2. The concept of the gray levels as a scalar potential to be valid requires that the Cauchy-Riemann conditions in 1-D and in 2-D must be satisfied at each point of the image. This implies that the gray levels and their successive derivatives are required to satisfy the continuity conditions expressed by Eqs. (1.14), (1.15), and (1.25)–(1.27), respectively. In [7], there are extensive statistical considerations to derive optimum values of orientation, phase and amplitude of signals using the Poisson's distribution that involve gray levels and successive derivatives. In [8], there are similar derivations utilizing Gaussians filters. In the case of fringe patterns, the solution is simpler at least for the small deformation theory of the continuum that requires continuous derivatives up to the third order.

Figure 1.8 represents a Gaussian filter in the physical space and in the frequency space.

Equation (1.38) relates both these filters.

$$I(ax, ay) \leftrightarrow \frac{1}{\|a\|} \tilde{I}\left(\frac{f_x}{a}, \frac{f_y}{a}\right) \tag{1.63}$$

Equation (1.63) gives the relationship between the components of the Gaussian filter in the physical space and the frequency space; the scale factor "a" is multiplicative in the physical space and it divides in the frequency domain. This is an important result because it indicates that in the process of filtering there is a scale effect that is a key in obtaining a satisfactory smoothing of the recorded signals. The scale depends on the gradients of the displacement function; large gradients require large scale factors in the physical space.
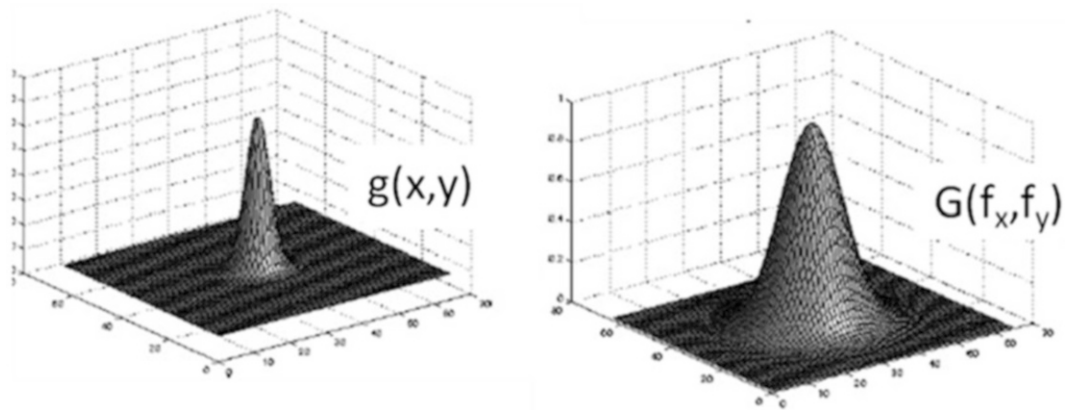
Fig. 1.8 Gaussian filters in the physical space and in the frequency space

Fig. 1.9 Gaussian filters and corresponding derivatives in the space domain and in the frequency domain
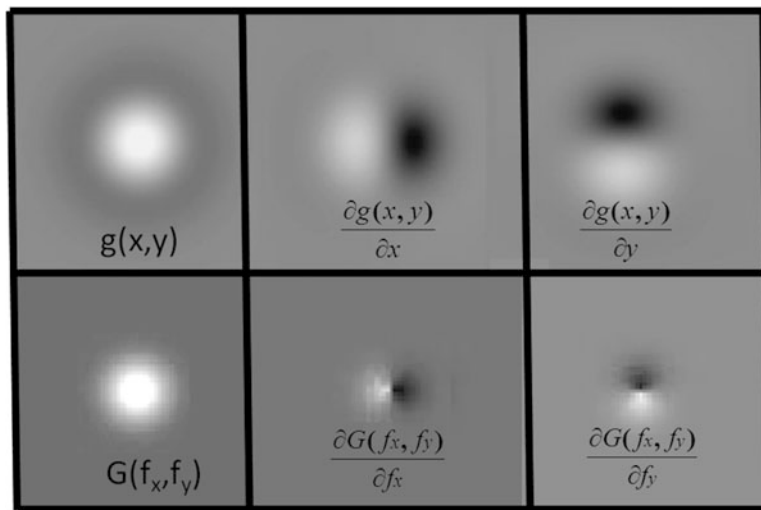
The 2D Gaussian filter represented in Fig. 1.8 is given by,

$$g(x, y) = \frac{1}{2\pi\sigma^2} e^{\frac{x^2 + y^2}{2\sigma^2}} \tag{1.64}$$

In this representation, it is assumed that the mean is $(0, 0)$ while $\sigma = 1$ is the standard deviation of the function. The Gaussian filter acts a point spread distribution and the effect in the smoothed function is determined by the selected value for σ. If σ is small, in the spatial domain a large number of frequencies will contribute to the filtered value of the signal and vice versa.

Figure 1.9 shows both the Gaussian function in the coordinate's domain and in the frequency domain as well as the corresponding derivatives. Gaussian derivatives in 2D are separable functions equivalent to a convolution in the x-direction and in the y-direction.

$$\frac{\partial g(x, y)}{\partial x} * *f(x, y) = \left(\frac{-x}{\sqrt{2\pi}\sigma^3} e^{-\frac{x^2}{2\sigma^2}}\right) * \left(\frac{1}{\sqrt{2\pi}\sigma} e^{-\frac{y^2}{2\sigma^2}}\right) * f(x, y) \tag{1.65}$$

Since we have discrete values of the function, it is necessary to produce discrete approximations to the Gaussian function. The function approaches zero at about 3σ, hence the kernel size is limited to this size.

1.8　Process of Phase Recovery

The preceding section covered the analysis of fringe patterns as 2D signals. One of the important concepts in this analysis is the definition of local phase. While the local phase concept is clear in the continuum theory, in the passage from the continuum to the actual signals one should note that the concept of local phase depends of the selected widows to smooth real signals.

In [1], it was concluded that in order to satisfy the quasi-harmonic condition that allows in 1D signals the utilization of in-quadrature signals for the computation of local phase, it is required to encode the displacement signal into a high frequency carrier. A similar argument must be introduced for 2D signals. In order to achieve this objective, we must consider again the concept of local phase, that in the general theory of 1D signal analysis is known as the definition of the instantaneous frequency, subject that has been the object of extensive studies [16, 17]. The phase computation is a point-wise operation that provides the local phase through the computation of the arc tan function and can be derived by the introduction of the concept of analytic functions [4]. Within the analytic function theory one has signals that are amplitude modulated or frequency modulated. Fringe patterns are both amplitude and frequency modulated signals. This creates a very difficult problem because amplitude and simultaneously phase modulated signals do not have a uniquely defined analytic signal representation [16]. The amplitude and the phase have their own frequency spectra and these spectra can overlap. In [1], it is observed that harmonics providing different optical information besides amplitude and phase can also overlap in the frequency space with amplitude and phase information. As a consequence of these facts, phase and amplitude recovery information is not possible unless steps are taken to minimize the effect of the mixing of different harmonics.

Two important tools are utilized to get solution to these two problems of real signals. The Bedrosian-Nuttal's theorems [18–20] provide solutions to the overlapping problem. If the Bedrosian-Nuttal's theorems are satisfied, the amplitude of the general phasor A($\mathbf{x}$) and the phase $\phi(\mathbf{x})$ are separated in the frequency space. The analytical function theory can provide the in-quadrature components that lead to a real signal with a well defined local frequency,

$$f(x) = \frac{1}{2\pi} \frac{d}{dx} \arg z(x) \qquad (1.66)$$

The possibility of satisfying the Bedrosian-Nuttal's theorems is related to the bandwidth of the involved signals. To get an intuitive picture of the problem of defining local phase at a given point of an image, let us return to the one dimensional signal. The simple harmonic function has been traditionally utilized to define instantaneous phase. A periodic motion is represented by a body that moves with constant speed along a circular path (see Fig. 1.10),

$$S(x) = A_0 \cos \phi(x) \qquad (1.67)$$

where A_o is the radius of the circle, $\phi(\mathbf{x}) = \omega x$, ω is the constant angular frequency connected with the spatial frequency $f_x = \omega/2\pi$.

In [1], it is concluded that for patterns where the amplitude modulation frequencies are much smaller than the frequencies of the phase modulation $f_a \ll f_\phi$, the in-quadrature signals provide accurate values of the phase. This conclusion is proven by the analysis of 1D signals extracted from moiré patterns both computer generated with known frequencies and actual optically produced moiré patterns. It is necessary to extend this conclusion to 2D signals,

Fig. 1.10 Simple harmonic motion as a model to define instantaneous frequency
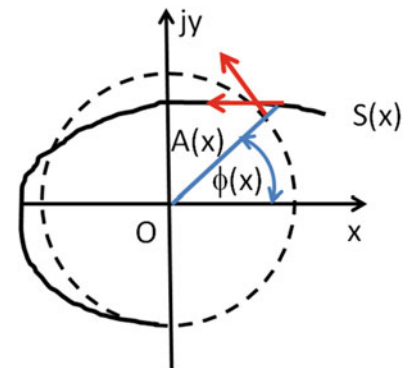
Fig. 1.11 Local power
spectrum of the signal
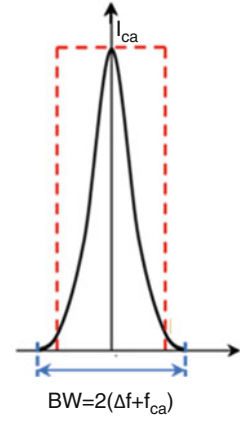
$$S_{mc}(x, y_c) = I_1 \cos \left[\frac{2\pi}{p_c} x + \phi(x, y_{ca}) \right] \tag{1.68}$$

In Eq. (1.68), it is assumed that we are operating along rows of the signal matrix and a carrier is introduced in the x-direction and has amplitude I_1 and the pitch is p_c. The y_c indicates the corresponding constant values of the y-coordinate. Now, if we consider a local region, the FT of the carrier is a pair of pulses at frequency $f_c = 1/p_c$. The frequency f_{ca} is selected such that,

$$f_{ca} \gg f_s \tag{1.69}$$

where f_s is the frequency of the signal $\phi(x, y_c)$ in the local region. Equation (1.69) indicates that locally the signal frequency is much smaller than the carrier frequency.

Figure 1.11 represents the spectrum of the signal plus carrier at a given location, Δf is the local change of frequency of the signal postulated to be such that $\Delta f \ll f_{ca}$ in order to have a narrow band signal. Through the Bedrosian-Nuttal's theorems, amplitude and phase of signals can be assumed to be independent if their respective spectra are separated in the frequency space. Hence, the closer the signal is to a narrow band condition, the more likely is that the Hilbert-transform analytical signal provides support to the validity of Eq. (1.67). This provides an accurate value for the local frequency. Looking from the point of view of Fig. 1.10, A(X) becomes a constant and,

$$\phi(\mathbf{x}) = \omega x \tag{1.70}$$

where ω is a constant angular frequency.

1.9 Application Examples

In the preceding sections two alternative ways of fringe pattern analysis have been discussed and the theory behind these two methods dealt with in some detail. There are many other approaches to fringe pattern processing, such as for example, the Gabor transform and a generalization of the Gabor transform through the concept of wavelet transforms that introduce more refined filters systems and that can be particularly useful for noisy signals. Actually recorded fringe patterns are processed and the results obtained with the different methods compared.

A disk under diametrical compression, *u–v* displacement patterns and their derivatives are chosen as an example of application of the FFT, the 2D Hilbert transform, the Gabor transform and the Morlet transform. Table 1.1 provides the parameters defining the utilized specimen mechanical properties and the applied load.

The recorded patterns of Fig. 1.12 were obtained with double illumination speckle interferometry. A preliminary analysis of the fringe patterns indicates that there are four orders in the *u*-pattern (Fig. 1.12a) and 17 orders in the *v*-pattern (Fig. 1.12c). Therefore, the horizontal diameter of the disk will expand by about 5 μm under the action of the applied load while the vertical diameter of the specimen will contract by about 21 μm. The computer generated patterns have been obtained utilizing a solution taken from the theory of elasticity [21]. The difference between theory and experiment is due to the modality of load application. The theoretical model assumes a point loading that generates a singular point in the theory

Table 1.1 Details of tested specimen

Material	Aluminum
Diameter	60 mm
Thickness	6.35 mm
Young's modulus	70 GPa
Poisson's ratio	$\nu = 0.336$
Pitch	1.222 µm
Applied load	3300 N
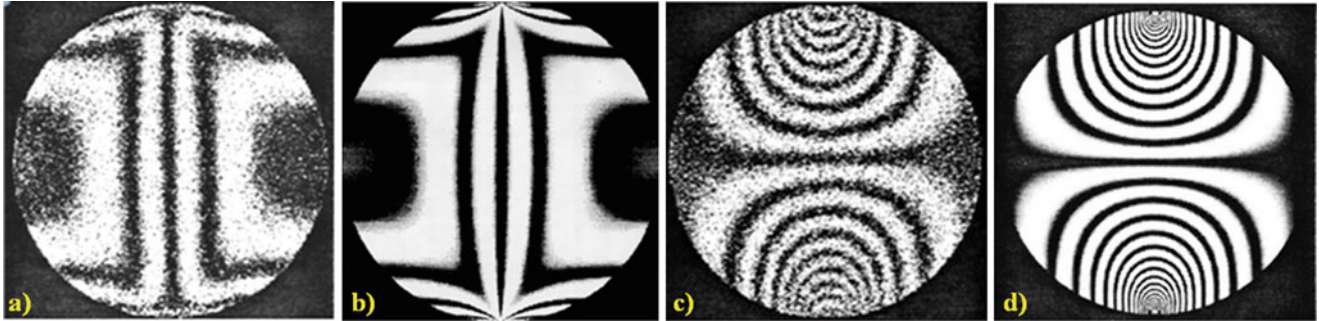
Fig. 1.12 (**a**) Recorded *u*-pattern; (**b**) computer generated *u*-pattern; (**c**) recorded *v*-pattern; (**d**) computer generated *v*-pattern
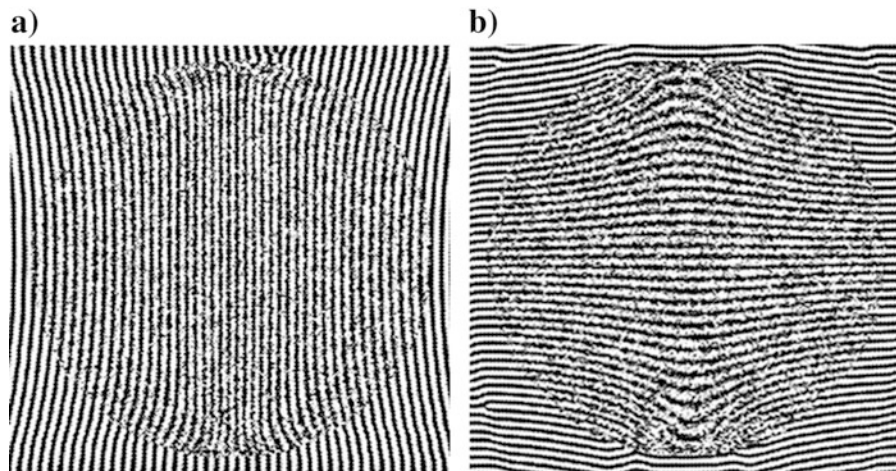
Fig. 1.13 *u*-extended (**a**) and *v*-extended (**b**) carrier fringes for the patterns of Fig. 1.12a, c

of elasticity solution while the actual loading is the result of the contact stresses between the loading application bar and the specimen. The fringe pattern analysis was not done directly on the recorded *u*–*v* patterns but in patterns where carrier fringes were introduced according to the theory presented in Sect. 1.6 (see Fig. 1.13).

There is an additional reason that is related to the adopted processing algorithms. In order to simplify the algorithm design, processing algorithms are derived under the assumption that computations are performed in a domain that asymptotically mimics an infinite domain. If an algorithm is developed for a finite region, this is a possible alternative, one has to design algorithms capable of changing as a function of the distance of the considered point to the boundaries (this distance depends on the domain geometry), which is not a simple task. An alternative choice is to keep the format of corresponding to an infinite domain and utilizing extended fringes to cover the full image area so that when one reaches the boundaries of the specimen either internal of external, the effect of the finite domain is removed [22]. The fringe extension is numerically feasible and converges faster if a high frequency carrier is present. The boundary problem is also present in both in the Gabor transform and in the wavelet transform. In the wavelet transform the edge problems present additional complications due to the different scales involved in the computation.

The above outlined path helps recovering the frequency information since it reduces the frequency spectrum to a narrower local band, resulting in a less populated energy matrix. This step is particularly useful for the Morlet wavelet transform since it reduces the number of scales and voices, thus reducing the amount of information that it is necessary to process. In this way the total amount of work required to compute frequencies is reduced and the accuracy of the results is enhanced.

In order to fully understand the comparison of different methods presented in this section, it is necessary to recall some fundamental relationships that arise from considering fringe patterns that encode displacement information as frequency modulated signals. The utilization of the energy representation of a signal in the coordinates-frequency space [23] provides powerful procedures to retrieve derivatives of displacements directly from fringe patterns without resorting to the differentiation of displacements. This alternative also simplifies the determination of displacements replacing complex unwrapping procedures by integration of the derivatives [24], a robust operation in the presence of noise. In view of the arguments presented in the preceding paragraphs, the comparison of results will be done between methods that provide displacements and methods that provide directly derivatives.

Figure 1.14 compares the theoretical distributions of u–v displacements (Fig. 1.14a) with the experimental values obtained from the FFT (Fig. 1.14b) and the experimental values obtained from the 2D Hilbert transform (Fig. 1.14c). The plots of Fig. 1.14b have been obtained starting from the extended fringe patterns of Fig. 1.13, utilizing the windowed FFT; the applied window is a Gaussian window like that displayed in Figs. 1.8 and 1.9. The plots of Fig. 1.14c have been obtained utilizing the 2D Hilbert transform described in this study. In the case of 2D Hilbert transform, displacement maps are presented in fashion of color contours; axes of symmetry of the disk are represented in order to highlight any asymmetry of the u–v fields.

Because of the pointed difference between the theory of elasticity solution and the experimental realization of this model, a FE solution was computed with the general purpose finite element software ANSYS. An elliptical distribution contact stress was assumed, the load contact width was determined from the recorded fringe patterns. Because of symmetry, only one half of the disk was modeled. Figure 1.15 shows the FE model and the u–v displacement maps computed by ANSYS; color bars for each displacement component are included in the figure. In order to obtain a mesh independent solution, convergence analysis was carried out and finally it was selected a mesh with 9242 elements (more specifically, in Fig. 1.15a, there are 9170 four-node plane elements, 60 target elements on the disk surface that may come in contact with 12 contact elements on the loading surface) connected by 9272 nodes. The FE model includes also auxiliary regions to apply the load to the disk and to support the specimen in the loading frame.

It can be verified that all these results are in good agreement. For example, the maximum u-displacement along the horizontal axis of the disk was determined as follows from experimental measurements and computations: 2.520 μm for the windowed FFT, 2.543 μm for the Hilbert transform, and 2.573 μm for ANSYS (similar to theoretical solution), respectively. A more detailed comparison is presented in Fig. 1.16 which shows the distribution of u-displacements measured or computed along the horizontal diameter: experimental data matched well the numerical simulations over the whole region of interest.

As far as it concerns the total v-displacement undergone by the vertical diameter of the disk, it can be seen that ANSYS predicted 20.7 μm (similar to theoretical solution) while the relative displacement extracted from the fringe pattern with windowed FFT and 2D Hilbert transform are about 18 μm. Both algorithms captured the asymmetry of the v-displacement pattern with respect to the horizontal diameter of the disk but could not reconstruct the whole pattern in the regions where the specimen is loaded (top) and fixed (bottom) as concentration of fringes caused a loss of resolution.

Figure 1.17a–d display the maps of strains ε_x and ε_y obtained directly from the fringe patterns of Fig. 1.12 utilizing the Gabor transform and the Morlet wavelet transform. It can be seen that the two patterns are very similar in their outlines.

Figure 1.18 shows the maps of ε_x and ε_y strains computed utilizing the patterns of Fig. 1.12 and the differentiation in the frequency space [25]. That is, derivatives are obtained directly from fringe patterns without going through the displacements similarly to what is done in the case of the Gabor and the Morlet wavelets. It is possible to see that distributions agree well in their outlines.

For a more detailed analysis, the distributions of strain ε_x along the horizontal axis obtained with the Gabor transform, the Morlet wavelet, the windowed FFT, the 2-D Hilbert transform and the finite element results are plotted in Fig. 1.19. Since values of contour lines do not match, data at the same locations along the control path are extracted. The agreement between the different methods is excellent (maximum strain is 190 με for Gabor/Morlet, 185 με for FFT, 193.5 με for Hilbert 2D and 201 με for finite elements) in spite of the fact that different numerical techniques and algorithms have been applied to obtain the corresponding values.

There is an exception that can be observed in the values of ε_y of Fig. 1.18 near the point of application of the load. In this region there is a large gradient of the displacements and this results in a concentration of fringes. If one processes the data and utilizes a single scale upon FT, filtering the field of the displacements is distorted because of the lack of spatial resolution in the region. Enlarging the scale of the contact region is possible to eliminate this error. The error is not present in the Gabor transform and in the Morlet wavelet because of a more comprehensive filtering resulting from the utilization of multiple scales.
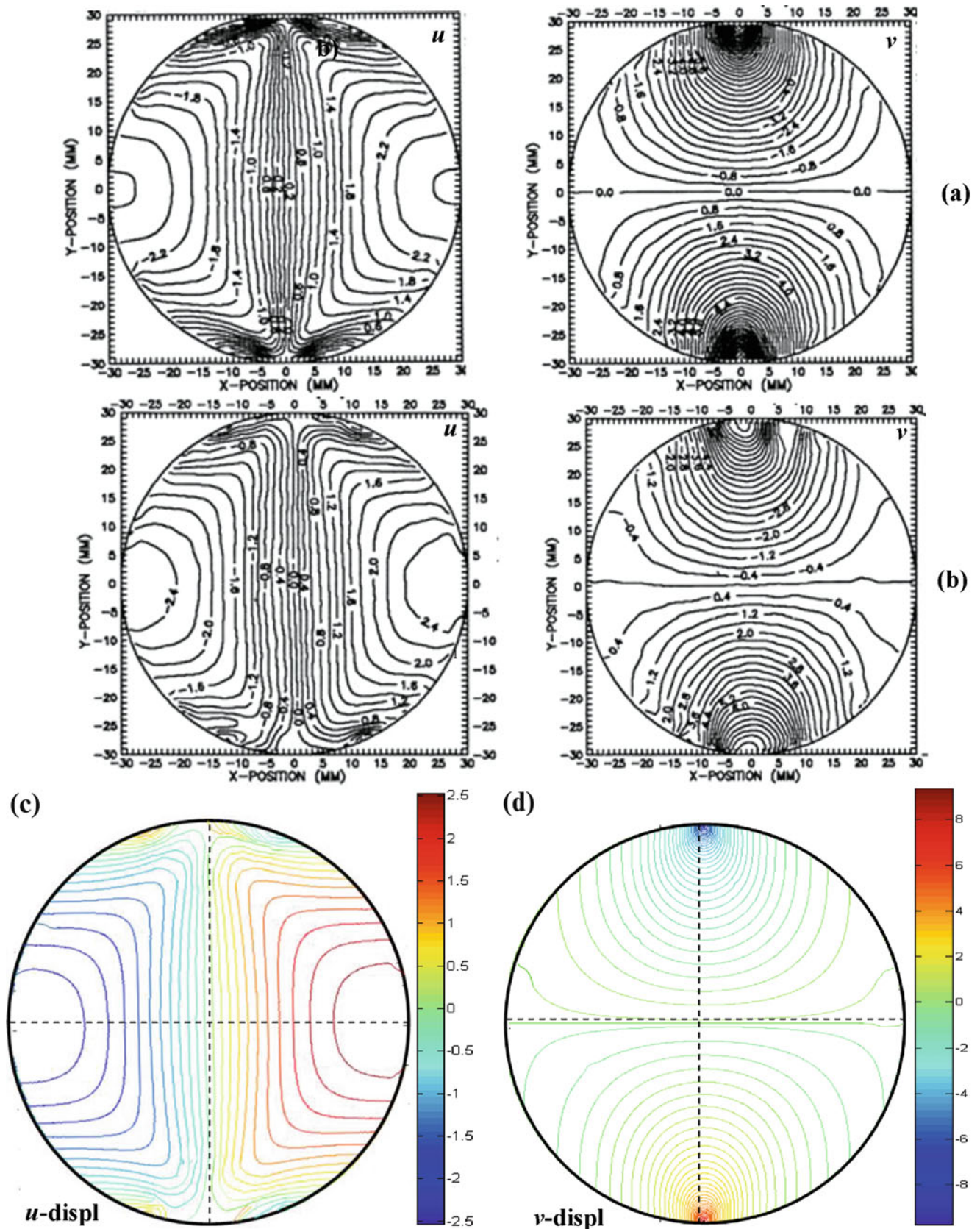
Fig. 1.14 (**a**) Theoretical *u–v* displacements (elasticity solutions from [21]); (**b**) experimental *u–v* displacements, windowed FFT [22]; (**c**, **d**) experimental u–v displacements, 2D Hilbert transform (present study). All scales are expressed in microns

u-scale [μm]

| -3.63 | -2.94 | -2.25 | -1.56 | -0.873 | 0.184 | 0.505 | 1.19 | 1.88 | 2.57 |

v-scale [μm]

| -10.35 | -8.3 | -5.95 | -3.6 | -1.25 | 1.1 | 3.45 | 5.75 | 8.05 | 10.35 |
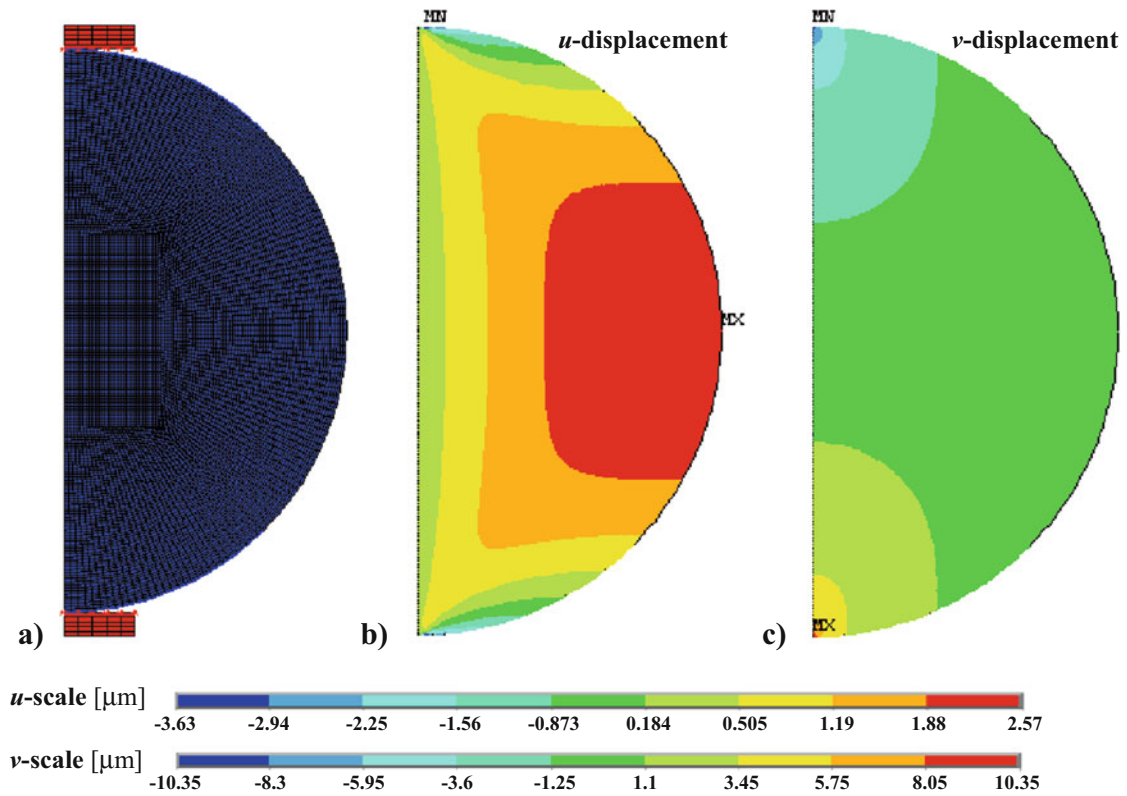
Fig. 1.15 Finite element model (**a**) and u-v displacement fields (**b-c**) computed by ANSYS for the disk under diametrical compression
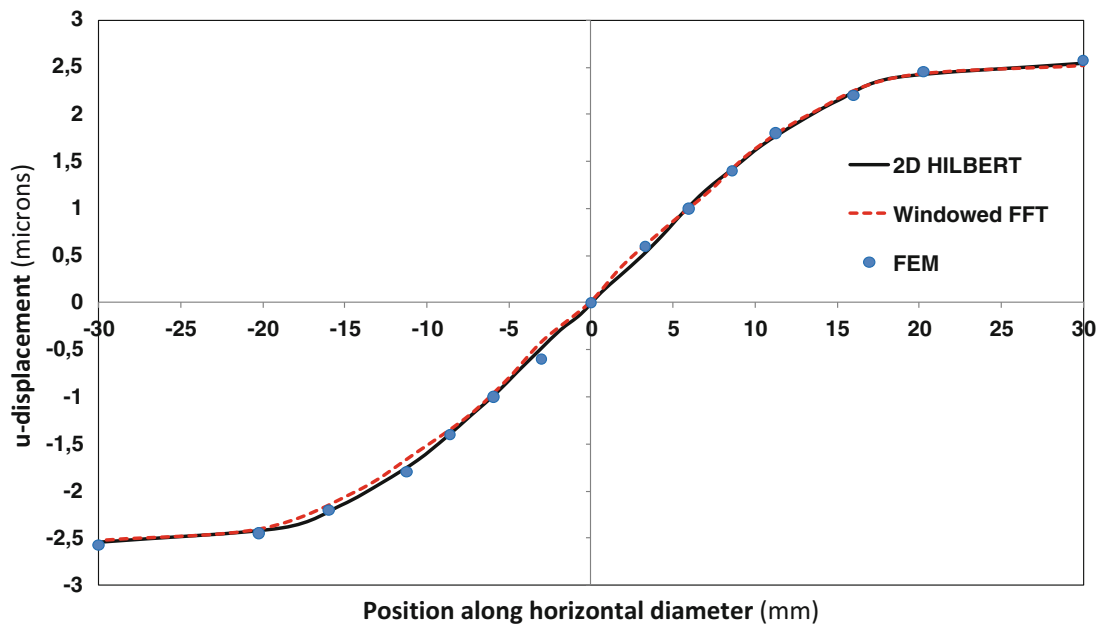
Fig. 1.16 Comparison of displacement fields obtained from fringe processing techniques and FE simulation for the horizontal diameter of the disk
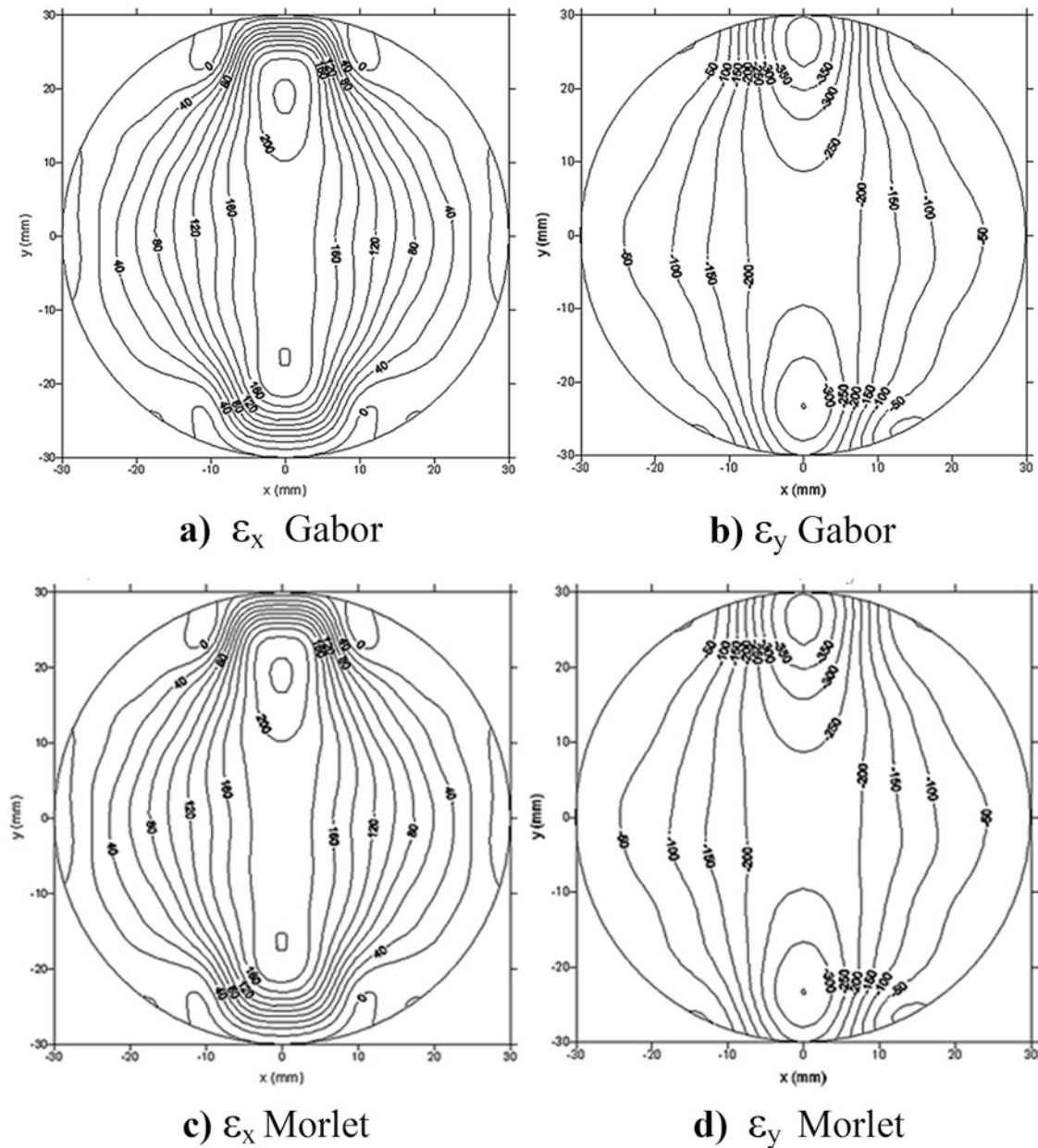
Fig. 1.17 Strains of the disk under diametrical compression utilizing the Gabor transform and the Morlet wavelet transform. (**a**) ε_x Gabor. (**b**) ε_y Gabor. (**c**) ε_x Morlet. (**d**) ε_y Morlet

1.10   Summary and Conclusions

Fringe pattern analysis is a sub discipline that is contained in the more general discipline of signal analysis. Early developments of signal analysis were done in applications to electrical engineering and communications engineering, thus basically concentrated in one dimensional signals. Image analysis has brought the generalization of this body of knowledge to two dimensions and more recently to 3-D. The fundamental idea of monogenic functions is to enclose all the mathematical derivations that apply to signals in general in a comprehensive multiple dimensional approach. An example of this comprehensive approach is found in [5, 8]. These references deal with a more general problem than the one dealt in the present publication. They deal with processes of statistical optimization in the computation of components of signals such as orientation θ, phase ϕ and signal amplitude A of the general monogenic signal defined by Eq. (1.37) and in many cases solutions of problems encountered in one dimensional signals [16, 17].
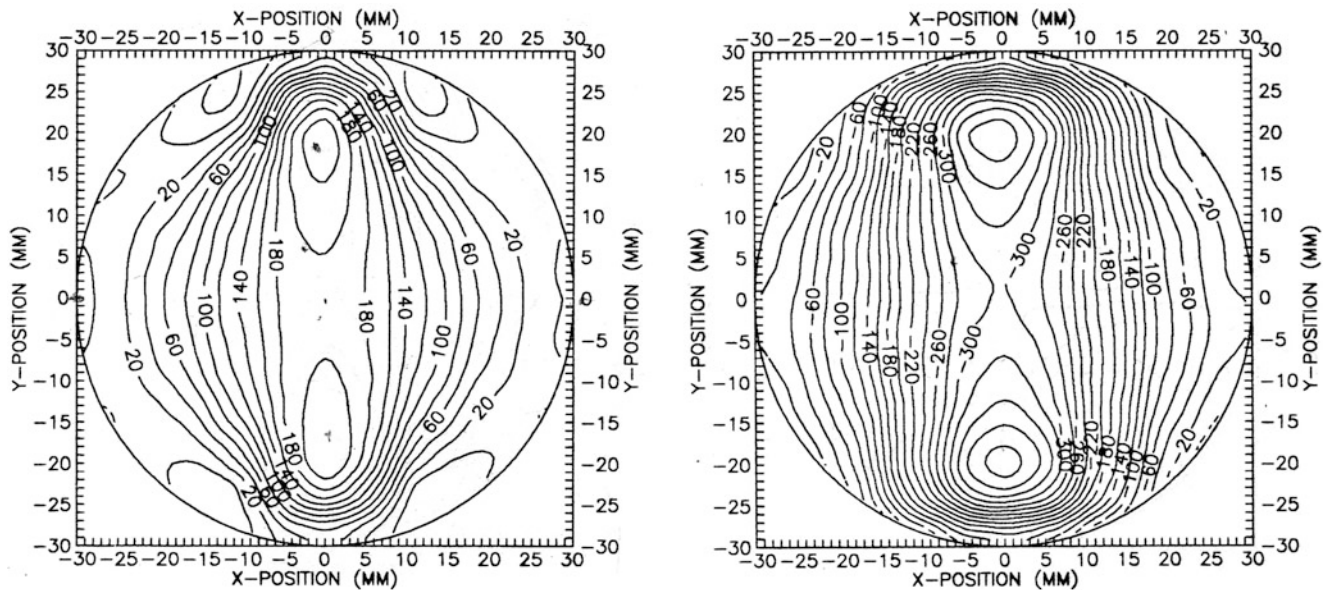
Fig. 1.18 Strains ε_x and ε_y of the disk under diametrical compression obtained from the FFT by differentiation in the frequency space [25]
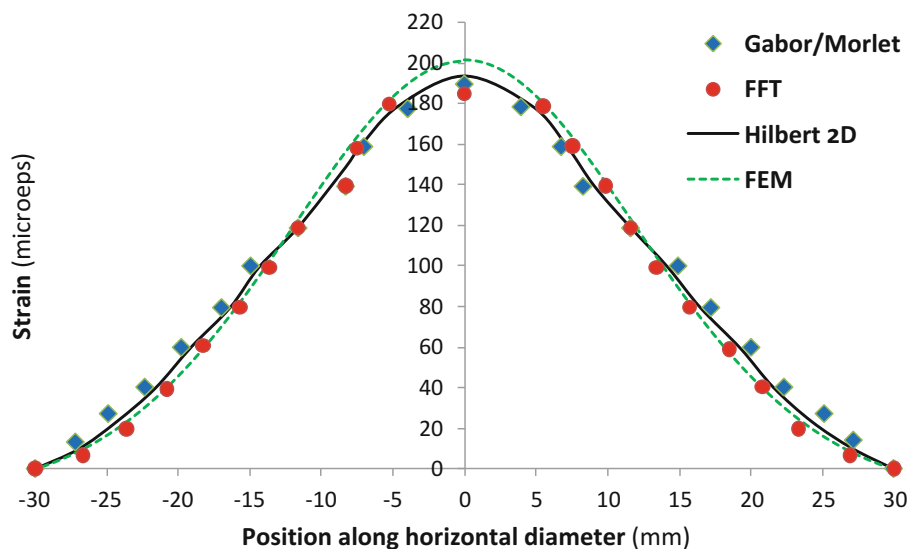
Fig. 1.19 Comparison of strains ε_x obtained by Gabor transform—Morlet wavelet and windowed FFT with finite element computation (control path corresponds to the horizontal diameter of the disk)

The current paper was devoted to put into the general theory of monogenic function, 2D fringe pattern analysis. This effort has an interesting sequel, the Poincare sphere well known to photoelasticians appears again on a different topic, the retrieval of displacement fields and their derivatives. This finding opens a new and interesting field of research in view of the fact that the phase concept has been attached in the past to the Poincare sphere [9–11]. As part of these developments the relationship between the FFT transform and the generalized Hilbert transform is analyzed. An important conclusion arrived to in [1], the equivalence of the multi phase method and the in-quadrature method, is extended to two dimensional signals. A more detailed analysis of these questions is presented in the discussion of the local phase concept closely related to the narrow band condition that makes more likely that the generalized Hilbert-transform to be a valid representation of the captured signals. Finally, the role of other transforms (Gabor transform and wavelet transform) in fringe pattern analysis is considered. The analysis of an actual fringe pattern, the fringes corresponding to a disk under diametrical compression by all the above described methods provides results that are numerically very close and also close to the finite element solution in spite of the quite different algorithms utilized in each case. This is also a very valuable outcome that provides a comparison of different approaches from the point of view of reliability and accuracy of the final results.

References

1. Sciammarella, C.A., Lamberti, L.: Mathematical models utilized in the retrieval of displacement information encoded in fringe patterns. Opt. Lasers Eng. **77**, 100–111 (2016)
2. Oppenheim, A.V., Lim, J.S.: The importance of phase in signals. Proc. IEEE **69**(5), 529–541 (1981)
3. Gabor, D.: Theory of communications. Part 1: the analysis of information. J. Inst. Electr. Eng. **93**(26), 429–441 (1946)
4. Papoulis, A.: Systems and Transforms with Applications to Optics. McGraw-Hill, New York (1968)
5. Felsberg, M.: Low-level image processing with the structure multivector. PhD Dissertation D-24098, Christian-Albrechts University of Kiel, Germany (2002)
6. Felsberg, M., Sommer, F.: The monogenic signal. IEEE Trans. Signal Process. **49**(12), 3136–3144 (2001)
7. Wietzke, L., Sommer, G.: The 2D analytic signal. Technical Report No. 0802, Christian-Albrechts University of Kiel, Germany (2008)
8. Langley, K., Anderson, S.J.: The Riesz transform and simultaneous representations of phase, energy and orientation in spatial vision. Vision Res. **50**(17), 1748–1765 (2010)
9. Pancharatnam, S.: Generalized theory of interference, and its applications—part I: coherent pencils. Proc. Indian Acad. Sci. A **44**, 247–262 (1956)
10. Berry, M.V.: The adiabatic phase and Pancharatnam's phase for polarized light. J. Mod. Opt. **34**(11), 1401–1407 (1987)
11. Gutierrez-Vega, J.C.: Pancharatnam–Berry phase of optical systems. Opt. Lett. **36**(7), 1143–1145 (2011)
12. Holm, D.D.: Geometric mechanics II: the poincare sphere $S^2 \subset s^3$. In: Lecture Notes. Imperial College, London, UK (2013)
13. Gaskill, J.D.: Linear Systems, Fourier Transforms, and Optics. Wiley, New York (1978)
14. Rabiner, L.R., Gold, B.: Theory and Application of Digital Signal Processing. Prentice-Hall International, London (1975)
15. Troncoso Romero, D.E., Dolocek, G.J.: Digital FIR Hilbert Transformers: Fundamentals and Efficient Design Methods. Intech Open, Rijeka (2012)
16. Boashash, B.: Estimating and interpreting the instantaneous frequency signal. Part 1: fundamentals. Proc. Inst. IEEE **80**(4), 520–538 (1992)
17. Boashash, B.: Estimating and interpreting the instantaneous frequency signal. Part 2: algorithms and applications. Proc. IEEE **80**(4), 540–568 (1992)
18. Bedrosian, E.: A product theorem for Hilbert transforms. Memorandum RM-3439-PM. The Rand Corporation, Santa Monica, CA (1962)
19. Bedrosian, E.: Hilbert transform of bandpass functions. Proc. IEEE **51**, 868–869 (1963)
20. Nuttall, A.H., Bedrosian, E.: On the quadrature approximation to the Hilbert transform of modulated signals. Proc. IEEE **54**(10), 1458–1459 (1966)
21. Timoshenko, S.: Theory of Elasticity. McGraw-Hill, New York (1970)
22. Sciammarella, C.A., Bhat, G.: Two-dimensional Fourier transform methods for fringe pattern analysis. In: Proceedings of the VII International Congress on Experimental Mechanics, vol. II, Las Vegas, NV (1992)
23. Sciammarella, C.A., Kim, T.: Frequency modulation interpretation of fringes and computation of strains. Exp. Mech. **45**(5), 393–403 (2005)
24. Sciammarella, C.A., Lamberti, L.: Basic models supporting experimental mechanics of deformations, geometrical representations, connections among different techniques. Meccanica **50**(2), 367–387 (2015)
25. Sciammarella, C.A., Narayanan, R.: The determination of the components of the strain tensor in holographic interferometry. Exp. Mech. **24**(4), 257–264 (1984)

Chapter 2
Full-Field High-Strain Evaluation from Wrapped ESPI Data Using Phasors

Juuso Heikkinen and Gary S. Schajer

Abstract Electronic Speckle Pattern Interferometry (ESPI) is a sensitive optical method commonly used for full-field measurements of surface displacements. It would be very desirable to be able to extend the technique also to indicate surface strains. This would provide a full-field, non-contact strain measurement method that avoids the substantial installation burden of strain gauges. A mathematical approach is described where the ESPI data from an in-plane interferometer are numerically differentiated to indicate surface strains. This is a challenging process because numerical differentiation is very sensitive to the presence of noise and ESPI data are inherently noisy. In addition, the phase information from ESPI data are wrapped modulo-2π. The resulting phase discontinuities make it difficult to use local averaging to smooth the data. A technique is described here where phasors are used to avoid the need for phase unwrapping. The effect of noise is reduced by a localized multiple smoothing technique that is effective in preserving spatial resolution, even near very high strain concentrations. Example measurements are shown and the effectiveness of the proposed method is illustrated.

Keywords Strain • ESPI • Phasor • Unwrapping • Smoothing

2.1 Introduction

The full-field, noncontact nature of optical methods makes them an attractive choice for surface deformation measurements [1, 2]. Electronic Speckle Pattern Interferometry (ESPI) is of particular interest because of its versatility and high sensitivity [3, 4]. Depending on the optical configuration used, the method can measure in-plane or out-of-plane displacements and other variations. It would be very attractive to extend the technique also to indicate surface strains. This would provide a full-field, non-contact strain measurement method that avoids the substantial installation burden of strain gauges. Direct surface strain measurement is possible, for example, using a shearography approach [5], but the strain measurements are very difficult to acquire accurately because they must be separated from much larger surface rotation effects. Alternatively, a compound interferometer divided into four illumination beams could be used [6]. The approach taken here is to determine surface strains mathematically by differentiating the data from an in-plane interferometer.

ESPI measurements involve illuminating the surface of a test object with two coherent laser beams originating from a common source and recording the reflected interference speckle pattern before and after deformation [1]. ESPI measurements yield a phase map indicating the surface displacements along the measurement sensitivity direction [7]. The raw phase map has phase discontinuities due to its modulo-2π nature and is called wrapped. It must be unwrapped in order to obtain continuous phase and displacement field [8]. However, the simultaneous presence of noise and of large strains makes unwrapping very challenging, leading to phase unwrapping errors and consequent displacement evaluation anomalies. These issues have very damaging effects during subsequent numerical differentiations to determine surface strains because differentiation greatly amplifies noise and is very sensitive to local displacement field anomalies.

Avoidance of unwrapping errors and reduction in phase noise are key requirements for effective strain field evaluation. Wrapped data cause difficulty when a 2π discontinuity occurs within the gauge length used for the strain evaluation. This opens the question as to whether it may be possible to avoid the need to do unwrapping. One approach is to do a local unwrapping of the phase angles within the gauge length [9]. This is reasonably effective, but limited to modest strain values. An alternative approach explored here is to avoid phase unwrapping issues by expressing the measured phase at each pixel in phasor format [10]. When phase is represented in this way it appears as a complex number of unit amplitude with phase angle φ as the argument. The real and imaginary parts respectively equal cos(φ) and sin(φ), both of which are continuous

---

J. Heikkinen • G.S. Schajer (✉)

Department of Mechanical Engineering, University of British Columbia, Vancouver, Canada

e-mail: schajer@mech.ubc.ca

functions. Thus, the phasor representation of the measured phase distribution can be mathematically manipulated without concern for the discontinuities associated with phase wrapping.

Even with the most careful ESPI measurements, speckle noise can be substantial, so some data filtering is needed in addition to the use of phasor notation. The continuous character of the phasor notation facilitates such filtering because it avoids any concerns for the discontinuities associated with wrapped phase data. Even so, the gauge length associated with the strain evaluation must be limited to encompass a phase difference less than 2π, else aliasing errors will occur.

Data filtering must be done sparingly to avoid data smearing and consequent loss of spatial resolution. In addition, care must be taken when using phasor notation because filtering can move the phasors away from their required unit magnitude. To combat both effects, repetitive filtering [11] is used, where a modest filter is repeatedly applied to the data, with phasor renormalization done after each filter application. Repetitive filtering is highly effective, with very smooth displacement maps obtained even with small filtering kernels. However, it must be done with moderation, else errors can propagate and distort large areas.

An ESPI strain calculation algorithm based on phasor format data and repetitive phasor mean filtering is described here. Particular focus is given to maintaining performance in areas of high strain concentrations.

2.2 Proposed Strain Calculation Approach

ESPI measurements indicate the phase change at each pixel that is caused by deformation of the imaged surface. Given knowledge of the ESPI interferometer geometry, this phase change enables direct evaluation of the surface deformation. The most common way of making ESPI measurements uses the phase stepping technique. A sequence of speckle pattern images is taken with a specified phase step added for each image using a piezo actuator mounted within one beam of the ESPI interferometer [4]. A popular choice is to take four images with a $\pi/2$ phase step between them. For this procedure, the local phase angle φ at a given pixel can be determined from the light intensities I_i measured at that pixel within the $1 \leq i \leq 4$ measured images:

$$\varphi = atan\left(\frac{I_4 - I_2}{I_1 - I_3}\right) = atan\left(\frac{n}{d}\right) \tag{2.1}$$

where n and d respectively are the numerator and denominator of the fraction within the atan function. The details of the contents of these quantities will vary according to the particular phase stepping technique used, but almost all will produce a atan(n/d) type of result. The phase angle φ can be determined within the range $-\pi < \varphi \leq \pi$ using the two-argument arctangent function. Phase angles outside this range are "wrapped" with modulo 2π, thus an angle $1.1\,\pi$ appears as $-0.9\,\pi$. Many mathematical techniques have been developed to unwrap the phase angle through comparisons with the phase of adjacent pixels [8]. However, such unwrapping can be difficult to do accurately in the presence of significant measurement noise and substantial phase gradients. Thus, it would be attractive to do the strain evaluations of interest here without the need for initial phase unwrapping.

ESPI measurement noise also seriously impedes attempts to determine the phase gradients to yield the desired surface strain information. This occurs because the needed differentiation is a numerically sensitive operation that enlarges the noise present in the measured data. Thus, it is necessary to do some initial smoothing of the measured phase data to reduce high-frequency noise and allow the strain evaluation to proceed reasonably. However, the amount of smoothing must be kept modest so that it does not significantly smear the underlying data and impair spatial resolution.

Initial smoothing to facilitate unwrapping is impeded by the presence of the 2π jumps present in the raw (wrapped) phase data. Conversely, initial unwrapping to facilitate smoothing is impeded by the presence of noise. A way forward is to choose a smoothing method that does not require prior phase unwrapping. The approach chosen here is to express the phase angle φ in Eq. (2.1) in phasor format [10]:

$$\Phi = cos\varphi + i\, sin\varphi = \frac{d}{r} + i\,\frac{n}{r} \tag{2.2}$$

$$\text{where} \qquad r = \sqrt{d^2 + n^2} \quad \text{and} \quad i = \sqrt{-1} \tag{2.3}$$

The phasor Φ has continuous real and imaginary parts, and so may be smoothed without concern for phase wrapping. Most modern mathematical software includes complex numbers as a native numerical format, so the smoothing can be done directly on Φ. Alternatively, the smoothing can be done separately on $\cos(\varphi)$ and $\sin(\varphi)$ [11]. Various smoothing methods can be suitable, for simplicity mean smoothing was chosen here. This process involves averaging the phase value at a pixel with the phase values at neighboring pixels, the group of pixels forming a template. Typical template sizes are $3 \times 3, 5 \times 5$, etc. Larger template sizes give greater smoothing, while smaller template sizes give greater spatial resolution. A side effect of smoothing is that it causes the phasor Φ to drift away from unit magnitude. The approach taken here is to seek to preserve spatial resolution by using the minimum 3×3 template, seeking sufficient smoothing by repeating the process several times, and maintaining unit phasor magnitude by renormalization after each smoothing.

Local strain can be determined directly by phase subtraction between neighboring pixels. To achieve second-order accuracy, a midpoint differentiation scheme is used to determine the strain at pixel i within a given row:

$$d\varphi_i \; = \; \frac{\varphi_{i+k} \; - \; \varphi_{i-k}}{2k} \; \text{rad/pixel} \tag{2.4}$$

where $2k$ is the number of pixels contained within the differentiation step. A difficulty when applying Eq. (2.4) is that it is susceptible to wrapping errors. This issue can be overcome by rewriting the equation in phasor format:

$$\arg[d\Phi_i] \; = \; arg \left[\sqrt[2k]{\Phi_{i+k} \cdot \Phi^*_{i-k}} \; \right] \; \text{rad/pixel} \tag{2.5}$$

where * denotes the complex conjugate. This form of equation is not affected by wrapping issues. A step size greater than the minimum $k = 1$ reduces the adverse effect of phase noise. However, k should not be so large that $2k$ pixels span a phase angle more than π, else aliasing will occur. The $2k$ root in Eq. (2.5) creates a further filtering effect. Without this root, the computed phase angle/pixel would lie in the range $-\pi < d\varphi_i \leq \pi$. For $k = 1$, the square root operator gives two solutions π apart. The smaller angle is returned by the solver, lying within the reduced range to $-\pi/2 < d\varphi_i \leq \pi/2$. For general k, the roots are π/k apart, with the returned value being the smallest angle, lying in the reduced range $-\pi/2k < d\varphi_i \leq \pi/2k$. The effect of this is that if phase noise creates an angle that would theoretically lie outside the reduced range, the smaller root is returned by the solver. This creates an inherent filtering where extreme outliers are automatically put into a more realistic range. To avoid the possibility of distortion due to noise and excessive filtering, the maximum value of k chosen should be such that the actual $|d\varphi_i| < \pi/4k$ rad/pixel.

Notwithstanding the beneficial effect of the 2k root solution in Eq. (2.5), the computed strain can still contain significant noise. Thus, it is useful to apply a further repetitive filtering of the computed strains in a similar way as was applied to the original raw phase data. The phasor format is retained, with mean filtering repeated several times with phasor renormalization done after each filter application.

In summary, the steps in the proposed method for determining the strains from an ESPI measurement of surface displacements are:

1. Represent the raw phase data in phasor format using Eqs. (2.2) and (2.3).
2. Repetitively apply a small-template mean filter to the phase data, with phasor renormalization after each step.
3. Calculate local strains at each pixel using Eq. (2.5).
4. Repetitively apply a mean filter with larger template to the computed strains, with phasor renormalization after each step.

The objective is to obtain a strain map that is acceptably smooth while preserving good spatial resolution. To achieve this, the filtering in steps 2 and 4 is done using small mean filter templates, repeated until the desired smoothing is achieved. The template size and the number of filtering repetitions required will depend on the noise level within the original ESPI data.

2.3 Measurement Setup

Experimental measurements were performed using an in-plane ESPI interferometer [9]. Figure 2.1 schematically shows the arrangement used. The measurement object was a rectangular nylon specimen $120 \times 98 \times 25$ mm^3. A 6 mm through-hole was drilled and two vertical slits sawn in the specimen to create localized strain concentrations. A thin layer of matte white paint was sprayed on the specimen surface to increase its reflectance. The specimen was fixed to an optical table and loaded compressively at the sides in a horizontal direction, parallel to the interferometer sensitivity direction. The specimen was

Fig. 2.1 Schematic diagram
of the in-plane ESPI
interferometer
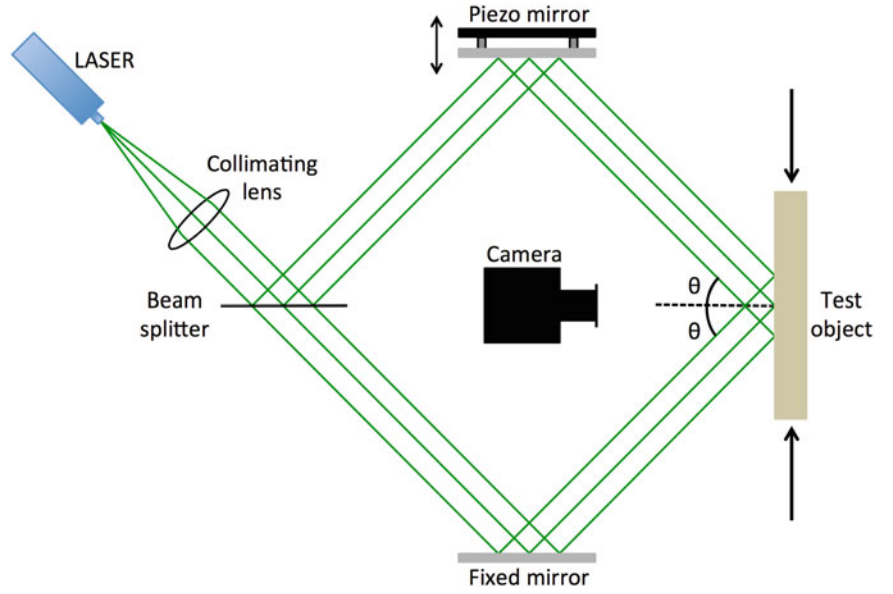
symmetrically illuminated using two expanded and collimated laser beams. The laser wavelength was 532 nm and the illumination angle 50° with respect to the object surface normal. Image resolution was 640 × 480, CCD pixel size $6 \times 6~\mu m^2$ and image magnification 0.12, so each pixel corresponded to 50 μm on the object surface.

The measured phase change directly indicates in-plane surface displacement [9]:

$$d_i = \frac{\varphi_i \lambda}{4\pi sin\theta} \tag{2.6}$$

where d_i and φ_i are the displacement and phase change in pixel i, respectively, λ is the laser wavelength and θ is the illumination angle. For the experimental setup configuration used, the displacement-phase relation was 55 nm/rad.

2.4 Phase Filtering

The noise amplification that occurs during numerical differentiation of displacement data to determine strain can have severe effects if the original data are very noisy. Noise filtering requires particular care in the case of high strains, as large displacements introduce additional speckle decorrelation noise [4, 12]. The filtering used here is a simple averaging filter where each pixel value is replaced by the average of the neighboring pixels. The range of pixels used in this process is called the template and has typical size 3 × 3, 5 × 5, etc., centered on the given pixel. The averaging is done directly on the phasors representing the phase at each pixel. After averaging, the resulting average phasors are renormalized to have unit amplitude. The size of the phase filtering template has to be restricted to preserve spatial resolution. In addition, the template size should be limited so that it spans less than one phase fringe, else aliasing errors will occur. Figure 2.2 shows an example of different levels of filtering applied on a phase map measured using the in-plane ESPI interferometer with slit-hole specimen. The raw phase map has substantial noise, so significant filtering is required. However, an oversized template leads to aliasing and phase smearing, so repeated application of a small template was chosen. Care must be taken to avoid excessive repetitions, else errors propagate into and damage nearby areas. Errors mostly occur within areas that have highest displacement gradients, notably around the hole and the slit tips. Since strain concentrations are of particular interest, such filtering errors must be controlled. In the example shown in Fig. 2.2d, five repetitions with a 3 × 3 template was found to give satisfactory results, with only some minor errors remaining near the slit tips. This moderate filtering provides the necessary phase data quality improvement but inevitably leaves some residual noise that will subsequently need to be filtered from the calculated strain field.

After the initial smoothing of the ESPI phase data, the numerical differentiation can be done using Eq. (2.5). Larger values of the differentiation span 2k seem desirable because they reduce noise sensitivity. However, if the span covers a phase angle greater than π, aliasing will occur and a false result will be returned. Thus, the chosen k should be limited.
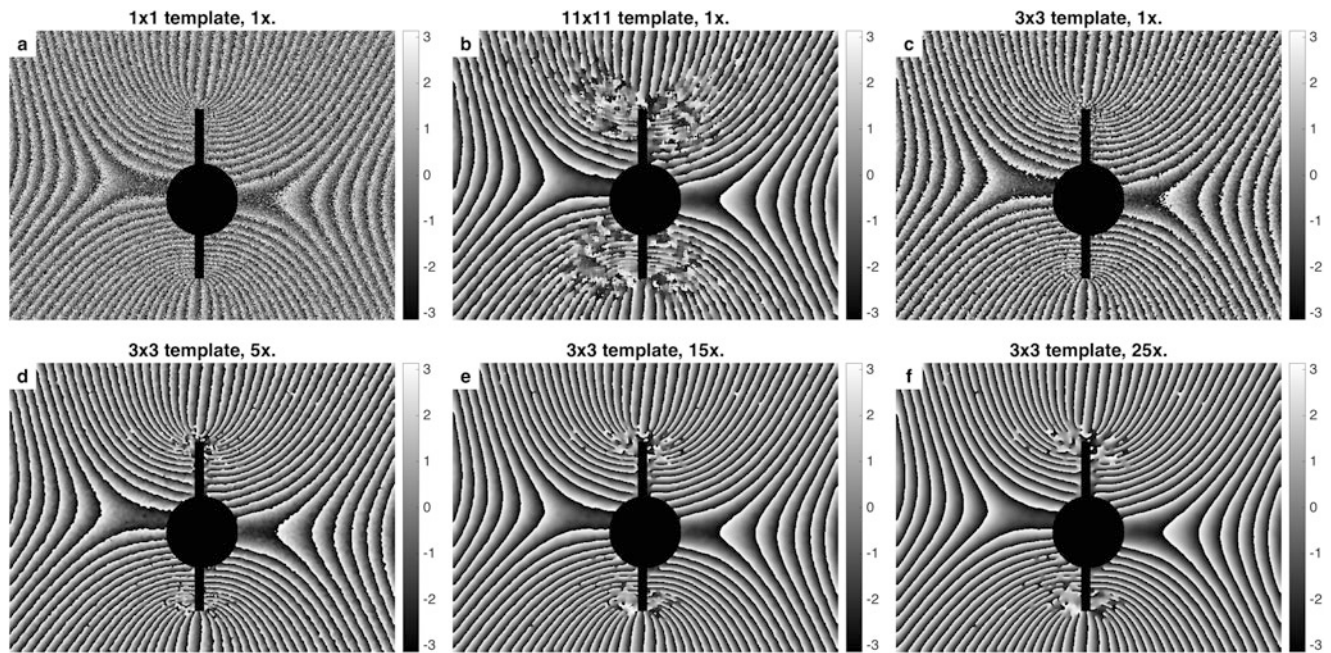
Fig. 2.2 An example phase map with large phase gradients. The hole and slits are masked and excluded from the calculations. (**a**) Raw phase map, (**b**) filtered phase map using 11 × 11 template and one repetition, (**c**) filtered phase map using a 3 × 3 template and one repetition, (**d**) filtered phase map using 3 × 3 template and five repetitions, (**e**) filtered phase map using 3 × 3 template and 15 repetitions, (**f**) filtered phase map using 3 × 3 template and 25 repetitions

The synthetic fringe pattern shown in Fig. 2.3 was created to study and quantify such effects. Strain in the generated phase fringe pattern is zero at the left edge. It increases linearly to a maximum value of 0.75 rad/pixel at three quarters of the total width from the left and decreases linearly back to zero at the right edge. A region of zero strain was added to mimic a hole. The interfaces between the hole and surrounding area have sharp phase jumps.

The effect of step size was first studied without any added noise. Figure 2.3 shows the synthetic fringe pattern together with the strain fields calculated using Eq. (2.5) with step sizes k = 1, 2 and 3. Since the phase data were synthetic without noise, no initial phase data filtering was needed nor applied. As expected, artifacts occur along the discontinuity lines aligned in the y-direction, perpendicular to the x-strain differentiation direction. When the step size is increased, these artifacts spread further. In addition, the step size determines strain calculation range. The upper limit is $|d\varphi_i| = \pi/2k$ rad/pixel, so the maximum absolute strains for step sizes k = 1, 2 and 3 are $\pi/2$, $\pi/4$ and $\pi/6$ rad/pixel, respectively. If the local strain exceeds the respective limit, aliasing occurs. This effect occurs for k = 3 on the right side of Fig. 2.3d in the region where the phase gradient exceeds the aliasing limit. Thus, to capture the highest strains in this example, the acceptable differentiation spans are k = 1 and k = 2.

Normally distributed numerical noise with standard deviation = 1.1 rad and zero-mean was added to the synthetic phase data to make the generated fringe pattern comparable with experimental data. The noisy phase map was first repetitively filtered using a 3 × 3 template and five repetitions. Strain was then calculated using a step size k = 1 to study the highest strains. Figure 2.4 shows the noisy and filtered phase maps and the corresponding calculated strains without any additional strain data filtering. Any values exceeding the range limits are seen in black or white. The general appearance of the strain map is very grainy. In addition, in the area of the largest strains on the right side of the strain map, phase filtering caused some errors that produced anomalies that appear as wrapped dark spots. It is evident that some additional strain filtering would be useful.

Repetitive filtering was applied on the calculated strain field. Figure 2.5 shows a comparison of different strain filtering parameters. Strain smoothing template sizes 3 × 3, 9 × 9 and 15 × 15 are displayed in the columns, while 1, 5, 10 and 15 repetitions are shown in the rows. It can be seen that increases in either template size or number of repetitions increases the smoothing effect. Viewing from left to right through the columns, it is also evident that large template sizes smear the spatial details. This can be seen clearly by observing the effect on the edges of the inset square. Alternatively, it can be seen that repetition with a modest size template can achieve reasonable smoothing without excessive blurring of sharp edges. In this example, a 9 × 9 smoothing template with 5–10 repetitions gives a reasonable compromise between smoothing effectiveness and data blurring. The choice of these numbers is not universal; they will depend on data quality and the strain concentrations to be observed.
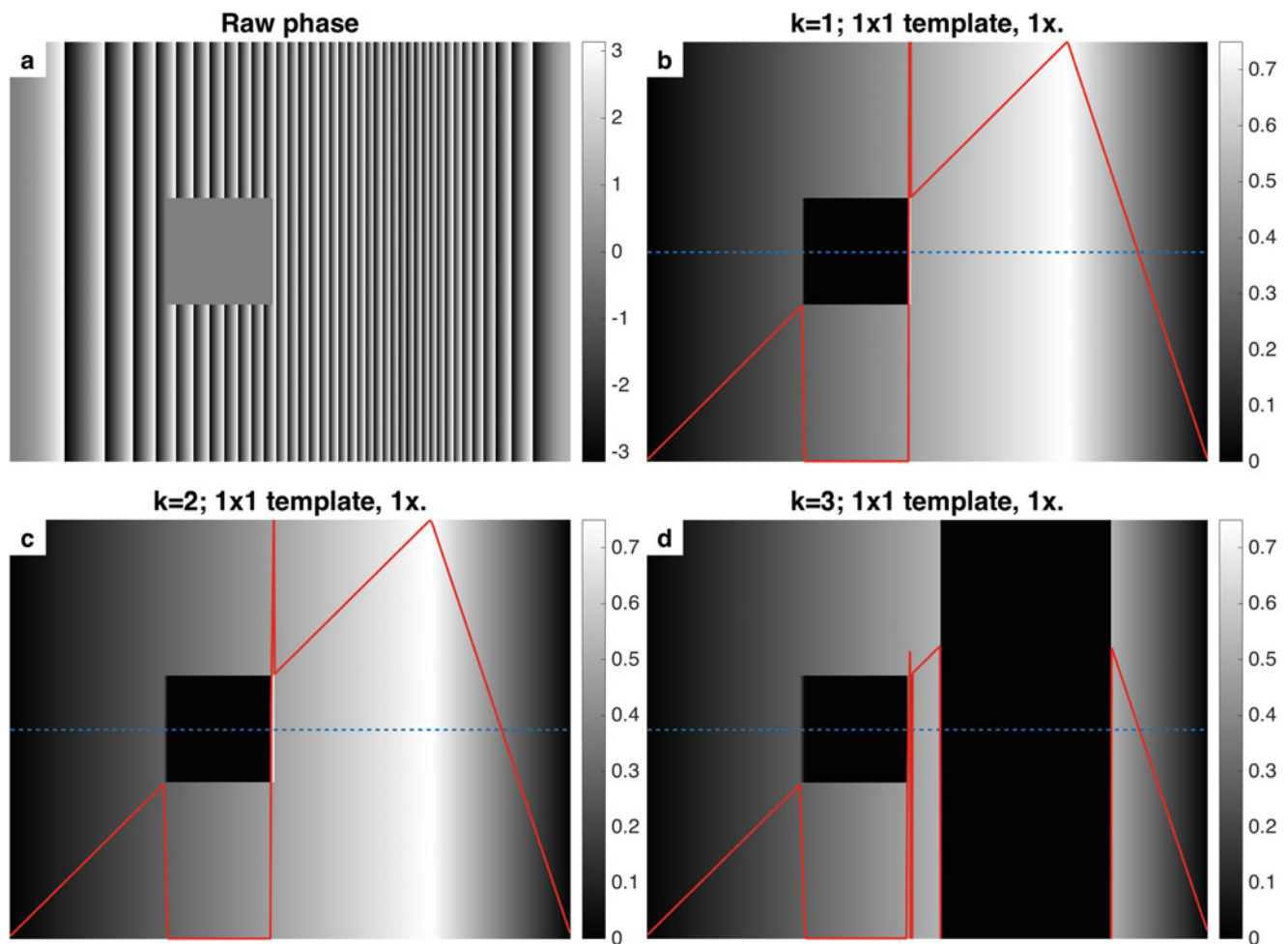
Fig. 2.3 The effect of step size under increasing strain. (**a**) Synthetic fringe pattern with strain increasing linearly from *left* to *right*. Minimum strain is zero and maximum strain 0.75 rad/pixel. The *square* has uniform zero phase and thus zero strain. (**b–d**) Horizontal strain calculated using Eq. (2.5) with step sizes k = 1, k = 2 and k = 3, respectively. The *solid red line* is a plot of strain along the *dashed blue line* in the *middle*

2.5 Example Experimental Measurements

Figure 2.6 presents experimental measurements and strain calculations done with the same slit-hole specimen used for Fig. 2.2. The successive rows of Fig. 2.6 show the results for increasing levels of horizontal compressive load. The left column shows the filtered phase maps, the center column shows the corresponding filtered strain maps computed using differentiation span k = 1, and the right column shows the filtered strain maps computed using differentiation span k = 2. (The electronic version of this document shows the strain results in color.) At the lowest loading level, the quality of the filtered phase map is very good and thus the strain calculation proceeds without problems. Both k = 1 and k = 2 give good results. When loading is increased, the fringe density and associated phase gradients increase correspondingly. These changes and the associated increase in noise level make filtering more challenging and prone to errors. At the third loading level, small phase and strain anomalies start to appear around the strain concentrations at the tips of the slits for both k = 1 and k = 2 strain evaluations, with the k = 1 results being slightly more robust. At the highest load level, the phase gradients around the tips of the slits have become sufficiently high to cause aliasing in the k = 2 strain calculations. This effect causes the strain distortions seen in the lower right image. The corresponding k = 1 strain map gives a more robust result, although still with some localized distortions due to the anomalies in the measured phase data. For the results shown, the maximum undistorted strains that could be resolved exceeded 700 microstrain (strain $\times 10^{-6}$).
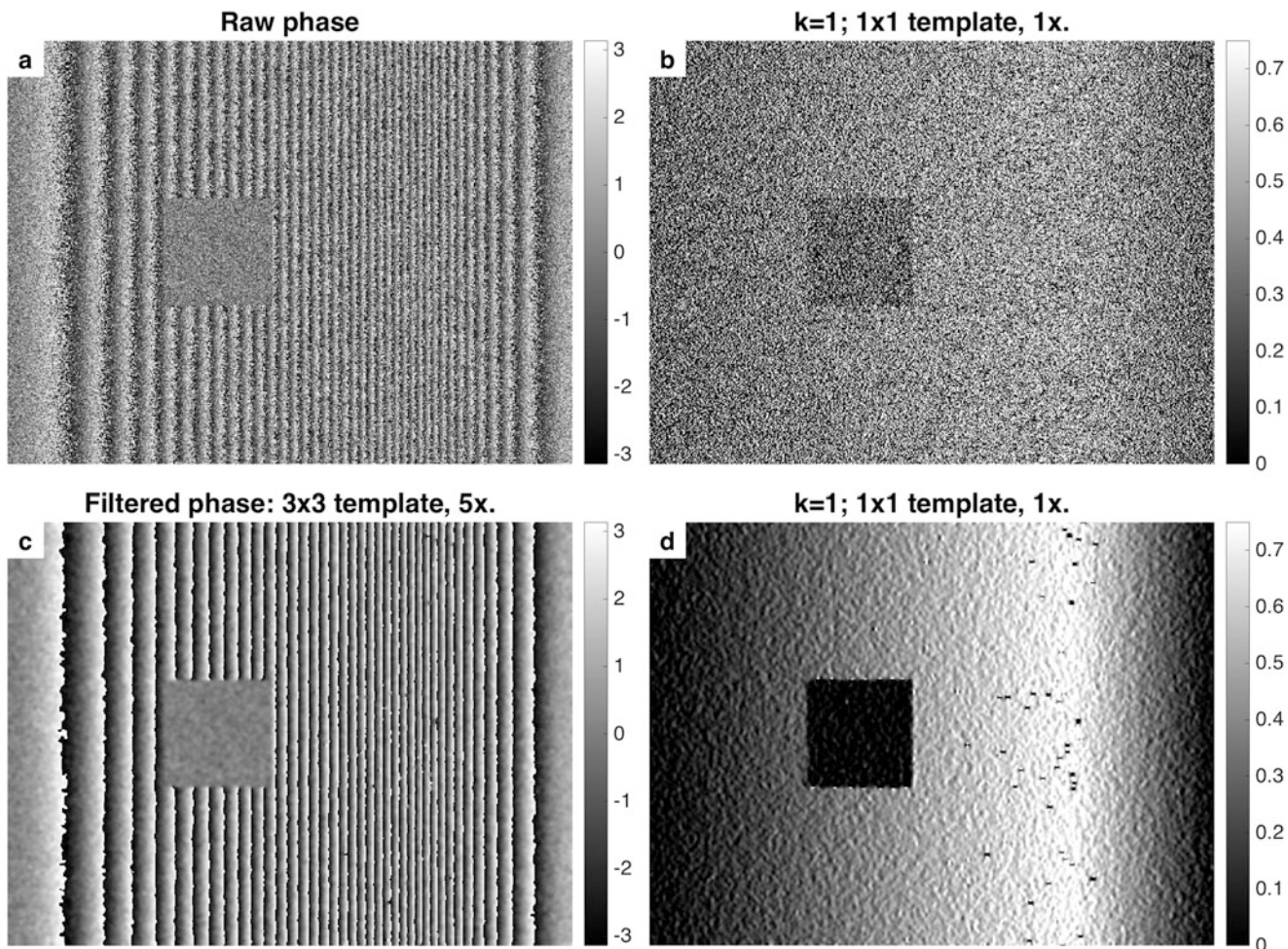
Fig. 2.4 The noise amplification phenomenon and the importance of phase filtering. (**a**) Noisy synthetic phase map, (**b**) strain calculated directly from the raw phase map using step size k = 1 and no filtering, (**c**) phase map after noise removal using a 3×3 filtering template and five repetitions, (**d**) strain calculated from filtered phase map using step size k = 1 and no additional strain filtering. Strain plots are omitted for clarity

2.6 Discussion

The inherently noisy character and the wrapped format of ESPI data make the differentiation required to evaluate strains from displacement measurements very challenging, especially in the presence of large strains. The procedure developed here seeks to address these concerns. To address the wrapping issue, the ESPI phase data are expressed in phasor format rather than as scalar angles. Then, an initial mild smoothing of the raw phase data is applied to remove outliers. The differentiation step is then done in phasor format using Eq. (2.5). The choice of the differentiation span 2k is important because on one hand it is desirable to use a large span to reduce noise in the results, while on the other hand it is desirable to use a small span to avoid wrapping errors. It turns out that the use of the smallest differentiation span with k = 1 is always an acceptable choice. This occurs because the noise reduction from the use of larger k affects only the shortest noise wavelengths, those with wavelengths of the order of k pixels. Longer wavelength noise is not affected. The further smoothing of the strain results using templates with larger numbers of pixels is designed to smooth the longer wavelength noise. Since this process also smooths the short wavelength noise, the prior choice of k has little effect on the subsequent smoothing results. Because of this, k = 1 is chosen in all cases because it provides the maximum strain range without wrapping issues.

Previous strain evaluation methods [4, 9] have sought to implement the needed smoothing during the differentiation step. This was done by averaging the strains evaluated over a large region surrounding the pixel of interest. However, with this arrangement, either only lower strains are acceptable or the region must be severely limited in size, else wrapping problems will occur. The localized unwrapping of scalar phase data used by [9] is effective only for modest strains and/or differentiation region size. The procedure proposed here reverses the focus of the operations. Instead of seeking to achieve smoothing by doing the differentiation over a large area, here the differentiation is done over a very small area, with controlled smoothing achieved by filtering both the raw phase data and the subsequent strain results.
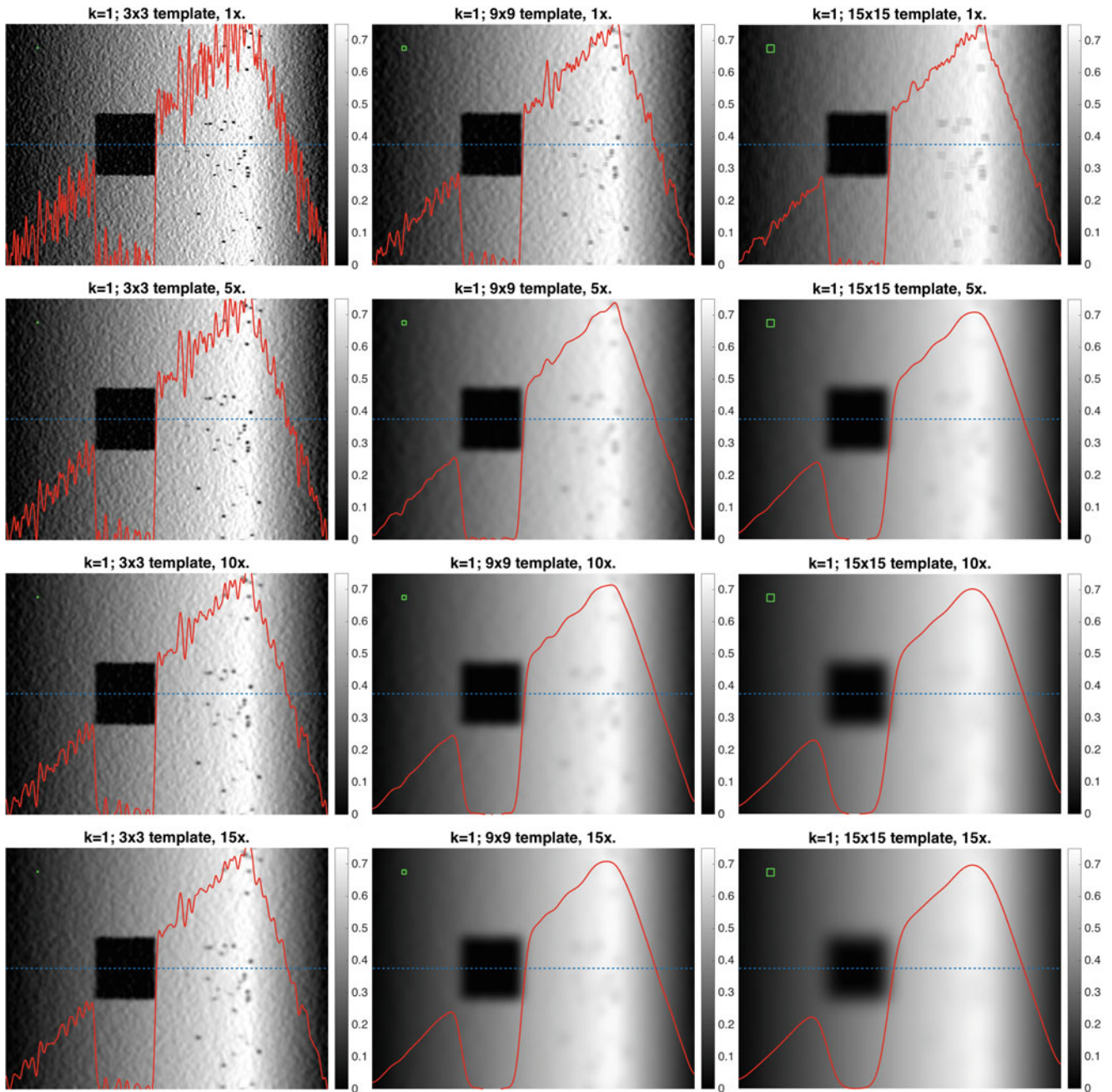
Fig. 2.5 Study of the effects of strain filtering template size and number of repetitions. From *left* to *right*, the template sizes in each *column* are 3×3, 9×9 and 15×15. From *top* to *bottom*, the numbers of repetitions in each *row* are 1, 5, 10 and 15. The *red lines* are plots of strain along the *dashed blue horizontal line*. The *green squares* show the filtering template size

2.7 Conclusions

A mathematical method for identifying surface strain from in-plane ESPI measurements has been developed and demonstrated. The approach used is tailored to the practical characteristics of ESPI data, notably their high noise content and phase wrapping. These issues are particularly challenging in areas of high strain because local data quality tends to deteriorate where there are high phase gradients. The numerical differentiation needed to evaluate strain from displacement data is very sensitive to the presence of noise, so significant smoothing is required. However, such smoothing must be applied in such a way as to minimize blurring of the results. This is done here by using a small mean filter template repeatedly applied to the raw displacement data. To accommodate the presence of phase wrapping, the raw phase data are expressed as phasors and the initial data filtering and all subsequent mathematical processes are kept within this format.
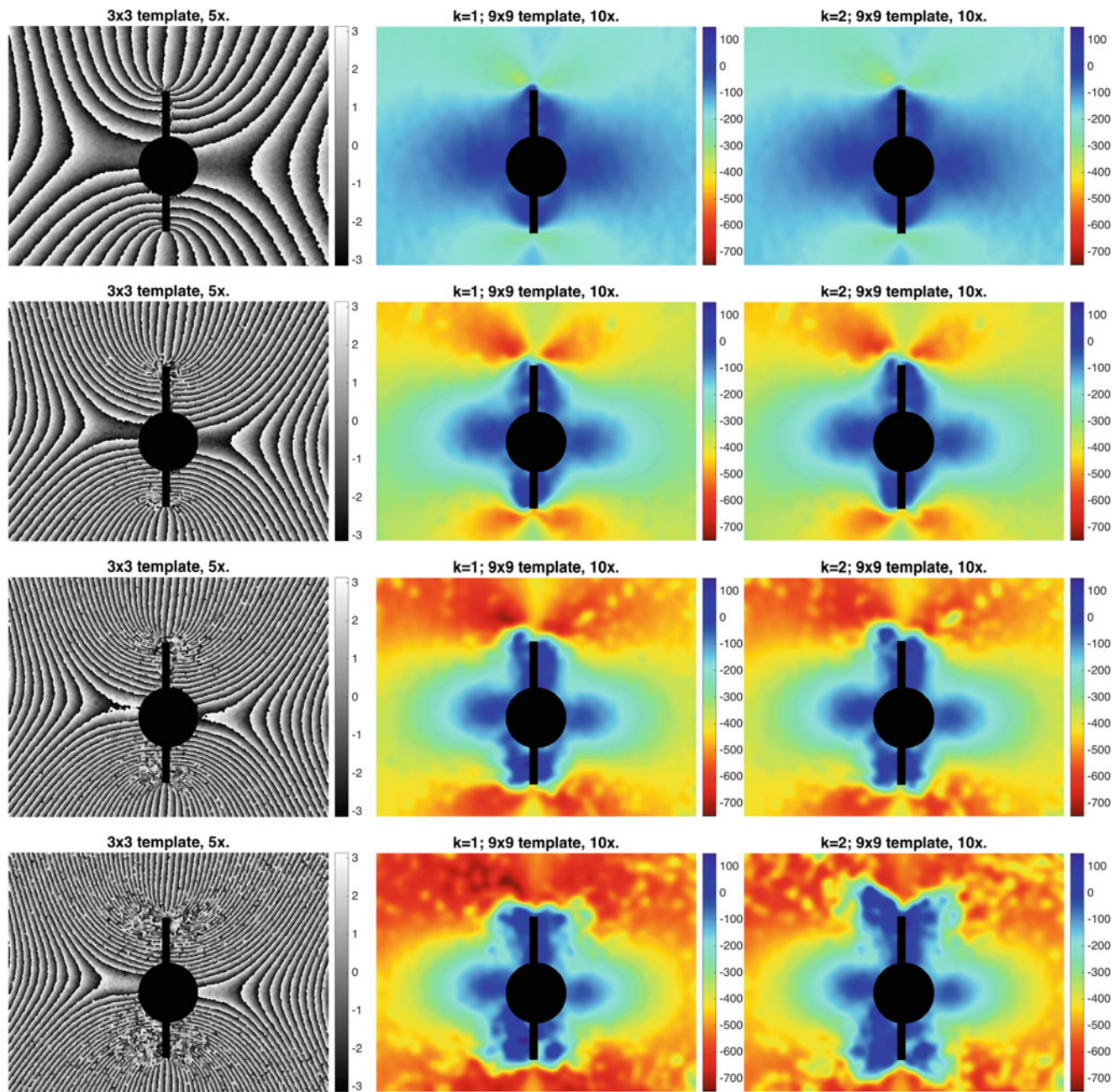
Fig. 2.6 Strain evaluation from experimental deformation measurements. *Rows*: increasing horizontal compressive loading on a slit-hole specimen. *Left column*: filtered phase maps. *Center column*: maps of horizontal strain $\varepsilon_{xx} = du/dx$ computed with differentiation span k = 1. *Right column*: maps of horizontal strain $\varepsilon_{xx} = du/dx$ computed with differentiation span k = 2. The unit of strain is microstrain (strain $\times 10^{-6}$)

After the initial raw data smoothing, a central difference differentiation function is applied to the data. The function has a short differentiation span so as to avoid aliasing associated with phase wrapping that may occur in regions of high phase gradient. Then, the resulting strain data are smoothed using a mean filter with larger template, again repeatedly applied. The approach taken here reverses those previously taken, which have sought to achieve filtering by evaluating strain by differentiation averaged over an extended area. However, with the previous approaches, aliasing associated with phase wrapping can occur in areas where the local strains and associated phase gradients are large.

The amounts of filtering to be used for the initial raw data smoothing and for the subsequent strain result smooth need to be chosen to accommodate the amount of noise in the raw ESPI data and the need for smoothness in the computed strain results. Both types of smoothing should be done in moderation, else excessive blurring and loss of spatial resolution will occur.

A single-axis in-plane interferometer was used for the example measurements shown here. It is conceptually straightforward to anticipate using a two-axis interferometer that is capable of measuring surface displacements in two orthogonal directions. With such a setup it would then be possible to use the techniques described here to identify the two normal in-plane strains and the associated shear strain. In this way, a full-field strain measurement can be achieved where effectively there is a three-axis strain gauge rosette at every pixel.

References

1. Jones, R., Wykes, C.: Holographic and Speckle Interferometry, 2nd edn. Cambridge University Press, Cambridge (1989)
2. Cloud, G.L.: Basics of optics. In: Sharpe, W.N. (ed.) Springer Handbook of Experimental Solid Mechanics, pp. 447–480. Springer, New York (2008)
3. Denby, D., Leendertz, J.A.: Plane-surface strain examination by speckle-pattern interferometry using electronic processing. J. Strain Anal. **9**(1), 17–25 (1974)
4. Vrooman, H.A., Maas, A.A.: Image processing algorithms for the analysis of phaseshifted speckle interference patterns. Appl. Optics **30**(13), 1636–1641 (1991)
5. Aebischer, H.A., Waldner, S.: Strain distributions made visible with image-shearing speckle pattern interferometry. Opt. Lasers Eng. **26**(4–5), 407–420 (1997)
6. Kim, K.-S., Jung, H.-C., Kang, K.-S., Lee, J.-K., Jang, S.-S., Hong, C.-K.: In-plane strains measurement by using the electronic speckle pattern interferometry. KSME Int. J. **12**(2), 215–222 (1998)
7. Steinzig, M., Ponslet, E.: Residual stress measurement using the hole drilling method and laser speckle interferometry: part I. Exp. Tech. **27**(3), 43–46 (2003)
8. Ghiglia, D.C., Pritt, M.D.: Two-dimensional phase unwrapping: theory, algorithms, and software. Wiley, Chichester (1998)
9. Lanza di Scalea, F.L., Hong, S.S., Cloud, G.L.: Whole-field strain measurement in a pin-loaded plate by electronic speckle pattern interferometry and the finite element method. Exp. Mech. **38**(1), 55–60 (1998)
10. Ströbel, B.: Processing of interferometric phase maps as complexvalued phasor images. Appl. Optics **35**(13), 2192–2198 (1996)
11. Aebischer, H.A., Waldner, S.: A simple and effective method for filtering speckleinterferometric phase fringe patterns. Opt. Commun. **162**(4–6), 205–210 (1999)
12. Steinchen, W., Yang, L.: Digital shearography: theory and application of digital speckle pattern shearing interferometry. SPIE, Bellingham (2003)

Chapter 3
Dynamic Deformation with Static Load

S. Yoshida, H. Ono, T. Sasaki, and M. Usui

Abstract We conduct a series of tensile analyses on metal-plate specimens to investigate the relation between the fatigue level and the material's response to external loads. We use Electronic Speckle-Pattern Interferometery (ESPI) to measures the in-plane displacement, and an acoustic transducer to assess the elastic modulus of the specimen via acoustic velocity measurement at various stress levels. We apply a tensile load at a constant pulling rate up to a certain stress level substantially lower than the yield stress, and analyze the strain field obtained with the ESPI setup at each time step. At the same time, we measure the acoustic velocity at various tensile stress levels. We have found repeatedly in the experiment on an aluminum-alloy specimen that (a) the strain field changes over several seconds after the tensile machine stops pulling, and (b) the acoustic velocity at the same point of the specimen considerably varies from measurement to measurement at the same stress level. These observations indicate that the specimen is deformed even if the crosshead of the tensile machine is stationary. This mysterious phenomenon is consistent with the observation made by Pappalettera et al. in their fatigue analysis that the acoustic emissions, which normally stops when the fatigue reaches a certain level, resumes if the specimen is dismounted from the test machine and remounted for continuation of the test.

Keywords Fatigue • Strain energy damping • Plastic deformation wave

3.1 Introduction

Fatigue of metals is a complex problem and its mechanism has not been fully understood. Fatigue tests [1, 2] utilize low level cyclic loading to the specimen until it breaks and evaluate the fatigue life. It is usually a long test, requiring the total cycle of the order of million. Often cyclic frequency is raised to save the time of experiment. There is always a question regarding the influence of the cyclic load frequency on the fatigue life. In polymer engineering, on the other hand, fatigue life is often discussed in conjunction with dynamic modulus [3, 4]. Dynamic modulus consists of the real part known as the storage modulus and imaginary part known as the loss modulus. The storage modulus represents elastic energy (conserved energy) and the loss modulus represents energy dissipation. In the context of metals, the conserved energy is elastic strain energy and the energy dissipation is irreversible (plastic) deformation. A recent theory of deformation and fracture [5] indicates that plastic deformation of metals can be described as loss modulus.

We have a series of studies on fatigue of metal specimens using electronic speckle-pattern interferometry [6, 7]. In these studies, we apply a cyclic load to metal plate specimens of the same material and dimension at various levels, and observe their response to a low level tensile load. Here we apply the tensile load at a constant pulling rate and observe the resultant in-plane strain at each time step in the form of the interferometric fringe pattern. The fringe patterns are generated via subtraction of interferogram obtained at the current time step from a previous step. Our goal is to develop a methodology to evaluate the fatigue level based on the shape of the fringe pattern. In the course of these studies, we repeatedly observe that interferometric fringe pattern is formed even after the tensile machine's grip stops. It is expected that the displacement field becomes constant when the tensile load becomes constant, and consequently, the subtraction of interferograms should not

---

S. Yoshida (✉)
Department of Chemistry and Physics, Southeastern Louisiana University, Hammond, LA 70402, USA
e-mail: syoshida@selu.edu

H. Ono
Department of Chemistry and Physics, Southeastern Louisiana University, Hammond, LA 70402, USA

Department of Engineering, Niigata University, Ikarashi-ninocho 8050, Nishi-ku, Niigata-shi, Niigata 950-2181, Japan

T. Sasaki • M. Usui
Department of Engineering, Niigata University, Ikarashi-ninocho 8050, Nishi-ku, Niigata-shi, Niigata 950-2181, Japan

form a fringe pattern. The subtracted image eventually becomes black, indicating that the specimen stops being deformed. However, fringe patterns are formed for a considerable duration, typically for a few seconds after the tensile load becomes constant. In other words, we find the strain-field keeps changing after the applied load becomes constant. This phenomenon is clearly different from creep in the time scale.

This observation is most naturally understood as the specimen recoils from the stretched state when the tensile machine's grip stops. Pappalettera et al. [8] observe in their fatigue analysis that the acoustic emissions, which normally stops when the fatigue reaches a certain level, resumes if the specimen is dismounted from the test machine and remounted for continuation of the test. The recoil behavior possibly represents the material's natural response. The fact that the fringe pattern eventually becomes black indicates that recoil motion decays due to viscosity. The decaying oscillatory behavior of this kind is sometimes called ring-down, and observed in various physical system such as LC oscillation of electric current and intra-resonator optical field after resonant condition of the optical resonator is broken. This interpretation leads to the possibility that the metal specimen's viscous property can be estimated from the ring-down characteristics, and that the fatigue can be quantitatively assessed based on the viscosity.

Hence, we conducted a simple experiment. In this experiment, we simply measured the change in load after the tensile machine's dynamic grip stops at a certain load lower than the yield point. The aim of this paper is to discuss the results of this experiment.

3.2 Experimental Arrangement

The material of the specimens was aluminum alloy A7075 [9] with the dimensions as shown in Fig. 3.1. The plate specimen was cut from a parent sheet produced with the cold-rolling method. The direction of the rolling was along the longer side of the specimen. Six specimens were prepared. Prior to the application of the low-level tensile load, five of the specimens were applied cyclic loads of 20, 100, 1000, 10,000, and 20,000 cycles, respectively. The amplitude and frequency of the cyclic load were 7.2 kN and 40 Hz. The sixth specimen, the control, was not fatigued at all.

Figure 3.2 presents the tensile characteristics of the specimen. The yield load was 13.5 kN. Thus, the amplitude of the cyclic load was 55 % of the yield load.

The experimental procedure was straightforward. A tensile load was applied to each specimen at a constant pulling rate (the dynamic grip speed) of 5 μm/s to the maximum load of 4 kN (less than 30 % of the yield load). The dynamic grip of the tensile machine was set to stop when the load sensor reading reached 4 kN. After the dynamic grip stopped, the load cell kept recording the load. When the load-cell reading plateaued, the direction of the dynamic grip was reversed to reduce the load to 0 N with the same speed 5 μm/s. A care was taken not to compress the specimen in the returning cycle. After the dynamic grip stopped at 0 N, the load-cell reading was recorded in the same fashion as when the grip stopped at the maximum load.

Fig. 3.1 Specimen used in the present study
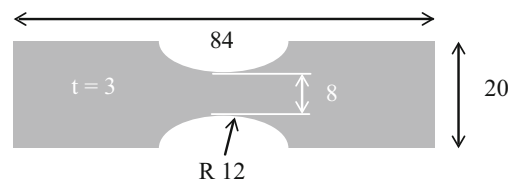
Fig. 3.2 Tensile load characteristics of the specimen used in the present study
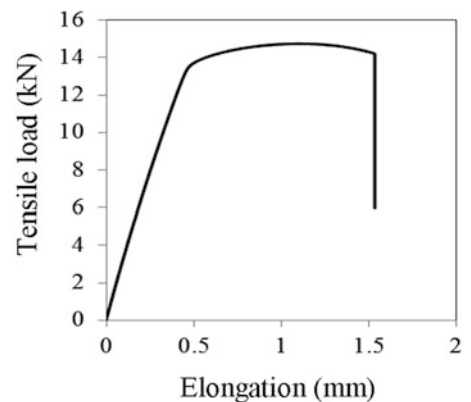
3.3 Results and Discussion

Figure 3.3 plots the load-cell reading after the dynamic grip stopped at the maximum load of 4 kN. The vertical axis is in the logarithmic scale and data are shown for four specimens, i.e., (a) is the control, (b)–(d) are fatigued specimens with 20, 1000 and 20,000 cycles, respectively. The horizontal axis is the elapsed time from the moment when the dynamic grip started to move at the constant pulling rate. Figure 3.3a–d present data only after the load decreased from the maximum load of 4 kN. The error associated with the load-cell's sensitivity is ±0.9 %. The straight lines inserted in the figures are best line fits for segments of the plots.

The following observations can be made in the data shown in Fig. 3.3. All cases indicate that the temporal trend of the load from the maximum load after the dynamic grip stops can be characterized by more than two segments. Of these segments, the last one (the one towards the end of the time window) has more scattered data indicating that the temporal variation is less exponential. The earlier segments present exponential decays, whereas the slope seems to become less steep with the elapse of the time. More careful examination of the four plots (a)–(d) reveals that in the data of fatigue cycles of 20 and 1000 (Fig. 3c, d) the initial slope is a factor of two steeper than the secondary slope, and that the secondary slope of these data sets is the same as (or very close to) the initial slope of the other two data sets.

(a)

(b)

(c)

(d)
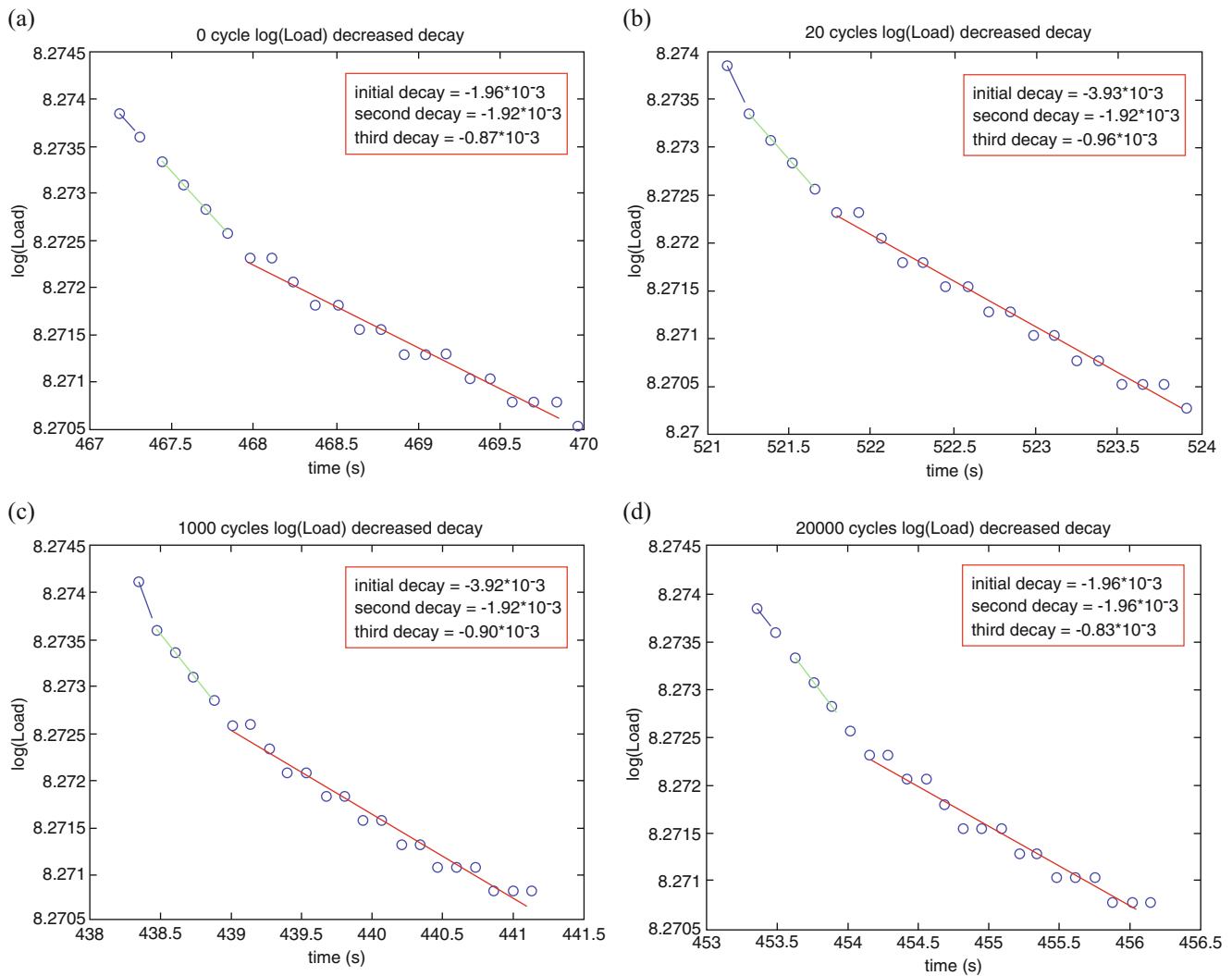
Fig. 3.3 Temporal variation of load-cell reading after dynamic grip stops at maximum load for four specimens; (**a**) control (no cyclic loading), (**b**) 200 cycles, (**c**) 1,000 cycles and (**d**) 20,000 cycles of fatigue (cyclcic) loading

In Fig. 3.4, the initial and secondary slopes are plotted as a function of the number of cycles (fatigue-load cycles). Here for the cycle of 20, the same low-level tensile load measurement was repeated and the resultant slope values are shown. The difference in the slope values between these particular two plots indicates the margin of errors and/or the deviation in the slope data. It is clear that the secondary slope has no dependence on the fatigue-load cycles. The initial slope decreases (becomes steeper with negative decay constant) with the fatigue-load cycles up to 1000 cycles.

Microscopic observation indicates that the specimen reveals crack after the fatigue cycle over 10,000 cycles.

The same load measurement was made after the dynamic grip returned to the initial position where the load-cell reading was 0 N. It was found that the load-cell reading did not fluctuate at all.

Based on the above observations on Figs. 3.3 and 3.4, and the fact that the load did not change at 0 N, the following interpretations are possible.

1. From the facts that the 0 N data does not show any change in load after the grip becomes stationary and that the data sets of the different fatigue levels show different initial slope (initial decay constant), it is unlikely that the observed decay in the load represents features of the tensile machine such as overshooting of the dynamic grip.
2. The reduction in the initial slope in fatigue-cycles of 20, 100 and 1000 can be interpreted as follows. As the fatigue-load cycle increases, the specimen experience more plastic deformation. Consequently, the decay rate increases negatively. Interestingly, the decay rates associated with initial and secondary slopes (1.96×10^{-3} to 3.92×10^{-3} 1/s) are of the same order of magnitude as the plastic deformation wave's decay constant (2.5×10^{-3} 1/s) observed in a similar aluminum alloy specimen as indicated in Fig. 3.5.
3. The increase in the initial slop after 10,000 cycles can be explained by the following scenario. When the fatigue-cycle reaches 10,000, the specimen is divided into two pieces due to the crack generation. Once this type of fracture occurs, the fractured portion does not change (stretched or compressed) as an external load is applied. Consequently, that portion does not contribute to the decay characteristics being discussed here. Instead, the non-cracked portion responds to the external load, showing the decay constant similar to the non-fatigued specimen. In a sense, the phenomenon is similar to the recovery process often discussed in conjunction with serration.

We also conducted acoustoelastic measurement using a contact acoustic transducer. The acoustic transducer on a surface of the specimen emitted longitudinal and shear waves through the thickness of the specimen and detected the wave signal reflected off the other surface. The decay rate evaluated from the comparison of the amplitude of the incident and reflected signals did not show clear dependence on the fatigue level. This result indicates that the above-discussed decay behavior represents plastic deformation associated with local weakness of the specimen, as opposed to the viscoelastic property that the aluminum alloy possesses intrinsically.
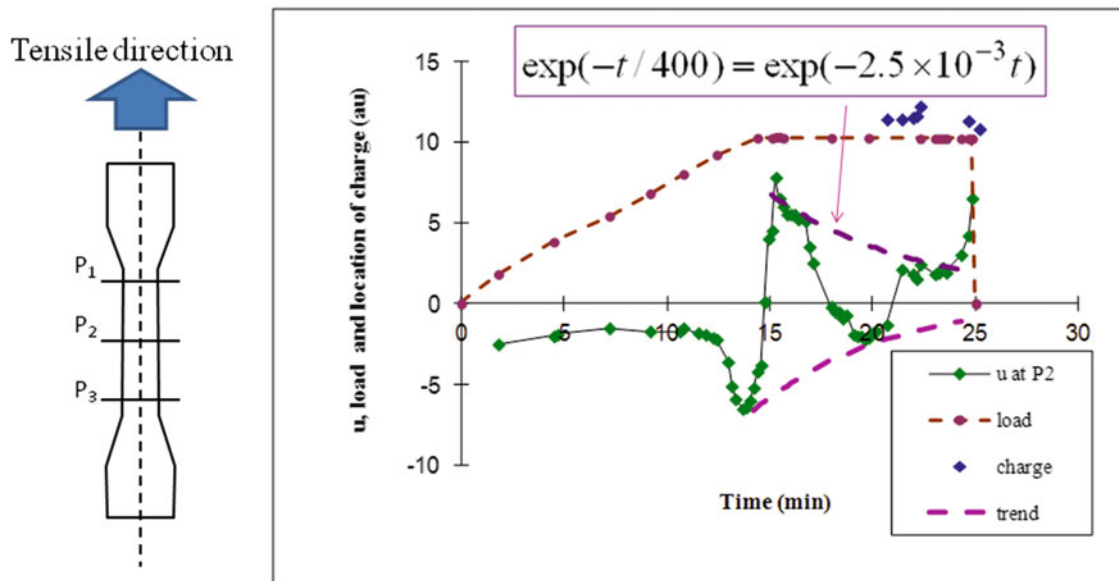
Fig. 3.5 Decay of plastic deformation wave observed in an aluminum alloy plate specimen. u is the particle velocity component perpendicular to the tensile direction. Charge is the shear band observed in the fringe pattern

3.4   Summary

Dynamic behavior of deformation in metal plate specimens have been discussed in conjunction with the degree of fatigue. Aluminum-alloy plate specimens fatigued at various levels were pulled by a tensile machine at a constant pulling rate to a maximum stress approximately one third of the yield load. The fatigue level was controlled by the number of cumulative fatigue-load cycles in a range of 20, 100, 1000, 10,000 and 20,000. After the dynamic grip of the tensile machine was stopped at the maximum load, the load-cell reading was found drop. The load-cell reading was recorded until the dropping trend plateaued. The time dependence of the load-cell reading indicates exponential decay of the vibrational displacement of the specimen. The exponential decay can be characterized by two decay constants. The initial decay constant has been found dependent on the fatigue level of the specimen whereas the secondary decay constant found independent of fatigue. Interestingly, the decay constants are of the order of the decay constant of the plastic deformation wave previously observed in separate experiment. It has been found that the cumulative fatigue-load cycles of 20–1000 causes the decay constant to increase by a factor of 2 whereas the fatigue load cycles over 10,000 showed the same decay constant as the non-fatigued specimen.

References

1. Committee E-9 on Fatigue, Manual on Fatigue Testing, ASTM, STP, 91-A (1949)
2. Fenner, A.J.: Mechanical Testing of Materials. (published by) George Newnes, London (1965)
3. Grover, E.B., Dillon, J.H., Suppiger, E.W.: Correlation of fatigue with the dynamic modulus of polymers. Text. Res. J. **36**(4), 346–355 (1966). 10p; (*AN 22713808*)
4. El Fray, M., Altstädt, V.: Fatigue behaviour of multiblock thermoplastic elastomers. 1. Stepwise increasing load testing of poly(aliphatic/aromatic-ester) copolymers. Polymer **44**(16), 4635–4642 (2003)
5. Yoshida, S.: Deformation and Fracture of Solid-State Materials. Springer, New York (2015)
6. Hasegawa, S., Sasaki, T., Yoshida, S., Hebert, S.L.: Analysis of fatigue of metals by electronic speckle pattern interferometry. In: Jin, H., Sciammarella, C., Yoshida, S, Lamberti, L. (eds.) Advancement of Optical Methods in Experimental Mechanics, vol. 3, Chap. 13, Springer, Berlin, pp. 127–134 (2014)

7. Sasaki, T., Hasegawa, S., Yoshida, S.: Fatigue damage analysis of aluminum alloy by ESPI. In: Rossi, M., Sasso, M., Connesson, N., Singh, R., DeWald, A., Backman, D, Gloeckner, P. (eds.) Residual Stress, in Thermomechanics and Infrared Imaging, Hybrid Techniques and Inverse Problems, vol. 9, Chap. 19, Springer, Berlin, pp. 147–154 (2015)
8. Pappalettera, G.: Politecnico di Bari, private communication (2015)
9. ASM International: Properties of Wrought Aluminum and Aluminum Alloys: 7075, Alclad 7075, Properties and Selection: Nonferrous Alloys and Special–Purpose Materials. In: ASM Handbook, vol. 2, Russell, Ohio, pp. 115–116. ASM International (1990)

Chapter 4
Full-Field Digital Holographic Vibrometry for Characterization of High-Speed MEMS

Payam Razavi, Cosme Furlong, and James D. Trolinger

Abstract Development of quantitative full-field high-speed imaging modalities are indispensable to monitor the real-time transient performance of Micro-electromechanical Systems (MEMS). Their performance is a direct result of how devices are designed and fabricated and any imperfection in either of them renders undesirable results. Furthermore, new devices are being designed to comply with tighter geometrical tolerances while operating at higher speeds. In this paper, we report progress in the development of a new High-speed Digital Holographic System (HDHS) for characterization of nanometer scale transient (i.e., >100 kHz) displacements of MEMS in full-field. Comparisons of the results obtained with our HDHS and those obtained with Laser Doppler Vibrometery (LDV) indicate a high level of correlation, which validates the measuring capabilities of our developed system. The high temporal and spatial (i.e., microseconds at >100k data points) resolutions of our HDHS enable concomitant measurements at all points to quantify spatially dependent motion parameters, including modal frequencies, time constants, Q-factors, changes in shapes, and surface strains. Representative results of the study of a high-speed MEMS deformable mirror are presented to show the capabilities of our method.

Keywords Digital high-speed holography • Full-field measurements • MEMS testing • Transient response

4.1 Introduction

It is estimated that up to 80 % of the fabrication costs of many MEMS involve final packaging and testing [1], which are critical for the development of reliable devices. In addition, as new MEMS devices operate at unprecedented speeds, suitable tools to measure their performance become an essence.

The need for high-speed full-field measurements is mostly due to the following factors:

- Unknown transient performance of MEMS devices under variations of environmental conditions such as surrounding medium, pressure, orientation, and temperature [2].
- Accuracy and performance of new devices require quantitative measurements as a feedback to their design and fabrication. In the case of kinematics of high-speed MEMS (i.e., >5 kHz), current operational MEMS testing devices such as Laser Doppler Vibrometery lack full-field capabilities with sufficient spatial resolutions. In addition, other testing methods to study kinematics of MEMS, such as stroboscopic holographic interferometry, require multiple measurements and characterization of the transient response of MEMS becomes difficult [3].

In this paper, we report advances in the development and application of a High-speed Digital Holographic System (HDHS) with the measuring capabilities that include high-measuring range (i.e., from nanometers to micrometers), full-field-of-view (i.e., >140,000 points), and high-speed (i.e., >40 kHz). Our methods, unlike others, have the unique capability of utilizing the full spatio-temporal resolution of high-speed cameras. These capabilities are suitable for characterization of high-speed transient events that occur in new MEMS designs. Measuring capabilities of our current HDHS are illustrated by characterizing high-performance adaptive optics such as deformable mirrors that have applications in microscopy, retinal imaging, laser communications, and wavefront correction.

P. Razavi (✉) • C. Furlong
Center for Holographic Studies and Laser Micro-mechaTronics (CHSLT), Worcester, MA, USA

Mechanical Engineering Department, Worcester Polytechnic Institute, Worcester, MA, USA
e-mail: prazavi@wpi.edu

J.D. Trolinger
MetroLaser, Inc., Laguna Hills, CA, USA

4.2   Methods

To perform high-speed holographic interferometry with high-measuring resolution, technological and methodological challenges relating to speed and spatial resolution need to be overcome. Because of this, existing phase sampling methods are unsuitable since they either sacrifice the spatial resolution (e.g., pixelated sensor phase sampling approach [4, 5]) to gain speed or sacrifice speed to gain spatial resolution (e.g., temporal phase sampling approach [6]). We are developing and implementing novel approaches to utilize the full spatio-temporal resolution of high-speed cameras by use of $2 + N$ frame acquisition methods based on a hybrid spatio-temporal local correlation phase sampling approach [7].

4.2.1   2 + N *Local Phase Correlation (LC) Method*

The method allows for quantification of transient deformations by utilizing two reference frames, $I_{ref}, I_{ref+\pi/2}$, and N consecutive deformed frames, $(I_{def})_i$, $i \in 1, 2, \ldots, N$, recorded before and throughout the evolution of transient event.

According to Fig. 4.1, $2 + N$ frame acquisition method starts by recording two $\pi/2$ phase shifted reference frames, I_{ref} and $I_{ref+\pi/2}$. While keeping the phase shifter at its $\pi/2$ position, a set of frames, $(I_{def})_i$, $i \in 1, 2, \ldots, N$, i.e., deformed frames, are recorded at a rapid sampling rate (e.g., >40 kHz) to capture transient deformations.

The corresponding spatio-temporal variation of the optical phase change, $\phi(m, n, t)$, is quantified by correlating the intensities of each deformed and reference frames with

$$\phi(m,n,t) = tan^{-1}\left[\frac{\rho\big(I_{ref}(m,n),\, I_{def}(m,n,t)\big)}{\rho\big(I_{ref+\pi/2}(m,n),\, I_{def}(m,n,t)\big)}\right] = tan^{-1}\left[\frac{\cos\big(\phi(m,n,t)\big)}{\sin\big(\phi(m,n,t)\big)}\right], \tag{4.1}$$

where m and n represent the local coordinate of the selected pixel, and ρ is the Pearson's correlation coefficient for finite discrete sets having the recoded intensities as arguments and computed based on a spatial kernel (e.g., with dimensions of 3×3 or 5×5 pixels) centered around each measurement point of a pair of reference and deformed frames [7–9].

4.2.2   *Continuous Phase Sampling Approach*

One of the advantages of LC method is that it requires only one phase shift. However, the method is highly sensitive to phase shifter calibration. In addition, due to the dynamical characteristics of the phase shifter and the speeds required for holographic acquisition, overshooting and ringing after $\pi/2$ phase shifting need to be taken into consideration. Furthermore, environmental
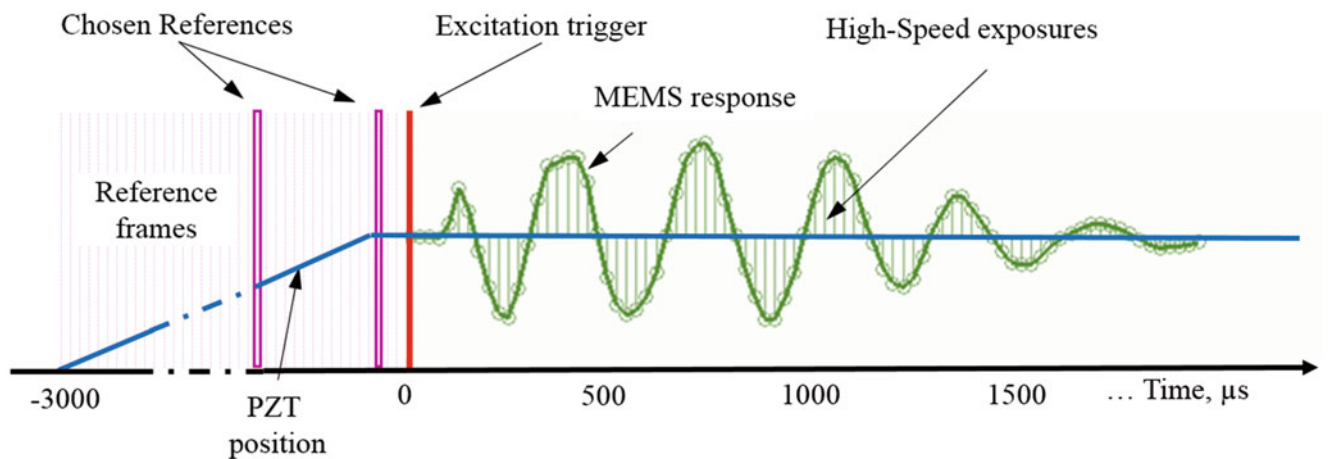
Fig. 4.1 Schematic representation of the events for $2 + N$ holographic acquisition with continuous phase shifting with a high-speed PZT nano-positioner

conditions and resolution of the driving electronics adversely affect the response of the phase shifter. To overcome the sensitivity of the LC method, we propose a continuous, rather than an instantaneous, phase shifting algorithm, as shown in Fig. 4.1. By using a phase-quality optimization algorithm the frames corresponding to the most accurate $\pi/2$ phase shift is identified. This modification produces repeatable and stable HDHS measurements. It also helps to eliminate precision issues caused by nanometer positioning errors and/or variations of other opto-mechanical elements in the setup.

4.2.3 Modular Interferometric Station (MIS)

We are developing a custom-made Modular Interferometric Station (MIS) for high-precision opto-mechanical measurements, shown in Fig. 4.2. MIS is capable of different measuring modalities including, confocal microscopy, white light interferometry, and Laser Doppler Vibrometery [10, 11]. In addition, MIS is equipped with a vacuum chamber having working channels to control environmental conditions and electromechanical components for testing a variety of samples. Moreover, MIS custom design contains pneumatic dampers and a large mass to cancel environmental vibrations. To expand the measuring modalities of MIS, an HDHS module has been developed and implemented, as shown in Fig. 4.2b, c.
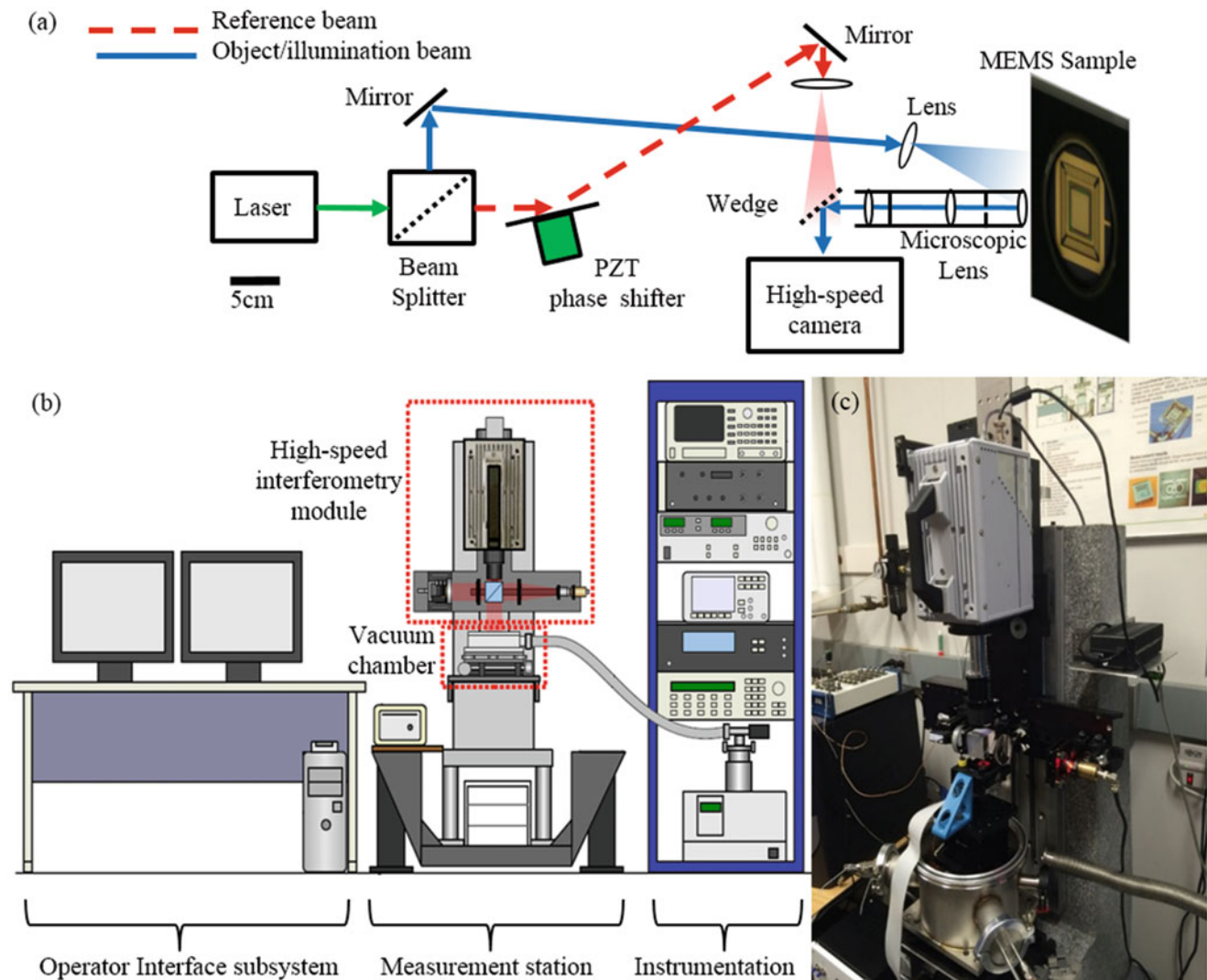
Fig. 4.2 Modular interferometric station updated with high-speed measuring capabilities: (**a**) schematic representation of the HDHS module; (**b**) schematic showing subsystems within the station; and (**c**) optical head of the HDHS module and vacuum chamber

4.3 Deformable MEMS Mirror Device (DMD)

4.3.1 Device Capabilities

Deformable mirrors have many applications that include microscopy, retinal imaging, laser communications, and wavefront correction in astronomy. The deformable mirror of interest is a MEMS device typically used as an integral part of wavefront correction mechanisms, as shown in Fig. 4.3. The MEMS device contains an array of 12 by 12 electrostatically driven actuators interacting with a deformable thin reflective surface and each actuator having a maximum stroke of 1.5 μm driven at speeds of up to 3 kHz [12].

4.3.2 Control System

A multipurpose control software interface was developed to synchronize the motions of the DMD with HDHS acquisition. As shown in Fig. 4.4, the desired pattern and amplitudes for each piston are entered in the user interface and the camera is adjusted to have enough temporal and spatial resolution matching the desired MEMS operational frequency. The measurements presented herein were obtained with a camera set at 42 kHz with spatial resolution of 384 × 384 pixels and 3.9 μs exposure time.

4.4 Representative Results

Transient response of the DMD under various loading conditions was investigated. First, the piston at location-1, shown in Fig. 4.5a, b, is activated by 90 % of its 1.5 μm stroke. In the next step, the piston is deactivated to its original position and is followed by activating piston in location-4 to 80 % of its stroke. The transient motions at five specific locations are shown in Fig. 4.5c. In addition, six temporal instances of the transient motions from 571 to 2595 μs are shown in Fig. 4.6.

4.5 Conclusions and Future Work

Some of the measuring capabilities of a HDHS under development were demonstrated by testing the transient response of a high-speed deformable MEMS device (DMD). High temporal and spatial (i.e., microseconds at >140,000 data points) resolutions of HDHS enables concomitant measurements at all points to quantify spatial and temporal motion parameters, including modal frequencies, time constants, Q-factors, changes in shapes, and surface strains. These measurements enable
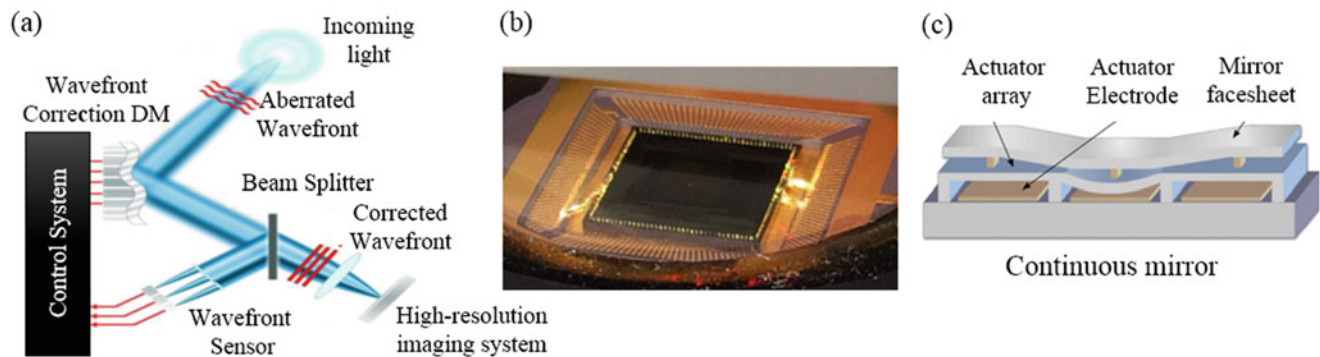
Fig. 4.3 MEMS deformable mirror of interest [12]: (**a**) schematic representation of a closed-loop wavefront correction system that includes adaptive optics in the form of a deformable mirror; (**b**) view of the reflective surface of the MEMS device of interest; and (**c**) schematic of the actuation mechanisms
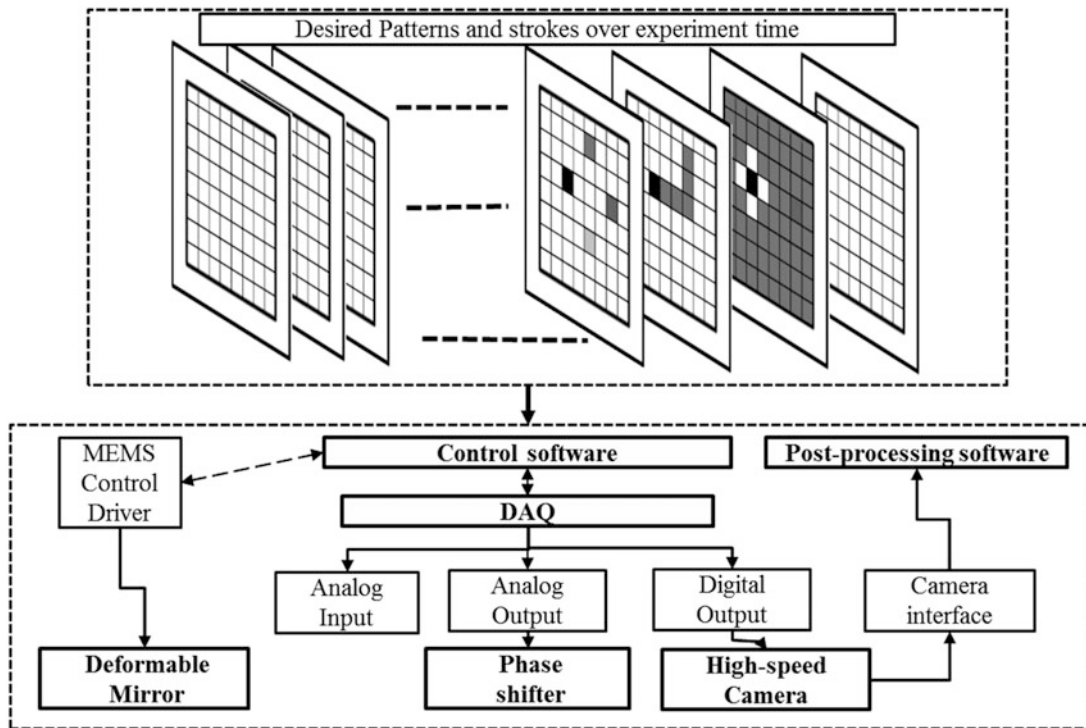
Fig. 4.4 Schematic representation of the HDHS control system synchronized with the driving mechanisms of the DMD
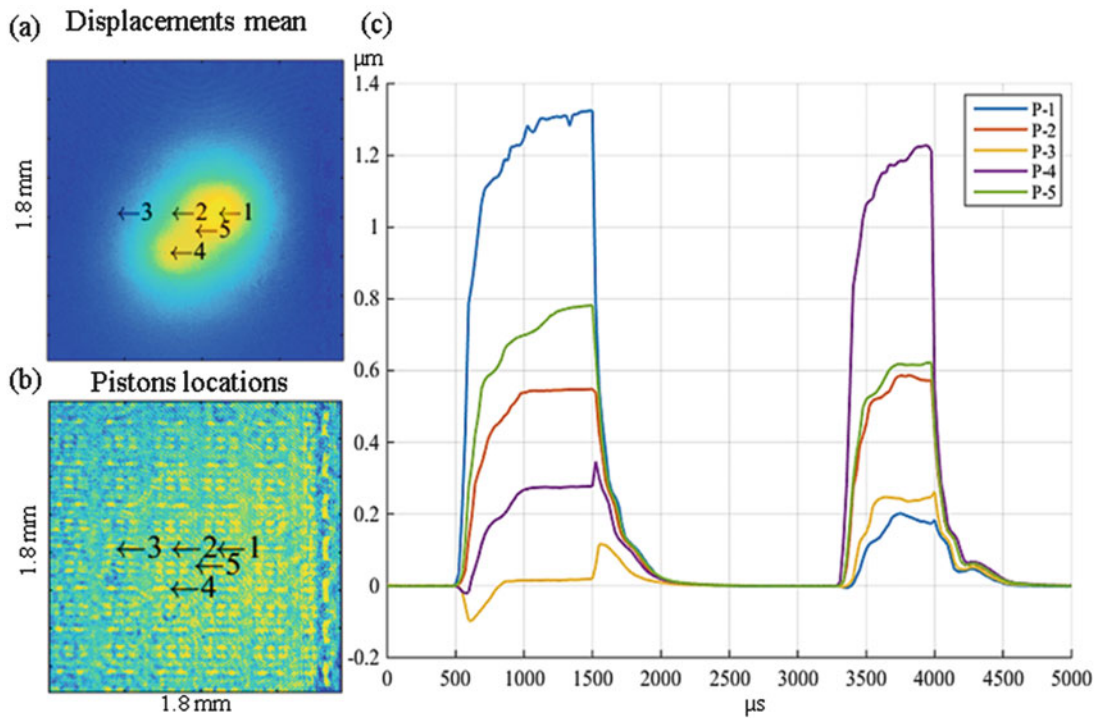
Fig. 4.5 Transient motions of the DMD after following a specific actuation sequence: (**a**) average mean of the displacements throughout the entire loading sequence; (**b**) undeformed DMD showing specific locations of interest; and (**c**) corresponding transient deformations at those selected points. Locations *1* and *4* are the activated pistons with 90 % and 80 % of their stroke, respectively
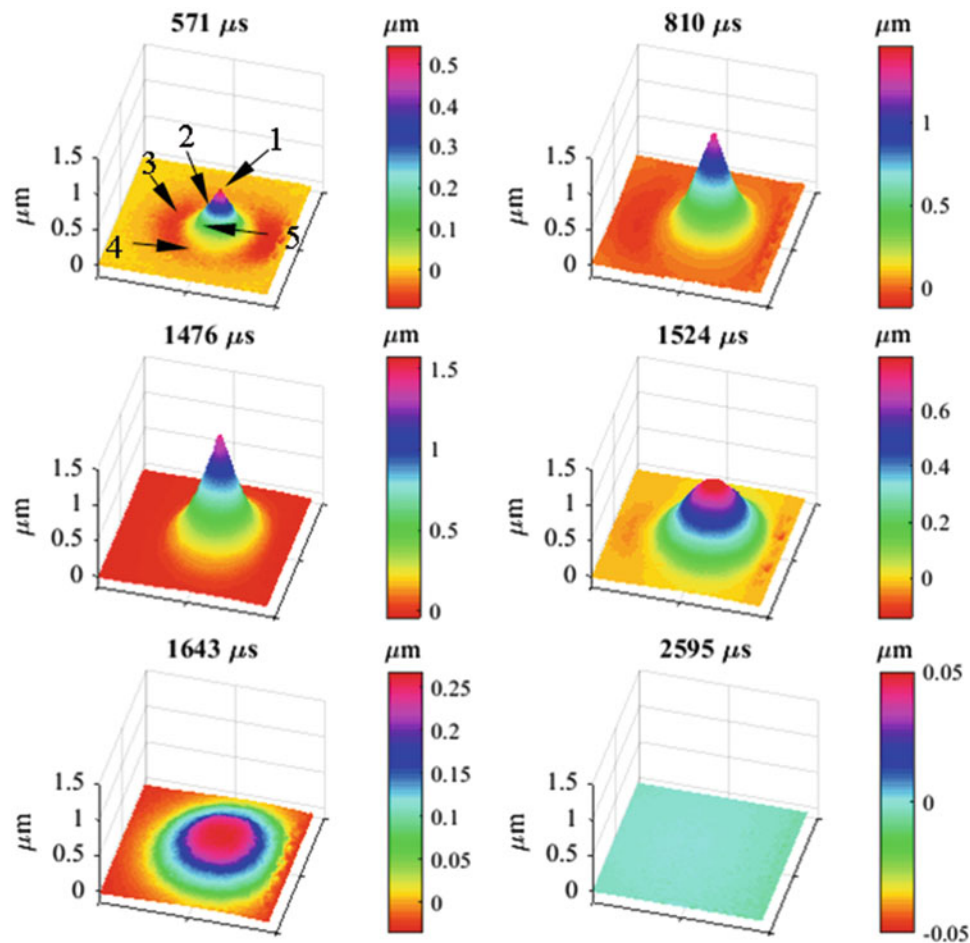
Fig. 4.6 Full-field of view 3D representation of motions at six selected temporal instances during the activation of the piston at location *1*

the design optimization of high-performance MEMS devices to reduce their fabrication costs and further improve their performance, specifically at higher speeds, which require full-field-of-view measurement tools such as HDHS.

References

1. Novak, E.: MEMS metrology techniques. In: Proc. SPIE 5716, Reliability, Packaging, Testing, and Characterization of MEMS/MOEMS IV, pp. 173–181 (2005). doi:10.1117/12.596989
2. Furlong, C., Pryputniewicz, R.J.: Optoelectronic characterization of shape and deformation of MEMS accelerometers used in transportation applications. Opt. Eng. **42**, 1223–1231 (2003)
3. Rembe, C., Kant, R., Muller, R.S.: Optical measurement methods to study dynamic behavior in MEMS. In: Proceedings of SPIE 4400, Microsystems Engineering: Metrology and Inspection, pp. 127–137 (2001)
4. Lal, A., Jo, J.S., Kupiec, S., Scott, E., Trolinger, J.:, Instrumentation for characterizing a new class of optical domes. In: Proceedings of SPIE 7302, Window and Dome Technologies and Materials XI, 73020P (2009)
5. Millerd, J.E., Brock, N.J.: Methods and apparatus for splitting, imaging, and measuring wavefronts in interferometry. US Patent 7,298,497, 2007
6. Creath, K.: Phase-shifting speckle interferometry. Appl. Opt. **24**, 3053–3058 (1985)

7. Dobrev, I., Furlong, C., Cheng, J.T., Rosowski, J.J.: Full-field transient vibrometry of the human tympanic membrane by local phase correlation and high-speed holography. J. Biomed. Opt. **19**, 096001–096001 (2014)
8. Georgas, P.J., Schajer, G.S.: Modulo-2pi phase determination from individual ESPI images. Opt. Lasers Eng. **50**, 1030–1035 (2012)
9. Razavi, P., Dobrev, I., Ravicz, M., Cheng, J.T., Furlong, C., Rosowski, J.J.: Transient response of the eardrum excited by localized mechanical forces. In: Tekalur, S.A., Zavattieri, P., Korach, C.S. (eds.) Mechanics of Biological Systems and Materials, vol. 6, pp. 31–37. Springer, New York (2016)
10. Klempner, A.R.: Development of a Modular Interferometric Microscopy System for Characterization of MEMS, MS Thesis, Worcester Polytechnic Institute, Worcester, MA (2006)
11. Klempner, A.R., Marinis, R.T., Hefti, P., Pryputniewicz, R.J.: Experimental determination of the Q-factors of microcantilevers coated with thin metal films. Strain **45**(3), 295–300 (2009)
12. BostonMicromachines Co. http://bostonmicromachines.com

Chapter 5
Surface Orientation Measurement Using Sampling Moire Method

Motoharu Fujigaki, Daiki Tomita, and Yorinobu Murata

Abstract A sampling moire method is one of a deformation measurement method of a large structure such as a building and a bridge. The accuracy of phase difference analysis is from 1/100 to 1/1000 of the grating pitches. This method can analyze two-dimensional phases from a two-dimensional grating image attached on the surface of a specimen. This method can be applied to measure the surface orientation accurately using this feature. In this paper, we propose a method to measure a surface orientation of a specimen. The surface orientation can be measured with accuracy of 0.1 degrees. The principle and an experimental result to confirm the effectiveness are shown.

Keywords Sampling moire method • Surface orientation measurement • Inspection of large structure • 3D displacement measurement

5.1 Introduction

It is required to develop a deformation measurement method without contact for large structures such as a bridge, a steel tower, and tall buildings in real-time. 3D displacement measurement of infrastructures is also required for a defect inspection on site and a fixed-point observation system for raising an alarm.

Phase analysis method of a grating is one of the useful methods to measure deformation accurately. It is better to measure deformation from one-shot image in the case of a moving object or a vibrating object. A spatial fringe analysis method using sampling technique to analyze phase distribution of moire images produced from one-shot grating image in a computer were proposed by Arai et al. [1]. This method is applied to phase analysis of two-dimensional grating image. We called this method a sampling moire method. This method was applied to deformation and strain measurement [2–4]. The accuracy of phase difference analysis is in the range between 1/100 and 1/1000 of the grating pitch. The accuracy of this method is very high. This is due to the phase of the grating pattern which is analyzed using a phase-shifting method. The phase-shifting method can be performed by generating phase-shifted moire images in a computer via a one-shot grating image.

The sampling moire method can analyze 3D displacement using several cameras. The calibration is important for the calculation. In the conventional calibration method, the parameters of the calculation can be obtained with moving a reference plane located on the object [5]. However, in this case of a large object, it is difficult to move the reference plane. It is necessary to know the camera angle for the calibration to measure the 3D displacement of a large object. In this paper, a method to measure a surface orientation of a specimen is proposed. The principle and an experimental result to confirm the effectiveness are shown.

M. Fujigaki (✉)
Graduate School of Engineering, University of Fukui, 3-9-1 Bunkyo, Fukui 910-8507, Japan
e-mail: fujigaki@u-fukui.ac.jp

D. Tomita
Graduate School of Systems Engineering, Wakayama University, 930 Sakaedani, Wakayama 640-8510, Japan
e-mail: s152029@sys.wakayama-u.ac.jp

Y. Murata
Faculty of Systems Engineering, Wakayama University, 930 Sakaedani, Wakayama 640-8510, Japan
e-mail: murata@sys.wakayama-u.ac.jp

5.2 Principle of Sampling Moire Method

The sampling moire method can analyze the phase distribution of a grating image. Figure 5.1 shows the scheme of a special fringe analysis method. The phase analysis algorithm of a sampling method for 2D grating is the same as this method. Figure 5.1a shows the brightness distribution of an original grating pattern on the specimen. Figure 5.1b shows the grating image taken by a digital camera. Figure 5.1c shows the sampling process. First, a starting sampling point is determined, and the original grating image is sampled at intervals. A length of sampling pixels does not fulfill the definition of sampling theorem. In Fig. 5.1c, the pitch of the grating pattern image is 5 pixels. In this case, the length of the sampling pixels is 4 pixels. Next, the starting sampling point is changed, and a sample is taken again. This process is repeated for the same numbers of times as the sampling pitch. Figure 5.1d shows the linear interpolation process for four sampling pattern images. Figure 5.1e shows an initial phase of the linear interpolation process, which can be analyzed in the phase shift moire method.

Figure 5.2 shows an *x*-directional phase analyzed by the sampling moire method. In this study, a 2D grating pattern pasted on an object is analyzed. Figure 5.2a shows the 2D grating pattern image captured by a digital camera. Figure 5.2b shows a grating image obtained after smoothing process in the y-direction. By this process, *x*-dimensional phase distribution can be analyzed because the 2-D grating is converted into the pattern image as one-dimensional grating pattern image. Figure 5.2c shows phase-shifted sampling moire images produced from Fig. 5.2b. Figure 5.2d shows the phase distribution for x-direction produced from Fig. 5.2c by phase-shifting method. Figure 5.1e shows a grating phase for the *x*-direction

Fig. 5.1 Special fringe analysis method. (**a**) Grating, (**b**) captured grating by digital camera, (**c**) thinned grating pattern, (**d**) linearly-interpolation, (**e**) phase distribution of moire
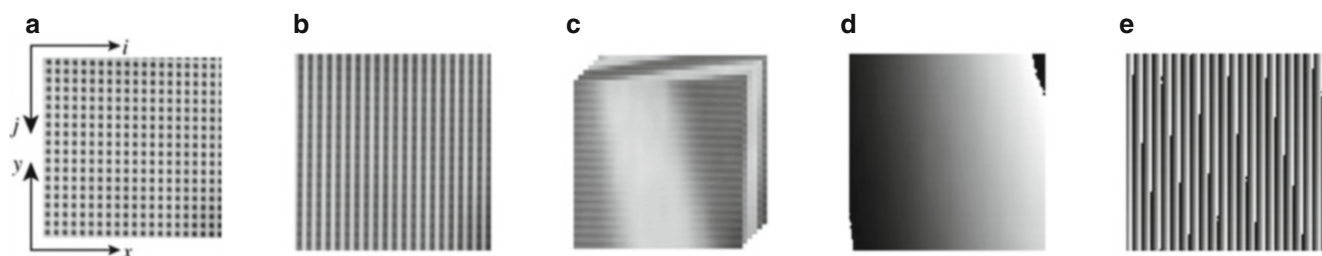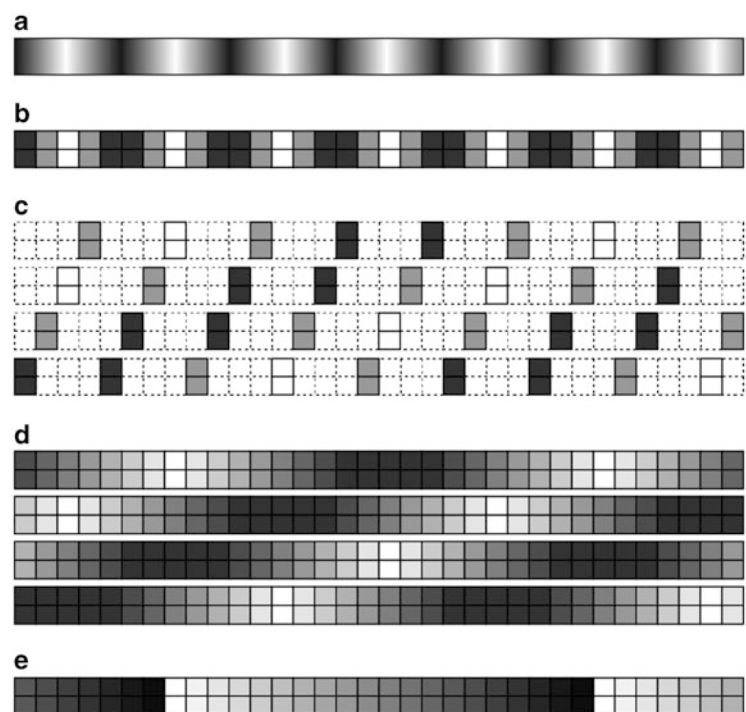
Fig. 5.2 Sampling moire method for *x*-directional analysis. (**a**) Original 2-D grating image, (**b**) grating image obtained after smoothing process in the *j*-direction, (**c**) phase-shifted sampling moire images produced from (**b**), (**d**) *x*-directional moire phase distribution, (**e**) *x*-directional grating phase distribution

obtained from Fig. 5.1d with subtracting the phase of grating of the reference sampling pitch. Next, a moire phase distribution θ_m, a reference phase distribution θ_r and a phase distribution of grid pattern θ_g can be calculated from Eq. (5.1):

$$\theta_g(i,j) = \theta_r(i,j) - \theta_m(i,j) \tag{5.1}$$

In the same process, the y-dimensional phase distribution can be obtained.

5.3 Method to Measure Surface Orientation

Figure 5.3a shows the arrangement of a target plate and a camera. The target has 2D grating on the surface. A camera is placed on a moving stage for the x' direction. The camera angle from the normal direction of a target is α. The position of the camera is changed with d_x' as shown in Fig. 5.3a. The displacement of the target in appearance becomes d_x as shown in Fig. 5.3b. The displacement of the target in appearance d_x can be obtained using a sampling moire method accurately. The angle α can be obtained from the following equation.

$$\alpha = \cos^{-1} \frac{d_x'}{d_x} \tag{5.2}$$

5.4 Experiment

Figure 5.4 shows an experimental setup. A camera is placed on a moving stage for the x' direction. A target plate with 2D grating of 10 mm pitches is placed on a rotary stage. The distance between the camera and the target is 2.3 m. The position of the camera is changed with 3.000 mm in each angle of rotary stage. A photograph of the target is shown in Fig. 5.4c. The horizontal and vertical pitches of the 2D grating on the surface are 10.00 mm and 9.96 mm, respectively.

A CMOS camera is used on this experiment. The image size taken by the camera is 512×512 pixels. The exposure time and the frame rate are set with 15 ms and 10 fps, respectively.

Firstly, the normal direction of the target surface is adjusted to the camera direction. Figure 5.5a, b shows the 2D phase distribution for the x- and the y-direcrions obtained by the sampling moire method when the angle is $0°$, respectively. Figure 5.6a, b shows the cross-sectional phase distribution along white lines in Fig. 5.5, respectively. The horizontal and vertical pitches of the 2D grating on the surface are obtained accurately from the phase distributions shown in Figs. 5.6a, b. Therefore, the normal direction of the target surface can be adjusted to the camera direction as the horizontal and vertical pitches become largest.

Figure 5.7a–g shows images taken by the camera at each angle. The target is tilted from the camera direction at intervals of $5°$ by a rotary stage. The surface angles are obtained by the above-mentioned method. The surface angles are analyzed at a center point of each image shown as a white cross mark in Fig. 5.8g. The results are shown on Table 5.1. The surface angles are also calculated as averaged values on a rectangle area shown as a white rectangle mark in Fig. 5.8g. The size of the rectangle area is 150×400 pixels. The results are shown on Table 5.2.

Fig. 5.3 Principle of identification method of a camera angle. (a) Arrangement, (b) relationship between camera angle and displacements
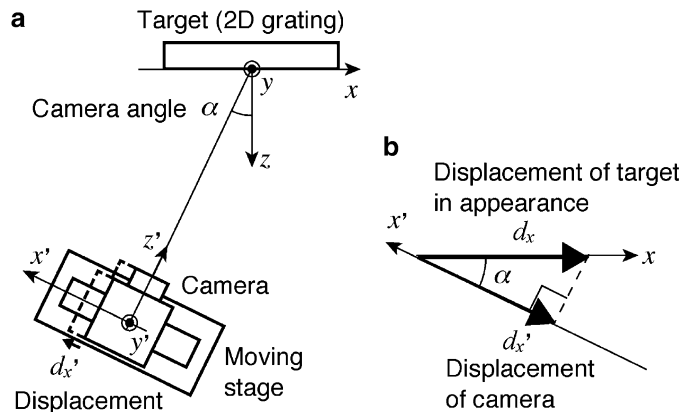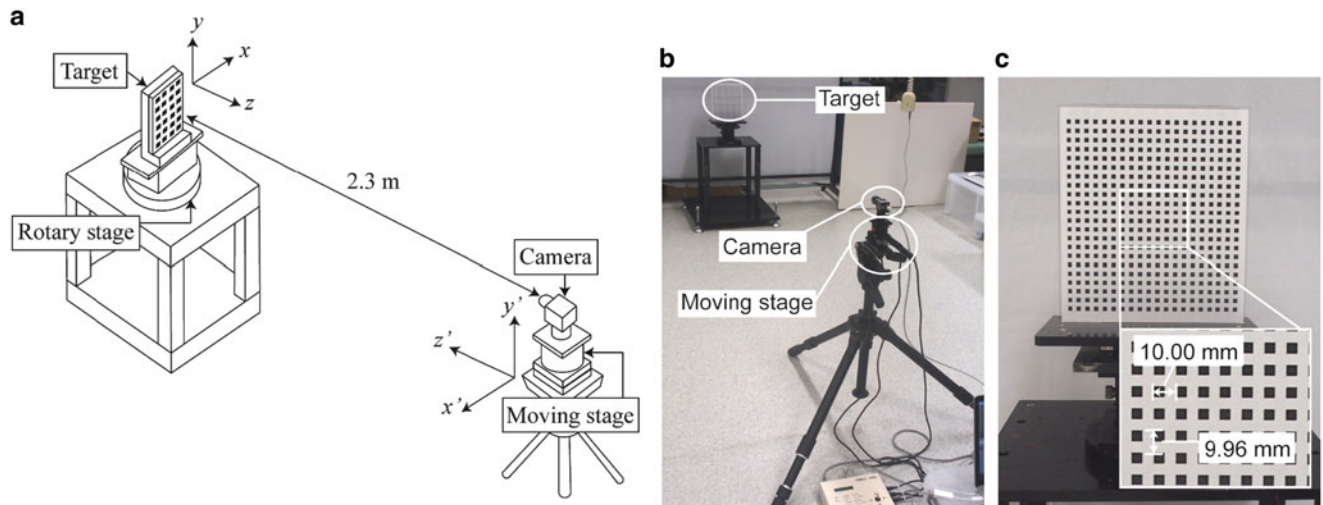
Fig. 5.4 Experimental setup. (**a**) Sketch, (**b**) photograph, (**c**) target

Fig. 5.5 Phase distribution
when the angle is 0°.
(**a**) *x*-Direction, (**b**) *y*-direction
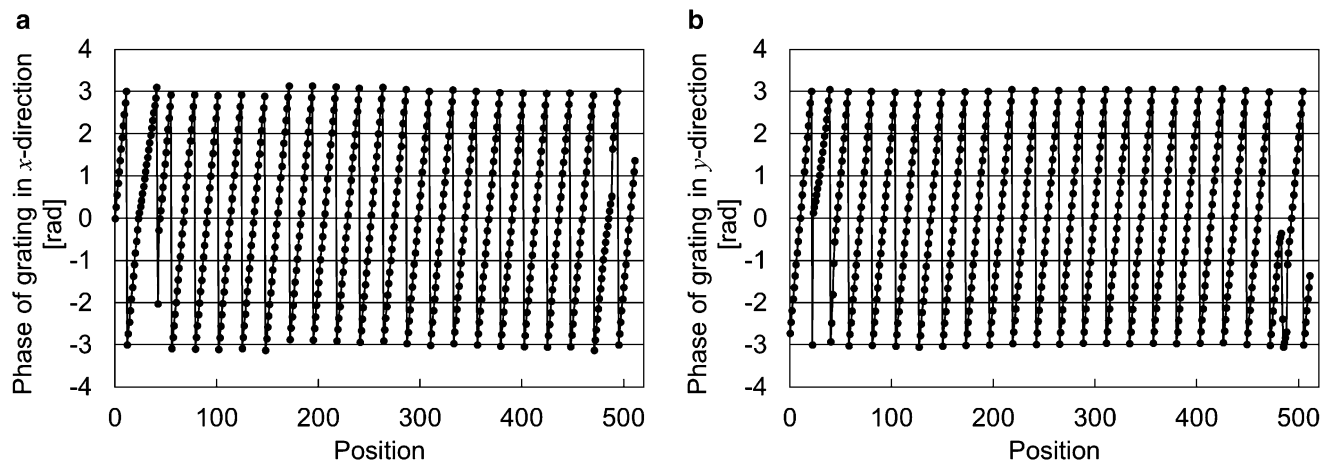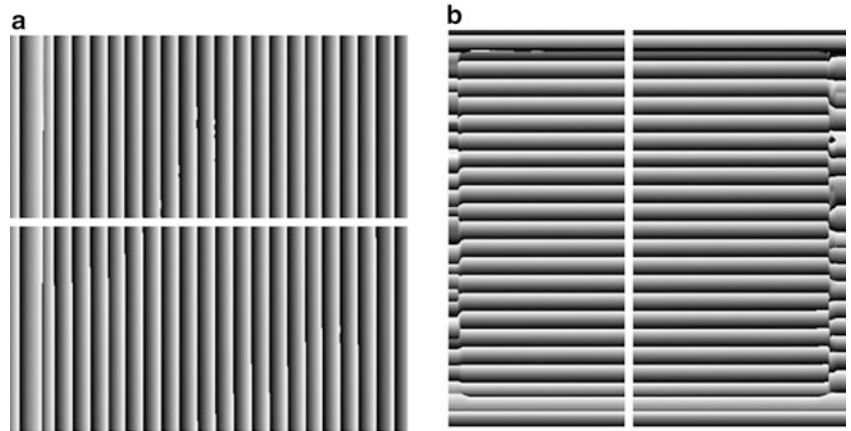
Fig. 5.6 Cross-sectional phase distribution along *white lines* in Fig. 5.5. (**a**) *x*-Direction, (**b**) *y*-direction
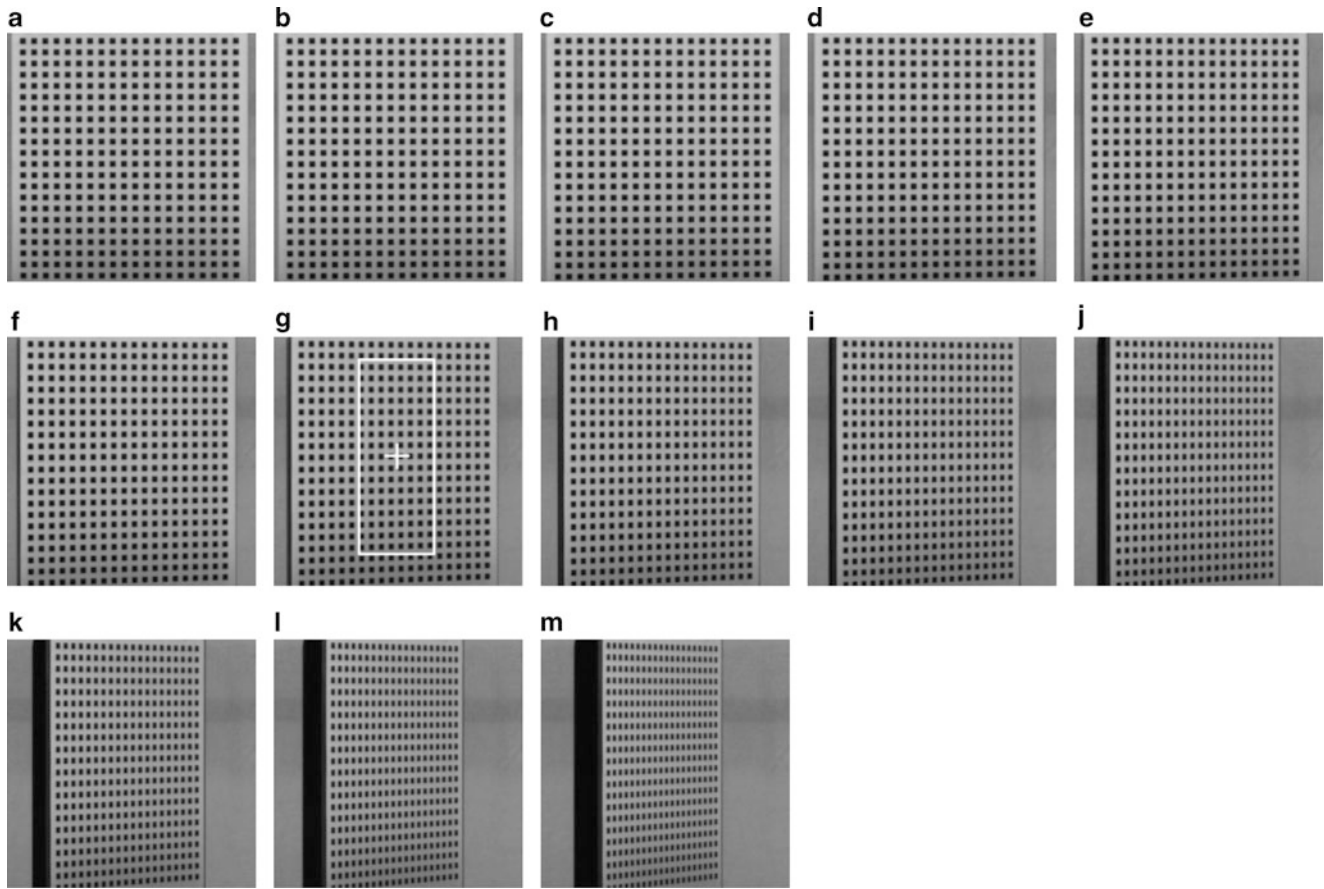
Fig. 5.7 Images taken by a camera with each camera angle. (**a**) 0°, (**b**) 5°, (**c**) 10°, (**d**) 15°, (**e**) 20°, (**f**) 25°, (**g**) 30°, (**h**) 35°, (**i**) 40°, (**j**) 45°, (**k**) 50°, (**l**) 55°, (**m**) 60°
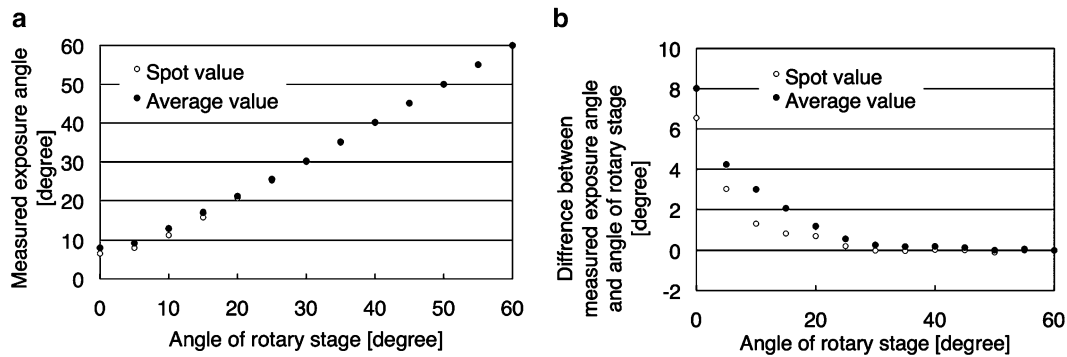
Fig. 5.8 Results of surface angle measurement. (**a**) Measured surface angle, (**b**) error

The results of the measured surface angle are shown in Fig. 5.8a. The errors between the given angle and the measured angle are shown in Fig. 5.8b. The error of the spot value and the average value when the rotating angle is 30° are 0.27° and −0.01°, respectively. The average and standard deviation of errors of the spot value from 30° to 60° are 0.42° and 0.09°. The average and standard deviation of errors of the average value from 30° to 60° are −0.01° and 0.04°. These results show effectiveness of the proposed method.

Table 5.1 Results of surface angle measurement at a center point

Angle of rotary stage (degree)	Measured exposure angle (degree)	Error (degree)
0.00	8.02	8.02
5.00	9.24	4.24
10.00	13.00	3.00
15.00	17.06	2.06
20.00	21.17	1.17
25.00	25.57	0.57
30.00	30.27	0.27
35.00	35.19	0.19
40.00	40.20	0.20
45.00	45.14	0.14
50.00	50.01	0.01
55.00	55.07	0.07
60.00	60.00	0.00

Table 5.2 Results of surface angle measurement on a rectangle area

Angle of rotary stage (degree)	Measured exposure angle (degree)	Error (degree)
0.00	6.55	6.55
5.00	8.02	3.02
10.00	11.29	1.29
15.00	15.84	0.84
20.00	20.71	0.71
25.00	25.21	0.21
30.00	29.99	−0.01
35.00	34.97	−0.03
40.00	40.03	0.03
45.00	45.01	0.01
50.00	49.90	−0.10
55.00	55.00	0.00
60.00	60.00	0.00

5.5 Conclusions

In this paper, a method to measure a surface orientation of a specimen using a sampling moire method was proposed. The surface orientations were measured with accurately. The error was smaller than $0.1°$ when the orientation is more than $30°$. The experimental results showed the confirmation of the effectiveness of the proposed method.

References

1. Arai, Y., Yokozeki, S., Shiraki, K., Yamada, T.: High precision two-dimensional spatial fringe analysis method. J. Mod. Opt. **44**(4), 739–751 (1997)
2. Ri, S., Fujigaki, M., Morimoto, Y.: Sampling moire method for accurate small deformation distribution measurement. Exp. Mech. **50**(4), 501–508 (2010)
3. Shimo, K., Fujigaki, M., Masaya, A., Morimoto, Y.: Development of dynamic shape and strain measurement system by sampling moire method. In: ICEM2009, Proceedings of SPIE, pp. 7522 (2009)
4. Hanada, R., Miyazawa, M., Fujigaki, M., Simo, K., Morimoto, Y.: A sampling moire method to measure the dynamic shape and strain of rotating tires. Tire Sci. Technol. **41**(3), 214–225 (2013)
5. Tomita, D., Fujigaki, M., Murata, Y.: Evaluation of accuracy for 3D displacement measurement using sampling moire method with multiple cameras. In: 9th International Symposium on Advanced Science and Technology in Experimental Mechanics (9th ISEM '14-New Delhi), #091 (CD-ROM) (2014)

Chapter 6
DD-DIC: A Parallel Finite Element Based Digital Image Correlation Solver

Jean-Charles Passieux, Robin Bouclier, and Jean-Noël Périé

Abstract The computational burden associated to finite element based digital image correlation methods (FE-DIC) is mostly due to the inversion of global FE systems and to global image interpolations. On the contrary, subset based approaches require only subimages, and allow solving small independent systems in parallel. A variable separation technique was recently proposed that alleviate mesh constraints in FE-DIC. However, in digital volume correlation, the question of the interpolation of the images becomes a real issue. For that reason, a non-overlapping dual domain decomposition method is proposed to rationalize the computational cost of high resolution FE-DIC measurements when dealing with large datasets. It consists in splitting the global mesh into submeshes and the images into subimages. The displacement continuity at the interfaces between subdomains is obtained iteratively by using a preconditioned conjugate gradient. It will be shown that the method combines the metrological performances of finite element based DIC and the parallelization ability of subset based DIC methods.

Keywords Digital image correlation • Parallelization • Dual domain decomposition • Finite element • Mechanical regularization

6.1 Introduction

The use of full-field measurements becomes increasingly relevant for the analysis of the mechanical behavior of materials and structures. It is mainly due the large quantity of data they provide. Because of the inexorable improvement of the hardware, this amount of data is rapidly rising. Efficient numerical methods have to be developed to be able to analyze these data within an affordable computational time.

Digital Image Correlation (DIC) has become one of the most popular full-field techniques because of a favorable ease of use to accuracy ratio [1] and because of its ability to deal with 3D measurements on the surface (stereo DIC) and also in the bulk with Digital Volume Correlation (DVC). In continuum solid mechanics, finite element based DIC (FE-DIC [2–9]) has proved to be a relevant choice since (a) it allows for interpolation-free communications with finite element simulations, (b) it significantly reduces the measurement uncertainties with respect to classical subset based approaches [10], since prescribed continuity of the unknown displacement fields acts as a regularization. The drawback of FE-DIC over subset-DIC [1] is the computational cost when high resolution is sought for [11]. Indeed, subset based DIC approaches lead to a set of small independent nonlinear systems of equations which are highly parallelizable, whereas FE-DIC methods lead to one global non-linear system whose inversion can become prohibitive with a large number of degrees of freedom [11].

In addition, due to the constantly increasing resolution of photographic sensors (standard sensors provide nowadays 29 million pixels, which can be extended up to 260 million pixels using a piezoelectric pixel shift), the manipulation and interpolation of images (large dense matrices) become more and more an issue [12]. This problem is even more acute with tomographic images for which even with a 2000×2000 pixels sensor, volume images may involve tens of billions of gray level data. The question of the computational time required for their analysis starts to be a burning issue.

J.-C. Passieux (✉) • J.-N. Périé
Université de Toulouse, Institut Clément Ader (INSA, ISAE, Mines Albi, UPS), CNRS UMR 5312,
3 rue Caroline Aigle, Toulouse 31400, France
e-mail: passieux@insa-toulouse.fr; jean-noel.perie@iut-tlse3.fr

R. Bouclier
Institut de Mathématiques de Toulouse, CNRS UMR 5219, INSA Toulouse, Université de Toulouse,
135 avenue de Rangueil, Toulouse 31077, France
e-mail: bouclier@insa-toulouse.fr

The two main causes responsible for the high computational cost of high resolution FE-DIC are thus (1) large system inversions and (2) large image interpolations. In this communication we will present a computational approach that addresses these limitations.

6.2 Finite Element Digital Image Correlation

Let us consider two grayscale images $f(\boldsymbol{x})$ and after $g(\boldsymbol{x})$ corresponding to the reference and deformed states of the specimen respectively. The displacement field between those two states is denoted $\boldsymbol{u}(\boldsymbol{x})$, where $\boldsymbol{x} \in \Omega$ is a point in the region of interest Ω of the (surface or volume) image. Given f and g, the DIC/DVC problem consists in finding the displacement field $\boldsymbol{u}^* \in \mathbf{L}^2(\Omega)$ (where $\mathbf{L}^2(\Omega)$ defines Hilbert space $[L^2(\Omega)]^d$ with $d = 2$ for DIC or 3 for DVC) that best fullfils the graylevel conservation equation [13]:

$$\boldsymbol{u}^{\star} = \underset{\boldsymbol{u} \in \mathbf{L}^2(\Omega)}{\mathrm{argmin}} \int_{\Omega} [f(\boldsymbol{x}) - g(\boldsymbol{x} + \boldsymbol{u}(\boldsymbol{x}))]^2 d\boldsymbol{x} \tag{6.1}$$

Problem (1) is nonlinear and solved by a Newton-like solver. At each iteration k, an estimate of $\boldsymbol{u}^k$ being known, the problem consists in finding the correction $\boldsymbol{\delta u}^k$ solution of the following variational problem:

$$\text{Find } \boldsymbol{\delta u}^k \in \mathbf{L}^2(\Omega) \text{ such that } \boldsymbol{a}(\boldsymbol{\delta u}^k; \boldsymbol{v}) = l^k(\boldsymbol{v}) \quad \forall \boldsymbol{v} \in \mathbf{L}^2(\Omega) \tag{6.2}$$

where $\forall (\boldsymbol{u}, \boldsymbol{v}) \in \mathbf{L}^2(\Omega) \times \mathbf{L}^2(\Omega)$,

$$\boldsymbol{a}(\boldsymbol{u}, \boldsymbol{v}) = \int_{\Omega} \boldsymbol{v}^T \nabla f \nabla f^T \boldsymbol{u} d\boldsymbol{x} \quad \text{and} \quad l^k(\boldsymbol{v}) = \int_{\Omega} \boldsymbol{v}^T \nabla f r(\boldsymbol{x}) d\boldsymbol{x} \tag{6.3}$$

where $r(\boldsymbol{x}) = f(\boldsymbol{x}) - g(\boldsymbol{x} + \boldsymbol{u}^k(\boldsymbol{x}))$ is the residual map. Then, the unknown displacement $\boldsymbol{\delta u}^k$ is searched for in an approximation subspace spanned by a set of basis functions $N_i(\boldsymbol{x})$, such that $\boldsymbol{\delta u}^k(\boldsymbol{x}) = \sum_i N_i(\boldsymbol{x}) q_i$ where $\boldsymbol{q}_i$ are the corresponding coefficients of the linear combination, referred to as degrees of freedom (dof). A galerkin approach yields the following linear system:

$$\boldsymbol{M} \boldsymbol{q}^k = \boldsymbol{b}^k \tag{6.4}$$

where $\boldsymbol{q}^k$ is a vector collecting the dof q^k_i and

$$\boldsymbol{M}_{ij} = \boldsymbol{a}(N_i(\boldsymbol{x}), N_j(\boldsymbol{x})) \quad \text{and} \quad \boldsymbol{b}_j^k = l^k(N_j(\boldsymbol{x})) \tag{6.5}$$

For the choice of the basis functions $N_i(\boldsymbol{x})$, finite element interpolation is more and more used in continuum solid mechanics. Indeed, besides the pioneer works of [2, 3], the studies using or developing FE-DIC is rich [4, 5] to name a few.

As mentioned in the introduction, high resolution finite element digital image correlation measurements induce high computational burden. A variable separation technique based on the Proper Generalized Decomposition (PGD) has first been proposed to reduce the computation time associated to the resolution of the FE systems [11, 14]. In two dimensions, the method allow for tremendous savings [11]. Nevertheless, in 3D-DVC, the manipulation of the images becomes more significant in the overall computing time, which makes the savings less impressive [14]. In the following, a non-overlapping dual domain decomposition method will be proposed to rationalize the computational cost of high resolution measurements when dealing with large images.

6.3   A Non-overlapping Dual Domain Decomposition Method

In the community of numerical simulation, a family of solvers, referred to as domain decomposition methods (DDM) has been developed for high performance computing on parallel computer architectures. The domain decomposition methods, such as Schwarz methods, were originally based on overlapping partitions of the studied region. Then non-overlapping methods were preferred because of their ease of implementation. The dual domain decomposition (such as Finite Element Tearing and Interconnecting, FETI [15]) seeks iteratively the displacement continuity at the interface assuming the equilibrium of the subdomains. On the contrary, primal domain decomposition methods (such as Balancing Domain Decomposition, BDD) prescribe displacement continuity and get iteratively equilibrium at the interface. Mixed and hybrid alternatives have also been proposed that mixes primal and dual approaches. See [16] for a review. Most often, the global problem is condensed onto the interface degrees of freedom and solved by a Krylov iterative algorithm [15]. The latter can be computed in parallel since it involves independent problems on each subdomain.

In the same way, a dual non-overlapping domain decomposition algorithm is proposed herein, in the context of FE-DIC, to alleviate both finite element system solving and image manipulation issues at the same time. The method consists in splitting the domain into a set of subdomains (with submeshes and subset images), see Figs. 6.1 and 6.2.

At iteration k of the quasi-Newton algorithm, standard FE-DIC formulations are first written in each subdomain $\boldsymbol{\Omega}_s$ (with $s = 1,\ldots, ns$) independently. Figure 6.3 present the typical displacements measured at this stage for the example presented in Fig. 6.2. Then, a set of Lagrange multipliers Λ are introduced in order to prescribe the displacement continuity across interfaces:
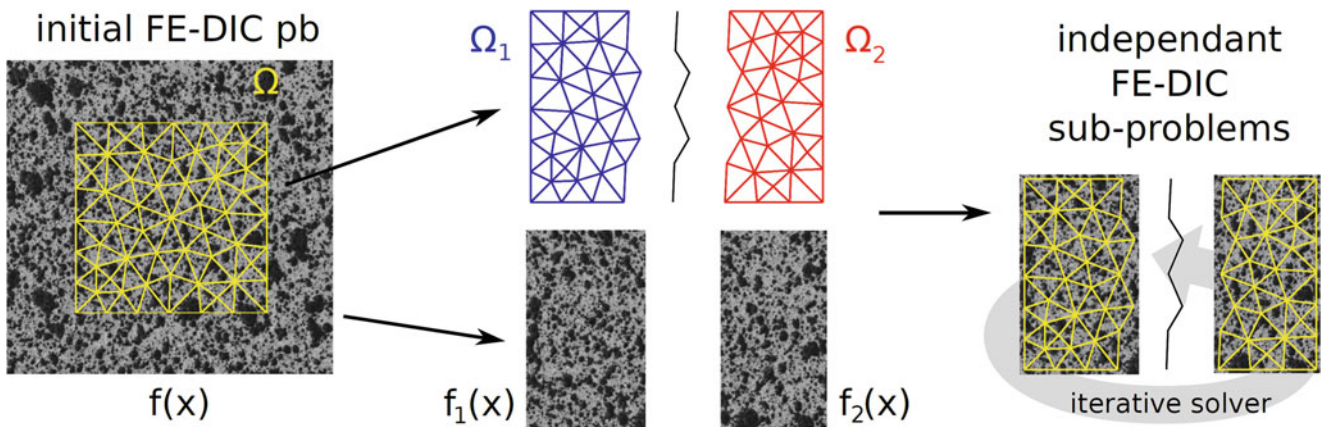
Fig. 6.1 Global image f and domain $\boldsymbol{\Omega}$ are decomposed in two subdomains $\boldsymbol{\Omega}_s$ and two subset images f_s. A set of subsets of image g is also built. Note that subdomains and submeshes are non-overlapping, but subset images presents some overlap
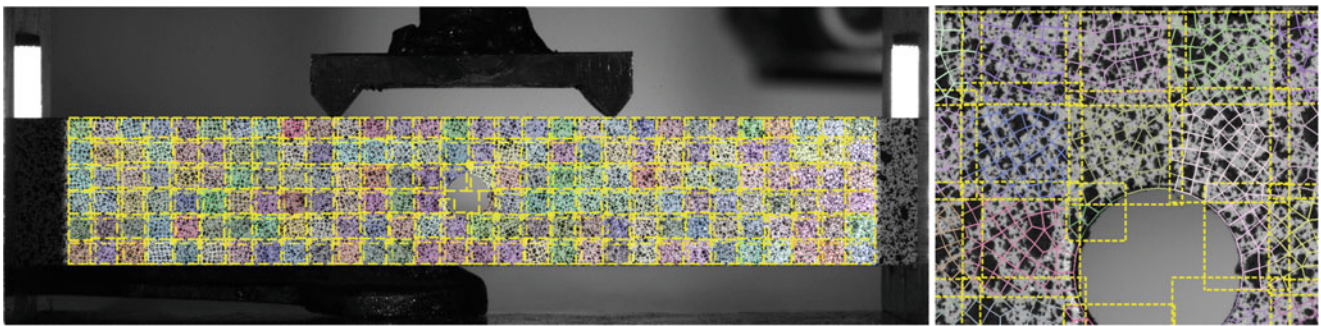
Fig. 6.2 Example of a four point bending test. A high resolution Charge-Coupled Device (CCD) camera (29 megapixels) has been used to capture images. The image and domain decomposition is presented here in the case of 179 subdomains. The overlapping subset images fs are in *yellow dashed line*. The finite elements belonging to a same subdomain are plotted with the same color. A zoom is provided on the *right*
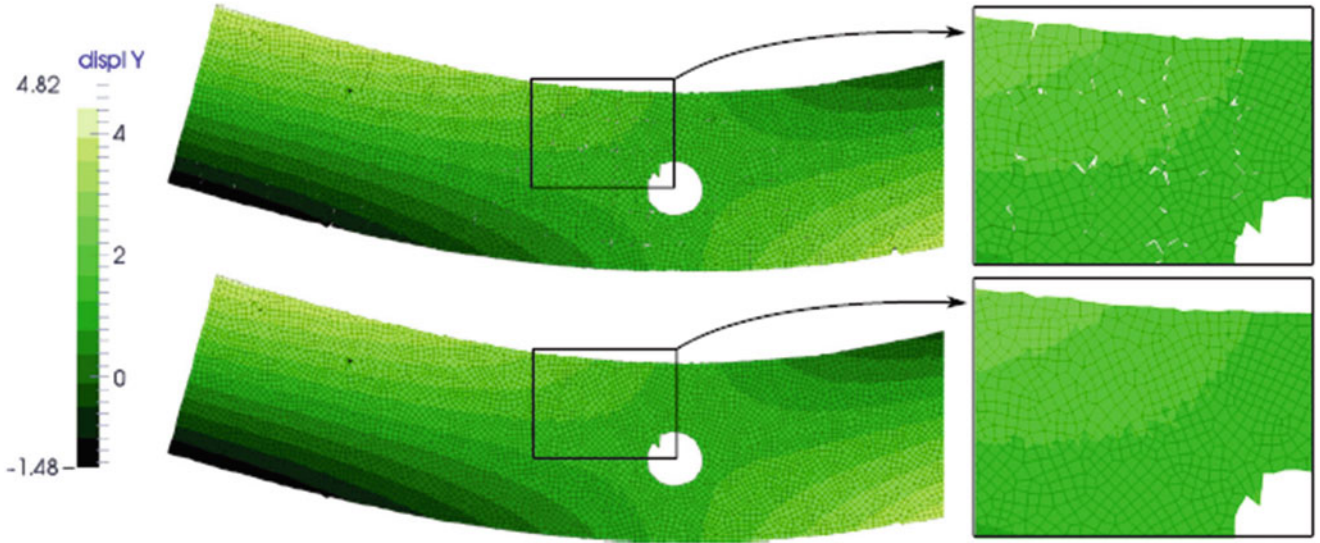
Fig. 6.3 Results for the four point bending test: displacement solution in pixels (amplification factor 50)—(*top*) finite element digital image correlation solution computed independently on each subdomain and (*bottom*) continuous solution computed by the domain decomposition method

$$\sum_s \boldsymbol{C}_s \left(\boldsymbol{q}_s^k + \boldsymbol{p}_s\right) = 0 \tag{6.6}$$

where $\boldsymbol{C}_s$ are coupling operators (which are signed boolean operators if the meshes are compatible at the interface) ans $\boldsymbol{p}s$ are the dof vector corresponding to the FE interpolation of $\boldsymbol{u}_s^{k-1}$. Then the problem is condensed onto the interface dofs Λ, which gives:

$$\boldsymbol{S}^d \Lambda = \boldsymbol{t}^k \tag{6.7}$$

where the condensed right hand side $\boldsymbol{t}^k$ and the so-called dual Shur complement operator $\boldsymbol{S}^d$ read:

$$\boldsymbol{t}^k = \sum_s \boldsymbol{C}_s \left(\boldsymbol{p}_s + \boldsymbol{M}_s^{-1}\boldsymbol{b}_s^k\right), \quad \boldsymbol{S}^d = \sum_s \boldsymbol{C}_s \boldsymbol{M}_s^{-1} \boldsymbol{C}_s^T. \tag{6.8}$$

Finally, the dual interface system is solved by a preconditioned conjugate gradient algorithm. This iterative solver only requires matrix–vector products of form $\boldsymbol{S}^d\boldsymbol{d}$, $\boldsymbol{d}$ being a given vector. As $\boldsymbol{S}^d$ is expressed as a sum on subdomains, performing the product corresponds to the following computation:

$$\boldsymbol{S}^d\boldsymbol{d} = \sum_s \boldsymbol{C}_s \boldsymbol{M}_s^{-1} \boldsymbol{C}_s^T \boldsymbol{d} = \sum_s \boldsymbol{C}_s \boldsymbol{y}_s \tag{6.9}$$

where $\boldsymbol{y}s$ is the solution of the set of local systems $\boldsymbol{M}_s\boldsymbol{y}_s = \boldsymbol{C}_s^T\boldsymbol{d}$, which corresponds to local correlation problems with different right hand sides. These system inversions are thus computationally affordable and, above all, independent from one subdomain to the other, which means that parallel processing can be used. Figure 6.3 (bottom) present the final displacements computed by the domain decomposition method for the example proposed in Fig. 6.2.

6.4 Mechanical Regularization

For more robustness, the proposed method is also extended to take into account a mechanical regularization of the optical flow. The addition of such regularization may appear necessary when dealing with poor textures (e.g. when dealing with tomographic images) or for identification purposes for instance [5]. The extension in this context relies on the introduction of

an additional Lagrange multipliers field that enforces the mechanical equilibrium at the subdomains interfaces. We thus end up with a three-field formulation involving the displacement unknown, the Lagrange multiplier associated to the kinematic compatibility and, the Lagrange multiplier corresponding to the equilibrium of the reaction forces. The obtained linear system can then be condensed onto the two sets of Lagrange multipliers. The resulting system has a four-block structure and can be efficiently solved in parallel by means of a specific Krylov iteration solver with a suitable preconditioning.

6.5   Conclusion

In this work, an efficient numerical tool is proposed to address the question of the computational cost associated to high resolution FE-DIC measurements and large datasets. It is based on a non-overlapping Dual Domain Decomposition method. The feasibility of the method is demonstrated on a set of synthetic and real examples. In practice, the proposed approach combines the advantages of FE-based DIC (lower uncertainties) and subset-based DIC methods (scalability). With the possibility of adding a mechanical regularization, the developed method may appear useful in a large variety of applications. It should constitute a good tool for performing regularized measurements and identification in challenging situations. For instance, the approach may be efficiently applied to extract relevant information from large tomographic images (involving poor image gradients in some localized regions).

References

 1. Sutton, M.A., Orteu, J.-J., Schreier, H.: Image Correlation for Shape, Motion and Deformation Measurements: Basic Concepts, Theory and Applications. Springer, New York (2009)
 2. Sun, Y., Pang, J.H.L., Khuen, W.C., Su, F.: Finite element formulation for a digital image correlation method. Appl. Optics **44**(34), 7357–7363 (2005)
 3. Hild, F., Roux, S.: Digital image correlation: from displacement measurement to identification of elastic properties—a review. Strain **42**, 69–80 (2006)
 4. Baldi, A., Francesconi, L., Medda, A., Bertolino, F.: Comparing two damage models under shear stress. Exp. Mech. **53**(7), 1105–1116 (2013)
 5. Réthoré, J., Muhibullah, Elguedj, T., Coret, M., Chaudet, P., Combescure, A.: Robust identification of elasto-plastic constitutive law parameters from digital image using 3D kinematics. Int. J. Solids Struct. **50**, 73–85 (2013)
 6. Fedele, R., Galantucci, L., Ciani, A.: Global 2D digital image correlation for motion estimation in a finite element framework: a variational formulation and a regularized, pyramidal, multi-grid implementation. Int. J. Numer. Methods Eng. **96**(12), 739–762 (2013)
 7. Passieux, J.-C., Bugarin, F., David, C., Périé, J.-N., Robert, L.: Multiscale displacement field measurement using digital image correlation: application to the identification of elastic properties. Exp. Mech. **55**(1), 121–137 (2015)
 8. Van Beeck, J., Neggers, J., Schreurs, P.J.G., Hoefnagels, J.P.M., Geers, M.G.D.: Quantification of three-dimensional surface deformation using global digital image correlation. Exp. Mech. **54**(4), 557–570 (2014)
 9. Wittevrongel, L., Lava, P., Lomov, S.V., Debruyne, D.: A self adaptive global digital image correlation algorithm. Exp. Mech. **55**(2), 361–378 (2015)
10. Hild, F., Roux, S.: Comparison of local and global approaches to digital image correlation. Exp. Mech. **52**(9), 1503–1519 (2012)
11. Passieux, J.-C., Périé, J.-N.: High resolution digital image correlation using proper generalized decomposition: PGD-DIC. Int. J. Numer. Methods Eng. **92**(6), 531–550 (2012)
12. Passieux, J.-C., Périé, J.-N., Salaün, M.: A dual domain decomposition method for finite element digital image correlation. Int. J. Numer. Methods Eng. **102**, 1670–1682 (2015)
13. Horn, B.K.P., Schunck, G.: Determining optical flow. Artif. Intell. **17**, 185–203 (1981)
14. Gomes Perini, L.A., Passieux, J.-C., Périé, J.-N.: A multigrid PGD-based algorithm for volumetric displacement fields measurements. Strain **50**(4), 355–367 (2014)
15. Farhat, C., Roux, F.X.: A method of finite element tearing and interconnecting and its parallel solution algorithm. Int. J. Numer. Methods Eng. **32**, 1205–1227 (1991)
16. Gosselet, P., Rey, C.: Non-overlapping domain decomposition methods in structural mechanics. Arch. Comput. Meth. Eng. **13**, 515–572 (2006)

Chapter 7
A New *In Situ* Planar Biaxial Far-Field High Energy Diffraction Microscopy Experiment

G.M. Hommer, J.S. Park, P.C. Collins, A.L. Pilchak, and A.P. Stebner

Abstract A new experimental platform that combines far-field high-energy diffraction microscopy (HEDM) and *in situ* planar biaxial loading is presented. The HEDM X-ray diffraction technique, which allows for non-destructive 3D microstructure measurements via serial reconstructions of 2D diffraction patterns, is briefly reviewed. Design attributes of a custom planar biaxial load frame and a new cruciform sample geometry for in situ HEDM experimentation are presented in detail. During the HEDM measurements, this new planar biaxial platform is capable of arbitrary combinations of tension and compression loading for studying full plane stress yield loci while localized gage stresses up to 1.8 GPa are generated with minimal influence from the cruciform geometry stress concentrations. The combination of these experimental capabilities demonstrates an ability to solve a long-standing problem of planar biaxial experimentation on nonlinear materials with unknown constitutive relations: how to measure the gage stress. Finite element results for isotropic elasticity are compared with classical plane stress analysis and digital image correlation (DIC) measurements, and all were found to be in good agreement.

Keywords Multiaxial • Experimental mechanics • Cruciform specimen design • Plane stress experiment • X-ray diffraction

Nomenclature

δ_{11}	Applied grip displacement in 11 direction
δ_{22}	Applied grip displacement in 22 direction
λ	δ_{11}/δ_{22}
ε_{11s}	FEA simulation gage strain in 11 direction
ε_{22s}	FEA simulation gage strain in 22 direction
λ_s	$\varepsilon_{11s}/\varepsilon_{22s}$
ε_{11a}	Analytic formulation gage strain in 11 direction
ε_{22a}	Analytic formulation gage strain in 22 direction
λ_a	$\varepsilon_{11a}/\varepsilon_{22a}$
ν	Poisson's ratio
E	Young's modulus
ε_{11}	Strain in 11 direction
ε_{22}	Strain in 22 direction
σ_{11}	Stress in 11 direction
σ_{22}	Stress in 22 direction

G.M. Hommer • A.P. Stebner (✉)
Mechanical Engineering Department, Colorado School of Mines, Brown Hall W350,
1610 Illinois Street, Golden, CO 80401, USA
e-mail: astebner@mines.edu

J.S. Park
Materials Physics and Engineering X-ray Science Division, Advanced Photon Source, Argonne National Laboratory,
9700 S. Cass Ave, Building 431-A004, Lemont, IL 60439, USA

P.C. Collins
Materials Science and Engineering, Iowa State University, 2240 Hoover Hall, 528 Bissell Road,
Ames, IA 50011-1096, USA

A.L. Pilchak
Air Force Research Laboratory, Wright-Patterson AFB, Ohio, OH 45433, USA

7.1   Introduction

7.1.1   Background

Advanced structural alloys often possess complex microstructures and low symmetry crystal structures that exhibit twinning, phase transformation and variations in strength between families of slip systems. These attributes may give rise to asymmetric mechanical behaviors, while processing (e.g., rolling, drawing, extruding, etc.) may further impart anisotropy. As such, their three-dimensional mechanical behaviors often cannot be fully understood through uniaxial characterizations. Historically, planar biaxial experiments have been developed to address the need for multiaxial characterizations during tension–tension loading of sheet metals—the primary mode of loading they experience during forming processes [1–11]. A standard cruciform geometry capable of tension–tension planar biaxial loading has been established [1]. A few planar biaxial experiments have been extended to tension–compression or compression–compression loading by clamping support plates on the specimen to prevent buckling [12, 13]. These approaches have been limited in their ability to drive localized deformation into the gage of the sample without influence from stress concentrations at the gage edges or the intersections of the arms of cruciform loading structures. Thus, the first challenge we aimed to address in designing a new experiment was to design planar biaxial specimen geometries capable of arbitrary compression–compression, tension–compression, and tension–tension gage deformations uninfluenced by the sample loading structure. We reported on the major features of such a sample at the 2015 Society of Experimental Mechanics meeting [14]. Here, we report on the final sample designs, including some modifications from last year's paper, and we also include a validation study. We also document the design of the custom planar biaxial load frame has been built that is capable of in situ multiaxial loading of these sample geometries during X-ray diffraction experimentation. The instrument and sample are capable of any arbitrary plane-stress deformation, in addition to load path change events. Thus, the micromechanics of full plane stress yield and transformation loci may be quantified in addition to path-dependent behaviors.

The 3D X-ray diffraction technique "far-field High Energy Diffraction Microscopy (HEDM)" allows for non-destructive micromechanics measurements via serial reconstruction of 2D diffraction patterns taken at small intervals (often $0.1°$ to $0.25°$) as samples are rotated (typically $360°$) [15–17]. Using Continuum Mechanics and crystallography, the (x, y, z) position of the center of mass of each grain within a polycrystalline sample, as well as the volume, phase, orientation tensor, and small strain tensor of each grain can be measured. From these data, multiscale micromechanical analyses can be performed to identify slip [18], twinning [19], and phase transformation mechanisms. The primary limitation of this technique is spatial resolution of X-ray diffraction measurements, which is on the order of 1 μm, meaning grain sizes must be larger than 5 μm for application of this technique to be feasible. Still, for large grain materials, it is possible to measure subgrain phenomena. Modern detector technologies and X-ray energies restrict the number of grains that can be observed at once to the order of 10,000, with 1000 or less grains being desirable. This latter limitation, however, is not a limiting factor in most experiments, as it is fairly easily overcome with X-ray focusing and collimation. In the past, computational analysis of the data were more limiting than any of these other challenges—analyzing the first data sets collected by a new research group took on the order of several years. However, years of focused and growing efforts has resulted in an ability to analyze some datasets as they are collected, and most data sets within several weeks. Users of the technique also have a variety of software choices including Fable [20], HEXRD [21], and MIDAS [22–25]—the best choice depends on the phenomena to be studied. Data analysis for far-field HEDM was carried out at the Advanced Photon Source (APS) of Argonne National Lab on their Orthros computing cluster using the MIDAS software package.

7.2   Methods

7.2.1   Experimental Setup

In situ diffraction experiments were carried out at Sector 1 in the 1-ID-E hutch of the Advanced Photon Source (APS) at Argonne National Lab. Key components of the experimental setup include incoming monochromatic X-ray beam that can be tuned to energies ranging from less than 30 to more than 120 keV (an energy of 71.676 keV was used in the experiments reported here), the planar biaxial load frame with mounted specimen, area X-ray detector in a far-field, transmission position, and stereo digital image correlation (DIC) assembly, all shown in Fig. 7.1a, b. Each of the four independent servohydrualic actuators built into the load frame has a 25 kN load capability and 50 mm of stroke. Each axis can be
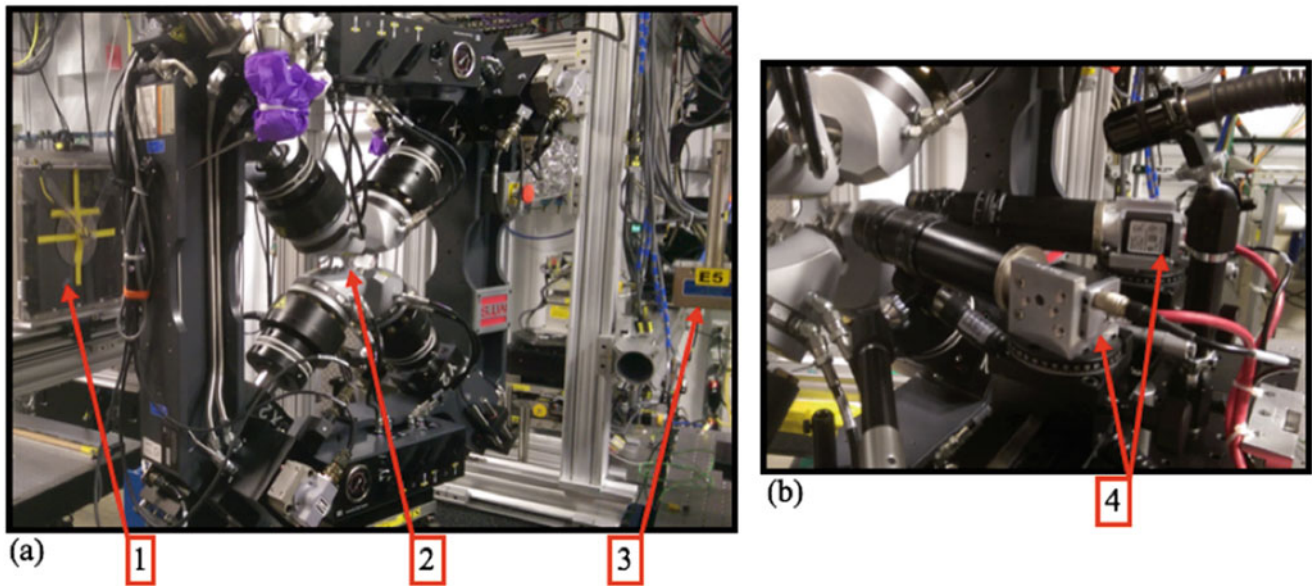
Fig. 7.1 Experimental setup in the 1-ID hutch of the APS at Argonne National Lab showing (*1*) the area detector, (*2*) the specimen mounted in the planar biaxial load frame, (*3*) the final X-ray beam collimation slits before it penetrates the sample, (*4*) and the DIC setup in image capturing position

corrected for concentric, angular, and rotational misalignment. For the experiments we report here, alignment was performed using a cruciform shaped alignment specimen instrumented with 32 strain gages. The maximum misalignment was less than 50 µε over all degrees of freedom as measured at 5 kN load and no-load conditions. The MTS controller has been verified to not move the specimen center more than 5 µm during 1 Hz out of phase cyclic loading, which represents a worst-case intended scenario. For the quasi-static loading used in the X-ray experiment, sample center position is held constant to better than 1 µm during loading. The sample is centered in the X-ray beam using a 6-axis goniometer. The top rotation stage is used to rotate the load frame 360° as each data point is recorded. For the experiments we report here, X-ray data collected during over 280° of this rotation is free from any shadowing from the load frame or grips. Furthermore, the "drift" of the sample center during the rotation was less than 5 µm over the entire 360° rotation. To achieve this result, stress in the hydraulic hoses was minimized by hanging them above the load frame in a helical configuration, which expanded and contracted uniformly during rotation in a manner that did not impose a bending moment on the goniometer. The DIC assembly was mounted on an actuator with better than 1 µm position repeatability that allowed it to extend into focal position to capture images and retract to prevent interference with load frame rotation.

7.2.2 Finite Element Analysis Approach

Finite element analysis (FEA) using ABAQUS [26] was used to design the specimen assuming isotropic linearly elastic material behavior with both aluminum 6061-T6 and fully annealed 4140 tool steel properties as inputs. Specimen symmetry allowed for one half-thickness quadrant of the geometry to be modeled with mirror boundary conditions, as is displayed for all FEA results (Figs. 7.4, 7.5, and 7.7). Displacement boundary conditions were used at the grips. Mesh convergence study was performed to ensure adequate element size. A minimum 10-element through-thickness was used to allow for out of plane stresses. The FEA elastic behavior was compared with an isotropic linearly elastic plane-stress analytic calculation for an infinite plate. Plane-stress comparison is supported by FEA results, as in-plane stresses in the gage were at least four orders of magnitude greater than out-of-plane stresses at all loads.

7.2.3 Specimen Preparation

Specimens were machined from fully annealed 4140 tool steel with ferrite surface grain sizes of approximately 5–10 μm. Larger grain sizes were desired for the HEDM technique, requiring heat treatment for grain growth. Thus, specimens were heat treated at 675 °C for 44 h in an argon evacuated bag with titanium alloy shavings to prevent oxidation. Resulting grain sizes were later determined through the HEDM analyses, as reported in Sect. 7.3.2.

7.3 Results and Discussion

7.3.1 Specimen Design

7.3.1.1 Geometries

Overall dimensions of the specimens are $5 \times 110 \times 110$ mm^3. These dimensions were chosen appropriately for load frame and load capacity. The 5 mm thickness is gradually reduced to 0.5 mm gage thickness through a 175 mm convex radius that starts at the end of the grips and connects to a 5 mm concave radius that leads into the 3.2 mm diameter gage, with all dimension interfaces being tangent. The 44.4° angle between grips and 12.2 mm arm intersection radii, and the radii itself are variable depending on the maximum stress desired in gage. A specimen geometry with these dimensions is shown in Fig. 7.2a. Maximum gage stresses are given relative to 22 kN proportional tension–tension or compression–compression biaxial loading for an isotropic linearly elastic material. Specimen geometries for maximum gage stresses of 400, 800, and 1700 MPa are shown in Fig. 7.3a–c, respectively. The 400 MPa specimen has arm intersection radii tangent and maximized relative to the grips. The 800 and 1700 MPa specimens have 12.2 mm are intersection radii which has been maximized with respect to overall and grip dimension requirements. Variable maximum gage stress is achieved by adjusting the angle between grips and arm intersection radii. This angle is 44.8° for 1700 MPa specimen, and 44.4° for 800 MPa specimen, as previously stated.
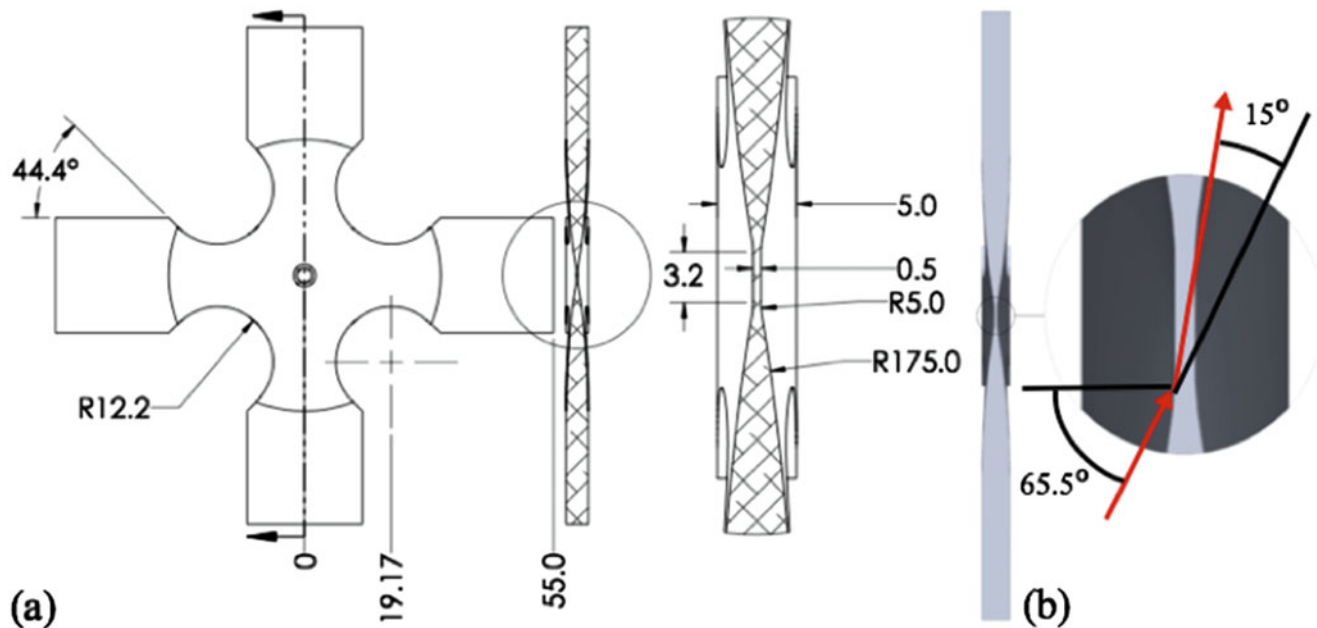
Fig. 7.2 Pertinent specimen dimensions with the 44.4° angle being specific to 800 MPa specimen shown (**a**) and schematic illustration of a beam incident at 65.5° on the gage perimeter, diffracting at 15° without intersection with material outside of gage (**b**)
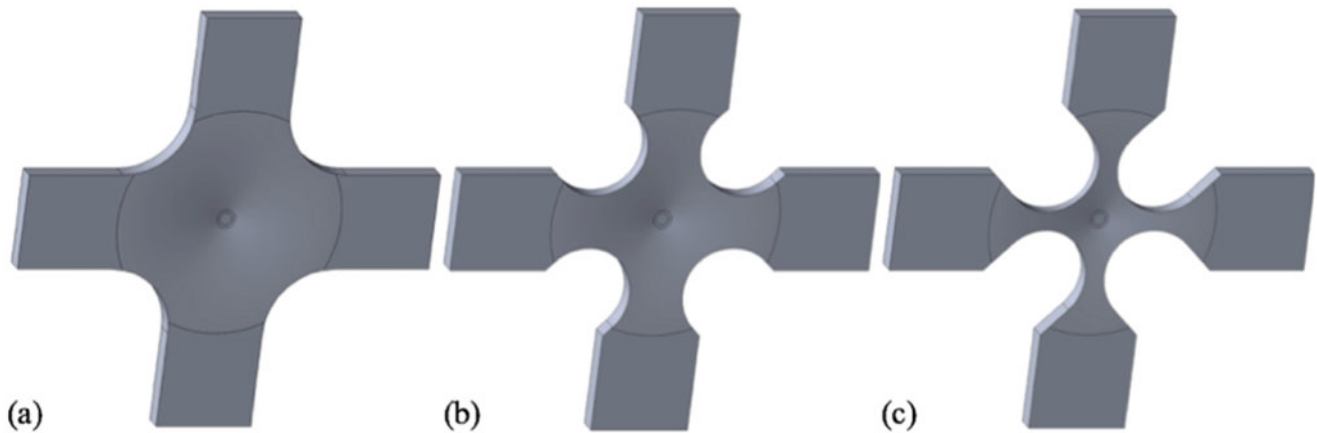
Fig. 7.3 Three specimen geometries with maximum gage stresses of 400 MPa (**a**), 800 MPa (**b**), and 1700 MPa (**c**)
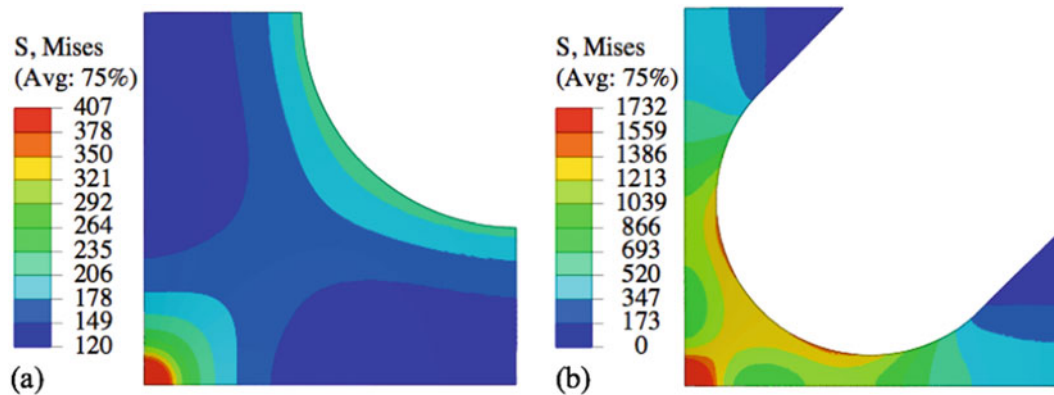
Fig. 7.4 FEA results showing maximum stress occurring in the gage under proportional tension–tension loading for 400 MPa and 1700 MPa specimens, (**a**) and (**b**), respectively

7.3.1.2 Diffraction Considerations

Gage geometry and lead-in radii to the gage were driven by diffraction considerations as well as mechanical behavior. Gage thickness and diameter combination results in maximum material penetration of 3 mm for a beam incident to the gage perimeter at 65.5° that diffracts at 15°, as is shown in Fig. 7.2b. These angles and material penetration represent extremes for diffraction without load frame shadowing and penetration issues related to beam energy. The lead-in radii are such that the aforementioned diffracted beam does not intersect the specimen after leaving the gage.

7.3.1.3 Mechanical Behavior

Maximum stress in specimen gage, shown in FEA results of Fig. 7.4a for 400 MPa specimen and Fig. 7.4b for 1700 MPa specimen, was achieved through reduction in thickness from 5 mm at grips to 0.5 mm in gage. Because dimensional gradients lead to stress concentration and disrupt load transfer, thickness reduction occurs as gradually as possible while still maintaining diffraction capability and maximum stress in the gage. The concave radius leading into the gage introduces an unavoidable stress concentration around the gage. The chosen 5 mm dimension causes a 10 MPa increase over gage stress. As a percentage of gage stress, it is worst in 400 MPa specimen at 2.5 %. Increasing the radius would reduce stress concentration, however, it would reduce definition of the gage as near maximum stresses would occur further outside due to a more gradual thickness increase stemming from the gage.

Fig. 7.5 FEA results for proportional tension–tension showing reduced stress zones at minimum arm width and uniform stress, units are Pa
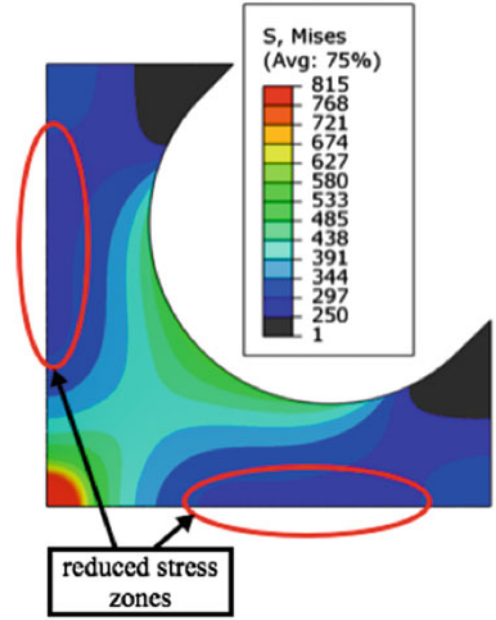
A consequence of removing material to increase maximum gage stress is increasing the stress concentration at arm intersection radii. This consequence is evident in Fig. 7.4a, b. This affects the extent to which plasticity can be studied. Stress fields at arm intersection radii of specimens with higher maximum gage stress will begin to interfere with the stress state of the gage, or even cause premature failure, at lower amount of gage plasticity. This behavior has also been considered by Van Petegem et al. [27].

Circular gage geometry was used to promote uniform elastic stress in, and axial load transfer to the gage. The disruption in load transfer imparted by specimen geometry is analogous to a hole in a plate, where a reduced stress zone occurs next to the hole. The gradual reduction in thickness leading into the gage prevents the reduced stress zone from occurring directly next to the gage, as was an issue in the G1 specimens of Hommer and Stebner [14]. Proportional tension–tension FEA results in Fig. 7.5 show reduced stress zone approximately centered at minimum arm width, as expected from classical stress concentration and crack-tip stress field formulations [28–30]. The load has sufficient distance after passing minimum arm thickness to redistribute and enter the gage uniformly.

FEA simulations were ran for 11 applied grip displacement ratios:

$$\lambda = \frac{\delta_{11}}{\delta_{22}} \tag{7.1}$$

Resulting strain data from the center of the gage was taken to formulate the corresponding FEA gage strain ratios:

$$\lambda_s = \frac{\varepsilon_{11s}}{\varepsilon_{22s}} \tag{7.2}$$

An analytic formulation for the gage strain ratio (Eq. (7.7)) as a function of the applied grip displacement ratio was derived from isotropic linearly elastic plane-stress in an infinite plate [31]:

$$\varepsilon_{11} = \frac{\sigma_{11}}{E} - \frac{\nu \sigma_{22}}{E} \tag{7.3}$$

$$\varepsilon_{22} = \frac{\sigma_{22}}{E} - \frac{\nu \sigma_{11}}{E} \tag{7.4}$$

As previously stated, the plane-stress assumption is supported by FEA results. When considering an infinite plate, strain and displacement are analogous. Rearranging and adopting the current work's nomenclature, Eqs. (7.3) and (7.4) become:

$$\varepsilon_{11a} = \delta_{11} - \nu \delta_{22} \tag{7.5}$$

$$\varepsilon_{22a} = \delta_{22} - \nu\delta_{11} \tag{7.6}$$

Through substitution of $\delta_{11} = \lambda\delta_{22}$ the analytic formulation for the gage strain ratio becomes:

$$\lambda_a = \frac{\lambda - \nu}{1 - \nu\lambda} \tag{7.7}$$

The analytic and FEA gage strain ratios are plotted against the applied grip displacement in Fig. 7.6. As the plane-stress assumption was previously justified, differences in gage strains can be attributed to stress concentration field effects occurring in 1700 MPa specimen and load dissipation effects occurring in 400 MPa specimen. As λ decreases, the points of maximum stress concentration move along the radii towards the axis of larger applied strain, analogously rotating and translating the corresponding stress fields. The stress concentration fields have minimum interference with the gage for proportional loading. As loading deviates from proportional, the stress concentrations move towards the gage, increasing interference. This explains gage strain difference trend between analytic and FEA of 1700 MPa specimen. This stress concentration field behavior is illustrated in Fig. 7.7, a simplified cruciform geometry with uniform thickness to emphasize

Fig. 7.6 Gage strain ratio vs. applied grip displacement ratio for FEA and plane stress of an infinite plate analysis formulation for strain
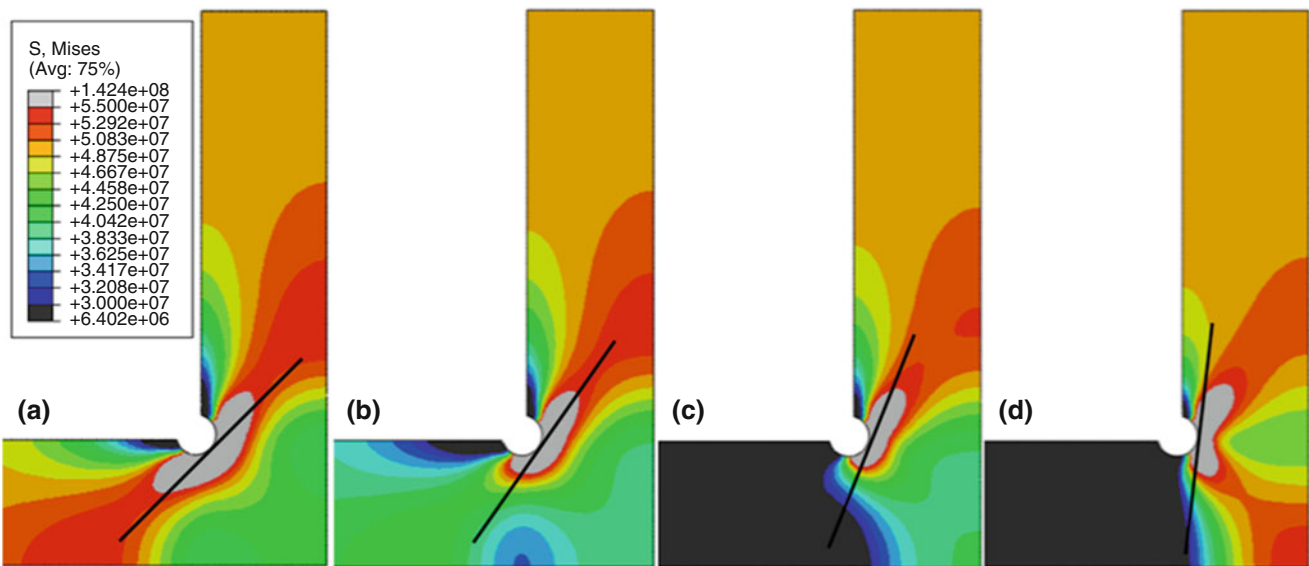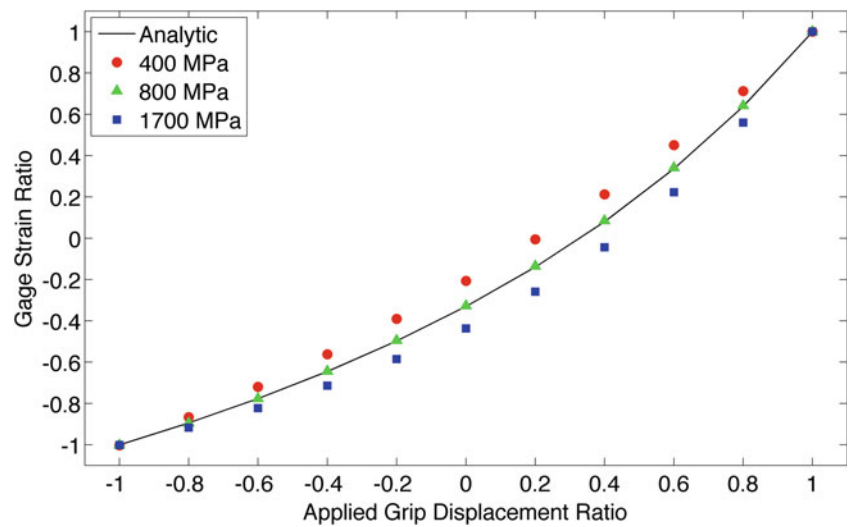
Fig. 7.7 Rotation and translation of stress concentration field with varying tension–tension applied grip displacement ratios of 1.0 (**a**), 0.8 (**b**), 0.5 (**c**), and 0 (**d**). As applied grip displacement ratio decreases, stress concentration field interference with the gage increases. The *black lines* are approximately tangent to point of maximum stress and rotate toward the vertical axis with decreasing λ. The geometry is a simplified cruciform specimen with uniform thickness. Units are Pa
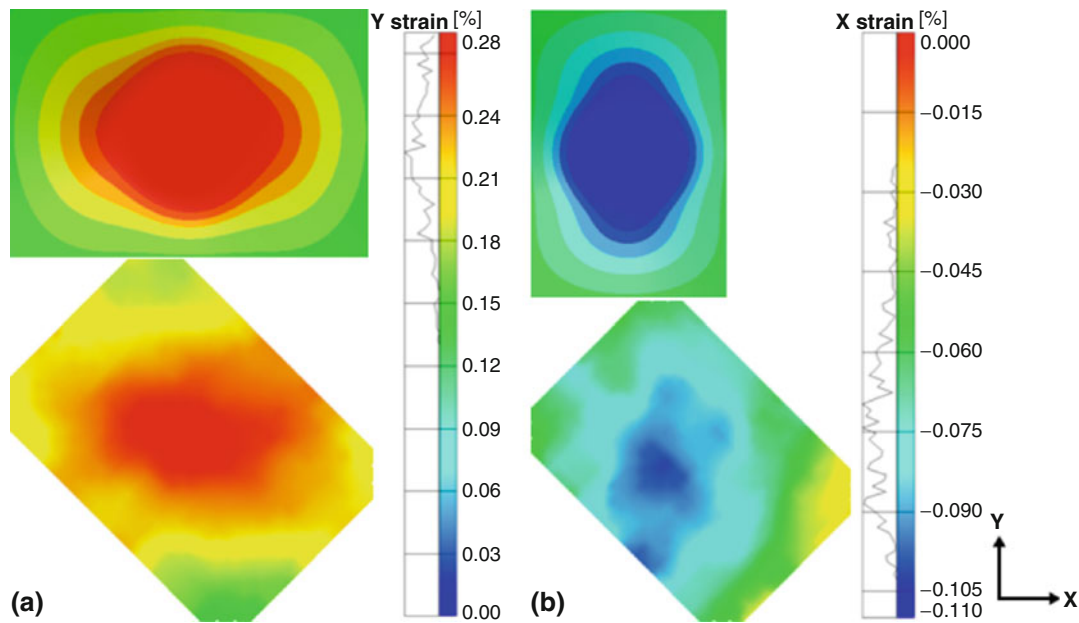
Fig. 7.8 FEA (*top*) and DIC (*bottom*) comparison of Y (**a**) and X (**b**) elastic gage strains in 4140 tool steel. FEA material model is isotropic. Applied load was 6 kN in Y and 0 kN in X

behavior of stress concentration fields, where the black lines are approximately tangent to point of maximum stress and rotate toward the vertical axis with decreasing λ. Additional material in 400 MPa specimen leads to incomplete load transfer, causing the gage strain difference trend between analytic and FEA.

7.3.1.4 Experimental Validation

DIC results of specimen gage from in-situ experiments at the APS provided preliminary experimental validation of FEA, shown in Fig. 7.8. Good agreement was found between the two. Specimen geometry used was 1100 MPa maximum gage stress. Quasistatic displacement rate to fixed loads of was 6 kN in Y and 0 kN in X was applied, which allowed for direct calculation of Poisson's ratio from gage strains. Poisson's ratio was found to be approximately 0.3, in good agreement with literature.

7.3.2 HEDM Grain Mapping

HEDM results from 4140 tool steel prior to loading are shown in Fig. 7.9. A large void is seen between the two surfaces of the gage where material is known to be present. A likely explanation is the heat treat performed grew only grains near the surface enough for the HEDM technique while interior grains remained below the threshold. Far-field HEDM can calculate grain volume but not morphology. Near-field HEDM must be used to obtain morphology. As a result, grain sizes are calculated assuming spherical shape. Grain radii, under this assumption, are accurately depicted in Fig. 7.9. Average grain radius was found to be 24.6 μm. Mises strain in principal form was calculated for each grain strain tensor using the average lattice parameter of all grains as the absolute lattice parameter, with an average of 0.00051. This is plausible considering the material was under no load. These results are in no way definitive, rather, they serve to demonstrate the capabilities of this experiment.
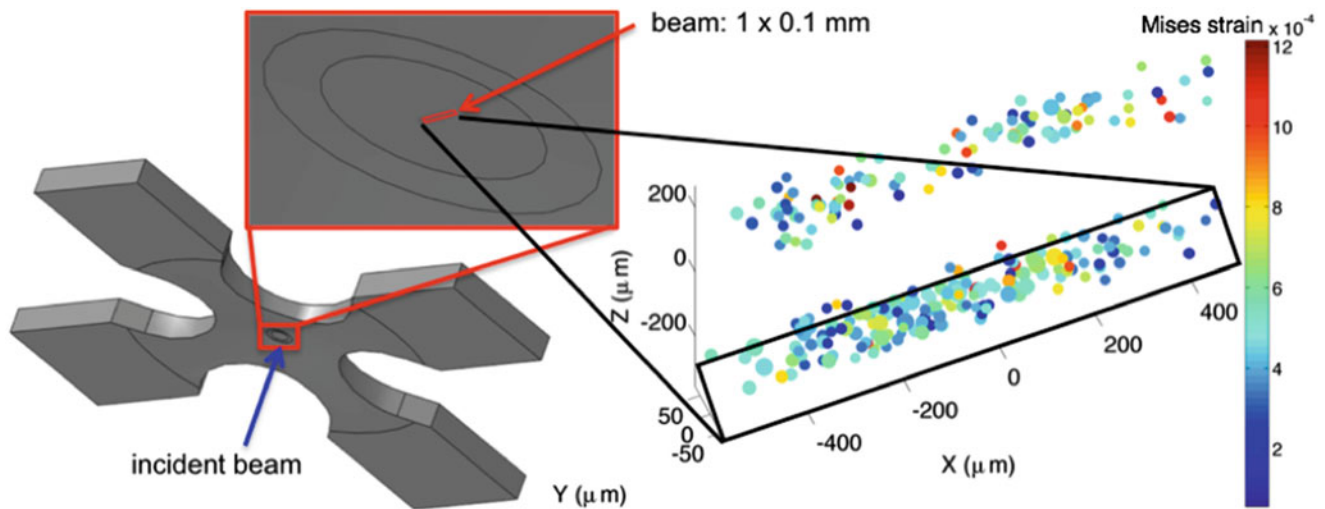
Fig. 7.9 HEDM grain mapping of 4140 tool steel prior to loading showing grain sizes and Mises strains. Data set location relative to specimen is shown schematically

7.4 Conclusions

A new *in situ* planar biaxial far-field high-energy diffraction microscopy (HEDM) experiment has been designed and demonstrated. Another benefit of combining far-field HEDM with planar biaxial loading that we have yet to demonstrate is that explicit stress analysis is possible given only the HEDM measurements and the single crystal elastic constants of the material, since a strain tensor is measured for individual grains of the gage. Stress can be calculated for each grain, and then aggregated to understand engineering stresses of the gage, without the need for finite element modeling. Thus, elucidating unknown planar biaxial constitutive responses is possible without iteration between the experiment and an assumed model, as was the previous state of the art. Hence, this new experimental platform creates an improved ability for studying multiaxial mechanics of solid materials.

References

1. Metallic Materials—Sheet and Strip—Biaxial Tensile Testing Method Using a Cruciform Test Piece. ISO 16842:2014
2. Abu-Farha, F., Hector Jr., L.G., Khraisheh, M.: Cruciform-shaped specimens for elevated temperature biaxial testing of lightweight materials. J. O. M. **61**(8), 48–56 (2009)
3. Demmerle, S., Boehler, J.P.: Optimal design of biaxial tensile cruciform specimens. J. Mech. Phys. Solids **41**(1), 143–181 (1993)
4. Hanabusa, Y., Takizawa, H., Kuwabara, T.: Numerical verification of a biaxial tensile test method using a cruciform specimen. J. Mater. Process. Technol. **213**(6), 961–970 (2013)
5. Hu, J.-J., Chen, G.-W., Liu, Y.-C., Hsu, S.-S.: Influence of specimen geometry on the estimation of the planar biaxial mechanical properties of cruciform specimens. Exp. Mech. **54**(4), 615–631 (2014)
6. Kuwabara, T., Kuroda, M., Tvergaard, V., Nomura, K.: Use of abrupt strain path change for determining subsequent yield surface: experimental study with metal sheets. Acta Mater. **48**(9), 2071–2079 (2000)
7. Makinde, A., Thibodeau, L., Neale, K.W.: Development of an apparatus for biaxial testing using cruciform specimens. Exp. Mech. **32**(2), 138–144 (1992)
8. Makris, A., Vandenbergh, T., Ramault, C., Van Hemelrijck, D., Lamkanfi, E., Van Paepegem, W.: Shape optimisation of a biaxially loaded cruciform specimen. Polym. Test. **29**(2), 216–223 (2010)
9. Shiratori, E., Ikegami, K.: Experimental study of the subsequent yield surface by using cross-shaped specimens. J. Mech. Phys. Solids **16**(6), 373–394 (1968)
10. Tiernan, P., Hannon, A.: Design optimisation of biaxial tensile test specimen using finite element analysis. Int. J. Mater. Form. **7**(1), 117–123 (2014)
11. Yu, Y., Wan, M., Wu, X.-D., Zhou, X.-B.: Design of a cruciform biaxial tensile specimen for limit strain analysis by FEM. J. Mater. Process. Technol. **123**(1), 67–70 (2002)
12. Kulawinski, D., Nagel, K., Henkel, S., Hübner, P., Fischer, H., Kuna, M., Biermann, H.: Characterization of stress–strain behavior of a cast TRIP steel under different biaxial planar load ratios. Eng. Fract. Mech. **78**(8), 1684–1695 (2011)

13. Kulawinski, D., Ackermann, S., Seupel, A., Lippmann, T., Henkel, S., Kuna, M., Weidner, A., Biermann, H.: Deformation and strain hardening behavior of powder metallurgical TRIP steel under quasi-static biaxial-planar loading. Mater. Sci. Eng. A **642**, 317–329 (2015)

14. Hommer, G.M., Stebner, A.P.: Development of a specimen for in-situ diffraction planar biaxial experiments. In: Beese, A.M., Zehnder, A.T., Xia, S. (eds.) Fracture, Fatigue, Failure and Damage Evolution, vol. 8, pp. 45–50. Springer International Publishing, Cham (2016)

15. Lienert, U., Li, S.F., Hefferan, C.M., Lind, J., Suter, R.M., Bernier, J.V., Barton, N.R., Brandes, M.C., Mills, M.J., Miller, M.P., Jakobsen, B., Pantleon, W.: High-energy diffraction microscopy at the advanced photon source. J. O. M. **63**(7), 70–77 (2011)

16. Lienert, U., Brandes, M.C., Bernier, J.V., Weiss, J., Shastri, S.D., Mills, M.J., Miller, M.P.: In situ single-grain peak profile measurements on Ti–7Al during tensile deformation. Mater. Sci. Eng. A **524**(1–2), 46–54 (2009)

17. Schuren, J.C., Shade, P.A., Bernier, J.V., Li, S.F., Blank, B., Lind, J., Kenesei, P., Lienert, U., Suter, R.M., Turner, T.J., Dimiduk, D.M., Almer, J.: New opportunities for quantitative tracking of polycrystal responses in three dimensions. Curr. Opin. Solid State Mater. Sci. **19**(4), 235–244 (2015)

18. Pagan, D.C., Miller, M.P.: Connecting heterogeneous single slip to diffraction peak evolution in high-energy monochromatic X-ray experiments. J. Appl. Crystallogr. **47**(3), 887–898 (2014)

19. Aydıner, C.C., Bernier, J.V., Clausen, B., Lienert, U., Tomé, C.N., Brown, D.W.: Evolution of stress in individual grains and twins in a magnesium alloy aggregate. Phys. Rev. B **80**(2), 024113 (2009)

20. FABLE: https://sourceforge.net/projects/fable/. Accessed 01 Mar 2016

21. HEXRD: https://github.com/praxes/hexrd. Accessed 01 Mar 2016

22. Sharma, H., Huizenga, R.M., Offerman, S.E.: A fast methodology to determine the characteristics of thousands of grains using three-dimensional X-ray diffraction. I. Overlapping diffraction peaks and parameters of the experimental setup. J. Appl. Crystallogr. **45**(4), 693–704 (2012)

23. Sharma, H., Huizenga, R.M., Offerman, S.E.: A fast methodology to determine the characteristics of thousands of grains using three-dimensional X-ray diffraction. II. Volume, centre-of-mass position, crystallographic orientation and strain state of grains. J. Appl. Crystallogr. **45**(4), 705–718 (2012)

24. Bernier, J.V., Barton, N.R., Lienert, U., Miller, M.P.: Far-field high-energy diffraction microscopy: a tool for intergranular orientation and strain analysis. J. Strain Anal. Eng. Des. **46**(7), 527–547 (2011)

25. Advanced Photon Source: "MIDAS," MIDAS, microstructural imaging using diffraction analysis software. https://www1.aps.anl.gov/science/scientific-software/midas. Accessed 01 Mar 2016

26. Dassault Systems: "Abaqus," Abaqus 6.13 online documentation, 02-Apr-2013. http://129.97.46.200:2080/v6.13/. Accessed 01 Mar 2016

27. Van Petegem, S., Wagner, J., Panzner, T., Upadhyay, M.V., Trang, T.T.T., Van Swygenhoven, H.: In-situ neutron diffraction during biaxial deformation. Acta Mater. **105**, 404–416 (2016)

28. Williams, M.L.: On the stress distribution at the base of a stationary crack. J. Appl. Mech. **24**, 111–114 (1957)

29. Irwin, G.R.: Analysis of stresses and strains near the end of a crack transversing a plate. J. Appl. Mech. **24**, 361–364 (1957)

30. Sanford, R.J.: A critical re-examination of the westergaard method for solving opening-mode crack problems. Mech. Res. Commun. **6**(5), 289–294 (1979)

31. Barber, J.R.: Plane strain and plane stress. In: Elasticity, 3rd edn, pp. 40–41. Springer, New York (2010). Chapter 3, Section 2

Chapter 8
Thermal Strain Measurement Using Digital Image Correlation with Systematic Error Elimination

Manabu Murata, Shuichi Arikawa, Satoru Yoneyama, Yasuhisa Fujimoto, and Yohei Omoto

Abstract This research aims to develop a method for measuring small strains at minute area on an electronic packaging using digital image correlation. To this end, the systematic error in the measured displacement is corrected by using the relation between measured displacement and actual displacement. This relation is obtained by measuring rigid rotation and in-plane translation. The strain distribution with high spatial resolution can be obtained from the displacement distribution because the systematic error that affects the resolution of the strain is eliminated. This error elimination method is applied to the thermal strain measurement of a bimaterial which is composed of copper and steel. Results show that high spatial resolution strain distributions at minute area can be obtained by using this method.

Keywords DIC • Electronic packing • Thermal strain • High magnification • Systematic error elimination

8.1 Introduction

Electronic packaging is the component of electronic devices. The packaging consists of heterogeneous materials such as solder and silicon, so its coefficient of thermal expansion on the packaging is not uniform. Therefore, thermal stress and strain occur when it is used. Because of this thermal stress, cracks in solder and delamination of silicon tip occur on a packaging, and these cause breakdowns of an electrical product. In the past, this thermal strain is evaluated by direct measurement such as strain gage and simulated by numerical analysis [1]. However, with offering technical advantages of mechanical products in recent year, electronic packaging is more downsizing, so evaluation of strain by strain gage is difficult. In addition, the selection of boundary condition for finite element analysis is difficult because some heterogeneous materials on electronic packaging complicate the condition. Meanwhile, in the condition like this, optical measurement is better because it can measure deformation in full visual field indirectly. There are some researches which measure thermal strain on electronic packaging by an optical method [2]. Digital image correlation (DIC) is one of the optical measurement methodologies [3]. The displacement distribution can be obtained from two pictures which are before and after the deformation. In addition, the experiment environment and the procedure of DIC are simpler than any other optical methods. However, displacement distribution obtained by DIC contains characteristic a systematic error. This is because of interpolation of gray level, speckle pattern of specimen and lack of gray level caused by gap between sensors in a CCD camera and so on. This systematic error is very small like few hundreds of a pixel, but this error affects strain obtained by DIC. The strain is calculated as the displacement gradient, so correct strain cannot be obtained if the displacement contains the systematic error. In the past, some researchers investigate the method for reduction of systematic error in displacement obtained by DIC.

Schireier et al. [4] picked up gray level distribution shapes in images and investigated the effects of this for the results of measurements. As a result, it was shown that systematic error increase when images contain high frequency contents, and the error could be reduced by reduction of high frequency content using a low pass filter. Bornet et al. [5] investigated the effect of speckle pattern size and the order of interpolation function for the measurement error. As a result, it was shown that

M. Murata (✉) • S. Yoneyama
Department of Mechanical Engineering, Aoyama Gakuin University, 5-10-1 Fuchinobe, Chuo-ku, Sagamihara-shi, Kanagawa 252-5258, Japan
e-mail: c5615123@aoyama.jp

S. Arikawa
Department of Mechanical Engineering Informatics, Meiji University, 1-1-1 Higashimita, Tama-ku, Kawasaki-shi, Kanagawa 214-0031, Japan

Y. Fujimoto • Y. Omoto
Mitsubishi Electric Corporation Advanced Technology Research and Development Center, 8-1-1 Tsukaguchi-honmachi, Amagasaki-shi, Hyogo 661-8661, Japan

smaller pattern size and higher order interpolation function can reduce the systematic error. Zhou et al. [6] believed the noises in image increase high frequency content in gray level distribution, and investigated the relation between the error and the presence of this high frequency content. As a result, it was shown that the error is reduced by applying some kind of filter such as Gaussian and Butterworth filter before analysis in order to suppress high frequency contents. However, to obtain correct strain distribution by DIC, systematic error should be eliminated completely. One method for eliminating the systematic error in DIC results has been proposed by Arikawa et al. [7].

This research aims to measure thermal strain at minute area on electronic packaging which is consist of heterogeneous materials such as solder and silicon. To this end, the error elimination method [7] is applied to the thermal strain measurement of a biomaterial specimen and the thermal strain measurement of an electronic packaging.

8.2 Eliminating Error in Displacement Obtained by DIC

As previously indicated, the factors causing systematic error in DIC are various. Figure 8.1a is an example of systematic error in measured displacement, which shows the relation between the measured displacement and the error. The error appears periodical, 1 cycle error to 1 pixel displacement, and it is constant amplitude. This systematic error vanishes at integer and its midpoint displacement. Figure 8.1b shows the relation between the measured and actual displacements in the interval of the displacement of 0–1 pixel. If the actual displacement is equivalent to the measured displacement, it is plotted on a graph as a straight line and its gradient is 1. However, the measured displacement distribution obtained by DIC is plotted as not a straight line, and its gradient is changed continuously. The gradient of the measured displacement in Fig. 8.1b is less than 1 firstly, and the gradient is changed to more than 1. Finally, the gradient is changed to less than 1 once again and ends the 1 cycle of the error. Now, if the gradient and the intercept of a linear approximation for the measured displacement at the area where its gradient exceed 1 can be obtained, the relation between the measured displacement and the actual displacement can be known. Arikawa et al. [7] suggested an error elimination method based on this idea. Before measuring the deformation, the rigid rotation and the translations are measured. The actual displacements of the translations are compared with the displacements measured by DIC. By this comparison, the relation between two displacements is obtained, and measured displacements with the systematic error are corrected.

In the experiment, the rigid rotation and the translations are given to the specimen before the specimen is deformed. The specimen at initial position is rotated at a certain angle. Next, specimen is translated to a unidirectional direction whose displacement is less than 1 pixel, and this translation is repeated several times. After measuring the rigid body rotation and the translations, a load is applied to the specimen and the deformed image is recorded. In the data analysis, the actual displacements of the translation and the measured displacements are obtained respectively. The initial image is analyzed with the translated images as a reference, and each displacements of the translation are obtained. Here, the actual displacement of the translation can be obtained by the analysis using only each translated images. However, the translation is too small
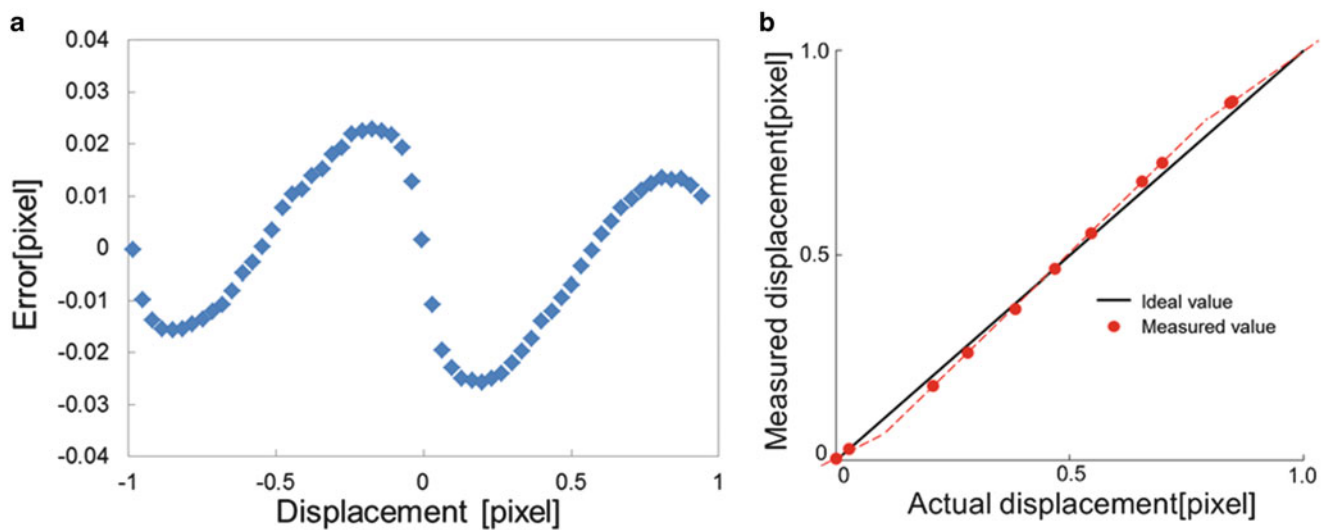

Fig. 8.1 The relations between (**a**) displacement and error (**b**) actual displacement and measured displacement

such as the displacement of 0.2 pixels so this displacement has the systematic error. In order to obtain the displacement without the influence of the systematic error, rigid rotation is given to the specimen. The actual displacements of the translation are obtained by subtracting each average of the displacement distribution of the rigid rotation and the translations. This is because the displacement gradient is uniform in the displacement distribution of the rigid rotation. If the distribution has the uniform displacement gradient, it means that there are some cycles of the systematic error in the displacement distribution. So, by subtracting the average of each displacement distribution, the displacements of the translation without the influence of the error can be obtained. This displacement is considered as the actual displacement of the translation. Next, the translated images are analyzed with the deformed image as the reference; these are the measured displacements obtained by DIC. The measured displacement is compared with this actual displacement, and the relation between these two displacements is obtained. This relation is obtained by using a least-square method.

In digital camera, there are sensors which sense the brightness of a measuring object. Also, there is a gap between sensors. If the speckle pattern on the measuring object is on this gap, the gray level of measuring object is not sensed by sensors. Therefore, this gap causes the lack of gray level of measuring object. For this reason, it is considered that the validity of measured displacement on this gap is poor. In this research, if the fractional value of the measured displacement is not greater than 0.1 pixel or greater than 0.9 pixel, this measured value is regarded as the displacement on the gap. The measured displacements are expressed by a linear approximation without these displacements on gap. Also, the relation obtained by this approximation is obtained at all evaluation points of the displacement, so error correction can be applied to all points on an image.

However, this method can eliminate only the systematic error in the unidirectional displacements. In fact, in order to eliminate the systematic error in in-plane displacements, the measurement of the rigid rotation and the translation must be conducted twice. Consequently, this research aims to develop this method to eliminate the systematic error in in-plane displacements. In the experiment, the y-directional translation is given to the specimen after the x-directional translation is given. After this, the deformation of the specimen is measured. In the analysis, the images translated to the x-direction are analyzed to correct the systematic error in the x-directional component of the displacement. Likewise, the images translated to the y-direction are analyzed to correct the systematic error in the y-directional component of the displacement.

8.3 Experiment

The schematic figure of the test equipment is shown in Fig. 8.2. A random pattern is painted on the surface of a test specimen. Then the specimen is placed in a temperature controlled chamber. The temperature can be controlled in the increments of 1 °C. A CCD camera is fixed on the stage above the temperature controlled chamber. The stage shown in Fig. 8.3 can give a

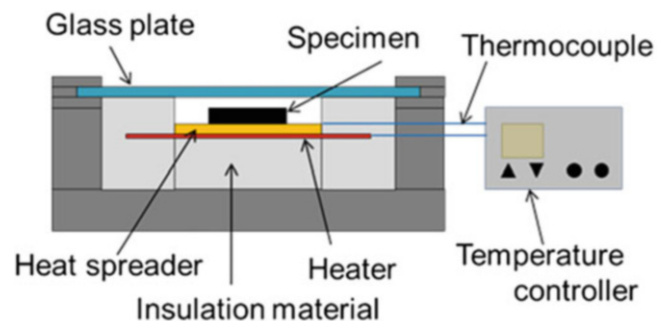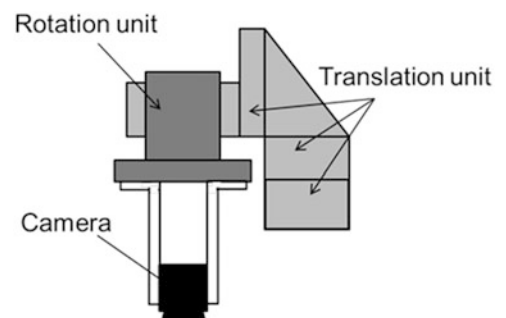**Fig. 8.2** Test equipment

Fig. 8.3 Translation-rotation stage

tri-axial translation and a rotation to the CCD camera. The images of the rigid rotation and the translation are recorded by applying the rotation and the translation to the CCD camera, instead of rotating and translating the specimen. Then, the thermal strains of a bi-material specimen are measured; this is the preliminary experiment of the measurement of the thermal strain of an electronic packaging.

The dimension of specimen is 15 (length) $\times$ 20 (width) $\times$ 3 (thickness) mm^3, a copper plate (C1020) and a steel (SS400) plate are adhered by silver brazing. On the specimen, speckle pattern is painted by a boron nitride spray and a lacquer spray. The condition of the temperature is incalescence from room temperature (26 $^\circ$C) to 194 $^\circ$C. The rigid rotation of 0.240° and the translations of the increment of 4 μm are given to the specimen. The magnification of the lens for the camera is 0.3 times. The resolution of CCD camera is 2048 $\times$ 2048 pixels and its bit depth is 8 bits. The interpolation function for DIC is bilinear. The subset size for analysis is 41 $\times$ 41 pixels and the analysis range is 840 $\times$ 1070 pixels, which is same as the range of the specimen in the image.

8.4　Result of DIC

Figure 8.4 shows an image of the specimen at the initial position. The left side of the specimen is steel and the right side of specimen is copper. The center in specimen is the bonded zone of silver brazing.

Figure 8.5 shows the thermal strain obtained from thermal displacement. The gage length, which is the range of applying least-square method to calculate the strain, is 41 pixels. The strain distributions in Fig. 8.5a, b are calculated from the displacements obtained by DIC without the error elimination. In each region of the homogeneous material, the uniform strain distribution should be observed, but it is not observed in these distributions. There are the vertical stripe in the horizontal strain distribution and the horizontal stripe in the vertical strain distribution. This is the result of the systematic error effect. This is because the displacement gradient in a local region is calculated to obtain strain. Nevertheless the systematic error is very small, this appears periodical to the displacement. Therefore, the displacement gradients change plus or minus from constant in each region of the homogeneous material. Thereby, the strain is changing constantly like stripe in the distribution. Also, the number of the stripe on the copper is more than that on the steel. This is because the coefficient of the thermal expansion of the copper is higher than that of the steel. The displacement of the copper is more than that of the steel.

On the other hand, this stripe is not observed in the strain distributions obtained from the displacement using the systematic error elimination method, shown in Fig. 8.5c, d. The uniform strain is obtained in each material. Consequently, the elimination of the in-plane systematic error is succeeded by conducting the in-plane translations.

To evaluate this result quantitatively, the average and the standard deviation of the strain in the region of the homogeneous materials in the analysis region is compared between before and after the systematic error elimination is applied. The result is shown in Table 8.1. In order to obtain the values in this table, the strain in the middle region of the specimen is excluded because there is the area adhered by silver brazing, and it is aimed to calculate these value in the region of homogeneous materials. The average strain is not great difference, but ε_x and ε_y of each material after correction are a little closer than before the correction. About the standard deviation of the strain before the error correction, they exceed 400×10^{-6} in the copper and 500×10^{-6} in the steel. On the other hand, that of strains after correction are about half of
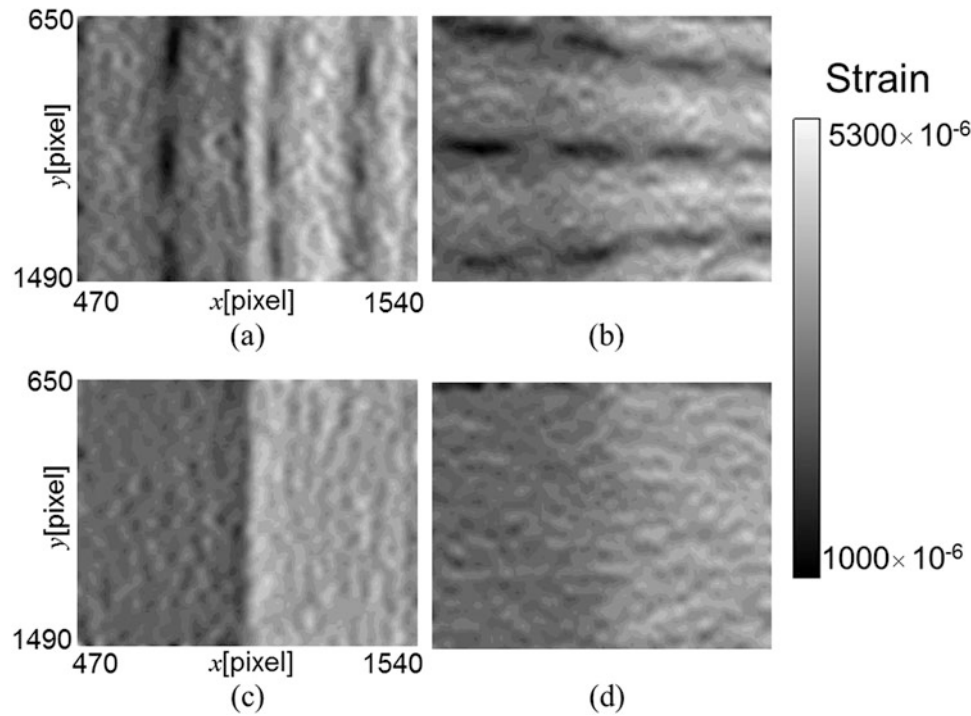
Fig. 8.4 Image of test specimen
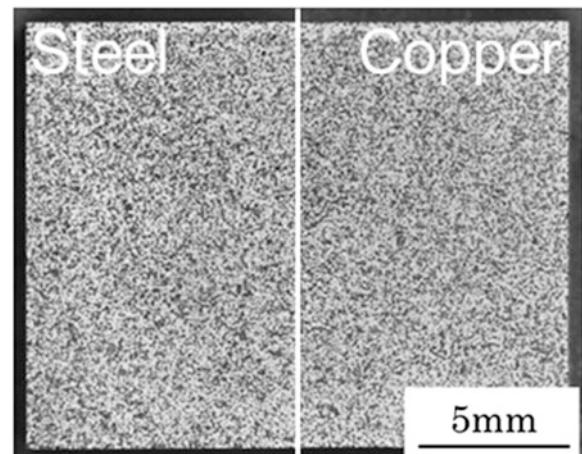
Fig. 8.5 Strain distribution of heat load test (**a**) ε_x (**b**) ε_y and after eliminating error (**c**) ε_x (**d**) ε_y

Table 8.1 Result of thermal strain measurement

		Before error correction		After error correction	
		Average ($\times 10^{-6}$)	Standard deviation ($\times 10^{-6}$)	Average ($\times 10^{-6}$)	Standard deviation ($\times 10^{-6}$)
Steel	ε_x	2699	434.1	2747	198.0
	ε_y	2717	426.7	2746	228.8
Copper	ε_x	3742	526.7	3660	251.6
	ε_y	3697	538.9	3678	277.5

that of the strains before correction. Thus, the strain measurement could be less variation in the homogeneous part of the specimen by using the error elimination method. Generally, the large gage length is not appropriate for the observation of the strain distribution on a minute area. This is because the calculated strain is smoothed in the region defined as a gage length. A small gage length can obtain the strain on a minute area, but the correct strain distribution is difficult to obtain because the displacement contains systematic error. However, in this research, it is shown that error elimination method can obtain the strains of the half standard deviation against before error correction. Therefore, this method can minify the gage length, so it makes to be able to observe the strain field on a minute area. Thus, due to this, the strain measurement resolution is improved by using the error elimination method.

8.5 Conclusions

The thermal strain of copper–steel silver brazing is measured by using DIC and its systematic error elimination method. To measure the in-plane displacements without the systematic error, the rigid rotation and the in-plane translation are given to the specimen before the thermal load is applied. Results show that the strain distribution without the influence of the error is obtained by using the error elimination method. The average and the standard deviation in the strain distribution can be reduced by the error elimination method. It is shown that the error elimination method improve the strain measurement resolution of DIC.

References

1. Tani, S., Yoshioka, S.: Stochastic finite element analysis of thermal deformation of electronic device mounted on circuit board. J. Jpn. Soc. Mech. Eng. **57**(541), 1999–2003 (1991)
2. Morita, Y., Arakawa, K.: Thermal Strain Analysis of SOJ Electronic Package by Phase-Shifting Moiré Interferometry. J. Jpn. Soc. Exp. Mech. **3**(1), 28–33 (2003)
3. Yoneyama, S.: Basic principle of digital image correlation for in-plane displacement and strain measurement. Adv. Compos. Mater. doi:10.1080/09243046.2015.1129681
4. Schireier, H.W., Braasch, J.R.: Systematic errors in digital image correlation caused by intensity interpolation. Opt. Eng. **39**(11), 2915–2921 (2000)
5. Bornet, M., Brémand, F.: Assessment of digital image correlation measurement error: methodology and results. Exp. Mech. **49**, 353–370 (2009)
6. Zhou, Y., Sun, C.: Image pre-filtering for measurement error reduction in digital image correlation. Opt. Lasers Eng. **65**, 46–56 (2015)
7. Arikawa, S., Yoshida, R.: A method for eliminating periodical error for highly accurate measurement in digital image correlation. In: Proceedings of International Conference on Advanced Technology in Experimental Mechanics 2015, p. 1 (2015)

Chapter 9
Investigating the Tensile Response of Materials at High Temperature Using DIC

Guillermo Valeri, Behrad Koohbor, Addis Kidane, Michael A. Sutton, and Hubert Schreier

Abstract Recent results from a DIC-based experimental analysis conducted to identify the tensile response of materials at high temperature are presented. Full-field deformation response of stainless steel specimen subjected to quasi-static tension at temperatures between 300 and 900 °C is examined using 3D digital image correlation. Band-pass filters along with a blue light source are used in the experimental setup, with images acquired using regular CCD cameras. A portable induction heating device equipped with water-cooled copper coils is used to heat the specimen. The use of this equipment allows for rapid heating of the designated area of interest in a specimen to the desired temperature with fairly uniform temperature distribution. Using the load history and measured full-field strain data as input, a VFM-based approach is implemented to identify the constitutive parameters governing the plastic deformation of the material at high temperatures.

Keywords Digital image correlation • Full-field deformation • Tensile properties • Virtual fields method

9.1 Introduction

Determination of the thermomechanical behavior of materials is a subject of great interest for both aerospace and metal forming industries. From an experimental perspective, there have been efforts in the past two decades to incorporate full-field measurement techniques such as Digital Image Correlation (DIC) in the analysis of the thermomechanical behavior of materials subjected to high temperature deformation [1]. For high temperature applications, DIC has various advantages compared with other conventional methods that use externally applied strain gauges, extensometers or other non-contact optical methods to measure specimen deformation. For high temperature applications, DIC provides a simple and versatile yet effective means for non-contact 2D and 3D full-field surface deformation measurements. The most significant limitation in the application of a conventional DIC technique for high temperature full-field deformation measurements is the progressive change in contrast of the speckle pattern at temperatures above 650 °C which can lead to decorrelation and reduced measurement accuracy [1, 2]. Another challenge documented in previous studies is the formation of a heat haze, which results from the sample heating the surrounding air, creating convective currents which change the refractive index of the surrounding air and consequently act as a source of image distortion [1]. In recent years, advances have been made to conduct successful DIC measurements at extreme temperature conditions. These include, but are not limited to, the application of novel speckling methods capable of sustaining integrity and efficiency at extreme temperatures [3], use of narrow band pass optical filters [2–5] and the application of monochromatic illumination sources, such as blue light or UV [2, 5–7]. However, the need for a simple and portable heating system that is compatible with multiple testing machine configurations and different specimen geometries remains an unresolved issue for high temperature DIC studies.

The present work extends a previous study [5], where a novel and portable 3D DIC-based high temperature measurement system was utilized to study the free thermal expansion of stainless steel specimens heated up to 1150 °C. In the current work, the same portable heating equipment is used along with a tensile testing machine to study the high temperature tensile response of 304 stainless steel specimens using blue light illumination and a band pass optical filter for image acquisition at temperatures ranging from room temperature up to 900 °C.

G. Valeri • B. Koohbor • A. Kidane (✉) • M.A. Sutton
Department of Mechanical Engineering, University of South Carolina, 300 Main Street, Columbia, SC 29208, USA
e-mail: kidanea@cec.sc.edu

H. Schreier
Correlated Solutions Inc., 121 Dutchman Blvd, Irmo, SC 29063, USA

9.2 Experimental

The high temperature tensile response of low carbon 304 stainless steel is evaluated. Flat dog-bone specimens are extracted from the as-received stainless steel sheets using a CNC waterjet system. Tensile specimens are coated with a thin layer of Yttrium oxide (Y_2O_3) white paint and then a fine black speckle pattern using high temperature silica-based ceramic paint. Tensile experiments are conducted in a Tinius Olsen 5000 tensile frame in displacement control mode and at a constant cross head speed of 10 mm/min, which is equivalent to a mean strain rate of $2 \times 10^{-3} \, s^{-1}$. Figure 9.1 illustrates the experimental setup and specimen geometry used in this work. Tensile experiments are performed at five different temperatures: 25 °C (room temperature), 300 °C, 500 °C, 700 °C, and 900 °C. Specimens are heated using a portable, table-top induction heating system equipped with custom-made water-cooled copper coils. The induction heating system used in this work can be employed in a wide range of specimen geometries and with different testing machines, as long as it is equipped with an appropriate coil system. The specimen is initially gripped at the bottom and heated until target temperature reached. Once the target temperature has been achieved, the temperature is maintained several minutes to optimize the uniformity of heating in the area of interest. Finally, the specimen is gripped at the top and the experiment is immediately initiated. Temperature of the specimen is measured using a non-contacting infrared thermometer facing the center of the specimen; reported accuracy of the temperature measurement is ±0.1 °C.

As mentioned earlier, the emission of light from the surface of a heated body (black-body radiation) at temperatures above 650–700 °C changes the contrast and intensity of the speckle pattern. To compensate for this issue, blue band pass filters (MIDOPT BP470-55) with a wavelength range of 435–495 nm are used in this work [5]. The filters are attached to 100 mm macro lenses of a 5 MP Point Grey® stereovision camera system used to acquire images during the experiment. Stereo images are acquired from a $25 \times 12.7 \, mm^2$ area of interest located at the center of the tensile specimen (see Fig. 9.1c). Blue LED light source is employed for illumination. Additional details regarding the imaging system can be found elsewhere [5].

Image acquisition is synchronized with temperature data collection at a rate of 1 Hz, from the start of the experiment until specimen failure. The acquired images are then used as input to the DIC software Vic-3D® (www.correlatedsolutions.com) for image correlation and further quantitative analysis. Subset and step sizes of 25 pixels and 6 pixels, respectively, are used for image correlation, with a magnification factor of approximately 0.021 mm/pixel. Full-field strain is computed over the area of interest using a Gaussian filter with a filter size of 15.

9.3 Identification of Temperature-Dependent Constitutive Response

The Johnson-Cook model is an empirical model that allows for the determination of flow stress as a function of equivalent plastic strain, plastic strain rate and temperature, as:
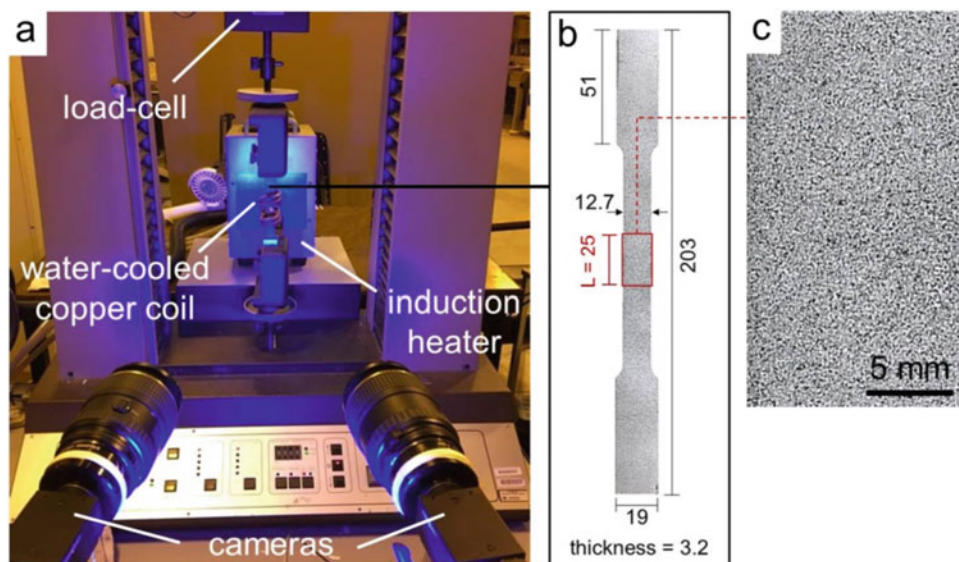

Fig. 9.1 (**a**) Experimental setup, (**b**) tensile specimen geometry with a magnified view of the area of interest shown in (**c**). All dimensions in mm

$$\overline{\sigma} = \left(A + B\overline{\varepsilon}_p^n \right) \left(1 + C \ln \dot{\varepsilon}^* \right) \left(1 - T^{*m} \right) \tag{9.1}$$

where $\dot{\varepsilon}^*$ is the plastic strain rate normalized with the reference quasi-static strain rate, and T^* is the homologous temperature. The parameters A, B and n are material constants that can be determined from quasi-static testing at reference temperature and strain rate and m is the temperature exponent. In this work, VFM-based analysisis employed to identify key material parameter in Eq. (9.1).

In the absence of body and acceleration forces, the global equilibrium of a solid can be expressed as:

$$-\int_V \sigma_{ij} \varepsilon_{ij}^* dV + \int_{\partial V} T_i \cdot u_i^* dS = 0 \tag{9.2}$$

where σ_{ij} and T_i represent the components of stress tensor and traction vector, respectively. u_i^* denotes components of a "virtual displacement field" and ε_{ij}^* denote components of the virtual strain tensor derived from u_i^*. Equation (9.1) can be simplified for the case of uniaxial tension by introducing an appropriate virtual displacement field. The virtual displacement field suggested by Avril et al. [8] is implemented in this work, as:

$$\begin{cases} u_x^* = 0 \\ u_y^* = y \end{cases} \quad \begin{cases} \varepsilon_{xx}^* = 0 \\ \varepsilon_{yy}^* = 1 \\ \varepsilon_{xy}^* = 0 \end{cases} \tag{9.3}$$

Accordingly, after further simplifications [8], the equilibrium equation can be expressed as:

$$\int_S \overline{\sigma}\left(\overline{\varepsilon}_p, T^*, m\right) dS = \frac{P(\tau) \cdot L}{t} \tag{9.4}$$

where P is the measured tensile load, L is the length of the area of interest (shown in Fig. 9.1), t is the specimen thickness and τ represents time, with. S the area on which full-field measurements are obtained. Assuming that the strain rate is constant over the area of interest and that its value remains equal to the reference strain rate, the only unknown parameter in Eq. (9.1) will be m. Note that the constants A, B and n have already been identified at this point from the stress–strain response of the material tested quasi-statically at room temperature. To compute the constant m, an iterative solution has been conducted to minimize the cost function, Φ, expressed as:

$$\Phi(m) = \sum_{i=1}^N \sum_{\tau=\tau_0}^{\tau=\tau_f} \left(\frac{1}{S} \int_S \overline{\sigma}\left(\overline{\varepsilon}_p, T^*, m\right) dS - \frac{P(\tau) \cdot L}{St} \right)^2 \tag{9.5}$$

with N being the total number of experiments conducted at different temperatures ranging from RT to 900 °C. τ_0 and τ_f denote the initiation of the plastic deformation and plastic instability (necking), respectively. As a final remark, it should be noted that Eq. (9.5) is valid as long as the temperature, strain rate and plastic strain remain spatially uniform over the entire area of interest. To evaluate the integral term in Eq. (9.5), strain values are computed by spatial averaging of this variable over the entire population of data points inside the area of interest. Note that the VFM analysis based on strain averaging is possible as long as there is negligible spatial variability of strain within the area of interest. Figure 9.2 depicts typical strain maps extracted at different stress magnitudes for the specimen tested at 900 °C. Relatively uniform distribution of strain over the area of interest is clearly indicated in this figure. In cases where a considerable spatial variability in strain (or strain rate) is present, the procedure detailed in [8] can be adopted.

9.4 Results and Discussion

Tensile stress–strain curve for the examined material is extracted at room temperature and reference strain rate. Figure 9.3 shows the reference stress–strain curve. The constants A, B and n (see Eq. (9.1)) are determined from the reference curve as: 393 MPa, 743.1 MPa and 0.568, respectively, by finding the best fit to the plastic part of the experimental curve.
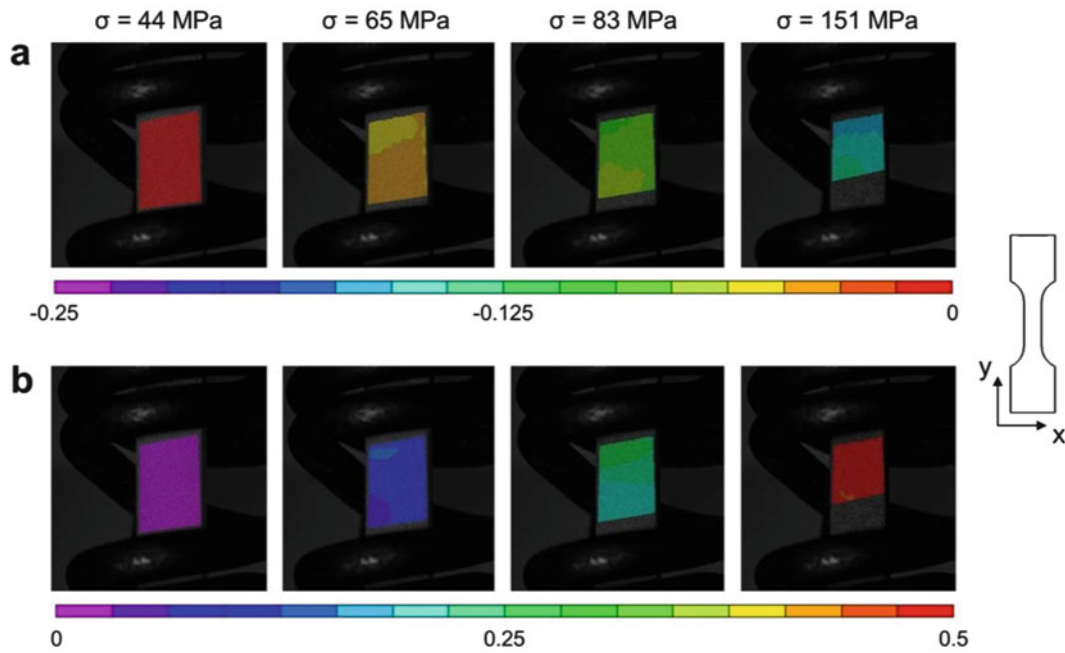
σ = 44 MPa   σ = 65 MPa   σ = 83 MPa   σ = 151 MPa

Fig. 9.2 Typical maps showing the distribution of (**a**) ε_{xx} and (**b**) ε_{yy} over the area of interest at different stress magnitudes ($T = 900\,°C$)

Fig. 9.3 Experimental and model curves obtained at room temperature and reference strain rate $2 \times 10^{-3}\,\mathrm{s}^{-1}$

$\bar{\sigma} = 393 + 743.1\,\bar{\varepsilon}_p^{0.568}$

$E = 199.3\,\mathrm{GPa}$
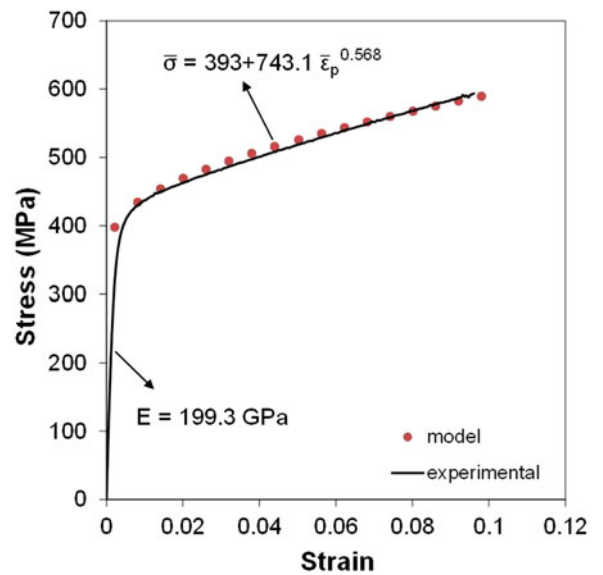
Next, to determine the temperature exponent m in Eq. (9.1), stress–strain curves obtained from high temperature tensile experiments are considered. Figure 9.4 illustrates the experimental curves obtained at each temperature. The 0.2 % offset method is used to obtain the plastic portion of the curves. It is clearly seen that specimen temperature varies spatially during the experiment. The reason for this might be due to the fact that as the specimen is stretched in axial direction, its cross-sectional area is reduced and consequently the distance between the specimen surface and the heating coil is changed. Thus the efficiency of induction heating is decreased. In the present work, the following procedure is followed to identify the temperature parameter m:

1. Collect the entire population of data points obtained from high temperature experiments and construct a full-grid material data set containing known strain-temperature-load information.

Fig. 9.4 Experimental stress–strain curves obtained at varying temperatures
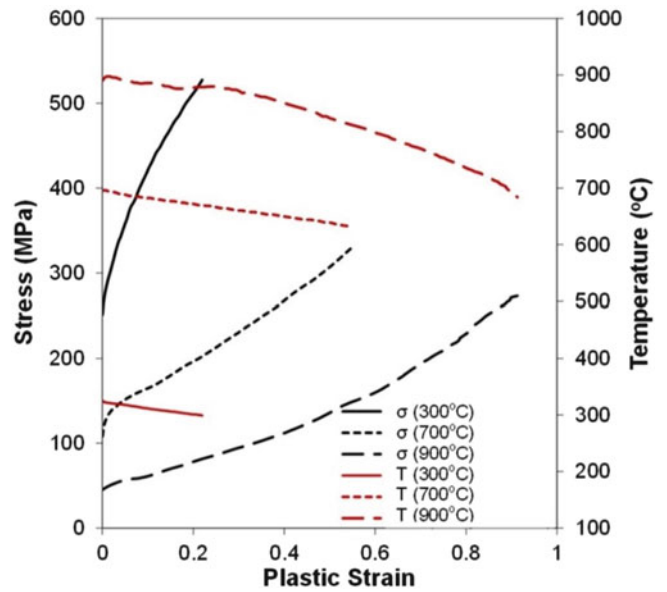
Fig. 9.5 Variation of normalized cost function with the temperature exponent m
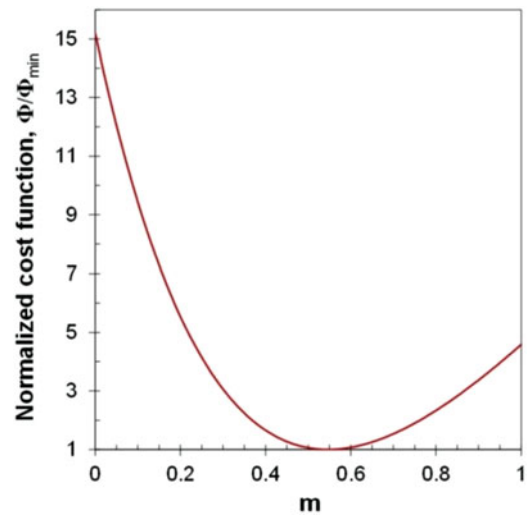
2. Select an initial guess for the parameter m and calculate the cost function (Eq. (9.5)) using the entire population of data points in the full-grid data set generated in step (1) and the selected value for m. *The initial value $m = 0$ is taken as the starting point in this work.*
3. Repeat step (2) for an updated value of m. Updating the temperature parameter m is conducted by progressively increasing m from $m = 0$ to $m = 1$ at increments of 0.001.
4. Identify the value of m that minimizes the cost function Φ.

   Figure 9.5 illustrates the variation of the cost function, Φ, with m. Accordingly, the optimum value of $m = 0.545$ is identified for the examined 304 stainless steel deformed at a strain rate of 2×10^{-3} s^{-1} and over a temperature range of 25–900 °C. Finally using the obtained temperature exponent, the stress–strain curves obtained at varying temperatures can be corrected and replotted at constant temperatures. Corrected stress–strain curves plotted at constant temperatures are shown in Fig. 9.6.

Fig. 9.6 Corrected stress–strain curves replotted at constant temperatures
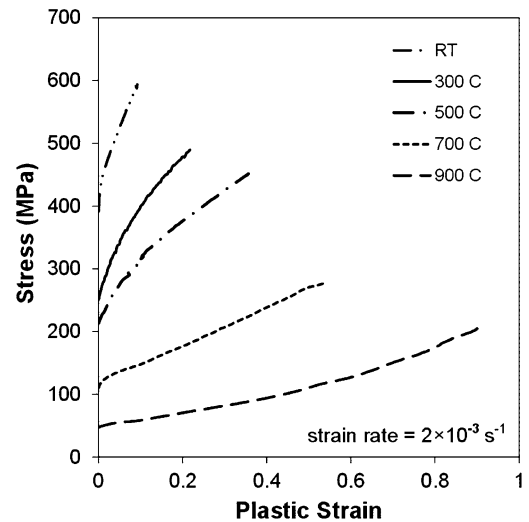
9.5 Summary

A portable and easy-to-implement experimental method based on 3D DIC is used to measure the full-field deformation of flat, stainless steel dog bone specimens under tension at temperatures ranging from 25 to 900 °C. The experimental setup consists of an induction coil heating and a stereo-camera system equipped with optical band-pass notch filters and blue LED illumination. Using the recorded load and full-field strain data as the input, a VFM-based approach is implemented to identify the constitutive parameters governing the plastic deformation of the material at high temperatures. Using these parameters, the stress–strain curves obtained at varying temperatures are corrected and replotted at constant temperatures.

References

1. Lyons, J.S., Liu, J., Sutton, M.A.: High-temperature deformation measurements using digital-image correlation. Exp. Mech. **36**, 64–70 (1996). doi:10.1007/BF02328699
2. Pan, B., Wu, D., Wang, Z., Xia, Y.: High-temperature digital image correlation method for full-field deformation measurement at 1200 °C. Meas. Sci. Technol. **22**, 1–11 (2011). doi:10.1088/0957-0233/22/1/015701
3. Guo, X., Liang, J., Tang, Z., Cao, B., Yu, M.: High-temperature digital image correlation method for full-field deformation measurement captured with filters at 2600 °C using spraying to form speckle patterns. Opt. Eng. **53**(6), 063101 (2014). doi:10.1117/1.OE.53.6.063101
4. Grant, B., Stone, H., Withers, P., Preuss, M.: High-temperature strain field measurement using digital image correlation. J. Strain. Anal. Eng. Des. **44**(4), 263–271 (2009). doi:10.1243/03093247JSA478
5. Koohbor, B., Valeri, G., Kidane, A., Sutton, M.: Thermo-mechanical properties of metals at elevated temperatures. In: Jin, H., Yoshida, S., Lamberti, L., Lin, M. (eds.) Advancement of Optical Methods in Experimental Mechanics, vol. 3, pp. 117–123 (2016). doi:10.1007/978-3-319-22446-6_15
6. Chen, X., Xu, N., Yang, L., Xiang, D.: High temperature displacement and strain measurement using a monochromatic light illuminated stereo digital image correlation system. Meas. Sci. Technol. **23**(12) (2012). doi:10.1088/0957-0233/23/12/125603
7. Berke, R.B., Lambros, J.: Ultraviolet digital image correlation (UV-DIC) for high temperature applications. Rev. Sci. Instrum. **85**(4), 1 (2014). doi:10.1063/1.4871991
8. Avril, S., Pierron, F., Sutton, M.A., Yan, J.: Identification of elasto-visco-plastic parameters and characterization of Lüders behavior using digital image correlation and the virtual fields method. Mech. Mater. **40**, 729–742 (2008). doi:10.1016/j.mechmat.2008.03.007

Chapter 10
Hybrid Stereocorrelation for 3D Thermomechanical Field Measurements

A. Charbal, J.-E. Dufour, F. Hild, S. Roux, M. Poncelet, and L. Vincent

Abstract Three dimensional displacement fields are measured thanks to an original stereo system made of InfraRed (IR) and visible light cameras. This configuration provides the thermal fields that drive the thermomechanical loading and the 3D surface displacement fields, i.e. the response of the studied material. The calibration of the stereo rig is performed by using a 3D target of known geometry and the large gray level variations that occur on the IR images are accounted for by applying a low-pass filter. Because of a slight disorientation of the target, a further calibration correction step revealed necessary. After correction of the target orientation, the measured displacement fields display a good qualitative agreement (no quantitative comparison has been performed yet) with the expected fields.

Keywords Stereocorrelation • Hybrid system • IR and visible light cameras • Calibration • Gray level corrections

10.1 Introduction

Thermal fatigue that may occur in components of nuclear power plants [1–3] is studied with a new experimental setup [4] in which cyclic thermal shocks are applied on an austenitic stainless steel plate by a pulsed laser [5]. The measurements of 2D thermal and 3D displacement fields of the impacted surface are performed with IR and visible light cameras. A finite element analysis of such experiment predicts the largest strain variations during loading to be in the out-of-plane direction, resulting in out-of-plane displacements of several micrometers [6]. In experimental mechanics stereocorrelation (SC) is commonly used in order to measure such displacement fields [7–11]. In the present study, it is proposed to perform SC by using an original hybrid combination of one IR and one visible light camera. The challenges to be addressed are to use two imaging systems with different properties (i.e., pixel sizes, definitions, gray level distribution and changes when the temperature evolves). A first feasibility analysis was performed [12] and proved on simple rigid body translations (RBT) that such a combination could be used for prescribed amplitudes varying from 5 to over 100 μm. It has also been shown that the scale factor could be readjusted by applying known RBTs during the calibration step. The RBTs were performed at room temperature. Therefore no digital level variations on the IR frames occurred. The assumption of 'gray' level conservation was still satisfied and low SC-residuals were obtained. In the present case, the laser shocks induce by locally heating-up the sample large gray level changes. This phenomenon has to be accounted for in order to be able to perform such measurements. The other issue is to calibrate the stereo rig when the characterized sample is a 2D plate. The use of a 3D target [13] to determine the projection matrices is necessary, which are later used for the SC measurements.

First, an overview of the experimental setup is presented, then the SC methodology is described, and finally the measured displacement and temperature fields are illustrated and discussed.

A. Charbal (✉)
LMT, ENS Cachan/CNRS/University of Paris-Saclay, 61 avenue du Président Wilson, Cachan 94235, France

CEA, DEN-SRMA, Université of Paris-Saclay, Gif sur Yvette 91191, France
e-mail: charbal@lmt.ens-cachan.fr

J.-E. Dufour • F. Hild • S. Roux • M. Poncelet
LMT, ENS Cachan/CNRS/University of Paris-Saclay, 61 avenue du Président Wilson, Cachan 94235, France
e-mail: dufour@lmt.ens-cachan.fr; hild@lmt.ens-cachan.fr; stephane.roux@lmt.ens-cachan.fr; poncelet@lmt.ens-cachan.fr

L. Vincent
CEA, DEN-SRMA, Université of Paris-Saclay, Gif sur Yvette 91191, France
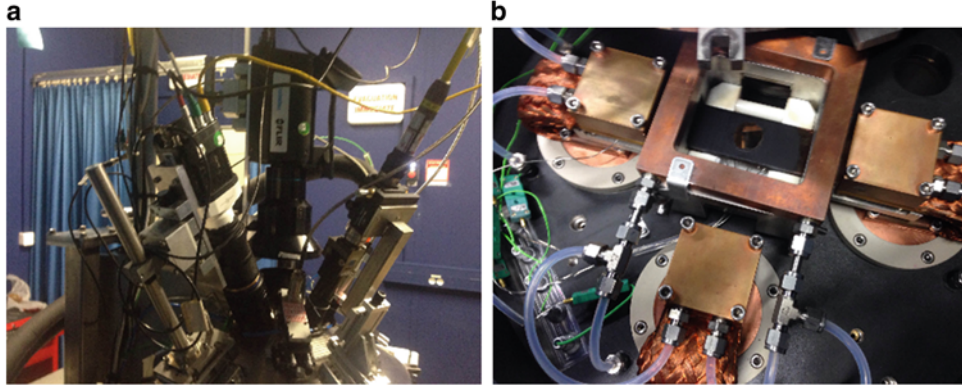e-mail: ludovic.vincent@cea.fr

Fig. 10.1 Experimental setup (**a**) and characterized sample (**b**) within the chamber

10.2 Experimental Setup

The use of such particular combination of cameras is mostly due to the fact that the experimental bench does not allow for having more than two cameras. The characterized sample is placed within an atmosphere controlled chamber in which secondary vacuum is first performed before introducing He gas. A pulsed laser (TruPulse 156, Trumpf™, $\lambda = 1064$ nm) is used to apply cyclic thermal shocks to stainless steel plates. In this case study, the shock frequency is 1 Hz, the pulse duration is 50 ms and the incident pulsed power is equal to 310 W. The applied temperature variation is 200 °C on the impacted zone and the initial sample temperature is 400 °C. A focusing optics allows a top-hat power density to be obtained over a 5-mm disk at a working distance of 29 cm. Due to the relatively low absorptivity of the polished then pre-oxidized surface an inclination of the beam is needed to reflect the incident beam onto an absorber. The latter gives access to the mean power reflected by the sample. An infrared camera (×6540sc FLIR™, definition: 640×512 pixels, $\lambda = [3\text{--}5\ \mu\text{m}]$ reduced to $\lambda = [3.97\text{--}4.01\ \mu\text{m}]$ with an internal filter for high temperature measurements) is used with a high magnification lens allowing for a pixel size of 15 μm. A visible light camera (MIRO M320S, Vision Research™, definition: 1920×1080 pixels) leads to a pixel size of 10 μm (Fig. 10.1).

10.3 Stereocorrelation

As for any stereoscopic system, camera calibration is needed. A two-step camera calibration is performed. The first one consists in optical distortion corrections. As the images are projected onto a supposed perfect numerical model (of the 3D object) such effects must be considered. The followed method to account for such biases uses integrated DIC (I-DIC) [14], which determines the intrinsic parameters such as radial, decentering and prismatic coefficients [15, 16] using a dedicated 2D calibration target. Once the images are corrected of their respective distortions, the projection matrices are estimated in a second step.

The determination of the projection matrices is based on the 3D coordinates of the numerical model projected onto the picture planes. The global approach proposed in Ref. [10] considers the 3D mathematical model of the sample and the use of an I-DIC algorithm allows for the optimization of the projection matrices by using a pseudo-kinematic basis. By working in the parametric space of the surface, it enables for images of different definition and nature to be registered. The homogeneous coordinates in each camera are related to the 3D positions by

$$\left\{ \begin{array}{c} s^l x^l \\ s^l y^l \\ s^l \end{array} \right\} = \left[\mathbf{M^l}\right][\mathbf{X}] \quad \text{and} \quad \left\{ \begin{array}{c} s^r x^r \\ s^r y^r \\ s^r \end{array} \right\} = \left[\mathbf{M^r}\right][\mathbf{X}] \tag{10.1}$$

where $[\mathbf{M^{l,r}}]$ denotes projection matrices for the left and right cameras, $[\mathbf{X}]$ the homogeneous coordinates, $x^{l,r}$ and $y^{l,r}$ the pixel coordinates in each camera, and $s^{l,r}$ the scale factors for the left and right cameras. I-DIC consists of minimizing the functional τ

$$\tau = \int_{\mathbf{ROI}} \left[f\left(\mathbf{x^l}(u, v, [\mathbf{M^l}])\right) - g(\mathbf{x^r}(u, v, [\mathbf{M^r}])) \right]^2 dudv \tag{10.2}$$

with respect to the unknown matrix components, where u and v denote the parametric coordinates of the surface model. Its linearization with respect to the corrections $dM_{ij}^{l,r}$ of the sought quantity yields

$$\tau_{\mathrm{lin}} = \int_{\mathbf{ROI}} \left[f\left(\mathbf{x^l}\right) - g(\mathbf{x^r}) + \left(\nabla f \cdot \boldsymbol{\delta x^l}\right)\left(\mathbf{x^l}\right) - (\nabla g \cdot \boldsymbol{\delta x^r})(\mathbf{x^r}) \right]^2 dudv \tag{10.3}$$

The positions in the IR and visible cameras are iteratively updated by computing the sensitivity fields

$$\boldsymbol{\delta x^{l,r}} = \frac{\partial \mathbf{x^{l,r}}}{\partial M_{ij}^{l,r}} dM_{ij}^{l,r} \tag{10.4}$$

At convergence, the gray level residual field shows that the black and white squares are matching (Fig. 10.2). The low level, i.e. 1.3 % of the dynamic range is due to the gray level corrections that are included (contrast and brightness). Before such corrections the residuals are as high as 19 % of the dynamic range. It is worth emphasizing that both images have not the same gray levels distributions.

In the following, it is assumed that the 3D sample used for the calibration phase and the characterized 2D surface share the same reference position. The calibration phase and a schematic view of the assumption are shown in Fig. 10.3.

Once the transformation matrices are determined, it is possible to perform SC analyses to measure 3D displacements by registering the reference and deformed images shot by the IR and visible light cameras. SC consists in minimizing the following functional [11]

Fig. 10.2 I-DIC residuals before (**a**) and after *gray* levels corrections (**b**) during the second calibration step
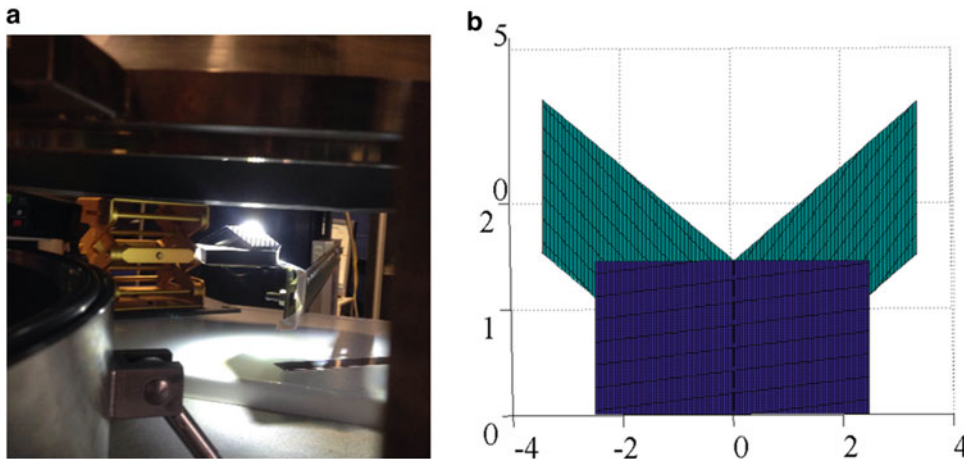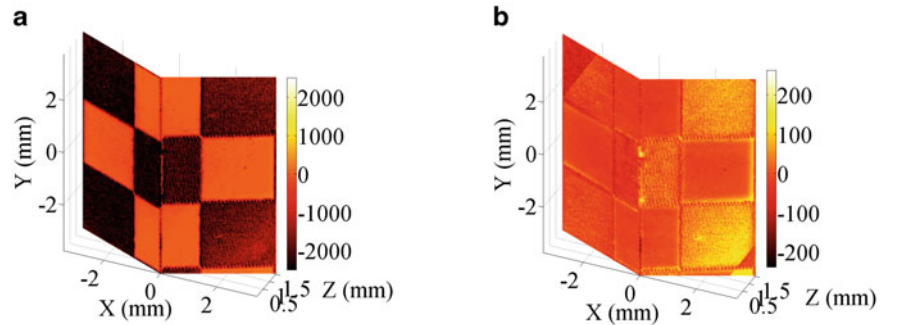

Fig. 10.3 3D target in an equivalent position (**a**). Due to experimental constraints, it is assumed that the 2-D and 3-D samples (**b**) are located at a same reference position

$$\boldsymbol{\tau} = \int_{ROI} \left[f(\mathbf{x^l}(u, v, \boldsymbol{P_{ij}})) - g(\mathbf{x^l}(u, v, \boldsymbol{P_{ij}} + d\boldsymbol{P_{ij}}))\right]^2 dudv + \int_{ROI} \left[f(\mathbf{x^r}(u, v, \boldsymbol{P_{ij}})) - g(\mathbf{x^r}(u, v, \boldsymbol{P_{ij}} + d\boldsymbol{P_{ij}}))\right]^2 dudv \quad (10.5)$$

where $\boldsymbol{P_{ij}}$ are the control points of the NURBS surface, that are in the present case 3×15 coordinates defining the 15 control points. The displacement fields are then obtained by estimating the motions $d\boldsymbol{P_{ij}}$ of the control points in the deformed images g. A Newton-Raphson algorithm is implemented to minimize the above functional. The linear equations to solve read [12]

$$[\mathbf{C}]\{\mathbf{dp}\} = \{\mathbf{b}\} \quad (10.6)$$

with the SC matrix

$$[\mathbf{C}] = \int_{ROI} \left(\frac{\partial \boldsymbol{x^r}}{\partial \boldsymbol{P_{ij}}} \cdot \nabla f^r \nabla f^r \cdot \frac{\partial \boldsymbol{x^r}}{\partial \boldsymbol{P_{ij}}} + \frac{\partial \boldsymbol{x^l}}{\partial \boldsymbol{P_{ij}}} \cdot \nabla f^l \nabla f^l \cdot \frac{\partial \boldsymbol{x^l}}{\partial \boldsymbol{P_{ij}}}\right) \boldsymbol{dudv} = [\boldsymbol{D^r}]^T[\boldsymbol{D^r}] + [\boldsymbol{D^l}]^T[\boldsymbol{D^l}] \quad (10.7)$$

where the unknowns are incrementally determined as

$$\{\mathbf{dp}\} = \{d\boldsymbol{P_{ij}}\} \quad (10.8)$$

and the SC vector

$$\{\mathbf{b}\} = [\boldsymbol{D^r}]^T(f^r - g^r) + [\boldsymbol{D^l}]^T(f^l - g^l) \quad (10.9)$$

At this stage the gray level corrections brought to the IR frames consist in removing the laser spot by first applying a Gaussian filter to the affected image and perform a subtraction to retain only the high frequencies. One may also use other methods available in the literature [17, 18].

10.4 Results and Discussions

The 3D target was not perfectly positioned on the reference position as illustrated in Fig. 10.4. This is visible on the residuals maps and the laser print present on both sides. The residuals are 3.4 and 1.2 % for the IR and visible light cameras, respectively. Hence, prior to calculations a correction was applied to the 2D model.

Before any corrections, the measured displacement and temperature fields are plotted in Fig. 10.5. The in-plane fields are expected to describe biaxial expansion. The amplitudes are close to the expected levels, namely, few micrometers for the applied loading, but they fail to reveal the expected expansion. This is due to the sample frame not being perfectly collinear to the 2D mathematical model of the surface or/and being rotated compared to the 3D frame used during the calibration step.

It is proposed to correct for this disalignment, through a corrected displacement expressed as

$$\{\underline{\mathbf{U}}\} = \left[\underline{\underline{R}}\right]\{\underline{\mathbf{U}}^{SC}\} \quad (10.10)$$

Fig. 10.4 Residual maps obtained with the (**a**) the visible light (in *gray* levels) and (**b**) IR (in *digital* levels) images after convergence (residuals interpolated in the parametric space)
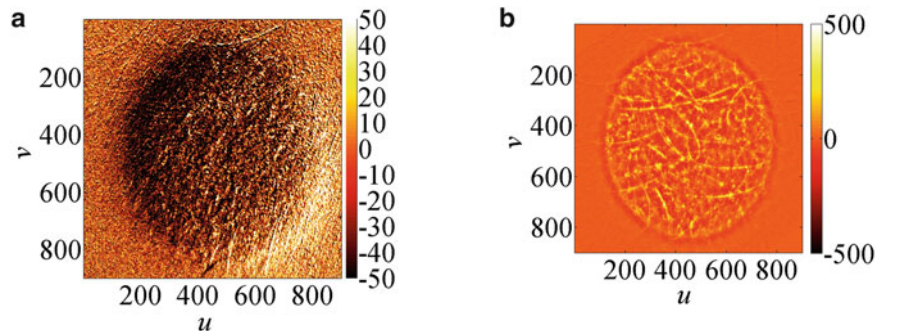
where $\left[\underline{\underline{R}}\right]$ denotes a 3D rotation matrix, and $\{\underline{U}\}$ the displacement field vector in the sample frame, while $\{\underline{U}^{SC}\}$ is the displacement vector determined in the rotated configuration. After corrections of a few degrees on each component the displacement field is in much better agreement with the expected biaxial expansion in the central part (Fig. 10.6).

To avoid such additional corrections, it is a necessity to perform reference RBTs on a 2D plate in which the same calibration procedures have been applied to preserve a unique frame.

Fig. 10.5 Displacement fields (**a**) Ux (**b**) Uy and (**c**) Uz (*color bar* in mm) before any rotation corrections, and (**d**) corresponding temperature field (*color bar* in °C)
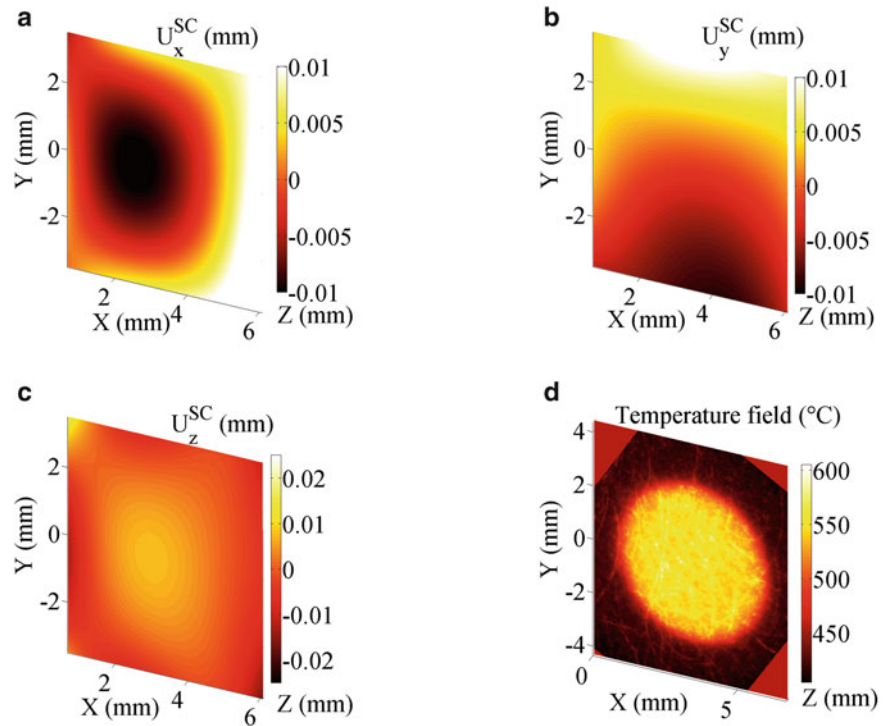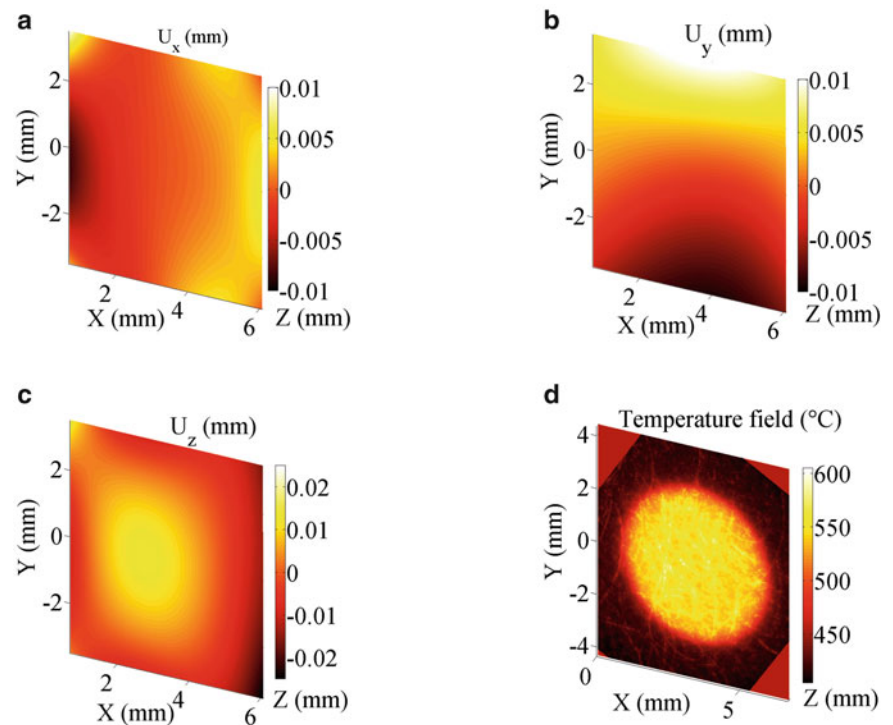

Fig. 10.6 Displacement fields (**a**) Ux (**b**) Uy and (**c**) Uz (*color bar* in mm) after a rotation correction and (**d**) the corresponding thermal loading (*color bar* in °C)

10.5 Conclusions and Perspectives

The new experimental setup designed to investigate thermal fatigue by using laser shocks allows 3D thermomechanical fields to be measured. Even if the testing machine only enables for the use of two cameras, global SC [10, 11] can be used to measure 3D surface displacements [12] *and* 2D thermal fields with a hybrid system. Its feasibility has been shown herein.

The calibration procedure needs to be further improved to have a better knowledge of the sample frame in comparison with that of the calibration target. The various uncertainties should also be investigated. The latter quantities need to be known when comparing or even performing material property identification with FE simulations [19, 20]. Last in this work a simple gray level correction was implemented for IR pictures. More advanced procedure may be implemented in order to enhance the sensitivity of the IR camera [17].

References

1. Amiable, A., Chapuliot, S., Contentinescu, S., Fissolo, A.: A computational lifetime prediction for a thermal shock experiment, part I: thermomechanical modeling and lifetime prediction. Fatigue Fract. Eng. Mater. Struct. **29**, 209–217 (2006)
2. Fissolo, A., Amiable, S., Ancelet, O., Mermaz, F., Stelmaszyk, J.M., Constantinescu, A., Robertson, C., Vincent, L., Maillot, V., Bouchet, F.: Crack initiation under thermal fatigue: an overview of CEA experience. Part I: thermal fatigue appears to be more damaging than uniaxial isothermal fatigue. Int. J. Fatigue **31**(3), 587–600 (2009)
3. Fissolo, A., Gourdin, C., Ancelet, O., Amiable, S., Demassieux, A., Chapuliot, S., Haddar, N., Mermaz, F., Stelmaszyk, J.M., Constantinescu, A., Vincent, L., Maillot, V.: Crack initiation under thermal fatigue: an overview of CEA experience: part II (of II): application of various criteria to biaxial thermal fatigue tests and a first proposal to improve the estimation of the thermal fatigue damage. Int. J. Fatigue **31**(7), 1196–1210 (2009)
4. Vincent, L., Poncelet, M., Roux, S., Hild, F., Farcage, D.: Experimental facility for high cycle thermal fatigue tests using laser shocks. In: Procceddings of Fatigue Design 2013, vol. 66, pp. 669–675 (2013)
5. Esnoul, C., Vincent, L., Poncelet, M., Hild, F., Roux, S.: On the use of thermal and kinematic fields to identify strain amplitudes in cyclic laser pulses on AISI 304L strainless steel. In: Photomechanics 2013, Montpellier, France (2013)
6. Charbal, A., Vincent, L., Hild, F., Poncelet, M., Dufour, J.-E., Roux, S., Farcage, D.: Characterization of temperature and strain fields during cyclic laser shocks. Quant. InfraRed Thermogr. J. **13**(1), 1–18 (2016)
7. Orteu, J.-J., Rotrou, Y., Sentenac, T., Robert, L.: An innovative method for 3-D shape, strain and temperature full-field measurement using a single type of camera: principle and preliminary results. Exp. Mech. **48**(2), 163–179 (2008)
8. Orteu, J.-J.: 3-D computer vision in experimental mechanics. Opt. Meas. **47**(3–4), 282–291 (2009)
9. Sutton, M.A.: Computer vision-based, noncontacting deformation measurements in mechanics: a generational transformation. Appl. Mech. Rev. **65**(5), 050802–050802 (2013)
10. Beaubier, B., Dufour, J.-E., Hild, F., Roux, S., Lavernhe, S., Lavernhe-Taillard, K.: CAD-based calibration and shape measurement with stereoDIC. Exp. Mech. **54**(3), 329–341 (2014)
11. Dufour, J.-E., Beaubier, B., Hild, F., Roux, S.: CAD-based displacement measurements with stereo-DIC: principle and first validations. Exp. Mech. **55**(9), 1657–1668 (2015)
12. Charbal, A., Dufour, J.E., Hild, F., Poncelet, M., Vincent, L., Roux, S.: Hybrid stereocorrelation using infrared and visible light cameras. Exp. Mech. **56**(5), 845–860 (2016)
13. Besnard, G., Lagrange, J.-M., Hild, F., Roux, S., Voltz, C.: Characterization of necking phenomena in high-speed experiments by using a single camera. EURASIP J. Image Video Process. 2010(1), 215956 (2010)
14. Dufour, J.-E., Hild, F., Roux, S.: Integrated digital image correlation for the evaluation and correction of optical distortions. Opt. Lasers Eng. **56**, 121–133 (2014)
15. Brown, D.C.: Decentering distortion of lenses. Photogramm. Eng. **32**, 444–462 (1966)
16. Brown, D.C.: Close-range camera calibration. Photogramm. Eng. **37**, 855–866 (1971)
17. Maynadier, A., Poncelet, M., Lavernhe-Taillard, K., Roux, S.: One-shot measurement of thermal and kinematic fields: infrared image correlation (IRIC). Exp. Mech. **52**(3), 241–255 (2012)
18. Poncelet, M., Leclerc, H.: A new digital images correlation algorithm to get rid of light reflection problems. In: Proceedings of Photomechanics 2015, Delft, The Netherlands (2015)
19. Avril, S., Pierron, F., Sutton, M.A., Yan, J.: Identification of elasto-visco-plastic parameters and characterization of Lüders behavior using digital image correlation and the virtual fields method. Mech. Mater. **40**(9), 729–742 (2008)
20. Mathieu, F., Hild, F., Roux, S.: Image-based identification procedure of a crack propagation law. Eng. Fract. Mech. **103**, 48–59 (2013)

Chapter 11
Experimental Characterization of the Mechanical Properties of 3D Printed ABS and Polycarbonate Parts

Jason Cantrell, Sean Rohde, David Damiani, Rishi Gurnani, Luke DiSandro, Josh Anton, Andie Young, Alex Jerez, Douglas Steinbach, Calvin Kroese, and Peter Ifju

Abstract Additive manufacturing (AM), more commonly referred to as 3D printing, has become increasingly popular for rapid prototyping (RP) purposes by hobbyists and academics alike. In recent years AM has transitioned from a purely RP technology to one for final product manufacturing. As the transition from RP to manufacturing becomes an increasingly accepted practice it is imperative to fully understand the properties and characteristics of the materials used in 3D printers. This paper presents the methodology and results of the mechanical characterization of acrylonitrile butadiene styrene (ABS) and polycarbonate (PC) 3D printed parts to determine the extent of anisotropy present in 3D printed materials. Specimens were printed with varying raster ([+45/−45], [+30/−60], [+15/−75], and [0/90]) and build orientations (flat, on-edge, and up-right) to determine the directional properties of the materials. Reduced gage section tensile and Isopescu shear specimens were printed and loaded in a universal testing machine utilizing 2D digital image correlation (DIC) to measure strain. Results indicated that raster and build orientation had a negligible effect on the Young's modulus or Poisson's ratio in ABS tensile specimens. Shear modulus and shear yield strength varied by up to 33 % in ABS specimens signifying that tensile properties are not indicative of shear properties. Raster orientation in the flat build samples reveal anisotropic behavior in PC specimens as the moduli and strengths varied by up to 20 %. Similar variations were also observed in shear for PC. Changing the build orientation of PC specimens appeared to reveal a similar magnitude of variation in material properties.

Keywords Digital image correlation • 3D printing • Additive manufacturing • Mechanical properties of materials • Rapid prototyping • Anisotropy • ABS • Polycarbonate

Nomenclature

3D	Three-dimensional
ABS	Acrylonitrile butadiene styrene
AM	Additive manufacturing
ASTM	American Society for Testing and Materials
CAD	Computer aided design
CI	Confidence interval
COV	Coefficient of variation
DIC	Digital image correlation
FDM	Fused deposition modeling
PC	Polycarbonate
RP	Rapid prototyping
SMP	Shape memory polymer
STL	Stereo lithography

J. Cantrell (✉) • S. Rohde • L. DiSandro • J. Anton • A. Young • A. Jerez • D. Steinbach • C. Kroese • P. Ifju
Mechanical and Aerospace Engineering Department, University of Florida,
571 Gale Lemerand Dr., MAE-C 134, Gainesville, FL 32611, USA
e-mail: jasontcantrell@gmail.com

D. Damiani
Bartram Trail High School, Saint Johns, FL 32259, USA

R. Gurnani
College of Engineering, University of California at Berkeley, Berkeley, CA 94720, USA

11.1 Introduction

Fused deposition modeling (FDM) is an additive manufacturing (AM) technique which works by a heated nozzle laying down molten material in layers to produce a desired part. FDM is one of the most common techniques used for 3D printers and has become one of the most popular rapid prototyping (RP) techniques in the last decade. FDM works by taking a part design by a computer aided design (CAD) model exported as a stereo lithography (STL) file and uploaded into a slicer program. The slicer program cross-sections the model into individual layers of a specified height and converts the desired height and other settings into G-Code to be read by the printer. The printer reads the G-Code, heats up a liquefier to the desired temperature to melt the polymer filament of choice, and begins extruding the material. The printing filaments used for this study were acrylonitrile butadiene styrene (ABS) and polycarbonate (PC). These filaments are fed through the heated liquefier by two drive wheels where the filament is then melted and extruded through a nozzle onto the build platform. The heating and extrusion of the filament to the specified diameter is all contained within the extrusion head which moves in the x-y plane depositing material on the build platform. A single line of material is called a road and the deposition of multiple roads side-by-side produces a single layer of a 3D printed part. After each layer is finished the build platform moves down a specified z or layer height and the process repeats for the next cross-sectioned layer until the part is completed. Figure 11.1 illustrates this process and highlights some of key parts within the extrusion head as well as the deposition of the extruded filament.

3D printing has increasingly progressed from a strictly prototyping technology to one used for production of final products intended for everyday use [1–4]. 3D printing has increasingly been used for advanced applications including the printing of adaptive structures utilizing shape memory polymer (SMPs) filaments and even printing cell structures in a granular gel medium [5–9]. This explosion in popularity has come with a proportionate increase in the study of 3D printed techniques as it is vital to comprehend the properties and characteristics of the parts which are created. Several previous studies utilized ASTM standard tensile test methods to determine the tensile properties as a function of the build and raster orientations the specimens were printed [10–20]. It has been widely publicized that in tension the road-to-road and layer-to-layer adhesion, shrinkage of the roads, and higher porosity in some orientations influences the material properties of the printed parts and causes anisotropy [15, 17, 21]. Several publications have worked to develop methods to reduce anisotropy by including the creation of polymeric blends and other blended materials or post-processing the parts via radiation [15, 16, 22, 23]. Creating polymeric blends and other blended materials did tend to reduce anisotropy but at the cost of the overall material strength. Radiation tended to have mixed results as some temperature/radiation combinations resulted in weakening of the parts while others did reduce anisotropy. Other studies did offer a more in depth look at the anisotropic properties of 3D printed materials and included the impact, flexural, or compression properties [24–26]. However, most studies on anisotropy of 3D printed materials generally give the Young's modulus, yield strength, and ultimate strength using extensometers and loads from a universal testing machine. These studies generally do not include other properties such as Poisson's ratio, strain energy density, or any shear data which are vital for complete understanding of the material behavior. Some publications did attempt to characterize shear properties of 3D printed materials; however, these properties are limited to those determined from the tension tests using the elastic modulus and the Poisson's ratio [18–20]. This approach assumes an isotropic relationship exists in the material on certain planes, which is somewhat of an over simplification. If the assumption is that the material is anisotropic, which is why such tests are performed, this approach neglects to take into

Fig. 11.1 Schematic of the standard FDM process with callouts for select parts within the extrusion head
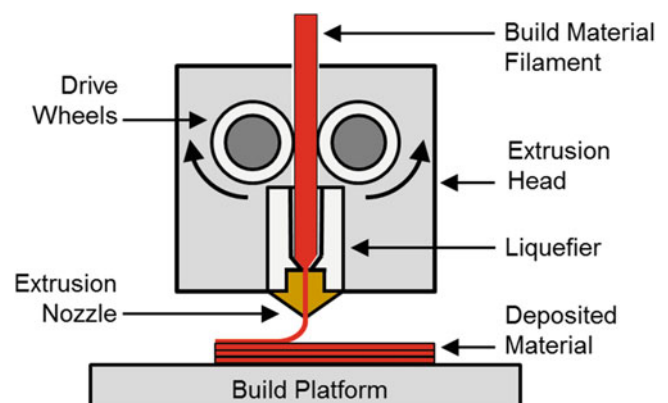
consideration the independence of the shear stress/strain behavior from the normal stress/strain behavior. Since the elastic moduli in all orientations don't vary significantly the assumption provides reasonably accurate shear moduli values. However, the shear strength as a function of orientation cannot be determined from tensile testing. In order to determine shear ultimate and yield strength a direct shear test method (specimen loaded in shear) should be utilized. Accurate shear strength measurements can only be made using a specimen that is loaded such that the test section is under both pure and uniform shear stress throughout the entire loading history. Pure shear means that normal stresses are minimized in the test section and shearing stresses dominate. Uniform shear stress is required to insure that failure, both in yielding and ultimate, occurs through the entire test section as a whole and is not localized. The most pure/uniform loading condition for shear testing is a hollow cylindrical specimen loaded in torsion [27]. This however cannot be utilized in this study because the specimen geometry is based on a cylindrical coordinate system whereas the printed material is oriented in a Cartesian coordinate system.

There are direct shear test methods that are specifically designed to achieve pure and uniform shear loading. Examples include; Iosipescu test [28–31], Arcan test [32, 33], Single and double shear rail tests [34–36]. The Iosipescu specimen was designed for testing anisotropic materials, is the most widely accepted test method for composites and has been shown to provide accurate shear modulus, when instrumented properly, as well as shear strength. The specimen is also relatively compact and well suited for 3D printed plastics. We propose to incorporate the use of the Iosipescu specimen for characterization of 3D printed materials in order to measurement of shear modulus, shear yield stress and shear strength.

In order to accurately measure shear modulus the average shear stress at any load is determined by dividing the load by the original cross-sectional area of the sample test-section. Typically the shear strain is measured via electrical resistance strain gages; however for 3D printed plastic materials gage reinforcement and self-heating complicate their use. Additionally, for this application with many dozens of specimens in our test program, application of electrical resistance strain gages would be prohibitively expensive and time consuming. We propose to utilize digital image correlation (DIC), a non-contact, full-field method instead. Using this experimental technique it is critical to measure the average shear strain in the test section rather than the shear strain at the center of the test section. This is because even though the specimen is designed to provide a uniform shear strain distribution in the test section, in reality the distribution is not perfectly uniform. The shear strain at the notches is zero, since it is a free surface with zero shear stress. The shear strain rises rapidly from the notches and forms a nearly uniform distribution. However the shear strain at the center of the test section does not equal the average value. Hence accurate shear stress/strain response can be determined by dividing the average shear stress by the average shear strain at any load, rather than by dividing the average shear stress by a local shear strain. This philosophy has been successfully utilized for composite material testing [37] using a specialized strain gage marketed by Vishay [38]. This methodology has been used on composites and plastics including PC and ABS; however, the studies on plastics were of injection molded specimens rather than 3D printed parts [39–42]. Using DIC the average shear strain in the test section was determined over an area that nearly spans the entire test section (19 mm) with a width of approximately 3 mm. Additionally, DIC is utilized in this manner on both sides of the specimen to account for potential differences cause by global specimen twist. This approach essentially integrates the shear strain through the entire volume of the test section [37].

Since the load path in the Iosipescu specimen must be transferred through the test section and since the shear strain is measured in the test section and not globally (displacement of one side of the fixture with respect to the other) any yielding of the stress strain diagram is representative of the material behavior. Thus even if the specimen ultimately fails outside of the test section, the shear stress strain diagram is representative of the material behavior to that point. However the stress/strain response is cut short and the actual ultimate strength and percent elongation may be higher.

The tensile and shear tests methods in this study utilize the same universal testing machine and digital image correlation setup for efficiency. The normal strain in the reduced gage section tensile specimens are measured over an area near the center of both sides of the specimen, much like the shear tests, and thus compensates for bending about both vertical axis of the specimen. This methodology is adopted rather than cross-head displacement because the latter is susceptible to errors caused by grip slippage and compliance in the load cell and loading fixtures.

Both the tensile and shear specimens are printed in various orientations within the 3D printer in order to assess the effect of build orientation and raster orientation on the anisotropy observed in the mechanical properties of ABS and PC test specimens. Both the ABS and PC specimens are evaluated for tensile and shear properties to give a complete picture of the mechanical behavior which will benefit researchers and undergraduates looking to incorporate 3D printed parts into their respective projects. This paper will describe fabrication methods, experimental procedure, and results from the characterization of ABS and PC.

11.2 Fabrication Methods, Experimental Set-Ups, and Procedures

11.2.1 Materials and Specimen Fabrication

The materials tested in this study were PC and ABS which were used to produce samples in a Stratasys® Fortus 360mc™ and an Ultimaker® 2 3D printer respectively. The specimen geometries followed specifications outlined in ASTM D-638 for the Type IV tensile specimens and ASTM D-5379 for the shear specimens [43, 44]. These specimens and select dimensions for both specimen types are shown in Fig. 11.2. Both specimen types were printed at a thickness of 4 mm (0.160 in.). The shear and tensile specimens were first created in Solidworks®, exported in stereo lithography (STL) format, and then imported into each 3D printer's respective slicer software to create the G-code used to print each specimen type.

The specimens printed on the Fortus 360mc™ machine used an extrusion width (the width of each layer of deposited material, also known as the road width) of 0.508 mm (0.020 in.) and a slice height (the height of an individual layer of deposited material) of 0.254 mm (0.010 in.). The Ultimaker® 2 used a default slice height of 0.1 mm (0.004 in.) and an extrusion width of 0.4 mm (0.016 in.). The slice height, extrusion width, air gap (the space between the bead of material), printer environmental temperature (the temperature of the air around the part and the bed temperature), build temperature (the temperature of the liquefier), nozzle size (width of the hole through which the material is extruded), and color (white for ease of use with DIC which is discussed in detail later) were all held to constant values. The entire list of constant or default values used during this study are shown in Table 11.1 for each printer. In order to completely understand the design space used by the printers, both the layer extrusion path, otherwise known as raster orientation and the part build orientation were selected as the parameters to vary during testing. These parameters were determined to be the most important and have been investigated by several other authors [10, 12, 13, 20, 45]. The raster orientations selected for investigation were [+45/−45], [+30/−60], [+15/−75], and [0/90]. The majority of specimens were printed in the [+45/−45] or [0/90] raster orientations unless large difference in material properties were discovered for a specific orientation. These orientations were selected instead of unidirectional orientations as a majority of 3D printers using an alternating raster pattern as the default printing scheme. Therefore, the data from this study will be directly relatable to the manufacturing of 3D printed parts. In addition to the four raster orientations, three build orientations were also investigated. These orientations are based upon which plane the front face of the specimen resides and were named accordingly. The three orientations investigated were flat (XY plane), on-edge (XZ plane), and up-right (ZX plane) and for clarification purposes are illustrated in Fig. 11.3 along with the raster orientation. An important item to note in Fig. 11.3 is that the primary printing axis differs from the primary raster axis by an angle of 45°. When a sample is printed parallel to the X or Y build plane the printers default raster orientation is [+45/−45]. Therefore, when a sample is printed at a raster orientation of [0/90] the sample is positioned at an angle of 45° on the printer bed surface. Ten specimens were printed for each printer/raster orientation and the results for all ten tests averaged to find the properties in each orientation.

Fig. 11.2 Schematic representation of the (**a**) ASTM D638 Type IV tensile specimen and (**b**) ASTM D5379 shear specimen geometries with relevant dimensions in mm
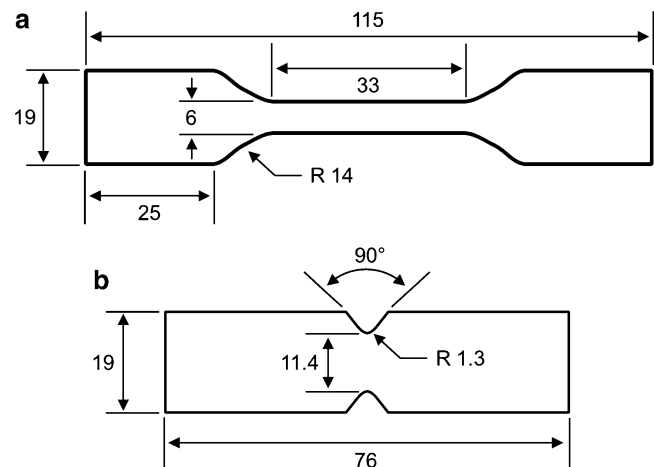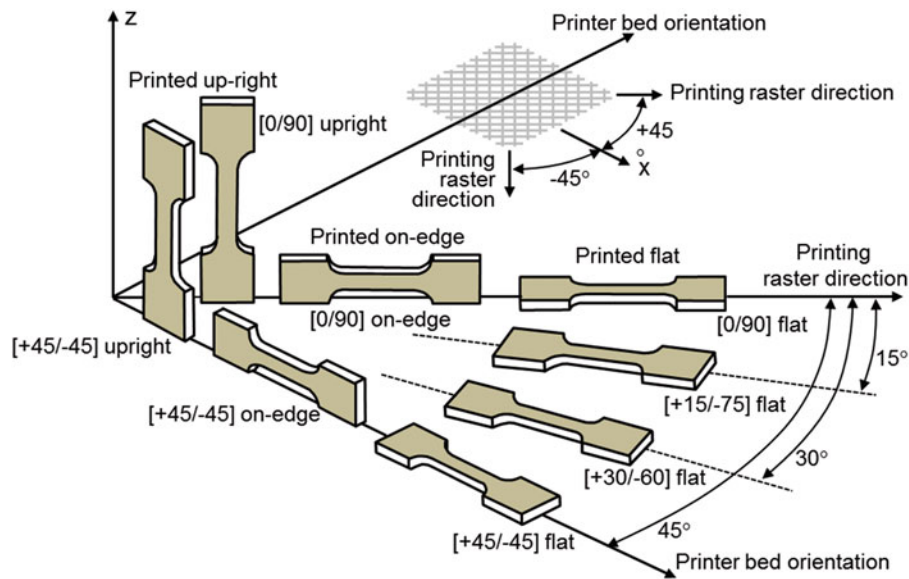
Table 11.1 Constant 3D printing process setting for the Fortus 360mc™ and Ultimaker® 2 printers

	Ultimaker® 2	Fortus 360mc™
Parameter	ABS value	PC value
Air gap (mm)	0.0	0.0
Slice height (mm)	0.1	0.254
Extrusion width (mm)	0.4	0.508
Nozzle size (mm)	0.4	0.4
Filament color	White	White
Fill (%)	100	100
Liquefier temperature (°C)	235	345
Environmental temperature (°C)	105 (Bed)	145 (Ambient)

Fig. 11.3 Graphic representation of the printer bed orientations (flat, on-edge, and up-right) and raster orientations ([+45/−45] [+30/−60], [+15/−75], and [0/90]) investigated

11.2.2   Testing Machine and Experimental Set-Up

A single test setup was developed for testing both tensile and shear properties of the material systems tested. The specimens were tested at a rate of 1.5 mm/min for both test methods at room temperature (~23 °C). Custom fixtures were manufactured to load the specimens in a Test Resources® 315 electromechanical universal testing machine equipped with a 22 kN load cell. The fixtures, shown in Fig. 11.4a, b, utilized multiple clevis joints to insure the load path through the sample was free of bending. Load values were recorded by Test Resources® Testbuilder™ software at a rate of 10 Hz. For tensile testing the average stress in the specimen, at any given load, was determined by dividing the load by the cross-sectional area. Collection of the necessary strain data was accomplished through the use of DIC, a non-contact, full-field shape and deformation measurement technique [46–48]. The strains were measured on both sides of the specimen using DIC over a rectangular region centered in the test section. This method compensates for a number of potential imperfections in loading and specimen geometry incurred during testing that cause inaccuracies. DIC was chosen for strain measurement rather than utilizing crosshead displacement because of potential grip slippage, loading mechanism compliance and load cell compliance, which is typical in such tests. Also, for testing polymers, electrical resistance strain gages mechanically reinforce the specimen as well as lead to strain gage self-heating issues. Additionally, extensometers typically only measure axial strain and in this study both axial and transverse strains are required to determine the Poisson's ratio. Although there are dedicated extensometers that measure both axial and transverse strain, such devices are bulky and the test section chosen for these studies is rather small. DIC strain measurement on both sides of the sample compensate for any bending during loading. Generally DIC can be
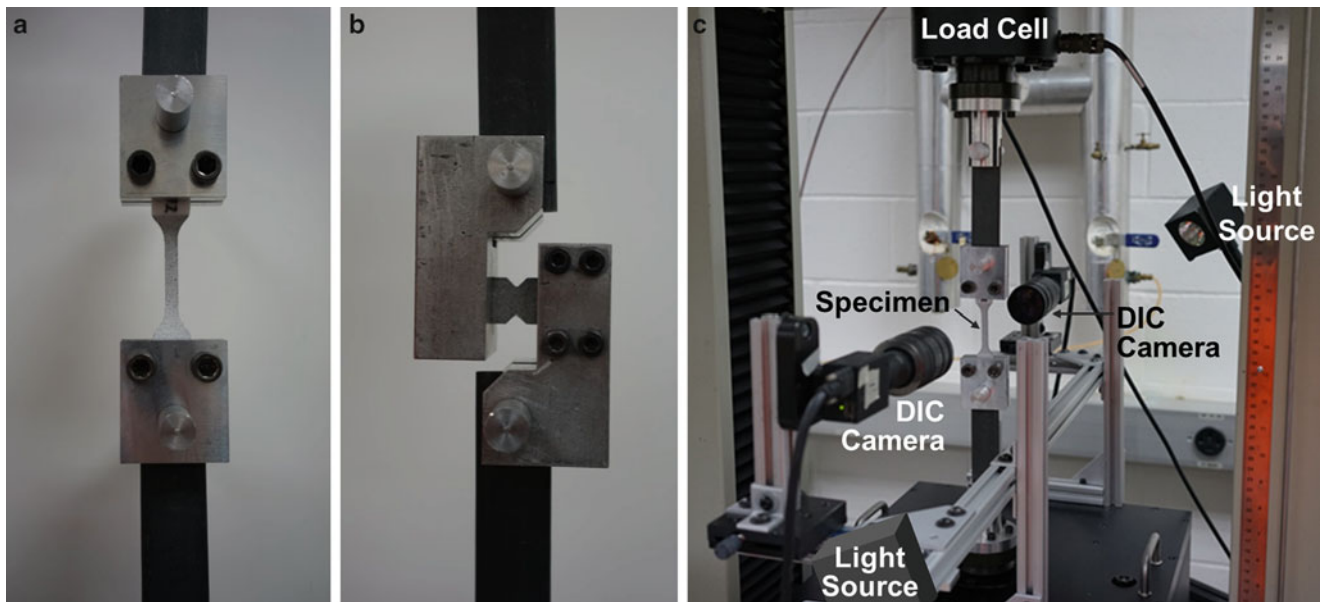
Fig. 11.4 Photographs of the (**a**) tensile specimen fixture, (**b**) shear specimen fixture, and (**c**) the experimental set-up and DIC camera set-up

performed either using a single camera or a pair in stereo. A single camera setup is susceptible to errors due to out-of-plane rigid body motion unless accounted for while the stereo setup can compensate for such motion. The DIC set-up used for this study consisted of two Point Grey® Research, 5-megapixel, grayscale cameras positioned on either side of the samples which simultaneously captured images of both sides of the samples. Using this single camera setup on both sides of the specimen allowed for compensation of rigid body motion by averaging the strain from the two sides. Specimen preparation only required a light speckle pattern of black paint over a light coat of white paint on the white plastic background, therefore had a negligible reinforcement effect. Images of the samples were captured via VIC-Snap™ 2009 at a rate of 1 Hz and later processed via VIC-2D™ to determine the strains. During processing in VIC-2D™ the standard subset size of 29 and step size of 5 were used which provided adequate strain and deformation data. After a sample was loaded into the testing machine and a preload applied, a pair of reference images (one image per camera) were taken of each side of the sample. These reference images were contrasted against images taken from the corresponding sides of the sample to determine the strains over the duration of the testing cycle. This methodology proved to be efficient and testing of a single specimen could be performed in a matter of minutes including mounting the specimen in the loading fixtures, taking initial undeformed DIC images, and loading the specimen through failure. The complete DIC and universal testing machine setup used for both tensile and shear testing is shown in Fig. 11.4c.

11.2.3 Experimental Procedure

Each shear and tensile test followed the same general experiment procedure throughout this study. After applying the high contrast DIC speckle pattern to the sample, it is loaded into its respective shear or tensile fixture shown in Fig. 11.4a, b. Once the specimen is loaded into the fixture the fixture/specimen combination is secured into the Test Resources® testing machine with multiple clevis joints. A preload of ~10 N is then applied and reference images are taken of both sides of the sample via the VIC-Snap™ software. The testing machine is set to a displacement rate of 1.5 mm/min and the VIC-Snap™ DIC software set to a rate of 1 Hz. The DIC and testing machine systems are started simultaneously and the testing is conducted through specimen failure. After specimen failure the test is concluded and the process repeated. Once all ten tests in a data set are completed the stress and strain behavior is analyzed via a MATLAB script, relevant properties determined, and stress-strain curves created for each specimen or set of specimens.

11.3 Results

11.3.1 Tension

The tension specimens were tested in batches of ten printed for each printer/raster orientation and the results for all ten tests averaged to find the properties in each orientation. Previous literature was primarily concerned with Young's modulus, yield strength, and failure modes for tensile specimens [11–16, 20, 45]. However, to give better insight into the complete material behavior the breaking strength (strength at sample failure), strain at failure, and the strain energy density were all calculated for each sample set. Each of these material properties are highlighted in Fig. 11.5 which illustrates where each property was calculated. The Young's modulus was calculated along the linear portion of the stress-strain curve, yield strength calculated using the 0.2 % offset method, and ultimate strength at the maximum stress value acquired. Strain at failure was calculated from the last DIC image available before sample failure. Breaking strength corresponds to the stress at that failure strain. Strain energy density was calculated by integrating the specimen stress strain curve. All seven of these properties were evaluated for each orientation combination and the results presented below.

The data from testing the ABS specimens showed some tensile properties appeared to behave isotropically while other properties exhibited anisotropic behavior with property differences of up to 91 %. All of the ABS tensile properties evaluated and orientation combinations tested are presented in Table 11.2. The Poisson's ratios and Young's moduli showed no statistically significant differences when comparing raster or print orientations as all values were within the 95 % confidence interval (CI). When evaluating the yield strength of each combination the [0/90] flat specimens had the highest value and raster orientation appeared to affect yield strength in the flat build orientation as the [+45/−45] flat specimens were 5.3 % weaker. Additionally, the [0/90] flat specimens had the highest ultimate strength; however, there were no statistically

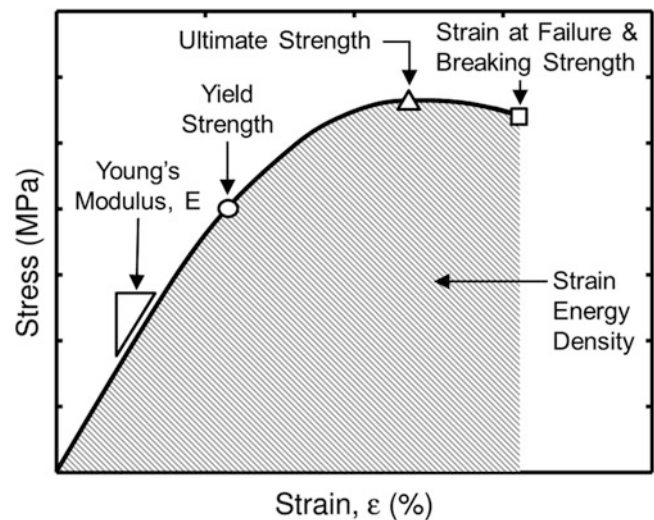**Fig. 11.5** Illustration of the relevant tensile stress-strain properties evaluated during this study

Table 11.2 Tension properties and 95 % CIs for the ABS specimen orientations tested

| Property | Orientation | | | | | |
| | [+45/−45] | [0/90] | [+45/−45] | [0/90] | [+45/−45] | [0/90] |
	Flat	Flat	On-edge	On-edge	Up-right	Up-right
Poisson's ratio	0.36 ± 0.03	0.37 ± 0.04	0.38 ± 0.03	0.36 ± 0.02	0.36 ± 0.03	0.36 ± 0.03
Young's modulus (MPa)	1960 ± 60	2020 ± 60	2020 ± 110	1910 ± 60	2040 ± 90	2050 ± 110
Yield strength (MPa)	30.3 ± 0.6	32.0 ± 0.8	30.0 ± 1.1	29.0 ± 0.6	29.3 ± 0.8	29.9 ± 1.6
Ultimate strength (MPa)	32.8 ± 0.6	33.5 ± 0.5	31.9 ± 0.9	30.7 ± 0.7	30.0 ± 0.8	30.9 ± 1.3
Strain at failure (%)	8.89 ± 2.34	7.14 ± 2.79	5.41 ± 1.13	5.82 ± 1.26	1.72 ± 0.16	1.84 ± 0.15
Breaking strength (MPa)	29.6 ± 0.5	30.7 ± 0.5	30.1 ± 0.9	29.4 ± 0.7	29.9 ± 0.8	30.8 ± 1.3
Strain energy density (MJ/m^3)	3.17 ± 1.04	2.14 ± 1.03	1.46 ± 0.37	1.66 ± 0.41	0.29 ± 0.04	0.32 ± 0.03

significant differences between the raster orientations. The up-right specimens had the lowest ultimate strengths and were on average 8 % weaker than the flat specimens. The up-right printer orientations also had the lowest strains at failure, averaging 5.6 % lower strain values than the flat orientation and 3.8 % lower values than the on-edge orientations. Like the yield and ultimate strength values explained previously, the [0/90] flat specimens again had the highest breaking strength and was 3.6 % higher than the [+45/−45] flat specimen. The only other statistically significant difference was between the [0/90] flat and on-edge specimens were there was a 0.1 MPa difference in the 95 % confidence intervals and a 4.2 % difference in the means. Finally, the property which exhibited the largest differences in values was the strain energy density. The flat orientations had the highest energy densities which were up to 91 % higher than the up-right orientations and 54 % higher than the on-edge orientations. Overall the [0/90] flat orientation had the highest tensile property performance while the [+45/−45] up-right orientation had the weakest properties. Anisotropy was found more often when varying printer orientation than when changing raster orientation and some ABS tensile properties exhibited isotropic behavior.

In addition to the results being detailed in Table 11.2 each tensile test was analyzed and plotted as a stress-strain curve to illustrate the data graphically. All ten tests from each orientation combination were plotted together to give an idea of the data spread and then averaged together to a representation of the typical stress-strain behavior for that combination. Two examples of the data scatter are shown in Fig. 11.6a, c. Figure 11.6a illustrates the relatively uniform behavior of the [+45/−45] flat ABS specimens through ultimate strength. The [+45/−45] flat specimens do have a large variation in strain at failure but have one of the lowest 95 % CIs for breaking strength. Figure 11.6c shows the behavior of the [0/90] up-right specimens which have a confidence interval nearly twice as wide as the [+45/−45] specimens. Furthermore, the [+45/−45] flat specimens behave in a ductile manner while the [0/90] up-right specimens appear to behave in a more brittle manner as many specimens fail at the ultimate strength. This brittle behavior and higher CI is most likely due to the up-right printing orientation as failure strain is entirely dependent upon the adhesion between layers rather than the ABS roads themselves. The average specimen orientation behaviors shown in Fig. 11.6b, d respectively further illustrate these findings as the [+45/−45] specimen average has a clear ultimate strength peak followed by a long period of plastic deformation while the [0/90] specimen average has an elastic region quickly followed by failure of the specimens. Finally, all six orientation combinations are shown in Fig. 11.6e which helps to visually present the entirety of the data displayed in Table 11.2. The [0/90] flat orientation specimen clearly outperforms the other five orientation combinations with respect to strength, followed closely by the [+45/−45] flat, and then the on-edge orientations. The flat and on-edge orientations exhibit ductile material behavior while both up-right orientations behavior in a brittle manner.

The data collected from the testing of the PC specimens, like the ABS specimens, showed that several tensile properties exhibited anisotropic behavior with property differences of up to 74 %. The flat printer orientation presented such a large degree of anisotropy when varying raster orientation between [+45/−45] and [0/90] that two additional orientations ([+30/−60] and [+15/−75]) were printed to be evaluated resulting in a total of eight orientation combinations being tested for PC. All of the PC orientation combinations and their respective tensile properties are presented in Table 11.3. The Poisson's ratio displays anisotropic behavior when evaluating raster orientation as the [+45/−45] flat orientation has a Poisson's ratio that is 26 % higher than the [0/90] flat orientation. While not all Poisson's ratios in the flat printer orientation had statistically significant differences there was a pattern of increasing Poisson's ratio through the raster sweep from [0/90] to [+45/−45]. The same results were found when evaluating Young's modulus as the [+45/−45] flat orientation was 14 % greater than the [0/90] flat orientation. The same increase in Young's modulus was found when sweeping through the raster angles in the flat orientation while the on-edge specimens appeared to be isotropic with respect to raster orientation. In the upright printer orientation anisotropic behavior was found as well as the [+45/−45] specimens had a Young's modulus that was 8 % higher than the [0/90] specimens. Furthermore, there were significant differences between print orientations as the [+45/−45] on-edge had a 6 % higher Young's modulus than the flat orientation and an 11.5 % higher modulus than the up-right orientation. The [0/90] on-edge orientation had a 17 % higher modulus than the other two print orientations whose moduli where approximately equal.

Anisotropic behavior was also present when evaluating the orientation combinations with respect to yield strength. Both the flat and on-edge orientations exhibited significant differences in raster orientation. The yield strength of the [+45/−45] raster specimen in the on-edge orientation was 8 % higher than the [0/90] specimen. The [+45/−45] raster specimen in the flat orientation had a yield strength that was 14 % higher than the [0/90] orientation and 23 % higher than the [+30/−60] orientation. This was an unexpected result as the yield strength did not appear to correlate with the raster orientation and actually alternated through the raster sweep. Varying the printer orientation also resulted in statistically significant differences in yield strength as the on-edge print orientation was up to 21 % greater than the up-right and up to 30 % larger than the flat orientations. Ultimate strength and strain at failure yielded similar behaviors as the [+45/−45] raster orientations generally yielded higher ultimate strength and strain at failure values. Additionally, the same alternating pattern of material behavior was seen in the flat orientation with the [+45/−45] flat samples having 55 % higher strain at failure values than [+30/−60] yet being only 30 % higher than the [+15/−75] orientation. Breaking strengths were similar for the [+45/−45]
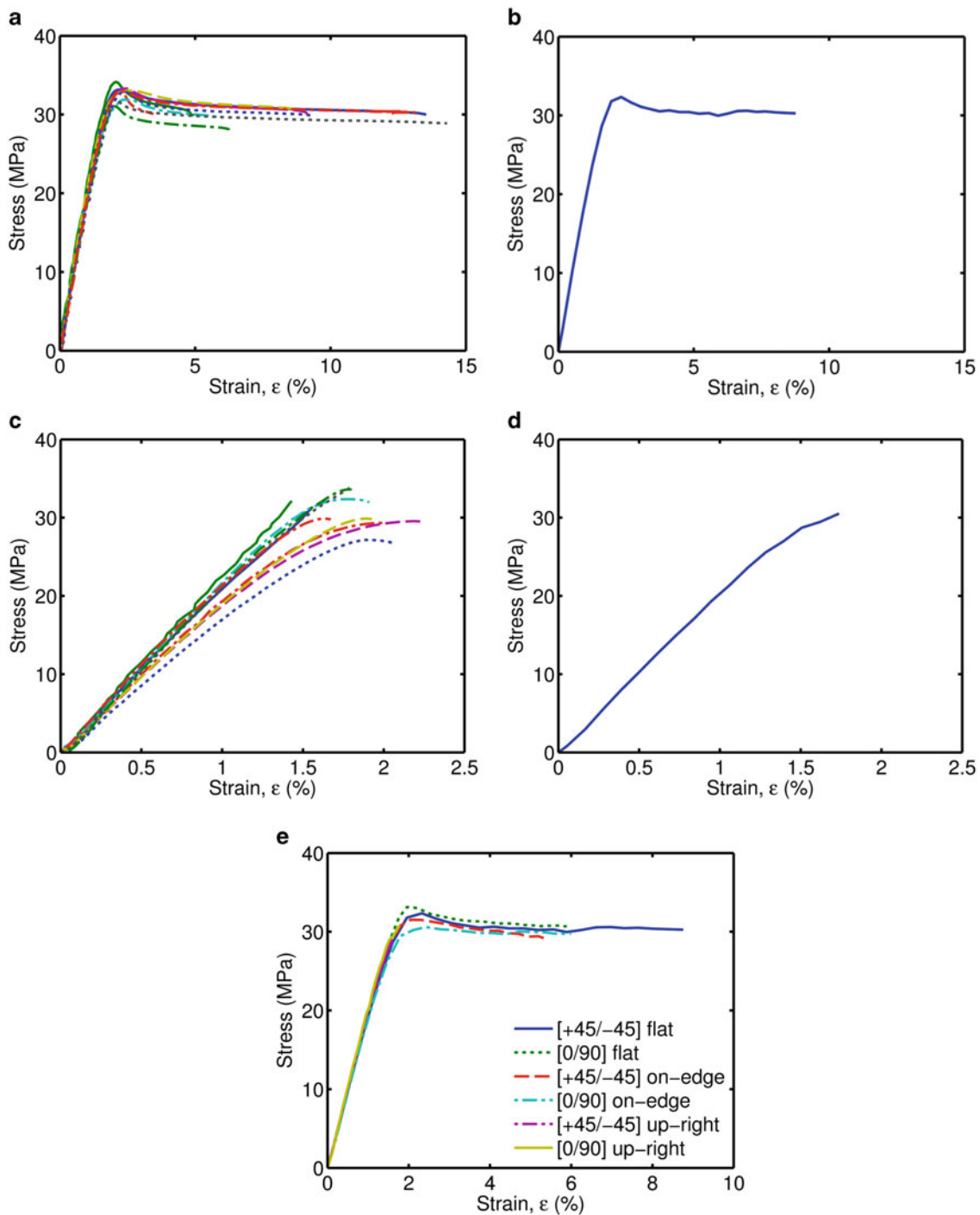
Fig. 11.6 Stress-strain curves for (**a**) ten [+45/−45] flat ABS tension specimens illustrating the data scatter of the samples tested and (**b**) the average of the ten [+45/−45] flat ABS tension specimens. The stress-strain curves illustrating (**c**) the data scatter for ten [0/90] upright ABS tension specimens, (**d**) the average of the ten [0/90] upright ABS tension specimens, and (**e**) the six major ABS raster/print orientation combinations

and [+15/-75] flat orientations which were 23 % higher than the breaking strengths of the [+30/-60] and [0/90] orientations. The on-edge specimens produced the highest breaking strengths while the upright specimens produced values similar to the weaker flat orientations. Finally, significant differences were seen in the strain energy density with respect to both the raster and print orientations. Again the on-edge orientations have much higher strain energy densities when compared to the up-right orientations. Overall the [+45/−45] on-edge orientation performed the best overall and had the highest or second highest tensile properties of the orientation combinations tested. The [+45/−45] flat and [0/90] on-edge orientations

Table 11.3 Tension test results and 95 % CIs for the PC specimen orientations tested

Property	Orientation			
	[+45/−45] flat	[+30/−60] flat	[+15/−75] flat	[0/90] flat
Poisson's ratio	0.39 ± 0.03	0.36 ± 0.02	0.33 ± 0.02	0.29 ± 0.02
Young's modulus (MPa)	1890 ± 60	1840 ± 20	1780 ± 30	1620 ± 60
Yield strength (MPa)	39.7 ± 0.9	30.4 ± 1.3	38.8 ± 1.2	34.3 ± 1.5
Ultimate strength (MPa)	56.6 ± 0.5	41.5 ± 2.3	54 ± 0.4	44.3 ± 0.4
Strain at failure (%)	6.72 ± 0.94	3.01 ± 0.19	4.57 ± 0.07	3.78 ± 0.21
Breaking strength (MPa)	54.0 ± 0.7	41.5 ± 2.3	53.7 ± 0.5	44.3 ± 0.4
Strain energy density (MJ/m^3)	2.91 ± 0.55	0.73 ± 0.09	1.49 ± 0.18	1.01 ± 0.08
Property	Orientation			
	[+45/−45] on-edge	[0/90] on-edge	[+45/−45] up-right	[0/90] up-right
Poisson's ratio	0.37 ± 0.02	0.38 ± 0.03	0.35 ± 0.03	0.31 ± 0.02
Young's modulus (MPa)	2000 ± 30	1950 ± 80	1770 ± 30	1630 ± 30
Yield strength (MPa)	43.5 ± 1.1	40.0 ± 1.9	35.8 ± 0.6	34.5 ± 0.8
Ultimate strength (MPa)	61.1 ± 0.5	57.9 ± 1.8	44.3 ± 1.1	42.4 ± 0.4
Strain at failure (%)	6.03 ± 0.57	4.72 ± 0.44	3.07 ± 0.11	3.18 ± 0.05
Breaking strength (MPa)	58.0 ± 1.4	57.8 ± 1.9	44.7 ± 1.2	42.2 ± 0.4
Strain energy density (MJ/m^3)	2.52 ± 0.19	1.75 ± 0.21	0.78 ± 0.06	0.76 ± 0.02

provided similar but slightly lower tensile properties. The on-edge specimens appeared to be isotropic in nature while large amounts of anisotropy were found when varying raster angle in the flat print orientation.

Generally the PC tests yielded confidence intervals and coefficients of variation (COVs) which were much smaller than the ABS specimens tested. The COV for the PC specimens averaged around 3.4 % for the Young's modulus while the COV for ABS specimens was nearly double at 6.5 %. This reduction in uncertainty was most likely due to the higher quality of the PC specimens printed by the Fortus 360mc™. This reduced scatter is clearly illustrated in Fig. 11.7a as all ten [+45/−45] flat samples have almost identical stress-strain curves with the exception of the strain to failure behavior. Figure 11.7c shows the average behavior of the six primary orientation configurations which illustrates that the on-edge specimens outperform the other two printer orientations. The [+45/−45] flat orientation has properties similar to the on-edge specimens and then there is a marked decrease in moduli and strength properties when observing the remaining orientations. The on-side and [+45/−45] flat specimens exhibit a more ductile material behavior while the other three primary orientations behave in a brittle fashion. Finally, Fig. 11.7d displays the raster sweep in the flat printer orientation which shows the discernible differences in material behavior with respect to raster orientation. The [+30/−60] and [0/90] orientations have much lower strength properties than the [+45/−45] and [+15/−75] orientations. The striking differences in material behavior could be due to a variety of factors like printer motor mechanics causing excessive air voids at the specimen boundaries or poor adhesion between PC layers.

While evaluating the PC and ABS specimens for the tensile material properties, the DIC images from each test were also evaluated to determine if patterns were present that could provide reasons for certain material characteristics. The PC specimens provided excellent DIC patterns and insight into material behavior; especially in the flat build orientation as individual PC roads in each layer could be seen when looking at the DIC results. Two sets of images depicting the longitudinal displacements and the strain fields for the [+45/−45] flat and [0/90] flat orientation combinations are shown in Fig. 11.8. These images clearly show the loading conditions of the raster and the strain variations within each specimen. The [+45/−45] orientation specimen has a more uniform strain pattern with slight peaks in strain along the PC roads while the [0/90] flat orientation specimen has a bimodal strain pattern. The [0/90] specimen has an alternating pattern of 0 and 2.5 % strain indicating that the individual roads are more likely to see higher strain values resulting in failure sooner than the more uniform [+45/−45] specimens where the entire structure is bearing the tensile load. This strain pattern also makes specimens more susceptible to failures due to printing imperfections as an imperfection could be printed along a road which would cause premature failure of the specimen due to the strain being concentrated in the individual roads. These observations support the results shown previously as the [0/90] flat specimens appear to perform worse than the [+45/−45] flat specimens in every tensile property category.

In addition to the stress-strain curve results, the fracture surfaces of the tensile specimens were evaluated for both the ABS and PC. The ABS specimens all behaved in a similar manner at fracture. These specimens all fractured cleanly in the plane perpendicular to the loading direction. The PC specimens fractured in a variety of ways and the most common failure
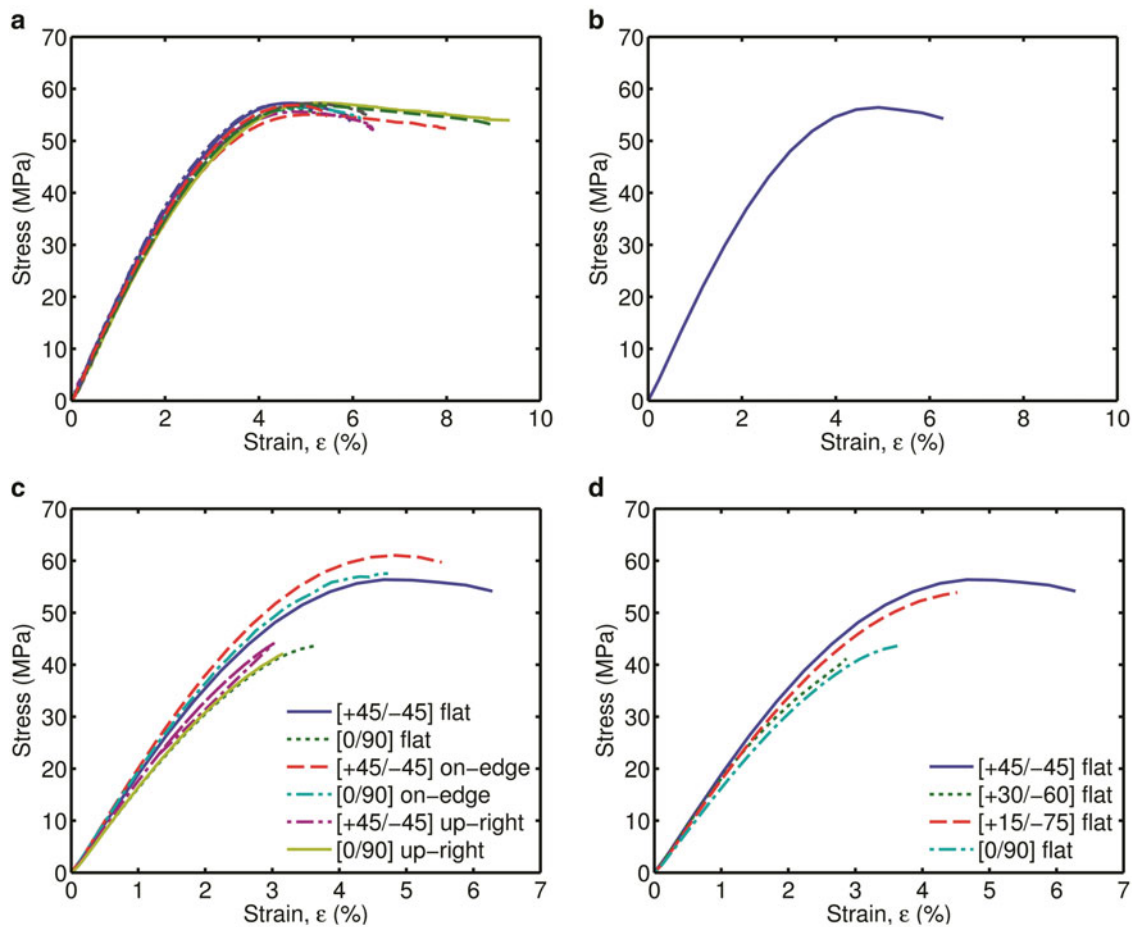
Fig. 11.7 Stress-strain curves for (**a**) ten [+45/−45] flat PC tension specimens and (**b**) the average of ten [+45/−45] flat PC tensile specimens. The average stress-strain curve behavior for (**c**) the six major PC raster/print orientation combinations and (**d**) a sweep of the flat PC raster orientations tested

modes for each orientation combination are shown in Fig. 11.9. Most specimens appeared to fracture cleanly in the same perpendicular plane that the ABS samples did. However, there were some notable differences as both on-edge specimens had jagged perpendicular fracture surfaces. The [+45/−45] flat PC specimen was also notably different from most fracture surfaces as the PC roads tended to tear apart rather than break cleanly resulting in a saw tooth-like pattern. Overall the specimens that exhibited cleaner fractures surfaces had markedly lower strain at failure values when compared to the three previously mentioned specimen orientations. Additionally, these specimens had a lower Young's modulus, ultimate strength, and strain energy density. These results indicate that some insight into the overall material properties can be gained from simply observing the specimen failure modes.

11.3.2 Shear

Like the results in the previous section, the shear specimen results were derived from ten tests for each printer/raster orientation and averaged to give a mean value as well as a 95 % confidence interval for each parameter evaluated. The results of these tests are displayed in Table 11.4. During shear testing only the shear modulus, yield strength, and ultimate strength were calculated as some specimens did not fail before the destruction of the DIC speckle pattern, making strain to failure calculations for some samples impossible. The PC specimens were more apt to fail during testing while the ABS specimens were ductile and very few ABS specimens failed completely. Unlike the results seen in tensile testing, there were several cases of anisotropy seen during shear testing in the ABS specimens. Despite the Young's modulus appearing isotropic in nature during tensile testing, differences of up to 25 % were found when comparing shear moduli. There was no

Fig. 11.8 DIC results showing the longitudinal displacement and strain fields results for [+45/−45] and [0/90] flat PC tensile specimens
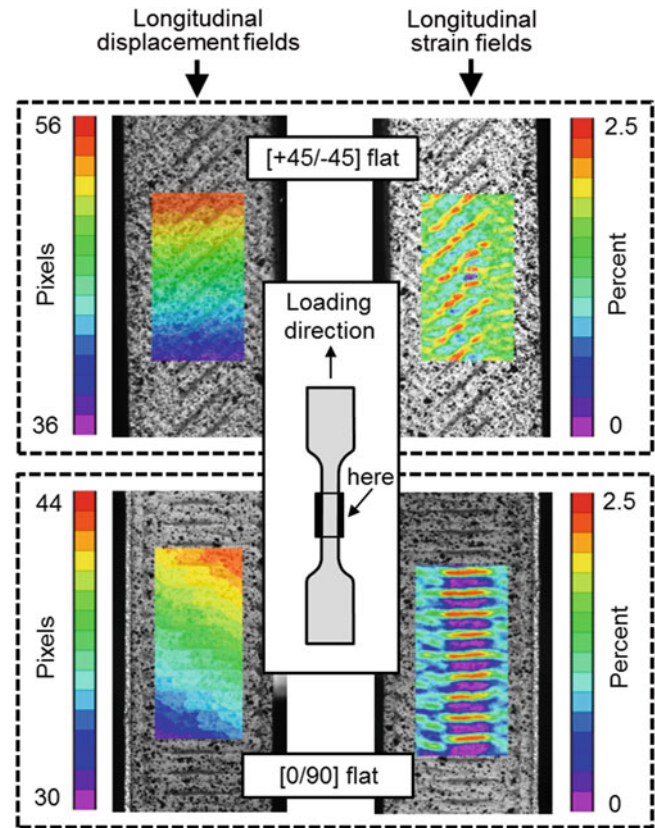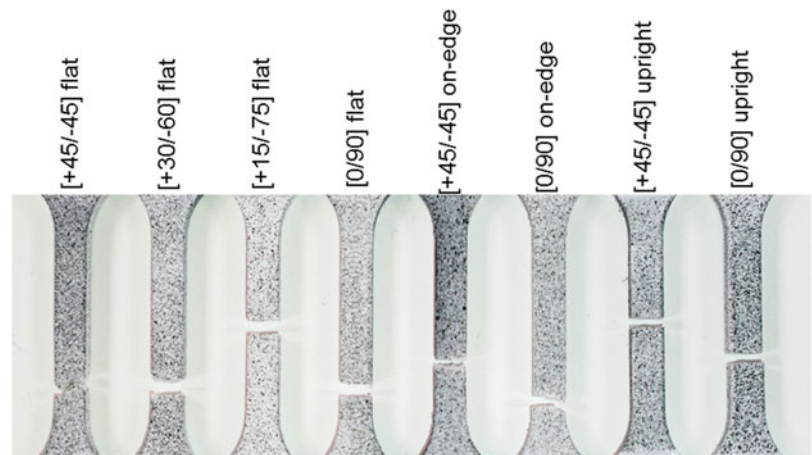

Fig. 11.9 A photograph of gage sections of the eight tensile PC specimens and the most common failure modes for each raster/printer orientation combination

significant effect on the shear modulus when varying raster orientation; however, when print orientation was varied the flat orientation was found to have a 25 % higher modulus than the on-edge samples and 12 % higher modulus than the up-right samples. The same results were seen when evaluating yield strength as raster orientation did not appear to have an effect on the sample strength. When evaluating printer orientation the flat orientations featured the highest values and the on-edge and up-right specimens being approximately equal in value. Finally, assessing the ultimate strengths revealed that the [0/90] on-edge specimens had 32 % lower values than the [0/90] flat specimens. This dissimilarity appeared to be due to weak adhesion between the deposited layers of material as the [0/90] on-edge specimens appeared to delaminate along the notched area while most specimens had shear flow along the notched region. The ultimate strength of the up-right specimens was also lower than the flat specimens; however, no delamination occurred and the maximum difference was halved to 16 %.

The PC specimens shear properties were much more varied and did see some anisotropy when comparing the orientation combinations. The [+45/−45] flat and [+45/−45] on-edge orientations had the highest shear moduli while the [0/90] flat

Table 11.4 Shear modulus, yield strength, and ultimate strength average values with 95 % CIs for the ABS and PC specimen orientations tested

Orientation	Shear modulus (MPa)	Yield strength (MPa)	Ultimate strength (MPa)
ABS			
[+45/−45] flat	740 ± 30	19.1 ± 0.5	28.8 ± 0.2
[0/90] flat	770 ± 40	21.5 ± 2.0	29.1 ± 0.3
[+45/−45] on-edge	610 ± 30	16.0 ± 1.1	23.9 ± 0.7
[0/90] on-edge	580 ± 20	14.5 ± 1.3	19.9 ± 1.8
[+45/−45] up-right	670 ± 30	15.5 ± 1.3	25.8 ± 0.3
[0/90] up-right	680 ± 40	15.4 ± 1.5	24.4 ± 0.5
Polycarbonate			
[+45/−45] flat	670 ± 10	22.8 ± 1.0	36.9 ± 0.3
[+30/−60] flat	640 ± 20	15.8 ± 0.6	30.4 ± 1.9
[+15/−75] flat	650 ± 20	18.2 ± 0.7	34.0 ± 0.8
[0/90] flat	540 ± 10	14.7 ± 0.8	29.5 ± 0.5
[+45/−45] on-edge	660 ± 10	19.9 ± 1.0	32.6 ± 0.7
[0/90] on-edge	650 ± 10	18.1 ± 0.9	30.0 ± 0.7
[+45/−45] up-right	680 ± 10	21.1 ± 0.6	34.0 ± 1.1
[0/90] up-right	630 ± 20	18.0 ± 0.6	30.0 ± 0.5

orientation had the lowest modulus value. Raster orientation did have an effect on shear modulus as the [+45/−45] samples had the highest moduli values across all printer orientations. Printer orientation appeared to have less of an effect on shear modulus as only the [0/90] flat and [0/90] up-right specimens were significantly different from the other orientations. Yield strength and ultimate strength showed similar results when evaluating raster orientation as the [+45/−45] flat orientation yield strength was 36 % higher and its ultimate strength was 20 % higher than the [0/90] orientation. The exceptions were the on-edge samples, which were isotropic in nature. Overall the [+45/−45] flat orientation had the highest material properties while the on-edge printer orientation appeared to be the most isotropic. When sweeping through the raster angles in the flat orientation, all of the shear moduli were nearly identical with the exception of the [0/90] orientation. However, when evaluating the ultimate and yield strengths the same alternating pattern seen in the tensile results was also present in the shear samples. The highest values were seen in the [+45/−45] raster orientation, followed by the [+15/−75], [+30/−60], and [0/90] orientations respectively.

Images illustrating the scatter seen in the shear stress-strain curves and the average stress-strain behavior of ten [+45/−45] flat orientation ABS samples are shown in Fig. 11.10a, b respectively. The scatter and confidence intervals for the PC samples resulted in a Young's modulus COV of 3.5 % while the ABS specimens produced an average COV of 7.7 %, again nearly doubling that of the PC tests. Fig. 11.10c shows the average behavior for the six primary orientation configurations for the ABS specimens. This figure helps to clearly illustrate the strength and superior properties of the flat orientation in shear. The up-right ABS specimens were the second best printer orientation and finally the on-edge specimens which appeared to perform poorly due to weak adhesion between the layers of material. Generally, the [+45/−45] specimens appeared to perform better in shear with the exception of the flat specimens were nearly identical. Fig. 11.10d illustrates the average performance of the PC specimens in the six primary orientation configurations. The graph shows that [+45/−45] specimens are clearly superior specimens in shear as all three have ultimate values which are higher than the [0/90] specimens. There is less certainty when comparing printer orientation as in the flat configuration the [+45/−45] specimen has the best properties of the six specimens but the worst when oriented in the [0/90] orientation suggesting shear is more dependent upon raster orientation. Finally, Fig. 11.10e presents the raster sweep in the flat printer orientation for the PC specimens. Again the results are mixed as the [+45/−45] configuration has the highest strength properties followed by the [+15/−75]. However, the moduli are similar for three of the four orientations despite the irregularity of the yield and ultimate strength properties.

Identical to the tensile testing procedure, DIC images were collected from each test to examine the strain fields during loading. The [+45/−45] flat and [0/90] flat orientation combinations showed some of the most noticeable patterns and images throughout the testing cycle. DIC results which display the longitudinal displacements and the strain fields at a point in the elastic portion of the stress-strain curve are shown in Fig. 11.11. The images were taken at similar points in the stress-strain curve and clear patterns can be seen in both the [+45/−45] and [0/90] flat specimens. Both strain patterns show the road orientation within the specimen as the peak strains follow the roads. The difference in the specimens is, like in the tensile tests, the [0/90] specimen has an alternating peak and valley pattern while the strain appears to be more uniform in the [+45/−45] specimen. The [+45/−45] specimens strain is averaged over the entire specimen while the [0/90] specimen has
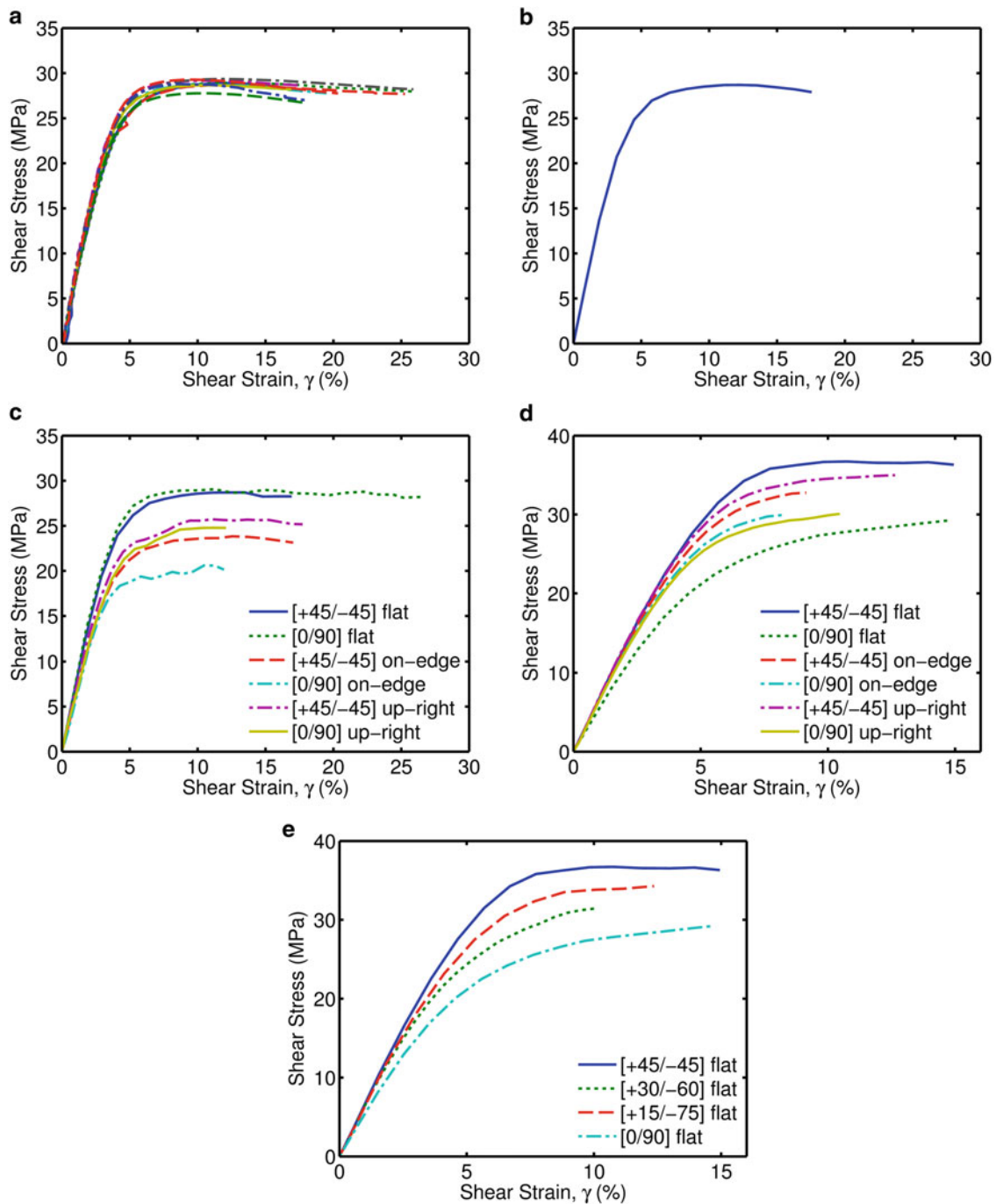
Fig. 11.10 Stress-strain curves for (**a**) ten [+45/−45] flat ABS shear specimens illustrating the data scatter and (**b**) the average of ten [+45/−45] flat ABS shear specimens. (**c**) The average stress-strain curve behavior for the six ABS raster/print orientation combinations tested. The average stress-strain curve behavior for (**d**) the six major PC raster/print orientation combinations and (**e**) a sweep of the flat PC raster orientations tested

concentrated loads at individual roads. These images support the outcomes shown previously as these concentrations appear to cause the [0/90] specimens to have a lower modulus and poorer strength values.

Finally, the fracture surfaces of the shear specimens were also evaluated. Due to the ductile behavior of the ABS specimens very few specimens were brought to complete failure as destruction of the DIC speckle pattern occurred well before specimen failure. Therefore, the ABS specimens fracture surfaces were not evaluated. However, the PC specimens were much more brittle in nature, and nearly all specimens experienced complete failure during testing. The PC specimens

Fig. 11.11 DIC results displaying the longitudinal displacement and strain fields for [+45/−45] and [0/90] flat PC shear specimens
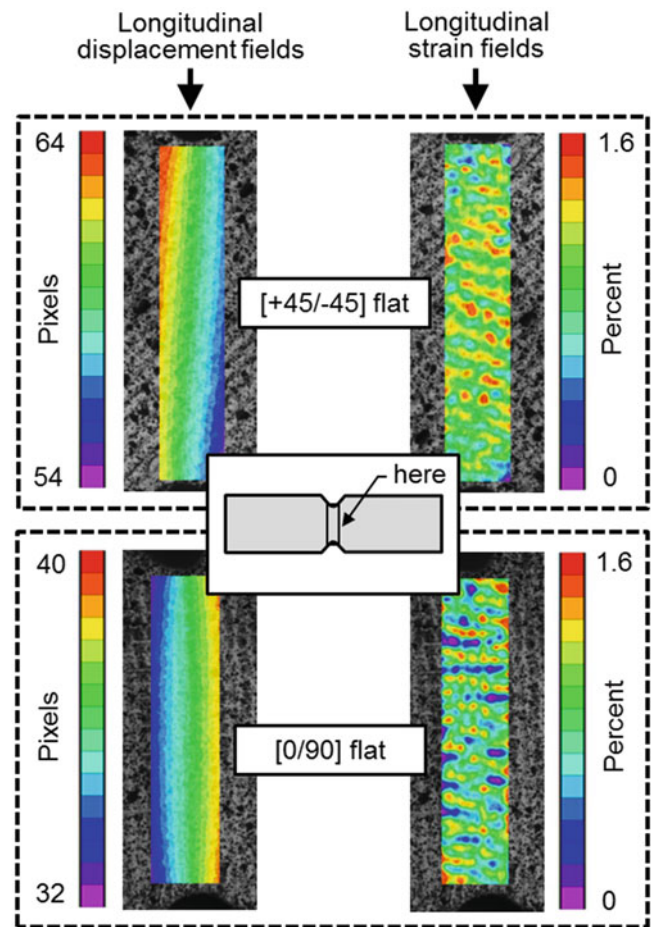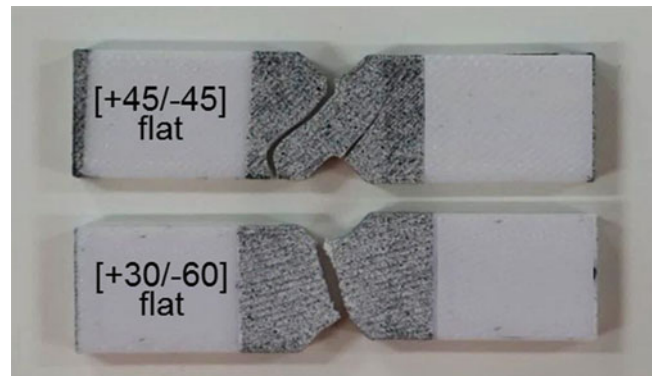

Fig. 11.12 Typical failure modes seen during the testing of PC shear specimens

fractured in two distinct ways which are pictured in Fig. 11.12. Most specimens failed a short distance away from the notch on the tension side which is still considered a valid test as only the ultimate strength could be marginally affected by this type of failure. Far fewer specimens were observed to fail across the notch area and failure across the notch often indicated lower yield and ultimate shear strengths. The [+30/−60] and [0/90] flat samples saw the most specimens with failures in the notch area while the other orientations featured failures just outside the notch area.

11.4 Conclusion

Polycarbonate (PC) and acrylonitrile butadiene styrene (ABS) specimens were created and evaluated according to ASTM standards D-638 (tensile) and D-5379 (shear) to determine if the specimens were anisotropic in nature. Four raster ([+45/−45], [+30/−60], [+15/−75], and [0/90]) and three build/printer orientations (flat, on-edge, and up-right) were selected to determine the directional properties of the materials. Images of the specimens during loading were captured via digital image correlation and processed to evaluate the properties of each raster and build orientation combination. The ABS specimens were isotropic in nature when comparing Young's modulus and Poisson's ratio; however, evaluating only these properties provides an incomplete and incorrect account of the behavior of ABS 3D printed materials. Anisotropy was found when comparing the ultimate strength, strain at failure, and strain energy density of the ABS specimens. The largest degree of anisotropy found was when comparing the strain energy densities as the [+45/−45] flat orientation had a density that was 91 % higher than the [+45/−45] up-right orientation. Raster orientation did not seem to affect the tensile and shear properties of the ABS specimens; however, printer orientation did appear to affect both the on-edge and up-right specimens. When evaluating the ABS shear specimens for anisotropy, differences of up to 25 % were found when comparing shear modulus with similar dissimilarities in the shear strengths reported. Performance of the ABS specimens in tension was a poor indicator of performance in shear as properties varied significantly across the same orientation combinations.

The PC tensile specimens revealed large amounts of anisotropy when varying raster orientation in the flat and upright printer orientations while appearing nearly isotropic in the on-edge orientation. An additional sweep of the raster orientations in the flat build orientation revealed a linear increase in Poisson's ratio and Young's modulus when rotating from [0/90] to [+45/−45]. Strength and strain energy density showed mixed results as the [+30/−60] and [0/90] raster orientations performed significantly worse than the [+15/−75] and [+45/−45] orientations. The on-edge PC specimens had the highest overall tensile properties while the [+45/−45] flat orientation appeared to have the highest shear strengths. The shear modulus was nearly identical for all [+45/−45] raster orientations regardless of print orientation. Identical to the tensile results, the [0/90] flat orientation had the worst material properties with a shear modulus which was 18 % lower than any [+45/−45] raster orientation. The PC specimens generally produced confidence intervals which were half the magnitude of the ABS specimens. This was likely due to the higher quality Fortus 360mc™ printer used to print the PC specimens. Overall specimens from both 3D printers displayed large amounts of anisotropy when build and raster orientation were varied which cannot be ignored when producing or modeling 3D printed parts.

References

1. Berman, B.: 3-D printing: the new industrial revolution. Bus. Horiz. **55**, 155–162 (2012). doi:10.1016/j.bushor.2011.11.003
2. Chulilla Cano, J.L.: The Cambrian explosion of popular 3D printing. Int. J. Interact. Multimed. Artif. Intell. **1**, 30 (2011). doi:10.9781/ijimai.2011.145
3. Espalin, D., Muse, D.W., MacDonald, E., Wicker, R.B.: 3D Printing multifunctionality: structures with electronics. Int. J. Adv. Manuf. Technol. **72**, 963–978 (2014). doi:10.1007/s00170-014-5717-7
4. Chua, C.K., Leong, K.F., Lim, C.S.: Rapid Prototyping: Principles and Applications, vol. 1. World Scientific, Singapore (2003)
5. Ge, Q., Dunn, C.K., Qi, H.J., Dunn, M.L.: Active origami by 4D printing. Smart Mater. Struct. **23**, 1–15 (2014). doi:10.1088/0964-1726/23/9/094007
6. Ge, Q., Qi, H.J., Dunn, M.L.: Active materials by four-dimension printing. Appl. Phys. Lett. **103**(3), 131901 (2013). doi:10.1063/1.4819837
7. Raasch, J., Ivey, M., Aldrich, D., et al.: Characterization of polyurethane shape memory polymer processed by material extrusion additive manufacturing. Addit. Manuf. **8**, 132–141 (2015). doi:10.1016/j.addma.2015.09.004
8. Yang, Y., Chen, Y., Wei, Y., Li, Y.: 3D printing of shape memory polymer for functional part fabrication. Int. J. Adv. Manuf. Technol. **84**(9), 2079–2095 (2016). doi:10.1007/s00170-015-7843-2
9. Bhattacharjee, T., Zehnder, S.M., Rowe, K.G., et al.: Writing in the granular gel medium. Sci. Adv. **1**, e1500655 (2015). doi:10.1126/sciadv.1500655
10. Bellini, A., Güçeri, S.: Mechanical characterization of parts fabricated using fused deposition modeling. Rapid Prototyp. J. **9**, 252–264 (2003). doi:10.1108/13552540310489631
11. Giannatsis, J., Sofos, K., Canellidis, V., et al.: Investigating the influence of build parameters on the mechanical properties of FDM parts. Innov. Dev. Virtual. Phys. Prototyp. In: Proceedings of 5th International Conference on Advanced Research in Rapid Prototyping, pp. 525–529 (2012). doi:10.1201/b11341-85
12. Hill, N., Haghi, M.: Deposition direction-dependent failure criteria for fused deposition modeling polycarbonate. Rapid Prototyp. J. **20**, 221–227 (2014). doi:10.1108/RPJ-04-2013-0039
13. Tymrak, B.M., Kreiger, M., Pearce, J.M.: Mechanical properties of components fabricated with open-source 3-D printers under realistic environmental conditions. Mater. Des. **58**, 242–246 (2014). doi:10.1016/j.matdes.2014.02.038
14. Wittbrodt, B., Pearce, J.M.: The effects of PLA color on material properties of 3-D printed components. Addit. Manuf. **8**, 110–116 (2015). doi:10.1016/j.addma.2015.09.006

15. Torrado Perez, A.R., Roberson, D.A., Wicker, R.B.: Fracture surface analysis of 3D-printed tensile specimens of novel ABS-based materials. J. Fail. Anal. Prev. **14**, 343–353 (2014). doi:10.1007/s11668-014-9803-9

16. Torrado, A.R., Shemelya, C.M., English, J.D., et al.: Characterizing the effect of additives to ABS on the mechanical property anisotropy of specimens fabricated by material extrusion 3D printing. Addit. Manuf. **6**, 16–29 (2015). doi:10.1016/j.addma.2015.02.001

17. Es-Said, O.S., Foyos, J., Noorani, R., et al.: Effect of layer orientation on mechanical properties of rapid prototyped samples. Mater. Manuf. Process **15**(1), 107–122 (2007)

18. Ahn, S.H., Baek, C., Lee, S., Ahn, I.S.: Anisotropic tensile failure model of rapid prototyping parts—fused deposition modeling (FDM). Int. J. Mod. Phys. B **17**, 1510–1516 (2003). doi:10.1142/S0217979203019241

19. Ahn, S.-H., Montero, M., Odell, D., et al.: Anisotropic material properties of fused deposition modeling ABS. Rapid Prototyp. J. **8**, 248–257 (2002). doi:10.1108/13552540210441166

20. Montero, M., Roundy, S., Odell, D.: Material characterization of fused deposition modeling (FDM) ABS by designed experiments. In: Proceedings of Rapid Prototyping and Manufacturing Conference, pp. 1–21 (2001)

21. Rodríguez, J.F., Thomas, J.P., Renaud, J.E.: Design of fused-deposition ABS components for stiffness and strength. J. Mech. Des. **125**, 545 (2003). doi:10.1115/1.1582499

22. Torrado Perez, A.R.: Defeating Anisotropy in Material Extrusion 3D Printing Via Materials Development. University of Texas at El Paso, El Paso (2015)

23. Shaffer, S., Yang, K., Vargas, J., et al.: On reducing anisotropy in 3D printed polymers via ionizing radiation. Polymer (United Kingdom) **55**, 5969–5979 (2014). doi:10.1016/j.polymer.2014.07.054

24. Ziemian, C., Sharma, M., Ziemian, S.: Anisotropic mechanical properties of ABS parts fabricated by fused deposition modelling. Mech. Eng. **23**, 167–180 (2012). doi:10.5772/34233

25. Lee, C.S., Kim, S.G., Kim, H.J., Ahn, S.H.: Measurement of anisotropic compressive strength of rapid prototyping parts. J. Mater. Process. Technol. **187–188**, 627–630 (2007). doi:10.1016/j.jmatprotec.2006.11.095

26. Sood, A.K., Ohdar, R.K., Mahapatra, S.S.: Parametric appraisal of mechanical property of fused deposition modelling processed parts. Mater. Des. **31**, 287–295 (2010). doi:10.1016/j.matdes.2009.06.016

27. Lee, S., Munro, M.: Evaluation of in-plane shear test methods for advanced composite materials by the decision analysis technique. Composites **17**, 13–22 (1986). doi:10.1016/0010-4361(86)90729-9

28. Iosipescu, N.: New accurate procedure for single shear testing of metals. J. Mater. **2**, 537–566 (1967)

29. Walrath, D.E., Adams, D.F.: The Iosipescu shear test as applied to composite materials. Exp. Mech. **23**, 105–110 (1983). doi:10.1007/BF02328688

30. Adams, D.F., Walrath, D.E.: Further development of the Iosipescu shear test method. Exp. Mech. **27**, 113–119 (1987). doi:10.1007/BF02319461

31. Adams, D., Lewis, E.: Current status of composite material shear test methods. SAMPE **31**, 32–41 (1995)

32. Arcan, M.: A new method for the analysis of mechanical properties of composite materials. In: Third International Congress on Experimental Mechanics (1973)

33. Arcan, M., Hashin, Z., Voloshin, A.: A method to produce uniform plane-stress states with applications to fiber-reinforced materials. A specially designed specimen yields material properties under pure shear or uniform plane-stress conditions. Exp. Mech. **18**, 141–146 (1978). doi:10.1007/BF02324146

34. ASTM International.: ASTM D7078/7078M-12 Standard Test Method for Shear Properties of Composite Materials by V-Notched Rail. 15 (2012) doi:10.1520/D7078

35. Whitney, J.M., Stransbarger, D.L., Howell, H.B.: Analysis of the rail shear test—applications and limitations. J. Compos. Mater. **5**, 24–34 (1971). doi:10.1128/JB.183.6.1909

36. Garcia, R., Weisshaar, T.A., McWithey, R.R.: An experimental and analytical investigation of the rail shear-test method as applied to composite materials. Exp. Mech. **20**, 273–279 (1980). doi:10.1007/BF02328411

37. Ifju, P.G.: The shear gage: for reliable shear modulus measurements of composite materials. Exp. Mech. **34**, 369–378 (1994)

38. Micro-Measurements Division MGI.: Strain Gages for Shear Modulus Testing of Composite Materials (1995)

39. Fang, Q.Z., Wang, T.J., Beom, H.G., Li, H.M.: Effect of cyclic loading on tensile properties of PC and PC/ABS. Polym. Degrad. Stab. **93**, 1422–1432 (2008). doi:10.1016/j.polymdegradstab.2008.05.022

40. Fang, Q.Z., Wang, T.J., Li, H.M.: Large tensile deformation behavior of PC/ABS alloy. Polymer (Guildf) **47**, 5174–5181 (2006). doi:10.1016/j.polymer.2006.04.069

41. Daiyan, H., Andreassen, E., Grytten, F., et al.: Shear testing of polypropylene materials analysed by digital image correlation and numerical simulations. Exp. Mech. **52**, 1355–1369 (2012). doi:10.1007/s11340-012-9591-7

42. Qin, L., Zhang, Z., Li, X., et al.: Full-field analysis of shear test on 3D orthogonal woven C/C composites. Compos. Part A Appl. Sci. Manuf. **43**, 310–316 (2012). doi:10.1016/j.compositesa.2011.11.006

43. ASTM International.: Standard test method for tensile properties of plastics. Annu. B ASTM Stand. 1–15 (2004). doi:10.1520/D0638-14.1

44. ASTM International.: (2011) Standard test method for shear properties of composite materials by the V-notched beam method. Annu. B ASTM Stand. 1–13. doi:10.1520/D5379

45. Smith, W.C., Dean, R.W.: Structural characteristics of fused deposition modeling polycarbonate material. Polym. Test. **32**, 1306–1312 (2013). doi:10.1016/j.polymertesting.2013.07.014

46. Sutton, M.A.: Springer Handbook of Experimental Solid Mechanics. Department of Mechanical Engineering, The Johns Hopkins University, Baltimore, MD, USA (2008)

47. Sutton, M.A., Orteu, J.J., Schreier, H.: Image Correlation for Shape, Motion and Deformation Measurements: Basic Concepts, Theory and Applications. Springer Science & Business Media, New York (2009)

48. Sutton, M.A., Turner, J.L., Bruck, H.A., Chae, T.A.: Full-field representation of discretely sampled surface deformation for displacement and strain analysis. Exp. Mech. **31**, 168–177 (1991)

Chapter 12
Experimental Determination of Transfer Length in Pre-stressed Concrete Using 3D-DIC

Sreehari Rajan, Michael A. Sutton, Ning Li, Dimtris Rizos, Juan Caicedo, Sally Bartelmo, and Albert Lasprilla

Abstract Since pre-stressed concrete structures have much higher tensile load carrying capacity, they are being used more often in the construction of highway bridges and railroad ties. Increased load-carrying capacity is achieved through transfer of the tensile loading in the reinforcement tendons into compressive stress in the concrete. The distance over which the pre-stress in the tendons is fully transferred to compressive stress in the concrete is known as the 'transfer length'. Since local tensile stresses in concrete are problematic, the transfer length is an important parameter in the design of pre-stressed concrete components to ensure that the concrete remains in compression when subjected to in-service loads. In this work, the authors developed a stereo-vision digital image correlation system for both laboratory and industrial environments to measure the relatively small surface strains that are imposed on the concrete during release of pre-tensioned reinforcement tendons. In comparison to the current approach that requires physically embedding of Whittemore gages in the concrete beam during the curing process, results for these studies show that the non-contacting optical measurement method is much less time-consuming, more accurate and more consistent, while requiring no physical placement of gages.

Keywords Pre-stressed concrete • Transfer length • Stereo-vision • DIC • Whittemore gage

12.1 Introduction

Pre-stressed concrete structures (PSCs) are being used in wide range of applications such as construction of bridges, railroad ties and nuclear reactor vessels. In the railroad industry, it has been suggested that significant reduction in the maintenance cost can be achieved by implementing pre-stressed concrete ties. The higher tensile load-carrying capacity and resistance to crack formation compared to conventional concrete makes PSCs ideal for such applications. In general, the release of pre-tensioned tendons is employed to compressively load the concrete that is poured and cured while maintaining tension on the tendons. Transfer of the pre-tension into the concrete as compressive load takes place over a distance which is termed 'transfer length'. For the pre-stressed concrete ties to be effective, the full transfer of the pre-tension should take place well before the position of the rail seat, which is the location in the tie where the primary loads are applied. Hence the transfer length is an importance parameter in determining the quality and long-term durability of pre-stressed ties. Conventionally, measurement of transfer length in pre-tensioned concrete is done by using Whittemore gages [1] and more recently by a laser speckle method [2]. As noted by Russel et al. [1], the authors estimated strains from longitudinal displacement data obtained from individual, embedded Whittemore gages placed 4 in. apart along the center line of pre-stressed beam. One of the conversional methods used to measure the transfer length with Whittemore gages measurements (similar approach can be used for any method that measures longitudinal displacement at discrete locations) assumes that the transfer length is the location where the compressive strain in the concrete has reached 95 % of the average maximum strain that is measured in the concrete. Designated the 95 % AMS method, the data reduction process involves finding the average strain in the strain plot along the length of the beam, oftentimes by visually inspecting the strain field. The transfer length is then obtained from the intersection of the 95 % AMS line with the measured strain profile. Another approach that has been employed to extract transfer length measurements from PSC strain measurements was described by Zhao et al. [3]. In their work, the authors proposed a least square bilinear fit to the strain data to obtain the transfer length. By fitting a rising straight line to the initial

S. Rajan (✉) • M.A. Sutton • N. Li
Department of Mechanical Engineering, University of South Carolina, Columbia, SC 29208, USA
e-mail: sreehari@email.sc.edu

D. Rizos • J. Caicedo • S. Bartelmo • A. Lasprilla
Department of Civil and Environmental Engineering, University of South Carolina, Columbia, SC 29208, USA

data and a horizontal straight line to the nominally uniform compressive strain in the central region, the transfer length is obtained from the intersection of the optimally fit bilinear curve.

It is important to note that both of these methods for measuring the transfer length have disadvantages. The Whittemore gage method requires that discrete brass markers are embedded in the concrete and the motion of the top point measured. This is a tedious, error-prone process that is impractical as a quality assessment method in a PSC production facility. The laser speckle method is well known to suffer from high sensitivity to rigid body translation and rotations that affect the robustness and accuracy of measurements, while also being limited to two dimensional measurement on a planar surface [4], making it very difficult to use in industrial settings. To overcome these issues, the authors selected stereo digital image correlation (e.g. 3D DIC or StereoDIC) to measure the surface deformations. StereoDIC or 3D-DIC is a non-contacting, full-field optical measuring technique that has been used extensively for shape, displacement and motion, measurements. Developed by researchers at University of South Carolina in the late 1980s [5–10], StereoDIC can be implemented for simultaneous measurement of both in plane and out of plane displacements on planar and curved surfaces on a wide range of length and time scales. The method is particularly useful in these studies since StereoDIC is nominally insensitive to industrial noise sources, including large rigid body motions and vibrations.

Recently, StereoDIC is receiving increased attention in the civil engineering community for measurement of deformation and strains on large structures [11]. In many cases the methods provide full field displacement and strain data to visualize deformation patterns and the evolution of failure modes of structures, measurements that were not possible with conventional sensor based point measurements. For example, Ghorbani et al. [12] measured full field deformations on a confined masonry wall subjected to horizontal in plane loads using StereoDIC, allowing the authors to map crack evolution on the wall during loading and visualize the load resistance mechanisms. In another example, Nonis et al. [13] used StereoDIC measurement in structural health monitoring of bridges to quantify spalling and identify cracks which are not visible by visual inspection.

In the current study, the authors used StereoDIC to measure full-field displacements and strains on the surface of a PSC beam after release of pre-tension to assess the potential of the method for quantifying the transition length in PSCs. Results obtained from one experiment conducted on a PSC beam in a high bay laboratory is presented in the following sections.

12.2 Experimental Setup

Figure 12.1 and the inset shows the lower portion of the structure used to develop pre-tension in the steel tendons as part of the PSC manufacturing process. As shown on both the left and right sides of Fig. 12.1, two vertical I section beams are bolted to the concrete floor and the top ends of the I-beams are joined to another horizontal I-beam to add structural integrity to this support structure. To perform pre-tensioning of the tendons, four holes at specified spacing are drilled through both flanges of the two vertical I-beams. The 12.7 mm diameter tendons are threaded through the holes and end-stops are attached on the outside of the right-side vertical I-beam; the inset in Fig. 12.1 shows a close-up of the lower region after the four tendons have been threaded through the holes. Just beyond the left vertical I-beam, a hydraulic system and a strong-back are used to apply the 53.4 kN pre-tension to each of the four tendons. While holding the pre-tension, end-stops are tightened against the left-side I-beam to maintain pre-tension. Figure 12.2 shows a photo of the upper portion of the pre-tensioning structure (horizontal I-beam spanning region between two vertical I-beams). On the left of the photo is a third vertical I-beam that is part of an independent structure that is used to support the L-brackets and the stereo camera pair at a height of 3.8 m above the PSC beam shown in Fig. 12.1. A separate camera support system is used in our experiment since preliminary studies showed that the method of pre-tension release used in the laboratory (flame cutting of the pre-tensioned tendons) introduced large transient vibrations of the structure supporting the pre-tension tendons, resulting in cameras to move relative to each other, which invalidated the calibration process required for accurate image-based measurements. It is noted that an additional precaution is taken by adding rubber damping material between the L-brackets and the vertical I-beam support to minimize the effect of foundation vibrations during the tendon release process.

To perform the imaging process, two 5 MP PointGrey cameras with 17 mm fixed focal length Schneider lens are used with VIC-Snap[1] software to obtain synchronized images of the beam surface. The distance between the cameras is 1 m with a stereo angle of $\approx 15°$. The deformation response of the pre-stressed beam is assumed to be symmetric about mid span, so the camera and lens system are set up to capture images of the top surface of the beam from one end to mid span. The field of

---

[1] Correlated Solutions Incorporated, 121 Dutchman Blvd, Columbia, SC 29063, www.correlatedsolutions.com
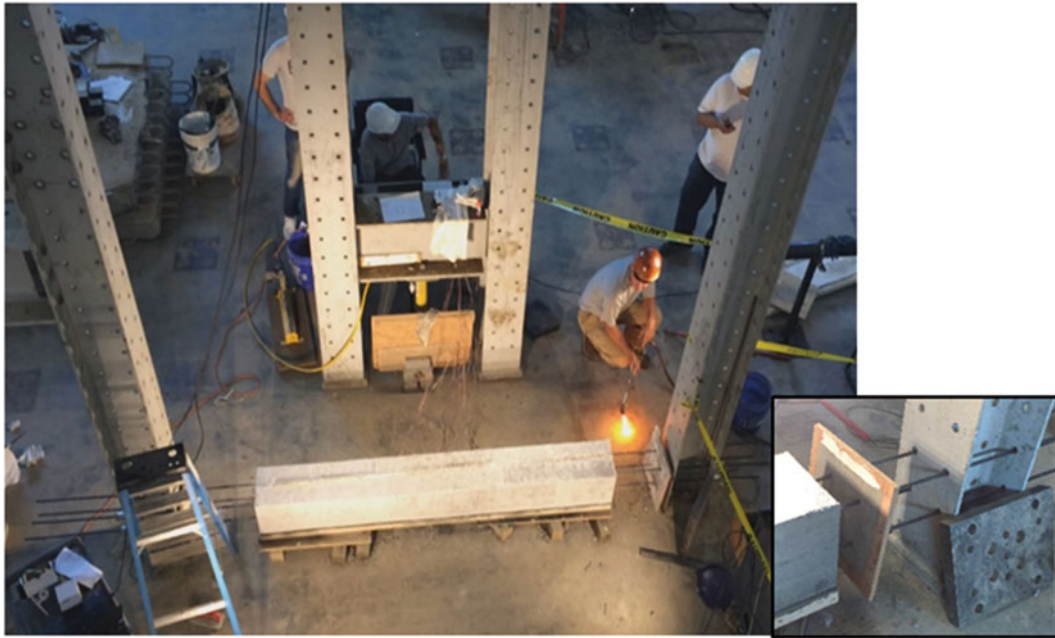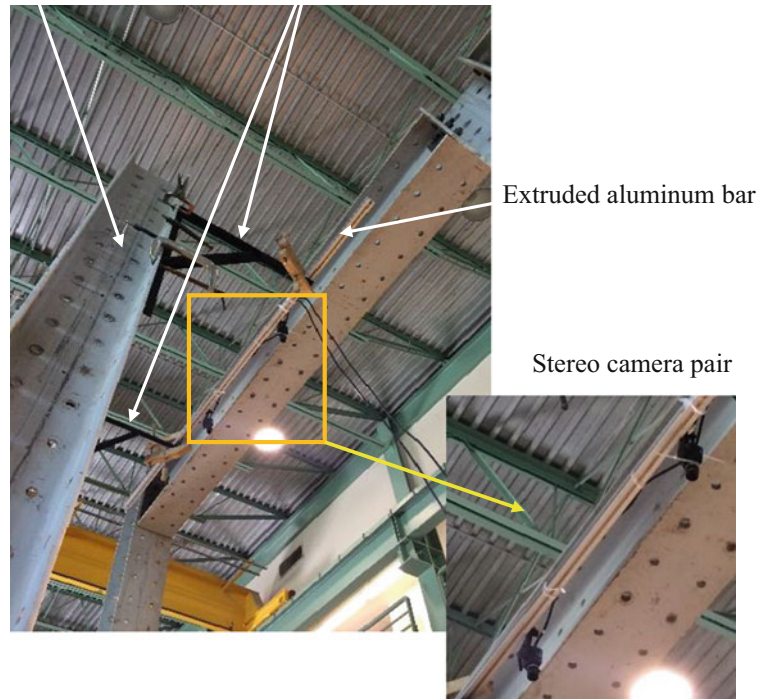
Fig. 12.1 View of PSC beam and the two vertical I-beams on left and right sides that form part of the structure used to perform pre-tensioning of steel tendons. *Inset*: Close-up view of the lower portion of I-beam with pass-through holes for tendons

Fig. 12.2 View of upper horizontal I-beam support attached to the two vertical I-beams on left and right sides forming pre-tensioning structure. Also shown is a portion of an independent vertical I-beam structure that supports the Stereo-DIC system. *Inset*: Close-up view of the stereo camera pair attached to a 2.5 m long extruded aluminum bar

view of both cameras is 1.78 m × 1.49 m, with an average magnification of ≈0.73 mm/pixel. Two LED-based light sources are employed that individually emitted 8000 lumens to illuminate the surface of the specimen.

The PSC beam is 2.4 m in length, having four pre-tensioned steel tendons (high strength, low relaxation) of 12.7 mm in diameter. The cross-section of the beam and position of the pre-tension tendons in the cross section are shown in Fig. 12.3. Each steel tendons are applied with an initial pre-tension load 53.4 kN using a hydraulic system. After applying the
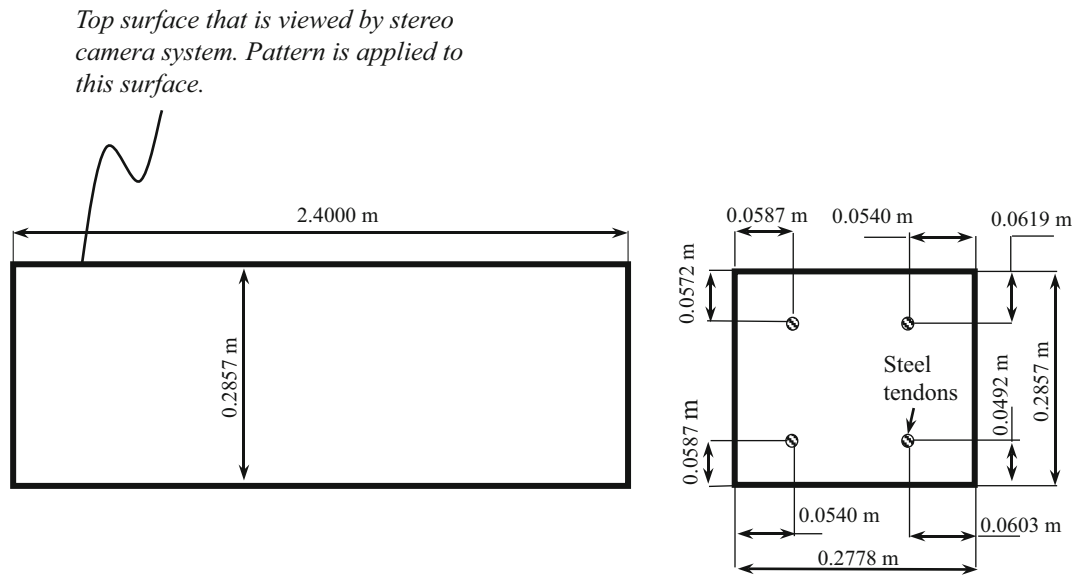
Fig. 12.3 View of PSC beam with location of steel tendons in cross-section. Note that tendons are note perfectly symmetric in the cross-section
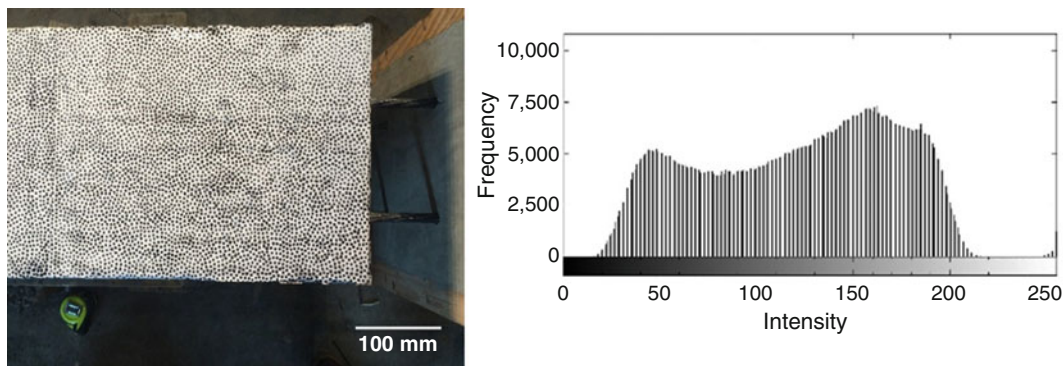

Fig. 12.4 Speckle pattern on the top surface of the concrete and the associated intensity histogram

pre-tension, concrete mix is poured in the mold and several experiment cylinders are made at the same time to determine the fracture strength of the concrete at the time of tendon release. The pre-tension in the tendons are released when the concrete reached a compressive strength of 27.6 MPa (12 h after pouring) determined from the experiment cylinders.

12.2.1 Specimen Surface Preparation for DIC

To obtain accurate methods with StereoDIC, a good contrast random speckle pattern of desired dimensions on the surface is required. Feature dimensions in the speckle pattern are determined by the average image magnification factor Since the features in the pattern should be sampled by at least 3×3 pixels to minimize aliasing [14], the minimum feature size in the pattern is calculated to be 2.2 mm (0.73 mm/pixel $\times$ 3 pixels). In our studies, a high contrast speckle pattern is applied on the concrete surface using a stencil with randomly distributed holes having a nominal diameter of 3 mm. The application of our speckle pattern required three stages. First, the concrete surface is painted with white matte finish paint. In the second stage, a low strength spray adhesive is applied to one side of the stencil to ensure good adherence to the painted surface. After smoothing the stencil onto the surface, in the third stage black paint is applied through the stencil to create a high contrast random pattern. Entire process of applying the random pattern on one half of the top surface of the concrete took less than 2 h. Figure 12.4 shows the speckle pattern that is painted on the surface, with the inset showing the intensity histogram of the speckle pattern. The histogram shows a relatively uniform distribution of pixel intensity values that range from 20 to

220 grey levels for our 8 bit gray scale image, indicating good contrast without image sensor saturation that would introduce measurement errors during the correlation process.

12.2.2 Stereo Camera Calibration and Image Acquisition

After application of a speckle pattern, the stereo cameras are mounted on the camera support structure, oriented to view the PSC top surface and the lens are adjusted to obtain well-focused images. Once the cameras reached steady state temperature (~1 h), calibration of the stereo camera pair is performed using a rigid calibration plate having 14 mm diameter circular dots arranged in a 12 × 9 grid with grid spacing of 35 mm. Two synchronized images of the grid locations are captured from the cameras using commercial software, VicSnap.[1] A total of 88 synchronized image pairs of the calibration grid are acquired at different positions and orientation, with calibration performed using Vic3D.[1] Third order distortion correction is used in the calibration to minimize errors in the DIC measurement due to lens distortions.

Once the calibration parameters are determined, a total of 50 pairs of synchronized reference speckle images of the pre-stressed concrete beam are captured before release of pre-tension; a large number of images are obtained at each step in the experiment to minimize the effect of intensity noise by image averaging; experimentally measured variability in the pixel intensity values is ±1 gray levels or 0.4 %. This is particularly important in these studies since the maximum strain developed on the concrete surface is less than 200 με. As soon as the reference images are captured, the top two tendons are flame cut using an acetylene torch. Then, another set of 50 pairs of synchronized speckle images are captured. This is followed by release of full pre-tension (cutting all four tendons). After completion of the release process, an additional 50 pairs of synchronized speckle images are captured.

12.3 Result and Discussions

Displacements and strains on the surface of the pre-stressed concrete after partial release and full release of pre-tension are calculated using commercial DIC software, VIC 3D.[1] In the DIC analysis, the subset size is 29 × 29 pixels with a step size of 9 pixels. Strains are calculated at the center point of an 11 × 11 set of measured displacements with Gaussian weighting. Hence the virtual gage length for strain calculation is 99 pixels (physical size of 72.3 mm). Figure 12.5a, b shows the full-field longitudinal strain data on the top surface of the concrete after release of pre-tension in the top two tendons and release of pre-tension in all four tendons, respectively. The average longitudinal compressive strain on the surface of the concrete after release of pre-tension in the top two tendons is 110 με. The average longitudinal compressive strain is 176 με after release of pre-tension in all four tendons.

12.3.1 Measurement of Transfer Length

When pre-tension of a set of tendons is released, the longitudinal compressive strain in the PSC beam will increase to a nominally uniform value in the concrete after some distance from the free edge. To estimate the transfer length, a line of strain data along the beam centerline is used. Figures 12.6a, b and 12.7a, b show the strain data measured after releasing the top two tendons in the PSC beam and all four tendons, respectively. Shown on the graphs are the results using both a bilinear fit and the 95 % AMS methods noted previously to estimate the transfer length. Table 12.1 summarizes the transfer length estimates. As shown in Table 12.1, the transfer length is on the order of 120 mm (5 in.) after partial release and 165 mm (6.5 in.) after full release.

12.4 Conclusions

Experimental studies conducted in a laboratory setting on PSC beams have shown that StereoDIC systems utilizing high resolution cameras are effective for measuring the transfer length. By averaging of images to reduce Gaussian noise, the variation of strain on pre-stressed concrete could be clearly identified, even though the beams are undergoing very small
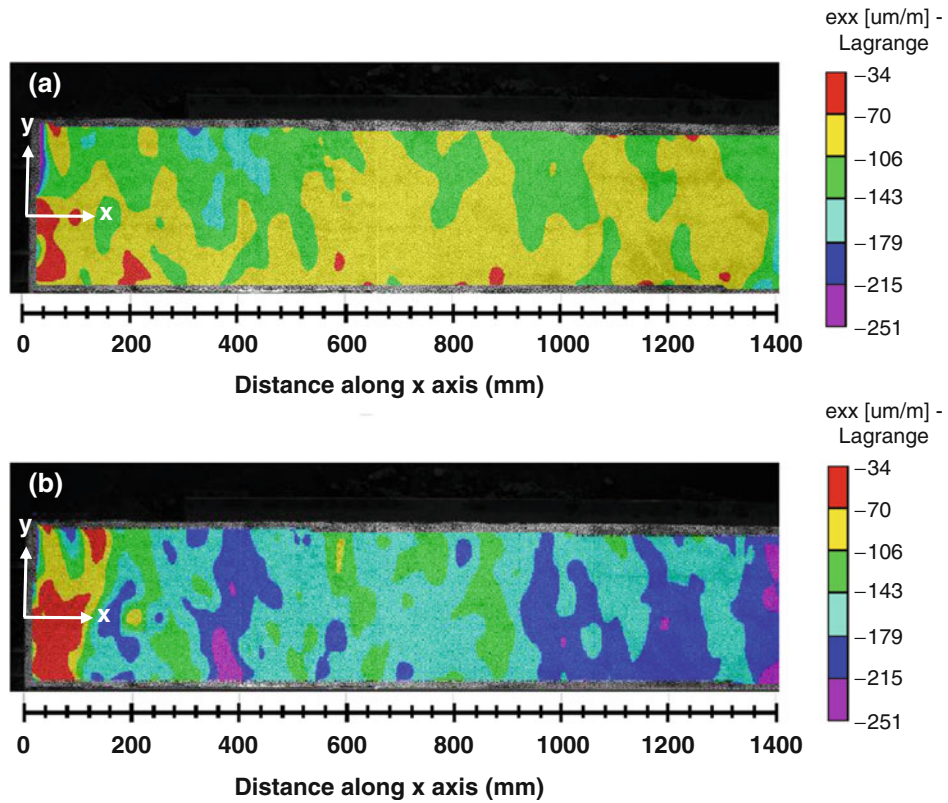
Fig. 12.5 Longitudinal strain field (ϵ_{xx}) on the top surface of concrete after release of pre-tension in (**a**) the top two steel tendons and (**b**) all four steel tendons

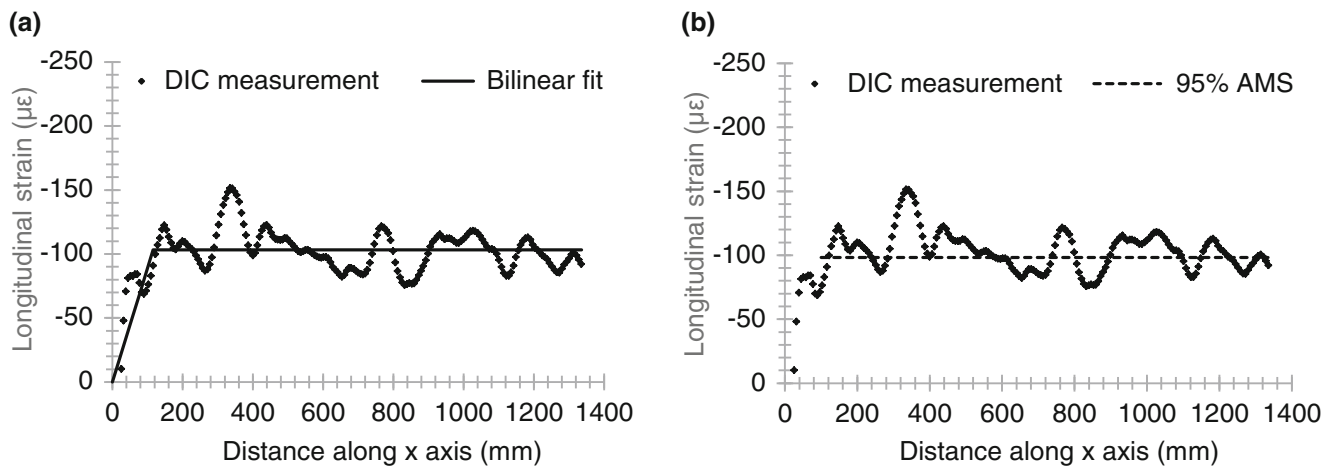**Fig. 12.6** Variation of longitudinal strain (ϵ_{xx}) along the length of beam after release of pre-tension in top two tendons showing (**a**) bilinear fit and (**b**) 95 % AMS line

deformation (less than 200 με). Transfer length results using both bi-linear fits and 95 % AMS are in good agreement for both partial and full release conditions. Results indicate that Stereo DIC has the potential to be used in quality control of pre-tensioned concrete structures in both laboratory and industrial settings.
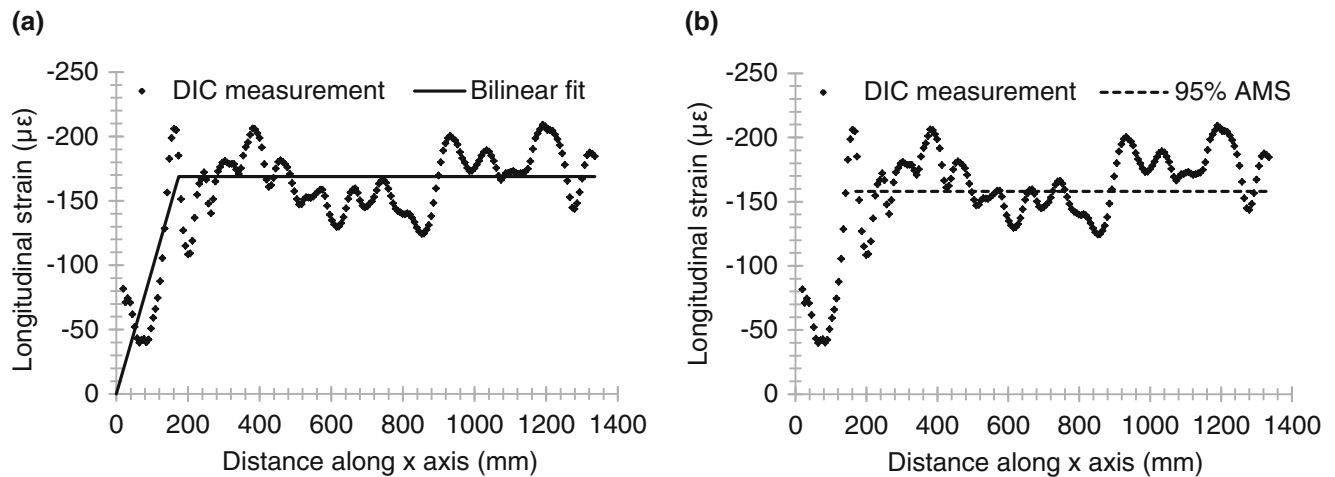
(a)

(b)

Fig. 12.7 Variation of longitudinal strain (ϵ_{xx}) along the length of beam after release of pre-tension in all four tendons showing (**a**) bilinear fit and (**b**) 95 % AMS line

Table 12.1 Transfer length after partial and full release of pre-tension obtained by bilinear curve fitting and 95 % AMS method

	Partial release of pre-tension	Full release of pre-tension
Transfer length from bilinear curve fitting (mm)	116	174
Transfer length using 95 % AMS (mm)	122	150

References

1. Russell, B.W., Burns, N.H.: Design Guidelines for Transfer, Development and Debonding of Large Diameter Seven Wire Strands in Pre-tensioned Concrete Girders, Research Report 1210-5F, Center for Transportation Research, University of Texas at Austin, Austin, TX (1993)
2. Zhao, W., Larson, K., Peterman, R.J., et al.: Development of a laser-speckle imaging device to determine the transfer length in pre-tensioned concrete members. PCI J. **57**(1), 135–143 (2012)
3. Zhao, W., Beck, B.T., Peterman, R.J., et al.: A direct comparison of the traditional method and a new approach in determining 220 transfer lengths in pre-stressed concrete railroad ties. In: Jt. Rail Conference. ASME (2013)
4. Parks, V.J.: The range of speckle metrology; Estimates of the largest and smallest displacements measurable with speckle methods are drawn from the literature and laboratory studies. Exp. Mech. **20**(6), 181–191 (1980)
5. Luo, P.F., Chao, Y.J., Sutton, M.A.: Application of stereo vision to three-dimensional deformation analyses in fracture experiments. Opt. Eng. **33**(3), 981–990 (1994)
6. Helm, J.D., Sutton, M.A., McNeill, S.R.: Improved three-dimensional image correlation for surface displacement measurement. Soc. Photo-Opt. Instrum. Eng. **35**(7), 1911–1920 (1996)
7. Luo, P.F., Chao, Y.J., Sutton, M.A., Peters, W.H.: Accurate measurement of three-dimensional deformations in deformable and rigid bodies using computer vision. Exp. Mech. **33**(2), 123–132 (1993)
8. Sutton, M.A., Yan, J.H., Tiwari, V., Schreier, H.W., Orteu, J.-J.: The effect of out-of-plane motion on 2D and 3D digital image correlation measurements. Opt. Lasers Eng. **46**(10), 746–757 (2008)
9. Sutton, M.A.: Computer vision-based, noncontacting deformation measurements in mechanics: a generational transformation. Appl. Mech. Rev. **65**(5), 050802 (2013)
10. Sutton, M.A., McNeill, S.R., Helm, J.D., Chao, Y.J.: Advances in two-dimensional and three-dimensional computer vision. In: Photomechanics. Springer, Berlin, pp. 323–372 (2000)
11. McCormick, N.J., Lord, J.D.: Practical in situ applications of DIC for large structures. Appl. Mech. Mater. **24–25**, 161–166 (2010)
12. Ghorbani, R., Matta, F., Sutton, M.A.: Full-field deformation measurement and crack mapping on confined masonry walls using digital image correlation. Exp. Mech. **55**(1), 227–243 (2015)
13. Nonis, C., Niezrecki, C., Yu, T.-Y., et al.: Structural health monitoring of bridges using digital image correlation. In: Health Monitoring of Structural and Biological Systems 2013, SPIE Proceedings, vol. 8695, p. 869507 (2013)
14. Sutton, M.A., Schreier, H., Orteu, J.-J.: Image Correlation for Shape, Motion and Deformation Measurements. Springer, New York (2009). ISBN 978-0-387-78746-6

Chapter 13
Hybrid Infrared Image Correlation Technique to Deformation Measurement of Composites

Terry Yuan-Fang Chen and Ren-Shaung Lu

Abstract Infrared thermography (IRT) inspections have become an accepted method for inspecting composite structures due to nondestructive and wider detecting area. In this study, a hybrid infrared image correlation method is proposed to measure the deformation of composite materials. The proposed method is based on performing a digital image correlation of the thermal images of specimen acquired under two different loads by step heating thermography. The thermograms of test specimens taken at different loads were processed to extract the bulk deformation from tiny changes in the thermograms using DIC. The DIC images were also taken by using visible light for comparisons. The digital image processing scheme developed, and its applicability are investigated and discussed.

13.1 Introduction

Carbon fiber reinforced polymers (CFRP) are increasingly being used in many aerospace/aircraft structural applications. However, one of the most significant issues of using adhesive bonding is the occasional occurrence of weaker bonds. Current NDE techniques have very few success in identifying kissing bonds/weak bonds in the bondline. Therefore, there is a greater need for an easy to implement experimental technique that can non-destructively quantify the strength of the bondline in composite structures. This is a key for monitoring and maintaining aerospace/aircraft structural integrity, safety, and reliability during their production process and in-service operations.

Infrared thermography (IRT) inspections have become an accepted method for inspecting composite structures due to nondestructive and wider detecting area. Various image processing methods have been adapted to analyze thermographic image to evaluate the defects quantitatively [1, 2]. By creating a dual-emissivity stochastic speckle pattern, a new method to assess the coefficients of thermal expansion of solid materials by infrared thermography and digital image correlation is reported [3]. The feasibility of using hybrid infrared image correlation method to measure the deformation of composite materials based on the embedded fiber features is also reported [4]. Since IR image represents the temperature field and contains high noises, it is difficult to obtain accurate result. In this study, the effect of using various image filtering techniques, the size of sub-image for correlation, and the image chosen from the time history images are compared. A digital scheme is developed to determine the deformation of various composite specimens. The result of IRT DIC is compared to the ones obtained by ordinary DIC, and discussed.

13.2 Materials and Methods

13.2.1 IRT Experimental System

Objects will emit infrared above 0 K, and the IR sensors receive infrared light generate electrical signal that is proportional to the radiation energy received. After amplification, the electrical signal will be converted into temperature data by data conversion circuit. In general, the temperature range and emissivity of IR camera need to be set for testing object and calibrated before starting the measurement. A photograph of step heating experimental system is shown in Fig. 13.1.
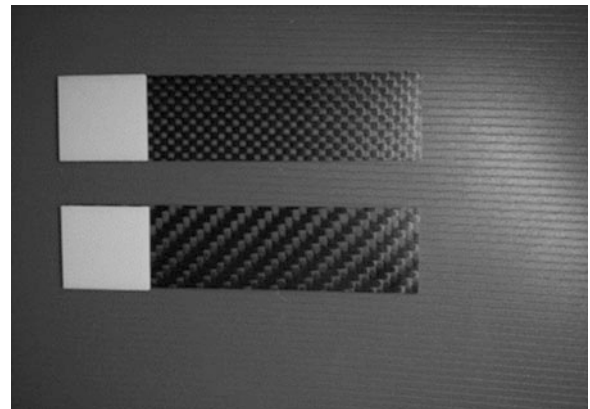
T.Y.-F. Chen (✉) • R.-S. Lu
Department of Mechanical Engineering, National Cheng Kung University, Tainan 70101, Taiwan, ROC
e-mail: ctyf@mail.ncku.edu.tw

Fig. 13.1 Step heating experimental system

Fig. 13.2 Photograph of CFRP samples

It consists of an IR camera, a computer system, and a hood with 4000 W of heat source lamp at the top inside. The IR camera (TAS-G100EXD, NEC, Japan) used in this study has wavelength of 8~14 μm and temperature range −40 to 1500 °C, with a resolution of 0.04 °C and a measurement accuracy of ±2 % or 2 °C of reading, 320 × 240 pixels and 30 frames/s. A shutter is set at the right end of hood to extract after preheating. A loading frame with a rotating wheel for tensile testing is set next to the shutter. Since the conversion of grey-level image to temperature field in not linear, a self-designed calibration method was applied to transfer the gray-level value image into a temperature image accurately [5].

13.2.2 Specimens and Tests

The CFRP specimen, as shown in Fig. 13.2, is made of AW146_HV957, with (0/90°) four plies, and dimensions of 100 mm × 25 mm × 1 mm. The thermography images of test specimens taken at different loads were processed to extract the bulk deformation from tiny changes in the images using DIC. The DIC images were also taken by using visible light for comparisons. One face of the specimen was subjected to a constant and uniform heat flux, and the surface temperature response was recorded on the other face. The hood was preheated for 5 s and applied for 5 s with heat source, and then the specimen was allowed to cool down. The IR camera recorded the data from the start of the heat flux application and up to 15 s after the heat source was turned off. The recorded thermogram was fed into computer directly for further image processing and image correlation.

In translation test, a displacement of 5 pixels (446 μm) was given, the correlation results of the thermograms recorded at different time was compared to find the proper ones among the 600 temperature-time history data for correlation. In tensile testing with preload, the variation of load with the step heating process were examined. The test results from thermogram are compared to the ones obtained using visible light.

13.2.3 Image Processing

Usually IRT images are analyzed for temperature difference which may indicate the suspected defects. Figure 13.3 shows the typical IRT and visible light images of the specimen after being enhanced. The features mainly caused by the 3D woven fiber inside the composites were used in deformation measurement by using image correlation. Since IRT image is very noisy and the features is repeatedly, the applicability of high-pass filters (gradient, Robert and Sobel) and low-pass filters (averaging and median) along with various size of sub-image, 31×31, 61×61 and 91×91, for better measurement is studied.

13.3 Test Results and Discussion

Figure 13.4 shows the displacement errors obtained for each filter with different sub-image size. It can be seen that low-pass filter reduces more errors than high-pass filter. An error less than 1 pixel can be achieved by using averaging filter with sub-image 61×61 or 91×91. Further correlation of the thermograms recorded at the same time, before and after translation, the errors plotted verse time is given in Fig. 13.5. It can be found that the average errors are bigger for the frame recorded during the step heating period, and are reduced to less than 0.6 pixels for the images recorded between 7 and 18 s with three-frame or five-frame averaging.

Fig. 13.3 Typical (**a**) IRT and (**b**) visible light images of the specimen after being enhanced
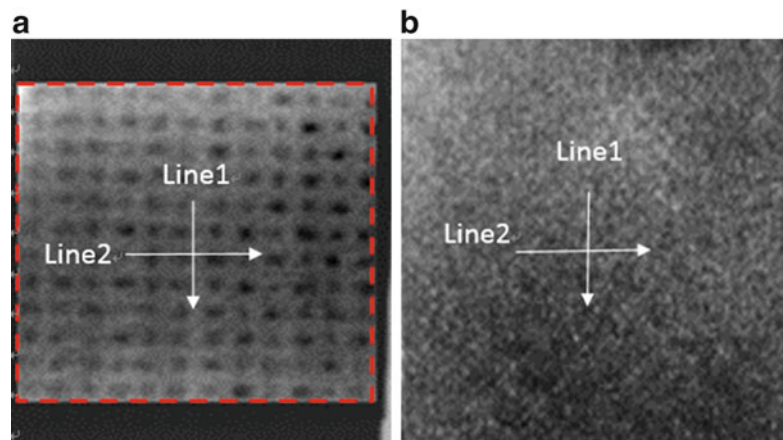

Fig. 13.4 Comparisons of displacement errors obtained for various filter with the three different sub-image sizes
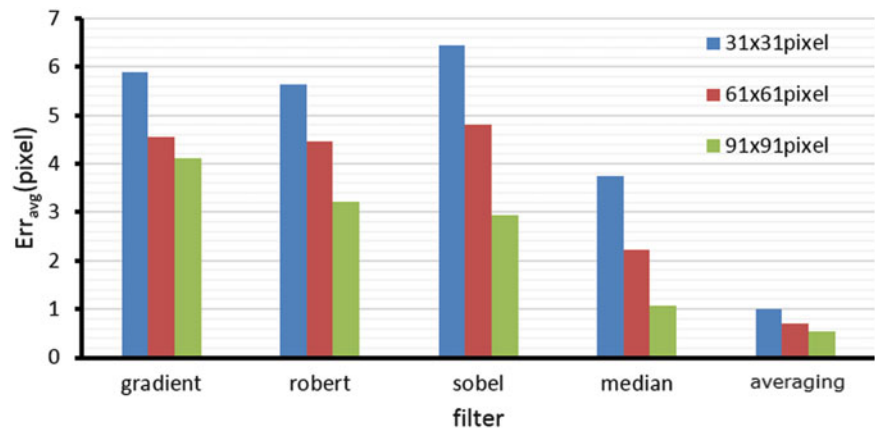
Fig. 13.5 The average errors obtained by correlating the thermograms recorded at the same time, before and after translation
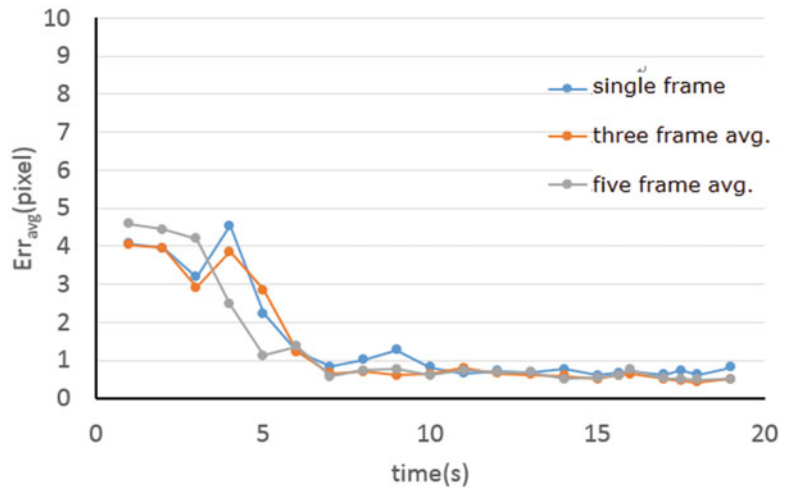

Fig. 13.6 Variation of load with the step heating process
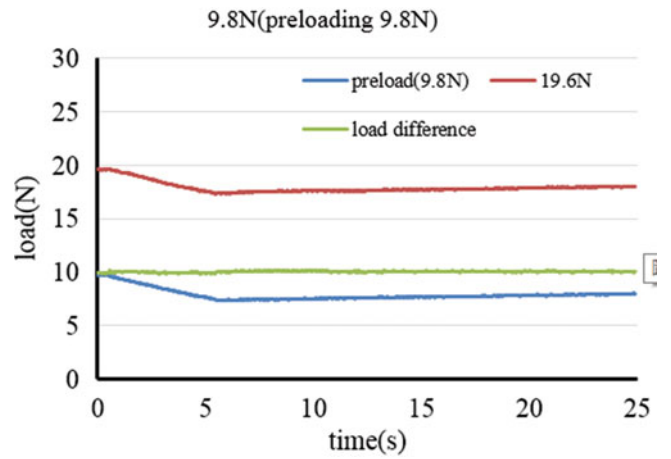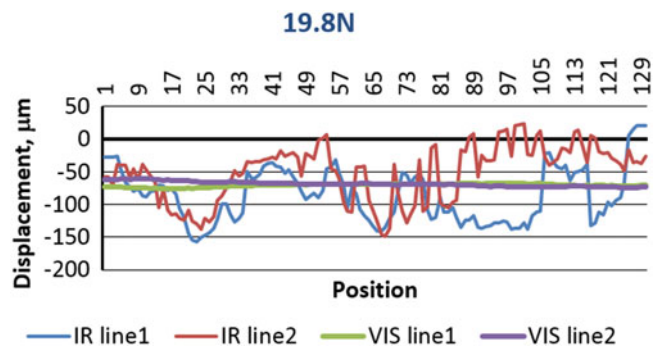

Fig. 13.7 Comparisons of the displacement measured by IRT and visible light, respectively, along line 1 and line 2 indicated in Fig. 13.3

In tensile testing with preload, the variation of load with the step heating process is shown in Fig. 13.6. It can be observed that the load drops during the heating process under either preload or load situation, however the loading difference is almost the same to the applied load. The average error is less than 2.5 %. Figure 13.7 shows the displacement measured by IRT and visible light, respectively, along line 1 and line 2 indicated in Fig. 13.3. An average displacement of 68 μm with standard deviation of 42 μm was obtained for IRT DIC, and that of visible light is 70 μm with standard deviation of 3 μm.

13.4 Conclusion

A hybrid method for digital image correlation of IR thermogram for deformation measurement of composites is presented. Through translation test, neighborhood averaging and frame averaging of the thermogram was found effective for image correlation, an average error of 0.6 pixels can be achieved from the tests. Form tensile testing, the loading was found decreased during the step heating period, however the applied load is almost the same. The displacement measured by IRT DIC compared fairly well to the ones by the ordinary DIC, but with relatively large standard deviation. Further study is required to improve the stability and accuracy of IRT DIC for practical use.

References

1. Vavilov, V., Maldague, X., Dufort, B., Robitaille, F., Picard, J.: Thermal nondestructive testing of carbon epoxy composites: detailed analysis and data processing. NDT&E Int. **26**, 85–95 (1993)
2. Maldague, X.: Applications of infrared thermography in nondestructive evaluation. In: Trends in Optical Nondestructive Testing, pp. 591–609 (2000)
3. Montanini, R., Freni, F.: A new method for the determination of the coefficient of thermal expansion of solid. In: 11th International Conference on Quantitative InfraRed Thermography, Italy, pp. 11–14 (2012)
4. Chen, T.Y.-F., Lu, R.-S.: Development of a hybrid infrared image correlation technique to deformation measurement of composites. In: ATEM'15, Japan (2015)
5. Chen, T.Y., Kuo, M.-H.: Converting the infrared thermal image into temperature field for detection the defects inside materials. In: Eighth International Symposium on Precision Engineering Measurement and Instrumentation, Proceedings of SPIE, vol. 8759, 87594L (2013). doi:10.1117/12.2015771

Chapter 14
DIC Anisotropic Denoising Based on Uncertainty

Manuel Grewer and Bernhard Wieneke

Abstract A typical challenge with subset based DIC algorithms is to find the optimal subset size for the problem. Small subsets may improve spatial resolution, but also increase noise. Larger subsets offer better noise rejection at the cost of resolved features. In general, the product of spatial resolution and noise is approximately constant. Therefore, changing the subset size offers limited options to achieve good spatial resolution and smooth data. To resolve this dilemma, an anisotropic denoising technique is presented which utilizes a DIC uncertainty estimator as an input. The anisotropic denoising will smooth the vector field only where local gradients are smaller than the uncertainty and preserve regions with strong gradients. We will give several examples of the performance of the anisotropic denoising, including DIC challenge sample 14.

Keywords DIC • Anisotropic denoising • Uncertainty • Automatic smoothing • Spatial resolution

14.1 Introduction

Nowadays, digital image correlation (DIC) is widely used for deformation measurements. Due to the non-intrusive nature of the technique, DIC is suited for difficult measurement environments where application of standard extensometers or strain gauges may not be possible. However, there are numerous error sources influencing the overall quality and accuracy of the resulting vector field, such as the performance of the optical system, speckle size and distribution, camera resolution, camera noise, as well as the processing parameters of the DIC algorithm. Especially for subset based DIC algorithms, the choice of the size of the interrogation window has a big impact on spatial resolution and noise rejection. Larger subsets generally give smoother results at the expense of spatial resolution. If the subset is too large to recover the spatial features of the experiment, the algorithm will underestimate the true displacement magnitude, which will in turn also affect spatial derivatives like strain. Therefore, choosing the best processing parameters for a given measurement is a formidable task, and may involve several reprocessing steps to optimize the result. Moreover, changing the subset size offers limited options to simultaneously achieve good spatial resolution and smooth data, since generally the product of spatial resolution and noise is approximately constant. Therefore, most image correlation algorithms feature post-processing schemes to reduce noise after vector computation. Simple smoothing filters involve spatial top-hat, Gaussian or polynomial regression fits, as well as POD analysis [1]. With post-processing the problem is shifted from setting a proper subset size to choosing the right filter kernel. Ideally, the algorithm would set the size of the filter kernel automatically depending on some error estimate.

Over the last decades DIC uncertainty measures have been subject of intense research. Today several approaches to determine DIC uncertainty have been published and most commercial DIC packages offer some kind of uncertainty estimator [2–5]. This information allows for an anisotropic denoising filter, which will smooth the vector field only where local gradients are smaller than the uncertainty and preserve regions with strong gradients. The algorithm will automatically adjust size and shape of the filter kernel according to a user set uncertainty band.

M. Grewer (✉) • B. Wieneke

Lavision GmbH, Anna-Vandenhoeck-Ring 19, Göttingen 37081, Germany

e-mail: mgrewer@lavision.de

14.2 Method

The denoising scheme takes as input the x-, y-, and possibly z-components of a computed vector field together with the related uncertainty values U_x, U_y, and U_z on a one-sigma level. Therefore, with a probability of 68 % the true displacement x_{true} is expected to fall within the interval $x \pm U_x$.

The denoising procedure is done independently for each vector. At start, an initial filter kernel of 5×5 vectors around the center vector is created. For each vector component (x, y, z) a second-order 2D-polynomial is fitted to the 5×5 vector neighborhood and the average uncertainties $U_{x,avg}$, $U_{y,avg}$, and $U_{z,avg}$ are calculated and will serve as a reference for the kernel. Next, the adjacent vectors outside the initial 5×5 region are checked if they should be added to the filter kernel. In Fig. 14.1 Vectors c and d will be added if all components (x, y, z) are within an uncertainty band around the fitted polynomial evaluated at positions a and b respectively. The uncertainty band is given by $\pm s$ times the average uncertainty ($x \pm sU_{x,avg}$, $y \pm sU_{y,avg}$, $z \pm sU_{z,avg}$), where s is the user selected filter strength, typically set to around 2–5. A band of $\pm 1 U_{avg}$ (or ± 1-sigma) is too tight and will severely hinder growth of the filter kernel.

To ensure that the center of gravity of the filter kernel remains at the center vector, c and d will only be added if both vectors match the acceptance criteria. Otherwise, c and d are rejected, subsequently preventing all vectors further out in this direction to be part of the smoothing kernel (Fig. 14.1). Once a new shell around the initial kernel is populated, the 2D polynomial is updated and the process is repeated. Growth of the kernel stops when no more vectors match the acceptance criteria or a user selected maximum kernel size is reached. Then the center vector is replaced by the value of the polynomial function at its position. Additionally, spatial derivatives, which are readily available from the polynomial, may be stored for further processing.

Finally, new uncertainty values are computed for each vector component by taking the reference uncertainty divided by $\sqrt{N_{eff} - 6}$, where N_{eff} is the number of independent vectors in the final filter kernel and 6 is related to the degrees of freedom (parameters) of the second-order 2D-polynomial function. N_{eff} will only be equal to the total number of vectors within the smoothing kernel, when non-overlapping interrogation windows were used during DIC processing. In general, N_{eff} is roughly the total number of vectors in the filter kernel divided by the number of vectors within the size of the interrogation window. For example at 75 % overlap there are 16 vectors within the size of one interrogation window, but all of them are closely correlated, thus smoothing over the 16 vectors would yield very little reduction of the uncertainty. The described scheme for uncertainty estimation is actually a simplified version of the uncertainty propagation rules described in [6] and may not be appropriate in all cases.

The spatial resolution of the vector field is related to the spatial auto-correlation coefficients between adjacent vectors. Due to varying kernel sizes and shapes, this is different for each vector in magnitude and direction. Therefore, calculating the spatial resolution of the smoothed vector field is a formidable task and a fully correct treatment is beyond the scope of this paper. As a rough estimate, the spatial resolution is assumed to be equal to the average linear dimension of the filter kernel. It remains to be seen whether or not this is a useful estimate.

Fig. 14.1 Sketch of the denoising procedure. A 2D-polynomial is fitted to the initial 5×5 filter kernel. Adjacent vectors c and d are probed and added to the kernel if all their components fall within an uncertainty band around the fitted polynomial at positions a and b respectively. To preserve the center of gravity of the filter kernel, c and d will only be added if both vectors match the acceptance criteria. Once a new shell around the initial kernel is populated, the 2D polynomial is updated and the process is repeated
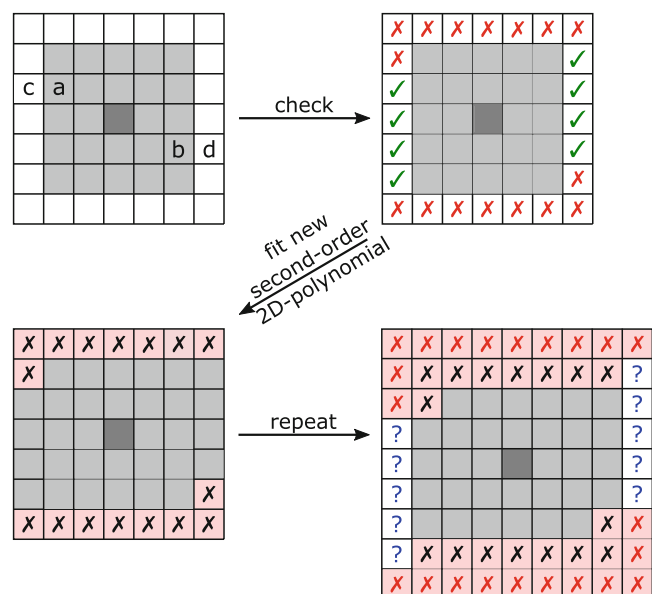
14.3   DIC Challenge Sample 14

DIC Challenge sample 14 provides an ideal test case to demonstrate the performance of the anisotropic denoising algorithm. Sample 14 features a sinusoidal x-displacement with increasing spatial frequency and a constant amplitude of 0.1 pixel. The DIC processing was done using an interrogation window size of 24×24 pixels and a step size of 5 pixels, resulting in the rather noisy displacement map displayed in the top section of Fig. 14.2. The lower part of Fig. 14.2 shows the corresponding uncertainties. On the left side of the image, where spatial frequencies are low, the uncertainties are within a range of 0.01–0.04 pixel and increase to a maximum of 0.07 pixel on the right side of the image. Obviously, the increasing uncertainty is correlated with the increasing spatial frequency of the displacements, clearly demonstrating the effect of the limited spatial resolution of the DIC algorithm.

Finally, the plot in Fig. 14.3 displays x-displacements and the associated uncertainties together, averaged over the full height of the vector field. Despite the large averaging area, noise is still visible in the plot, especially in regions with small displacement gradients. Nevertheless, the displacement amplitude is close to the true 0.1 pixel magnitude for all visible peaks.

The initial or raw vector field has been filtered using the proposed denoising scheme and increasing filter strengths s in the range of 1–4. The maximum kernel size was set to 21×21 vectors. The smoothed displacement maps are shown in Fig. 14.4 for the various filter strengths. As stated before, a filter strength of 1-sigma is too tight and consequently there is very little
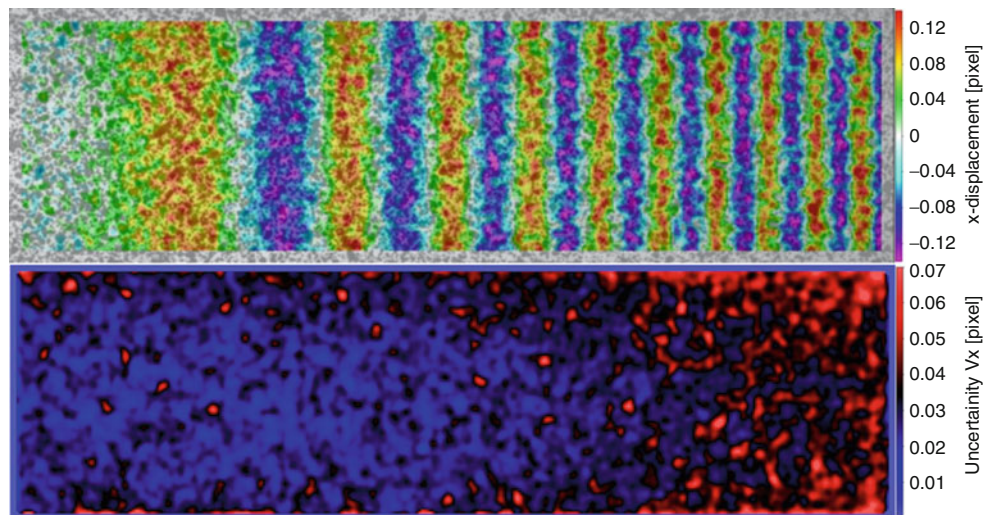

Fig. 14.2   DIC results using 24×24 pixel subsets at a step size of 5 pixel for DIC Challenge sample 14 featuring a constant amplitude (0.1 pixel) sinusoidal displacement with horizontally increasing frequency. X-displacement (*top*) and associated uncertainty map (*bottom*)
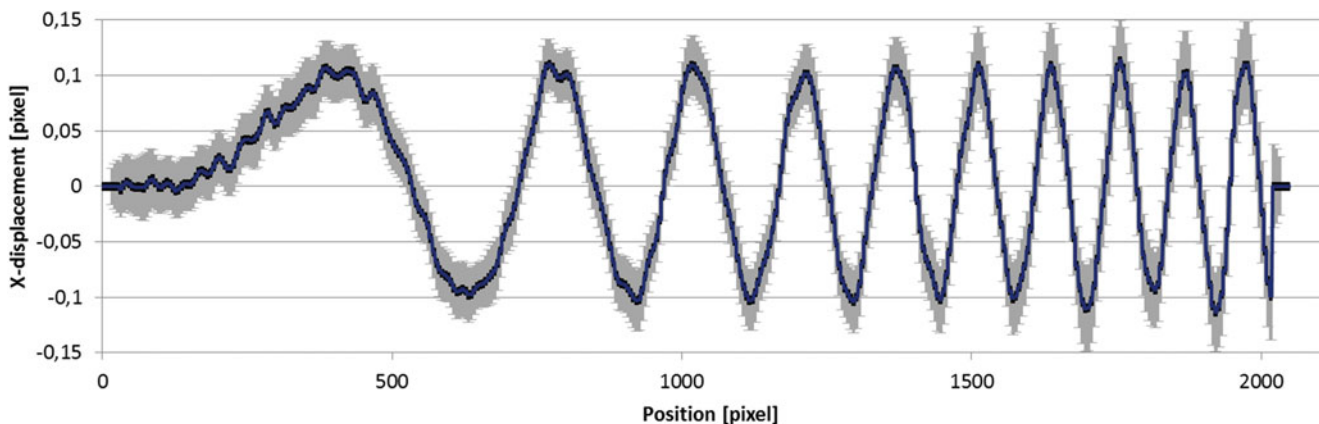

Fig. 14.3   Plot of the x-displacements and associated uncertainties of the vector field in Fig. 14.2, averaged over the full height of the image
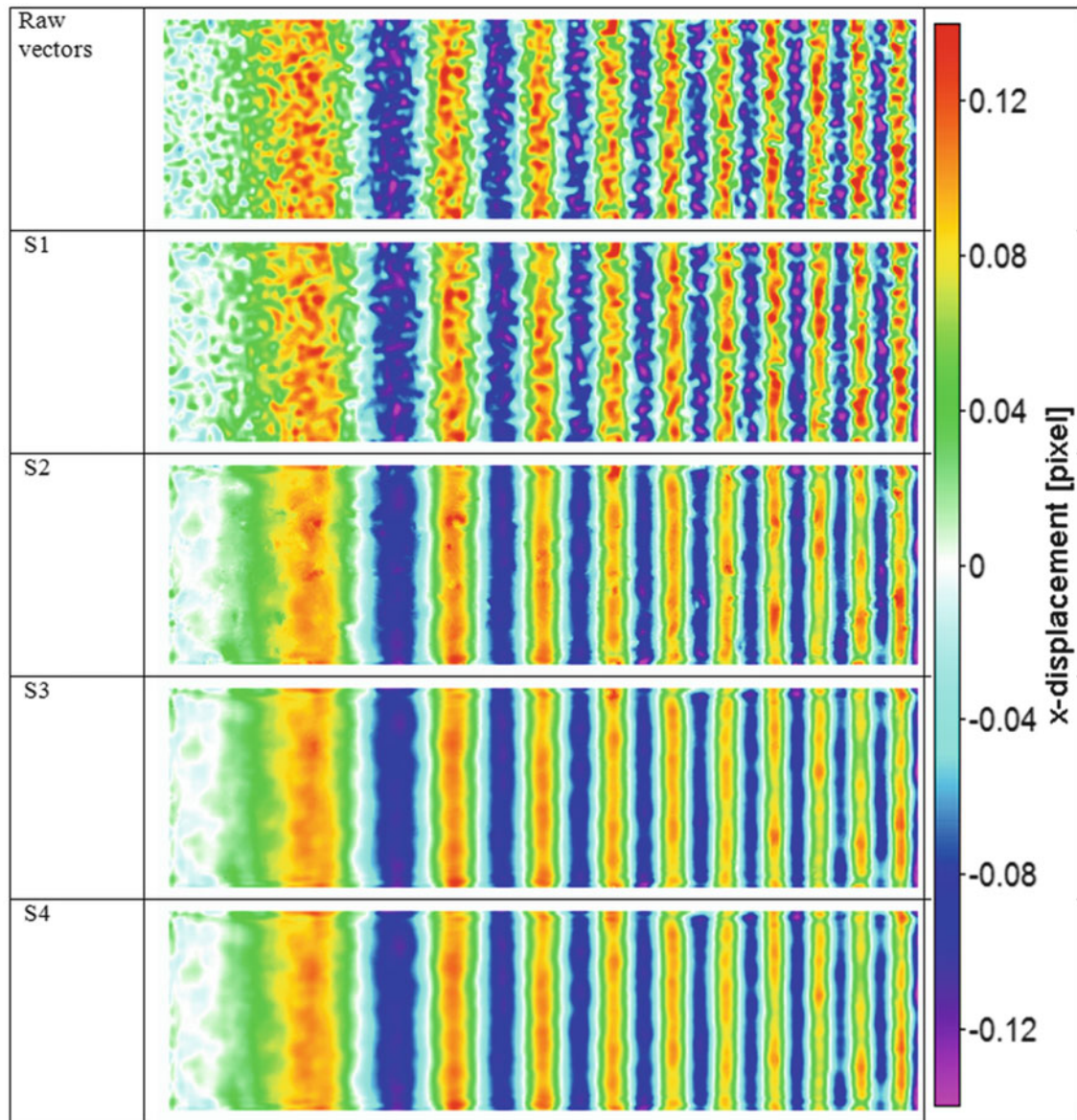
Fig. 14.4 Comparison of x-displacement maps at various levels of anisotropic denoising. Improvements are clearly visible for filter strengths above S1. Differences between S3 and S4 are marginal due to S4 being cut-off by the maximum kernel size of 21 × 21 vectors

noise improvement between the initial vector map and the S1 vector field. At a filter strength of 2, improvements are clearly visible and the noise is significantly reduced. The anisotropic denoising is predominantly removing noise along the vertical direction while still preserving the horizontal displacement gradients. At filter strength 4 the denoising is cut-off by the maximum kernel size of 21 × 21, thus only marginal differences between S3 and S4 are observed. In both cases S3 and S4, the smoothing leads to a slight loss of the displacement magnitude, indicating that the optimal filter strength is between 2 and 3.

Figure 14.5 displays ε_{xx} strain maps corresponding to the displacements in Fig. 14.4. The anisotropic denoising has an even bigger impact on the spatial derivatives than on the raw displacements. At filter strength S2 the stain values are already smooth and most of the high frequency noise components have been removed. The S3 and S4 cases further reduce the noise but differences to S2 are marginal. This is emphasized by the plot at the bottom of Fig. 14.5, which shows the evolution of the strain magnitude for filter strength up to S3. In all cases the loss of strain amplitude is minimal and the S2 and S3 graphs are almost superimposable. The only exception is the last peak on the right, where the S3 peak is approximately 25 % lower than the raw signal and 15 % below S2.
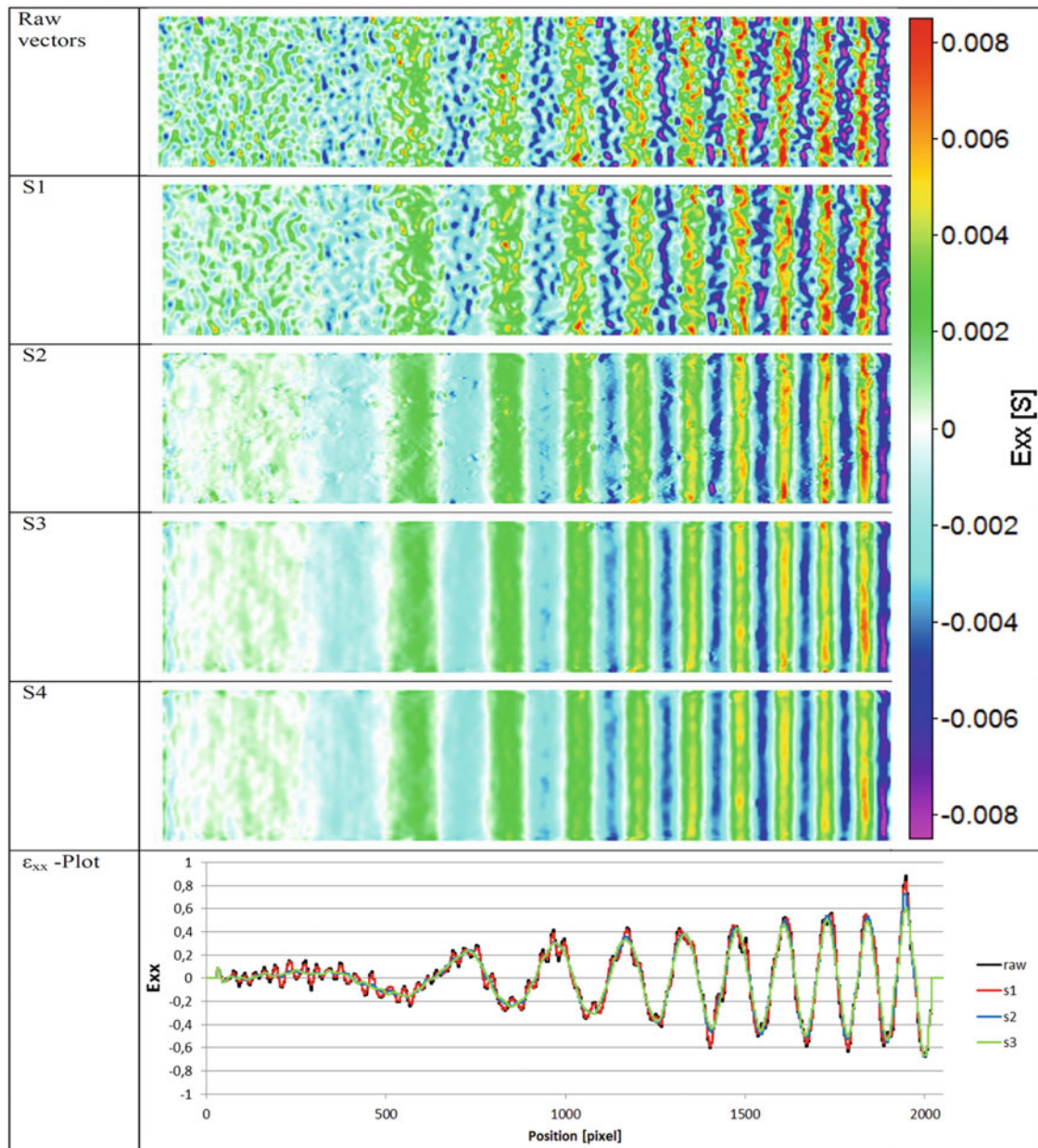
Fig. 14.5 Comparison of ε_{xx}-strain maps at various levels of anisotropic denoising. The denoising has an even bigger impact on the derivatives, than on the displacements displayed in Fig. 14.4. The plot at the bottom demonstrates that there is virtually no loss in strain amplitude up to S2.

14.4 DIC Challenge Sample 12

Sample 12 of the DIC challenge is a tensile test featuring a specimen with a hole in the middle. Tension along the vertical axis leads to characteristic butterfly-shaped strain concentrations around the hole. The displacements are much larger than in the previous case, thus there is hardly any visible noise in the displacement maps. Obviously noise is still present in the raw displacement data, but it is obscured by the scaling of the displacement map. However, strain maps reveal the noise and, as shown in Fig. 14.6, do benefit from anisotropic denoising. The filter does mainly smooth low strain regions far away from the hole while preserving strain localizations around the hole.
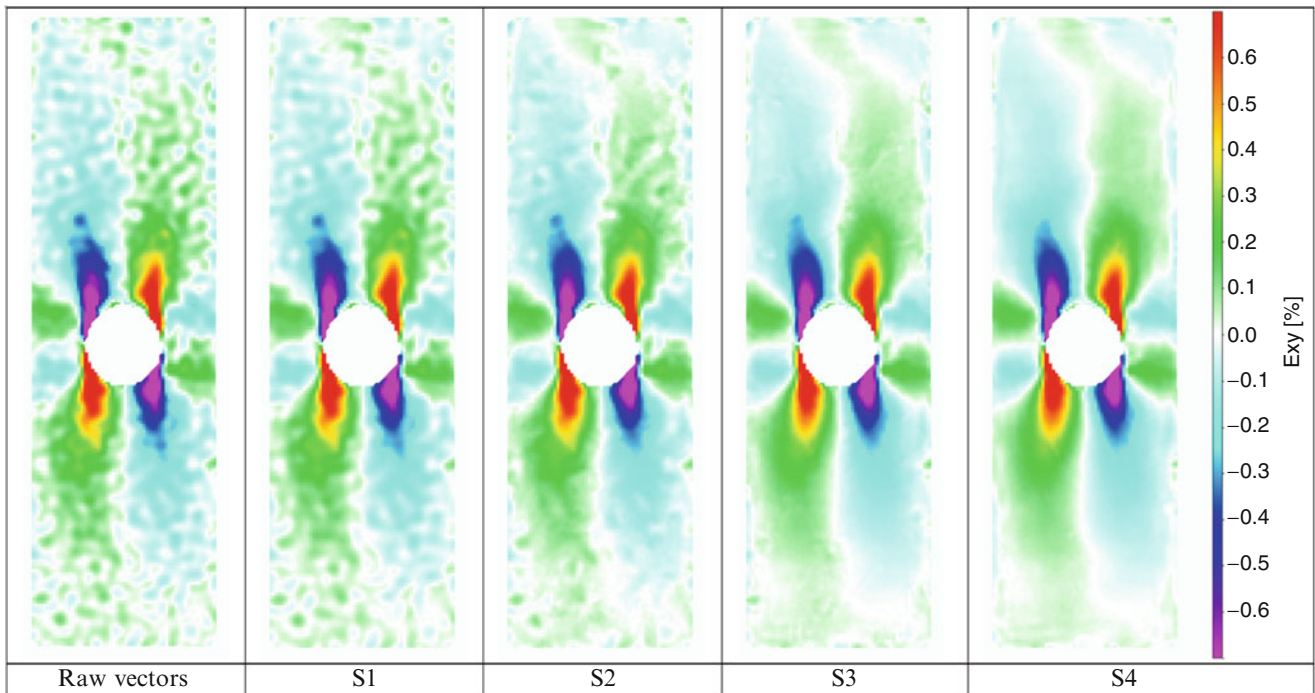
Fig. 14.6 Comparison of ε_{xy}-strain maps of DIC challenge sample 12 at different levels of anisotropic denoising. The butterfly-shaped strain concentrations around the hole are rather unaffected by the smoothing, while noise patterns in the low strain regions far away from the hole are subsequently removed at increasing filter strength

14.5   Conclusion

An anisotropic denoising technique based on DIC uncertainty has been developed, which will smooth the vector field only where local gradients are smaller than the uncertainty and preserve regions with strong gradients. The performance of the denoising algorithm was demonstrated on samples 12 and 14 of the DIC challenge. It offers robust automatic smoothing with only little loss in displacement or strain magnitude.

References

1. Raiola, M., Discetti, S., Ianiro, A.: On the suppression of PIV measurement noise with a POD based filter. In: 17th International Symposium on Applications of Laser Techniques to Fluid Mechanics, Lisbon, Portugal (2014)
2. Reu, P.L., Sutton, M., Wang, Y., Miller, T.J.: Uncertainty quantification for digital image correlation. In: Proceedings of the SEM Annual Conference, Albuquerque, NM, USA (2009)
3. Mazzoleni, P., Matta, F., Zappa, E., Sutton, M.A., Cigada, A.: Gaussian pre-filtering for uncertainty minimization in digital image. Opt. Lasers Eng. **66**, 19–33 (2015)
4. Bornert, M., Brémand, F., Doumalin, P., Dupré, J.-C., Fazzini, M., Grédiac, M., Hild, F., Mistou, S., Molimard, J.: Assessment of digital image correlation measurement errors: methodology and results. Exp. Mech. **49**(3), 353–370 (2009)
5. Zappa, E., Mazzoleni, P., Matinmanesh, A.: Uncertainty assessment of digital image correlation method in dynamic applications. Opt. Lasers Eng. **56**, 140–151 (2014)
6. Wieneke, B., Sciacchitano, A.: PIV uncertainty propagation. In: 11th International Symposium on PIV, Santa Barbara, CA, USA (2015)

Chapter 15
An Applications-Oriented Measurement System Analysis of 3D Digital Image Correlation

Jordan E. Kelleher and Paul J. Gloeckner

Abstract The purpose of this paper is to document a measurement system analysis (MSA) for a stereo digital image correlation (DIC) system such that ISO 9001 specifications are met. Many of the prior uncertainty or error studies on DIC have focused on the numerical calculations alone or only specific stages of the metrological process. Thus, there is a need to conduct an MSA to understand the various sources of uncertainty introduced over the entire process and their individual contributions on the final results. The focus of the present MSA was for the practicing engineer in an industrial environment/ laboratory. Therefore, the primary sources of uncertainty investigated in this study were the common adjustable parameters that are available to the end user during the system setup and operation. The interdependence of all the factors, both controllable and concealed, elucidated in the literature is acknowledged and conveyed. The measurand of interest was displacement and the particular software utilized to compute the displacements was Vic-3D™ (version 2012) from Correlated Solutions, Inc. The procedure outlined in ISO 98-3 "Guide to the expression of uncertainty in measurement" (GUM) was followed.

15.1 Introduction

One of the primary responsibilities of any laboratory is to provide good quality data to its customers to guide product design and development decisions. However, to definitively show that data is valid and of good quality can be a challenging endeavor, especially for more complex measurement techniques. This is a key requirement in order for a laboratory to obtain ISO 9001 "Quality Management Systems" certification. A measurement system analysis (MSA) is one of the foundational exercises to prove that a measurement system is capable and suitable for the test at hand.

The term MSA was originally coined by the Automotive Industry Action Group (AIAG). The purpose of a MSA is to assess the quality of a measurement system and the associated measurement process. In the present investigation, the term "MSA" is used rather than measurement uncertainty analysis (MUA). The key difference is that a MSA includes variations due to both the measurement system *and* the process while a MUA generally concentrates only on variations due to specific sources of the measurement system. Other than this clarification, the nomenclature in this paper is consistent with that defined in ISO 98-3 "Guide to the expression of uncertainty in measurement" (GUM).

The DIC uncertainty quantification that is common in the scholarly and commercial literature primarily focuses on the numerical calculations or a particular segment of the equipment [1–8]. While these studies provide useful information regarding a specific source of uncertainty, they fail to capture the uncertainty due to the entire measurement process. Additionally, the error sources that pertain to the DIC numerical calculations alone are not beneficial to the practicing engineer because the software is typically provided by an academic or commercial third-party; hence, it is not controllable to the user. A recent article raised similar concerns and questioned the relevance of synthetic image studies claiming improvements on the order of 0.0002 pixels [9]. Have the potentially more significant contributors been neglected, especially when using DIC outside of a well-controlled laboratory setting, simply because they are difficult to control or too setup-specific? The goal of this study was to quantify the uncertainties at key steps of the DIC process in a representative environment of an industrial laboratory.

J.E. Kelleher (✉) • P.J. Gloeckner
Cummins Technical Center, Cummins Inc., 1900 McKinley Avenue, Columbus, IN 47201, USA
e-mail: jordan.kelleher@cummins.com

15.2 Materials and Methods

15.2.1 Experimental Setup

The imaging setup was rigidly fixed on an anodized aluminum optical table/breadboard. An aluminum plate of dimensions $12 \times 12 \times 0.125$ in. ($305 \times 305 \times 3.2$ mm) was used as the target specimen. The specimen was mounted vertically onto a precise translation stage[1] using an L-bracket. The translation stage had a Mitutoyo micrometer head with a travel of 1.0 in. (25.4 mm) and engraved gradations every 0.001 in. (25.4 μm).

The specimen was divided into four equally-spaced columns so that four unique speckle patterns were applied by four trained operators. The speckle patterns on the specimen were created by applying a base coat of flat (non-glossy) white spray paint and then black spray paint to create the speckles (see Fig. 15.1).

Images of the specimen were acquired using in Vic-Snap™ 2010 with two 5.0 megapixel cameras.[2] This camera model uses a Sony ICX625 charge-coupled device (CCD) 2/3″ sensor with a pixel size of 3.45 μm × 3.45 μm. The output images were saved as 8-bit tagged image file format (.tif) with 2448 × 2048 pixels. Schneider-Kreuznach 23 mm focal length prime lenses[3] were utilized and the apertures were set to roughly f/8. Two external arrays of LED lights[4] with a maximum output of 6000 Lumens each were mounted off-angle to provide uniform illumination while minimizing glare and saturation. After the stereo-rig was setup, the cameras and lenses were focused to achieve sharp images. The exposure time for each camera was set to 890 μs. The pixel size in the object space was approximately 110 μm/pixel; thus, the total field of view (FOV) was roughly 270 mm (10.6 in.) horizontally and 225 mm (8.9 in.) vertically. An overview of the stereo-rig setup is displayed in Fig. 15.2.

Fig. 15.1 A camera's FOV showing the four columns of unique speckle patterns applied to the specimen by four individuals

---
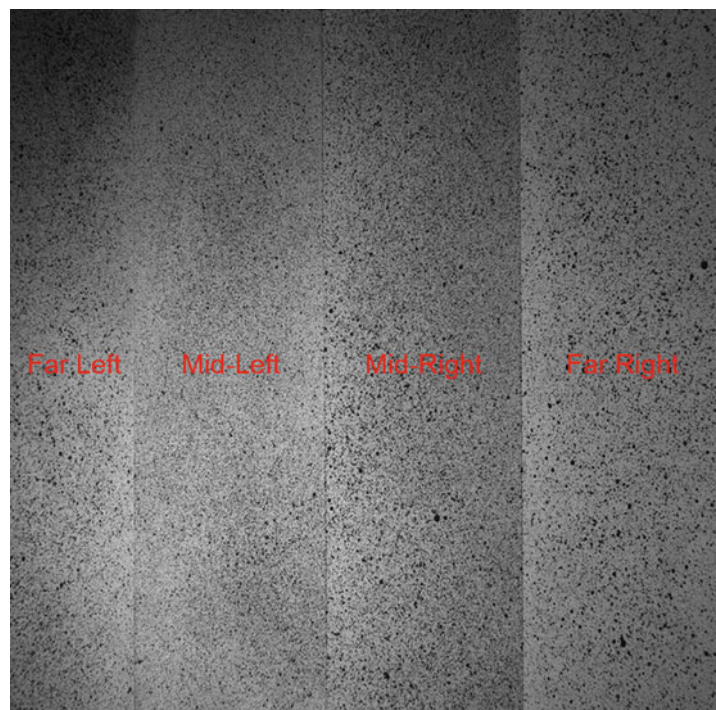
[1] Single-Axis Translation Stage, PT1, Thorlabs, Inc., Newton, NJ, USA.

[2] GRAS-50S5M-C, Point Grey Research, Inc., Richmond, BC, Canada.

[3] Xenoplan 1.4/23-0902, Schneider-Kreuznach. Bad Kreuznach, Rhineland-Palatinate, Germany.

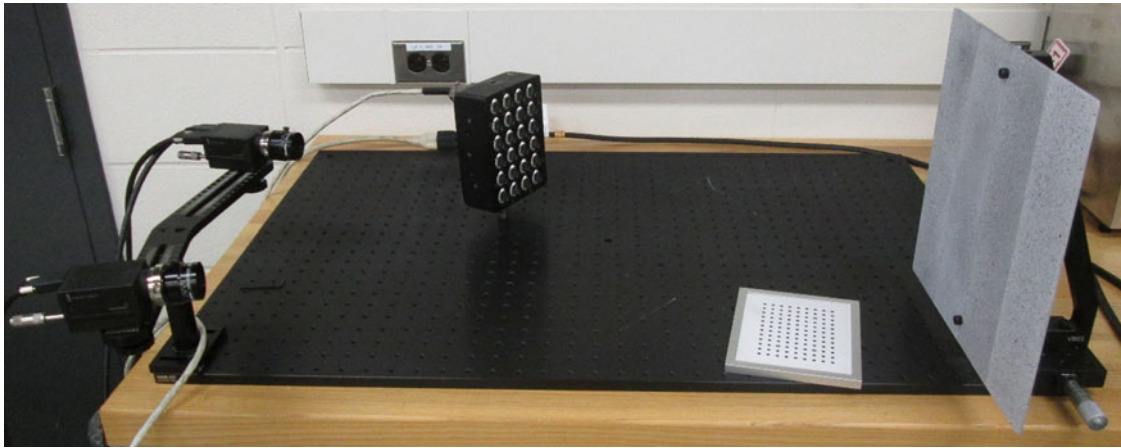[4] Model 900445, Visual Instrumentation Corporation, Lancaster, CA, USA.

Fig. 15.2 An overview of the test setup including the cameras, lights, specimen, translation stage, and the calibration grid

15.2.2 Measurement Process

Four trained operators were utilized to acquire images in order to quantify the variability due to the user. The stereo-rig was calibrated by acquiring 20 image pairs of a grid with 12×9 dots and a dot spacing of 9 mm. The calibration grid was rotated about all three axes, translated in-plane, and plunged out-of-plane such that it filled the entire measurement volume. Twenty calibration image pairs were captured because the "Vic-3D v7 Testing Guide" by Correlated Solutions, Inc. recommends 15–20 image pairs so this is the standard practice at Cummins Inc. However, a more recent study suggests that a *minimum* of 25 and ideally around 100 calibration image pairs should be captured in order for the nonlinear minimization process to accurately calculate the intrinsic and extrinsic camera parameters [10]. Nevertheless, the goal of this MSA is to capture uncertainties for a typical, representative measurement process and setup which is why only 20 calibration image pairs were acquired.

Once the calibration was complete, five static/stationary images of the specimen were acquired for the noise floor test also known as the self-correlation test [7]. The specimen on the precision stage was then translated 0.1 in. (2.54 mm) to the right (from the camera's view) and another five images were acquired before returning the stage back to its original position. This entire process (i.e. calibration, static images, and rigid body translation) was completed five times for each operator. Thus, there were a total of 20 distinct data sets—leading to a grand total of 400 calibration image pairs, 100 static image pairs, and 100 rigid body translation image pairs.

15.3 Uncertainty Sources

15.3.1 MSA Scope

Defining the scope and assumptions is one of the most critical steps in the design of a MSA. The scope of the present MSA entails the DIC measurement process beginning with equipment that is already setup and ending with the image correlation results obtained via software. Effects of post-processing (e.g. coordinate transformation, smoothing, calculating strains, etc.) the image correlation results will not be considered in this study. The following is a list of assumptions regarding the scope of this particular MSA:

1. Camera synchronization was negligible since the test was quasi-static.
2. The subset and step sizes were held constant at 23 pixels and 7 pixels, respectively.
3. The DIC software package utilized was Vic-3D™ (version 2012) from Correlated Solutions, Inc.
4. The subset weighting function, interpolation function, and optimization criterion were fixed as Gaussian, optimized 8-tap, and zero-mean normalized sum of squared differences (ZNSSD), respectively. The subset shape function is affine plus a perspective transform.

5. The effect of post-processing options (e.g. coordinate transformation, removal of rigid body motion, filtering or smoothing of the displacement field, etc.) on the displacement data were not examined.
6. The impact of lens distortion on in-plane displacement variability is insignificant which has been proven for a 23 mm focal length Schneider lens with a stereo angle of 30° or greater [3, 6].
7. Only random/variance errors are considered in the present study and not bias/systematic errors.

The stereo-DIC measurement process can be broadly divided into five main categories: (1) specimen preparation, (2) stereo-rig setup, (3) calibration (4) conducting the test (i.e. acquiring images), and (5) image correlation and post-processing. With a measurand of in-plane displacement, the uncertainty sources that were investigated in this study were: (1) stereo-calibration, (2) speckle pattern, (3) image noise and environmental influences, and (4) the "hidden" DIC computations (i.e. subset shape function, interpolation, and optimization criterion). These four uncertainty sources were intended to generally follow the five main steps of the DIC measurement process. The uncertainties associated with the stereo-rig setup were not pursued because the equipment (i.e. cameras, lenses, mounting system, lights, etc.) was the common hardware used for a test at Cummins Inc. Additionally, the effects of stereo-angle on the in-plane and out-of-plane uncertainties is already well understood [3].

15.3.2 Displacement Uncertainty Due to the Calibration

The stereo-calibration was performed in Vic-3D™ (version 2012) by Correlated Solutions, Inc. The same five image pairs—one reference static image and four rigid body translation images—were processed with each calibration run and the mean of the displacement field was analyzed. The area of interest (AOI), which was also the same for all calibration runs, was chosen to be the middle vertical half (i.e. from pixel row 512 to 1536) of the mid-right speckle pattern. The standard deviation of the mean displacement was calculated for the four images separately for all 20 calibration runs and then averaged.

15.3.3 Displacement Uncertainty Due to the Speckle Pattern

The in-plane displacement of 80 static image pairs (four separate operators, five iterations for each operator, with four images per iteration) was analyzed for each speckle pattern similar to other studies [11]. The same stereo-calibration parameters, calculated using 99 image pairs, was applied to process all the static images. The four unique speckle patterns were labeled "far left," "mid-left," "mid-right," and "far right" as shown in Fig. 15.1. The standard deviation of the horizontal displacement field was computed for each speckle pattern. In order to mitigate the contributions of image noise, the variation between speckle patterns within each image was computed and then averaged for all 80 images. This is a satisfactory approach assuming the image noise is consistent over the entire FOV, which was confirmed via the Image Processing Toolbox™ in MATLAB®.[5]

15.3.4 Displacement Uncertainty Due to Image Noise

The in-plane displacement of 80 static image pairs was analyzed for the same AOI, which was chosen to be the middle vertical half (i.e. from pixel row 512 to 1536) of the mid-right speckle pattern. The same stereo-calibration parameters, calculated using 99 image pairs, was applied to process all the static images in order to reduce influences due to the calibration. The standard deviation of the horizontal displacement field was computed for each image and the average value was reported.

---

[5] MATLAB®, version 8.2.0.701, R2013b, The MathWorks, Inc., Natick, MA, USA.

15.3.5   Displacement Uncertainty Due to DIC Computations

The final source of uncertainty that was explored in the current study was due to the "hidden" computations of DIC [12–14]. These "hidden" computations included the subset shape and weighting functions, gray level interpolation, and the optimization criterion for pattern matching. These were aggregated and categorized as a Type B uncertainty source according to the GUM nomenclature. The uncertainty value was taken from a survey of the estimates provided in the literature for the specific settings (i.e. affine plus a perspective transform subset shape function with a Gaussian weighting function, optimized 8-tap interpolation function, and ZNSSD optimization criterion) used in this investigation.

15.4   Results and Discussion

The mean and standard deviation of the calibration parameters and the calibration score/residuals for all 20 calibration runs are listed in Table 15.1. There were two calibration runs (from the same operator) where the residuals were approximately 0.09, which is higher than what would typically be accepted. If these two runs are removed from the data set then the standard deviation of the parameters is reduced by more than half. Nevertheless, the calibrations were generally of good quality.

The mean horizontal displacement of the same 4 images after the specimen was translated 2.54 mm (0.1 in.) is displayed in Fig. 15.3 for 20 different calibration runs. The mean displacement was very consistent from calibration-to-calibration but a larger spread was observed from image-to-image—likely due to image noise and environmental influences. Thus, the standard deviation was computed for each of the four translated images and then the average of the four standard deviations was reported as the calibration uncertainty value which was 0.16 μm or approximately 0.0015 pixels. There is an apparent bias in the mean displacements of approximately 5 μm (0.0002 in.). However, this is well within the uncertainty of the translation stage which had engraved gradations every 25.4 μm (0.001 in.); therefore, it is disregarded as a true bias error.

Table 15.1 The mean and standard deviation of the calibration parameters and the calibration score/residuals for all 20 calibration runs with four operators

			Mean	St dev
Intrinsic parameters	Camera 0	Center X (pixels)	1256.265	20.970
		Center Y (pixels)	1001.614	11.276
		Focal length X (pixels)	6643.471	62.808
		Focal length Y (pixels)	6643.679	62.682
		Skew (degrees)	0.886	0.339
		Kappa 1 (pixels^{-2})	−0.179	0.004
		Kappa 2 (pixels^{-4})	0.533	0.182
	Camera 1	Center X (pixels)	1266.656	73.502
		Center Y (pixels)	1028.635	13.523
		Focal length X (pixels)	6634.636	57.109
		Focal length Y (pixels)	6636.073	64.039
		Skew (degrees)	−0.252	2.898
		Kappa 1 (pixels^{-2})	−0.181	0.004
		Kappa 2 (pixels^{-4})	0.425	0.184
Extrinsic parameters	Angles	X (degrees)	0.445	0.043
		Y (degrees)	−22.446	0.578
		Z (degrees)	0.420	0.047
	Distances	X (mm)	298.754	0.726
		Y (mm)	1.452	0.140
		Z (mm)	66.797	2.937
	Residuals	Overall score	0.033	0.014
		Camera 0 score	0.023	0.003
		Camera 1 score	0.030	0.023

Fig. 15.3 The mean of the horizontal displacement field for four rigid body translation images for all 20 calibration runs. The average of the standard deviation for each image was used to quantify the uncertainty due to the calibration
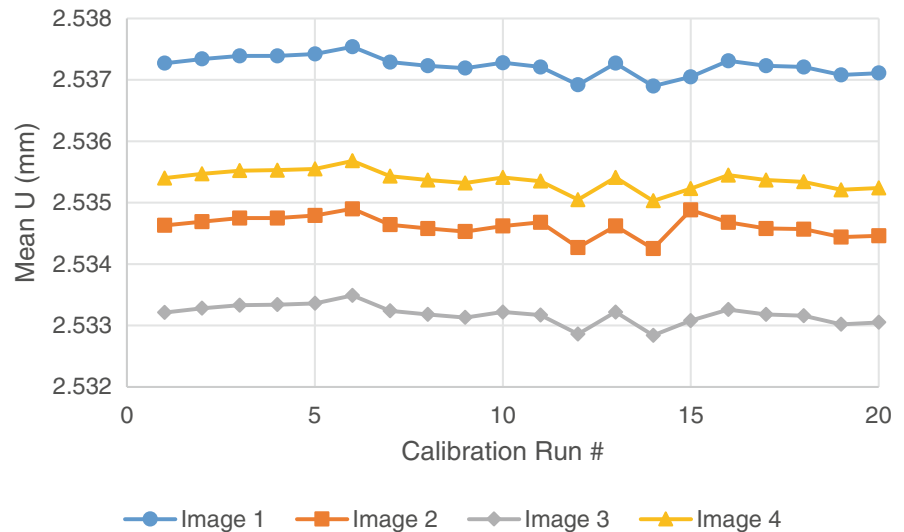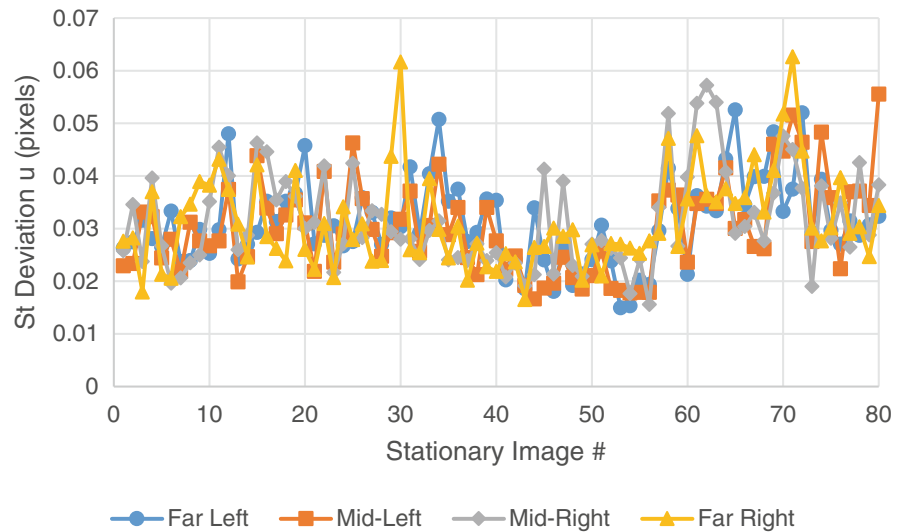

Fig. 15.4 The standard deviation of the horizontal displacement field for each speckle pattern for 80 static/stationary images. The variation between speckle patterns within each image was averaged for all 80 images to quantify the uncertainty due to the speckle pattern

The standard deviation of the horizontal displacement field is shown in Fig. 15.4 for each speckle pattern for 80 static images. The standard deviation amongst speckle patterns is quite consistent and there is no obvious trend. The average standard deviation between speckle patterns within each image was 0.0063 pixels.

The standard deviation of the horizontal displacement field (of the mid-right speckle pattern) for all 80 static images is presented in Fig. 15.5. A slightly higher magnitude and more volatility is exhibited in the last 20 images, which are from the same operator. This could potentially indicate that some environmental effect(s), such as vibrations induced by the heating, ventilation, and air conditioning system turning on, were present then but absent or diminished during the other runs. The average of the standard deviation of the horizontal displacement was 0.033 pixels.

Finally, the uncertainty attributed to the "hidden" computations of DIC was assumed to be 0.01 pixels. This was obtained by a careful assessment of the values presented in the literature for the subset shape and weighting functions, gray level interpolation, and the optimization criterion for pattern matching [15, 16].

All of the uncertainty sources are listed in Table 15.2 and then pooled to give a combined standard uncertainty of 0.035 pixels and an expanded uncertainty at 95 % confidence of 0.07 pixels or roughly 7.7 μm for this particular experimental setup. The terminology and calculations employed to combine and expand the uncertainties followed the GUM procedure.

Fig. 15.5 The standard deviation of the horizontal displacement field (of the mid-right speckle pattern) for 80 static/stationary images
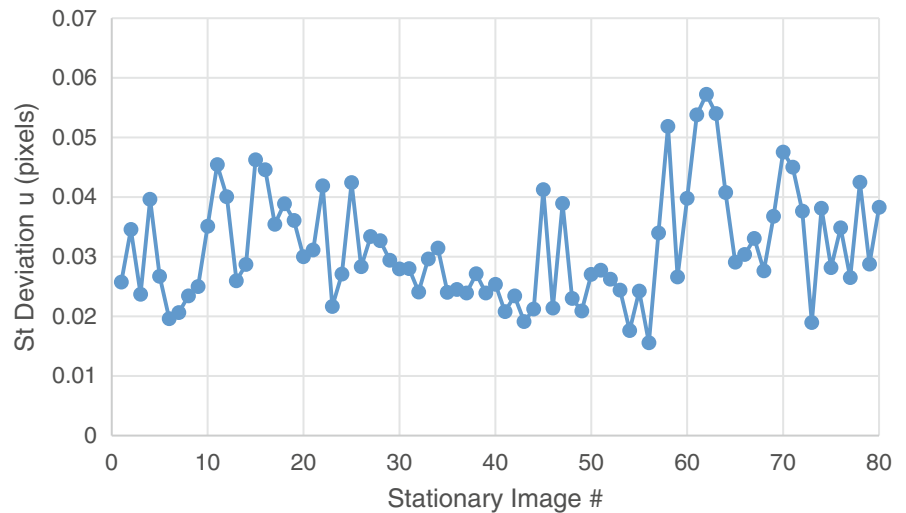

Table 15.2 The uncertainty budget of the four sources examined in this study along with the combined and expanded uncertainty estimates following the GUM

Source of uncertainty	Limits (±a) or 1 sigma	Distribution type	Evaluation method	Standard uncertainty	Sensitivity coefficient	Individual uncertainty contributor as % of combined
Stereo calibration	0.0015 pixels	Normal	A	0.0015 pixels	1	0.2 %
Speckle pattern	0.0063 pixels	Normal	A	0.0063 pixels	1	3.2 %
Image noise and environmental effects	0.033 pixels	Normal	A	0.033 pixels	1	88.5 %
DIC "hidden" computations	0.010 pixels	Normal	B	0.010 pixels	1	8.1 %
			Combined standard uncertainty:		0.035 pixels	
			Confidence limit:		95.0 %	
			Coverage factor:		2	
			Expanded uncertainty:		0.070 pixels	

15.5 Conclusions

The expanded uncertainty at 95 % confidence was 0.07 pixels or roughly 7.7 μm for this particular experimental setup with a FOV of 270 mm × 225 mm. The effect of the stereo calibration had a minor effect on the noise floor displacement results (assuming an acceptable calibration residual was obtained)—on the order of 0.1 μm in this study. However, the calibration had a more significant impact when assessing the specimen's 3D position or shape. The impact of the speckle pattern was modest, provided that the pattern obtained (i.e. speckle size and contrast) is appropriate for the desired FOV. By far the largest uncertainty contributor examined was found to be image noise and environmental effects. While image noise has been investigated in synthetic image studies, there is no clear way to study environmental influences using synthetically generated images. The effects of air turbulences, temperature/humidity fluctuations, slight vibrations, dust particles suspended in the air, camera mounting stability, etc. are all factors that are very hard to control but play a large role in the overall uncertainty of a DIC measurement. Practicing engineers who use DIC in an industrial laboratory must give careful consideration to the measurement setup and process. Reassuringly, DIC proved to be a robust technique since the measurement uncertainties did not significantly vary from operator to operator. There are dozens of other parameters which were omitted from this MSA. Additionally, the interdependence of the many factors is one of the most challenging aspects of a DIC uncertainty study. Even though the uncertainty values presented in this study are specific to this setup, the general findings should transcend and be applicable to a variety of scenarios.

The scope of the current MSA did not include the equipment setup (i.e. cameras, lenses, tripod mounting, lighting, etc.) and how variability in the setup process could influence the measurement uncertainty. The focus of future research will be to examine the impacts of equipment setup from operator-to-operator via a gage repeatability and reproducibility (R&R) study.

References

1. Bornert, M., Brémand, F., Doumalin, P., Dupré, J.-C., Fazzini, M., Grédiac, M., Hild, F., Mistou, S., Molimard, J., Orteu, J.-J., Robert, L., Surrel, Y., Vacher, P., Wattrisse, B.: Assessment of digital image correlation measurement errors: methodology and results. Exp. Mech. **49**(3), 353–370 (2009)
2. Dupré, J.C., Bornert, M., Robert, L., Wattrisse, B.: Digital image correlation: displacement accuracy estimation. EPJ Web Conf. **6**, 31006 (2010)
3. Ke, X.-D., Schreier, H.W., Sutton, M.A., Wang, Y.Q.: Error assessment in stereo-based deformation measurements, Part II: experimental validation of uncertainty and bias estimates. Exp. Mech. **51**(4), 423–441 (2011)
4. Lecompte, D., Smits, A., Bossuyt, S., Sol, H., Vantomme, J., Van Hemelrijck, D., Habraken, A.: Quality assessment of speckle patterns for digital image correlation. Opt. Lasers Eng. **44**(11), 1132–1145 (2006)
5. Pan, B., Xie, H.M., Wang, Z.Y., Qian, K.M., Wang, Z.Y.: Study of subset size selection in digital image correlation for speckle patterns. Opt. Express **16**(10), 7037–7048 (2008)
6. Reu, P.L., Sweatt, W., Miller, T., Fleming, D.: Camera system resolution and its influence on digital image correlation. Exp. Mech. **55**(1), 9–25 (2015)
7. Wang, Z.Y., Li, H.Q., Tong, J.W., Ruan, J.T.: Statistical analysis of the effect of intensity pattern noise on the displacement measurement precision of digital image correlation using self-correlated images. Exp. Mech. **47**(5), 701–707 (2007)
8. Wang, Y.Q., Sutton, M.A., Bruck, H.A., Schreier, H.W.: Quantitative error assessment in pattern matching: effects of intensity pattern noise, interpolation, strain and image contrast on motion measurement. Strain **45**(2), 160–178 (2009)
9. Reu, P.L.: A realistic error budget for two dimensional digital image correlation. Adv. Opt. Methods Exp. Mech. **3**, 189–193 (2015)
10. Reu, P.L.: A study of the influence of calibration uncertainty on the global uncertainty for digital image correlation using a Monte Carlo approach. Exp. Mech. **53**(9), 1661–1680 (2013)
11. Haddadi, H., Belhabib, S.: Use of rigid-body motion for the investigation and estimation of the measurement errors related to digital image correlation technique. Opt. Lasers Eng. **46**(2), 185–196 (2008)
12. Reu, P.: Hidden components of DIC: calibration and shape function—Part 1. Exp. Tech. **36**(2), 3–5 (2012)
13. Reu, P.: Hidden components of 3D-DIC: interpolation and matching—Part 2. Exp. Tech. **36**(3), 3–4 (2012)
14. Reu, P.: Hidden components of 3D-DIC: triangulation and post-processing—Part 3. Exp. Tech. **36**(4), 3–5 (2012)
15. Schreier, H.W., Braasch, J.R., Sutton, M.A.: Systematic errors in digital image correlation caused by intensity interpolation. Opt. Eng. **39**(11), 2915–2921 (2000)
16. Sutton, M.A., Orteu, J.-J., Schreier, H.W.: Image Correlation for Shape, Motion and Deformation Measurements—Basic Concepts, Theory, and Applications. Springer, New York (2009)

Chapter 16
Preliminary Study on Determination Pointing-Knowledge of Camera-Pair Used for 3D-DIC

Chi-Hung Hwang, Wei-Chung Wang, and Shou Hsueh Wang

Abstract While digital image correlation method (DIC) implemented for displacement measurement of large scale object, the pointing knowledge is an important parameter of the measurement. The 2D DIC system always uses a single camera for imaging, the pointing knowledge is known as the point where camera line-of-sight intersects object surface. Knowing from the previous study, DIC determined displacement field has an additional error if the camera line-of-sight is not perpendicular to the object surface because in-plan measurement sensitivity of 2D-DIC is higher than out-of-plan one. In-plan displacement along object surface can be decomposed into normal and parallel to line-of-sight respectively. 2D-DIC can evaluate the displacement vector normal to the camera line-of-sight well. 3D-DIC has a similar problem, the in-plan and out-of-plan displacement resolutions are different. Comparing with 2D-DIC, 3D-DIC system has more complex parameters. For a typical camera pair of 3D-DIC imaging system always consists of two cameras. The cameras can be considered as two sub-apertures of an imaging device. The line-of-sight of assembled imaging system defines the pointing knowledge of an imaging system with respect to the subject. In this paper, the errors introduced by pointing knowledge of a camera pair used for 3D-DIC is investigated and discussed.

Keywords Digital image correlation • Different formats • Displacement • Strain

16.1 Introduction

In this paper, errors introduced by ill pointing are estimated by a simple experiment, this study is part of a project on developing a method of implementing exist surveillance imaging systems as an imaging sensor network for health monitoring. To secure the safety of important public infant structures, many surveillance imaging systems has been installed around main bridges, tunnels, dams, tanks, and even the historical buildings to provide a video stream to the security department [1]. Among all image-processing-based strain measurement technology, the digital image correlation (DIC) method can be used to determine the field of displacement and strain by tracing two images captured at different status and the maximum measurable diameters are determined by imaging system that provides a great freedom for measuring applications and the spatial resolution can research sub-pixel level.

Digital image correlation method (DIC) is a strain optical measurement method based on tracking the characteristic pattern of an object among series captured images. The displacement, deformation, strain and even the stress field can be evaluated. The DIC method can also be implemented with a different imaging system for a different scale. Traditional optics, camera and microscope, can be used for evaluating strain field of an object with meters to micrometers in size. By using SEM and TEM the object characteristic diameters in nanometer scale. The geometrical relation between the testing object to the imaging system can be well defined by imaging system frame if an imaging system such as the microscope, SEM and TEM. However, in general application, there are no frames between the imaging system and the object which can be used to define the geometric relation between the imaging sensor and the object. Pointing knowledge is defined to be the spatial relations between the observer and the object under measurement, especially the intersection of camera-line-of-sight to the object, that is, the angle defined by the line-of-sight and surface vector of the testing object and the pixel corresponding object point are both need to be determined.

C.-H. Hwang (✉)
ITRC, NARLabs, Hsinchu 30073, Taiwan, ROC
e-mail: chhwang@narlabs.org.tw

W.-C. Wang • S.H. Wang
Department of Power Mechanical Engineering, National Tsing Hua University, Hsinchu 30013, Taiwan, ROC

Fig. 16.1 Experimental setup of a 2D DIC to reveal how the poor pointing knowledge degrades the measurement accuracy. (**a**) 2D DIC setup. (**b**) Operation scenarios, introducing artificial pointing by rotating the camera
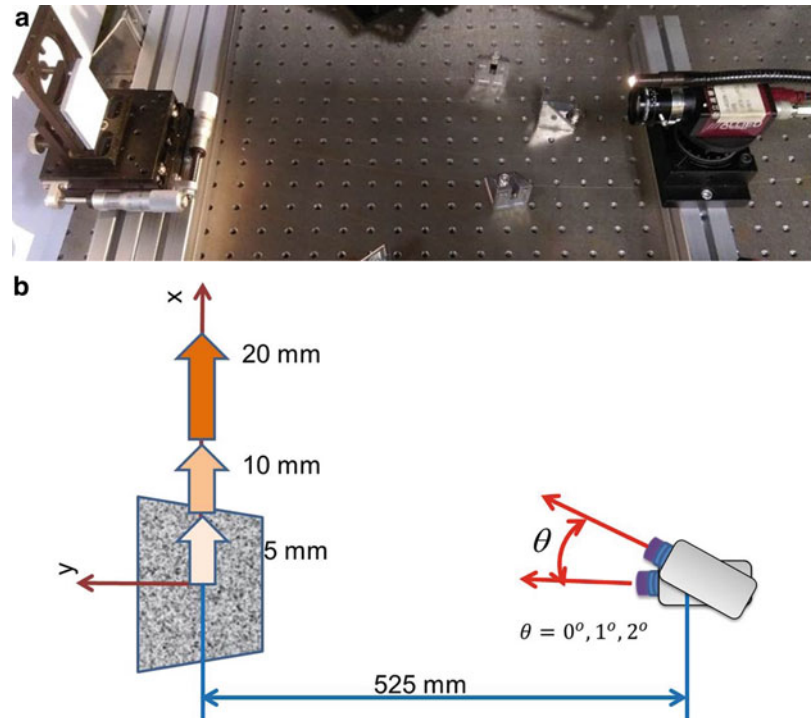
16.2 Experimental Setup

To reveal the fact that pointing-knowledge affects the DIC measurement results; simple and easy setup experiments need to be designed for this study. However, in general, there is always a small angle exist between the optics and test object, especial the test object is at the reference position. It is very difficult to eliminate the angle and observe the object from the normal direction. The remaining angle would change the observing coordinate system and alter the measurement sensitivity of the system. Considering the definition of pointing knowledge and the existing of small angle between the optics and object, in this study, to understanding how the pointing knowledge degrades the DIC measurement results the specimen is designed to move along the x-axis and the movements are recorded by the imaging system at different rotated angles.

As showing in Fig. 16.1, for 2D DIC, the camera is mounted on a rotating stage, the specimen is moved to +5, +10 and +20 mm with the help of a linear stage to generate strain free displacement.. Series images have been captured as the camera is rotated by the rotating stage to angles $\theta = 0°$, $1°$, $2°$. The operation scenario is shown in Fig. 16.1b. Similar experiment setup and procedure of 3D DIC system are also implemented, as showing in Fig. 16.2. The camera pair is mounted on a camera-rod and again installed to a rotating stage. The heading angle, Ω, of both camera with respect to the camera-rod, and the baseline, B, of the camera pairs keep the same value as the object moved to two position, x = +9 mm and x = +23.5 mm (as showing in Fig. 16.2b). As for the rotating angle of the 3D DIC camera pair, same as 2D DIC, there are defined to be $0°$, $1°$, $2°$. It is worthy of notice that the 3D DIC has a measurement sensitivity of the out-of-plane displacement, to well generate an ideal in-plane displacement field; a positioning plate with holes drilled in predefined pitch, as shown in Fig. 16.3, is utilized to mount the object to the giving position to simulate displacement; this positioning plate provides repeatability positioning of the test aluminum plate, the initial angle between the object and the camera pair can be ensured. In this study, the CCD camera and the camera pair are rotated clock-wisely, by this way, the object can be seen after moved.

The test object is made of an aluminum plate, and followed with standard surface preparing process [2] to yield a random speckle pattern on the surface.

16.3 Results and Discussions

In this study, both 2D DIC and 3D DIC are implemented to evaluate the displacement and strain field of a flat aluminum plate. With no doubt, in this study the initial pointing angle between the optics and the test object are also unknown which is the typical measurement condition of the application of DIC method. Therefore, all measurements performed in this study has to be done carefully to avoid any change of the initial pointing angle.

Fig. 16.2 Experimental setup of a 3D DIC to reveal how the poor pointing knowledge degrades the measurement accuracy. (**a**) 3D DIC setup. (**b**) Operation scenarios, introducing artificial pointing by rotating the base
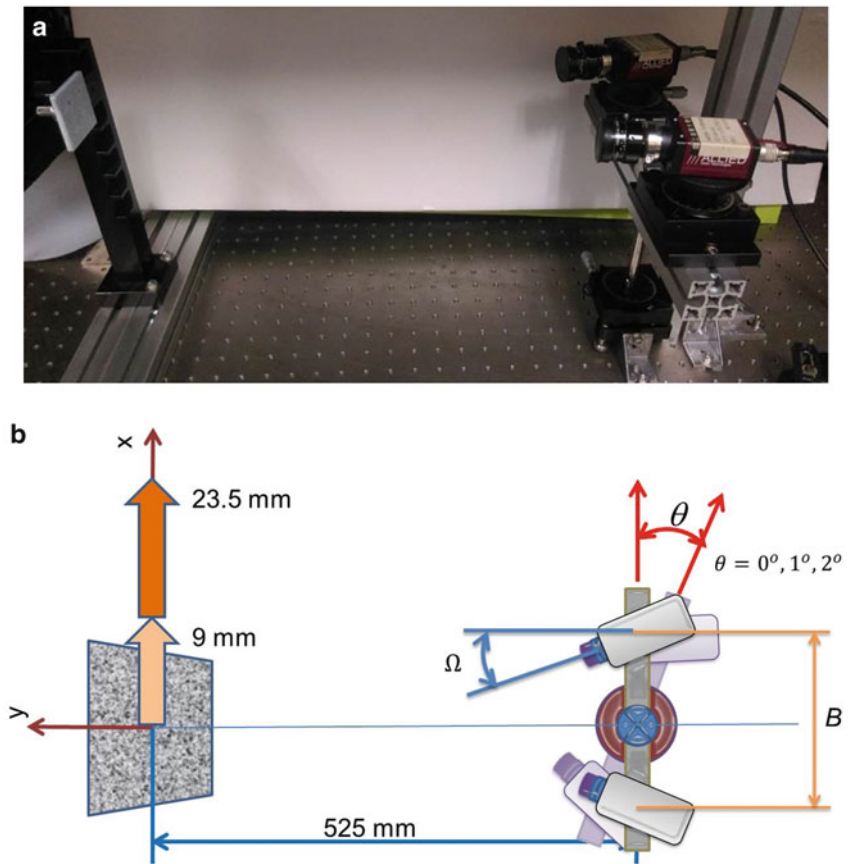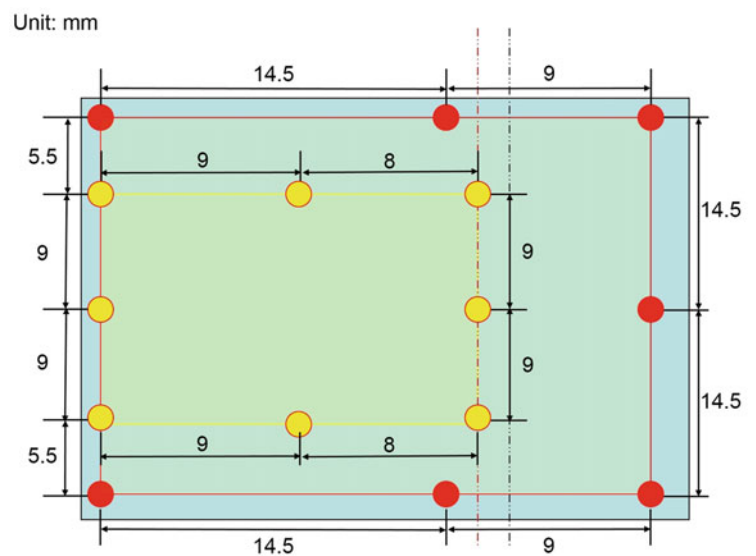

Fig. 16.3 Positing plate provides repeatability positioning of the test aluminum plate

16.3.1   2D DIC

In this study, the camera was rotated to different angles to simulate the impact of poor pointing knowledge; Fig. 16.4 is the U-displacement field calculated from different images captured at different rotation angles as the test object moved towards +x-direction. The images indicate that the displacement fields are changed from left upper corner down to right-hand lower
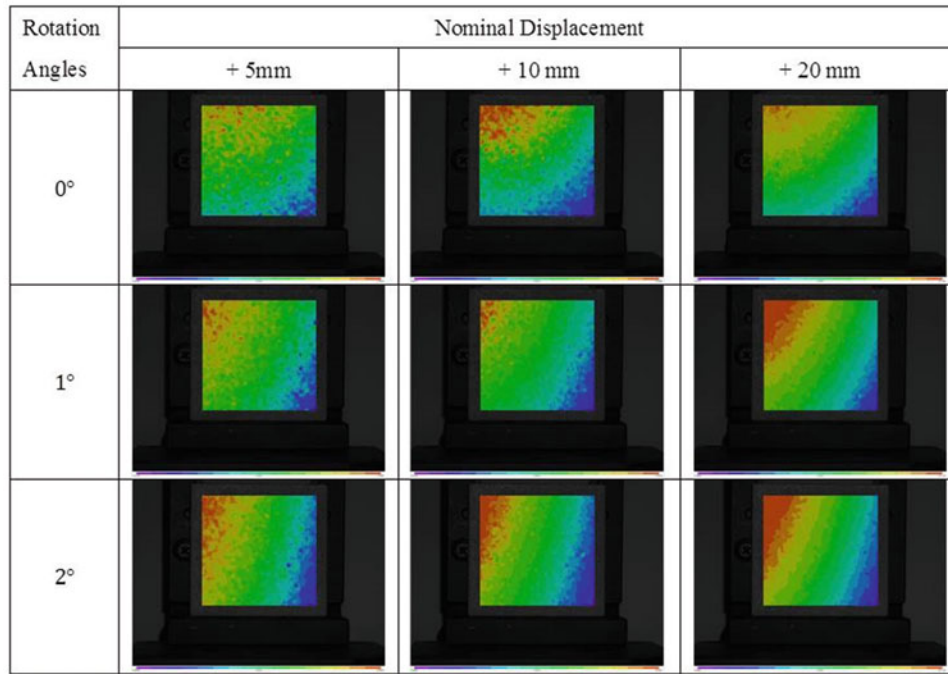
Rotation Angles	Nominal Displacement		
	+ 5mm	+ 10 mm	+ 20 mm
0°			
1°			
2°			

Fig. 16.4 The U-displacement field calculated by 2D DIC

part. Based on the observed, the displacement and strain data are taken from the calculated displacement and strain field along diagonal for further analysis and discussion. The displacements along diagonals have been plotted in Fig. 16.5, the results show that the displacement span is minimum as the rotation angle is 0°, and in general, the displacement span increased as the rotation angle increased, it is interesting to know from the displacement plots that the maximum displacements of three rotation angles are almost the same. In addition, the displacement determined from images captured at 1° and 2° are close for small displacement, +5 and +10 mm, but the difference becomes significant as the nominal displacement increased to +20 mm, as shown in Fig. 16.4c. The displacement differences between the calculated averaged and the nominal displacement is shown in Fig. 16.4d, it indicates that the errors are increased as either rotation angle increased or the displacement increased; the results also reveal that the pointing issue can be improved by controlling the displacement measurement error.

As for the strain field, since the object is moved by linear stage with subjected to any external force, in principle the strain field should be zero; for discussion convenience, pseudo strain defined by the following equation is introduced for further discussion,

$$\text{pseudo strain, } \varepsilon_{ij} = \left[\sum_l^n \sum_k^m \frac{\left(\varepsilon_{ij}|kl\right)^2}{(m+n)} \right]^{1/2}$$

where $i, j = 1, 2, 3$ for coordinates, k and l are an index of the pixel along row and column, the maximum pixel numbers of row and column are m and n.

Table 16.1 shows the pseudo strain for different rotation angle and nominal displacement; from the table, ε_{xx} and ε_{yy} are related small as rotation angles are small, but ε_{xy} are not changed with respect to the rotation angle. Meanwhile, all pseudo strains are increased as nominal displacement increased. Figure 16.6 shows the pseudo strain-displacement relations at given rotation angle. The plots indicates the pseudo strain-displacement is almost linear, in this study, and The pseudo strain field obtained from different rotation angles which indicate larger rotation angle would conduct higher pseudo strain, and the pseudo strain increased as nominal displacement increased.
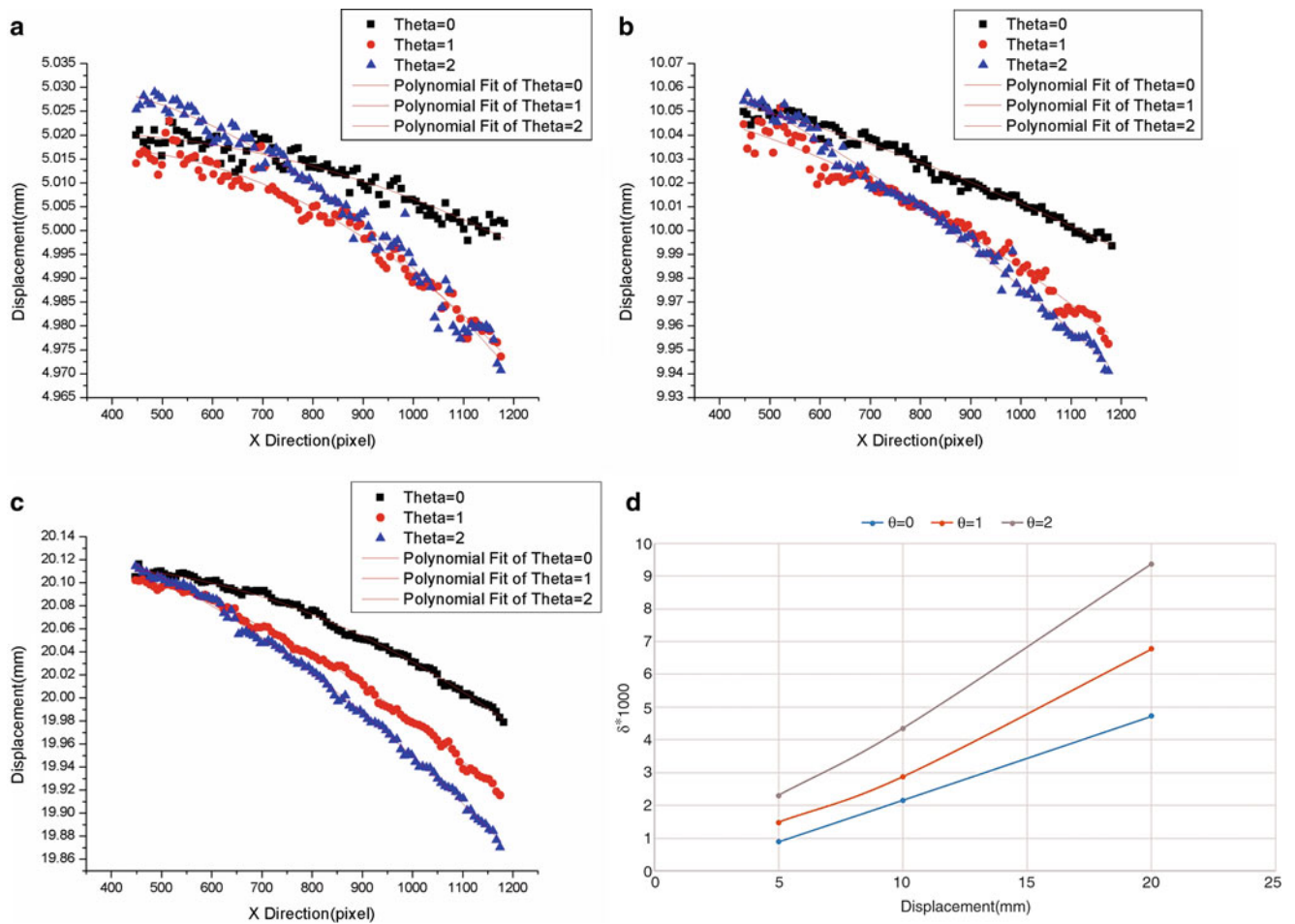
Fig. 16.5 Comparing the difference between the nominal in-plane displacements with 2D-DIC determined ones which are evaluated by using images obtained from different rotation angles. (**a**) Calculated displacement field for nominal displacement +5 mm. (**b**) Calculated displacement field for nominal displacement +10 mm. (**c**) Calculated displacement field for nominal displacement +20 mm. (**d**) Difference between the calculated averaged displacement to the nominal displacement

Table 16.1 The pseudo strain obtained from 2D DIC

Nominal displacement		+5 mm			+10 mm			+20 mm		
Pseudo strain		ε_{xx}	ε_{yy}	ε_{xy}	ε_{xx}	ε_{yy}	ε_{xy}	ε_{xx}	ε_{yy}	ε_{xy}
Rotation angles	0°	0.00059	0.00066	0.00043	0.00102	0.00063	0.00058	0.00193	0.00109	0.00077
	1°	0.00091	0.00061	0.00040	0.00163	0.00081	0.00054	0.00315	0.00155	0.00081
	2°	0.00126	0.00095	0.00047	0.00232	0.00138	0.00057	0.00442	0.00224	0.00079

16.3.2   3D DIC

As for 3D DIC, considering the test plate is mounted to a given position, therefore, in principle there should be U-displacement available, and the test object should be stress-free because of no external force acts on. Again, for convenience, the averaged displacement is determined by the following equation are given in Table 16.2.
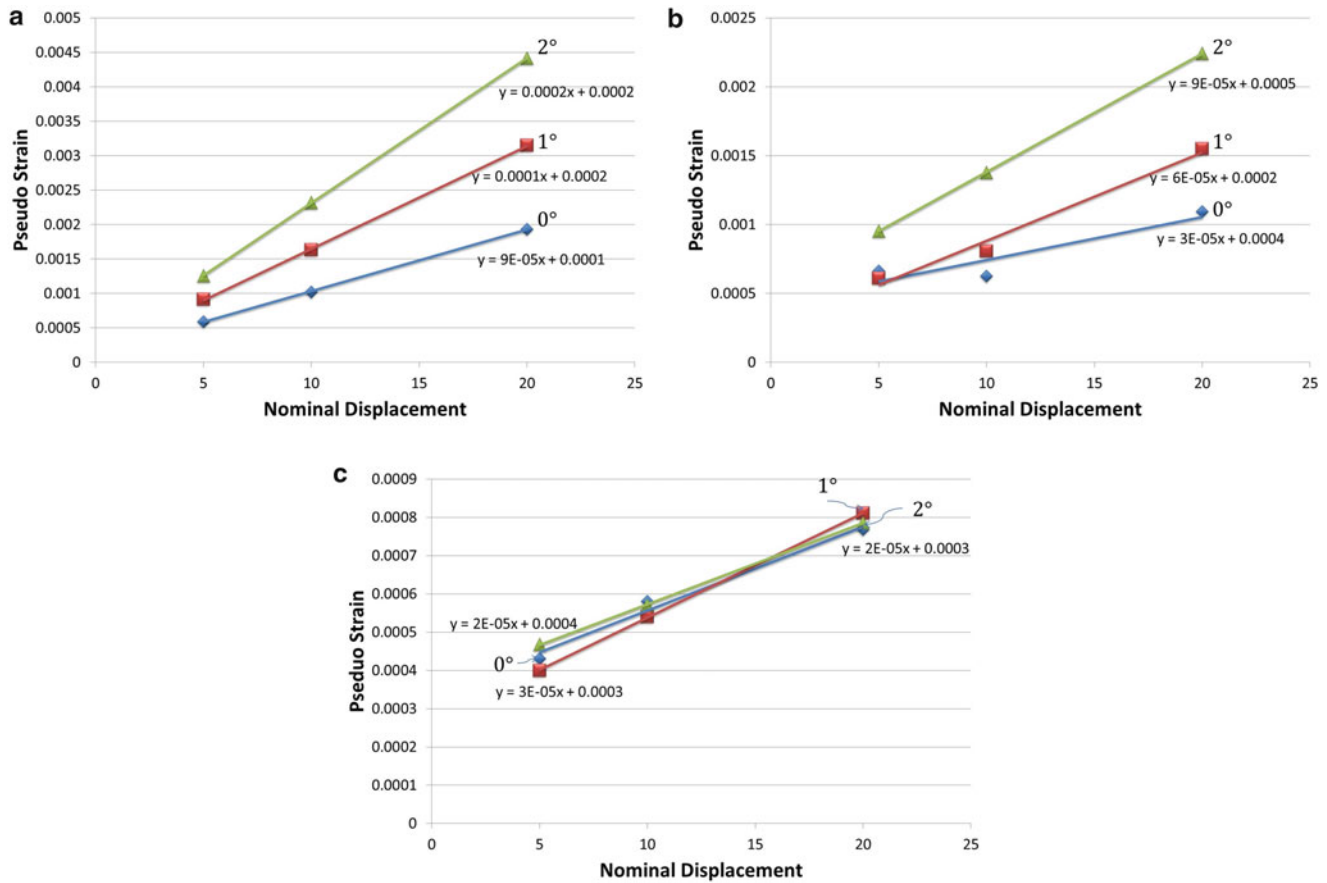
Fig. 16.6 The pseudo strain-nominal displacement relations. (**a**) Pseudo strain ε_{xx}. (**b**) Pseudo strain ε_{yy}. (**c**) Pseudo strain ε_{xy}

Table 16.2 The displacement obtained from 3D DIC

Nominal displacement		+9 mm			+23.5 mm		
Averaged displacement		U	V	W	U	V	W
Rotation angles	0°	9.081	0.057	0.233	23.363	0.086	0.280
	1°	9.147	0.090	0.029	23.421	0.044	0.858
	2°	9.126	0.094	0.515	23.377	0.087	0.671

$$\text{Averaged Displacement, } U_i = \left[\sum_l^n \sum_k^m \frac{(U_i|kl)^2}{(m+n)} \right]^{1/2}$$

where $i = 1, 2, 3$ for coordinates, that is $(U_1, U_2, U_3) = (U, V, W)$, k and l are index of pixel along row and column, the maximum pixel numbers of row and column are m and n. The averaged displacements determined by 3D DIC show that as the rotation angle is 0°, the difference between the averaged U displacement and the nominal U displacement is minimum where the nominal displacement is +9 mm; as for +23.5 mm, the minimum U-displacement departure occurs at rotation angle is 1°, for both case, the V displacements are also minimum compared with others. However, the W displacements in both cases are relative large. Figure 16.7 shows the difference U displacements between the nominal and the 3D-DIC determined. For U = +9 mm case, the displacement span increased as the rotation angle increased, different from 2D DIC results, only when rotation angles at 0° and 2°, the maximum displacements are almost the same. As for U = +23.5 mm, as shown in Fig. 16.7b, the U displacement is decreasing from left-upper corner to bottom right corner when the rotation angles are 0° and 1°, but the displacement is increasing from left-upper corner to bottom right corner at 2° rotation angle. The results indicate that the pointing issues have to consider all three displacement vectors. Again, from Fig. 16.7c, the error-nominal
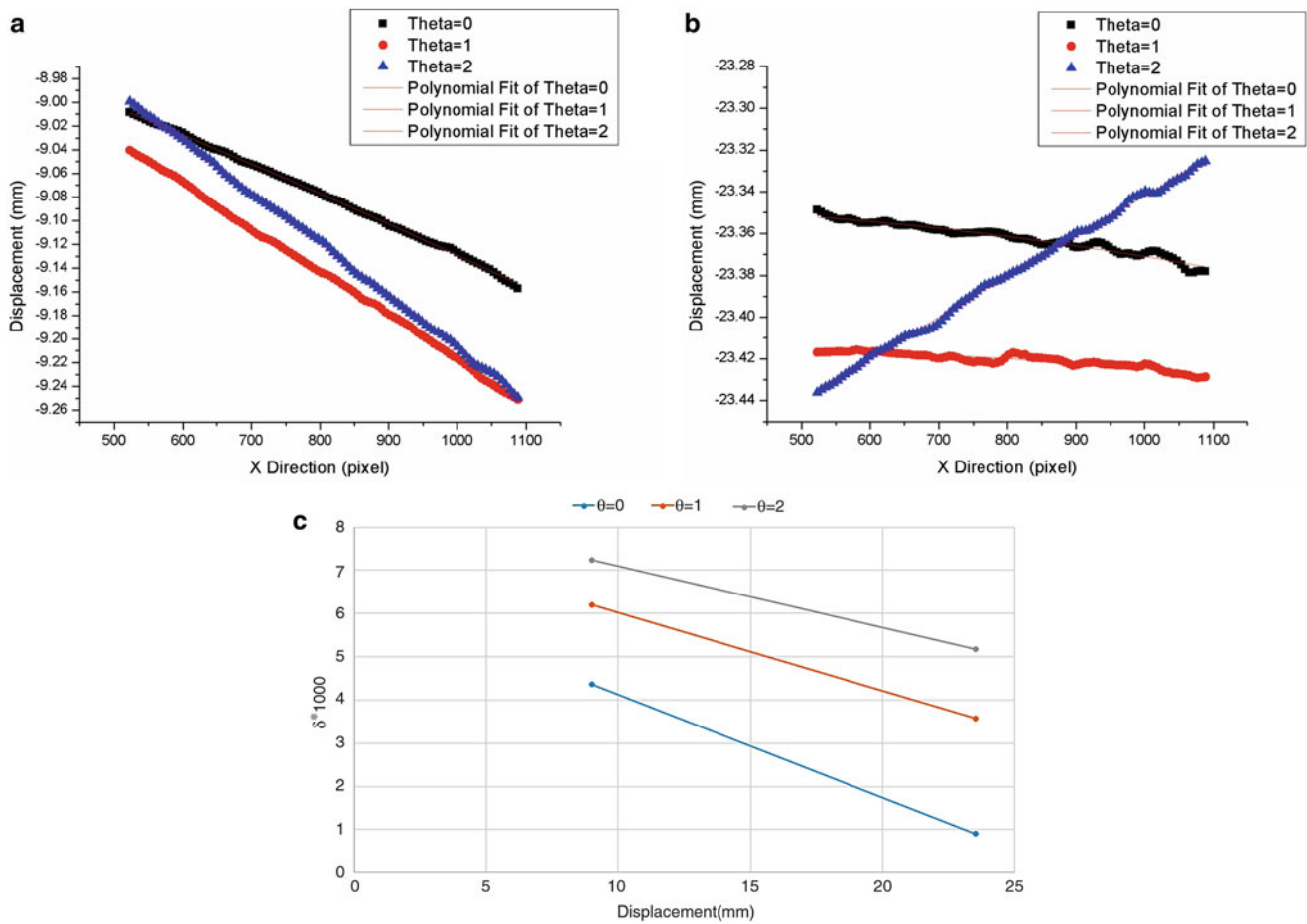
Fig. 16.7 Comparing the U displacement difference between the nominal displacements and 3D-DIC determined. (**a**) Calculated displacement field for nominal displacement +9 mm. (**b**) Calculated displacement field for nominal displacement +23.5 mm. (**c**) Difference between the calculated averaged displacement to the nominal displacement

Table 16.3 The pseudo strain obtained from 3D DIC

Nominal displacement		+9 mm			+23.5 mm		
Pseudo strain		ε_{xx}	ε_{yy}	ε_{xy}	ε_{xx}	ε_{yy}	ε_{xy}
Rotation angles	0°	0.00029	0.00023	0.00027	0.00039	0.00029	0.00020
	1°	0.00022	0.00020	0.00021	0.00036	0.00026	0.00018
	2°	0.00024	0.00021	0.00024	0.00038	0.00024	0.00026

displacement plot shows the U displacement errors are decreased with the nominal displacement increased, the results are different from 2D DIC.

As for the pseudo strain, as shown in Table 16.3, the values are much more stable with respect to 2D DIC. For U = +9 mm, the pseudo strain is about 0.00025, and the pseudo strain increasing to 0.00037 for ε_{xx}, and there are no significant changes for ε_{yy} and ε_{xy}.

16.4 Conclusions

In this paper, the pointing knowledge issues are studied by rotating the camera and camera pair to generate additional pointing errors to understand how poor pointing knowledge would affect the measurement results. From this study, the results show that, for 2D DIC, the error is increased if the initial pointing angle is increased. As for 3D DIC, the pseudo

strains are relative stable. But there is no specific rule can be established for the nominal displacement and averaged displacement at different rotation angles. More detail studies are needed to fully understand the pointing effect on DIC measurement.

References

1. Hwang, C.-H., et al.: Displacement measurement by DIC method with cameras of different formats. Advancement of Optical Methods in Experimental Mechanics, vol. 3. Springer International Publishing, Cham, pp. 95–101 (2016)
2. Vic-2D Testing Guide, Correlated Solutions (2007)

Chapter 17
Analysis of Dynamic Bending Using DIC and Virtual Fields Method

Behrad Koohbor, Addis Kidane, Michael A. Sutton, and Xing Zhao

Abstract The present work is aimed to analyze the dynamic bending response of a copper specimen. The specimen is impacted in a three point bending configuration using a Hopkinson bar apparatus. The impact force is measured by the use of two piezoelectric load-cells located behind the supports of the three point bending fixture. Dynamic deformation response of the specimen is studied and analyzed through the use of ultra-high speed photography in conjunction with digital image correlation. To do this, an ultra-high speed HPV-X camera is utilized to capture images of the specimen during deformation time at a frame rate of 10^6 frames per second. Full-field distributions of in-plane displacement and strain components are studied and used to calculate the strain rate and acceleration distributions in the specimen. An analytical approach based on the Virtual Fields Method (VFM) is then implemented which allows for the calculation of inertia forces developed in the specimen. In addition, the method of virtual fields is used in this work to identify the rate-dependent constitutive response of the material at plastic deformation regime.

Keywords Digital image correlation • Hopkinson bar • Ultra-high speed camera • Virtual fields method • Dynamic bending

17.1 Introduction

Several mechanical testing procedures have been devised over the past century to enable the study and characterization of the mechanical behavior of materials at high strain rate loading conditions. Kolsky or split Hopkinson pressure bar (SHPB) is one of the most common apparatuses in this area. However, there are certain limitations associated with the use of SHPB. Such limitations are basically the results of simplifying assumptions in extracting the dynamic constitutive response of the specimens tested in SHPB [1]. The most significant of these limitations are the restriction of the test procedure to uniaxial loading conditions, as well as the assumption of stress equilibrium within the specimen. The latter becomes even more important as the applied strain rates are increased and/or the dynamic response of a low impedance material is to be investigated [2–4]. In such cases, the accuracy of the results obtained from conventional test procedure may not be assured unless "inertia effects" are incorporated in the analysis [5]. Direct measurement of inertia force and its resultant stress has been extremely challenging, if not impossible, from an experimental standpoint. Hdowever, recent advances in the fields of high speed photography and full-field measurements have facilitated an accurate means for direct quantification of inertia effects in dynamic testing of materials [6–9].

In light of this, the present work aims to employ the recently developed ultra-high speed HPV-X camera to study the full-field deformation response during central impact of a three-point bend copper specimen. The impact tests were carried out in a Hopkinson apparatus, modified for dynamic bending experiments. The intention in the present study has been to extend the work of Pierron et al. [9], conducted on aluminum bars subjected to dynamic bending within the elastic regime, by pushing the measurements range further into the plastic regime. In an effort to highlight the significance of ultra-high speed imaging coupled with full-field measurements, an analysis based on the Virtual Fields Method (VFM) has been conducted to identify the visco-plastic constitutive response of the copper specimen within the range of strain and strain rate applied.

B. Koohbor (✉) • A. Kidane • M.A. Sutton • X. Zhao

Department of Mechanical Engineering, University of South Carolina, 300 Main Street, Columbia, SC 29208, USA

e-mail: koohbor@email.sc.edu

17.2   Experimental

Figure 17.1 illustrates the experimental setup used in this work. A custom made three-point bend fixture mounted in a Hopkinson bar apparatus was used to perform dynamic bending experiments. The fixture and the input bar were made from high strength 7075 aluminum alloy. The impactor side of the bar, as shown in Fig. 17.1b, was machined into a U-shaped configuration and was placed against the beam specimen prior to the test. A projectile fired by an air gun was utilized to impact the input bar. The velocity of the projectile upon impact to the input bar was ~28 m/s. A strain gage located 1575 mm away from the tip of the impact bar was used to provide an off-set trigger to the oscilloscope, strobe and the camera. The triggering delay time was calculated as 309 µs using the one-dimensional elastic wave speed in the input bar material (c_{Al} = 5091 m/s). To measure the reaction force history, two piezoelectric load-cells were inserted behind the supports of the three-point bend fixture (see Fig. 17.1b). The load data was recorded at a rate of 5 MHz by the same oscilloscope used with the strain gauge.

The specimen tested here was a 10 mm thick copper 110 alloy with 80×6 mm^2 (L × W) side dimensions, extracted from the as-received stock. Figure 17.2 illustrates a schematic view of the specimen configuration in the three-point bend fixture. Quasi-static stress-strain response of the as-received material was evaluated in-house at room temperature and at a 5×10^{-4} s^{-1} mean strain rate. Quasi-static experimental flow curve of the specimen was fitted with a Hollomon power-law equation as $\bar{\sigma} = 344\bar{\varepsilon}^{0.078}$.
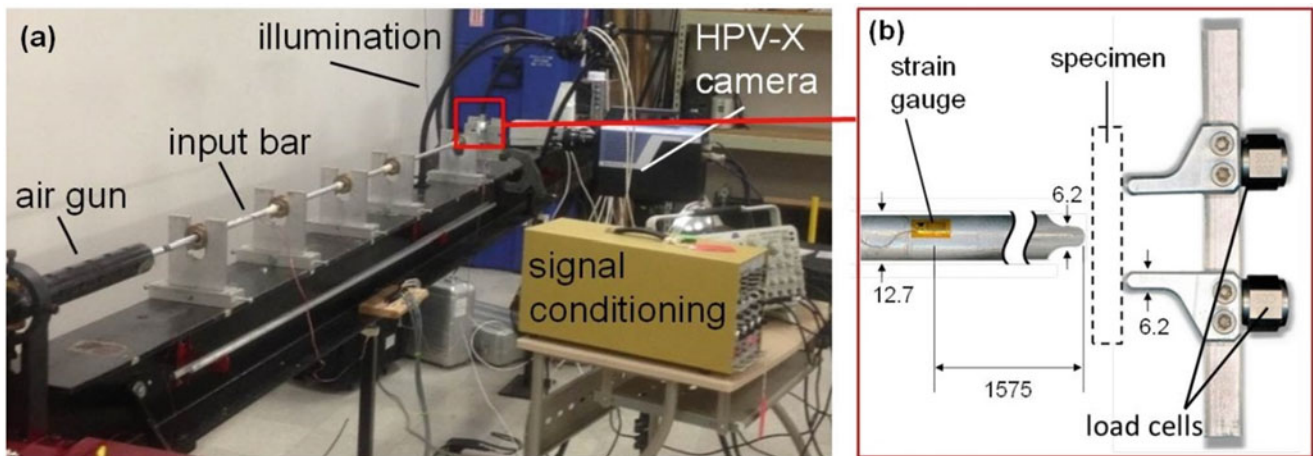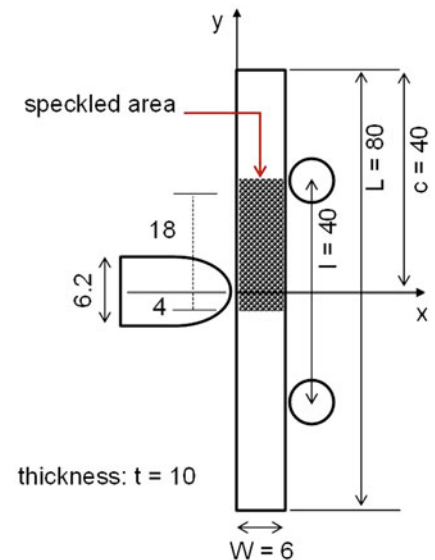

Fig. 17.1 (**a**) Experimental setup used in dynamic bending tests and (**b**) three-point bending fixture

Fig. 17.2 Schematic of the test specimen configuration in the three-point bend fixture. Dimensions in mm

17.3 Ultra-High Speed Imaging and DIC

A single Shimadzu Hyper Vision HPV-X ultra-high speed camera was used to capture images of the specimen during deformation time. The utilized camera is capable of capturing 128 frames at a full-field resolution of 400×250 pixel^2 and at frame rates up to 10×10^6 fps. A framing rate of 1×10^6 fps was used in this work, allowing for the record of 128 μs duration after the impact. External illumination containing a flash unit and high intensity white LED light source was used.

Image correlation was conducted in the software Vic-2D (Correlated Solutions, Inc.). Full-field in-plane displacement and strain distributions were computed in this software using 23×23 pixel^2 subset and 6 pixel step size between the subset centers. The spatial resolution of the displacement was measured as 90 μm/pixel. Image correlation was performed using the 'normalized squared differences' matching criterion, with an optimum 4-tap interpolation and affine shape functions. Temporal derivatives—strain rate and acceleration—were computed from the full-field displacement and strain output by applying a central difference scheme as:

$$a_i(t) = \frac{u_i(t + \Delta t) - 2u_i(t) + u_i(t - \Delta t)}{\Delta t^2} \tag{17.1}$$

$$\dot{\varepsilon}_{ij}(t) = \frac{\varepsilon_{ij}(t + \Delta t) - \varepsilon_{ij}(t - \Delta t)}{2\Delta t} \tag{17.2}$$

where u_i and a_i are the in-plane components of the displacement and acceleration, respectively. ε_{ij} and $\dot{\varepsilon}_{ij}$ represent in-plane strain and strain rate components, and Δt is the interframe time ($=1$ μs). Temporal smoothing was performed using second-order polynomial applied over 7 μs time span.

17.4 Full-Field Displacement and Strain

In-plane displacement fields computed over the area of interest are illustrated in Fig. 17.3. Displacement maps in Fig. 17.3 exhibit patterns that are characteristic of three-point bending experiments. Figure 17.4 illustrates the distribution of in-plane strain components over the entire area of interest. For all in-plane strain components, a region of localized strain is identified
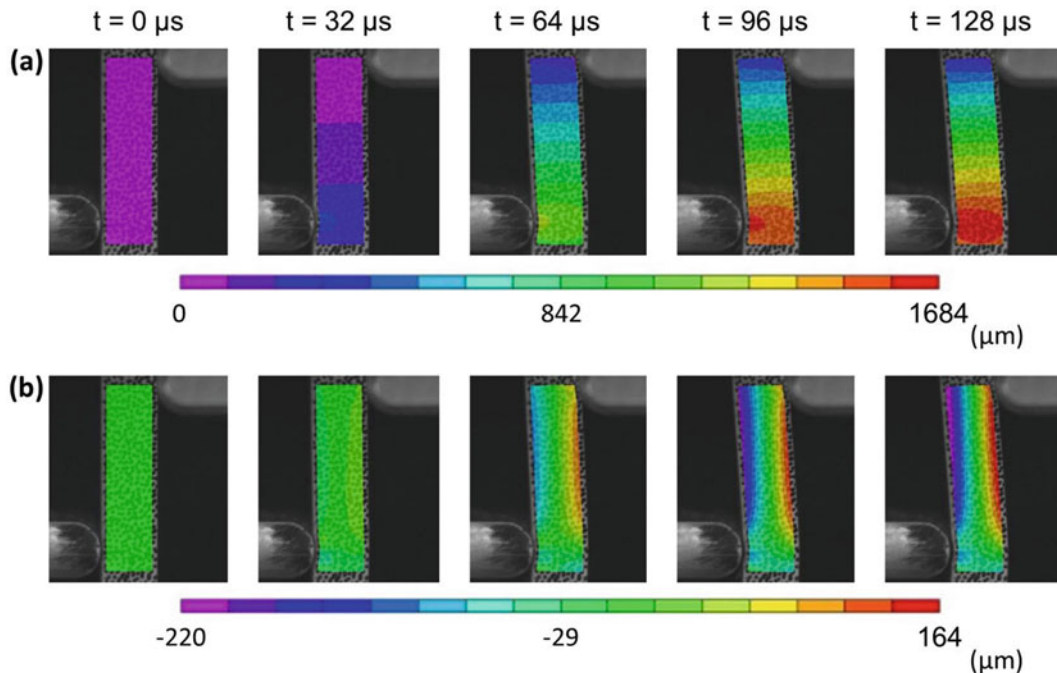

Fig. 17.3 Full-field (**a**) horizontal, u, and (**b**) vertical, v, displacement distributions in the bar
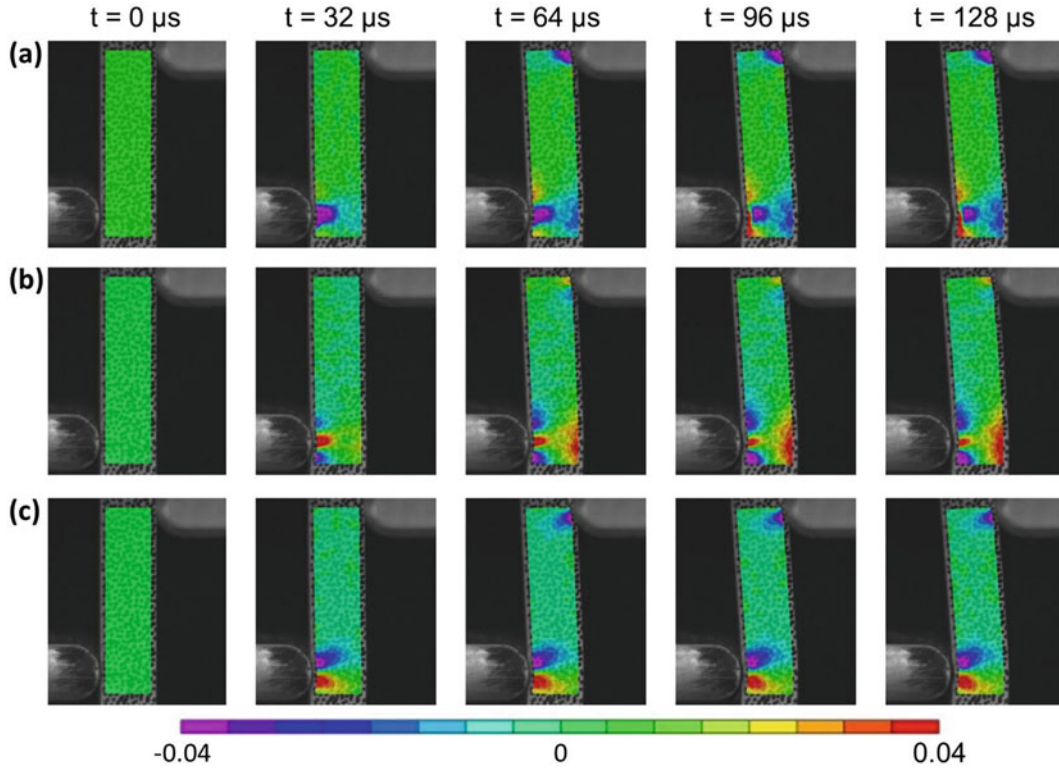
Fig. 17.4 Distribution of (**a**) ε_{xx}, (**b**) ε_{yy} and (**c**) ε_{xy} over the area of interest

in the vicinity of the impact area. Also, strain magnitudes of up to 4 % are developed in the impact region vicinity, confirming the occurrence of plastic deformation in the bar. ε_{yy} contour maps represent the bending strain with negative (compressive) and positive (tensile) values on the impacted and free faces of the bar, respectively. Figure 17.4c exhibits a typical distribution of shear strain in three-point bending, having a symmetric pattern about the projected line of impact [9].

Equivalent strain, ε_{eq}, and strain rate, $\dot{\varepsilon}_{eq}$, can be determined in the bar, using the full-field strain data and Eq. (17.3), as:

$$\varepsilon_{eq}(x,y,t) = \left[\frac{2}{3}\left(\varepsilon_{xx}(x,y,t)^2 + \varepsilon_{yy}(x,y,t)^2\right) + \frac{4}{3}\varepsilon_{xy}(x,y,t)^2\right]^{1/2} \tag{17.3a}$$

$$\dot{\varepsilon}_{eq}(x,y,t) = \left[\frac{2}{3}\left(\dot{\varepsilon}_{xx}(x,y,t)^2 + \dot{\varepsilon}_{yy}(x,y,t)^2\right) + \frac{4}{3}\dot{\varepsilon}_{xy}(x,y,t)^2\right]^{1/2} \tag{17.3b}$$

Figure 17.5 shows the variations of Equivalent strain and strain rate averaged over a 4×5.5 mm^2 area at the vicinity of the impact point. Equivalent strain shows a progressive increase during a ~70 μs period after the impact and remains constant afterwards. The unchanged magnitude of Equivalent strain is attributed to the loss of contact between the impactor and the specimen after $t = 70$ μs.

Equivalent strain rate curve shows significant oscillations during the first 30 μs after the impact, and becomes relatively constant with an average value of 250 s^{-1} after $t = 30$ μs. The large oscillations observed in strain rate in the early stages of impact may be due to the transient stress state during the first 30 μs.

17.5   Viscoplastic Constitutive Parameter Identification

An analytical solution based on the Virtual Fields Method (VFM) was implemented to identify the viscoplastic constitutive response of the copper specimen in this work. For this purpose, the analytical study of dynamic bending conducted previously by Pierron et al. [9] was adopted here. Neglecting the influence of volumetric forces, the principle of virtual work can be expressed as:
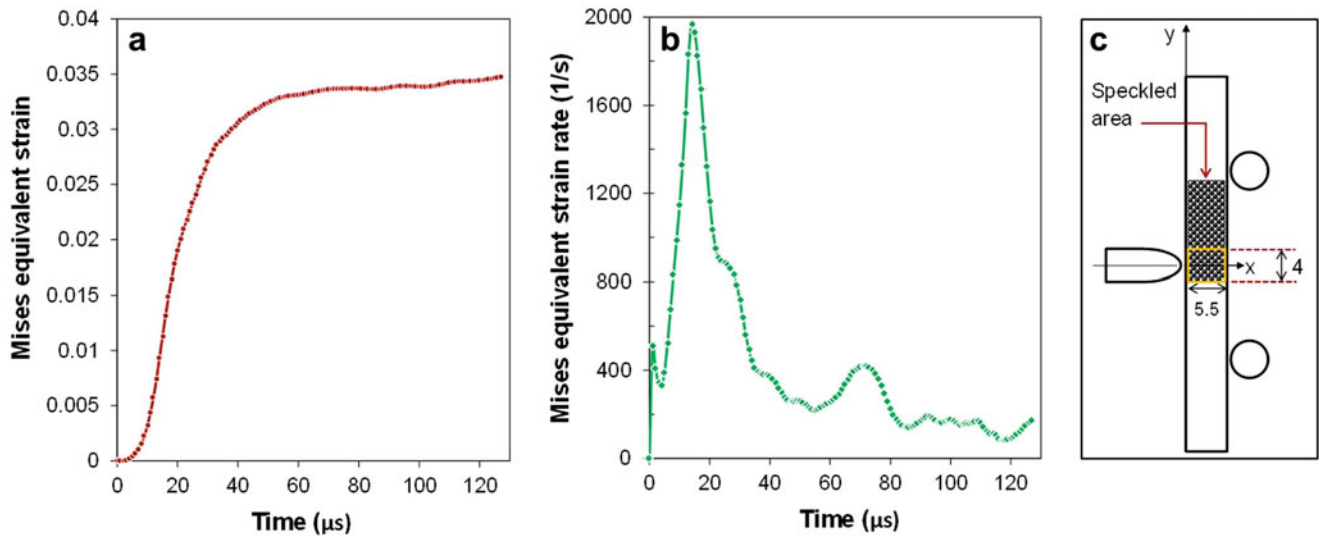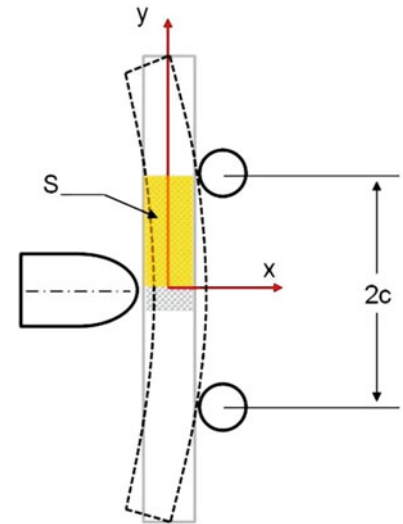
Fig. 17.5 Variation of average (**a**) Equivalent strain and (**b**) Equivalent strain rate over a 4×5 mm^2 area marked in (**c**)

Fig. 17.6 Schematic of the virtual field used for constitutive model identification

$$-\int_V \underline{\underline{\sigma}} : \underline{\underline{\varepsilon}}^* dV + \int_{S_f} \underline{T} \cdot \underline{u}^* dS = \int_V \rho \underline{a} \cdot \underline{u}^* dV \tag{17.4}$$

where $\underline{\underline{\sigma}}$ and $\underline{\underline{\varepsilon}}^*$ are stress and virtual strain tensors, respectively. $\underline{T}$ denotes the traction vector acting on S_f; $\underline{u}$ is the virtual displacement. ρ is mass density, $\underline{a}$ is the acceleration vector and V represents volume. The principle of virtual work is valid for any arbitrary displacement and its resultant strain fields, as long as the fields are kinematically admissible. For the specific case of dynamic bending problem, Pierron et al. [9] have suggested a kinematically admissible virtual displacement and its resultant strain field expressed in Eq. (17.5), defined over an area of interest shown schematically in Fig. 17.6.

$$\begin{cases} u_x^* = \dfrac{1}{2}(c^2 - y^2) \\ u_y^* = xy \end{cases} \quad \begin{cases} \varepsilon_{xx}^* = 0 \\ \varepsilon_{yy}^* = x \\ \varepsilon_{xy}^* = 0 \end{cases} \tag{17.5}$$

Note that this is a Bernoulli-like bending virtual displacement with no virtual shear strain. Using the virtual strain fields detailed in Eq. (17.5), virtual equivalent strain can be determined as:

$$\varepsilon_{eq}^* = \sqrt{\frac{2}{3}}x \tag{17.6}$$

Assuming that the in-plane measurements conducted on the surface of the material remain valid through the thickness direction, the first integral on the left hand-side of Eq. (17.4) can be redefined using the definition of flow stress, $\overline{\sigma}$, and equivalent virtual strain, ε_{eq}^*, as:

$$-\int_V \underline{\underline{\sigma}} : \underline{\underline{\varepsilon}}^* dV = -t \int_S \overline{\sigma} \varepsilon_{eq}^* dS \tag{17.7}$$

with t being the specimen thickness. In this work, the rate sensitivity in the constitutive response of the material was incorporated using a simple power-law term as:

$$\overline{\sigma} = K \overline{\varepsilon}^n \left(\frac{\dot{\varepsilon}}{\dot{\varepsilon}^0} \right)^m \tag{17.8}$$

where parameters K and n were obtained at quasi-static conditions ($\dot{\varepsilon}^0 = 5 \times 10^{-4}\,\mathrm{s}^{-1}$) as 344 MPa and 0.078, respectively. Our goal here is to determine the rate sensitivity component m. Combining Eqs. (17.7) and (17.8), and replacing the integral form with a simple spatial averaging, the first term in Eq. (17.4) can be further simplified to:

$$-\int_V \underline{\underline{\sigma}} : \underline{\underline{\varepsilon}}^* dV = -\sqrt{\frac{2}{3}} tw^2 c \left[\overline{\left(K\overline{\varepsilon}^n \left(\frac{\dot{\varepsilon}}{\dot{\varepsilon}^0} \right)^m \right)} \right] \tag{17.9}$$

where the overline indicates the spatial averaging over area S indicated in Fig. 17.6. At the location of impact, i.e. $y = 0$, the only non-zero displacement component is $u_x^* = c^2/2$, which is multiplied by the impact force, F, to simplify the second term on the left-hand-side of Eq. (17.4) as $\frac{Fc^2}{2}$. The impact force in this work was measured by superimposing the reaction force recorded by the load-cells, with the average inertia force [9]. Figure 17.7 shows the reaction force history plotted against time.

The integral term on the right-hand-side of Eq. (17.4) represents the inertia term and can be simplified as [9]:

$$\int_V \rho \underline{a} \cdot \underline{u}^* dV = t\rho \left[\int_S \frac{1}{2} a_x (c^2 - y^2) dx\,dy + \int_S a_y xy\,dx\,dy \right] \tag{17.10}$$

This equation requires the determination of the in-plane horizontal, a_x, and vertical, a_y, acceleration component. However, the contribution of vertical acceleration component will be neglected here, since its value is one order of magnitude lower than that of the horizontal acceleration. Also, according to Pierron et al. [9] the first integral on the right hand-side of Eq. (17.10), containing a_x, can be further simplified by approximating the acceleration profile along y with a simple quadratic term as:

$$a_x \approx \frac{c^2 - y^2}{c^2} a_x^{\mathrm{max}} \tag{17.11}$$

where a_x^{max} is maximum acceleration along x at $y = 0$. Finally, by rearranging Eq. (17.4) and substituting the simplified terms, the final expression for the bending force can be written as:

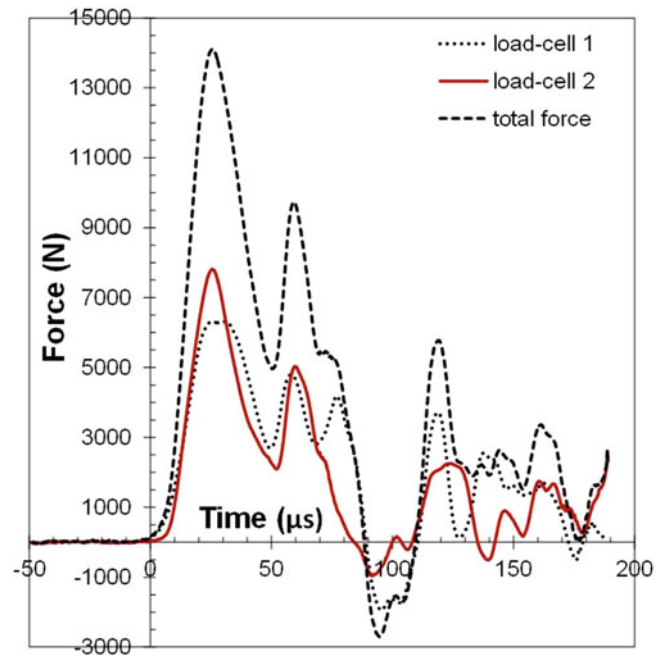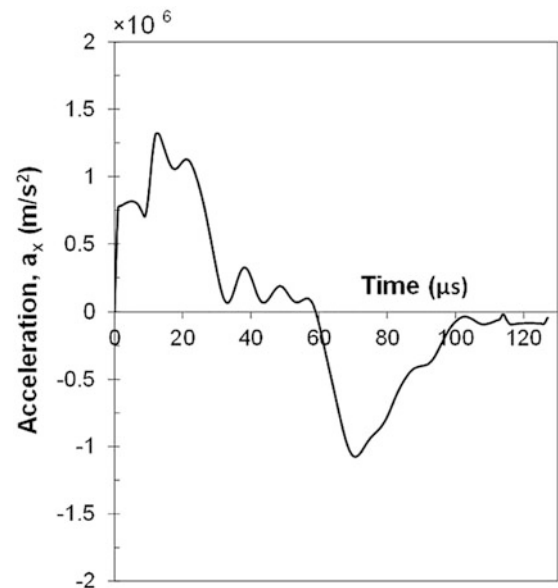**Fig. 17.7** Temporal variation of reaction force measured by the load-cells

Fig. 17.8 Temporal variation of a_x^{max}

$$F = F_i + F_d \tag{17.12a}$$

$$F_i = \frac{16}{15} twc\rho a_x^{max} \quad F_d = \sqrt{\frac{8}{3} \frac{tw^2}{c}} \left[\overline{\left(K\bar{\varepsilon}^n \left(\frac{\dot{\varepsilon}}{\dot{\varepsilon}^0} \right)^m \right)} \right] \tag{17.12b}$$

Equations (17.12a) and (17.12b) indicates that the impact force is consumed in accelerating the specimen, as well as deforming it. The inertia force, F_i, can be measured from the acceleration, as discussed earlier. Figure 17.8 shows the temporal variation of a_x^{max}. It is clearly seen that the acceleration curve follows a periodic pattern. Such periodic behavior can be explained through the bending wave traverse along the 80 mm length of the copper specimen. A more detailed discussion on the periodic patterns observed in the acceleration curves is presented in [9].

The only unknown parameter in Eqs. (17.12a) and (17.12b), i.e. m, can be determined following the procedure documented in [10]. The procedure is based on the construction of a cost function, Φ, the value of which depends on the parameter m. This cost function is expressed in Eq. (17.13), as the summation of the quadratic differences between $F - F_i$, i.e. the difference between the impact and inertia forces; and F_d, i.e. the deformation force.

$$\Phi(m) = \sum_{t=t_0}^{t_f} \left[F - \frac{16}{15} twc\rho a_x^{max} - \sqrt{\frac{8}{3}} \frac{tw^2}{c} \left[\overline{\left(K\overline{\varepsilon}^n \left(\frac{\dot{\varepsilon}}{\dot{\varepsilon}^0} \right)^m \right)} \right] \right]^2 \tag{17.13}$$

The lower (t_0) and (t_f) bounds of the summation in Eqs. (17.12a) and (17.12b) represent the time period during which the specimen undergoes plastic deformation. Accordingly, an optimized value of $m = 0.014$ was obtained for the copper specimen dynamically deformed at plastic strains <0.035 and the strain rates ranging from 400 to 1800 s^{-1}.

17.6 Summary

Ultra-high speed photography with full-field deformation measurements were used to analyze the dynamic bending response of a copper specimen in a three-point bending configuration. An ultra-high speed HPV-X camera was utilized to capture 128 images of the specimen during deformation time at a rate of 10^6 fps. Strain rate and acceleration fields were derived from the full-field displacement and strain data by simple numerical differentiations. Periodic patterns were observed for acceleration curves, indicating the significance of bending waves. In-plane strain, strain rate and acceleration fields were used as the input for a VFM-based analysis to determine the inertia loads. Experimentally-measured reaction forces were used along with the results obtained from the VFM analysis to investigate the viscoplastic constitutive response of the examined material.

References

1. Field, J.E., Walley, S.M., Proud, W.G., Goldrein, H.T., Siviour, C.R.: Review of experimental techniques for high rate deformation and shock studies. Int. J. Impact Eng. **30**, 725–775 (2004). doi:10.1016/j.ijimpeng.2004.03.005
2. Zhao, H.: Testing of polymeric foams at high and medium strain rates. Polym. Test. **16**, 507–516 (1997). doi:10.1016/S0142-9418(97)00012-3
3. Othman, R., Aloui, S., Poitou, A.: Identification of non-homogeneous stress fields in dynamic experiments with a non-parametric method. Polym. Test. **29**, 616–623 (2010). doi:10.1016/j.polymertesting.2010.03.013
4. Song, B., Chen, W.: Dynamic stress equilibrium in split Hopkinson pressure bar tests on soft materials. Exp. Mech. **44**, 300–312 (2004). doi:10.1007/BF02427897
5. Pierron, F., Zhu, H., Siviour, C.: Beyond Hokinson's bar. Philos. Trans. R. Soc. A **372**, 20130195 (2014). doi:10.1098/rsta.2013.0195
6. Koohbor, B., Kidane, A., Lu, W.Y., Sutton, M.A.: Investigation of the dynamic stress-strain response of compressible polymeric foam using a non-parametric analysis. Int. J. Impact Eng. **91**, 170–182 (2016). doi:10.1016/j.ijimpeng.2016.01.007
7. Pierron, F., Forquin, P.: Ultra-high-speed full-field deformation measurements on concrete spalling specimen and stiffness identification with the virtual fields method. Strain **48**, 388–405 (2012). doi:10.1111/j.1475-1305.2012.00835.x
8. Moulart, R., Pierron, F., Hallet, S.R., Wisnom, M.R.: Full-field measurement and identification of composites moduli at high strain rate with the virtual field method. Exp. Mech. **51**, 509–536 (2011). doi:10.1007/s11340-010-9433-4
9. Pierron, F., Sutton, M.A., Tiwari, V.: Ultra high speed DIC and virtual fields method analysis of a three point bending impact test on an aluminum bar. Exp. Mech. **51**, 537–563 (2011). doi:10.1007/s11340-010-9402-y
10. Le Louedec, G., Pierron, F., Sutton, M.A., Siviour, C., Reynolds, A.P.: Identification of dynamic properties of Al 5456 FSW welds using the virtual fields method. J. Dyn. Behav. Mater. **1**, 176–190 (2015). doi:10.1007/s40870-015-0014-6

Chapter 18
Elimination of Periodical Error for Bi-directional Displacement in Digital Image Correlation Method

Shuichi Arikawa, Manabu Murata, Satoru Yoneyama, Yasuhisa Fujimoto, and Yohei Omoto

Abstract A technique for eliminating the periodical systematic error in bi-directional displacements by a digital image correlation method is investigated. The technique is based on a periodical error elimination method for single directional displacements which has been developed by the authors. In this technique, rotated and multiple translated images for the horizontal and the vertical directions are captured before a deformation. Translation amounts are determined from the rotation and the translated images. After the deformation, a single image is captured. The periodical error is eliminated using a calculation based on the translation amounts and the measured multiple displacements from the single deformed state image with the initial translated images. The elimination is applied to a thermal deformation measurement. As a result, periodical errors for bi-directional displacements can be eliminated. Therefore, it is expected that accurate in-plane displacements and strain components can be obtained using the proposed technique.

Keywords Deformation measurement • Digital image correlation • Displacement • Error

18.1 Introduction

Recently, digital image correlation method (DIC) [1] is widely used in various fields. Since DIC is an image-based measurement technique, measurements in various scales are possible, such as a bridge diffraction measurement [2] and a micro-scale measurement in a scanning electron microscope [3]. Additionally, the measurement error level has been much reduced by improving the calculation process in DIC [4–6].

In DIC measurement, a window called subset is set on an initial state image and the displacement is calculated by searching a matched pattern with the initial subset in a deformed state image. Then a subpixel calculation by an interpolation in a region between adjacent pixels is performed for obtaining high accurate displacements. The displacement calculation accuracy has been improved by investigating the image correlation coefficient and the interpolation for the subpixel calculation. In the beginning of the research in DIC, a periodical systematic error occurred using bi-linear interpolation for the subpixel calculation. Recently, improving measurement accuracy and reducing the periodical error have been achieved by applying high-order polynomial interpolations or spline interpolations. Incidentally, the measurement accuracy in DIC is increased by an enlargement of subset size, and it leads to the decreased spatial resolution. With the improvement in the measurement accuracy as described above, the spatial resolution has been improved more than before. However, further improvement of the spatial resolution is very important for measuring complicated deformation fields in detail.

In displacement field measurements by DIC, it is inappropriate to assume the spatial resolution as the subset size. Spatial resolutions in general measurements depend on regions for obtaining physical information. Therefore, not only the subset and also the region for the subpixel interpolation should be considered for deciding the spatial resolutions. The area for the interpolation is 2×2 pixels for bi-linear interpolation, 4×4 pixels for bi-cubic interpolation, and so on. Hence, the area size increases with increasing degree of functions. Such subpixel interpolations using high-order functions can improve the measurement accuracy by an effective utilization of large area data. On the other hand, the authors have developed a method

---

S. Arikawa (✉)
Department of Mechanical Engineering Informatics, Meiji University, 1-1-1 Higashimita, Tama-ku, Kawasaki, Kanagawa 214-8571, Japan
e-mail: arikawa@meiji.ac.jp

M. Murata • S. Yoneyama
Department of Mechanical Engineering, Aoyama Gakuin University, 5-10-1 Fuchinobe, Chuo-ku, Sagamihara, Kanagawa 252-5258, Japan

Y. Fujimoto • Y. Omoto
Mitsubishi Electric Corporation Advanced Technology Research and Development Center, 8-1-1 Tsukaguchi-honmachi, Amagasaki, Hyogo 661-8661, Japan

for improving the measurement accuracy by increasing data amount in small areas [7]. In this method, bi-linear interpolation is used for the subpixel calculation, and the generated periodical systematic error in calculated displacements is eliminated using multiple images captured with physical subpixel-translations. However, the method has been applied for single directional measurements such as a horizontal or a vertical direction. It is expected that improving the error elimination method will contribute for improving the spatial resolution in DIC measurements. For this reason, we propose a technique for bi-directional displacement measurement using the error elimination method, and investigate the measurement accuracy of the measurement result.

18.2 Periodical Error Elimination

Figure 18.1 shows a schematic figure of a relationship between the measured and actual displacement at a single point using bi-linear interpolation for the subpixel calculation in DIC. The measured value fluctuates periodically around the ideal value. The error profile is periodical to multiple of a single pixel, and becomes zero at the actual values of 0, 0.5 and 1. The line of measured value has three linear sections with two different slopes, however a practical measured value shows a curved line with the similar behavior. The principle of the periodical error elimination method is described as follows. In this figure, there are four points shown as P_0 to P_3 on the center long linear section. P_0 is a displacement point where an actual displacement is determined. Points of P_0 to P_3 are obtained by subpixel translations with known amounts. The translations mean physical translations of the relative position of a digital camera and an object. The gradient of the line along the points can be then obtained using the translation amounts and the measured displacements. Additionally, since the error becomes zero at the displacement of 0.5 pixel, a linear function equation can be determined, and the actual displacement can be then found using the measured displacement of P_0 and the equation. To obtain the actual displacement distribution, the error elimination process is carried out for all points in the measurement region.

In this method, highly accurate translation amounts should be obtained. If the camera or the object is translated and the translation amount is measured by a displacement sensor, the translation amount is obtained. However, the change of relative position does not match with the measured value because of effects of environmental disturbances in experimental conditions. So, the authors have developed a technique for obtaining highly accurate translation amounts using an in-plane rotation. When a displacement distribution of an in-plane rigid-body rotation around a center of an image is measured, the periodical error distribution shows a symmetrical profile. If the rotation does not include a translation, the average value of the displacements becomes zero. If the rotation includes some translation amount, the average value is equal to the translation amount. A schematic figure of the practical process is shown in Fig. 18.2. Firstly, a single image, image BR, is captured before the rotation, and multiple translated images, image 0 to image n, are captured after the rotation. Secondly, displacements with and without translations, u^*_{0R} to u^*_{nR}, are obtained by DIC using image BR and image 0 to image n. Finally, the translation amounts can be obtained by subtractions of each displacement field.

Fig. 18.1 Schematic figure of relationship between actual and measured displacements with image translation
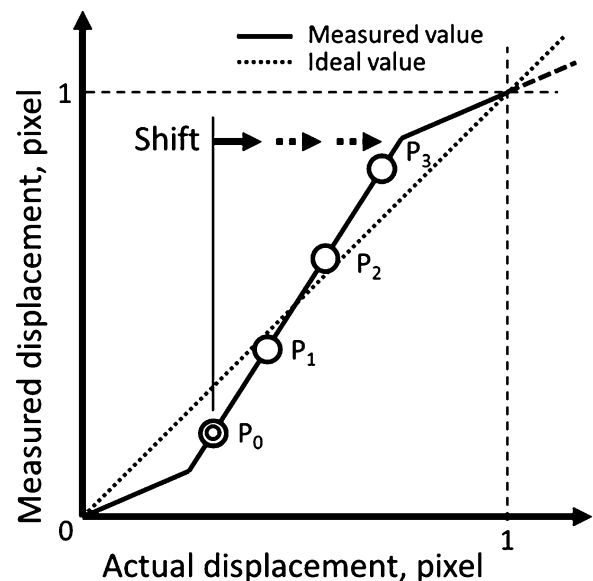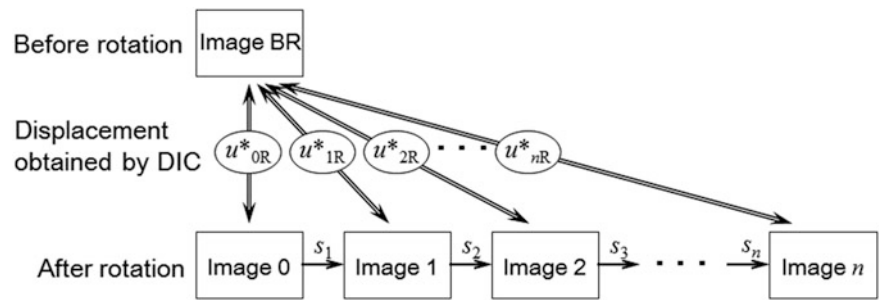
Fig. 18.2 Schematic figure of translation amounts with rotated and translated images

For applying the method to deformation measurements, deformation images of each stage are captured continuously, after image recording of the initial and the rotation images. Then, the direction of the translations should be the same with the direction of the displacement for the error elimination. Hence, for applying the method to bi-directional displacement measurement, multiple images with translations along the horizontal and the vertical direction should be captured after the rotation. Each deformation stage images are then recorded after capturing these images. The error elimination for the bi-directional displacement of the deformation measurement is possible using images recorded by the process.

18.3 Experiment

In this study, a rigid-body rotation and a thermal deformation measurement are performed to evaluate the effectiveness of the proposed technique in cases with and without deformation. A 5 mm thick aluminum plate is used for the rotation measurement and a 3 mm thick copper plate is used for the thermal deformation measurement. Random patterns are set on the specimen surfaces by a white and black paint. A digital camera used in this study has a 2048×2048 pixels image resolution and a gray 8 bit color depth. The camera is attached on a stage including a rotation and a bi-directional translation stage. In both measurements, firstly, a single image of an initial state is captured, secondly, ten translation images for the horizontal and vertical direction are captured after a rotation of $0.230°$ in anti-clockwise. After that, the rotation or the thermal deformation states are recorded. The given angle for the rotation measurement is set to $0.460°$ in anti-clockwise. The temperature change for the thermal deformation measurement is set to 170 K using a heat-chamber. In calculation of the correlation coefficient in DIC, the subset size is set to 41×41 pixels, the deformation of the subset shape is considered, and bi-linear interpolation is used for the subpixel calculation.

18.4 Results and Discussion

Figures 18.3a, b show horizontal and vertical displacement distributions of the in-plane rotation measurement. In addition, Fig. 18.3c, d shows corrected displacements for each direction. In these contour maps, differences in before and after the correction are not distinguished by the naked eye. To investigate the measurement accuracy, errors in each displacement field are evaluated. Since plane approximations by least squares method for each displacement field are assumed to be the ideal values, errors are then calculated by subtractions of the ideal and the measurement results. The resulting error maps are shown in Fig. 18.4a–d. Periodical errors are clearly observed in error maps of displacements without the correction as shown in Fig. 18.4a, b. In contrast, the periodical errors are eliminated for each direction in corrected displacements as shown in Fig. 18.4c, d. Therefore, the proposed technique is effective.

Figures 18.5a, d show displacement distributions of the thermal deformation. Displacement maps for each direction without the correction are shown as Fig. 18.5a, b, and displacements with the correction are shown as Fig. 18.5c, d. Differences in displacements with and without the correction cannot be distinguished by the naked eye as the rotation measurement results. The thermal deformation can be assumed to be a constant strain distribution, because the copper plate specimen is a homogeneous material. So, errors of the measurement results are evaluated by a subtraction of a plane-approximation for each displacement field and of each measured displacement field. Obtained error maps are shown in Fig. 18.6a–d. Typical periodical errors are observed in displacement maps without the correction as shown in Fig. 18.6a, b.
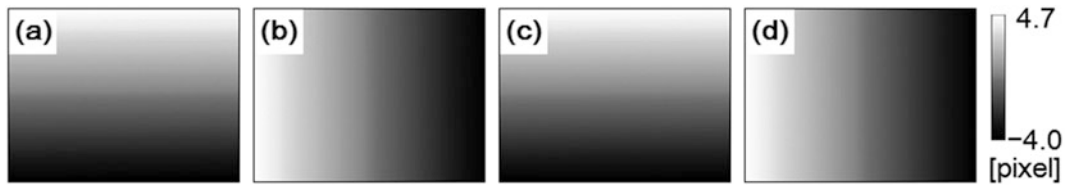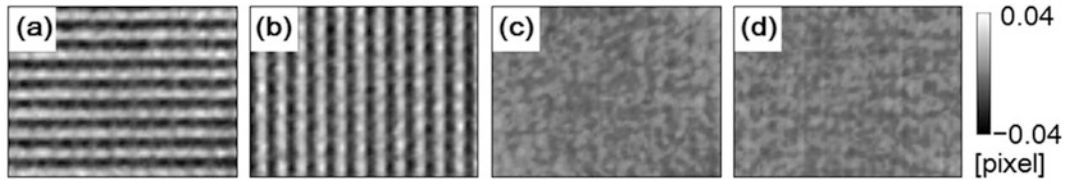
Fig. 18.3 Displacement maps of in-plane rotation measurement; (**a**) horizontal displacement, (**b**) vertical displacement, (**c**) corrected horizontal displacement and (**d**) corrected vertical displacement
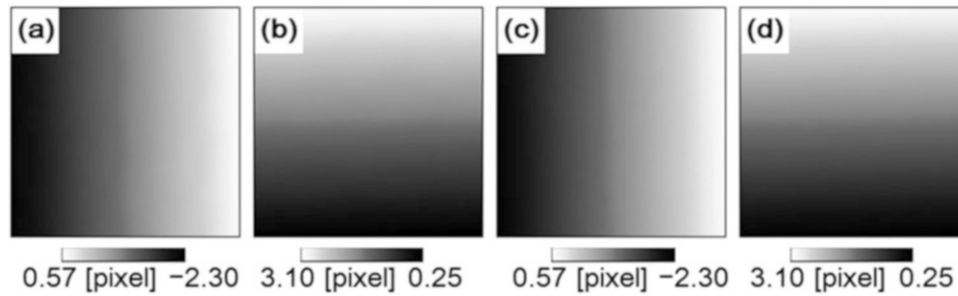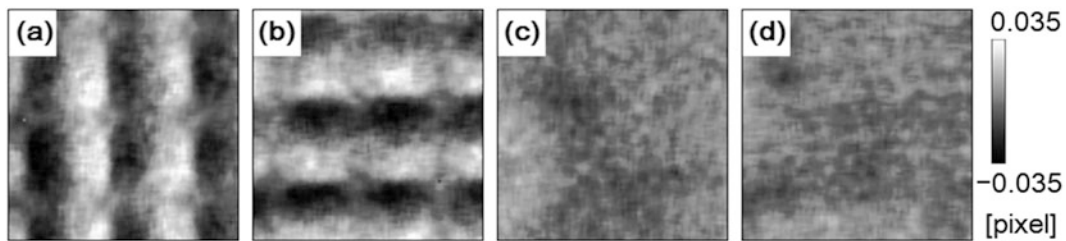

Fig. 18.4 Error maps of in-plane rotation measurement; (**a**) horizontal displacement, (**b**) vertical displacement, (**c**) corrected horizontal displacement and (**d**) corrected vertical displacement

Fig. 18.5 Displacement maps of thermal deformation measurement; (**a**) horizontal displacement, (**b**) vertical displacement, (**c**) corrected horizontal displacement and (**d**) corrected vertical displacement

Fig. 18.6 Error maps of thermal deformation measurement; (**a**) horizontal displacement, (**b**) vertical displacement, (**c**) corrected horizontal displacement and (**d**) corrected vertical displacement

In contrast, the periodical errors are eliminated for each direction in the corrected displacements as shown in Fig. 18.6c, d. According to above results, the accuracy of the bi-directional displacement measurements is greatly improved by the proposed technique whether the displacement includes a deformation or not. Thus, the effectiveness of the technique is verified. It is expected that the concept of this error elimination will contribute to improve spatial resolution in DIC measurement by enhancements of the proposed method such as a reduction of the subset area size.

18.5   Conclusion

In this study, we propose a technique for applying the periodical error elimination method for a bi-directional displacement measurement, and its effectiveness is evaluated by experiments. As a result, the periodical errors can be removed and good displacement distributions are obtained in both conditions for the displacement field with and without deformation. Additionally, it is expected that the error elimination will contribute to improve spatial resolution in DIC measurement by enhancing the method.

References

1. Sutton, M.A., Wolters, W.J., Peters, W.H., Ranson, W.H., McNeill, S.R.: Determination of displacements using an improved digital correlation method. Image Vis. Comput. **1**(3), 133–139 (1983)
2. Yoneyama, S., Ueda, H.: Bridge deflection measurement using digital image correlation with camera movement correction. Mater. Trans. **53**(2), 285–290 (2012)
3. Maschmann, M.R., Ehlert, G.J., Park, S.J., Mollenhauer, D., Maruyama, B., Hart, A.J., Baur, J.W.: Visualizing strain evolution and coordinated buckling within CNT arrays by in situ digital image correlation. Adv. Funct. Mater. **22**(22), 4686–4695 (2012)
4. Schreier, H.W., Braasch, J.R., Sutton, M.A.: Systematic errors in digital image correlation caused by intensity interpolation. Opt. Eng. **39**(11), 2915–2921 (2000)
5. Schreier, H.W., Sutton, M.A.: Systematic errors in digital image correlation due to undermatched subset shape functions. Exp. Mech. **42**(3), 303–310 (2002)
6. Pan, B.: Bias error reduction of digital image correlation using Gaussian pre-filtering. Opt. Lasers Eng. **51**, 1161–1167 (2013)
7. Arikawa, S., Yoshida, R., Yoneyama, S., Fujimoto, Y., Omoto, Y.: A method for eliminating periodical error for highly accurate measurement in digital image correlation. In: Proceedings of International Conference on Advanced Technology in Experimental Mechanics 2015, p. 1 (2015)

Chapter 19
The Cluster Approach Applied to Multi-Camera 3D DIC System

Thorsten Siebert, Karsten Splitthof, and Marek Lomnitz

Abstract In material testing optical techniques take more and more over the role of classical mechanical length changing tools. Beside simple 1-dimensional measurement methods, full field techniques like digital image correlation (DIC), allow 2- or 3-dimensional characterisation of the materials and components. Especially for anisotropic materials the multidimensional information is important. E.g. up to now this is limited to 2D strain information on plane surfaces.

Nowadays, the application of the DIC technique moves from academic to industrial fields. In this interest, one needs to prove the DIC technique on real components. The conventional 2-cameras 3D DIC inspection becomes then non-optimal since complex geometries imply hidden areas. The approach of using more than minimum required number of camera views overcome these limitations. An efficient way to overcome these limitations is to take advantage of the use of multi-cameras DIC system. This idea is already commonly used in other fields like photogrammetry.

This publication describes the idea and principle of using the Cluster Approach for multi-cameras DIC systems. In order to illustrate the implications of this new technique, we present strain measurements in tensile testing and deformation measurements on complex geometrical structures.

Keywords Digital image correlation • Multi camera DIC • Strain measurement • Material testing

19.1 Introduction

In mechanical engineering, optical measurement techniques are very popular tools for non-invasive and non-contact full-field deformations, strains and vibrations analyses. The optical techniques are classified by the spatial field-of-view they can measure. Concerning camera based systems, these are 2D or 3D mostly. A very popular technique is the Digital Image Correlation (DIC) technology. Depending on the number of used cameras, one can obtain 2D (one camera) or 3D (two or more cameras) measurements.

Historically speaking, the DIC technique was first implemented with only one camera, which limited the inspections to plane objects with in-plane displacement only. This limitation was caused by the technical state-of-the-art of digital image processing and by the camera technology. Nevertheless, the results of these early measurements gave a big advantage in the understanding of e.g. inhomogeneous materials. The next historical step increased the number of cameras from 1 to 2. This additional camera offered to the DIC technology the possibility to measure 3D objects and to perform in-plane and out-of-plane deformations measurements [1].

Having access to a complete 3D information of the inspected object implied a huge additional complexity in the determination of the projection parameter, geometrical setup and the DIC algorithm [2]. This effort has paid off since an exhaustive determination of the object's contour and deformation became available.

19.2 DIC Using the Cluster Approach

As 3D information can only be calculated from objects points which are simultaneously imaged by two cameras, the field-of-measurement is limited to the overlap of the field-of-views of the cameras. A sufficient overlap zone can become tedious to obtain when non-planar objects are measured. By directing a third camera on the same common measurable area, issues as

T. Siebert (✉) • K. Splitthof • M. Lomnitz
Dantec Dynamics GmbH, Kässbohrerstr. 18, Ulm D-89077, Germany
e-mail: Thorsten.Siebert@Dantecdynamics.com

curved objects or corners can be overcome. Additionally, the accuracy of the measurement is increased in the area where all three cameras view the object [3]. This additional third camera doesn't implies any further changes in the principle of how the DIC algorithm is used. The facets used for the identification of the measurement points on the object surface are defined in the image of one, so called "reference camera". Starting from this image, the positions of the facets are detected in the other images and the corresponding 3D position can be reconstructed. Figure 19.1 illustrates this process for a 3 camera DIC setup.

The sole drawback of this enhancement is that the area which can be evaluated is still restricted by the view of one, so called "reference camera", since the image of this camera defines which points are to be measured. In the same trend, an additional fourth camera may increase the accuracy of the DIC system. If the fourth camera shall be used to enlarge the field of measurement, one does need to change the way of defining the measurement points on the object, since no camera can capture the entire field of view.

By using the Cluster Approach for DIC systems, the restrictions by using a reference camera can be overcome. The points to be evaluated are not defined in a single camera view but on the object itself [4]. Every object point seen by at least any pair of two cameras is followed. This innovative approach opens new realms in applications and information acquisitions for the DIC technique. The principle of this approach is illustrated in the next figure (Fig. 19.2).

The principle used for the 3D reconstruction of the object points is identical to the one used in conventional DIC. By using the information of the projection parameter the pixel positions are projected back and the intersection of these lines defines the 3D coordinate of the corresponding object point.

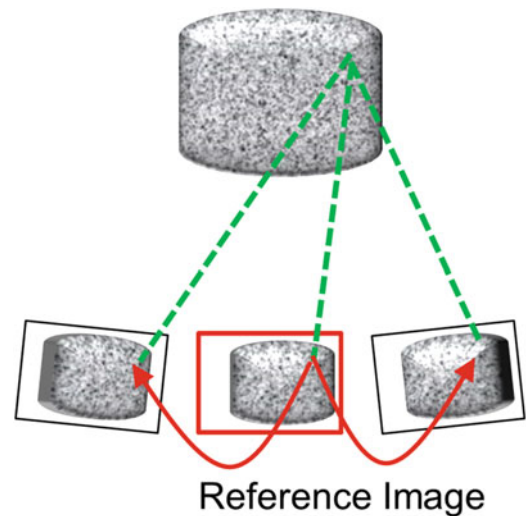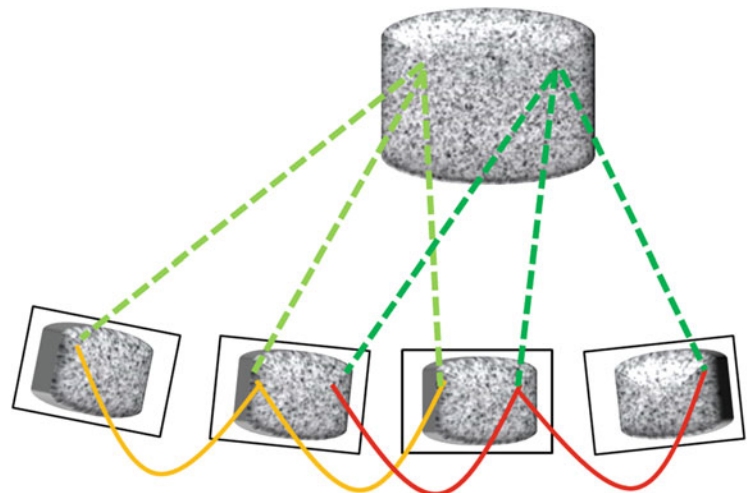**Fig. 19.1** Definition of facets in a conventional 3 camera DIC setup

Fig. 19.2 Definition of facets in Multi Camera DIC setup using the cluster approach

19.3   DIC Multi Camera Setup Using Four Cameras

By using e.g. a 4-cameras setup and the Cluster Approach, different configurations are possible. Table 19.1 summarizes principle arrangements of the cameras:

One examples for the corner arrangement is the measurement of carton boxes under pressure load. The deformation of the adjacent sides and the corner are of importance. Since the behavior is not reproducible all information needed to be measured simultaneously. As a result the entire behavior and full information can be analyzed. Figure 19.3 shows the 3D model of the measured area with the amplitude of the displacement mapped as a result on the surface of the model.
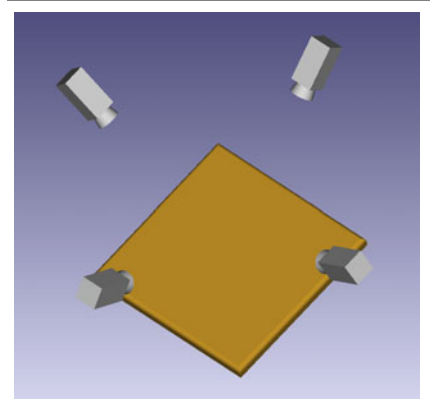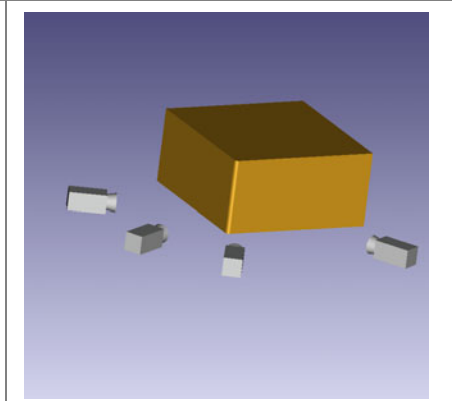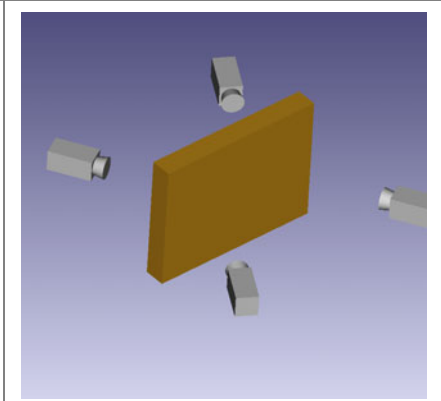
The double side arrangement is predestinate for material testing applications in tensile load [5]. Using the four camera configuration, both sides of the sample are measured simultaneously. As all cameras are calibrated in a common coordinate system the thickness of sample and any changes are measured directly. In this way the strain in thickness direction is measurable directly as well. This enables the determination of the strains as full-field data in three dimensions: in longitudinal, transverse and thickness direction at the same time.

Figure 19.4 shows a typical result of a tensile test of a steel sample using a frond back side measurement configuration. The measured strain is plotted over the average strain in loading direction. The solid triangles are strain values measured at the point of failure, where the maximum load occurs. The open triangles are results from the base material. The blue line represents the longitudinal strain in loading direction, the green line displays the transverse strain, measured on the surface perpendicular to the loading direction and the red line is the strain in thickness direction. For isotropic materials the transverse and thickness strain is expected to be identical, the differences are caused by inhomogeneous material properties introduced e.g. by the production process. This information can now be measured directly without need of any model assumption.

19.4   DIC Multi Camera Setups in One Side Arrangement

Starting from the one side arrangement of the cameras, various configurations can be realized. Each has advantages in terms of flexibility and improvements for measurable object geometry. A listing of some applications can be found in the following table (Table 19.2).

Table 19.1 Principle configurations of a 4 camera Multi Camera setup

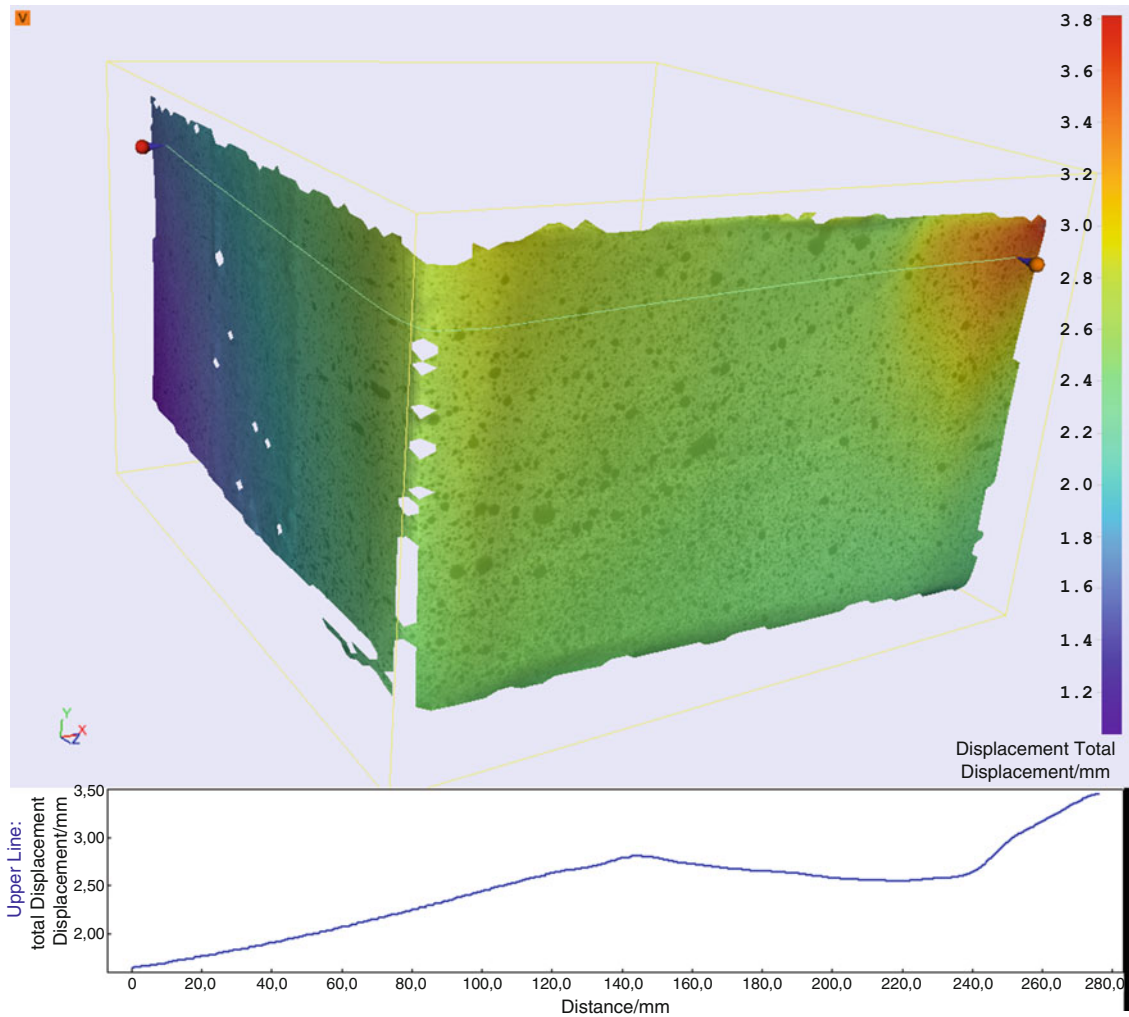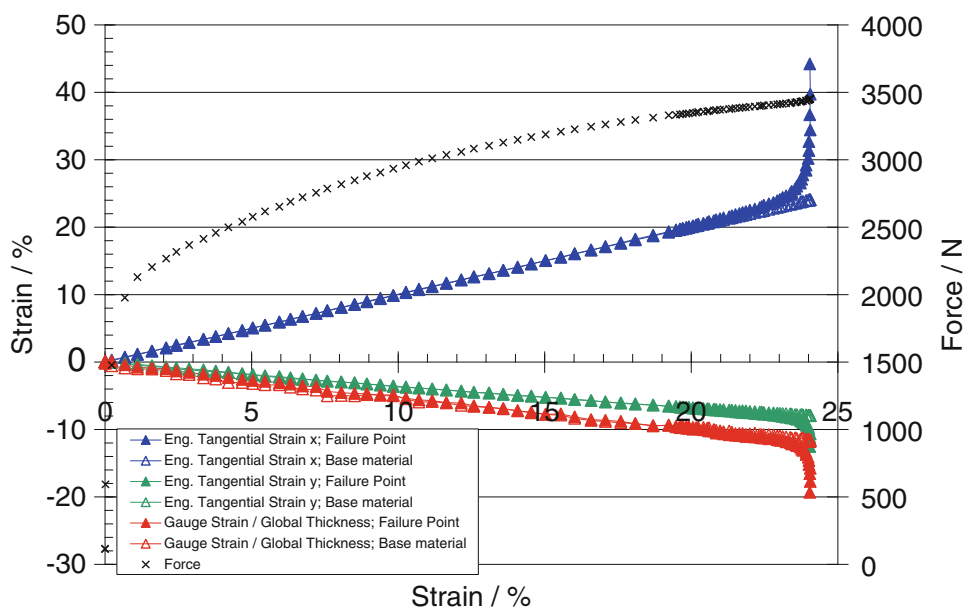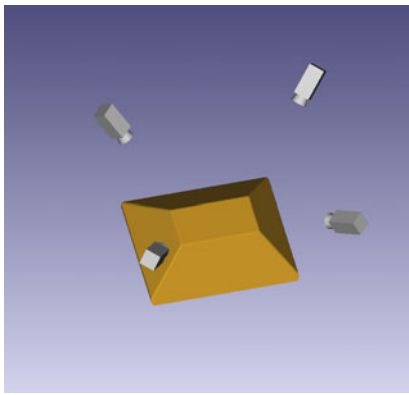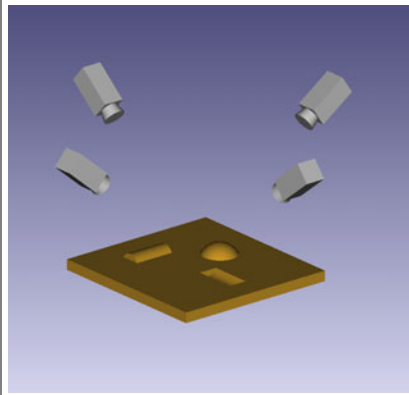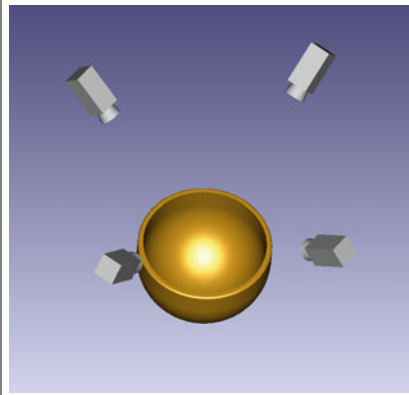| One side arrangement	Corner arrangement	Double side arrangement
All cameras see the object from one side	Cameras look at two adjacent sides and the corner	Cameras look at front and back side
• Increased accuracy	• Measurement around a corner	• Simultaneous measurement of front and back side
• Extension of field of measurement	• Increased accuracy on the sides and at the corner	• Data in common coordinate system
		• Direct measurement of thinning

Fig. 19.3 Deformation of a carton box

Fig. 19.4 Strain results measured in a tensile test using Multi Camera DIC

Table 19.2 Different applications of a 4 camera Multi Camera setup in one side arrangement

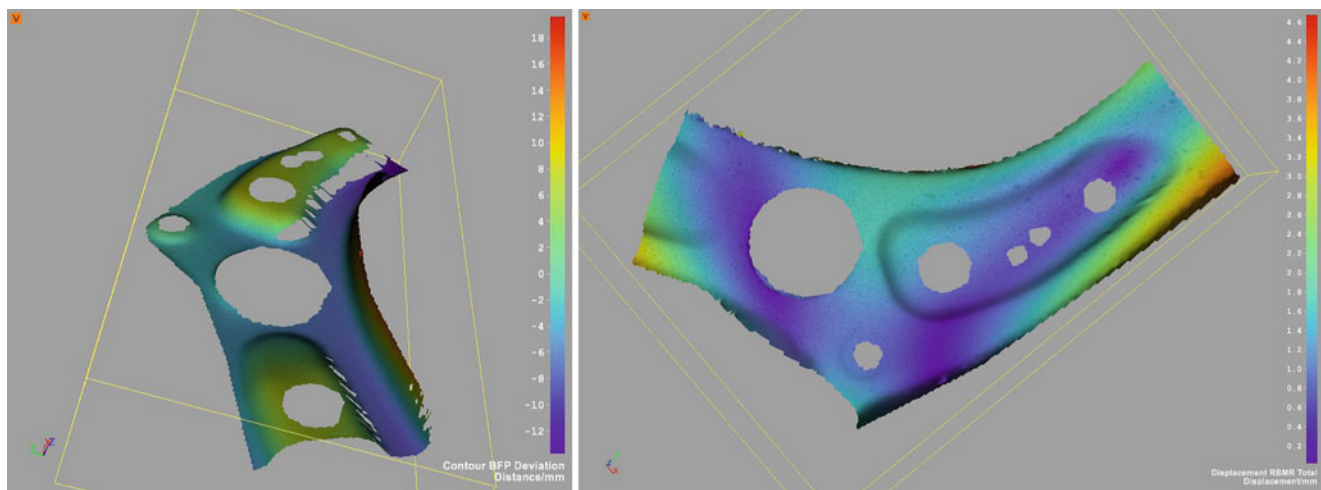| All side arrangement	Component testing	Concave objects
Cameras look around the object	Cameras look from different directions	Cameras look into the concave shape
• Full view of object	• Full view of object shape	• 360° view of bowl shaped object
• Measurement of discontinued areas	• Measurement of curvature and bulges	• Measurement of entire shape

Fig. 19.5 Comparison between 2 camera DIC (*left*) and 4 camera DIC (*right*) measurement off a car component

19.4.1   Component Testing

The advantages of configurations based on the one side arrangement are described in the following more in detail. Depending on the shape of the object under investigation and the requirements of the measurement, the use a conventional 2 camera DIC system may not be able to capture enough measuring area. The contour does not allow a single camera viewing all of the surface, areas will be shadowed by the contour and shape of the object. In this situation the Cluster Approach can overcome these restrictions.

By moving from scientific use into more industrial applications, the objects move from simple samples into components. The geometry of the objects gets more challenging. Starting form pure plane object surfaces even simple components are equipped with dents, hollows, buckles and so on. Areas of interest are often close to these irregularities and a reliable analysis is required. A comparison between a standard 2 camera 3D DIC system and a 4 camera Multi Camera DIC shows the next figure (Fig. 19.5) [5].

19.5 Hemisphere Testing

A quite demanding object geometry is a half shell item. The goal here is the investigation of the complete inner surface of hemisphere under pressure load from the button. From the beginning it is not clear at which position of the circumference the surface will deform first. That's why a measurement of the complete inner surface is required. The setup is made as in Table 19.2 proposed. Four cameras look into the concave surface from top. A single camera covers more than 90°, each object point is viewed by at least cameras and the complete surface can be measured by this Multi Camera setup.

A picture of a setup for the measurement of a half shell shows Fig. 19.6. The object is a hemisphere of about 25 cm diameter and a 5 cm rim on top. This experiment was used demonstrating the feasibility of the system measuring the complete surface even with an irregular shape.

A small pressure from the button causes a buckling of the inner surface. Figure 19.7 shows the reconstructed inner surface of the test object as a 3D model. The complete 360° of the surface is captured and can be reconstructed as a full model of the object. The magnitude of the displacement is mapped as color coded texture on the surface. The maximum displacement is about 8 mm. A line along the circumference verify the local buckling with a positive and negative amplitude.

19.6 Conclusion

The advantages of using more than two cameras for performing DIC measurements were discussed and highlighted.

In component testing, the object's shape is more complex than in the academic field. One still need to be able to characterize the component's behaviour. Therefore, the Multi-Cameras Approach helps reducing the areas of shadowing and extends the measurable area significantly. Moreover, the use of the Cluster Approach for multi-cameras DIC measurements of tensile test sample allows the direct access to all three strain directions for each object point. This is one more dimension than conventional DIC systems are able to deliver.
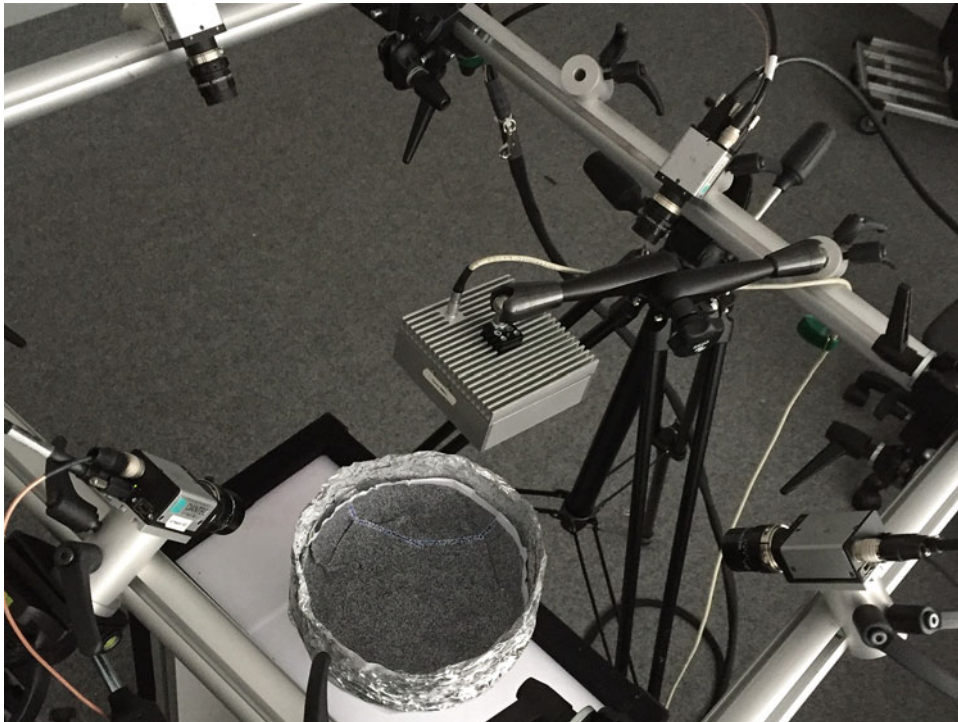

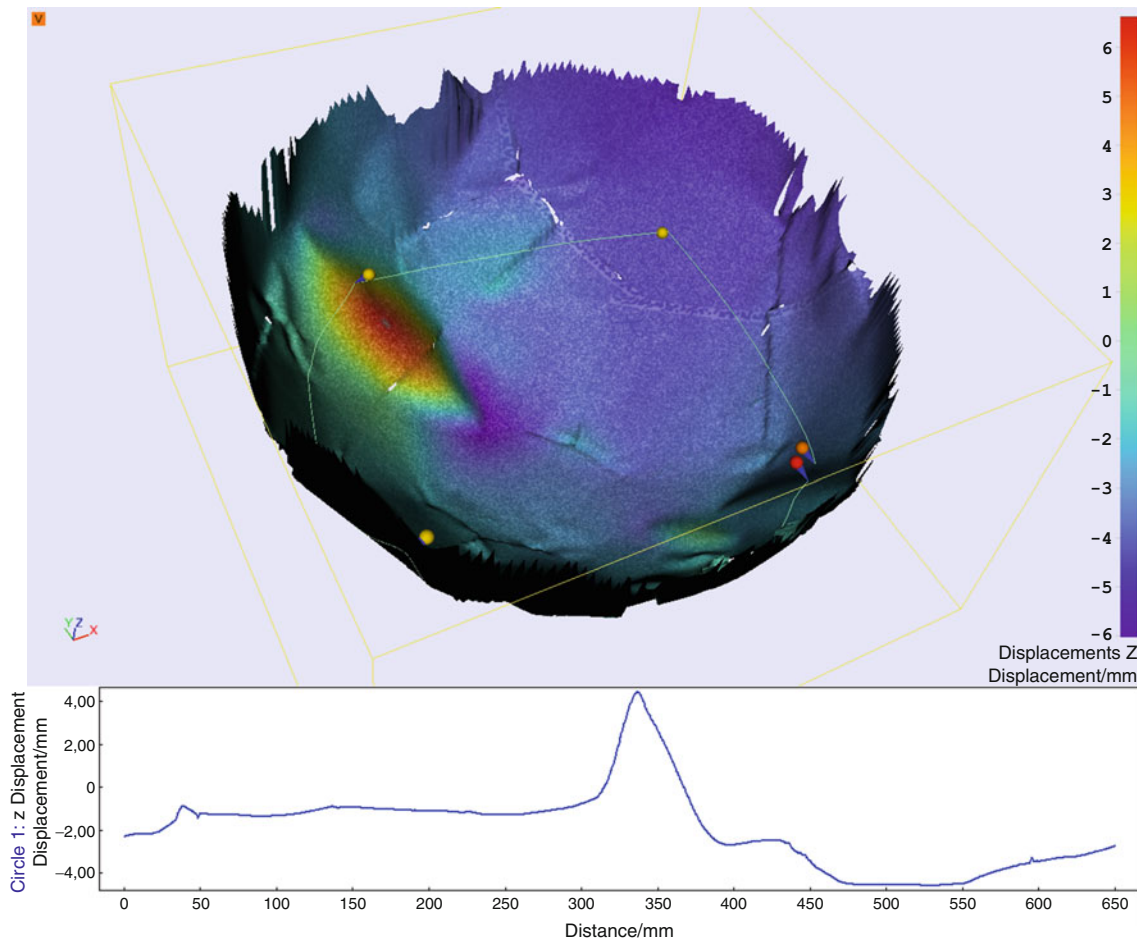**Fig. 19.6** Setup of multi camera system for measurement of a hemisphere

Fig. 19.7 Displacement of hemisphere object

The extension of standard DIC systems to Multi-cameras Systems requires a new way of defining how the points must be correlated. Nevertheless, this innovative approach increases the flexibility of the arrangement of the multi-cameras and thus the applications range dramatically. Furthermore, complex shapes like a hemisphere, can be captured and reconstructed as a single object.

References

1. Sutton, M.A., McNeil, S.R., Helm, J.D., Chao, Y.J.: Advances in 2-D and 3-D computer vision for shape and deformation measurements. In: Rastogi, P.K. (ed.) Photomechanics. Topics in Applied Physics, vol. 77, pp. 323–372. Springer, New York (2000)
2. Sutton, M.A., Orteu, J.-J., Schreier, H.W.: Image Correlation for Shape, Motion and Deformation Measurements. Springer Science + Business Media, Berlin (2009). ISBN 978-0-387-78746-6
3. Siebert, Th., Crompton, M.J.: An approach to Strain measurement uncertainty for DIC using the SPOTS calibration procedure. In: Proceedings of the SEM International Conference and Exposition on Experimental and Applied Mechanics, June 11–12, Paper 107 (2012)
4. Orteu, J., Bugarin, F., Harvent, J., Robert, L., Velay, V.: Multiple-camera instrumentation of a single point incremental forming process pilot for shape and 3D displacement measurements: methodology and results. Exp. Mech. **51**, 625–639 (2011)
5. Siebert, Th., Tran, V.: Multi-camera DIC offers new dimensions in material testing. In: Proceedings of the SEM International Conference and Exposition on Experimental and Applied Mechanics, Paper 381 (2014)

Chapter 20
Self-adaptive Isogeometric Global Digital Image Correlation and Digital Height Correlation

J.P.M. Hoefnagels, S.M. Kleinendorst, A.P. Ruybalid, C.V. Verhoosel, and M.G.D. Geers

Abstract This work explores the full potential of isogeometric shape functions for global digital image correlation. To this end, a novel DIC and DHC (digital height correlation) methodology have been developed based on adaptive refinement of isogeometric shape functions. Non-Uniform Rational B-Spline (NURBS) shape functions are used employed of their flexibility and versatility, which enables a wide range of kinematic descriptions. In the adaptive refinement algorithm, the shape functions are automatically adjusted to be able to describe the kinematics of the sought (2D or 3D) displacement field with an optimized number of degrees of freedom. Both methods show high accuracy as demonstrated by various virtual experiments with predefined, highly localized (2D and 3D) displacement field. For adaptive iso-GDIC, real tensile tests of complex sample geometries demonstrate its effectiveness in practice, showing local refinement at the areas of localization, without the need of making problem-specific choices regarding the structure of the shape functions. For adaptive iso-GDHC, the correlation of surface height profiles of deforming stretchable electronics structures shows successful autonomous refinement at two localized buckles, thereby strongly reducing the 3D residual, while also analytical differentiation of the C1-continuous 3D displacement field yields the curvature field of the deforming stretchable interconnect.

Keywords Digital image correlation • NURBS • Adaptive refinement • GDIC • Digital height correlation

20.1 Introduction, Motivation, and Goal

Digital Image Correlation (DIC) is a computational technique used for determining displacement fields from digital images. The technique is used for a wide range of applications, ranging from glacier movement tracking and weather predictions by storm system movement detection to the working principle of an optical computer mouse. DIC was first developed in the 1980s and introduced in the field of solid mechanics by Peters, Sutton and Chu, see Pan et al. [1] for an extensive review on the development of the digital image correlation method. For materials scientists DIC is an important technique to couple experiments and numerical simulations by analyzing displacement fields from mechanical tests.

Digital Image Correlation (DIC) is a computational technique used to determine displacement fields, for example from mechanical tests. In the DIC algorithm the displacement field is regularized with a limited amount of degrees of freedom and shape functions. Many choices for shape functions are possible, however an isogeometric approach using Non-Uniform Rational B-Splines (NURBS) has proven to be promising. In combination with an adaptive refinement algorithm, NURBS show promise to improve DIC compared to results acquired with conventional regularization techniques. This is because due to adaptive refinement the NURBS shape functions are smooth in locations where the sought displacement field does not exhibit strong variations, while at positions where the displacement field shows high gradients, the NURBS adapt to capture these fluctuations. Therefore, in this work the full potential of Isogeometric Digital Image Correlation is explored, both for regular 2D DIC and Digital Height Correlation (i.e. Quasi-3D DIC) in which topological surfaces are correlated to measure the three-dimensional displacement field.

J.P.M. Hoefnagels (✉) • S.M. Kleinendorst • A.P. Ruybalid • C.V. Verhoosel • M.G.D. Geers
Department of Mechanical Engineering, Eindhoven University of Technology, P.O. Box 513, Eindhoven 5600 MB, The Netherlands
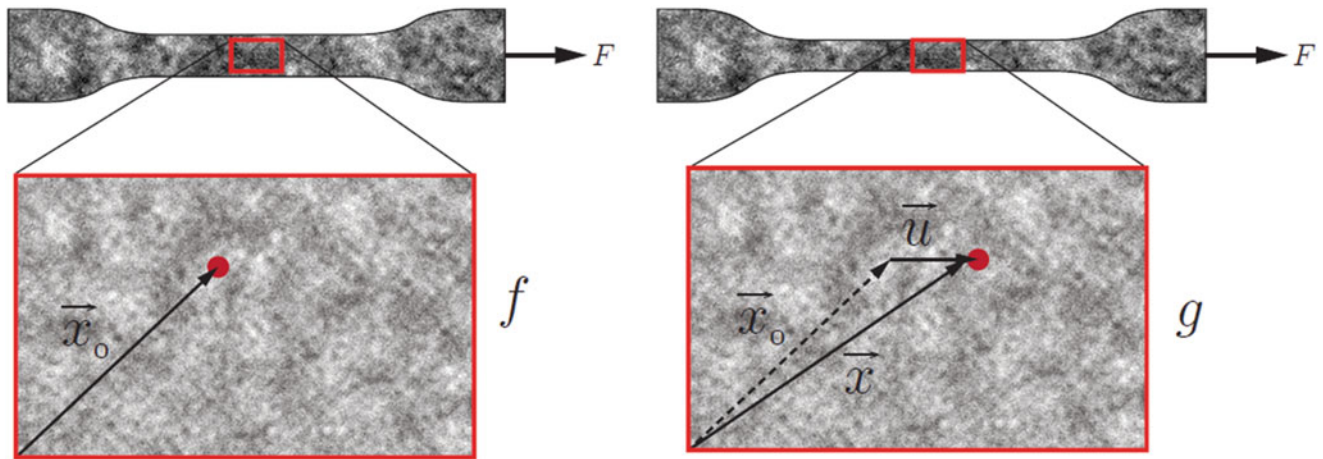e-mail: j.p.m.hoefnagels@tue.nl

Fig. 20.1 Illustration of GDIC applied on a tensile bar that is deformed due to load F. The reference image f and the deformed image g are shown, in which a material point with initial coordinates $\vec{x}_0$ is indicated. After deformation this material point is positioned at $\vec{x}$. With GDIC the global deformation field $\vec{u}(\vec{x}_0)$ of all material points is computed

20.2 Digital Image Correlation

The DIC method consists of an algorithm searching for the displacement field that best matches two images, f and g, of a specimen taken during an experiment. In Fig. 20.1 the method is graphically represented. This displacement field is found by minimizing the residual image $f - g$ and solving the resulting system of equations. The problem is ill-posed by nature since the number of unknowns equals twice the number of pixels, because the vector displacement per pixel is sought, while only one brightness value per pixel is known. Furthermore the number of unique gray values is typically less than the number of pixels. In an experimental setting also noise plays a role. To solve this problem the system is spatially regularized by a combination of shape functions and degrees of freedom (DOF's). The choice of these shape functions is important, since they need to be able to describe the kinematics of the displacement field.

Different approaches of DIC exist, referred to as global and local approaches. They differ in the way the displacement field is computed: either by solving the entire domain at once or by taking a small subset of the image into account at the time. First the method referred to as local DIC was developed. Herein the region of interest (ROI) is divided in small subsets, zones of interest (ZOIs), which are correlated in both images in order to find their displacement. The total displacement field then is interpolated. In the early attempts this method only accounted for pure translation of the ZOIs, but over the years the kinematics could also capture more complex displacement fields, such as warping and rotation [1].

Later on an alternative approach, referred to as global DIC (GDIC), was advanced. Herein the correlation of the two images is executed over the whole domain at once, hence the term 'global' [2]. In the global DIC method continuity of the displacement field is imposed and therefore the problem is more regularized. Hild et al. have shown that the method is less sensitive to noise than the local DIC implementation [3]. In contrast to the local method, where displacement are calculated at every subset center, the global approach provides a displacement at every pixel. Therefore the spatial resolution is higher and the accuracy of the solution is better. However, because of the higher amount of regularization the global method is more reliant on the choice of certain important variables the user makes. In particular the choice of the shape functions is important, since these must be able to capture the kinematics of the sought displacement field. However, this field is generally unknown in advance, which can make this choice very difficult. The local method is somewhat more user friendly, since only few choices have to be made in advance, like the subset size. Local DIC is more versatile and less dependant on problem-specific information supplied to the algorithm in advance.

20.3 NURBS Shape Functions

Many choices for shape functions are possible. In this work the potential of NURBS shape functions is investigated. NURBS originate from computer aided design (CAD) modeling, where they are the industry standard. NURBS are able to represent many geometric shapes—in particular conic sections—exactly, whereas standard finite element shape functions

Fig. 20.2 Second order NURBS shape functions in one-dimensional space. The knots are indicates by ξ_I
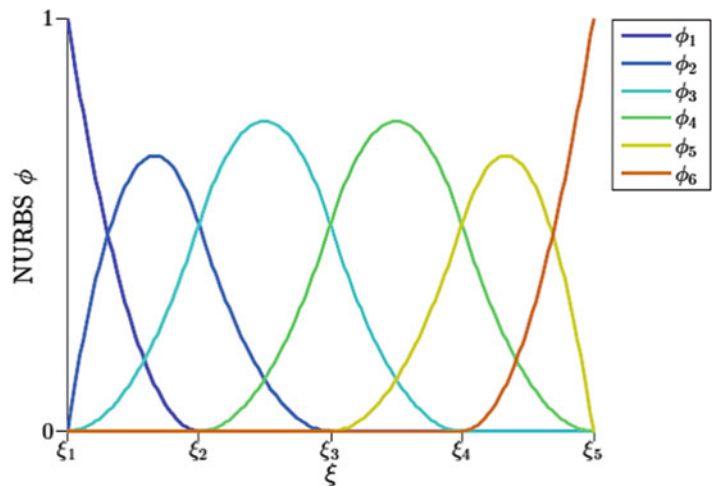
approximate them. Hughes et al. proposed to use the geometrical representation of CAD-models directly for finite element analysis: Isogeometric Analysis (IGA) [4]. The use of B-Splines in a digital image correlation setting was pioneered by Cheng et al. [2]. Beaubier et al. directly utilized the CAD-representation of their subject for the correlation algorithm [5]. Advantages of NURBS were investigated by Elguedj et al. [6], who concluded that, compared to high order Lagrange shape functions, NURBS need fewer functions to adequately describe the displacement field, which improves the conditioning of the problem and thereby the noise robustness of the correlation algorithm.

NURBS are versatile and can be used for describing the kinematics of many types of problems. They have several advantages over other types of shape functions, such as traditional finite element method (FEM) shape functions, which are in fact a subclass of NURBS. Firstly the geometry can be described exactly, whereas FEM shape functions approximate. This is beneficial for capturing for example edge effects. Secondly NURBS shape functions are smoother than standard finite element shape functions. Where FEM basis functions are C^0 continuous at the element boundaries, NURBS are C^{p-1} continuous, where p is the polynomials order. In a isogeometric analysis setting this property is proven to lead to better convergence properties in many cases [7].

An example of NURBS functions is shown in Fig. 20.2. The form of the NURBS basis functions, and thereby the kinematics that they describe, are determined by the polynomial order and by the so called knot vector. The knots divide the parametric domain in intervals and are positions where the continuity of the basis functions is decreased. They determine the amount of regularity applied to the problem. An interesting idea is to optimize the knot locations automatically in order to adjust the NURBS such that they are able to describe the kinematics of the displacement field best.

20.4 Hierarchical Refinement

The most straightforward way of refining an isogeometric mesh is by adding knots in the knot vectors Ξ and Z. However, due to the tensor product structure of the mesh, the refinement propagates as is illustrated in Fig. 20.3b. Therefore the total number of degrees of freedom can increase rapidly in the refinement process, although they are not necessarily added at useful positions. In DIC particularly this is disadvantageous, due to the ill-posed nature of the problem.

A second approach for refining the mesh, is hierarchical refinement. In contrast to propagated mesh refinement the idea is to refine the mesh in a more local fashion, as illustrated in Fig. 20.3c. The key idea to hierarchical refinement is to replace some of the shape functions in the initial basis by shape functions of the refined basis. The bases are constructed hierarchically, which implies that multiple levels of basis functions exist, which represent subsequent levels of refinement of the underlying geometry. This is illustrated in one dimension in Fig. 20.4. In Fig. 20.4a the initial basis is shown and in Fig. 20.4b the refined basis. The last three elements are marked for refinement and all shape functions that are entirely contained within these elements are selected to be replaced, as indicated by the dashed line in Fig. 20.4a. They are replaced by the shape functions of the refined basis that completely lie within this domain, as indicated by the solid lines in Fig. 20.4b. The resulting set of shape functions is shown in Fig. 20.4c. It should be noted that in 1D-space the same effect could be obtained by knot insertion. In 2D-space the refinement remains local, this in contrast to tensor product B-splines.
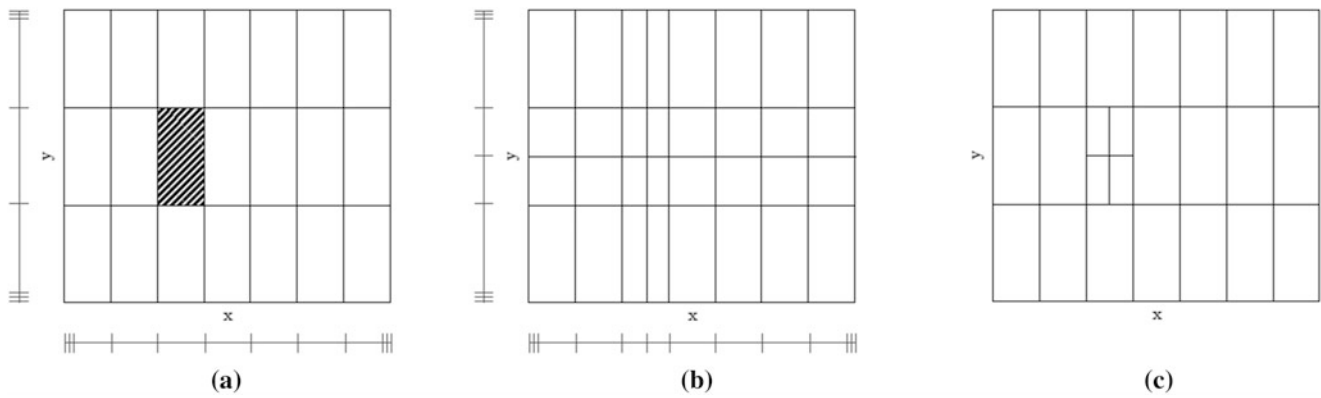
Fig. 20.3 Mesh before and after refinement of one element. Knot vectors associated with the x- and y-direction are shown below and to the left of the mesh respectively. (**a**) Initial mesh with one element marked for refinement, (**b**) propagated refined mesh, and (**c**) hierarchically refined mesh

Fig. 20.4 The concept of hierarchical refinement. In the *top* figure an initial basis is shown and in the *middle* figure a refined basis. The *dashed* basis functions in the initial basis are replaced by the *solid* shape functions of the refined basis. In the *lower* figure the result of this refinement step is shown. Element boundaries (knot locations) are indicated by *vertical black dashed lines*
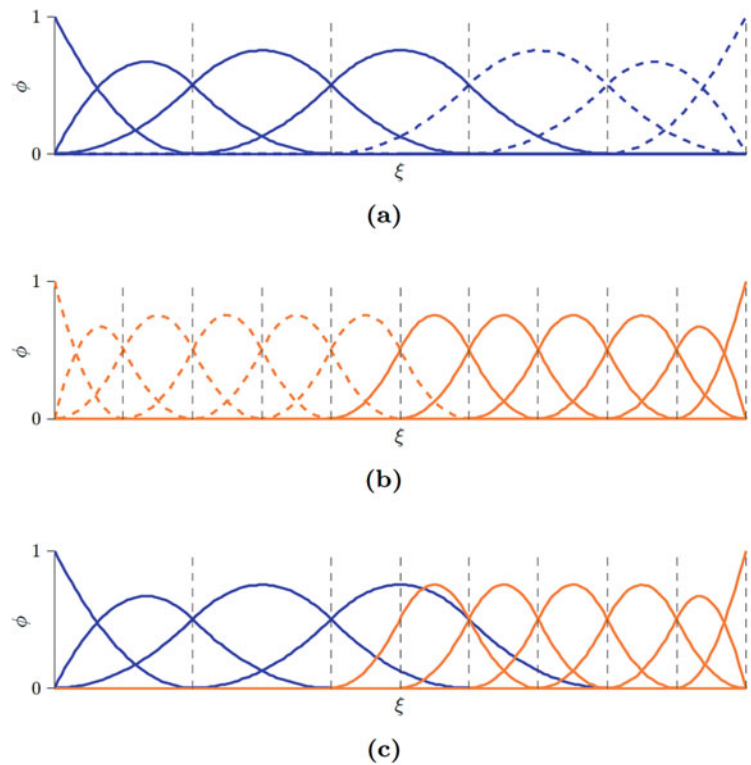
An important property of hierarchical splines is that they are linearly independent, which makes them suitable to use as basis functions. The details of the procedure to automatically optimize the knot locations has been described in [8].

20.5   Adaptive Refinement in 2D Isogeometric Digital Image Correlation

A (real) experiment is performed in order to investigate the performance of the adaptive isogeometric GDIC method to a practical problem. A uniaxial tensile test is performed in a microscopic setup. The tensile sample before and after deformation can be seen in Fig. 20.5. These images, along with a number of intermediate images taken during the experiment, are used in the correlation process as reference image f and deformed image g. Some additional steps are taken in order to make the mesh conforming the hole, as described in [8]. Four elements that are located in or near the hole, and their corresponding shape functions are removed. Next the control points of the elements surrounding the hole are
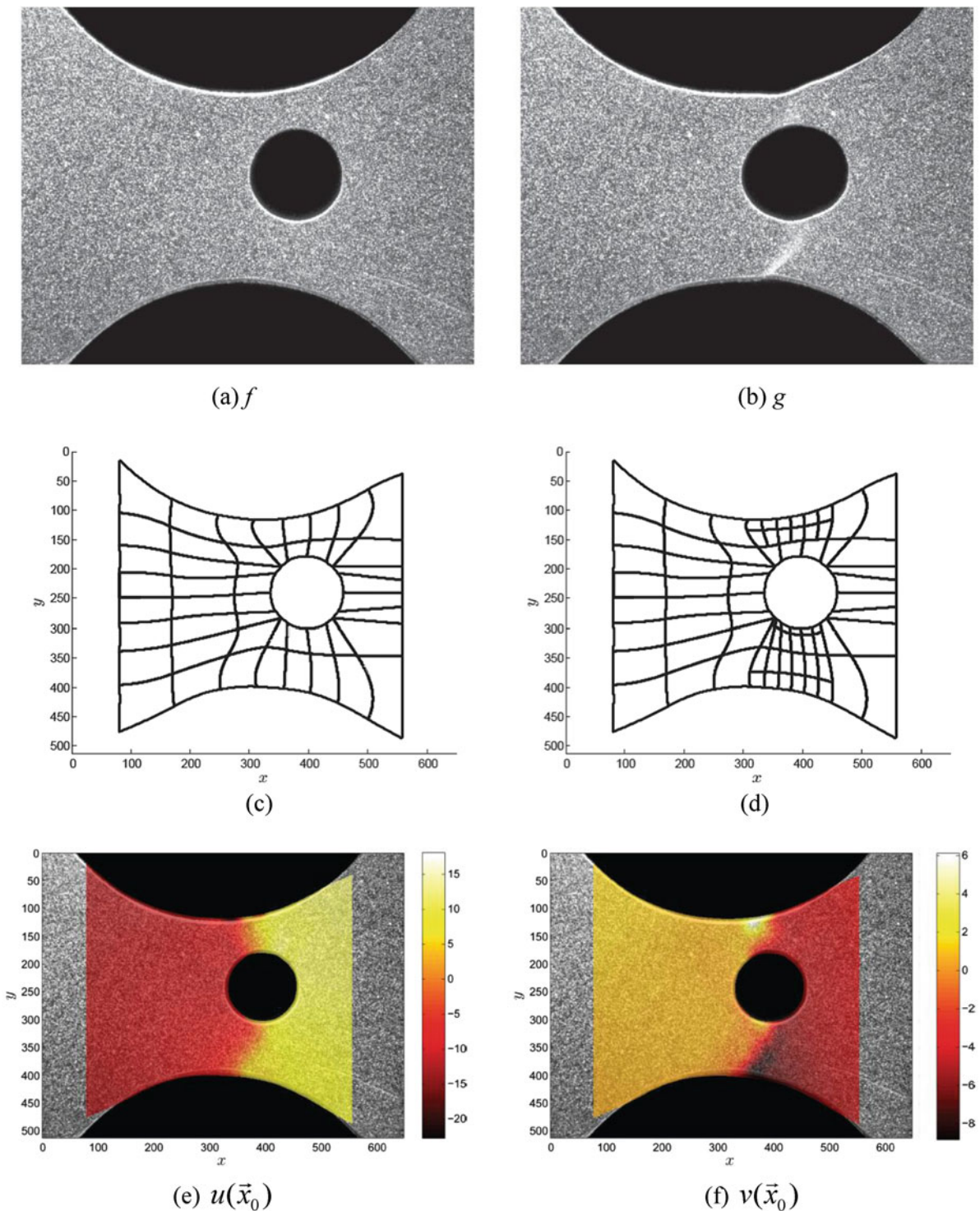
Fig. 20.5 Validation experiments of the adaptive refinement in 2D isogeometric DIC: (**a**) images of the sample before and after deformation. (**b**) Evolution of the mesh during the refinement process. (**c**) Calculated displacement fields u in x-direction and v in y-direction. The displacement is expressed in terms of pixels (Reproduced from [8])

translated to the edge of the hole, such that the mesh forms a fit around the hole. In order to describe the hole accurately at least 12 elements around the hole are required, resulting in a quite fine mesh, see Fig. 20.5c. The correlation procedure is executed using adaptive refinement of second order NURBS shape functions. The evolution of the mesh is shown in Fig. 20.5d. It can be seen that refinement takes place in the area where the largest deformation, i.e. localization, is expected;

the least wide material regions. Only one level of refinement is reached. This is attributed to the fact that the elements surrounding the hole are rather small in the initial mesh. This is because the length scale of the elements needed to describe the geometry around the hole is comparable to the length scale needed to capture the shape of the displacement field. Consequently after one refinement step, the shape functions are fine enough to describe the localized kinematics in the displacement field.

The final calculated displacement field u in x-direction and v in y-direction can be seen in Fig. 20.5e, f. From the deformed image it is observed that necking occurs in the small regions around the hole. Indeed in Fig. 20.5f this localization is visible: the displacement in y-direction is largest in this area. Furthermore a localization in x-displacement in the same area is recognized in Fig. 20.5e. Displacement in both directions combined indicate shearing.

A more thorough validation of the new methodology is given in [8], where the method is compared to the case without adaptive refinement algorithm and to local DIC. This comparison is done both on virtual experiments and real experiments. There, the virtual experiments show that for a test-case with a strong localization of the displacement, where refinement is desired, the new method yields a good result compared to conventional DIC implementations. Most importantly, this result is obtained automatically. The user doesn't need to supply the program with specific prior information about the problem, as is required for the conventional DIC method to obtain accurate results. The validation comparison based on a real experiment with a complex geometry demonstrates that the novel method also performs well in practice. A notched tensile sample with a hole was chosen, which shows a localized displacement field under deformation. Indeed localization takes place in the area around the hole. Mesh refinement also appears in this region. It was shown that the isogeometric GDIC adaptive refinement algorithm has some major advantages. The most important advantage is its flexibility, which makes the method rather robust. Furthermore the method provides accurate results, without the need of supplying problem-specific information to the algorithm in advance. Last it is shown in [8] that in specific cases the method provides a more accurate result that any conventional DIC method.

20.6   Adaptive Refinement in 3D Isogeometric Digital Height Correlation (DHC)

Another recent development concerns the correlation of profilometric images in order to identify both in-plane and out-of-plane deformation fields: Digital Height Correlation (DHC). So far three examples have been published in the literature where this technique is applied; in all three cases accurate results were obtained on the microscale [9–11]. The results in these cases are convincing, however, in all cases the discretization of the DHC problem (necessary because of the intrinsic ill-posed nature of a DHC formulation) was adapted to the specific mechanics of the considered experiment. However, in most mechanics problems it is not possible to assess the kinematics of the unknown displacement field a priori, for instance in the case of Fig. 20.6, where a copper stretchable electronic interconnect delaminates from the rubber substrate and buckles in specific local areas, which is an active field of research [12, 13]. Therefore, a more generic DHC framework is called for, which preferably autonomously adjusts to the kinematics, without using prior knowledge.

For the case of in-plane, two-dimensional DIC, it was shown above that the use of NURBS shape function is versatile and able to capture a wide range of kinematics. Moreover, NURBS originate from CAD-modeling and are able to describe many shapes exactly. In the case of stretchable electronics, it is very useful to be able to describe both the complex shape of the interconnects and the buckle pattern, which occurs mainly at the edges of the interconnect. Furthermore, the continuity of NURBS functions across the element edge is adjustable by inter alia choosing the polynomial order of the shape functions.

Fig. 20.6 A stretchable electronics interconnect, showing buckles under applied deformation. (Reproduced from [13])
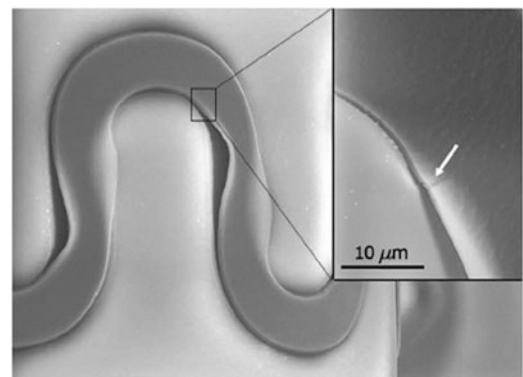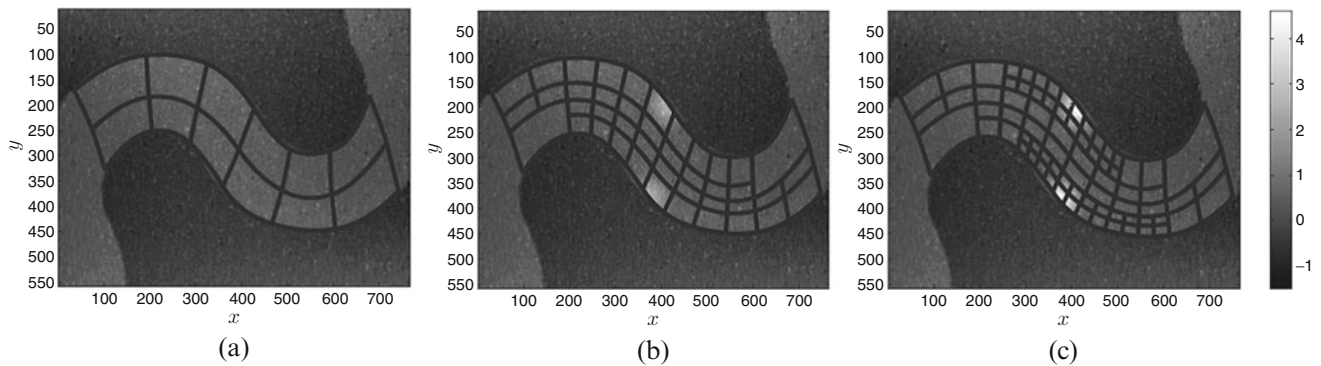
Fig. 20.7 Virtual experiment to test the potential of the self-adaptive isogeometric DHC algorithm. The gray scale corresponds to the measured height in micrometers. The applied displacement field again represents localized buckles, corresponding to the buckles seen in Fig. 20.6. The reference image f (*left*) is shown along with deformed images g_2 (*middle*) and g_4 (*right*). The initial mesh and refined meshes are plotted on *top* [14]

Therefore, a generic autonomous DHC framework has been developed by adapting the 2D adaptive iso-GDIC formulation toward quasi-3D: DHC. An advanced meshing framework has thereby been implemented, which is generic for a myriad of shape function types, polynomial orders and mesh generating interfaces.

The potential of the novel method is demonstrated here on a virtual experiment with interface delamination of stretchable interconnects, see Fig. 20.7. The applied displacement field again represents localized buckles, corresponding to the buckles seen in Fig. 20.6. Figure 20.7 shows that the self-adaptive isogeometric DHC algorithm successfully refines at the location of the buckles. The refined mesh also shows that the implemented refinement is again a hierarchical refinement, similar to the one implemented in the 2D self-adaptive isogeometric DIC algorithm. Further validation of the self-adaptive isogeometric DHC algorithm has been performed and is given in [14], in which also much more details of the algorithm are given.

20.7 Conclusions

A novel method was developed where isogeometric global digital image correlation was combined with an adaptive refinement algorithm. The potential advantage of this method is that it is flexible and can be used for a wide variety of DIC and DHC problems. The NURBS shape functions are able to capture the kinematics of many displacement fields, depending on the structure of the knot vector. In combination with adaptive refinement the shape functions are automatically adjusted to be able to describe the kinematics of the sought displacement field with an optimized number of degrees of freedom. A hierarchical mesh refinement algorithm is used in order to prevent inefficient refinement, providing DOF's only where needed, which is beneficial for the conditioning of the problem. Iterating towards the optimum number of DOF's is incorporated in the procedure of marking shape functions for refinement. Shape functions are merely refined if the residual in its region of support is significantly higher than the average.

It was found that adaptive refinement in isogeometric digital image correlation improves results for cases that are difficult to solve with the conventional method. Furthermore the new method is more user friendly, since the user does not have to make certain choices in advance, like the type of shape functions and the structure of the mesh, based on limited knowledge. This method is applicable to a wide variety of cases and therefore gives an interesting perspective for the future of DIC and DHC.

References

1. Pan, B., Qian, K., Xie, H., Asundi, A.: Two-dimensional digital image correlation for in-plane displacement and strain measurement: a review. Meas. Sci. Technol. **20**(6), 062001 (2009)
2. Cheng, P., Sutton, M.A., Schreier, H.W., McNeill, S.R.: Fullfield speckle pattern image correlation with b-spline deformation function. Exp. Mech. **42**, 344 (2002)
3. Hild, F., Roux, S.: Comparison of local and global approaches to digital image correlation. Exp. Mech. **52**, 1503 (2012)
4. Hughes, T.J.R., Cottrell, J.A., Bazilevs, Y.: Isogeometric analysis: CAD, finite elements, NURBS, exact geometry and mesh refinement. Comput. Methods Appl. Mech. Eng. **200**, 4135 (2005)

5. Beaubier, B., Dufour, J.-E., Hild, F., Roux, S., Lavernhe, S., Lavernhe-Taillard, K.: Cad-based calibration and shape measurement with stereodic. Exp. Mech. **54**, 329 (2014)
6. Elguedj, T., Réthoré, J., Buteri, A.: Isogeometric analysis for strain field measurements. Comput. Methods Appl. Mech. Eng. **200**, 40 (2011)
7. Bazilevs, Y., Beir ao da Veiga, L., Cottrel, J.A., Hughes, T.J.R., Sangalli, G.: Isogeometric analysis: approximation, stability and error estimates for h-refined meshes. Math. Models Methods Appl. Sci. **16**, 1031 (2006)
8. Kleinendorst, S., Hoefnagels, J.P.M., Verhoosel, C.V., Ruybalid, A.P.: On the use of adaptive refinement in isogeometric digital image correlation. Int. J. Numer. Methods Eng. **104**, 944 (2015)
9. Han, K., Ciccotti, M., Roux, S.: Measuring nanoscale stress intensity factors with an atomic force microscope. Europhys. Lett. **89**, 66003 (2010)
10. Bergers, L.I.J.C., Hoefnagels, J.P.M., Delhey, N.K.R., Geers, M.G.D.: Measuring time-dependent deformations in metallic fMEMSg. Microelectron. Reliab. **51**, 1054 (2011)
11. Neggers, J., Hoefnagels, J.P.M., Hild, F., Roux, S., Geers, M.G.D.: Direct stress-strain measurements from bulged membranes using topography image correlation. Exp. Mech. **54**, 717 (2014)
12. Van Der Sluis, O., Hsu, Y.Y., Timmermans, P.H.M., Gonzalez, M., Hoefnagels, J.P.M.: Stretching-induced interconnect delamination in stretchable electronic circuits. J. Phys. D Appl. Phys. **44**, 034008 (2011)
13. Lucchini, R., Catarinuzzi, E., Maraghechi, S., Gastaldi, D., Adami, A., Lorenzelli, L., Vena, P.: Delamination phenomena in aluminum/polyimide deformable interconnects: in-situ micro-tensile testing. Mater. Des. **89**, 121 (2016)
14. Kleinendorst, S., Hoefnagels, J.P.M., Fleerakkers, R., van Maris, M.P.F.H.L., Cattarinuzzi, E., Verhoosel, C.V., Geers, M.G.D.: Adaptive isogeometric digital height correlation: application to stretchable electronics, accepted for publication in Strain (2016)

Chapter 21
Ultrasonic Test for High Rate Material Property Imaging

F. Pierron and R. Seghir

Abstract In order to perform experimental identification of high strain rate material models, engineers only have a very limited toolbox based on test procedures developed decades ago. The best example is the so-called Split Hopkinson Pressure Bar (SHPB) which has proved extremely useful but has important intrinsic limitations due to the stringent assumptions required to process the test data. The recent advent of full-field deformation measurements using imaging techniques has allowed novel approaches to be developed and exciting new testing procedures to be imagined for the first time. One can then use this full-field information in conjunction with efficient numerical inverse identification tools such as the Virtual Fields Method (VFM) identify material parameters at high rates. The underpinning novelty is to exploit the inertial effects developed in high strain rate loading.

This paper presents results a new inertial ultrasonic test to obtain stress-strain curves at high strain rates (here, up to 300/s). The idea is to excite a flat rectangular specimen at its first longitudinal resonance frequency. Images are recorded with an HPV-1 camera from Shimadzu at 250 kfps. It is shown that meaningful stress-strain curves can be obtained using acceleration as a stress gauge.

Keywords High strain rate • High speed imaging • Ultrasonic testing • Virtual fields method • Digital Image Correlation

21.1   Introduction

The identification of the high strain rate properties of materials is a very important topic for many engineering applications like crash, blast, forming, among others. It is also a very challenging experimental task mainly because of the difficulty in measuring impact loads accurately in regimes where inertia effects are significant. The most popular technique to obtain material parameters at strain rates between several hundred to several thousands of s^{-1} is undoubtedly the Kolsky (or split Hopkinson) bar. This technique is well understood and produces useful results but suffers from limitations arising from the strong assumptions on which its data analysis relies. In particular, the fact the specimen needs to be at quasi-static equilibrium (*i.e.*, forces at both loading ends are equal in magnitude and opposite in sign) is a strong limitation which does not allow to obtain data in the transient regime of the test when inertia effects are significant. As a consequence, this technique is not very good at determining elastic stiffness of materials.

A recent alternative is to use the acceleration information as an image-embedded load cell, where the density of the material acts as the load cell factor, in conjunction with an inverse identification tool called the 'Virtual Fields Method' (VFM, [1]). The first time that this was used was to extract orthotropic stiffness components from vibrating plates [2]. This was extended to complex stiffnesses in [3]. In this case, the assumption of harmonic response makes the calculation of the acceleration much easier as it is simply proportional to the displacements for a given excitation frequency. However, it is possible to extend this approach to transient waves by deriving the acceleration through double temporal differentiation. This was adopted in several papers on composites [4], concrete [5] and welds [6].

However, such impact tests are difficult to set up, potentially dangerous and acceleration derivation requires significant regularization. Therefore, harmonic loading would be preferable if large enough strain rates can be achieved. To obtain large strain rates, testing at high frequencies is necessary. Recently, a very interesting article was published [7] where a sawbone specimen was submitted to longitudinal vibrational excitation in the ultrasonic range. The authors showed that it was

---

F. Pierron (✉)

Engineering Materials Group, Faculty of Engineering and the Environment, University of Southampton, Southampton SO17 1BJ, UK
e-mail: f.pierron@soton.ac.uk

R. Seghir
Engineering and the Environment, University of Southampton, Southampton, UK

possible to measure time resolved strain response maps by combining Digital Image Correlation (DIC) and ultra-high speed imaging. This paper builds up on this.

21.2   Objectives and Methodology

Dynamic Mechanical Analysis (DMA) is a well-known tool in polymer testing. The idea is to use a simple test like torsion or bending and from force and displacement measurements, complex stiffness values are obtained. However, this technique suffers from some shortcomings. First, only global average values are achieved. Moreover, stiffnesses from load/displacements are generally less accurate as they do not take into account the compliance of the test set-up or indentation at the loading point. And damping include dissipation arising from contacts between specimen and fixture. Finally, only low strains are achievable with this technique. Based on the experiment in [7], the present paper illustrates a route towards a new imaged-based DMA technique that has great potential for the future.

Figure 21.1 shows the specimen dimensions and loading configuration from [7]. A thin strip of polyurethane foam (known as 'sawbone') is excited ultrasonically close to its first longitudinal resonance. This creates longitudinal standing waves. Digital Image Correlation (DIC) from images acquired with an HPV-1 ultra-high speed camera was used to obtain displacements at 250 kfps. The images were processed by the MatchID software,[1] more details in Data can be visualized in the videos available online.[2] From the acceleration obtained from the displacement and the angular velocity, stress profiles along the length can be reproduced using Eq. (21.1), see [8], where $\overline{\sigma_{yy}}^y$ is the average stress in a transverse cross-section, ρ is the material density, L is the specimen length and $\overline{a_y}$ is the average acceleration over the surface area between the considered cross-section and the free end. Strain rates up to 300 s^{-1} are achieved at the excitation frequency of 20 kHz.

$$\overline{\sigma_{yy}}^y = \rho(L - y)\overline{a_y} \tag{21.1}$$

21.3   Results and Analysis

Figure 21.2 shows a stress-strain curve obtained at two locations in the sawbone specimen. The value of the Young's modulus is compatible with the manufacturer's data, about 500 MPa. Unfortunately, the images are not good enough here to extract the damping coefficient but using the latest state of the art camera as in, this will be possible, turning the technique

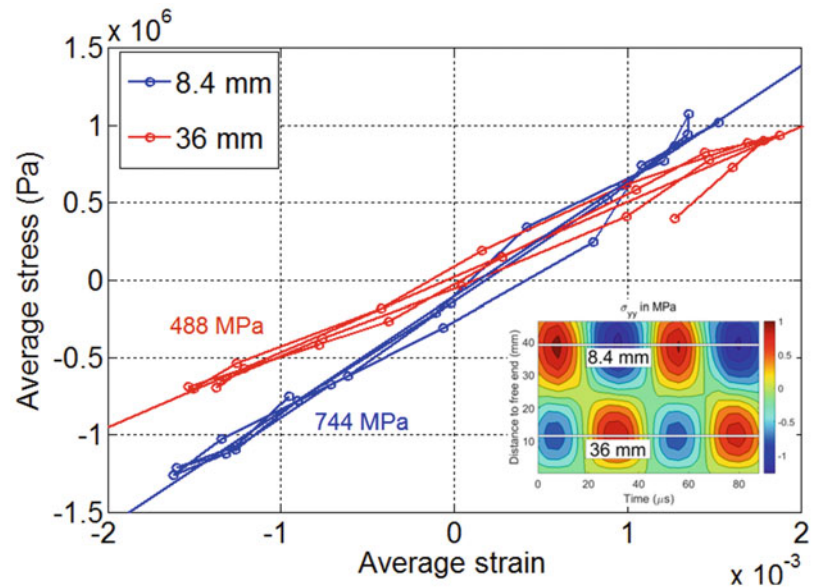**Fig. 21.1** Specimen dimensions and loading configuration from [7]
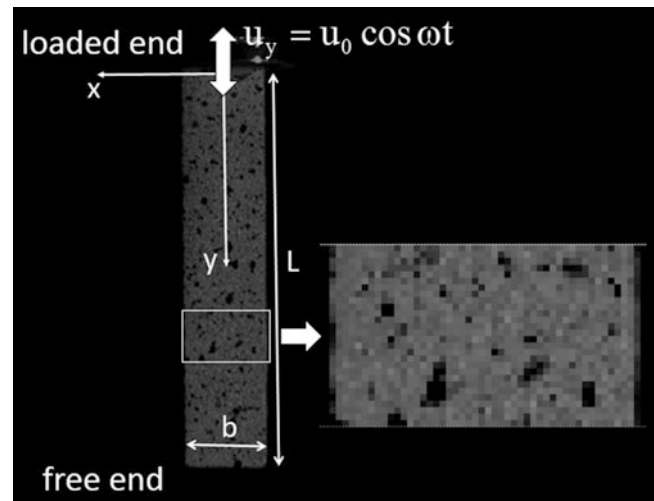
into an image-based DMA technique that can image complex stiffness within the material. This is believed to be particularly

---

Fig. 21.2 Stress-strain curve for two locations in the sample

interesting in the future to address heterogeneous materials. The presentation will be based on simulated and further experimental data on PMMA.

21.4 Conclusion

The test proposed in [7] coupled with the analysis described in this article has great potential to explore the strain, strain-rate and temperature dependence of materials constitutive behaviour. [7] also reported temperature measurements. Because of the high excitation frequency and high associated strain rates, self-heating is significant and temperatures reached up to ~160 °C before fracture of the specimen. With better quality measurements, it will be possible to include the identification of temperature dependent stiffness and damping as the test evolves. Therefore, this test has the potential to become an 'imaged-based DMA (Dynamic Mechanical Analysis)' technique. Varying the excitation frequency and will enable to shift the high strains from some parts of the specimen to others. This will overcome the problem of the vibration nodes for which no data can be obtained at a particular excitation frequency. Finally, different specimen shapes can also be used to concentrate the strains, or activate more stress components for anisotropic materials.

However, to deliver the above, significant improvement of the measurement quality needs to be achieved. This will be possible by the recent progress in ultra-high speed imaging where better quality images and higher performances are currently at hand.[3] This is confirmed when comparing the quality of the stress-strain curves obtained in [5, Fig. 26] with the Shimadzu HPV-1 camera (the same as that used for the present data) and in [4, Fig. 13] with the more recent HPV-X camera (see footnote 3). Improvement will also arise from the use of better speckle patterns with less aliasing, or the use of the grid method when the material allows a grid to be bonded onto it as in [4].

References

1. Pierron, F., Grédiac, M.: The virtual fields method. Extracting constitutive mechanical parameters from full-field deformation measurements, p. 517. Springer, New-York (2012)
2. Grédiac, M., et al.: Direct identification of elastic constants of anisotropic plates by modal analysis: experimental results. J. Sound Vib. **210**(5), 643–659 (1998)

---

[3] Like the Shimadzu HPV-X2 camera, http://www.shimadzu.com/an/test/hpv/hpv-x2/, last accessed March 4th 2016.

3. Giraudeau, A., Pierron, F., Guo, B.: An alternative to modal analysis for material stiffness and damping identification from vibrating plates. J. Sound Vib. **329**(10), 1653–1672 (2010)

4. Pierron, F., Zhu, H., Siviour, C.: Beyond Hopkinson's bar. Philos. Trans. R. Soc. Math. Phys. Eng. Sci. **372**(2023), 20130195 (2014)

5. Pierron, F., Forquin, P.: Ultra high speed full-field deformation measurements on concrete spalling specimens and stiffness identification with the Virtual Fields Method. Strain **28**(5), 388–405 (2012)

6. Le Louëdec, G., et al.: Identification of the dynamic properties of Al 5456 FSW welds using the virtual fields method. J. Dyn. Behav. Mater. **1**(2), 176–190 (2015)

7. Wang, D., Lucas, M., Tanner, K.E.: Characterising the strain and temperature fields in a surrogate bone material subject to power ultrasonic excitation. Strain **49**(5), 409–419 (2013)

8. Pierron, F.: Addendum to "Characterising the strain and temperature fields in a surrogate bone material subject to power ultrasonic excitation." Strain **52**(3), 186–190 (2016)

Chapter 22
The Virtual Fields Method to Rubbers Under Medium Strain Rates

Sung-ho Yoon and Clive R. Siviour

Abstract This paper describes a dynamic experimental technique for characterizing the uniaxial stress-strain relationship of rubbers under medium strain rate deformation. This method combines the Virtual Fields Method (VFM) and high-speed imaging with digital image correlation. The VFM can be expressed so that force measurement during dynamic loading is no longer required but acceleration data on the specimen surface, which occurs as a result of wave propagation in the specimen, are measured and used as a 'virtual load cell'. In a previous paper, the authors have utilized this technique for characterizing material parameters for the dynamic behaviour of rubbers using a drop-weight apparatus [Int. J. Solids Struct. 69–70:553–568, 2015]. One limitation of this technique is that the stability of the parameter estimation depends on the length of a specimen. When the loading stress wave reaches the fixed end of the rubber specimen, a static equilibrium state is instantaneously achieved. At this instant, the acceleration fields are no longer able to provide information, and the identification is unstable. In order to overcome this limitation, the present paper proposes a VFM able to produce stable identification even at the equilibrium instant. This procedure utilizes both inertial and material forces, and a new experiment apparatus has been developed for simultaneously measuring these two sets of data. This new procedure is described using results from simulations; then, the experimental system and its results will be presented.

Keywords Elastomers • High-strain rate • Mechanical characterization • Virtual Fields Method • Inverse method

22.1 Introduction

Rubbers have been used for many engineering applications from aerospace to military fields. One of the useful characteristic of rubbers is energy dissipation, allowing the material to be used for energy absorption, which is of particular interest for impact protection. For example, one application is elastomeric coatings on concrete masonry unit walls, elastomers are also used to predict mobile devices such as cell phones. When rubbers are used in such dynamic applications, the strain rate induced by impact loading can fall into the so-called dynamic range (1–10^4 s^{-1}) [1]. For example, the strain rate of a rubber protective layer of masonry walls can reach the order of 100 s^{-1} [2]. The mechanical behaviour of rubbers is very sensitive to deformation rate even between quasi-static rates (10^{-4}–1 s^{-1}) [3]. Understating the dynamic and rate dependent behaviour is important to not only achieve cost-effective use of the materials but also ensure a targeted safety level. These two aspects can be achieved by appropriate engineering design, but engineering design cannot be reliable unless material behaviour in the service conditions is well understood. Thus, it is clear that the mechanical characterization of rubbers over a wide range of strain rates is essential.

The most widely used test method for mechanical characterizations of materials at dynamic strain rates is the split Hopkinson bar. This technique has been used for characterizing the dynamic stress-strain curve of rubbers in compression [3–5]. Alternative dynamic techniques have been developed for testing rubbers in tension [6–8]. Although many efforts have been made in the design and performance of these tests, there are several experimental difficulties due to the low Young's modulus of rubbers. The first difficulty is low signal-to-noise ratio of force measurement during dynamic loading. This difficulty is typically expected when the split Hopkinson pressure bar (SHPB) experiment is conducted with high impedance metallic bars on a low impedance rubber specimen [9]. The second limitation is the achievement of static stress (equilibrium in the dynamic experiment). This limitation needs to be considered for all Hopkinson bar type dynamic experiments, in which remote measurement of specimen behaviour are made, but it is more difficult for rubbers to obtain this equilibrium state within the initial loading period due to their low wave speed [10]. Thus, the force data measured from one end of a

S.-h. Yoon (✉) • C.R. Siviour
Department of Engineering Science, University of Oxford, Parks Road, Oxford OX1 3PJ, UK
e-mail: sung-ho.yoon@eng.ox.ac.uk

specimen will differ from that at the other end, and these measurements are affected by both specimen and material response, rather than measuring material response alone.

Recently, the authors developed an entirely different approach [11]. The new method is based on the combination of two modern experimental techniques: full-field measurement supported by high-speed imaging and digital image correlation [12] and the Virtual Fields Method (VFM) [13]. The VFM is an inverse method by which material constitutive parameters are inversely characterized by applying experimental observations such as strain and force data to the principle of virtual work equation. This equation is written as

$$-\int_v \boldsymbol{\sigma} : \boldsymbol{\varepsilon}^* \mathrm{dv} + \int_{s_f} \mathbf{T} \cdot \boldsymbol{u}^* \mathrm{d}s = \int_v \rho \boldsymbol{a} \cdot \boldsymbol{u}^* \mathrm{dv} \tag{22.1}$$

where

$\boldsymbol{\sigma}$	actual stress tensor
$\mathbf{T}$	actual loading $(=\boldsymbol{\sigma}\boldsymbol{n})$
$\boldsymbol{u}^*$	virtual displacement vector
$\boldsymbol{\varepsilon}^*$	virtual strain tensor $(=\partial \boldsymbol{u}^*/\partial \boldsymbol{x})$
v	current volume of the body
s_f	current loaded surface
':' and '·'	the dot products for matrices and vectors

For a quasi-static experiment, the inertial force term (the right-hand side of Eq. (22.1)) is negligible and can be omitted. When materials are dynamically loaded, this inertial term becomes significant due to the high accelerations, causing a non-uniform deformation of a test sample. Several previous works have modified this equation to remove the traction force term (the second term of the left-hand side of Eq. (22.1)) by applying appropriate virtual fields [14], for example,

$$\begin{cases} u_x^{*(1)} = x(x-L) \\ u_y^{*(1)} = 0 \end{cases} \Rightarrow \begin{cases} \varepsilon_x^{*(1)} = 2x - L \\ \varepsilon_y^{*(1)} = 0 \\ \varepsilon_{xy}^{*(1)} = 0 \end{cases}$$
$$\begin{cases} u_x^{*(2)} = 0 \\ u_y^{*(2)} = x(x-L)y \end{cases} \Rightarrow \begin{cases} \varepsilon_x^{*(2)} = 0 \\ \varepsilon_y^{*(2)} = x(x-L) \\ \varepsilon_{xy}^{*(2)} = (2x-L)y \end{cases} \tag{22.2}$$

where x and y are the axial and transverse coordinates and L indicates the axial distance from the fixed to loaded boundary. With these virtual fields, Eq. (22.1) can be rewritten as

$$-\int_v \boldsymbol{\sigma} : \boldsymbol{\varepsilon}^* \mathrm{dv} = \int_v \rho \boldsymbol{a} \cdot \boldsymbol{u}^* \mathrm{dv} \tag{22.3}$$

The cancellation of the traction force term in Eq. (22.1) means that the force measurement during dynamic loading is not required but instead the inertial force term is utilized as load cell. The fact that the traditional force measurement is not required is significantly advantageous for a dynamic test on rubbers since the aforementioned experimental difficulties in terms of force measurement do not need to be considered. The application of this equation can be referred to as the dynamic VFM and has been adopted for characterizing various materials such as metal [15, 16], composites [14, 17] and concrete [18]. The present authors used Eq. (22.3) to identify the Young's modulus of a silicone rubber under a small amplitude dynamic loading, in tension, produced by a drop-weight apparatus; the identification and experimental procedures are described in a previous paper [11]. The Young's modulus identification is also conducted with different pre-stretching levels imposed on the rubber specimen. A series of the Young's moduli (averaged values from each test) is collected and used in a special optimization with the assumption that each modulus is a tangent to the actual stress-strain curve of the test specimen. A suitable hyperelastic model is assumed in this optimization procedure, and the unknown model parameters are obtained. The drop-weight apparatus is schematically described in Fig. 22.1.

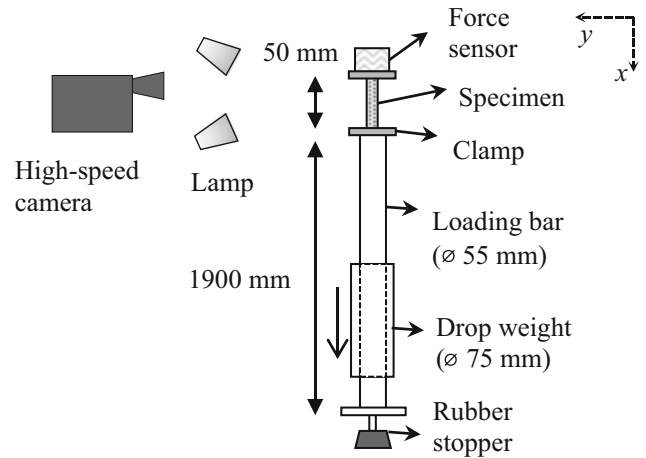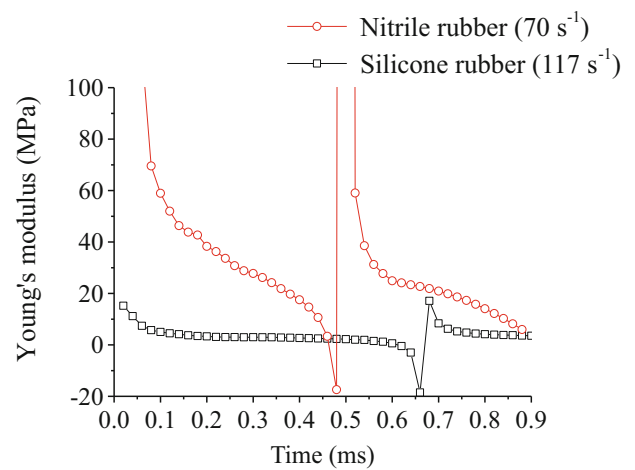**Fig. 22.1** Schematic diagram of the drop-weight dynamic test

Fig. 22.2 Young's modulus identifications from the VFM application on the drop-weight experiment

However, this technique does have a limitation. To demonstrate this, experiments have been performed on silicone (Sylgard 184 silicone elastomer, Dow Corning) and nitrile rubbers (Coru118, Coruba). The uniaxial type specimens were prepared from these two rubber sheets with the dimensions of width = 13 mm and length = 80 mm. The thickness is uniformly about 1 mm. After inserting the specimens between the two clamps in the drop-weight apparatus as shown in Fig. 22.1, the gauge length is approximately 50 mm. The dynamic experiment was identically conducted as presented in the previous work [11]. The procedure is briefly described here again. First, the specimen is located on top of the drop-weight apparatus. Both ends of the specimen are clamped by the two fixtures. The cylindrical weight is manually dropped from a certain location; when the end of the loading bar is impacted by the weight, the tensile loading wave travels toward the specimen. The bottom clamp is displaced downward and hence the rubber specimen is dynamically stretched. At this instant, a high-speed camera (FASTCAM SA 5, Photron) is triggered in order to capture the dynamic deformations at 50 000 fps. Each digital image taken by this camera is analysed by means of a commercial digital image correlation package (Davis 7.2, Lavision 2007). From this analysis, the strain and acceleration data fields are obtained at each imaging time step. These data are applied to Eq. (22.3) in which the stress term σ is described by the linear elastic constitutive model with the two unknown parameters: Young's modulus E and Poisson' ratio ν. Eq. (22.3) can then be rewritten in the form of the system of linear equations. The calculation of this equation leads to the identification of E and ν at each time step. The identification results for the silicone and nitrile rubber are given in Fig. 22.2.

The identification period shown in Fig. 22.2 is approximately the initial incident loading period after which slight unloading period occurs due to wave reflection within the loading bar. Within this initial loading period, there is at least one wave reflection; that is, the stress wave reaches the fixed end of the specimen. According to the observation of the strain data field, the stress wave reached the fixed end at about 0.5 and 0.7 ms for the case of the silicone and nitrile rubbers, respectively. At a similar instant, it can be seen that the Young's modulus identification falls below zero before returning to positive values. The reason for this unstable identification is that static stress equilibrium is achieved for a short period

when the stress wave reaches the fixed end. During this temporary equilibrium state, the inertial force term of Eq. (22.3) is close to zero; this means that no force data exist in the principle of virtual work equation.

In the previous work, the averaged Young's moduli need to be obtained from the identification results at different pre-stretch levels in order to conduct the optimization procedure with the assumed hyperelastic model. For example, the averaged value for the silicone rubber case can be calculated with the Young's modulus from 0.2 to 0.5 ms, over which the identifications are stable. The way to determine the stable identification period is to consider the assumption that rubbers should exhibit reasonable compressibility so that the Poisson's ratio, identified during the averaging period, should be close to that obtained from a quasi-static test. This method works well for determining the starting point of the averaging period. However, the unstable identification of the Poisson's ratio at the temporary equilibrium state is not as significant as that of the Young's modulus. Thus, it is not clear when to define the final point. This problem can significantly affect the identification result of the averaged Young's modulus, especially when rubbers exhibit a large amount of stress relaxation as shown in Fig. 22.2 in that the identification result of the nitrile rubber decreases more than that of the silicone rubber during the identification period. For this case, the averaged Young's modulus is largely influenced by the length of the averaging period. Furthermore, if the rubber specimen is shorter or stiffer, the unstable identification moment occurs earlier so that the determination of the averaging period can be more difficult, and its significance on the averaged modulus can be higher.

In the present paper, a new VFM and experimental procedure is proposed in order to overcome the experimental limitation of the current dynamic VFM technique on rubbers. The next section will describe this new VFM procedure using finite element simulation, which resembles the new experimental conditions, and explain how to remove the unstable identification moment and extend the stable identification period. The next section also explains an alternative way to reconstruct the stress-strain curve without using the optimization procedure introduced in the previous work [11].

22.2 Simulation

Finite simulation studies were conducted using ABAQUS. A two-dimensional rectangular specimen was designed with similar dimensions as used in the actual experiment. The geometry is schematically described in Fig. 22.3 (left). The left-hand boundary is fixed, and the velocity boundary condition (Fig. 22.3 (right)), which was obtained from the actual experiment, is imposed on the right-hand side boundary. The fixed boundary condition in the y direction is applied on both ends. ABAQUS/explicit simulations were performed with a CPS4R (four-node plane stress) element type and the maximum calculation time increment of 1 μs. The element size was chosen as 0.5 mm. The same simulation procedure is described more in detail in the previous work [11]. For the material model, the two-term Ogden [19] and linear viscoelastic models (Prony series) are adopted to simulate the rate-dependent hyperelastic behaviour. The parameters for the Ogden model were obtained from a quasi-static uniaxial test (0.01 s^{-1}) on the same nitrile rubber. The dynamic mechanical analysis (DMA) with the aid of time-temperature superposition was used to obtain the relaxation curve of the same material, which was then fitted to the Prony series in order to obtain the parameters for the viscoelastic part. The same description of the quasi-static experiment and DMA application can be found in the previous work [11]. The material parameters are listed in
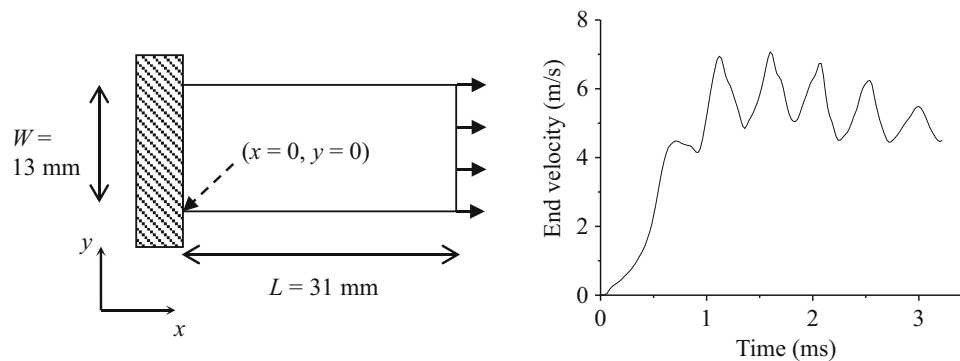

Fig. 22.3 (*Left*) Two dimensional simulation geometry (the hatching pattern rectangle represents the fixed boundary condition, and the solid arrows on the right-hand side boundary indicates the velocity boundary condition); (*right*) the velocity boundary condition imposed on the right-hand side boundary

Table 22.1 Simulation parameters for the two-term Ogden and Prony sereis models: $\log(\tau_i)$ and g_i are respectively logarithmic relaxation time and normalized shear modulus terms

Two-term Ogden			
μ_1 (MPa)	α_1	μ_2 (MPa)	α_1
0.028	0.004	0.014	0.014

Prony series										
$\log(\tau_i)$	-19	-18	-17	-16	-15	-14	-13	-12	-11	-10	-9
g_i	0.028	0.004	0.014	0.014	0.024	0.020	0.046	0.047	0.149	0.027	0.201
$\log(\tau_i)$	-8	-7	-6	-5	-4	-3	-2	-1	0		
g_i	0.156	0.198	0.056	0.010	0.003	0.001	0.001	0.0002	0.001		

Table 22.1. It should be noted that for the hyperelastic model a large bulk modulus ($K = 400$ MPa) is given to simulate an almost incompressible behaviour.

The strain and acceleration data fields were extracted, using the method as in the previous work [11], from the simulation result at a time interval of 0.02 ms, which is the same interval as the imaging speed, 50 000 fps, in the experiment. The extracted data fields were applied to the principle of virtual work equation, Eqs. (22.2) and (22.3), in order to obtain the Young's modulus identifications at each time step. The identification result from Eq. (22.3) is referred to as the Old VFM from this section onwards.

The meaning of the first virtual field of Eq. (22.2) is to impose zero (axial) virtual displacements on both ends of the specimen: the term x and $(x - L)$ respectively are null at the left- and right-hand side ends so that the tractions from both ends can be cancelled from the principle of virtual work equation. If the virtual fields can cancel the contribution of the traction over the fixed boundary, it is referred to as the kinematically admissible (KA) virtual field [13]. The principle of virtual work equation, Eq. (22.1), is only valid when such a KA virtual field is applied. However, a non-KA virtual field can be also used if the traction from the fixed boundary is known. In this case, however, it is assumed that in the experiment we can measure the traction of the fixed boundary during dynamic loading. This assumption allows the removal of the term x from Eq. (22.2). The term $(x - L)$ remains to cancel the traction from the loaded boundary, because it can be difficult to measure the reaction force from a dynamically loaded boundary. With this assumption, the first virtual field is rewritten as

$$\begin{cases} u_x^{*(1)} = (x - L) \\ u_y^{*(1)} = 0 \end{cases} \Rightarrow \begin{cases} \varepsilon_x^{*(1)} = 1 \\ \varepsilon_y^{*(1)} = 0 \\ \varepsilon_{xy}^{*(1)} = 0 \end{cases} \tag{22.4}$$

The second virtual field remains the same to be KA for cancelling any lateral traction contribution which is experimentally difficult to measure. With this new virtual field, the principle of virtual equation is written as

$$-\int_v \boldsymbol{\sigma} : \boldsymbol{\varepsilon}^* \mathrm{dv} + \int_{s_f} \mathbf{T} \cdot \boldsymbol{u}^* \mathrm{d}s = \int_v \rho \boldsymbol{a} \cdot \boldsymbol{u}^* \mathrm{dv} \tag{22.5}$$

where s_f indicates the fixed boundary. The same simulation data fields were also applied to this new equation. For the virtual work term of the traction force, the reaction force data were extracted from the nodes over the fixed boundary to supply the axial traction, T_x.

The identifications of the Young's modulus from the Old and New VFMs are given in Fig. 22.4. The black solid line represents the identification history from the Old VFM, in which the unstable identification instants can be observed as similarly shown in the preliminary experimental result in Fig. 22.2. The stable identification period between these instants becomes shorter with increasing time during the loading. This reduction could be due to not only the temporally equilibrium state but also the complex loading history as shown in Fig. 22.3 (right). In contrast, the result (red line) from the New VFM shows a very stable identification for the whole loading period. No unstable identification instant is found, except for the very early loading period, although there are multiple wave reflections within the specimen. The two identification results are almost coincident during the initial loading period ($t < 1$ ms). Thus, the old method to obtain the averaged Young's modulus can work for this period. However, after this period, the result from the Old VFM significantly deviates from that of the new method; the stable identification period becomes shorter and, so, only for short periods of time the two results are coincident.

Fig. 22.4 Young's modulus
identification results obtained
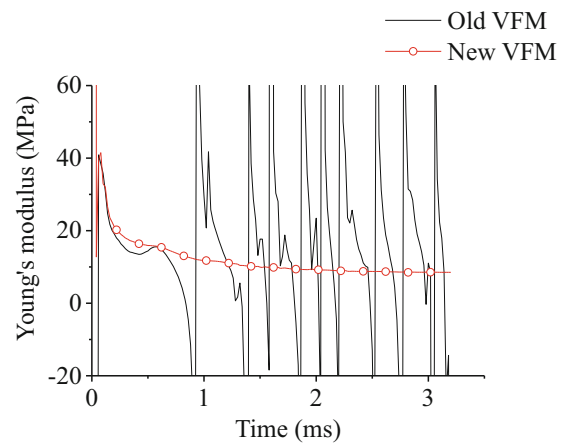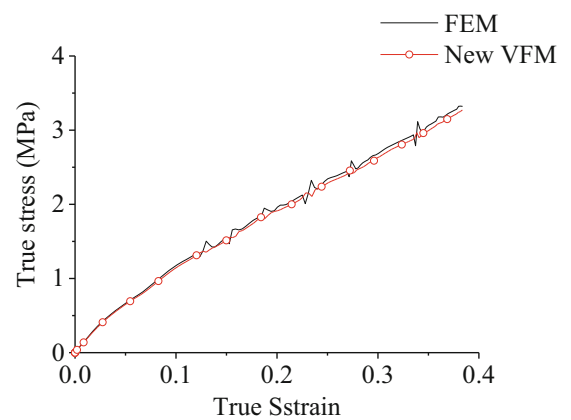from the old (Eq. (22.2)) and
new (Eq. (22.5)) VFMs

Fig. 22.5 Comparison with
the true stress-strain curves
obtained from the New VFM
and extracted from the
simulation

In the previous work [11], the averaged Young's modulus obtained during the initial loading period is assumed to be a tangent slope of the actual stress-strain curve. This assumption was made because the strain amplitude during this initial loading period is relatively small ($\varepsilon < 0.05$), so static pre-stretching was used to obtain data at larger strains. The identification result of the New VFM can be also used to obtain the averaged modulus within a small strain amplitude loading period. Then, each averaged modulus obtained from the dynamic test with different pre-stretching levels can be applied to the optimization procedure with an assumed hyperelastic model in order to find the optimized material parameters.

One limitation of this method is that a hyperelastic model needs to be assumed prior to knowing the actual stress-strain behaviour. With regard to this limitation, the new approach can be applied to the new identification result to reconstruct the stress-strain curve without assuming any particular model. This new approach is allowed by the fact that the new identification result is stable for a long loading period (i.e. large deformation). With this advantage, the axial stress is simply calculated by multiplying the spatially averaged axial true strain at each time step to the corresponding Young's modulus. This can be mathematically expressed as

$$\sigma_x(t) = E_{\text{VFM}}(t) \times \overline{\varepsilon}_x(t) \tag{22.6}$$

where the overbar of ε indicates a spatially averaged value. This equation is used to reconstruct the true stress-strain curve during the whole dynamic loading period. The reconstructed curve (red line) is given in Fig. 22.5. For comparison, the stress-strain curve directly extracted from the FEM simulation is given as a black solid line. The stress-strain curve from the simulation is obtained by averaging the stress and strain values at each time step. The comparison shows that the reconstructed curve from the New VFM is well matched with the given behaviour of the simulation. This result means that the constitutive model assumption is not required to reconstruct a nonlinear stress-strain curve when the identification result of the New VFM is used with the simple reconstruction approach of Eq. (22.6).

22.3 Experiment

The New VFM procedure was identically applied to a dynamic experiment using a new apparatus which produced the boundary condition given in Fig. 22.3 (right). This new experiment system was developed with the requirements to produce a longer deformation amplitude than that of the drop-weight apparatus introduced in the previous work [11] and to provide force measurement during the dynamic loading. The new experimental system satisfying these two requirements is described in Fig. 22.6 and consists of three parts: incident bar, specimen clamps and impacting bar. The impacting bar travels at 6–8 m/s in the direction as indicated by the arrow. The bar passes through the metal plate attached to the end of the gas-gun barrel. Next to the end of the gun barrel, a uniaxial piezoelectric force sensor (PCB Piezotronics, 208C02) is attached to the metal plate. The other side of the force sensor is connected to the clamp, which is used to apply the fixed boundary condition on one end of the uniaxial type rubber specimen. The other end of the specimen is attached to the other clamp which is connected to the end of the incident bar. The incident bar is dynamically displaced by the impact of the impacting bar on the middle of the clamp. In order to remove high frequency oscillation, two EPDM rubber layers (thickness = 2 mm) are attached on the impacting place of the moving clamp. The movement of the bar and clamp introduces dynamic tensile loading on the specimen. At the same time, the high-speed camera is triggered to capture the dynamic deformations at 50,000 fps. The images were analysed by a digital image correlation package with the same procedure introduced in the previous work [11]. One of the axial displacement fields obtained from the image analysis is shown in the right-hand side of Fig. 22.6. For a testing material, the same nitrile rubber sheet was used. After inserting this rubber specimen, the width and gauge length are similar to those shown in Fig. 22.3 (left). Three tests were performed with different impact speeds.

The data fields: strain, acceleration and coordinates obtained from the image analysis were applied to the Old (Eq. (22.3)) and New (Eq. (22.5)) VFMs in the same way as in the simulation work. One of the VFM analysis results is shown in Fig. 22.7 (left) presenting the history of the Young's modulus identifications from the two VFMs. The identification result is similar to the simulation results given in Fig. 22.4. The identification result of the Old VFM shows the unstable identification instants. Over the first loading period, the two results are almost matched, but after the first unstable identification the two results are not exactly matched; it seems that, after each unstable identification, the Old VFM reaches the similar identification level of the New VFM for only a short period. The reason of this fluctuation can be explained by the averaged acceleration profile (shown in Fig. 22.7 (left)). It can be seen that when the averaged acceleration becomes close to zero, i.e. the vicinity of dynamic stress equilibrium state, the unstable identification starts to occur. When the specimen is in or very close to the equilibrium state, the actual acceleration amplitude can be very low. However, the actual low-amplitude acceleration fields can be obscured by imaging processing noise as the acceleration data used in the VFM are calculated by double differentiation of the displacement data fields, which include imaging noise. When the New VFM, Eq. (22.5), is used, the virtual work contributed by the acceleration lessens due to the use of the new virtual field, Eq. (22.4), and instead, the proportion of the virtual work from the traction force is large. Therefore, the effect of unreliable measurements or calculations of the acceleration field at the temporally equilibrium state can be mitigated. This mitigation is the reason for the smooth and stable identification result of the New VFM shown in Fig. 22.7 (left). This result is used to reconstruct the true stress-strain
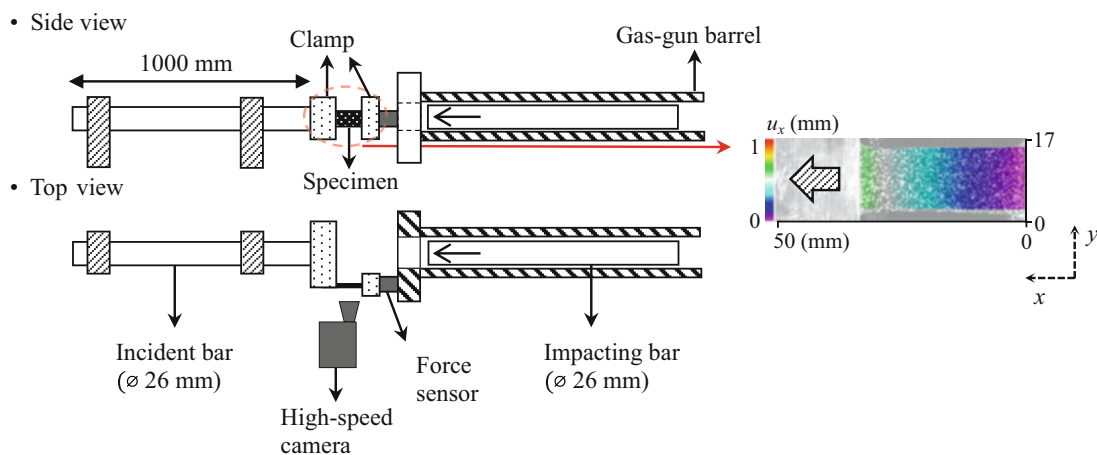

Fig. 22.6 Schematic representation of the dynamic tension test on a rubber sheet; the picture on the right-hand side shows one of the dynamic displacement field in the axial direction, which is overlayered on an actual picture of the specimen
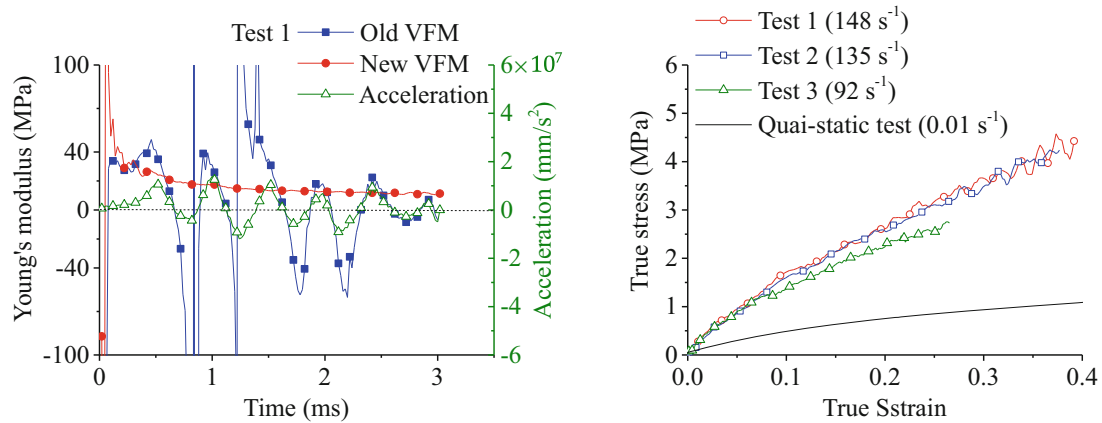
Fig. 22.7 (*Left*) Young's modulus identification results of the old (Eq. (22.2)) and new (Eq. (22.5)) VFMs applied on the experimental data (Test 1) and the averaged acceleration profile; (*right*) Stress-strain curves reconstructed from the Young's modulus identifications of the new VFM.

curve by using Eq. (22.5). The result is plotted in Fig. 22.7 (right); the reconstructed curves from the other two tests are presented as well. The legend in this figure provides the strain rate of each test. The stress curves of Test 1 and 2 shows a good repeatability of the present technique; the comparison between Test 1, 2 and 3 as well as the quasi-static test indicates that the present technique is able to capture the rate dependency of the chosen rubber.

22.4   Conclusions

A new experimental technique is proposed, an improvement to the previous VFM analysis and drop-weight test procedure introduced in a previous work [11], to characterize the dynamic behaviour of rubbers in uniaxial tension. The previous method utilized the dynamic VFM, in which the principle of virtual work equation is implemented to cancel the traction force term induced from the loaded boundary so that only acceleration data are used to identify the Young's modulus. One limitation is that although a rubber specimen is continuously deformed in tension, there are stress wave reflections during which the specimen is in an approximate equilibrium state, where the acceleration field is close to zero, for a short period of time. During this period, the Young's modulus identification is unstable. For this reason, the modulus identification history is discontinuous at the temporarily equilibrium instants. In order to overcome this limitation of the previous VFM, a modified VFM was made in which one of the virtual fields is modified so that the traction, which can be measured at the fixed boundary of a testing specimen, is included in the principle of virtual work equation. A new dynamic experiment system was also developed to introduce dynamic loading in tension and simultaneously to measure the traction forces. The test data (full-field and force measurement data) was applied to the new VFM; it is found that the modulus identification is smooth and continuous over a whole loading period. With this advantage of the new VFM result, a simple way to reconstruct the true stress-strain curve simply by applying the spatially averaged strain to the modulus identification result. Using this way, a dynamic true stress-strain curve is successfully reconstructed without assuming any nonlinear constitutive model.

At the moment, using the current experiment system it is difficult to produce a strain amplitude higher than 0.4 as the specimen deformation goes out of the imaging area. One way to make a larger strain could be to use a short specimen or make a longer distance between the high-speed camera and a specimen surface. The first of these methods is well-suited to the new technique, which is able to cope with the increased number of wave oscillations that would result; however, a short specimen may induce complex strain states. The second method may increase the imaging noise amplitude due to the smaller image resolution. Another possible way to characterize the dynamic behaviour at a larger deformation is to implement the pre-stretching scheme introduced in the previous work [11]. This implementation is currently in progress.

References

1. Field, J.E., Walley, S.M., Proud, W.G., et al.: Review of experimental techniques for high rate deformation and shock studies. Int. J. Impact Eng. **30**(7), 725–775 (2004). doi:10.1016/j.ijimpeng.2004.03.005
2. Davidson, J.S., Fisher, J.W., Hammons, M.I., et al.: Failure mechanisms of polymer-reinforced concrete masonry walls subjected to blast. J. Struct. Eng. **131**, 1194–1205 (2005). doi:10.1061/(ASCE)0733-9445(2005)131:8(1194)
3. Sarva, S.S., Deschanel, S., Boyce, M.C., Chen, W.: Stress–strain behavior of a polyurea and a polyurethane from low to high strain rates. Polymer (Guildf) **48**, 2208–2213 (2007). doi:10.1016/j.polymer.2007.02.058
4. Song, B., Chen, W.: One-dimensional dynamic compressive behavior of EPDM rubber. J. Eng. Mater. Technol. **125**, 294 (2003). doi:10.1115/1.1584492
5. Harrigan, J.J., Ahonsi, B., Palamidi, E., Reid, S.R.: Experimental and numerical investigations on the use of polymer Hopkinson pressure bars. Philos. Trans. A Math. Phys. Eng. Sci. **372**, 20130201 (2014). doi:10.1098/rsta.2013.0201
6. Fatt, M.S.H., Bekar, I.: High-speed testing and material modeling of unfilled styrene butadiene vulcanizates at impact rates. J. Mater. Sci. **39**, 6885–6899 (2004). doi:10.1023/B:JMSC.0000047530.86758.b9
7. Mohotti, D., Ali, M., Ngo, T., et al.: Strain rate dependent constitutive model for predicting the material behaviour of polyurea under high strain rate tensile loading. Mater. Des. **53**, 830–837 (2014). doi:10.1016/j.matdes.2013.07.020
8. Niemczura, J., Ravi-Chandar, K.: On the response of rubbers at high strain rates—I: Simple waves. J. Mech. Phys. Solids **59**, 423–441 (2011). doi:10.1016/j.jmps.2010.09.006
9. Chen, W., Zhang, B., Forrestal, M.J.: A split Hopkinson bar technique for low-impedance materials. Exp. Mech. **39**, 81–85 (1999). doi:10.1007/BF02331109
10. Song, B., Chen, W.: Dynamic stress equilibration in split Hopkinson pressure bar tests on soft materials. Exp. Mech. **44**, 300–312 (2004). doi:10.1007/BF02427897
11. Yoon, S., Giannakopoulos, I., Siviour, C.R.: Application of the Virtual Fields Method to the uniaxial behavior of rubbers at medium strain rates. Int. J. Solids Struct. **69–70**, 553–568 (2015). doi:10.1016/j.ijsolstr.2015.04.017
12. Sutton, M.A., Orteu, J.-J., Schreier, H.: Image Correlation for Shape, Motion and Deformation Measurements. Springer, New York (2009)
13. Pierron, F., Grédiac, M.: The Virtual Fields Method: Extracting Constitutive Mechanical Parameters from Full-Field Deformation Measurements. Springer, New York (2012)
14. Moulart, R., Pierron, F., Hallett, S., Wisnom, M.: Full-field strain measurement and identification of composites moduli at high strain rate with the virtual fields method. Exp. Mech. **51**, 509–536 (2011). doi:10.1007/s11340-010-9433-4
15. Kim, J.H., Lee, G.A., Lee, M.G.: Determination of dynamic strain hardening parameters using the virtual fields method. Int. J. Autom. Technol. **16**, 145–151 (2015). doi:10.1007/s12239-015-0016-3
16. Pierron, F., Sutton, M.A., Tiwari, V.: Ultra high speed DIC and virtual fields method analysis of a three point bending impact test on an aluminium bar. Exp. Mech. **51**, 537–563 (2010). doi:10.1007/s11340-010-9402-y
17. Pierron, F., Zhu, H., Siviour, C.: Beyond Hopkinson's bar. Philos. Trans. R. Soc. A Math. Phys. Eng. Sci. **372**, 20130195 (2014). doi:10.1098/rsta.2013.0195
18. Pierron, F., Forquin, P.: Ultra-high-speed full-field deformation measurements on concrete spalling specimens and stiffness identification with the virtual fields method. Strain **48**, 388–405 (2012). doi:10.1111/j.1475-1305.2012.00835.x
19. Ogden, R.W.: Large deformation isotropic elasticity—on the correlation of theory and experiment for incompressible rubberlike solids. Proc. R. Soc. Lond. A Math. Phys. Sci. **326**, 565–584 (1972). doi:10.1098/rspa.1972.0026

Chapter 23
Inertial Impact Tests on Polymers for Inverse Parameter Identification

F. Davis, F. Pierron, and Clive R. Siviour

Abstract In aircraft and automotive components, polymeric materials such as PMMA are subjected to dynamic loading and deform at moderate (1–100 s^{-1}) and high strain rates (>10^2 s^{-1}). A methodology for calculating the strain-rate dependent parameters of PMMA at high strain rates will be presented. Images of each sample deforming were collected during an inertial impact test with an ultra-high speed camera, recording at 3 Mfps. The full field displacement, strain, and acceleration were input to the virtual fields method to perform an inverse identification of the material parameters.

Keywords High-strain rate • Ultra-high speed camera • Virtual fields method (VFM) • PMMA

23.1 Introduction

Due to its low density and transparency, PMMA is frequently used as a glass substitute. Polymer windows are expected to resist impact loads and can be subjected to high strain rate loading (>10^2 s^{-1}). While the quasi-static behavior of PMMA is well characterized [1, 2], significantly fewer studies have looked into its high strain rate response. PMMA exhibits rate-dependent elastic and failure behavior, with both the modulus and the yield stress becoming sensitive to strain rate above a threshold of approximately 10^3 s^{-1}. The goal of this study is to propose a new experimental technique for quantifying the viscoplastic behavior of glassy polymers at high strain rates. In this manuscript, the results of a preliminary test campaign to validate this novel approach at a single strain rate are presented. First, the protocol for performing inertial impact tests, which relies upon ultra-high-speed imaging, is described. Next, an inverse technique used to identify parameters from full field imaging data called the virtual fields method is introduced. Finally, the results of the test campaign and accuracy of the parameter identification are discussed.

23.2 Experimental Methods

The inertial impact tests were performed on PMMA samples using the gas gun facilities at the Solid Mechanics and Materials Engineering Group at Oxford. Figure 23.1 shows a schematic of the experiment. A gas gun is used to fire a cylindrical projectile towards the waveguide and specimen. The specimen is L = 55 mm long by H = 32 mm tall with a thickness of 4 mm. A grid with a pitch of 1 mm was applied to the specimen using transfer paper. Contact between the waveguide and the projectile closed a custom copper make trigger. A delay time of 13 µs was used when triggering the camera from the copper make trigger to account for the time it takes the wave to propagate through the waveguide to the sample. An ultra-high-speed camera (Kirana, Specialized Imaging) was used to image the sample during the impact test. A total of 180 frames were recorded at a rate of 3 Mfps.

From the images collected, displacement fields were calculated using the grid method. The Grid Method GUI [3] (v. 2.09) was used to generate time-resolved displacement maps of the deformation. Due to the presence of camera noise, the displacement field at each pixel was filtered in the time domain using a third order low pass Butterworth digital filter with a
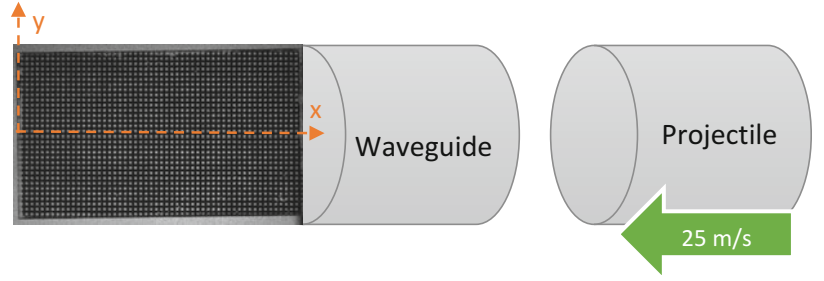
F. Davis (✉) • F. Pierron
Engineering Materials Group, Faculty of Engineering and the Environment, University of Southampton, Southampton SO17 1BJ, UK
e-mail: frances.davis@soton.ac.uk; f.pierron@soton.ac.uk

C.R. Siviour
Department of Engineering Science, University of Oxford, Oxford, UK
e-mail: clive.siviour@eng.ox.ac.uk

normalized cut-off frequency of 0.07. The smoothed displacement was numerically differentiated to obtain the acceleration field. To minimize the influence of spatial noise on the strain, the displacement was spatially filtered using a median filter with a radius of 2 mm.

23.3 Virtual Fields Method

The virtual fields method (VFM) is an inverse technique for the identification of material properties based on the weak form of the equilibrium equation. For dynamic problems, the VFM capitalizes on the inertia developed during high strain-rate tests, treating the acceleration as a volume distributed load cell. The VFM has been well developed for linear elastic problems and the material parameters can be identified by solving a set of linear equations [4].

From the weak from of the equilibrium equation, the principle of virtual work can be written as:

$$-\int_V \boldsymbol{\sigma} : \boldsymbol{\varepsilon}^* dV + \int_S \boldsymbol{T} \cdot \boldsymbol{u}^* dS = \int_V \rho \, \boldsymbol{a} \cdot \boldsymbol{u}^* dV \tag{23.1}$$

where the influence of body forces has been neglected. In Eq. (23.1), $\boldsymbol{\sigma}$ is the stress tensor, $\boldsymbol{u}^*$ and $\boldsymbol{\varepsilon}^*$ are the virtual displacement vector and associated virtual strain tensor, respectively, $\boldsymbol{T}$ is the traction vector on the boundary of the body, ρ is the density of the material, and $\boldsymbol{a}$ is the acceleration vector. The dot product of two vectors is denoted $\boldsymbol{l} \cdot \boldsymbol{m}$, and the double dot product between two tensors is denoted $\mathbf{L} : \mathbf{M}$. The virtual displacement is simply a test function in the weak form of the equilibrium equations and has no physical meaning. The virtual strain is calculated from the virtual displacement using the traditional strain-displacement relationship. If no measurement of the external force is available, their contribution to Eq. (23.1) can be sent to zero by an appropriate selection of $\boldsymbol{u}^*$.

For the particular case of a thin homogenous isotropic sample in a state of plane stress Eq. (23.1) becomes

$$-Q_{11}\int_S \varepsilon_x \varepsilon_x^* + \varepsilon_y \varepsilon_y^* + 2\varepsilon_{xy}\varepsilon_{xy}^* \, dS - Q_{12}\int_S \varepsilon_y \varepsilon_x^* + \varepsilon_x \varepsilon_y^* - 2\varepsilon_{xy}\varepsilon_{xy}^* \, dS = -\int_l \boldsymbol{T} \cdot \boldsymbol{u}^* dl + \rho \int_S \left(a_x u_x^* + a_y u_y^* \right) dS \tag{23.2}$$

where the stress tensor has been written in terms of strain and the stiffness components Q_{11} and Q_{12}. From these stiffness values Poisson's ratio, $\upsilon = Q_{12}/Q_{11}$, and Young's Modulus, $E = Q_{11}(1 - \upsilon^2)$, can be calculated. Using the spatially dense data collected using an imaging technique, such as the grid method or DIC, the integrals in Eq. (23.2) can be approximated as discrete sums. Note that since the area associated with each strain value is the same size, those sums can be written as spatial averages over the field of view (denoted by the over bar).

$$\int_S \varepsilon_x \varepsilon_x^* dS \cong \sum_{n=1}^m \varepsilon_x^{(n)} \varepsilon_x^{*(n)} s^{(n)} = S \overline{\varepsilon_x \varepsilon_x^*} \tag{23.3}$$

Equation (23.2) contains two unknown materials parameters, so two sets of virtual displacements must be defined to form the set of linear equations. To analyze the collected experimental data the following virtual displacements were chosen:

$$\text{Set } 1 : \begin{cases} u_x^* = L - x \\ u_y^* = 0 \end{cases} \quad \text{Set } 2 : \begin{cases} u_x^* = 0 \\ u_y^* = (L - x)\, y/H \end{cases} \tag{23.4}$$

No measurement of the impact force was made during the experiments so the value of the traction on the impact edge is not known. This was easily addressed using the VFM by setting the value of $\boldsymbol{u}^*$ on the impact edge ($x = L$) to zero for both sets of virtual displacements. Substituting Eq. (23.4) into Eq. (23.2), the following linear system was found:

$$\left[\begin{array}{cc} \overline{\varepsilon_x} & \overline{\varepsilon_y} \\ -\varepsilon_y\left(\dfrac{L-x}{H}\right) - 2\varepsilon_{xy}\left(-\dfrac{y}{H}\right) & -\dfrac{\varepsilon_x(L-x)}{H} + 2\varepsilon_{xy}\left(-\dfrac{y}{H}\right) \end{array} \right] \begin{bmatrix} Q_{11} \\ Q_{12} \end{bmatrix} = \begin{bmatrix} \rho\,\overline{a_x(L-x)} \\ \rho\,\overline{a_y(L-x)\,y/H} \end{bmatrix} \tag{23.5}$$

23.4   Results and Discussion

The three PMMA specimens tested were impacted at nominal speed of 25 m/s. Maps of the acceleration, strain, and strain rate in the x direction for sample 2 are shown in Fig. 23.2. The concentrated band in the acceleration map is the stress wave, propagating from right to left in the sample. The strain map shows a band of compressive strain following behind the inertial front. The strain rate reaches a maximum value of around $1100\ \text{s}^{-1}$ as the stress wave passes. Clearly in Fig. 23.2 the wave propagation results in highly heterogeneous maps of acceleration, strain, and strain rate.

By solving Eq. (23.5) at each time step, the value of the Young's Modulus and Poisson's ratio can be identified as a function of time. Figure 23.3 shows the evolution of the elastic parameters for sample 3. While the modulus is relatively stable overtime, Poisson's ratio is far more sensitive to measurement noise leading to oscillations in the identified value. This difference in sensitivity has been previously observed and discussed in [5].

A single value of Young's Modulus and Poisson's ratio can be identified for each sample by assembling a matrix with Eq. (23.5) written for every time step. This will result in an over-determined linear system that can be solved in a least squares sense. To identify Young's Modulus and Poisson's ratio the data collected between 10 and 40 μs was used. The resulting values for each specimen can be found in Table 23.1.

In the literature, the values for E and ν were reported to be 3–6 GPa and 0.33, respectively, at quasi-static strain rates [1, 2]. The values reported in Table 23.1 are in line with the range of quasi-static values found in literature and with previous findings that PMMA shows limited strain rate sensitivity at strain rates below $10^3\ \text{s}^{-1}$ [1]. There is limited data on the strain rate sensitivity of ν, but the results in Table 23.1 suggest that below $10^3\ \text{s}^{-1}$ Poisson's ratio is also insensitive to strain rate.

In summary, full-field deformation data was obtained from the images collected using an ultra high-speed camera. This full-field data was then used as an input to the VFM to perform an inverse identification of the material parameters. In the VFM, no external measurement of the impact force was necessary since the acceleration field was used as a load cell. By solving a set of linear equations, the VFM was able to identify the Young's Modulus and Poisson's ratio of PMMA. In the future, additional test campaigns will be performed increasing the speed of the projectile. If the velocity of the impact is sufficiently high, plastic deformation will be developed and the rate-dependent yield stress of PMMA can be examined.
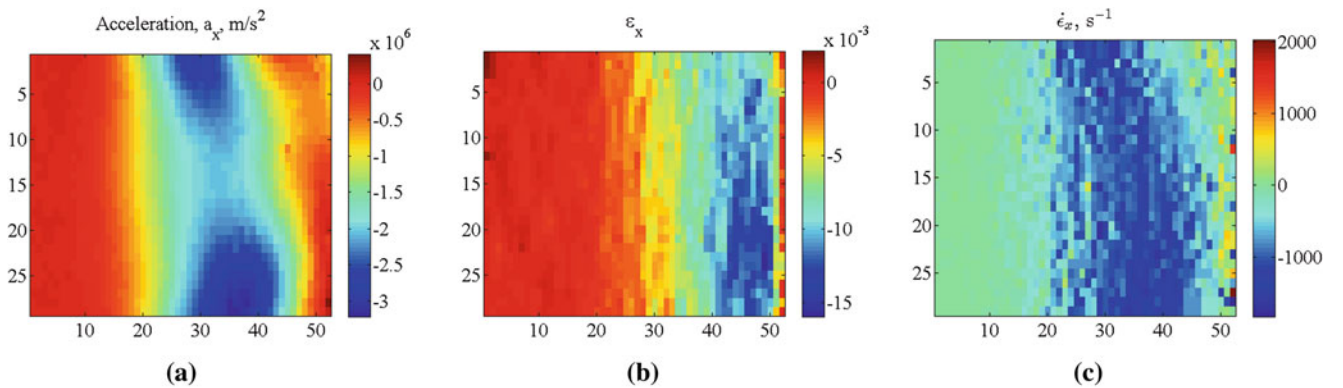

Fig. 23.2 Maps of (**a**) acceleration, (**b**) strain, and (**c**) strain rate in the x-direction for sample 2 at 17 μs
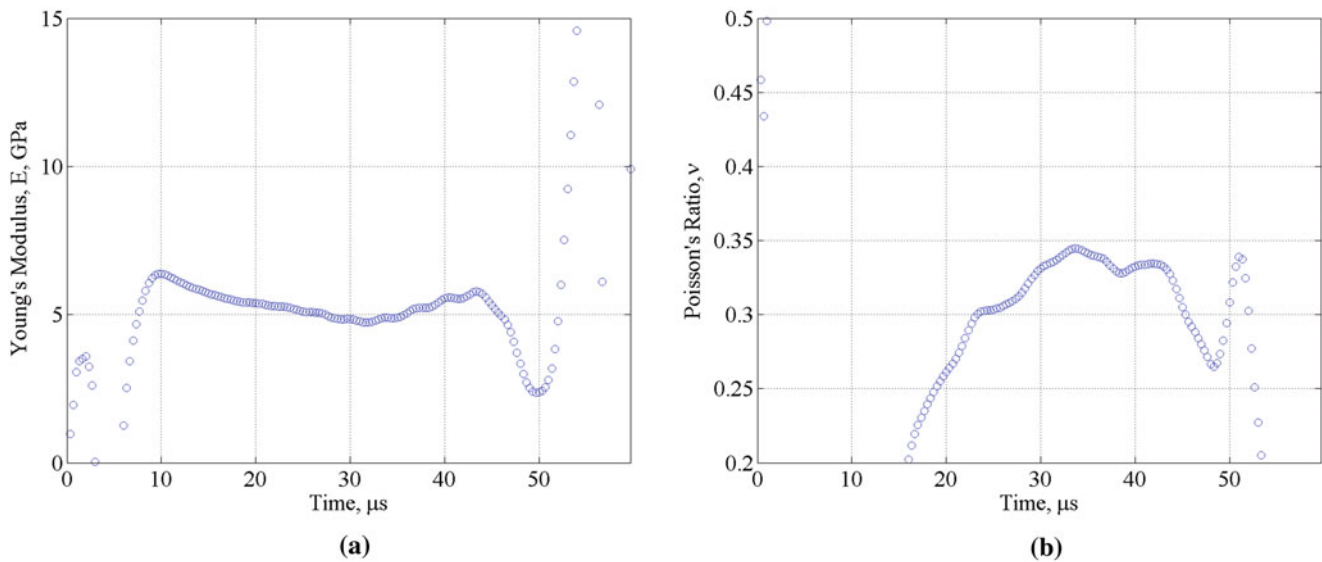
Fig. 23.3 Identified values of (**a**) Young's Modulus and (**b**) Poisson's ratio as a function for time for sample 3

Table 23.1 Identified elastic parameters for PMMA

Specimen No.	Young's Modulus, E (GPa)	Poisson's ratio, ν
1	5.3	0.32
2	5.0	0.31
3	5.0	0.34

References

1. Li, Z., Lambros, J.: Strain rate effects on the thermomechanical behavior of polymers. Int. J. Solids Struct. **38**(20), 3549–3562 (2001). http://doi.org/10.1016/S0020-7683(00)00223-7
2. Greaves, G.N., et al.: Poisson's ratio and modern materials. Nat. Mater. **10**(11), 823–37 (2011). http://doi.org/10.1038/nmat3134
3. Devivier, C., Pierron, F.: Grid method GUI: a tool to process grid images. http://gridmethod.tk/GMGUI_r.php. Last accessed 4 Mar 2016
4. Pierron, F., Grédiac, M.: The Virtual Fields Method. Springer, New York (2012)
5. Pierron, F., et al.: Beyond Hopkinson's bar. Philos. Trans. R. Soc. A Math. Phys. Eng. Sci. **372**(2023), 20130195 (2014). http://doi.org/10.1098/rsta.2013.0195

Chapter 24
Full-Field Identification Methods: Comparison of FEM Updating and Integrated DIC

A.P. Ruybalid, J.P.M. Hoefnagels, O. van der Sluis, and M.G.D. Geers

Abstract Full-field identification methods are increasingly used to adequately identify constitutive parameters to describe the mechanical behavior of materials. This research investigates the more recently introduced, one-step method of Integrated Digital Image Correlation (IDIC) with respect to the most commonly used, two-step method of Finite Element Model Updating (FEMU), which uses a subset-based digital image correlation algorithm.

To make the comparison as objective as possible, both methods are implemented in the most equivalent manner and use the same FE-model. Various virtual test-cases are studied to assess the performance of both methods when subjected to different error sources: (1) systematic errors, (2) poor initial guesses for the constitutive parameters, (3) image noise, (4) constitutive model errors, and (5) experimental errors.

Results show that, despite the mathematical similarity of both methods, IDIC produces less erroneous and more reliable results than FEMU, particularly for more challenging test-cases exhibiting small displacements, complex kinematics, misalignment of the specimen, and image noise.

Keywords Full-field measurement • Inverse methods • Parameter identification • Finite element model updating • Integrated digital image correlation

24.1 Introduction

Proper identification of constitutive model parameters is essential for trustworthy prediction of mechanical material response. Thanks to increased computing power, large data sets can be processed efficiently, enabling rich, *full-field* kinematic information to be analyzed for the identification of such parameters through a single experiment, while relaxing the design requirements on the specimen and the loading conditions.

The most widely used full-field identification method is that of finite element model updating (FEMU) [1, 4, 8, 14], in which model parameters are optimized by iteratively minimizing the difference between a measured displacement field, acquired through, e.g., Digital Image Correlation (DIC) and a simulated displacement field, acquired through finite element (FE) analysis.

More recently, another identification method has been introduced [5, 7, 10–12] that more intimately integrates mechanical descriptions with full-field measurements. The method is termed *Integrated DIC*, and it integrates the (image) correlation procedure and identification procedure into a one-step approach, making it distinct from other methods (such as FEMU), which are two-step approaches whereby post-processing of experimental data precedes the identification procedure.

In the following proceeding, the objective comparison between the performances of the one-step method of IDIC and the two-step method of FEMU is described. To make a fair comparison, both methods are implemented in an equivalent manner and are applied to the same experimental data, and the most important error sources are triggered: (1) systematic errors, (2) poor initial guesses for the parameters of interest, (3) image noise, (4) model errors, and (5) experimental errors.

A.P. Ruybalid • J.P.M. Hoefnagels (✉) • O. van der Sluis • M.G.D. Geers
Department of Mechanical Engineering, Eindhoven University of Technology, P.O. Box 513,
5600 MB Eindhoven, The Netherlands
e-mail: a.p.ruybalid@tue.nl; j.p.m.hoefnagels@tue.nl

24.2 Full-Field Identification Methods

Both identification methods: FEMU and IDIC, will be briefly explained. At the heart of both techniques lies digital image correlation (DIC), in which pixel intensities of subsequent images that have captured the deformation of a material, are correlated in order to calculate *full* displacement fields (encompassing the *full* imaged region of interest of the deformed material).

24.2.1 FEM Updating

In the method of FEM Updating, subset-based DIC is first used to calculate displacement fields $\vec{m}$ of a deforming material during an experiment. Subsequently, these measured fields are compared to simulated displacement fields $\vec{h}$, coming from FE-simulation of a model of the experiment, making use of initial guesses for the constitutive model parameters θ. For a perfect model with accurate model parameters, the simulated field equals the measured field, assuming no errors are made in the determination of either of the fields. Hence, by minimizing a squared residual of the measured and simulated displacements, the model parameters used for simulation are updated in an iterative fashion. The objective function to be minimized is mathematically expressed as follows:

$$\vec{J} = \int_{\tau}\int_{\Omega}\frac{1}{2}\left(\vec{m}(\vec{x},t) - \vec{h}(\vec{x},t,\theta_i)\right)^2 \mathrm{d}\vec{x}\mathrm{d}t. \tag{24.1}$$

The data from all time instances is not sequentially processed, but considered in a single objective function. Displacement fields, whose values depend on the spatial coordinates $\vec{x}$, of different time instances t are stacked to form displacement *blocks* $\vec{m}(\vec{x},t)$ and $\vec{h}(\vec{x},t,\theta_i)$, which are subtracted to produce the block residual $\vec{J}$. The residual is minimized at once for all displacements in space-time, which is defined by the spatial domain Ω and the temporal domain τ.

FEMU is considered a *two-step* method, comprising two iterative procedures, namely: (1) the DIC algorithm, providing the measured displacement fields m and (2) the subsequent identification procedure, in which the residual $\vec{J}$ is iteratively minimized by a Gauss-Newton scheme. A flowchart of this two-step FEMU method is shown in Fig. 24.1.

24.2.2 Integrated DIC

In the method of IDIC only one iterative scheme exists, because the parameter optimization (identification) is integrated directly into the DIC procedure, in which the residual between images is minimized, assuming conservation of brightness, which is mathematically expressed as:

$$f(\vec{x},t_0) \approx g\left(\vec{\Phi}(\vec{x},t)\right) = g\circ\vec{\Phi}(\vec{x},t), \tag{24.2}$$

$$\vec{\Phi}(\vec{x},t) = \vec{x} + \vec{U}(\vec{x},t), \tag{24.3}$$

where f and g are the scalar intensity fields of, e.g., light sensed by a camera sensor, and $\vec{\Phi}$ represents the vector function that maps the pixel coordinates $\vec{x}$ of image f, corresponding to the reference material state, to the pixel coordinates of image g, corresponding to the deformed state. Important to realize is that the mapping function $\vec{\Phi}(\vec{x},t)$ depends on a displacement field $U(\vec{x},t)$, which can be approximated by FE-simulation of a model of the experiment: $U(\vec{x},t) \approx \vec{h}(\vec{x},t,\theta_i)$, which, in turn, depends on the constitutive model parameters θ_i. The image residual Ψ to be minimized is written as:

$$\Psi = \int_{\tau}\int_{\Omega}\frac{1}{2}\left(f(\vec{x},t_0) - g\circ\vec{\Phi}(\vec{x},t,\theta_i)\right)^2 \mathrm{d}\vec{x}\mathrm{d}t. \tag{24.4}$$
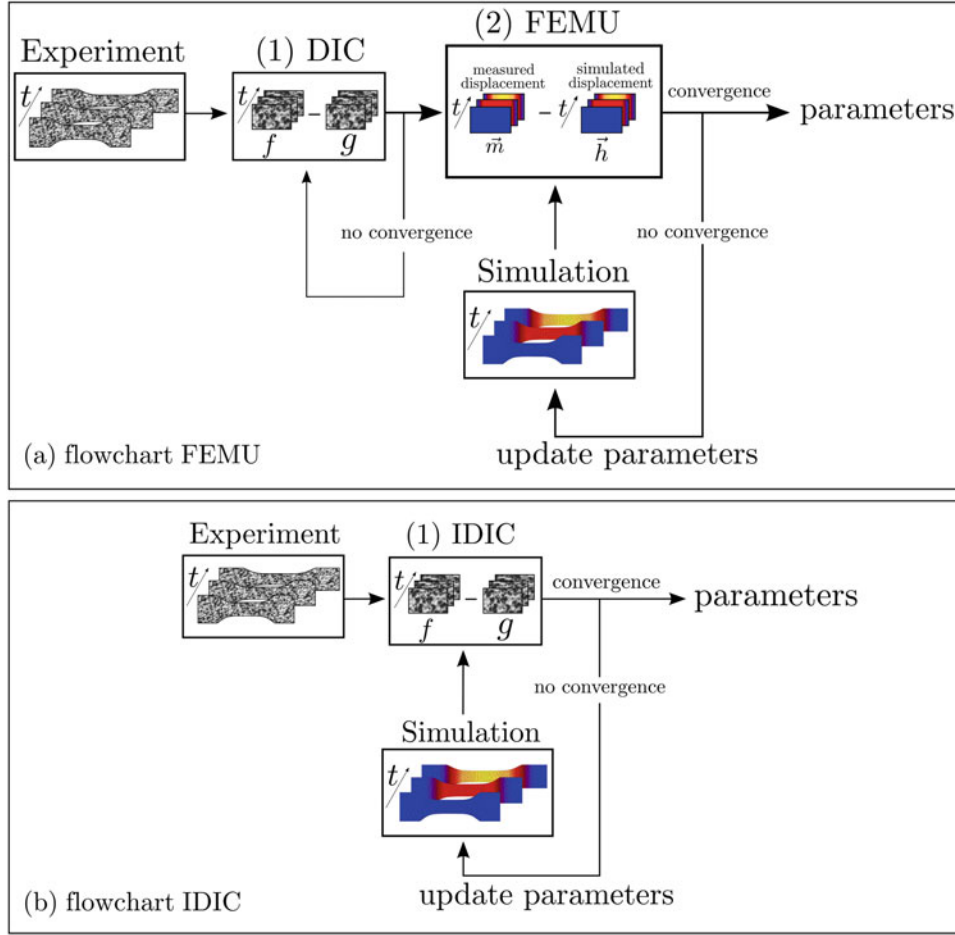
Fig. 24.1 Flowcharts of (**a**) the two-step method of FEMU (note the two iteration loops) and (**b**) the one-step method of IDIC

Hence, optimization of the constitutive parameters θ_i is directly achieved by minimizing this image residual in an iterative manner. Because of the single iterative solution scheme, this method is considered to be a *one-step* procedure. A flowchart of the IDIC method is shown in Fig. 24.1.

24.2.3 Load Residuals

So far, only kinematic information is considered in both identification methods. However, loading data, which is typically measured during mechanical testing, is generally required in the identification process for certain parameters, as conventionally done in FEMU [3, 6] and similarly in IDIC [10]. This is mandatory for parameters that directly influence the force level when only Dirichlet boundary conditions are applied in the FE-simulation of the identification methods.

Similar to the displacement and image residuals, a load residual can be defined as:

$$\vec{P}_F = \int_{\tau} \left(\vec{F}_{\text{exp}}(t) - \vec{F}_{\text{sim}}(t,\theta_i) \right)^2 \mathrm{d}t, \tag{24.5}$$

where $\vec{F}_{\text{exp}}(t)$ is the experimentally measured force, and $\vec{F}_{\text{sim}}(t,\theta_i)$ is the numerically obtained reaction force, which depends on the constitutive parameters θ_i. This objective function is minimized by optimizing the parameters θ_i according to Gauss-Newton optimization, and it can be combined with the minimization processes of the kinematic objective functions of Eqs. (24.1) and (24.4), for FEMU and IDIC, respectively.

24.3 Virtual Experiment

In order to quantitatively assess the errors made by IDIC and FEMU and exclude effects of errors that cannot be quantified, virtual experiments are conducted. An artificial speckle pattern in reference image $f(\vec{x}, t_0)$ is deformed by numerically imposing displacements to produce subsequent images $g(\vec{x}, t)$.

Virtual, uniaxial tensile tests (2D plane stress simulations) were performed on a virtual tensile bar of which an illustration is shown in Fig. 24.2.

To trigger different realistic complexities in material parameter identification, two types of test-case materials were studied, using the above-described specimen and speckle pattern. Tensile stress-strain curves of both test-cases are also shown in Fig. 24.2.

One test-case concerns an isotropic, elastoplastic material, of which the elastic behavior is described by Young's modulus $E = 134$ GPa and Poisson's ratio $\nu = 0.36$. A Von Mises plasticity model is used with isotropic power-law hardening that describes the relation between the yield stress σ_y and the equivalent plastic strain $\overline{\varepsilon}_p$ by the parameters A and m [9].

The second test-case corresponds to a cubic orthotropic, linear elastic material, which is described by three independent model parameters [2]; Young's modulus $E_x = 130$ GPa, Poisson's ratio $\nu_{xy} = 0.28$, and the shear modulus $G_{xy} = 79.6$ GPa. The orthotropy axes coincide with the x- and y-direction of Fig. 24.2. The virtual tensile bar is loaded in x-direction by an applied horizontal tensile force of 2500 N. This results in small displacements with an average value of 0.64 pixel and a maximum strain of 0.25 %, in the center of the tensile specimen (where the strain is largest due to the presence of the notches).

24.4 Results and Conclusions

Both identification methods; FEMU and IDIC, were used to identify the parameters of the two test-case materials. Different error sources were considered in order to assess the methods' robustness to:

1. poor initial guesses for the constitutive parameters
2. modeling errors
3. the presence of image noise
4. experimental errors

Both methods were found to perform equivalently with respect to the first two error sources of (1) poor initial guesses for the parameters and (2) modeling errors.
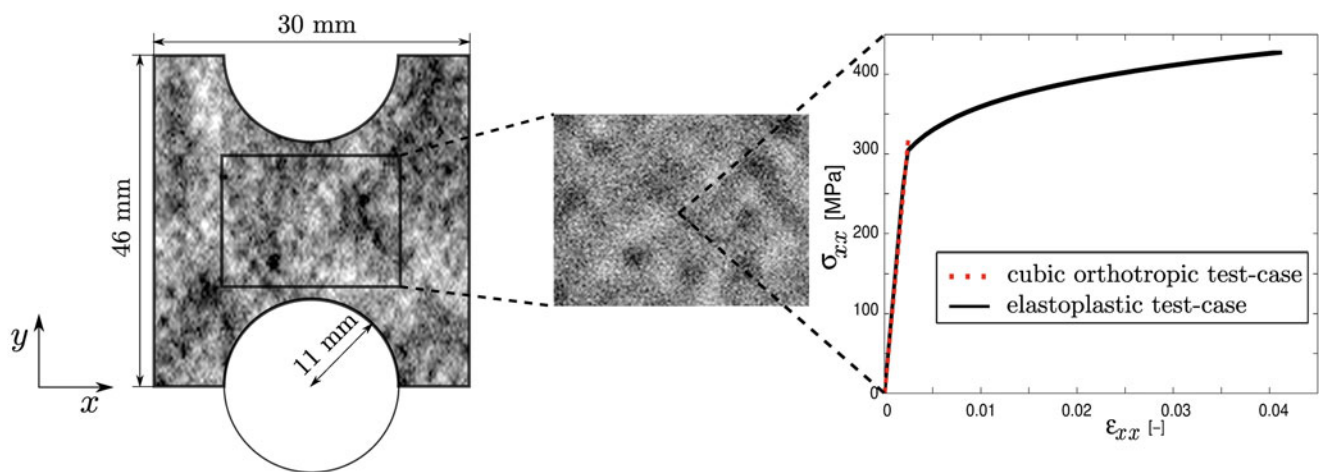

Fig. 24.2 Sketch of a tensile bar with circular notches, used in virtual uniaxial tensile tests, in which loading is applied in the x-direction. The indicated imaged region of the tensile specimen is used for parameter identification purposes. Two test-cases were studied, for which tensile stress-strain curves illustrate the corresponding constitutive behavior
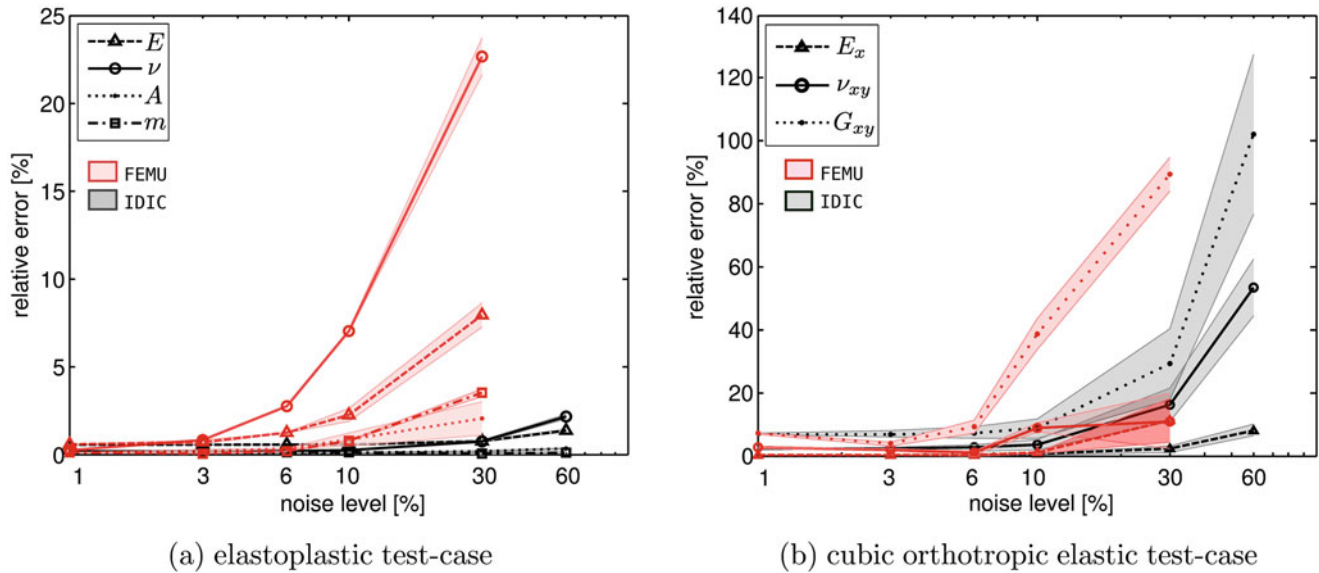
Fig. 24.3 The relative errors of the parameters plotted against different noise levels for (**a**) the elastoplastic and (**b**) cubic orthotropic elastic test-cases

Significant differences between the methods were revealed in the presence of image noise and experimental errors. IDIC is less sensitive to image noise than FEMU, as shown in Fig. 24.3. This results from the high level of regularization of the image correlation procedure by a limited set of degrees of freedom: the mechanical parameters. On the contrary, in FEMU, local subsets are individually correlated during the DIC procedure, requiring a large number of degrees of freedom. The ill-posed DIC problem is thereby less regularized, and the signal-to-noise ratio within each subset is lower.

In the case of an experimental error in the form of misalignment of the specimen with respect to the loading direction of $0.5°$, $1°$, and $2°$, IDIC is found to be more robust when no extra degrees of freedom (DOF) are considered in the identification routine. This is regarded to be caused by the locally, strongly varying speckle pattern resulting in a narrower global minimum in the objective functions minimized in IDIC, while in FEMU, the objective functions contain more gradually varying displacement field differences, resulting in a broader global minimum.

When the y-displacement is considered to be an additional DOF that is optimized along with the mechanical parameters, the FEMU routine is improved and produces results with similar accuracy as IDIC. In Fig. 24.4, these results are summarized.

Furthermore, a test-case of higher complexity, involving a tensile specimen with two sharp notches, reveals the criticality of the subset size in the DIC algorithm of FEMU. Subsets that are too large to capture fine kinematics result in erroneous identification of model parameters, as do subsets smaller than speckle-pattern features. The correctness of the chosen subset size is difficult to assess from the DIC results (e.g., the correlation coefficient), jeopardizing the reliability of FEMU results. The specimen geometry with the notches is shown in Fig. 24.5, together with the results for IDIC and FEMU, utilizing a DIC algorithm with different subset sizes. The subset-size selection, regarded as a DIC-related setting is absent in IDIC, making this method insusceptible to errors resulting from such choices.

These results lead to the conclusion that, despite the mathematical resemblance between both methods, IDIC is less laborious than FEMU and, more importantly, contains less potential error sources because of its one-step nature, resulting in more reliable identification results. This becomes especially pronounced for test-cases involving small displacements, significant image noise, misalignment of the specimen with respect to the loading direction, or more complex kinematics [13].
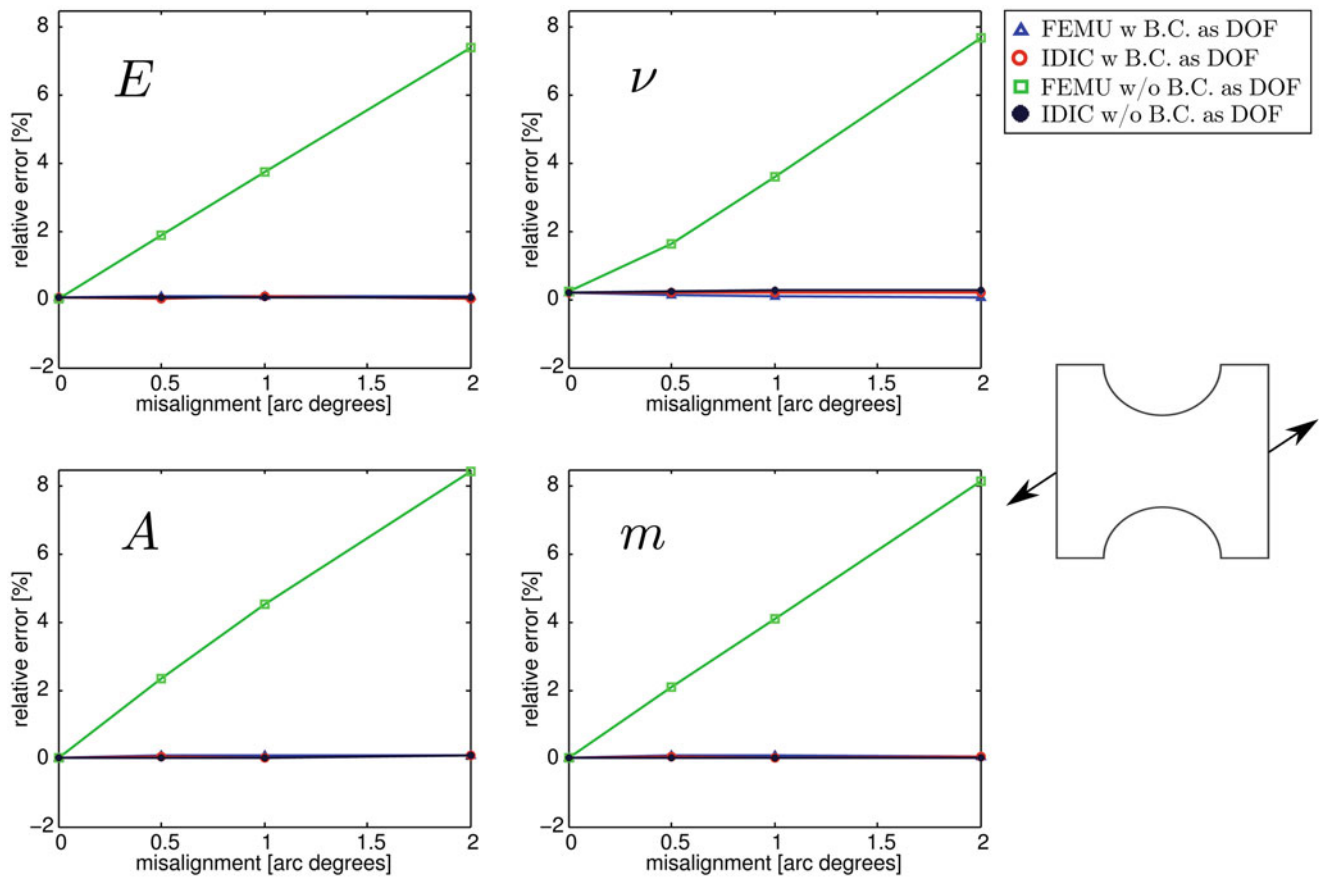
Fig. 24.4 Relative errors of elastoplastic parameters (each in a separate plot) identified by FEMU and IDIC for the case of misalignment of the specimen with respect to the loading direction (schematically illustrated on the right), either with (w) or without (w/o) the boundary condition (B.C.) of y-displacement as a degree of freedom (DOF) in the procedure
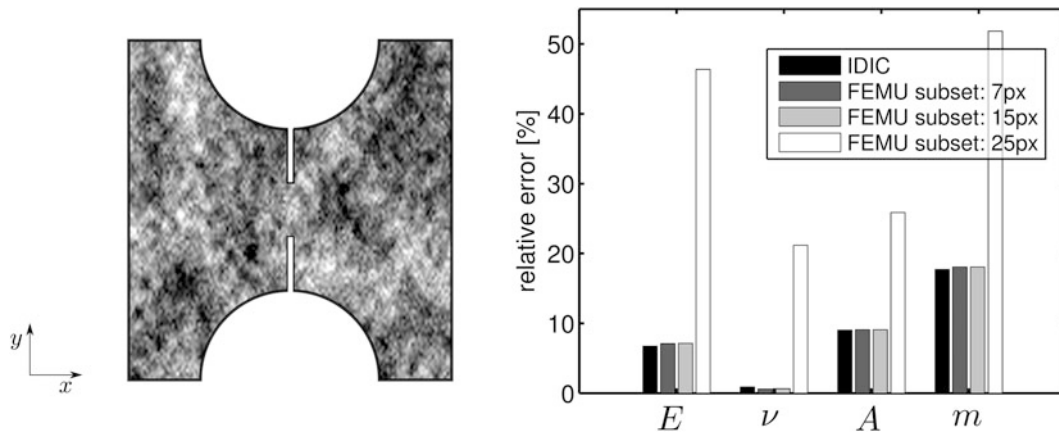

Fig. 24.5 Virtual, sharply notched, elastoplastic tensile bar (*left*). The results of IDIC and FEMU, utilizing different subset sizes in its DIC procedure, reveal the importance of this regularization choice in FEMU

References

1. Collins, J.D., Hart, G.C., Haselman, T.K., Kennedy, B.: Statistical identification of structures. AIAA J. **12** (2), 185–190 (1974)
2. Hopcroft, M.A., Nix, W.D., Kenny, T.W.: What is the Young's modulus of silicon? J. Microelectromech. Syst. **19** (2), 229–238 (2010)
3. Kajberg, J., Lindkvist, G.: Characterisation of materials subjected to large strains by inverse modelling based on in-plane displacement fields. Int. J. Solids Struct. **41** (13), 3439–3459 (2004)
4. Kavanagh, K.T., Clough, R.W.: Finite element applications in the characterization of elastic solids. Int. J. Solids Struct. **7** (1), 11–23 (1971)
5. Leclerc, H., Périé, J.N., Roux, S., Hild, F.: Integrated digital image correlation for the identification of mechanical properties. Lect. Notes Comput. Sci. (Including Subseries Lect. Notes Artifi. Intell. Lect. Notes Bioinform.) **5496** (LNCS), 161–171 (2009)
6. Mahnken, R., Stein, E.: Parameter identification for finite deformation elasto-plasticity in principal directions. Comput. Methods Appl. Mech. Eng. **147** (1–2), 17–39 (1997)
7. Mathieu, F., Leclerc, H., Hild, F., Roux, S.: Estimation of elastoplastic parameters via weighted FEMU and Integrated-DIC. Exp. Mech.. DOI: 10.1007/s11340-014-9888-9 (not yet in print), 2014
8. Mottershead, J.E., Friswell, M.I.: Model updating in structural dynamics: a survey. J. Sound Vibr. **167** (2), 347–375 (1993)
9. MSC Software Corporation: Volume A: Theory and User Information (2013)
10. Réthoré, J., Muhibullah, Elguedj, T., Coret, M., Chaudet, P., Combescure, A.: Robust identification of elasto-plastic constitutive law parameters from digital images using 3D kinematics. Int. J. Solids Struct. **50** (1), 73–85 (2013)
11. Réthoré, J., Roux, S., Hild, F.: An extended and integrated digital image correlation technique applied to the analysis of fractured samples. Eur. J. Comput. Mech. **18**, 285–306 (2009)
12. Roux, S., Hild, F.: Stress intensity factor measurements from digital image correlation: Post-processing and integrated approaches. Int. J. Fract. **140** (1–4), 141–157 (2006)
13. Ruybalid, A.P., Hoefnagels, J.P.M., van der Sluis, O., Geers, M.G.D.: Comparison of the identification performance of conventional fem updating and integrated DIC. Int. J. Numer. Methods Eng., **106** (4), 298–320 (2015)
14. Simon, D., Golinval, J.-D.: Use of whole-field displacement measurements for model updating of blades. Proc.IMAC XXI (131):3–6 (2003)

Chapter 25
Finite Element Stereo Digital Image Correlation Measurement for Plate Model

Jean-Emmanuel Pierré, Jean-Charles Passieux, and Jean-Noël Périé

Abstract The aim of this study is to measure accurately the boundary conditions, namely the displacements and rotations, along the edges of a large part of a composite panel subjected to complex loadings. With classical Stereo Digital Image Correlation techniques (Stereo DIC), the displacement field can only be measured on the upper skin. The rotations are usually estimated *a posteriori* by numerical differentiation and smoothing. Unfortunately additional uncertainties may arise with these steps. Conversely, the use of a Finite Element plate model is proposed here to regularize a Stereo Finite Element-DIC measurement (Stereo FE-DIC). The idea is to use the 3D displacement as the primary unknown of the correlation problem. This approach thus requires projection operators (here based on a pinhole camera model). It allows taking into account distortions directly.

Keywords Stereovision • Digital Image Correlation • Mechanical regularization • Finite element • Distortion

25.1 Introduction

This study is part of a project (ANR VERTEX) that aims to perform tests on composite plates of dimensions $500 \times 500\,\mathrm{mm}^2$ in order to validate damage models (Fig. 25.1). This sample size allows an original scale of structural details and allows treating fundamental problems. The drawback is that non-conventional testing resources in which instrumental *ad hoc* resources have to be used. In this project, it is for instance proposed to use stereo DIC to provide the boundary conditions needed by the partners in order to validate a damage model. For a plate model, boundary conditions are three displacements and two rotations. A stereo correlation method is more likely to measure the displacements of the upper skin, and the rotations are not directly estimated. The rotations can be obtained by *a posteriori* numerical differentiation. Since the measured displacement is noisy, smoothing techniques which usually do not consider the mechanical nature of the measured field are usually exploited. In this work, an integrated DIC approach is preferred. A plate finite element model is used to regularize *a priori* the stereo correlation measurement. A dedicated FE Stereo DIC method was developed accordingly.

More precisely, Digital Image Correlation (DIC) [1–3] consists in measuring the displacement field $\boldsymbol{u}$ between two images, f and g in two different loading conditions (at t_0 and t_1). The displacement field measured on the images is assumed to correspond to the actual displacement of the object. Finite element interpolations have been proposed which allow bridging more efficiently numerical models and experiments [4–8]. Classically, the optical flow problem is written in a weak form over a region called Region of Interest (ROI) which is usually defined by a subset of the reference state image f (Eq. (25.1)).

$$\boldsymbol{u}^{\star} = \underset{\boldsymbol{u}\in L^2(ROI)}{\mathrm{argmin}} \int_{\mathrm{ROI}} [f(\boldsymbol{x}) - g(\boldsymbol{x} + \boldsymbol{u}(\boldsymbol{x}))]^2 d\boldsymbol{x} \tag{25.1}$$

For one increment of Stereo Correlation [2, 9–11], two image registrations are performed independently. Both correlation problems involve unknowns that are not directly related to the physical (3D) displacement $\boldsymbol{U}$ calculated after triangulation and shape variation. Thus, in FE studies, it is difficult to do an Integrated Correlation with a mechanical model in which the unknown is a 3D displacement [12, 13].

J.-E. Pierré (✉) • J.-C. Passieux • J.-N. Périé
Université de Toulouse, Institut Clément Ader (INSA, ISAE, Mines Albi, UPS), CNRS UMR 5312, 3 rue Caroline Aigle, Toulouse 31400, France
e-mail: jepierre@insa-toulouse.fr; passieux@insa-toulouse.fr; jean-noel.perie@iut-tlse3.fr
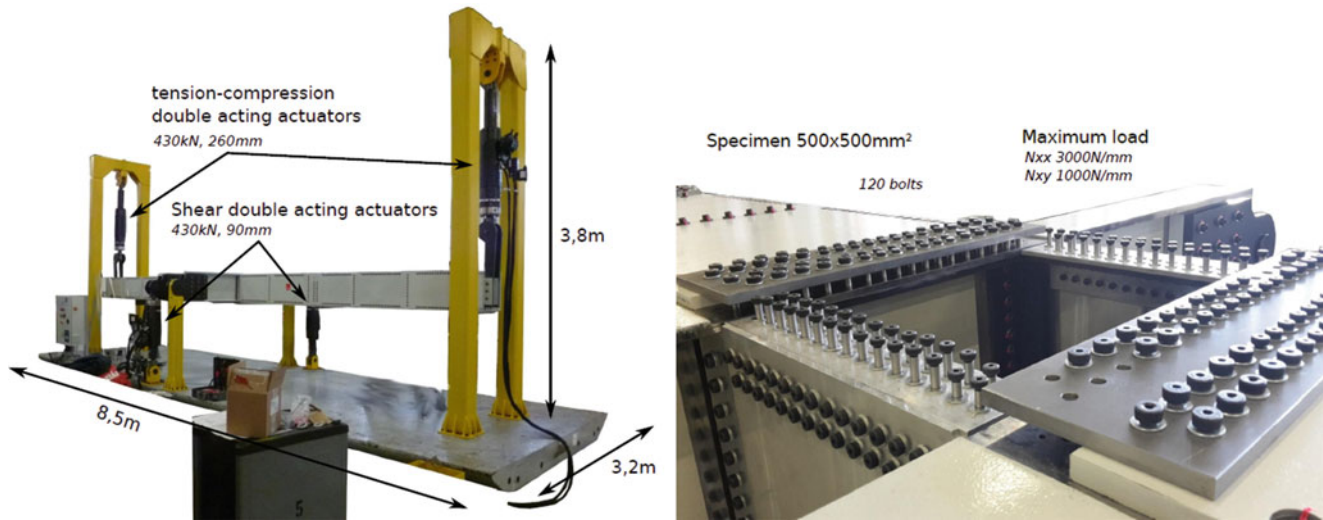
Fig. 25.1 Vertex testing machine: a beam in which a $500 \times 500 \, \text{mm}^2$ plate is fixed on the upper skin

25.2 Physical Quadrature Formulation

In order to consider U as the unknown, the problem is written by considering the projectors P_c of each camera (Eq. (25.2)), extending to Stereo Correlation what is done in [14] in the context of calibration:

$$U^{\star} = \underset{U \in L^2(\Omega)}{\text{argmin}} \sum_c \int_\Omega [f_c(P_c(X)) - g_c(P_c(X + U(X)))]^2 dX \tag{25.2}$$

A classical quadrature in FE-DIC implies a bias because the quadrature is done after projection of the nodes of the mesh. Here, this method considers for each camera c a projection model, denoted P_c, which maps the coordinates X (in meter) of a point in the physical space to the coordinates x (in pixel) of its projection onto the image plane (Fig. 25.2). The quadrature is in the physical space Ω defined by the mesh instead of a ROI included on an image. Moreover, with the projectors, it is possible to consider the calibration, and so, the distortions [15].

25.3 Mechanical Regularization

Since physical displacement U the can now be measured, it is easier to add mechanical regularization terms. In this study, a Mindlin-Reissner plate model is used as an example. It involves five parameters: three displacements and two rotations at the middle plane (U^0, θ^0) (Fig. 25.3). With the cameras, the displacement U is measured on the upper skin, *i.e.*, at $x_3 = h/2$ (Eq. (25.3)).

$$\begin{cases} U_1\left(x_1, x_2, \dfrac{h}{2}\right) = U_1^0(x_1, x_2) + \dfrac{h}{2}\theta_1^0(x_1, x_2) \\[2mm] U_2\left(x_1, x_2, \dfrac{h}{2}\right) = U_2^0(x_1, x_2) + \dfrac{h}{2}\theta_2^0(x_1, x_2) \\[2mm] U_3\left(x_1, x_2, \dfrac{h}{2}\right) = U_3^0(x_1, x_2) \end{cases} \tag{25.3}$$

The rotations could be obtained indirectly by measuring the displacement on a band of elements [16]. Here, the idea is to consider a simple projector which gives the upper skin displacement U with a five dimensions field $V = \left(U^0, \, \theta^0\right)$ describing the middle plane behavior. Thus, with two more unknowns, a mechanical regularization based on an "Integrated" formulation is needed [13, 17, 18]. The goal is to consider both optical and mechanical contributions (Eq. (25.4)):

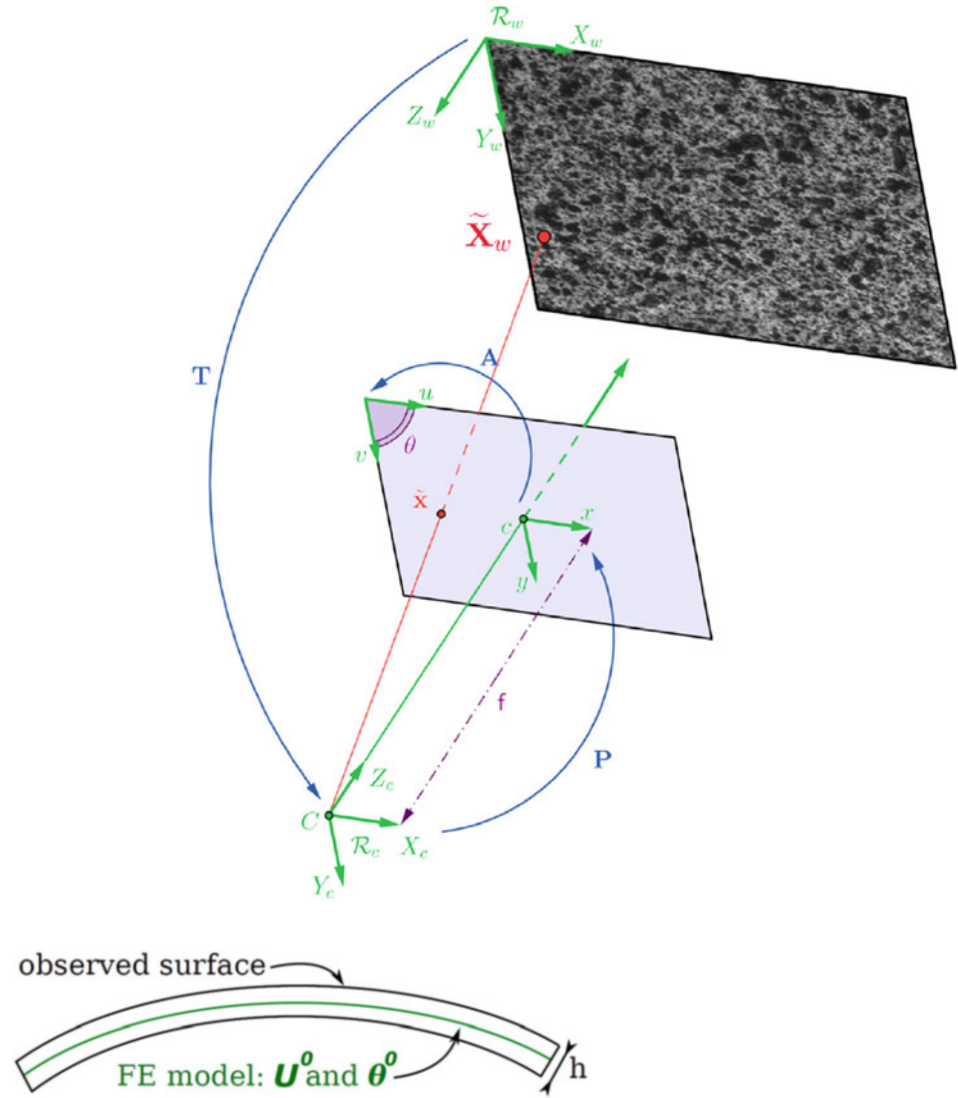**Fig. 25.3** Plate model: the observed surface gives access to the displacement U, but the main unknowns are both displacements and rotations at the middle plane $V = \left(U^0, \, \theta^0 \right)$

$$V^{\star} = \underset{V \in L^2(\Omega)}{\operatorname{argmin}} \frac{1 - l_0 - l_1}{m_0} \sum_c \int_{\Omega} [f_c(P_c(X)) - g_c(P_c(X + U(X)))]^2 dX + \frac{l_0}{k_0} \overline{F}_{int}^T \overline{F}_{int} + \frac{l_1}{k_1} TV \qquad (25.4)$$

The rotations could be obtained indirectly by measuring the displacement on a band of elements [16]. Here, the idea is to consider a simple projector which gives the upper skin displacement U with a five dimensions field $V = \left(U^0, \, \theta^0 \right)$ describing the middle plane behavior. Thus, with two more unknowns, a mechanical regularization based on an "Integrated" formulation is needed [13, 17, 18]. The goal is to consider both optical and mechanical contributions (Eq. (25.4)):

25.4   Conclusion

A Finite Element Stereo Digital Image Correlation method directly written in the world reference system is presented. It enables the use of the physical displacement as the primary unknown. A linear elastic model based on a plate formulation is used to measure regularized FE degrees of freedom in a band of elements around a detail. The latter measurements are then

used as boundary conditions in nonlinear FE simulation of the behavior of the inner part of the composite specimen. The long-term goal is to perform multiscale identification following the approach [8] initially developed in 2D.

References

1. Horn, B.K.P., Schunck, B.G.: Determining optical flow. Artif. Intell. **17**(1–3), 185–203 (1981)
2. Lucas B.D., Kanade T.: An iterative image registration technique with an application to stereo vision. In: Proceedings of Imaging Understanding Workshop, pp. 121–130 (1981)
3. Sutton, M.A., Wolters, W.J., Peters, W.H., Ranson, W.F., McNeill, S.R.: Determination of displacements using an improved digital correlation method. Image Vis. Comput. **1**(3), 133–139 (1983)
4. Sun, Y., Pang, J.H.L., Wong, C.K., Su, F.: Finite element formulation for a digital image correlation method. Appl. Optics **44**(34), 7357–7363 (2005)
5. Hild, F., Roux, S.: Digital image correlation: from displacement measurement to identification of elastic properties—a review. Strain **42**(2), 69–80 (2006)
6. Fehrenbach, J., Masmoudi, M.: A fast algorithm for image registration. C.R. Math. **346**(9–10), 593–598 (2008)
7. Hild, F., Roux, S.: Comparison of local and global approaches to digital image correlation. Exp. Mech. **52**(9), 1503–1519 (2012)
8. Passieux J.-C., Bugarin F., David C., Périé J.-N., Robert L.: Multiscale displacement field measurement using digital image correlation: application to the identification of elastic properties. Exp. Mech. 55(1):121– 137 (2015)
9. Kahn-Jetter, Z.L., Chu, T.C.: Three-dimensional displacement measurements using digital image correlation and photogrammic analysis. Exp. Mech. **30**(1), 10–16 (1990)
10. Luo, P.F., Chao, Y.J., Sutton, M.A., Iii, W.H.P.: Accurate measurement of three-dimensional deformations in deformable and rigid bodies using computer vision. Exp. Mech. **33**(2), 123–132 (1993)
11. Orteu, J.-J., Bugarin, F., Harvent, J., Robert, L., Velay, V.: Multiple-camera instrumentation of a single point incremental forming process pilot for shape and 3d displacement measurements: methodology and results. Exp. Mech. **51**(4), 625–639 (2010)
12. Besnard, G., Hild, F., Lagrange, J.-M., Martinuzzi, P., Roux, S.: Analysis of necking in high speed experiments by stereocorrelation. Int. J. Impact Eng. **49**, 179–191 (2012)
13. Réthoré, J., Muhibullah, Elguedj T., Coret M., Chaudet P., Combescure A.: Robust identification of elastoplastic constitutive law parameters from digital images using 3d kinematics. Int. J. Solids Struct. **50**(1), 73–85 (2013)
14. Beaubier, B., Dufour, J.-E., Hild, F., Roux, S., Lavernhe, S., Lavernhe-Taillard, K.: CAD-based calibration and shape measurement with stereoDIC: principle and application on test and industrial parts. Exp. Mech. **54**(3), 329–341 (2014)
15. Pierré, J.-E., Passieux, J.-C., Périé, J.-N., Bugarin, F., Robert, L.: Unstructured finite element-based digital image correlation with enhanced management of quadrature and lens distortions. Opt. Lasers Eng. **77**, 44–53 (2016)
16. Sztefek, P., Olsson, R.: Tensile stiffness distribution in impacted composite laminates determined by an inverse method. Compos. A Appl. Sci. Manuf. **39**(8), 1282–1293 (2008)
17. Roux, S., Hild, F.: Stress intensity factor measurements from digital image correlation: post-processing and integrated approaches. Int. J. Fract. **140**(1–4), 141–157 (2006)
18. Réthoré, J.: A fully integrated noise robust strategy for the identification of constitutive laws from digital images. Int. J. Numer. Methods Eng. **84**(6), 631–660 (2010)

Chapter 26
Measurement of Orthogonal Surface Gradients and Reconstruction of Surface Topography from Digital Gradient Sensing Method

Chengyun Miao and Hareesh V. Tippur

Abstract Shape and surface topography evaluation from measured orthogonal slope/gradient data is of considerable engineering significance as many full-field optical sensors and interferometers readily output such a data accurately. This has applications ranging from metrology of optical and electronic elements, surface profile estimation, wave front and shape reconstruction, to name a few. In this context, a recently developed non-contact, full-field optical method called Digital Gradient Sensing (DGS) capable of measuring small angular deflections of light rays (~10^{-4} degree) is used to measure surface slopes of a silicon wafer subjected to mechanical deformations. A robust Higher-order Finite-difference-based Least-squares Integration (HFLI) scheme in the Southwell configuration is developed to reconstruct the surface topography. It involves solving a set of integration equations to compute the values of out-of-plane deflections based on least-squares approach.

Keywords Digital gradient sensing • Reconstruction of surface topography • Electronic elements • Integration based on least-squares • Southwell configuration

26.1 Introduction

There is a demand for an accurate, non-contact evaluation of surface topography of objects. Some optical sensors such as the Shack–Hartmann wave-front sensor [1], the lateral shearing interferometers [2], and the pyramid sensor [3] have all been used to measure the surface gradients. Integration algorithms are applied then to convert the measured gradients into topographic information. It can be concluded that a highly accurate, non-contact method for measuring surface gradients in combination with an accurate integration method are among the key factors to satisfactorily reconstruct surface topography.

In recent years, digital image correlation (DIC) methods have become rather popular for measuring deformations, two or all three orthogonal displacements in the whole field, as they offer many advantages besides directly providing the required information in the digital form [4]. By taking advantage of this, a new full-field optical method called reflection-mode Digital Gradient Sensing (r-DGS) method has been proposed recently for measuring two orthogonal small angular deflections of light rays [5]. Converting the orthogonal slope data into surface topography is quite valuable. There are several two-dimensional integration methods reported in the literature that could be employed for this purpose. Huang et al. [6] compared three families of two-dimensional integration methods: (a) the Finite-difference-based least-squares integration methods, (b) the transform-based integration methods and (c) the Radial basis function based integration methods. Their performance, advantages and weaknesses are discussed in details for specific cases. Based on their observations, Li et al.'s algorithm [7] called the Higher-order Finite-difference-based Least-squares Integration (HFLI) scheme in the Southwell configuration is selected in the current work.

26.2 Experimental Setup and Working Principles

A schematic of the experimental setup for (r-DGS) used to measure surface slopes is shown in Fig. 26.1. A digital camera, a reflective planar specimen, a micrometer, a beam splitter and a target plate are included in the figure. The target plate is decorated with random speckles using alternate mists of black and white paints. The beam splitter is placed between the

C. Miao • H.V. Tippur (✉)

Department of Mechanical Engineering, Auburn University, Auburn, AL 36849, USA

e-mail: htippur@eng.auburn.edu

Fig. 26.1 Schematic of
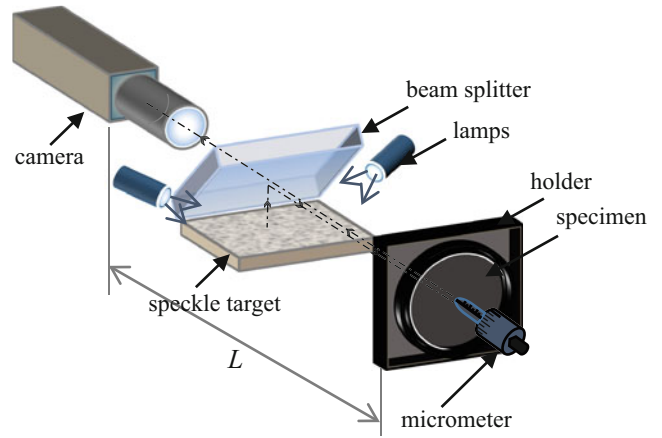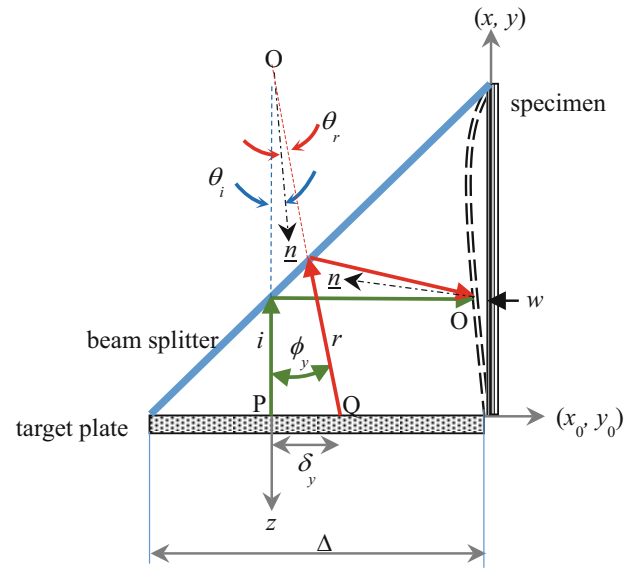r-DGS experimental setup

Fig. 26.2 Schematic
explaining the working
principle of r-DGS

specimen and target plate at an angle of 45° to the optical axis of the setup. For simplicity, the angular deflections of light rays only in the y-z plane are shown in Fig. 26.2. Initially, a point P on the target plate is recorded by the camera through a point O when the specimen is in its undeformed state. When the specimen suffers out-of-plane deformation, a neighboring point Q on the target gets recorded by the camera through O. OP makes an angle ϕ_y with OQ and $\phi_y = \theta_i + \theta_r$ where θ_i and θ_r ($=\theta_i$) are incident and reflected angles relative to the normal to the specimen. The two orthogonal surface slopes can be expressed as $\frac{\partial w}{\partial y:x} = \frac{1}{2}\tan(\phi_{y:x})$. The local displacements $\delta_{y\,:\,x}$ can be measured by correlating the undeformed image of the specimen with respect to the deformed image. Finally, the two orthogonal surface slopes can be determined using [5]:

$$\frac{\partial w}{\partial y : x} = \frac{1}{2}\tan(\phi_{y:x}) \approx \frac{1}{2}(\phi_{y:x}) \approx \frac{1}{2}\left(\frac{\delta_{y:x}}{\Delta}\right) \tag{26.1}$$

where Δ is the distance between the specimen and target plate and small angle approximation is evoked.

26.3 Wafer Subjected to Central Loading

The feasibility of HFLI method used in conjunction with r-DGS to obtain mechanically applied out-of-plane deformation maps for a deformed thin silicon wafer subjected to central loading was considered next. A polished 360 μm thick silicon wafer was used in the experiment. A Nikon D100 digital SLR camera was focused on the target via the polished face of the

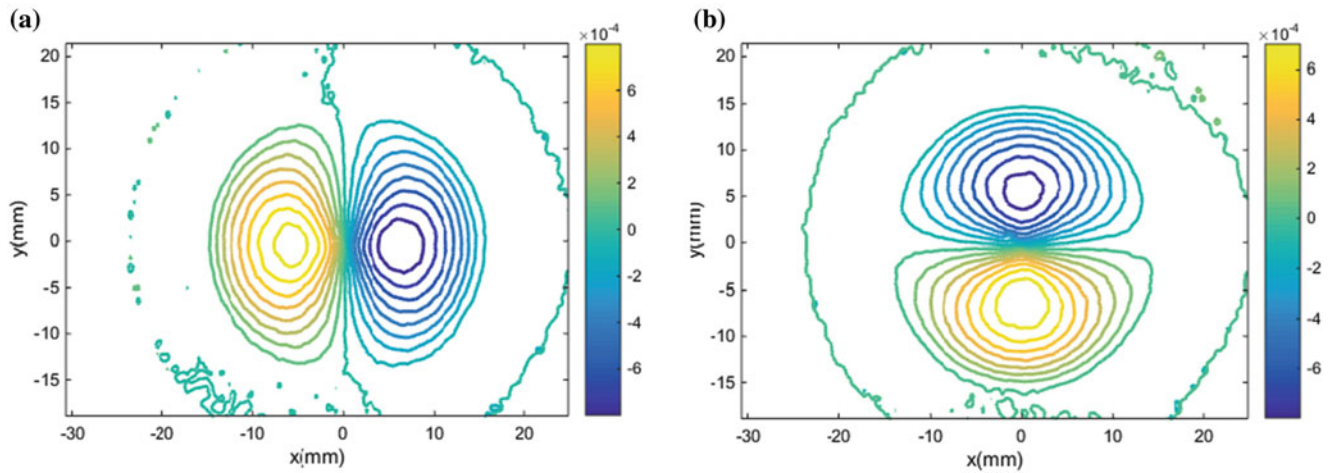**Fig. 26.3** Results from r-DGS for a clamped silicon wafer subjected to central deflection of 10 μm: (**a**) contours of $w_{,x}$ (**b**) contours of $w_{,y}$. *Note*: (0, 0) is made to coincide with the loading point
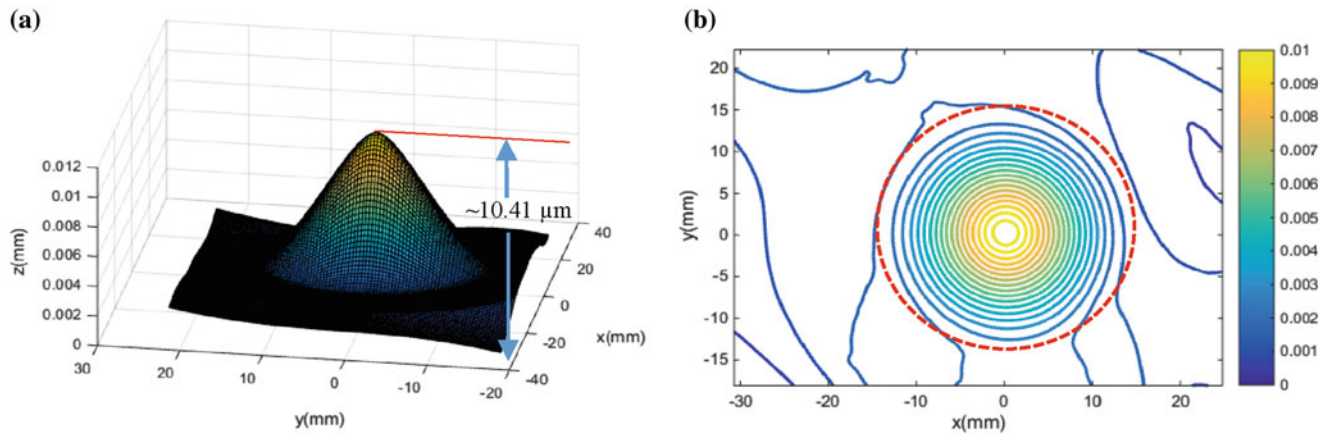

Fig. 26.4 Surface topography calculated via 2D integration using surface slope data and HFLI method: (**a**) 3D surface representation of reconstructed surface, (**b**) out-of-plane displacement (*w*) contours (0.5 μm increments). *Note*: (0, 0) is made to coincide with the loading point; red circle indicates the edge of the circular aperture of the steel washer

silicon wafer. When the silicon wafer was under no load, an 8-bit reference image was recorded. Then, a known central out-of-plane displacement, $w = 10 \pm 1$ μm, was imposed on the silicon wafer using the micrometer tip and speckle images corresponding to the deformed states of the wafer were recorded. By correlating each of these speckle images with the reference image, the local displacements $\delta_{y \,:\, x}$ in the region of interest were measured.

The two orthogonal surface slope contours, $\frac{\partial w}{\partial x}$ and $\frac{\partial w}{\partial y}$ measured from r-DGS are shown in Fig. 26.3. The contours are plotted at increments of 100 micro-radians in the figure. It can be observed that the magnitude of contours of $\frac{\partial w}{\partial x}$ and $\frac{\partial w}{\partial y}$ are symmetric about $x = 0$ and $y = 0$ with a high concentration of contours near the loading point. As expected, slopes are zero along the circular edge (and beyond) of the Si wafer in the glued portion and near the loading point with a gradual transition in the intermediate region. The reconstructed 3D surface computed using integration of surface slope data and HFLI computations is plotted in Fig. 26.4a. Figure 26.4b shows the corresponding contours of out-of-plane displacements (*w*) at 0.5 μm increments. The circular contours in Fig. 26.4b demonstrate that the shape of the reconstructed figure matches well with the reality of the experiment both qualitatively and quantitatively. (Note that for all the plots in Figs. 26.3 and 26.4, the origin is made to coincide with the loading point.) The peak value of the height of the reconstructed 3D surface is 10.41 μm with an acceptable error of about 4 %. The errors are attributed to a combined effect of (a) micrometer backlash and human errors while imposing the out-of-plane displacement, (b) the non-uniformity and finite compliance of the epoxy adhesive used to 'clamp' the Si wafer to the steel plate, (c) errors due to DGS measurements as well as integration errors in the HFLI method. It should also be mentioned that the reconstructed surface along the glued boundary of the wafer shows non-zero deflection (approximately 1 μm instead of zero). This is attributed to a combination of reconstruction errors as well as compliance of the epoxy glue layer.

26.4   Conclusion

In this work, the feasibility of surface profile evaluation from reflection mode Digital Gradient Sensing (r-DGS) method is demonstrated. This is accomplished by coupling r-DGS output with a Higher-order Finite-difference-based Least-squares Integration (HFLI) scheme implemented in the Southwell configuration. The surface profile measurement is demonstrated successfully using a 'clamped' reflective Si wafer subjected to out-of-plane concentrated load applied centrally in the experiment. The imposed deflection has been recovered using the HFLI scheme with good accuracy relative to the accuracy of the micrometer used. The recovered values show approximately 5 % deviation from the expected value. The reconstruction has also revealed non-zero out-of-plane deflections in the 'clamped' regions of the plate due to the compliance of the epoxy adhesive layer.

References

1. Malacara-Doblado, D., Ghozeil, I.: Hartmann, Hartmann–Shack, and other screen tests. In: Optical Shop Testing. Wiley (2007)
2. Strojnik, M., Paez, G., Mantravadi, M.: Lateral shear interferometers. In: Optical Shop Testing. Wiley (2007)
3. Ragazzoni, R.: Pupil plane wavefront sensing with an oscillating prism. J. Mod. Opt. **43**, 289–293 (1996)
4. Sutton, M.A., Orteu, J.J.: Image Correlation for Shape, Motion and Deformation Measurements. Springer, New York (2009)
5. Periasamy, C., Tippur, H.V.: A full-field reflection-mode digital gradient sensing method for measuring orthogonal slopes and curvatures of thin structures. Meas. Sci. Technol. **24**, 025202 (2013)
6. Huang, L., Idir, M., Zuo, C., Kaznatcheev, K., Zhou, L., Asundi, A.: Comparison of two-dimensional integration methods for shape reconstruction from gradient data. Opt. Laser Eng. **64**, 1–11 (2015)
7. Li, G., Li, Y., Liu, K., Ma, X., Wang, H.: Improving wave front reconstruction accuracy by using integration equations with higher-order truncation errors in the Southwell geometry. J. Opt. Soc. Am. A **2013**, 1448–1459 (2013)

Chapter 27
Opportunities for Inverse Analysis in Dynamic Tensile Testing

Steven Mates and Fadi Abu-Farha

Abstract Dynamic tensile testing using Kolsky Bar methods are used to assess crashworthiness of new structural materials needed for lightweight automotive design. High speed Digital Image Correlation (DIC) measurements routinely show that the strain experienced by dynamic tensile specimens deviates markedly from what is expected from the original strain wave analysis techniques used in tensile Kolsky bar metrology. Deviations can be manifest either by different average strain values over the gage section, or by departures from strain uniformity, or both. The former can be attributed to plastic yielding in the specimen outside the gauge section, while the latter concerns specimen geometry and material hardening effects. These issues are sometimes difficult to eliminate through simple modifications of the sample or the test design. Finally, it is of interest to make use of the data beyond necking, where the strain state departs significantly from ideal conditions. These metrology issues lend themselves to solution by inverse methods, where full field strain measurements and global load measurement data are available. In this paper we describe typical measurement data and explore methods to identify the constitutive response from dynamic tensile tests.

Keywords High strain rate • Advanced high strength steels • Digital image correlation • Finite element analysis • Virtual fields method

27.1   Introduction

High strain rate tensile testing of Advanced High Strength Steels (AHSS) are of interest to automotive manufacturers who need to assess the crashworthiness of these new materials that are being developed to make lighter, more fuel-efficient vehicles. Crashworthiness, in a relative sense, is estimated from dynamic strength and ductility obtained from stress-strain curves measured to failure. Crash performance is analyzed in a more absolute sense by large finite element simulations of full-scale vehicle impact problems, which relies on full stress-strain curves over a range of strain rates, to define the material response up to, but not including, the fracture point. Modeling fracture requires many additional mechanical tests that are not discussed here [1].

In the past several years it has become apparent that traditionally-designed dynamic tensile tests, performed using Kolsky Bar methods can produce flawed results. High speed Digital Image Correlation (DIC) measurements show that the strain experienced in specimens can deviate markedly from what is indicated using traditional Kolsky bar data analysis methods [2]. These deviations can be manifest in a variety of ways. Typically the strain measured by DIC methods in the gage section is substantially less than indicated by Kolsky bar data analysis, owing to some amount of plastic strain occurring outside the nominal gage section. In addition, strain non-uniformities arise when small gage length specimens are used to achieve high overall strain rates, rapid force equilibration and to promote fracture. The ASTM E8 standard for static tensile testing calls for a minimum ratio of gage length to gage width of 8, whereas ISO 26203-1:2010, a standard for dynamic testing, allows for ratios as low as 2. For some materials, particularly high strength ones that have limited strain hardening capacity such as most AHSSs, highly non-uniform strain distributions can result [3]. One way to combat this is to customize the specimen geometry for each individual material. However, this is a daunting prospect and makes it difficult to compare different materials on an equivalent strain rate basis. An alternative is to use so-called inverse methods, which may be employed to provide more accurate estimates of material behavior from non-ideal experiments. In addition, opportunities exist to use

S. Mates (✉)
National Institute of Standards and Technology, 100 Bureau Drive, Gaithersburg, MD, USA
e-mail: smates@nist.gov

F. Abu-Farha
Clemson University—International Center for Automotive Research, Greenville, SC 29607, USA

inverse methods to extract material information from portions of a Kolsky bar test that traditionally are ignored: the ringup portion of the test, where the forces and strain rates are varying, and the post-necking behavior where tri-axial stresses develop that cannot be analyzed using load-deflection measurements unless approximate Bridgeman-type correction methods are applied [4].

The literature is rich and growing fast on inverse method techniques and applications. Review papers on inverse methods have described different methods considered and benefits and drawbacks of the various approaches [5]. One significant distinction we note is whether or not finite element analysis (FEA) is performed. The Virtual Fields Method (VFM) is a powerful technique that can identify material parameters directly from DIC strain field data without performing expensive FEA. Instead, parameters can be obtained simply by solving a small linear system of equations for elasticity problems, or by minimizing a cost function for plasticity problems [6]. More recently, the dynamic VFM (dVFM) has been developed that uses acceleration field information derived from DIC displacement field measurements to estimate internal forces [7]. Avoiding expensive FEA computations greatly improves speed and reduces the cost of the analysis, and many practical applications have shown remarkable accuracy when the method is expertly applied. The VFM method is limited, however, to two dimensional problems because the DIC measurements upon which it relies can measure only surface strain fields [6]. FEA-based methods avoid this problem, in that results can be obtained without three dimensional data. Another benefit of using FEA-based inverse methods is that one can use the same numerical approximation method to identify material behavior that is used to solve problems of practical significance. This ability minimizes errors that can arise when numerical approximation methods are mismatched.

In this paper we explore opportunities to apply either VFM or FEA-based inverse methods to better leverage experimental measurements from Kolsky bar strain gage signals and high speed DIC displacement field data to experimental results that may be flawed due to specimen geometry or to portions of the experiments that have not traditionally been used to enhance our understanding of material behavior.

27.2 Results

Three aspects of dynamic tensile testing that may lend themselves to inverse methods are considered here. First, an initial "ringup" period exists in the Kolsky bar test where force equilibrium has yet to develop and the data are therefore considered unreliable and ignored. Second, depending on the test geometry and material hardening characteristics, the strain in the gage section can be non-uniform after force equilibrium is established due to end effects. Third, after the onset of localized necking through to failure when uni-axial analysis becomes inappropriate. We note that other localization phenomena exist that may provide opportunities for inverse analysis, such as strain localization due to Portevin-Le Chatelier banding, are not considered here. The three portions of the dynamic tensile test are now considered in order.

27.2.1 Ringup

The ordinary way to treat data during the ringup portion of a Kolsky bar test is to ignore it, on the reasonable grounds that the stress and strain state is highly non-uniform and the strain rate is varying rapidly. These are, however, the exact conditions that are exploited by the dVFM [7], which depends on the presence of significant accelerations within the test piece that can be measured with DIC to provide dynamic force information. Typical high speed digital cameras used for dynamic material measurements, such as the ones used in this study, operate at about 100,000 frames per second (100 kHz) and can measure displacement and strain fields with adequate spatial resolution for a tensile Kolsky Bar test. We also note that force and displacement information provided by Kolsky bar strain gage data must be acquired at 200 kHz or more to be fully resolved [8]. Thus typical high speed cameras may not acquire DIC information fast enough to capture the real acceleration fields to make proper use of the dVFM method. Although there are more advanced cameras that can meet or exceed strain gage measurement rates, they can be quite expensive and may also be limited in terms of the total number of frames that can be captured.

In Fig. 27.1 we compare the acceleration obtained from a three dimensional (3D) surface DIC measurement using typical high speed camera equipment and resolution (90,000 fps, 128 × 288 pixels, 1 μs exposure, 15 pixel DIC subset with 3 pixel offset) with the acceleration predicted from an analysis of the reflected strain pulse from the bar end, which is recorded at 2 MHz using a high speed oscilloscope. The sample in this test is a QP-980 high strength steel, and the gage section measures 2.9 mm wide by 7 mm long by 1.0 mm thick. The DIC acceleration is averaged over a slice of the sample taken perpendicular

Fig. 27.1 Comparison of the acceleration of the incident side of a steel tension specimen obtained from DIC measurements at 90,000 frames/s with the acceleration of the incident bar obtained from the reflected strain pulse recorded at 2 MHz. Accelerations are determined by central differencing
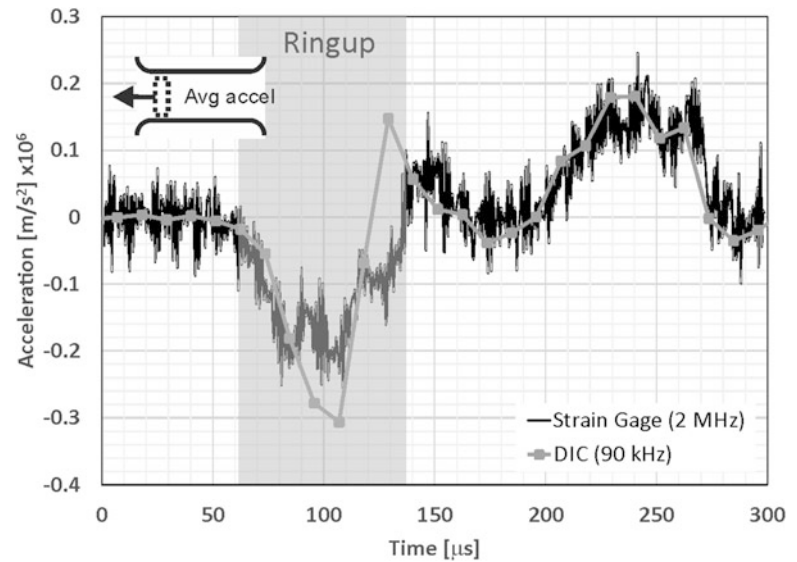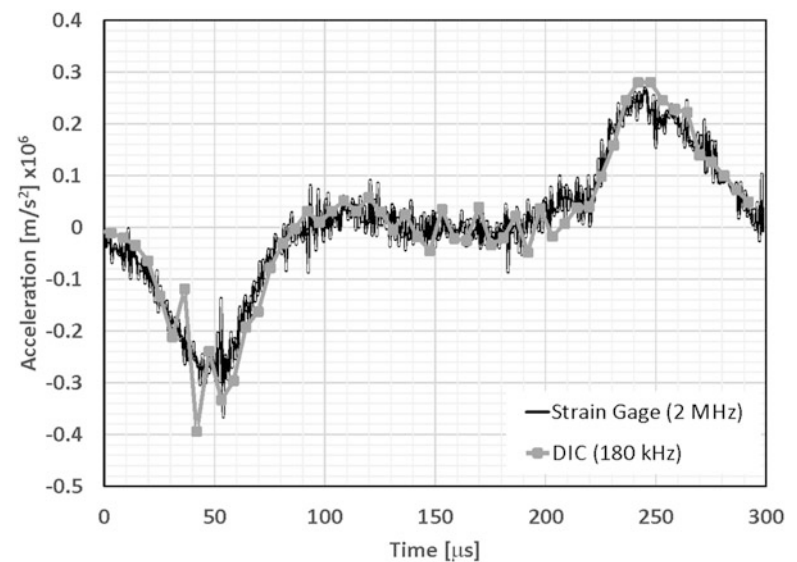

Fig. 27.2 Comparison of the acceleration of the free end of the incident bar with no sample obtained from DIC measurements at 180,000 frames/s with strain gage results obtained at 2 MHz using central differencing

to the load axis, located nearest the incident bar where the acceleration is highest during ringup. Further, the accelerations obtained from both DIC field information and strain gage data are smoothed by central differencing. As this figure shows, the DIC acceleration field data differ from the strain gage result nearest the acceleration period during ringup. Some of this difference may be real and caused by slippage between the sample and the grip, which is typical but undesirable in Kolsky bar testing. To compare accelerations between DIC and strain gage data at higher recording rates without grip effects, Fig. 27.2 plots DIC measurements obtained directly on the end of the incident bar, this time at 180 kHz, against the strain gage signal. With grip slippage eliminated there is better agreement between DIC and strain gage results, but we still see larger noise in the DIC data near the peak accelerations compared to the strain gage result. Clearly, obtaining acceleration information from DIC displacement field measurements is quite prone to noise because the data must be differentiated twice, amplifying any displacement noise. Noise levels are quite significant in the 2 MHz strain gage signals that have only been differentiated a single time. Thus even with higher speed cameras for DIC measurements, noise in the derived acceleration data during the ringup portion of a Kolsky bar experiment presents a challenge to obtaining accurate dVFM results. As discussed by its inventors [7], dVFM may be better suited to experiments that are intentionally designed to provide large, smoothly changing accelerations. Turning to FEA-based inverse techniques, the question arises whether data obtained during ringup is useful for identification purposes since in principle the optimized FEA solution would be able to capture this portion of the experiment. Displacement data could be used to guide the identification process so double differentiation is avoided. However, because more constitutive parameters are sensitized during this portion of the test (strain rate sensitivity, for example), the identification process becomes more difficult.

27.2.2 Equilibrium Deformation

In Fig. 27.3 shows dynamic tensile test results for a second-generation AHSS using a gage length of 7 mm and a length-to-width ratio of 1.4. An estimate of the dynamic true-stress, true strain response of this material shows limited strain hardening in the material. High speed 3D DIC measurements using the same settings as the previous data (90,000 fps, 128 × 288 pixels, 1 μs exposure, 15 pixel DIC subset with 3 pixel offset) show highly peaked true strain profiles across the cross section of the specimen for global average true strains exceeding a few percent. For a material with very little strain hardening such as the QP-980 material studied here, achieving uniform strain along the gage section is very difficult. In the limit of a zero strain hardening material, one can demonstrate with finite element analysis that localized necking begins almost immediately because the material is incapable of diffusing a neck by hardening. In Fig. 27.4 the same steel is tested with the same gage length (7 mm) but a reduced thickness such that the gage length-to-width ratio is now 2.4. Clearly the strain profile is more uniform, but the strain falls off significantly at the edges even within the gage section. We note that the strain rate is higher in the second test because of reduced cross sectional area of the specimen lowers the transmitted load which, in turn, increases the overall strain and strain rate in the test. Thus even seemingly minor changes to the specimen geometry can impact the test conditions significantly.
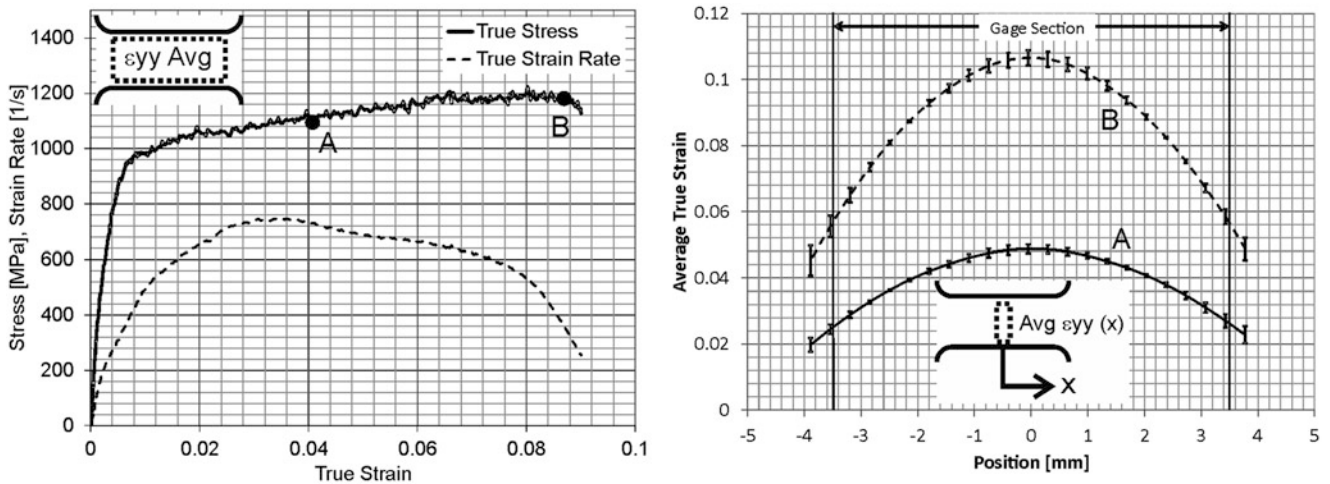

Fig. 27.3 *Left*: Dynamic average stress-strain behavior of an AHSS with a gage length-to-width ratio of 1.4. *Right*: True strain distribution along the load axis at two average true strain values (labeled *A* and *B*), from DIC data averaged across planes perpendicular to the load axis
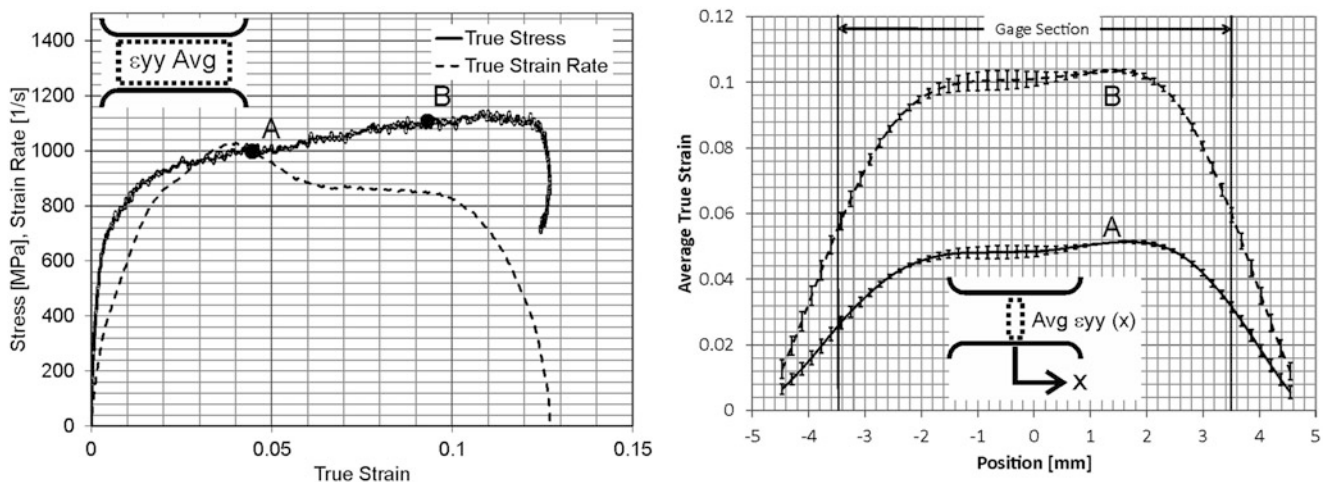

Fig. 27.4 *Left*: Dynamic average stress-strain behavior of an AHSS with a gage length-to-width ratio of 2.4. *Right*: True strain distribution along the load axis at two average true strain values (labeled *A* and *B*), from DIC data averaged across planes perpendicular to the load axis

Equilibrium deformation can be analyzed by the ordinary (non-dynamic) VFM because the strain fields are quite non-uniform, the equilibrated forces acting to cause the strain field are available from strain gage data, and the specimen is assumed to be in a state of plane stress up to the point of localized necking. Again, depending on the assumptions made and the complexity of the plasticity model, plastic parameters may need to be identified by minimizing a cost function rather than solving a set of algebraic equations. Additionally, the dynamic nature of the test introduces an additional complication that is unique to dynamic plasticity experiments: adiabatic heating of the specimen due to rapidly accumulating plastic strain. In this case an additional step is needed to evaluate the temperature field and its effect on the virtual work estimate which affects the resulting identified material parameter values. Accounting for adiabatic heating has been recognized as a significant challenge by the developers of the VFM [6]. An iterative updating scheme, combined with an assumption, based on measurement data, regarding the fraction of plastic work converted to heat, might be used to account for adiabatic heating effects in this case. FEA-based inverse methods can also be applied to this portion of the test, albeit at considerably greater complication and computational expense, and with no obvious advantage over the VFM other than providing consistent numerical approximations between the identification problem and the application problem.

27.2.3   Necking

Once localized necking begins, ordinarily no more information can be obtained from a dynamic tensile test. Acceleration levels are much lower during necking than at the onset of the test except when fracture occurs. In addition, the stress state within the developing neck transitions from plane strain to tri-axial, which by itself precludes the use of the VFM because one can no longer accurately estimate virtual work quantities where stresses vary through the thickness of the sample. Further, because the gradients in strain become large in the neck and, in general, high speed cameras have limited spatial resolution, the strain or displacement field resolution is too limited to accurately capture these gradients. This problem also affects the quality of FEA-based identification techniques but it does not preclude their use to estimate material parameters in the neck region up until the fracture point.

27.3   Conclusions

Measuring the dynamic tensile stress-strain curves of advanced high strength automotive sheet steels presents opportunities for inverse analysis to better leverage experimental data obtained when imperfect test conditions arise due specimen geometry effects that are exacerbated by the relatively low hardening rates in these steels. Three portions of the dynamic test were examined regarding the potential of various inverse techniques to improve the value of the test. The dVFM may be very useful to analyze material behavior during ringup, but DIC data must be obtained at very high sampling rates for accurate results in this kind of experiment. After ringup and before necking, ordinary (non-dynamic) VFM can be applied and should perform well if adiabatic heating effects can be adequately accounted for. Once localized necking begins, finite element based inverse methods must be used because the tri-axial stress state that develops in the neck precludes use the VFM. More costly FEA-based identification methods can be applied to all three portions of the test, although the accuracy of the identified parameters can be limited by the quality of the approximations needed in the absence actual of three dimensional data. FEA-based methods can also be selected to minimize approximation errors between the identification problem and the application problems. It is also noteworthy that the present paper deals only with dynamic tests designed using the traditional approach that seeks a uni-axial strain state and rapid development of force equilibrium. As pointed out in [7], there may be significant benefits to designing material tests very differently in order to maximize the utility of the dVFM method in making use of internal accelerations within the test sample that are intentionally avoided by the traditional materials testing approach.

References

1. Bao, Y., Wierzbicki, T.: On fracture locus in the equivalent strain and stress triaxiality space. Int. J. Mech. Sci. **46**, 81–98 (2004)
2. Gilat, A., Schmidt, T., Walker, A.: Full field strain measurement in compression and tensile split Hopkinson bar experiments. Exp. Mech. **49**, 291–302 (2009)
3. Mates, S., Abu-Farha, F. Dynamic tensile behavior of a quenched and partitioned high strength steel using a Kolsky Bar. In: Proceedings of the Society for Experimental Mechanics 2015 Annual Meeting. Society for Experimental Mechanics, Costa Mesa (2015)
4. Bridgman, P.: Studies in Large Plastic Flow and Fracture. McGraw-Hill, New York (1952)
5. Avril, S., et al.: Overview of identification methods of mechanical parameters based on full-field measurements. Exp. Mech. **48**, 381–402 (2008)
6. Pierron, F., Grédiac, M.: The Virtual Fields Method. Springer, New York (2012)
7. Pierron, F., Zhu, H., Siviour, C.: Beyond Hopkinson's bar. Philos. Trans. R. Soc. A **372**(2023), 24 (2014)
8. Chen, W., Song, B.: Split Hopkinson (Kolsky) Bar. Springer, New York (2010)

Chapter 28
Determination of the Dynamic Strain Hardening Parameters from Acceleration Fields

J.-H. Kim, D.-H. Leem, F. Barlat, and F. Pierron

Abstract The aim of the present study is to determine dynamic strain hardening parameters accurately using an inverse method so that accurate hardening properties at intermediate or high strain rates can be provided for automotive crash analysis simulations. In order to validate the identification procedure, a proper constitutive model was selected and a finite element (FE) analysis was carried out to obtain simulated measurements. The same identification procedure as that which will be implemented in the experiments was adopted. The virtual fields method (VFM) was used as an inverse method to retrieve the constitutive parameters. Since precise measurement of the applied force is not an easy task at high strain rates due to the inertial effect, the identification was performed without using the force information. Instead, the acceleration fields were used for the identification. The obtained parameters using the VFM were compared with the reference ones, which were fed into the FE simulations and very promising results were acquired from the VFM. In addition, a novel high speed tensile tester for sheet metal specimens was developed to validate the proposed methodology in the experiments.

28.1 Introduction

Crash analysis using finite element (FE) simulation is now essential in auto companies to evaluate automobile crashworthiness. In order to acquire reliable simulation results, precise material behaviors at intermediate or high strain rates should be fed as input. However, the dynamic hardening behavior of materials at high strain rates is not easily characterized because accurate measurement of load is difficult due to the inertial effect [1]. The aim of the present study is to characterize the dynamic strain hardening behavior of thin steel sheet specimens using the virtual fields method (VFM) [2]. The identification is carried out using the acceleration fields without utilizing load information. To determine the hardening parameters at high strain rates, high speed tensile tests are conducted on advanced high strength steel (AHSS) sheet specimens and full-field displacement fields are measured by a digital image correlation (DIC) technique using a high-speed camera. Then, a proper elasto-plastic constitutive model is chosen and the VFM is used as an inverse analytical tool to determine the constitutive parameters. In this study, the methodology is introduced and a validation of the proposed identification procedure against simulated and experimental data is presented.

28.2 Identification Procedure

28.2.1 Logarithmic (True) Strain

In order to simulate the measurement points from DIC, fine mesh size was employed first. Three nodes triangular shell elements were used. Reference (undeformed) and deformed coordinates of measurement points were recorded and the whole area of interest (AOI) was meshed using triangular elements.

J.-H. Kim (✉) • D.-H. Leem • F. Barlat
GIFT, POSTECH, 77 Cheongam-Ro, Nam-Gu, Pohang, Gyeongbuk 790-784, South Korea
e-mail: jinkim@postech.ac.kr

F. Pierron
Engineering Materials Group, Faculty of Engineering and the Environment, University of Southampton, Southampton SO17 1BJ, UK

The deformation gradient F for each triangle was calculated from the undeformed and deformed coordinates of measurement points using the analytical approach adopted in [3] and the theory of finite deformation [4]. A plane stress state and incompressibility ($\det(F) = 1$) in plasticity were assumed. Then the logarithmic strain tensor ε_{ln} was obtained from the deformation gradient F through the left stretch tensor V ($V^2 = F^{\mathrm{T}}F$) as in Eq. (28.1).

$$\varepsilon_{\ln} = \sum_{i=1}^{3} \ln(\lambda_i) r_i \otimes r_i \tag{28.1}$$

where λ_i and r_i are the eigenvalues and eigenvectors of the left stretch tensor V respectively.

28.2.2 Constitutive Model

Choosing a constitutive model which can describe the dynamic strain hardening behavior properly is important. In this study, von Mises yield criterion for isotropic material and Swift model for a rate independent hardening law were chosen as an initial study. The associated flow rule was assumed.

$$\text{Swift model}: \sigma_s = K\left(\varepsilon_o + \varepsilon_p\right)^n \tag{28.2}$$

where σ_s is the current yield stress and ε_p the equivalent plastic strain. K, ε_0 and n are the material parameters to be identified.

28.2.3 The Virtual Fields Method

In this study, the virtual fields method (VFM) was used for an inverse method to retrieve the constitutive parameters from the measured deformation fields. The VFM makes use of the principle of virtual work which describes the condition of global equilibrium. The equilibrium equation in the case of elasto-plasticity for dynamic loading, and in absence of body forces, can be written as follows:

$$-\int_V \left[\int_0^t \dot{\sigma}_{ij} dt\right] \varepsilon_{ij}^* dV + \int_{S_f} T_i u_i^* dS = \int_V \rho a_i u_i^* dV \tag{28.3}$$

where $\dot{\sigma}$ is the stress rate which is a function of $\dot{\varepsilon}$ (actual strain rate), σ (actual stress) and unknown constitutive parameters, V the measurement volume, T the distribution of applied forces acting on S_f, e^* the virtual strain field derived from u^* (the virtual displacement field), ρ the density and a the acceleration.

Material parameters can be determined from the acceleration fields by choosing proper virtual fields which can get rid of the external virtual work (EVW) term including the loads. For an elasto-plasticity problem, the identification is carried out using an iterative procedure [5] to minimize the quadratic gap between the internal virtual work (IVW) and the acceleration term (the right hand side of Eq. (28.3). Since the constitutive parameters are unknown, initial guesses are required to initiate the iteration. Then, the stress components are recalculated until the equilibrium equation is satisfied by updating the parameters. Nelder-Mead algorithm was used for the minimization. In this study, simple virtual fields were applied to find the material parameters as in Eq. (28.4).

$$u_x^* = 0, \quad u_y^* = (y - y_{\min})(y - y_{\max}) \tag{28.4}$$

where y is the vertical coordinate of the measurement points in the current (deformed) configuration. The chosen virtual fields cancels out the EVW term. The parameters were determined in less than 5 min.

28.2.4 Speed and Acceleration

The speed fields can be obtained from the measured displacement fields using simple finite difference.

$$v_i\left(t + \frac{\Delta t}{2}\right) = \frac{u_i(t + \Delta t) - u_i(t)}{\Delta t} \tag{28.5}$$

where i can be either x or y and t is time.

The acceleration fields can be computed from the displacement fields by double temporal differentiation as in Eq. (28.6). Due to the nature of the quantities, the speed is defined at time $t + \Delta t/2$ and the acceleration is at time t.

$$a_i(t) = \frac{u_i(t + \Delta t) + u_i(t - \Delta t) - 2u_i(t)}{\Delta t^2} \tag{28.6}$$

28.3 FE Simulation

28.3.1 FE Model

In this study, virtual dynamic tensile tests were carried out using the FE software ABAQUS/Explicit. A specimen geometry was chosen as in Fig. 28.1. The dimensions of the specimen were 80 mm (height) $\times$ 30 mm (width) $\times$ 1 mm (thickness). The width for the AOI was 10 mm. In ABAQUS/Explicit, input parameters for Swift hardening law were; K: 1514.2 MPa, ε_0: 0.0011, n: 0.168. Those parameters were obtained from a static uniaxial tensile test on a dual phase (DP) 780 steel specimen. Dynamic tensile tests were simulated by constraining the lower edge and by applying vertical constant speed at the upper edge. During the deformation, the deformed coordinates of each measurement point were saved at evenly spaced time intervals (100 loading steps). Then, the logarithmic strain fields of the AOI were calculated using the procedure described in Sect. 28.2.1.

Speed magnitude was adjusted so that average axial (y-direction) strain rate in the AOI reached to approximately 50 s^{-1} (case A), 750 s^{-1} (case B), and 1500 s^{-1} (case C) after the initial stage. Also, total time elapsed was controlled to make the maximum local axial strain as near 20 % at the final step of the simulations. Imposing constant speed as a boundary condition is to simulate the actual experimental conditions with a servo hydraulic dynamic tensile tester.

Fig. 28.1 Specimen geometry
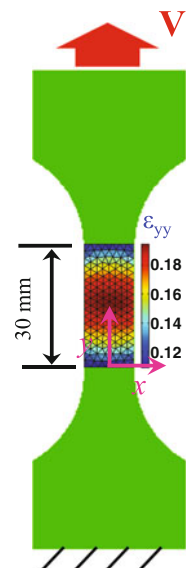
28.3.2 Effect of Strain Rates

Then, the effect of strain rates on the identification was investigated. For a fair comparison, the identification was conducted for all the cases when the maximum ε_{yy} in the loading direction was around 20 % at the central area. The material parameters were extracted from the central AOI. As can be seen in Table 28.1, the parameters of Swift hardening law were reasonably retrieved for the cases of B (strain rate of 750 s^{-1}) and C (1500 s^{-1}), but the identification is unsatisfactory for the case of A (50 s^{-1}). The deviation between the calculated true stress values from the identified parameter sets and the reference values are is quite large for case A as shown in Fig. 28.2. In addition, the relative error for ε_0 is relatively large. It is the most difficult term to identify accurately because the influence of ε_0 on the cost function is negligible [3].

In order to check the temporal variation of acceleration, the averages of acceleration fields in the loading direction are plotted in Fig. 28.3. The average acceleration is significantly low for case A compared to that of cases B and C. It is considered that the acceleration information is insufficient for the identification with the VFM for case A, low strain rate. In this case, the material parameters should be obtained using the external virtual work term including loads instead of the acceleration term in Eq. (28.3).

Table 28.1 Comparison between target and identified parameters (case A: strain rate of 50 s^{-1}, case B: 750 s^{-1}, case C: 1500 s^{-1}, R. E.: relative error)

	K	ε_0	n
Target	1514.2	0.0011	0.168
Identified (case A)	836	0.00476	0.325
R.E. (case A)	44.7 %	332 %	93.6 %
Identified (case B)	1436	0.000540	0.163
R.E. (case B)	5.13 %	50.9 %	2.80 %
Identified (case C)	1519	0.000880	0.165
R.E. (case C)	0.34 %	20 %	1.79 %

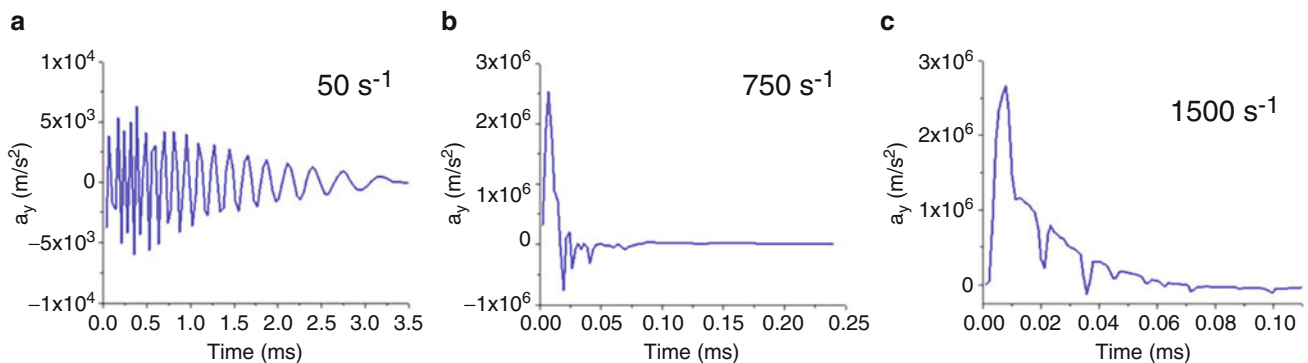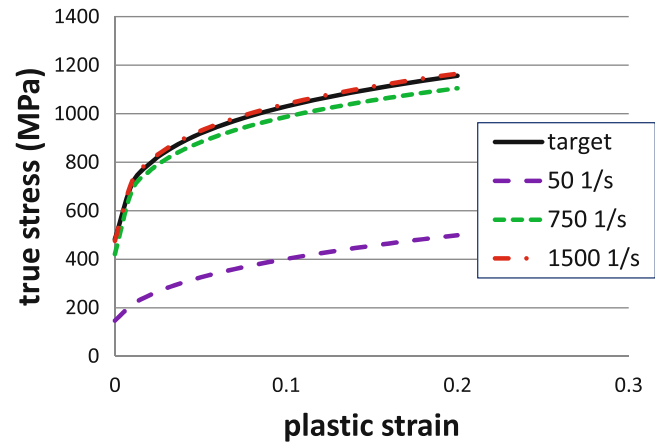**Fig. 28.2** Comparison of the calculated true stress values from the identified parameter sets

Fig. 28.3 Average acceleration in the loading direction (**a**) case A: 50 s^{-1}, (**b**) case B: 750 s^{-1}, (**c**) case C: 1500 s^{-1}

28.4   A Novel High Speed Tensile Tester

28.4.1   Impact Frame High Speed Test (IFHS Tests)

In order to validate the proposed methodology in the experiments, a novel high speed tensile tester for sheet metal materials based on [6] has been developed, and the experimental set-up is shown in Fig. 28.4. In the high speed tensile tester, two metallic frame bars are connected to a hydraulic pump through a coupler, which is designed to be broken when it is put under a certain amount of load. When the pump starts to impose tensile load on the coupler, the coupler endures the load until it reaches to critical load value and elastic strain energy is accumulated in the frame bars at the same time. If the load is increased to break the coupler, the energy within the frame bars is released so that the specimen connected to a frame module is pulled in tension and acceleration fields are generated on the specimen.

28.4.2   Experiments

For the experimental application, Dual Phase (DP) 780 advanced high strength steel (AHSS) material was used. The sheets were 1 mm thickness, and all the specimens were cut in the rolling direction (RD).

In the experiments, high speed tensile tests on sheet metal specimens were conducted and full-field displacement fields were measured by a digital image correlation (DIC) technique using a high-speed camera (Photron FASTCAM SA-X2).
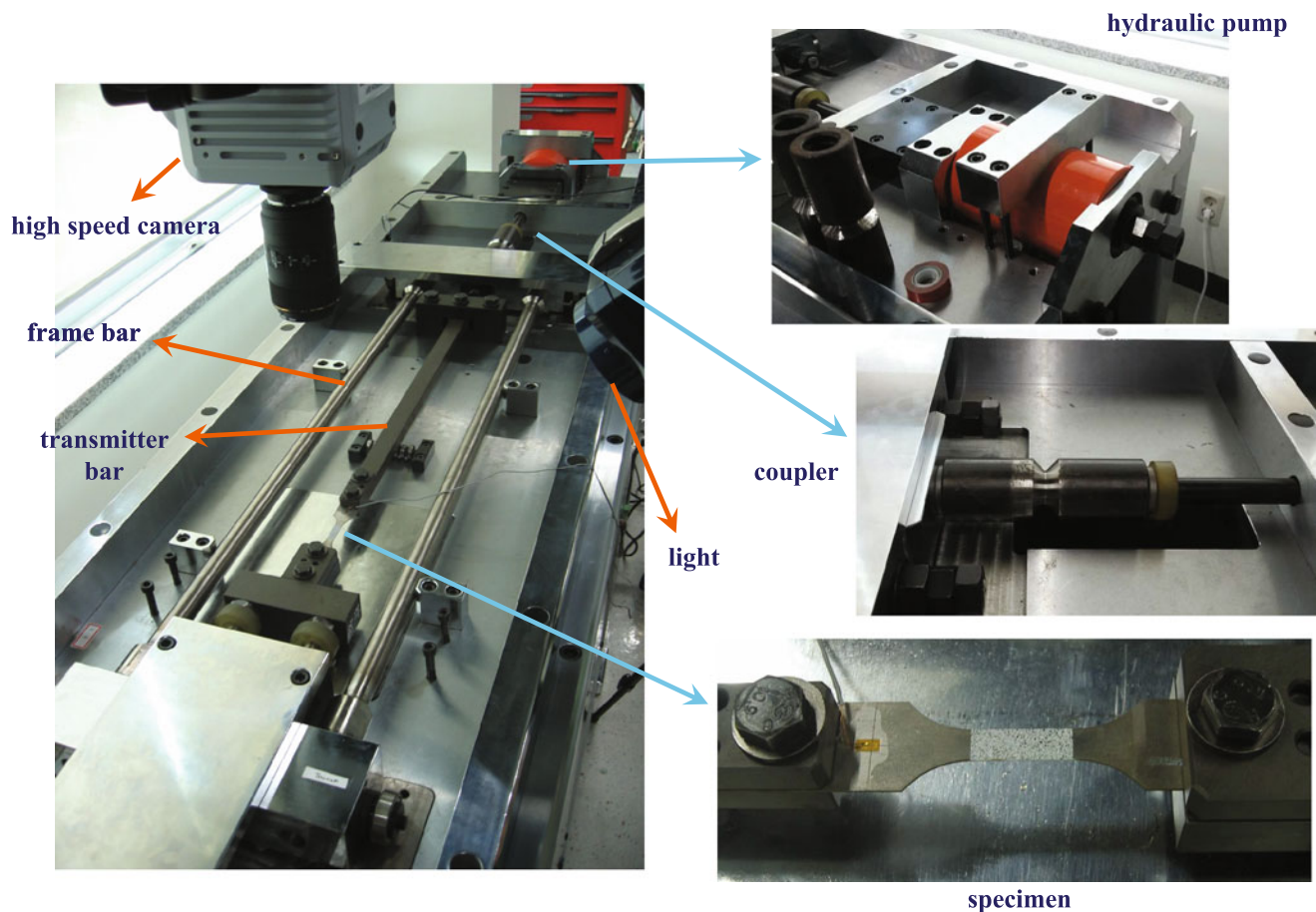

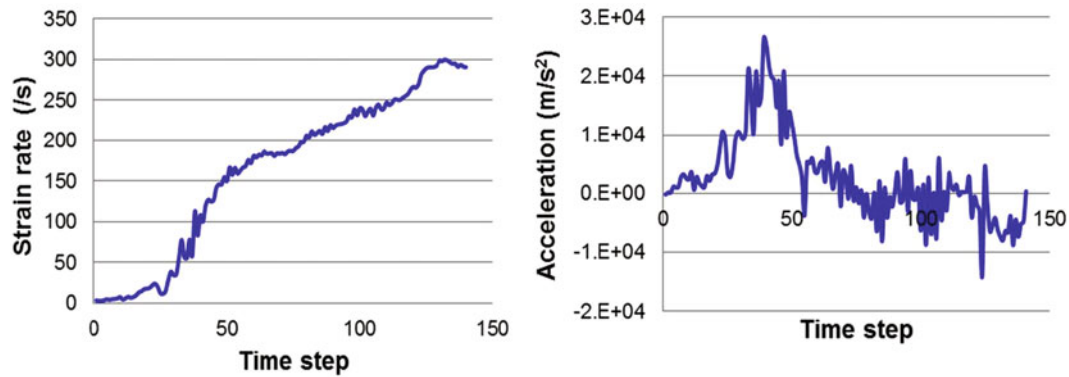**Fig. 28.4** Impact frame high speed tester

Fig. 28.5 Temporal variation of strain rate and acceleration

In order to check the temporal variation of strain rate and acceleration, the averages of strain rate and acceleration fields in the loading direction are plotted in Fig. 28.5. It was observed that maximum strain rate up to 300 s^{-1} and maximum acceleration up to 25 km/s^2 were obtained from the newly built IFHS tester.

28.5 Conclusion

In this study, a new methodology has been applied to determine the dynamic true stress-strain curve of sheet metals using the virtual fields method (VFM) without measuring loads. In the FE simulation, parameters of the Swift hardening law were retrieved successfully from the acceleration fields by introducing appropriate virtual fields which can remove the virtual work term including the external loads. A new high speed tensile tester was built and high speed tensile tests were carried out on sheet metal specimens using a high-speed camera. The validation of the proposed methodology against experimental measurements will be performed. The identification results with the Swift model at various strain rates will be compared with those from the conventional identification procedure using a load-cell.

References

1. Pierron, F., Sutton, M.A., Tiwari, V.: Ultra high speed DIC and virtual fields method analysis of a three point bending impact test on an aluminium bar. Exp. Mech. **51**(4), 537–563 (2011)
2. Pierron, F., Grédiac, M.: The Virtual Fields Method. Springer, New York (2012)
3. Kim, J.H., Serpantié, A., Barlat, F., Pierron, F., Lee, M.G.: Characterization of the post-necking strain hardening behavior using the virtual fields method. Int. J. Solids Struct. **50**(24), 3829–3842 (2013)
4. Dunne, F., Nik, P.: Introduction to Computational Plasticity. Oxford University Press, New York (2005)
5. Grédiac, M., Pierron, F.: Applying the virtual fields method to the identification of elasto-plastic constitutive parameters. Int. J. Plasticity **22**(4), 602–627 (2006)
6. Kim, D.J., Wille, K., El-Tawil, S., Naaman, A.E.: Testing of cementitious materials under high-strain-rate tensile loading using elastic strain energy. J. Eng. Mech. **137**(4), 268–275 (2010)

Chapter 29
Image-Based Inertial Impact Tests on an Aluminum Alloy

S. Dreuilhe, F. Davis, Clive R. Siviour, and F. Pierron

Abstract This paper presents the development of a novel inertial test for the identification of non-linear parameters for elasto-plastic constitutive models at high strain rates. After briefly presenting the principle of the approach using the virtual fields method, the experimental implementation is detailed. Using the virtual fields method, the yield stress and hardening modulus of aluminum 6082-T6 were identified.

Keywords High-strain rate • Ultra-high speed imaging • Virtual fields method (VFM) • Grid method • Inertial test

29.1   Introduction

A number of experimental techniques have been developed to study the high strain rate response of materials. However, the most popular technique for characterizing material behavior at high strain rates (10^2–10^4 s^{-1}) is the Kolsky (or split Hopkinson) bar. In a compression test, the specimen is placed between two long bars, the incident and output bars which are upstream and downstream of the sample, respectively. An impact is used to generate a stress wave in the incident bar. This stress wave then propagates into the sample and the output bar. Assuming that the stress wave is one-dimensional, the stress, strain, and strain-rate in the sample are determined from the stress wave in the incident and output bars. This is readily accomplished by placing strain gauges on the incident and output bars. Embedded in the calculation of stress, strain, and strain rate is the assumption that the deformation of the sample is homogenous. In addition, the forces on the front and back faces of the specimen must be equal for the stress calculations to be valid. These requirements limit the size and impedance of materials that can be tested using a Kolsky bar.

Our current understanding of the mechanical response of materials at high strain rates is still hampered by the lack of more robust and detailed experimental data. Recent advances in ultra-high speed imaging have now made it possible to record images at a rate of 5 Mfps with a resolution of 0.67 Mpixels. Using an imaging technique such as digital image correlation (DIC) or the grid method, the time-resolved displacement fields on the specimen surface during dynamic loading can be captured. Further, by applying an inverse identification technique such as the virtual fields method, the material parameters can be identified. This approach has already been implemented to determine the elastic parameters of quasi-isotropic composite specimens subjected to inertial impact tests [1]. The approach has also been paired with the classic Kolsky bar test to identify the material parameters for glass epoxy composites [2]. The strength of the virtual fields method is that it does not require any load measurement. Instead the acceleration field, derived from the time-resolved displacement field, is used as a load cell. In fact, this approach also has the advantage of relieving the constraint on specimen size and impedance, as quasi-static force equilibrium is no longer required.

The objective of this paper is to use inertial impact tests and the virtual fields method to identify the parameters that describe the elasto-plastic response of aluminum 6082-T6, an aircraft grade aluminum, at high strain rates. First, a brief introduction to the virtual fields method is given. Next, to validate the approach, the inertial impact test was simulated using finite element analysis. The virtual fields method was then used to identify yield stress and hardening modulus from the finite element displacement data. Finally, inertial impact tests were performed in collaboration with the Impact Engineering Group at Oxford on aluminum 6082-T6 samples. An ultra-high speed camera was used to capture the dynamic response of each

S. Dreuilhe (✉) • F. Davis • F. Pierron

Engineering Materials Group, Faculty of Engineering and the Environment, University of Southampton, Southampton SO17 1BJ, UK
e-mail: smd2e13@soton.ac.uk; frances.davis@soton.ac.uk; f.pierron@soton.ac.uk

C.R. Siviour
Department of Engineering Science, University of Oxford, Oxford, UK
e-mail: clive.siviour@eng.ox.ac.uk

impacted sample. The grid method was used to analyze the collected images and obtain full field displacement data on the sample surface. These full field data were used as inputs to the virtual fields method to identify the yield stress and hardening modulus.

29.2 The Virtual Fields Method

The Virtual Fields Method is a computationally efficient technique for the identification of constitutive model parameters from full-field kinematic measurements. The general formula derived from the principle of virtual work is given by [3]

$$-\int_V \boldsymbol{\sigma} : \boldsymbol{\varepsilon}^* dV + \int_S \boldsymbol{T} \cdot \boldsymbol{u}^* dS = \int_V \rho \, \boldsymbol{a} \cdot \boldsymbol{u}^* dV \tag{29.1}$$

where $\boldsymbol{\sigma}$ is the stress tensor, $\boldsymbol{u}^*$ and $\boldsymbol{\varepsilon}^*$ are the virtual displacement vector and associated virtual strain tensor, respectively, $\boldsymbol{T}$ is the traction vector on the boundary of the body, ρ is the density of the material, and $\boldsymbol{a}$ is the acceleration vector. The scalar product between vectors is $\boldsymbol{l} \cdot \boldsymbol{m}$ whereas $\mathbf{L} : \mathbf{M}$ is the scalar product for between matrices. In Eq. (29.1), the virtual displacement does not have any physical meaning, and can be any function that is continuous and differentiable over the body [3]. Note that the virtual strain is calculated from the virtual displacement using the traditional linearized strain-displacement relationship.

For the thin rectangular specimen shown in Fig. 29.1, Eq. (29.1) reduces to:

$$-t_h \int_S \boldsymbol{\sigma} : \boldsymbol{\varepsilon}^* dS + t_h \int_{-b/2}^{b/2} \boldsymbol{T} \cdot \boldsymbol{u}^* \, dx_2 = t_h \int_S \rho \, \boldsymbol{a} \cdot \boldsymbol{u}^* dS \tag{29.2}$$

where the specimen is assumed to be in a state of plane stress and t_h is the specimen thickness. Imposing a virtual displacement of $u_1^* = 1$ and $u_2^* = 0$, the first term in Eq. (29.2) vanishes. The second integral in Eq. (29.2) will equal the average stress in the x_1 direction on the surface S_1 (Fig. 29.1 in green). When the integrals in Eq. (29.2) are replaced by discrete sums the following relationship is found:

$$\overline{\sigma_1(x_1, t)}^{x_2} = \rho x_1 \overline{a_1(x_1, t)}^{S_2} \tag{29.3}$$

In Eq. (29.3), the overbars indicate averages over the line or area specified in the superscript. Since the full-field imaging techniques measure the displacement at a large number of points on the specimen surface the integrals in Eq. (29.2) can be approximated using discrete sums. The acceleration field is obtained by double differentiation of the time-resolved displacement field. By varying the value of x_1, $\overline{\sigma_1(x_1, t)}^{x_2}$ can be identified from the acceleration for any transverse section. Since the strain field is also known, average stress-strain curves can be constructed.

To identify the elasto-plastic material parameters, a set of non-linear equations must be minimized. The cost function to be minimized is the sum of the squared difference between the average stress in each section calculated from the acceleration (Eq. (29.3)) and the average stress in each section calculated using the constitutive model. The identification of material

Fig. 29.1 Schematic showing the test configuration for an inertial impact test
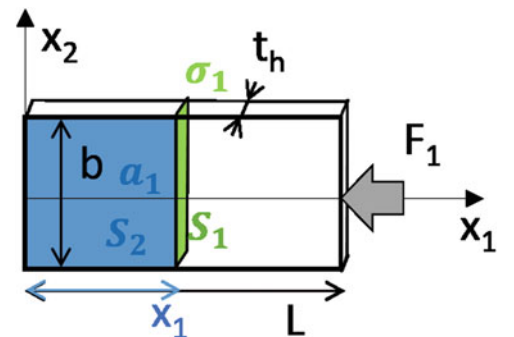
parameters for non-linear constitutive equations is iterative; the cost function is evaluated for several different combinations of the material parameters (through the constitutive model) searching for the set of parameters that minimizes the cost function.

29.3 Methods

29.3.1 Validation Using Simulated Measurements

The inertial impact test was simulated using a two-dimensional plane stress model in Abaqus Explicit (v. 6.13). A rectangular impactor (50 mm × 34 mm × 4 mm) was placed 0.03 mm from the end of the specimen and given an initial velocity of 50 m s^{-1}. A mesh size of 0.25 mm was used for the aluminum specimen (55 mm × 32 mm × 4 mm) and the impactor. Both were meshed with reduced integration plane stress elements (CPS4R). The aluminum specimen and steel impactor were modeled using an elasto-plastic material model with linear isotropic hardening (Table 29.1). The results of the finite element analysis were saved at 180 time steps spaced 0.2 µs apart, to match the acquisition rate of the camera.

The identification procedure was validated on the finite element strain and acceleration data, producing errors of 0.14 % on the yield stress, σ_0, and 11.1 % on the hardening modulus, H. The higher identification error on H is due to the small sensitivity of the cost function to H. This is amplified when the values of H are very small when compared with the Young's Modulus. The study was repeated using a hardening modulus of 1.8 GPa and the error on the hardening modulus was only 0.6 %, supporting this conclusion.

29.3.2 Experimental Protocol

Inertial impact tests were carried out on aluminum 6082-T6 samples using the gas gun facilities in the Impact Engineering Group at Oxford. A grid with a pitch of 0.3 mm was bonded to each aluminum specimen. A steel waveguide was employed to ensure that the impactor made even contact. Each specimen was glued to a waveguide as shown in Fig. 29.2. When the

Table 29.1 Finite element material model parameters

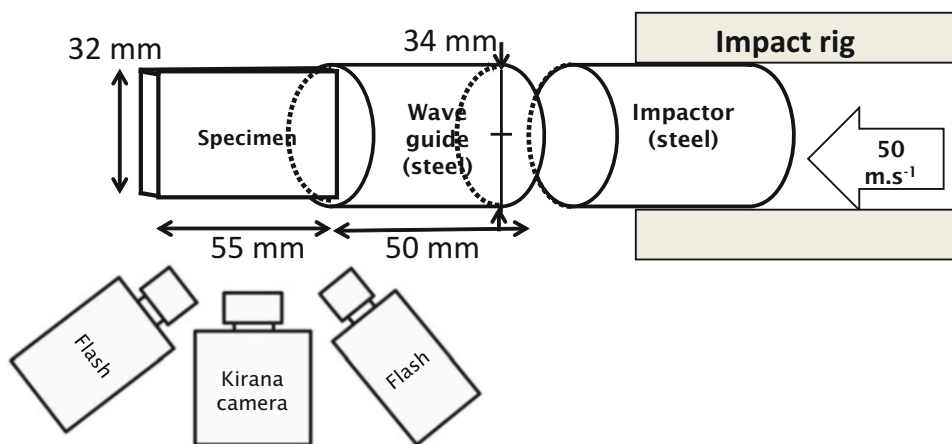|	Specimen—Al6082-T6	Impactor—mild steel
Density	2700 kg m^{-3}	7850 kg m^{-3}
Young's Modulus, E	70 GPa	205 GPa
Poisson's ratio, ν	0.30	0.29
Yield stress, σ_0	350 MPa	370 MPa
Hardening modulus, H	150 MPa	2.3 GPa

Fig. 29.2 Schematic of the experimental setup

impactor and the waveguide make contact a stress wave forms; the wave then propagates along the waveguide and into the specimen. An ultra-high speed camera (Kirana, Specialized Imaging) collecting 180 images at 5 Mfps was used to image the propagation of the stress wave in each aluminum specimen. A total of four specimens were impacted all at a nominal speed of 50 m s^{-1}.

29.3.3 Data Processing

In order to obtain exploitable strain and acceleration fields, the raw images were processed using the Grid Method GUI (v. 2.09) [4] to produce displacement maps. Due to the presence of random and periodic noise in the images obtained with the camera, the displacement was filtered in the time domain using a low-pass Butterworth digital filter of order 7 with a normalized cut-off frequency of 0.06. From this smoothed displacement, double temporal differentiation was performed to obtain the acceleration. A robust spatial spline smoothing technique [5, 6] of smoothing parameter 6 was also applied to the displacement to prevent the numerical differentiation from amplifying the spatial noise in the strain.

29.4 Results and Discussion

A total of four aluminum specimens were successfully tested. After the data processing, it became clear that the last 85 images could not be used for the inverse material parameter identification due to the high levels of noise. The cause of the camera noise amplification with specimen speed is unclear and will be the focus of future investigation. To ensure that these noisy images did not bias the filtering, the last 85 images were not processed. This effectively reduced imaging time from 36 to 19 μs. Using the remaining images Eq. (29.3) can be used to generate stress-strain curves at any transverse section. Figure 29.3 shows one representative stress-strain curve for specimen 1. The early behavior is linear elastic where elastic modulus can be identified from the slope. In this case, the Young's Modulus was found to be 67 GPa. Figure 29.3 also indicates that specimen 1 yields at approximately 270 MPa.

A cost function for each sample was built up by taking the sum over space and time of the squared difference between the average stress in each section calculated from the acceleration (Eq. (29.3)) and the average stress in each section calculated using a linear isotropic hardening constitutive model. The values of the yield stress and hardening modulus identified can be found in Table 29.2. At quasi-static strain rates, the expected yield stress is between 250 and 300 MPa [7, 8]. Since aluminum 6082-T6 shows limited strain rate sensitivity at strain rates below 10^3 s^{-1} [7], the values identified in Table 29.2 correspond well with the expected yield stress. The hardening modulus for aluminum 6082-T6 is insensitive to strain rate and was expected to be approximately 130 MPa [7]. While the hardening moduli identified are of the right magnitude, there is clearly

Fig. 29.3 Average stress-strain response for specimen 1 at a distance of 7 mm from the impact edge
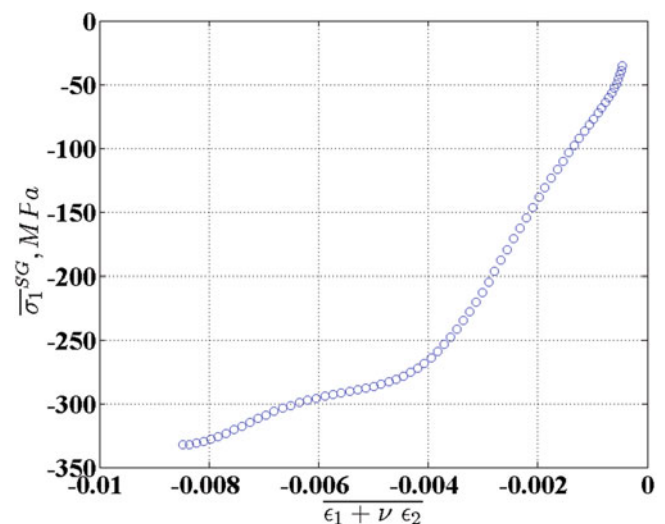
Table 29.2 Identified plastic parameters for the four specimens tested

Specimen no.	Yield stress, σ_0 (MPa)	Hardening modulus, H (MPa)
1	272	358
2	275	−303
3	–	–
4	266	521

no consistency in the identified values. These results suggest that the cost function is not sensitive enough to the hardening modulus. This limited sensitivity to the hardening modulus was expected based on the results of the finite element validation. Notably, for specimen 3 no values for the yield stress or hardening modulus could be identified.

29.5 Conclusions

In this manuscript, the virtual fields method was used to inversely identify the elasto-plastic parameters of aluminum 6082-T6, an aircraft grade aluminum, from an inertial impact test. The feasibility of this novel protocol was shown using simulated finite element data. The virtual fields method was implemented to recover the plastic parameters input in the finite element model. As a proof of concept, a short test campaign was performed impacting four samples of aluminum 6082-T6 at a speed of 50 m s^{-1}. The material parameters identified using the virtual fields method are in line with published results on the high strain rate response of aluminum [7, 8]. Although it is also possible to identify the parameters using finite element updating, it is worthwhile to remember that the virtual fields method is at least an order of magnitude less computationally expensive than finite element model updating since there is no need for a finite element computation to evaluate the cost function. In the future additional testing campaigns will be performed to more thoroughly examine the source of the camera noise in the final 85 frames, and to increase the strain rate by impacting at higher speeds. Other materials with more significant hardening will also be investigated.

References

1. Pierron, F., et al.: Beyond Hopkinson's bar. Philos. Trans. R. Soc. A Math. Phys. Eng. Sci. **372**(2023), 1471–2962 (2014)
2. Moulart, R., et al.: Full-field strain measurement and identification of composites moduli at high strain rate with the virtual fields method. Exp. Mech. **51**(4), 509–536 (2011)
3. Pierron, F., Grédiac, M.: The Virtual Fields Method. Springer, New York (2012)
4. Devivier, C., Pierron, F.: Grid method GUI: a tool to process grid images. http://gridmethod.tk/GMGUI_r.php. Accessed 14 Mar 2016
5. Garcia, D.: Robust smoothing of gridded data in one and higher dimensions with missing values. Comput. Stat. Data Anal. **54**(4), 1167–1178 (2010)
6. Garcia, D.: A fast all-in-one method for automated post-processing of PIV data. Exp. Fluids **50**(5), 1247–1259 (2011)
7. Moćko, W., et al.: Compressive viscoplastic response of 6082-T6 and 7075-T6 aluminium alloys under wide range of strain rate at room temperature: experiments and modelling. Strain **48**(6), 498–509 (2012)
8. Vignjevic, R., et al.: Effects of orientation on the strength of the aluminum alloy 7010-T6 during shock loading: experiment and simulation. J. Appl. Phys. **92**(8), 4342–4348 (2002)

Chapter 30
Inverse Material Characterization from 360-Deg DIC Measurements on Steel Samples

L. Cortese, K. Genovese, F. Nalli, and M. Rossi

Abstract A tension-torsion testing machine is used for the elasto-plastic characterization of an isotropic steel grade for offshore pipeline applications. The machine is capable of performing multiaxial tests using different sample geometries and load combinations. It is equipped with an optical rig for stereo digital image correlation (DIC) such that, while load is hold at different steps up to final fracture, a set of high resolution images is taken framing the full 360° view of the specimen. Image capturing is synchronized with standard load-displacement and torque-rotation acquisition. Illustrative results obtained from tensile tests are presented. In particular, the 3D shape and surface deformation are retrieved with DIC throughout a stepwise axial test of an isotropic steel sample. Different constitutive models, previously calibrated with the aid of FE analysis using multiaxial global experimental data (i.e. load-displacement curves), are here validated based on tension-torsion tests results. Afterwards, the local information from DIC (i.e. cross-section dimensions at different axial positions, deformation along significant surface paths) is compared with the corresponding FEM data implementing the validated material model. Evidence on the accuracy of the optical measurements, and on the benefits in terms of material characterization deriving from the additional local information available with such approach are here presented and discussed in detail.

Keywords 3D-DIC • Inverse calibration • Multi-axial tests • Large strain plasticity • Strain field measurement

30.1 Introduction

An accurate elasto-plastic material characterization is mandatory to use FE Analysis effectively both in metal forming simulations and in the structural assessment of critical components of mechanical systems. As regards forming, this information would help in designing tools and processes to obtain a feasible manufactured shape; for structural assessment, the stress and strain field evolution need to be correctly described, since it is responsible for damage accumulation, up to the ultimate failure. The effects of stress on plasticity have been broadly investigated for years [1–6]. Many authors have proposed advanced formulations, depending often in complex ways on the stress state [7–9]. A suitable selection of plasticity models for a specific application depends on the material type (isotropic/anisotropic, high/low ductility) and on the loading conditions (uniaxial/multiaxial, monotonic/cyclic). Commonly, constitutive models are calibrated with simple axial tests, and validated through similar loading conditions. The lack of accuracy of some formulations is revealed when complex tests, generally multiaxial, are performed [10–13]. In these cases, a poor transferability has been observed. This could be attributed to inherent limits of a specific formulation, or it could be a consequence of an inadequate calibration of the models themselves. Often, the experimental information is limited, averaged, and global, leading to a non optimal determination of the material constants. To overcome these issues, several studies implementing full-field techniques applied to material characterization have been proposed in literature [14–17].

In this paper it is investigated the possibility of using 3D digital image correlation (3D-DIC) techniques [18, 19] to collect detailed local information from experimental tests, in addition to standard quantities conventionally acquired. To achieve this, a 3D digital image correlation framework was integrated into a biaxial testing machine to collect 360-deg digital images during experiments. The optical measurement rig consisted in a dedicated frame, camera, lens and lighting system. Using

L. Cortese (✉) • F. Nalli
Faculty of Science and Technology—Free University of Bozen, Piazza Università 5, Bolzano 39100, Italy
e-mail: luca.cortese@unibz.it

K. Genovese
School of Engineering, University of Basilicata, Viale dell'Ateneo Lucano 10, Potenza 85100, Italy

M. Rossi
Università Politecnica delle Marche, Via Brecce Bianche, Ancona 60131, Italy

this arrangement, 3D shape and surface full-field deformation of Grade X65 steel specimens were measured, at different stages of axial test, until fracture. These data were then compared with the corresponding numerical FE results, making use of constitutive models calibrated on the same material by means of inverse methods in previous studies [20–22]. In this works a standard J2 and a more advanced J2–J3 plasticity models were adopted, and the calibration was achieved with tension, torsion and tension-torsion tests executed with the same equipment. A thorough additional validation of this calibration procedure is carried out, to grant the accuracy of the numerical simulation. The effectiveness of the full field measurement is assessed by comparing the DIC and numerical data. The results reported in this paper prove that the 360-deg DIC technique can be used to provide alternative data for calibration purposes, or be complementary to standard inverse material identification procedures. This is expected to be especially advantageous when local or directional experimental information is required (such for the case of anisotropic material characterization) and that it can reduce the number of the required experimental tests.

30.2 Experimental Setup and Test Methodology

An isotropic Grade X65 grade steel for pipeline applications was used for the tests. A biaxial machine was used, capable of axial and torsional loads up to 100 kN and 1000 Nm respectively. The translational and rotational actuators can be controlled independently such that pure tension, pure torsion and mixed tension-torsion tests are possible. Load, torque, displacement and rotation are acquired by a biaxial load cell and digital encoders embedded in the actuators themselves. Additional details on the equipment can be found in [21]. Hollow cylindrical specimens are used, whose geometry is shown in Fig. 30.1a. They have threaded ends with machined parallel faces, to be held by custom-designed grips, thus allowing their correct constraining, as well as the application of tensional and torsional loads. The hollow shape is optimized by trading-off the need of homogenizing the stress and strain states in the radial direction, while avoiding geometrical instabilities. The biaxial machine was equipped with a Nikon D7000 SLR camera with a 60 mm Micro Nikkor lens, mounted on a slewing ring bearing coaxial with the specimen axis (Fig. 30.2). The frame allows a manual positioning of the camera around 14 fixed positions to cover the full 360° view of the specimen surface [23, 24].

In this paper an axial test was performed, measuring the deformation by 3D-DIC technique. Prior to testing, specimens were sprayed with a light gray primer paint as a base, and later with black acrylic paint to provide the speckle pattern needed for correlation. A calibration pattern was fixed on one specimen end (Fig. 30.1). The test was run applying a progressive and quasi-static displacement up to fracture. During the experiment, the actuator was put on hold at different stages to allow the acquisition of the image sequences [24]. The number of stages was selected to have a limited strain variation from one acquisition to another, to obtain accurate DIC matching. Each step corresponded to an estimated (by FE analysis) nominal strain increment ($\Delta L/L_0$) of about 0.01 mm/mm. At the end, 30 sequences of 4000×3000 pixel^2 images at different load levels were collected. For each stage, load and displacement were also recorded in synchronization with images timestamps. Optical acquisition was interrupted when the paint started to present appreciable detachments from the specimen surface,
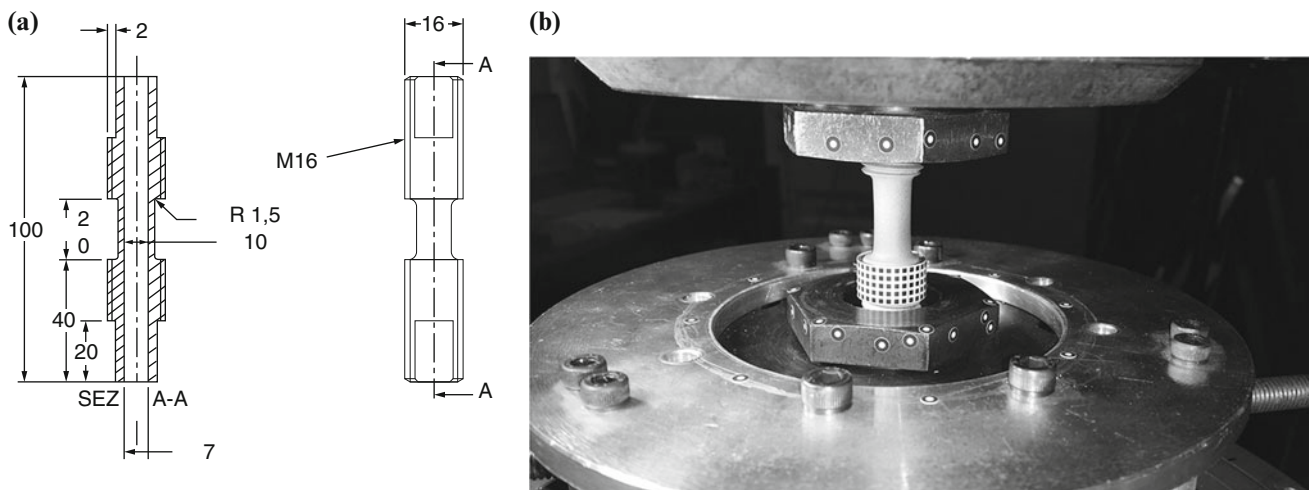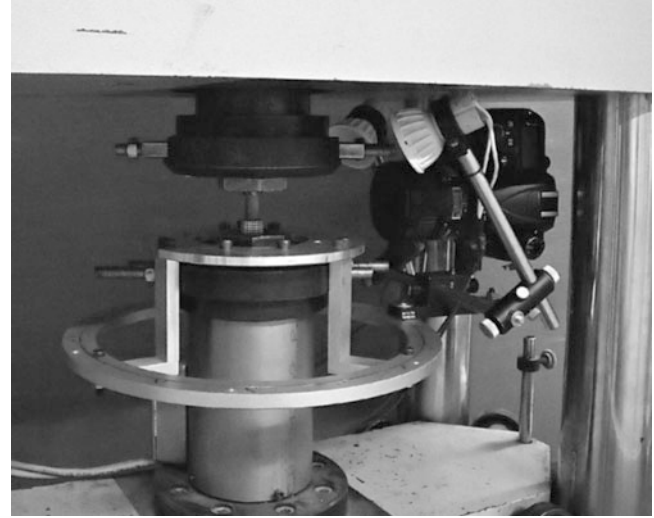

Fig. 30.1 (a) Specimen geometry. (b) Specimen setup and details of the calibration pattern

Fig. 30.2 Optical rig for the 360-deg acquisition of digital images

Tab. 30.1 Test type definitions and displacement to rotation ratios

Test type		Proportional				Non-proportional		
Test number		Test 1	Test 2	Test 3	Test 4	Test 5	Test 6	Test 7
Loading path: u/θ ratio	Stage 1	Tension	0.28	0.67	1.57	0.17	0.17	Tension
	Stage 2					0.15	0.02	Torsion

which occurred at medium-high strain levels, but, unfortunately, before the final fracture. Additional tension-torsion tests are here reported, that were executed at an earlier stage of the work without the use of DIC [20] and that were employed for the calibration of the plasticity models. Different displacement to rotation ratios (u/θ ratio) were applied, both under proportional and non-proportional conditions. For these tests, load/displacement and torque/rotation curves were collected up to the instant of fracture. In this work, shape measurements on fractured specimens were additionally made, using a 3D scanner (Atos Core 300 from GOM), to obtain the gauge minimum section. Table 30.1 reports all test definitions and related data.

30.3   Validation of Constitutive Laws, Experimental Results, and Discussion

Both a J2 von Mises plasticity and an enhanced J2–J3 plasticity model were already tuned on the selected material, based on tensile and torsion tests, using inverse methods [21]. In this work, it was also proved that the more advanced model needs to be used when complex multiaxial loading conditions are implied. Such advanced plasticity model, differently from the J2 formulation, accounts for the effect of the third deviatoric invariant on the flow rule. As yield function it was used:

$$q \frac{g(X = 1, \beta, \gamma)}{g(X, \beta, \gamma)} - \sigma_Y \left(\varepsilon_p \right)^{Tens} = 0 \tag{30.1}$$

where:

$$g(X, \beta, \gamma) = \frac{1}{\cos \left[\beta \frac{\pi}{6} - \frac{1}{3} \arccos(\gamma X) \right]} \tag{30.2}$$

is the function that modifies the standard von Mises yield function shape according to the deviatoric parameter:

$$X = \frac{3\sqrt{3}}{2} \frac{J_3}{J_2^{3/2}} \tag{30.3}$$

terms β and λ are material constants to be identified. Details of the theoretical formulations, calibration procedures and material constants can be found in [21]. In the following, a validation of the abovementioned calibration is provided, in terms of experimental-numerical match of both global quantities and local data, adopting the J2–J3 model. Results from multiaxial tension-torsion tests are presented, which provided stress states on the material very different from the ones used for tuning. Tension test results are reported for reference, too. Particularly, Fig. 30.3 illustrates the level of agreement in terms of global quantities, which is very good. Instead, Table 30.2 summarizes a "local" comparison, between the actual fracture diameters (measured at minimum cross-section), and the prediction from numerical simulation. This kind of data is critical, being more sensitive to elasto-plastic behavior variations. Also in this case, the experimental-numerical match is fairly good for almost all tests, with maximum error below 9 %. Analyzing these results, it can be stated that the J2–J3 model is properly calibrated, and that the numerical simulation is capable to accounts for all experimental observations.

These results highlight the great importance and significance of local data, here used for validation. Indeed, such information could be as well used in a multi-objective calibration, along with global quantities, thus achieving a more robust characterization. In this context, apart from the basic measurements adopted here, great benefits could derive from the usage of 3D-DIC which would permit the identification of the full radial profile of specimens during deformation, as well as the components of the strain tensor along any arbitrary surface path. All these quantities might be compared with the corresponding numerical ones coming from FE analysis, such that numerical constitutive laws could be setup accordingly. To explore this possibility, the results from the tensile test run using DIC analysis are now presented. Figure 30.4 illustrates a sequence of images acquired at different loading stages, for a given angular position of the camera system. These images were post-processed, to retrieve the specimen profile, and the axial and circumferential strain on the profile itself.
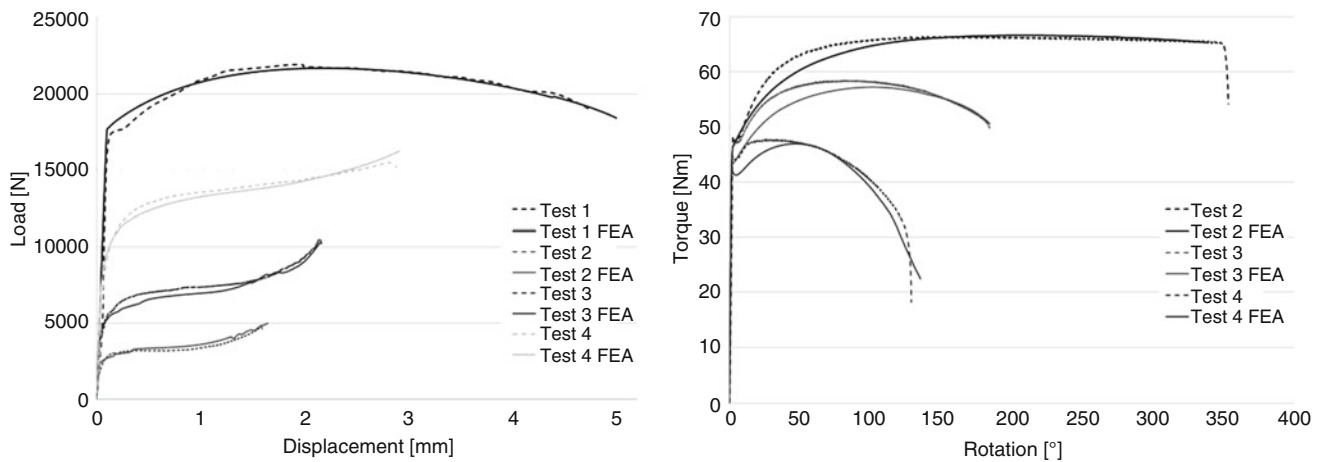

Fig. 30.3 Load-displacement and torque-rotation experimental and numerical data for proportional tests

Tab. 30.2 Gauge fracture cross-section diameters, experimental-numerical comparison: percentage errors

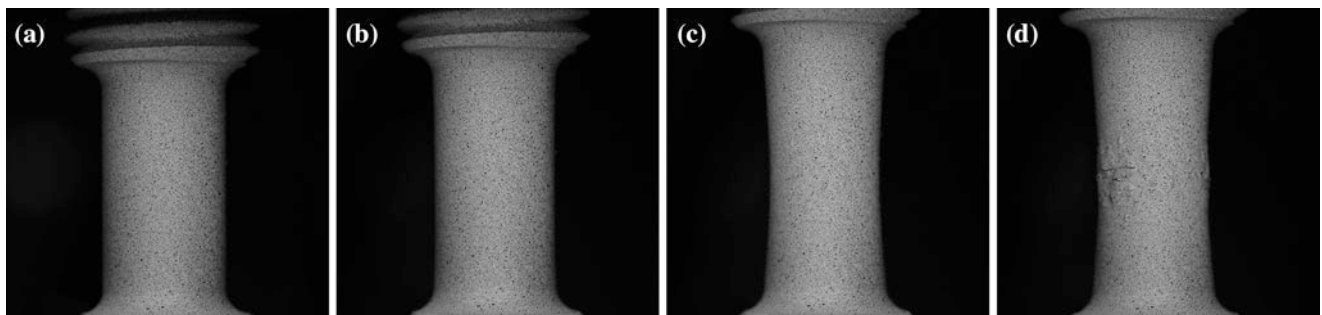|	Test 1	Test 2	Test 3	Test 4	Test 5	Test 6	Test 7
External diameter	0.27	−1.20	0.34	3.51	4.27	1.27	−0.10
Internal diameter	−1.08	−2.70	−8.49	−8.40	0.88	−0.86	−0.29

Fig. 30.4 Details of the images acquired at different elongations during the axial test: (**a**) 0 mm; (**b**) 1.35 mm; (**c**) 3.3 mm; (**d**) 3.75 mm

Fig. 30.5 Radial profile, 3D-DIC—numerical comparison, at two different average equivalent plastic strain values
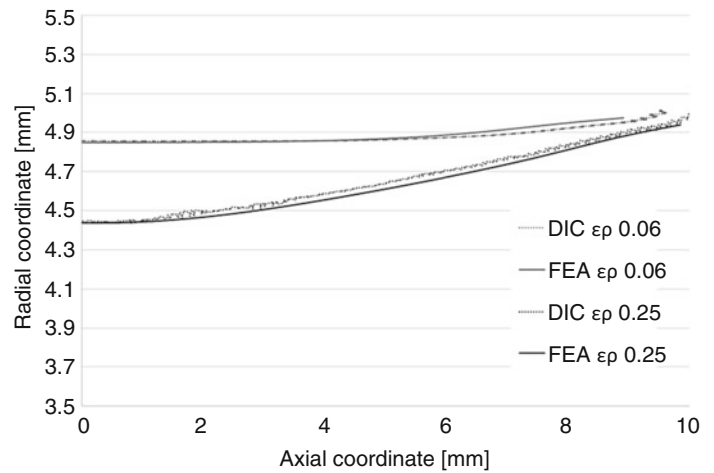

Fig. 30.6 Axial strain, 3D DIC—numerical comparison, at two different average equivalent plastic strain values
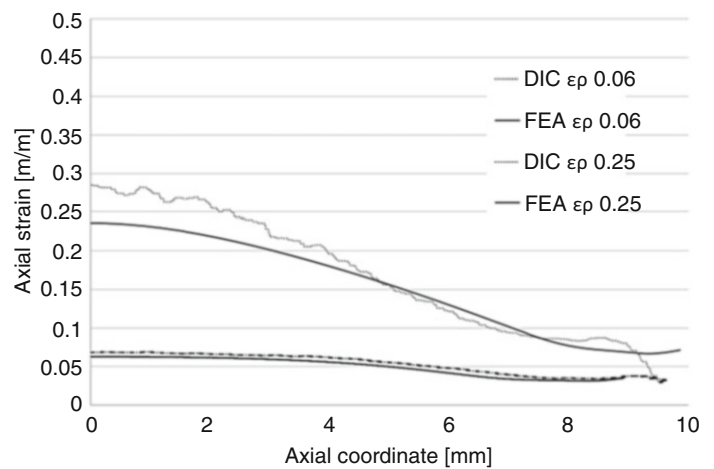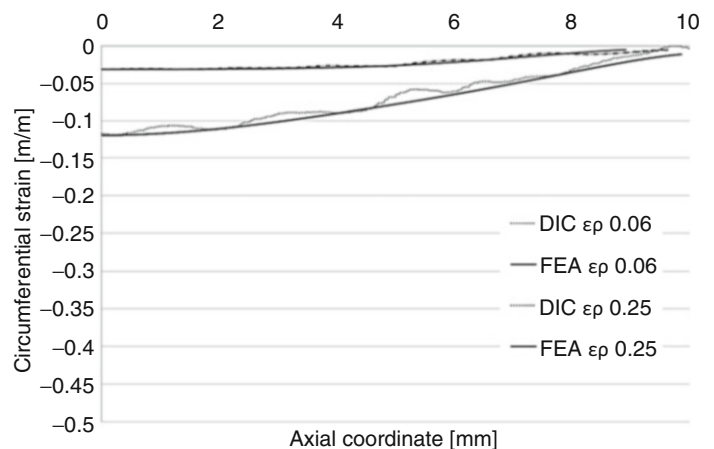

Fig. 30.7 Circumferential strain, 3D DIC—numerical comparison, at two different average equivalent plastic strain values

The technique used for the data processing is described in detail in [23, 24]. Given the accuracy of the material calibration, as demonstrated by data shown above, it can be assumed that the numerical simulation of the tensile test is reliable, and its output can be checked against DIC results to prove that the technique can capture the local material behavior in terms of displacements, and strains fields. The main outcomes of this comparison are shown in Figs. 30.5, 30.6 and 30.7. Two stages are here reported, both relative to large deformation, in the post-necking regime. The latter corresponds to the last stage before paint detachment (at an axial strain of about 0.3 m/m), after which the correlation was lost. In all graphs, the quantities

are plotted against the actual axial coordinate of the specimen, zeroed on the minimum deformed cross-section. The pictures shows a satisfactory agreement between DIC measurement and numerical models.

The technique, here illustrated for a tensile test, can be profitably used on more complex multiaxial tests. This is particularly valuable, since advanced plasticity models, such as the J2–J3 here presented, cannot be calibrated on tension only, requiring several non-conventional tests, and resulting in a high experimental effort. It would be therefore possible, using DIC to setup an inverse calibration based on the local information, which can help to reduce the number of tests to be performed. Anyway, the method expresses its greatest potential in the characterization of anisotropic materials. In this case, profiles, radial and circumferential deformation should be acquired along different directions, and could be useful to identify the principal directions and quantify the level of anisotropy of the specific material. In addition, numerical models used for anisotropy require several material constants to be identified, based on tests from specimen machined from different anisotropy directions. In this case, using 360-deg DIC, with a very limited number of tests it would be possible to provide an effective calibration, given the larger amount of information that can be collected.

30.4 Conclusions

The present paper investigates the possibility of using a 360-deg DIC measurement system to characterize the mechanical properties of material in large strain plasticity. To this purpose, firstly the elasto-plastic properties of an isotropic material were identified from typical data coming from tension and tension-torsion tests (force-displacement, torque-rotation). A J2–J3 plasticity model was calibrated, and verified in terms of global quantities and specimen sections at fracture prediction. Then, new axial tests were performed on the same material using the 360-deg DIC technique to measure the profile and the deformation of the sample during the test. The comparison of these experimental measurements with the calibrated FE simulation showed a good agreement, thus demonstrating the reliability of the proposed approach. In future works, the measurement technique, here validated for the isotropic case, will be used to study the behavior of anisotropic materials, looking at the non-symmetrical evolution of the necking profile, and considering mixed tension-torsion tests.

References

1. Bridgman, P.W.: Studies in Large Plastic Flow and Fracture with Special Emphasis on the Effects of Hydrostatic Pressure. McGraw-Hill, New York (1952)
2. Clausing, D.P.: Effect of plastic strain state on ductility and toughness. Int. J. Fract. Mech. **6**, 71–85 (1970)
3. Hu, W., Wang, Z.R.: Multiple-factor dependence of the yielding behavior to isotropic ductile materials. Comput. Mater. Sci. **32**(1), 31–46 (2005)
4. Bardet, J.P.: Lode dependences for isotropic pressure-sensitive elastoplastic materials. J. Appl. Mech. **57**(3), 498–506 (1990)
5. Brunig, M.: Numerical simulation of the large elastic–plastic deformation behavior of hydrostatic stress-sensitive solids. Int. J. Plast. **15**(11), 1237–1264 (1999)
6. Gao, X., Zhang, T., Zhou, J., Graham, S.M., Hayden, M., Roe, C.: On stress-state dependent plasticity modeling: significance of the hydrostatic stress, the third invariant of stress deviator and the non-associated flow rule. Int. J. Plast. **27**(2), 217–231 (2011)
7. Bai, Y., Wierzbicki, T.: A new model of metal plasticity and fracture with pressure and Lode dependence. Int. J. Plast. **24**(6), 1071–1096 (2008)
8. Yoon, J.W., Lou, Y., Yoon, J., Glazoff, M.: Asymmetric yield function based on the stress invariants for pressure sensitive metals. Int. J. Plast. **56**, 184–202 (2014)
9. Kuroda, M.: A phenomenological plasticity model accounting for hydrostatic stress-sensitivity and vertex-type of effect. Mech. Mater. **36**(3), 285–297 (2004)
10. Prager, W.: Strain hardening under combined stresses. J. Appl. Phys. **16**(12), 837–840 (1945)
11. Ohashi, Y., Tokuda, M.: Precise measurement of plastic behaviour of mild steel tubular specimens subjected to combined torsion and axial force. J. Mech. Phys. Solids **21**(4), 241–261 (1973)
12. Miller, M.P., McDowell, D.L.: Modeling large strain multiaxial effects in FCC polycrystals. Int. J. Plast. **12**(7), 875–902 (1992)
13. Faleskog, J., Barsoum, I.: Tension-torsion fracture experiments—part I: experiments and a procedure to evaluate the equivalent plastic strain. Int. J. Solids Struct. **50**, 4241–4257 (2013)
14. Dufour, J.-E., Hild, F., Roux, S.: Shape, displacement and mechanical properties from isogeometric multiview stereocorrelation. J. Strain Anal. Eng. Des. **50**(7), 470–487 (2015)
15. Wang, Y., Lava, P., Coppieters, S., Houtte, P.V., Debruyne, D.: Application of a multi-camera stereo DIC set-up to assess strain fields in an Erichsen test: methodology and validation. Strain **49**, 190–198 (2013)
16. Rossi, M., Lava, P., Pierron, F., Debruyne, D., Sasso, M.: Effect of DIC spatial resolution, noise and interpolation error on identification results with the VFM. Strain **51**(3), 206–222 (2015)

17. Sasso, M., Chiappini, G., Rossi, M., Cortese, L., Mancini, E.: Visco-hyper-pseudo-elastic characterization of a fluoro-silicone rubber. Exp. Mech. **54**(3), 315–328 (2014)
18. Sutton, M.A., Orteu, J.-J., Schreier, H.: Image Correlation for Shape, Motion and Deformation Measurements. Springer, New York (2009). ISBN 978-0-387-78747-3
19. Wang, Z., Kieu, H., Nguyen, H., Le, M.: Digital image correlation in experimental mechanics and image registration in computer vision: similarities, differences and complements. Opt. Lasers Eng. **65**, 18–27 (2015)
20. Cortese, L., Coppola, T., Campanelli, F., Campana, F., Sasso, M.: Prediction of ductile failure in materials for onshore and offshore pipeline applications. Int. J. Damage Mech. **23**(1), 104–123 (2014). doi:10.1177/1056789513485967
21. Cortese, L., Coppola, T., Campanelli, F., Broggiato, G.B.: A J2-J3 approach in plastic and damage description of ductile materials. Int. J. Damage Mech. **25**(2), 228–250 (2016). doi:10.1177/1056789515577228
22. Cortese, L., Broggiato, G.B., Coppola, T., Campanelli, F.: An enhanced plasticity model for material characterization at large strain. In: Conference Proceedings of the Society for Experimental Mechanics Series, p. 287 (2014). ISBN:978-331900875-2
23. Spera, D., Genovese, K., Voloshin, A.: Application of stereo-digital image correlation to full-field 3-D deformation measurement of intervertebral disc. Strain **47**(s1), e572–e587 (2011)
24. Genovese, K., Cortese, L., Rossi, M., Amodio, D.: A 360-deg digital image correlation system for material testing. Opt. Lasers Eng. **82**, 127–134 (2016)

Chapter 31
Identification of Plastic Behaviour and Formability Limits of Aluminium Alloys at High Temperature

G. Chiappini, L.M. Mattucci, M. El Mehtedi, and M. Sasso

Abstract In order to simulate accurately the stamping process of sheet metals, their constitutive behaviour, as well as their formability limits, must be accurately evaluated. In this work, tensile and Nakazima tests are conducted at high temperature on aluminium alloys of the 5000 series. The tensile tests are mainly used to determine the flow stress curve of the material, while the Nakazima tests, are used to determine the admissible elongation before failure at different strain ratios. The raw load-displacement curves and the deformation of the samples, measured by the optical grid method, are included in an inverse FEM procedure to best identify the real elasto-plastic law of the material and its formability limits.

Keywords Aluminium alloys • Grid method • Inverse method • Plastic behaviour • Formability

31.1 Introduction

The hot-forming process has reached a preminent position in most of the mechanical fields, like automotive or aerospatial industry; as obvious, the trend is to obtain, even in mass production, finished products with the best quality characteristics as well a reduction of the waste due to breaking or surface defects or overcoming of the geometrical tolerance limits. In this scenario, the necessity to product semi-finished or finished parts with a low order of wasted material involved by process errors or surface defects, has determinated a concentration of sperimental, theoretical and numerical studies about the sheet metal forming.

For a correct process simulation [1, 2] it is necessary to obtain the mechanical and formability characteristics of the material, in ordered to simulate even the most complex products, most of all for the barely workable materials. The deformation behaviour of aluminium alloys has been frequently object of researches to determinate the principal mechanisms involved.

The easiest test to characterize the deformation behaviour of a material is the tensile one, however it is just valid in uni-axial tensile cases. To investigate more complex deformation processes, like the hot forming ones, it is necessary to lead a test where all the tensile directions, or at least two of them, are involved like the bi-axial ones. Among them, one of the most diffuse is the Nakazima test, which allows to analyze the material in different deformation conditions, through its own specimen having different width. In this job, a semi-automatical optical technique, has been used for the measure of the deformation, based on the measure of a grid previously printed on the specimen surface: the calculation of the spatial position of the grid intersections obtained by a stereoscopic couple of camera, three-dimensionally calibrated according to the Heikkila algorithm, allowed to reconstruct the 3D surface of the specimen. Then the right Cauchy-Green tensor has been created that allowed to obtain the logarithmic strain field.

The results of the tensile test, together with the optical technique, made possible to obtain the mechanical characteristics of the 5000 aluminium alloy: the breaking load (Rmax), the yield load at the 0.2 % of the plastic strain (Ry), the elongation at break (A%), and the forming limit diagrams.

G. Chiappini • L.M. Mattucci • M. El Mehtedi • M. Sasso (✉)

Dipartimento di Ingegneria Industriale e Scienze Matematiche, Università Politecnica delle Marche,
via Brecce Bianche, Ancona 60131, Italy
e-mail: m.sasso@univpm.it

31.2 Materials and Experimental Techniques

31.2.1 Materials

Magnesium is one of the most effective and widely used alloying elements for aluminium, and is the principal element in the 5000 series alloys. When it is used as the major alloying element or combined with manganese, the result is a moderate- to high-strength, non-heat-treatable alloy. Alloys in this series are readily weldable and have excellent resistance to corrosion, even in marine applications. When magnesium content exceeds 3 % corrosion resistivity is reduced depending on the application and temperature of operation (more than 1000 °C). Most of aluminium-magnesium alloys are characterized by good corrosion resistance (in general under stress and other means of corrosions). It is necessary to note their good corrosion resistance in the sea water. High strength of magnesium alloys is achieved by a thin oxide film that appears on the surface.

In order to improve the strength and corrosion resistance characteristics, manganese and chromium are added. As strengthening agents in small portions scandium and zirconium are used. Magnesium content in the alloy is 0–37.5 % which is eutectics. Eutectics exist at the temperature equal to 449 °C and magnesium content 34.5 %. Dissolution of magnesium at this temperature is maximum and equals to 17.4 % (in some sources 16.5 %). At the temperature of 300 °C in liquid-solid solution only 6.7 % magnesium can be dissolved; at 100 °C—1.9 % magnesium. Magnesium that was not dissolved remains in the form of liquid-phase. Implementation of 0.5–0.7 % magnesium into aluminium increases dramatically the incidence of hot cracks formation (65 %). Further on this characteristics (K) is reduced and stabilized at a level of 30 % with 6–7 % magnesium.

31.2.2 Experimental Tests

The characteristics of the sheets, such as formability, generally depend on many factors [3, 4]. Some features are dependent on the application of the load conditions, for example from the speed of load application, and are also affected by temperature. The tensile tests were performed at three different temperatures on proportional test specimen (UNI EN 10002); the tests were performed with displacement control, with a crosshead speed of 3 mm/min. The Nakazima test [5] consists in forming a rectangular specimen having different widths using a hemispherical punch, a die and a blank holder, until it reaches the necking or fracture (Fig. 31.1). By varying the length of the specimen and the lubrication conditions, are obtained different levels of deformation, from those typical of the deep drawing to those of the stretch forming [6]. By varying the ratio of the initial size of the sheet, entirely different deformations conditions, are derived: while, for a ratio of the sides equal to 1 (a square initial blank) acts on the blank holder around the contour of the sheet metal and have conditions of fully balanced biaxial stretching; to vary the ratio between the sides of the blank holder operates on a limited part of the contour of the sheet and the stretching conditions are increasingly unbalanced.
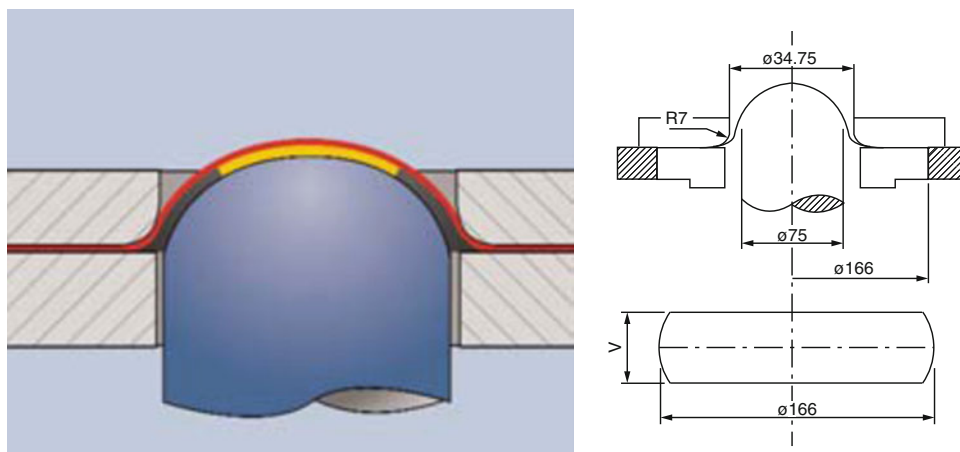

Fig. 31.1 Nakazima test

The advantages of the Nakazima test consist of the simplicity of the equipment and the specimen shape, as well as the ability to track the entire domain of the formability limit curve. The disadvantages, however, consist in the probability of causing wrinkling and crinkle of the material and in the possibility to have measurement errors since the latter occur practically in the rupture zone that occurs on a curved surface by the action of the hemispherical shape of the punch and so on a curved surface. The use of a stereoscopic optical technique has allowed to eliminate this type of measurement error.

31.3 Optical Methods

The principle on which is based the measurement of the deformations is the calculation of spatial positions of the intersections of a grid, initially equispaced, imprinted on the specimen undeformed which deforms during tensile test or during the Nakazima test. The specimen surface is taken up by a stereoscopic two-camera system CMOS with a resolution of 1280×1024 pixel (Pixelink®B371F) at 25 frame/s. Cameras are three-dimensionally calibrated using the calibration algorithm Heikkila with a common reference system. For calibration it used a grid of dots 50×50 with 1 mm pitch, shoot in different positions from the two cameras.

Through a calculation program developed in Matlab [7] the intrinsic parameters (focals, coordinates of the optical center, skewness), the extrinsic parameters (rotation angles, the position vector) and the radial distortion coefficients for the two cameras, were calculated. Then, these parameters were used for the calculation of stereoscopic triangulation necessary for the reconstruction of the specimen surface. In Fig. 31.2 it is shown a graphical view of the location of the two cameras with respect to the surface of the specimen obtained by stereoscopic calculation carried out with the obtained parameters, as listed in the table. In Fig. 31.3 shows the images acquired by the two cameras for the tensile test specimens.
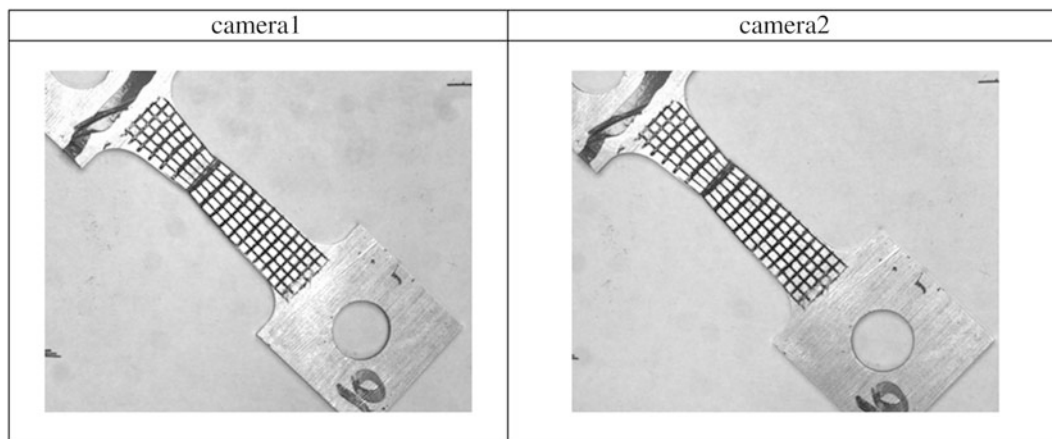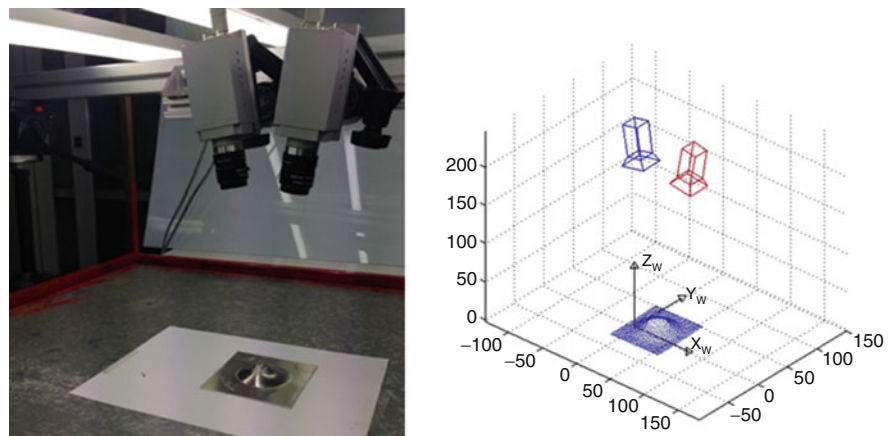

Fig. 31.2 Calibration results

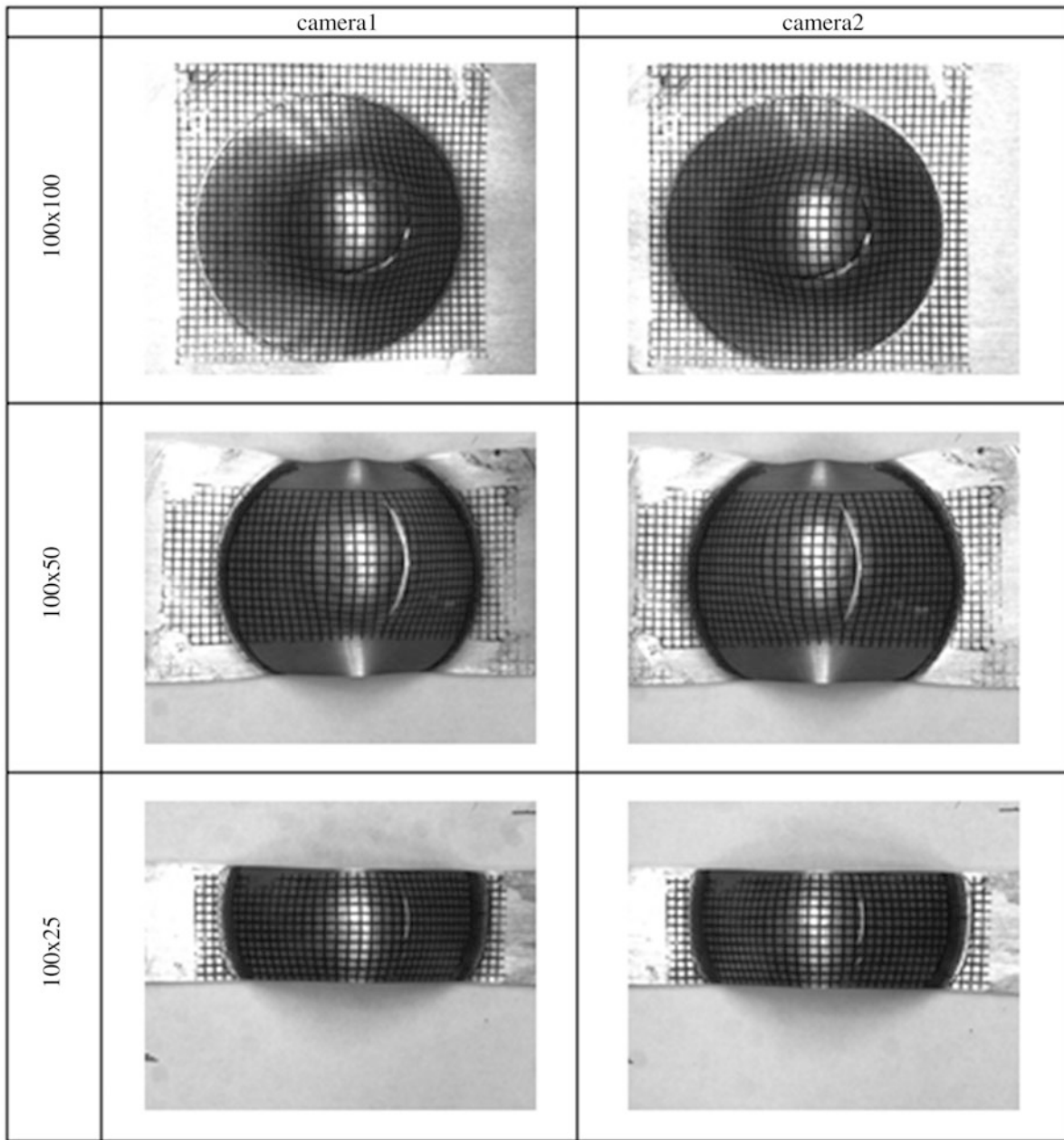**Fig. 31.3** Deformed grid for tensile tests

Fig. 31.4 Deformed grid for Nakazima tests

Figure 31.4 shows the images acquired for the Nakazima test specimens: were used two different types of specimens with different aspect ratio. The images were processed with a semiautomatic Matlab® program for the recognition of the pixel coordinates of the cross centers based on an algorithm in which we can distinguish three main phases:

- image segmentation,
- determination of the center point of the marker,
- sorting centers according to their referential position

After the binarization of the image through an algorithm based on search of the Convex Hull polygons, the coordinates of the center point of intersections of the grid, are determined. Sorting problem refers to the process of association between markers found on the surface and the respective referential coordinates. In the case of square mesh grids each marker corresponds to a pair of integer coordinates. This step is essential to identify the intersections between the two cameras.
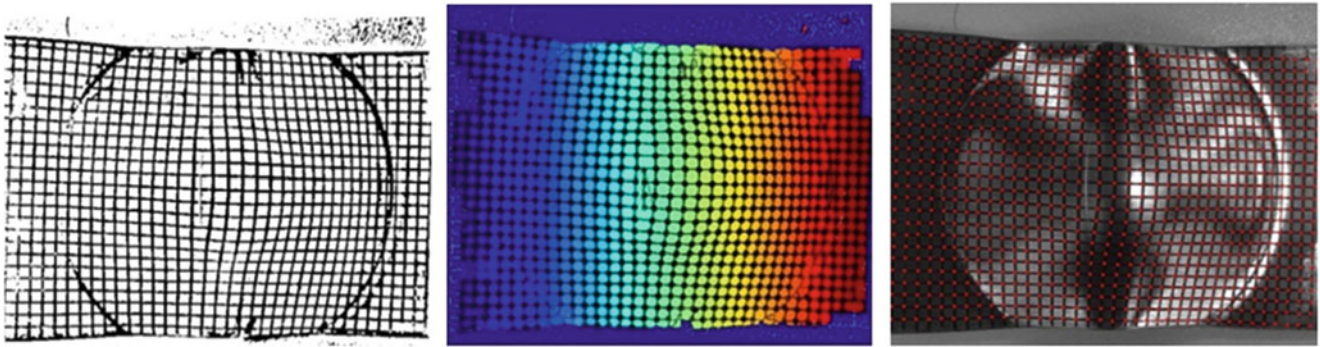
Fig. 31.5 Corner search algorithm
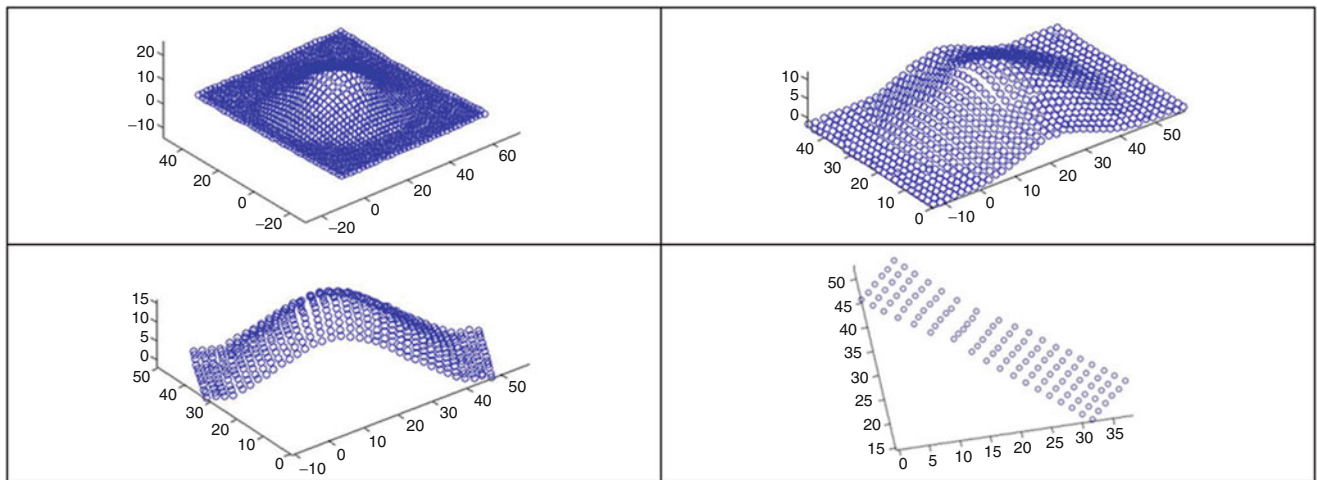
Fig. 31.6 3D representation 3D—test Nakazima and tensile test

Figure 31.5 shows the sequence of operations carried out for an image of Nakazima test: the binarized image, the map of convex polygons used to obtain the center of the crosses and the original image with highlighted found centers, are visible: the results of the automated process are filtered and optimized to eliminate false intersections and insert any crossings undetected due to uneven illumination.

Starting from the pixel coordinates, using the referential coordinates automatically assigned on the two images, pairs of corresponding points are determined. Through a stereoscopic calculation based on the pinhole model and epipolar geometry, the 3D surface of the specimen, displayed as a cloud of points in Fig. 31.6, is determined.

Comparing the marker coordinates in the deformed configuration with those of the undeformed configuration, according to the theory of large deformations, defining the shape functions is then calculated the gradient tensor of deformations from which it was obtained the right Cauchy-Green tensor which allowed to obtain the logarithmic deformation. In Fig. 31.7 is shown the map of the principal deformations ε_1 and ε_2 calculated for a Nakazima test.

The deformation maps were plotted directly superimposed to the scanned images to identify exactly the location of points of interest for further processing. In Fig. 31.8 is shown the map of the deformation along the thickness calculated by considering the conservation of volume.

31.4 Results

In Fig. 31.9 are shown the experimental curves obtained by the tensile tests made at different temperatures (200 and 300 °C) and speeds (0.5 and 5 mm/s).

The results of the optical elaborations have been used to obtain the forming limit diagrams (FLD) shown in Fig. 31.10.
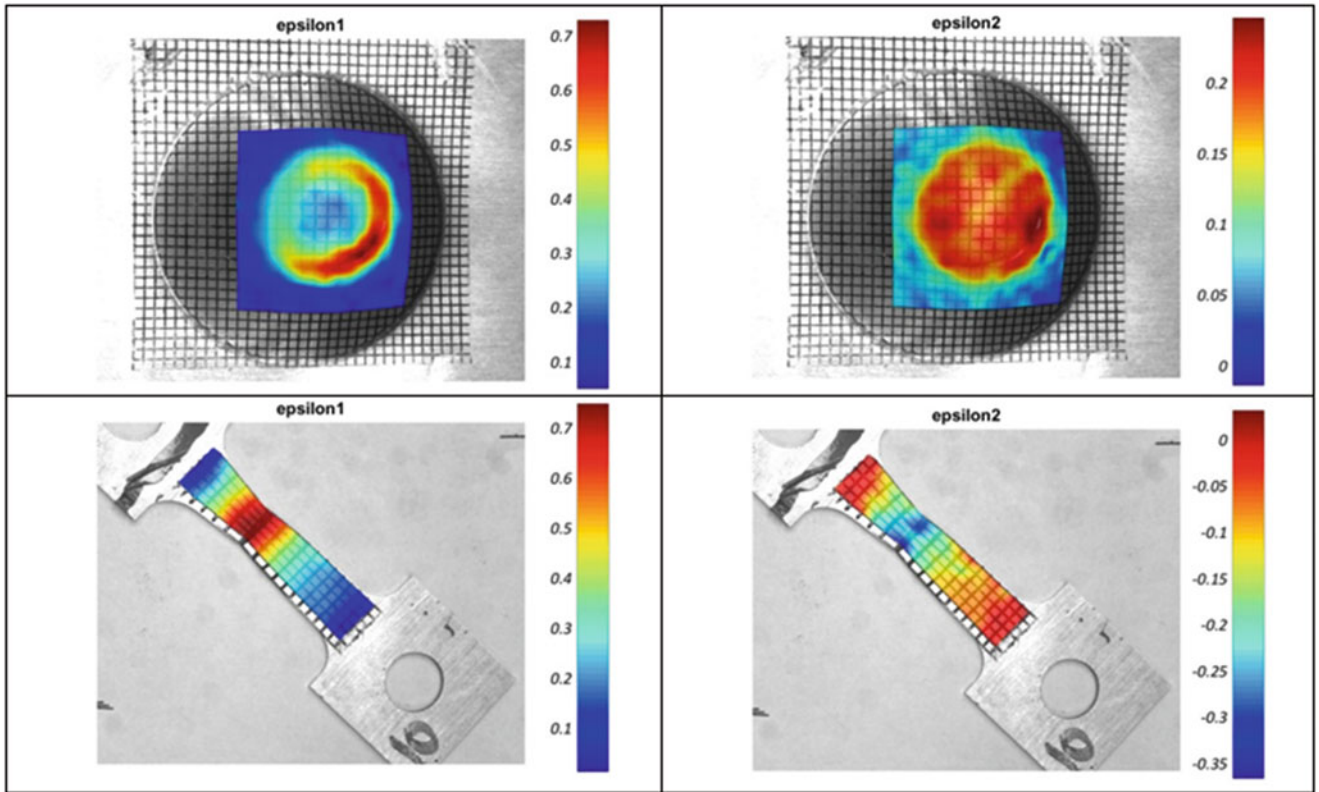
Fig. 31.7 Maps of major/minor strain
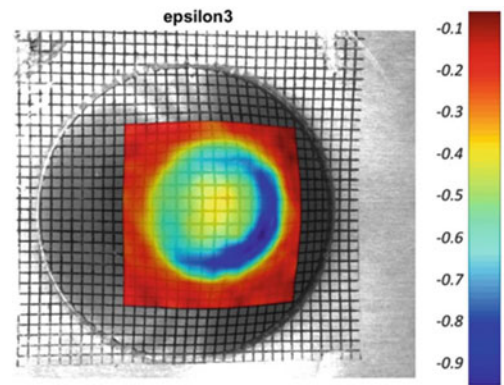

Fig. 31.8 Map of the thickness deformation

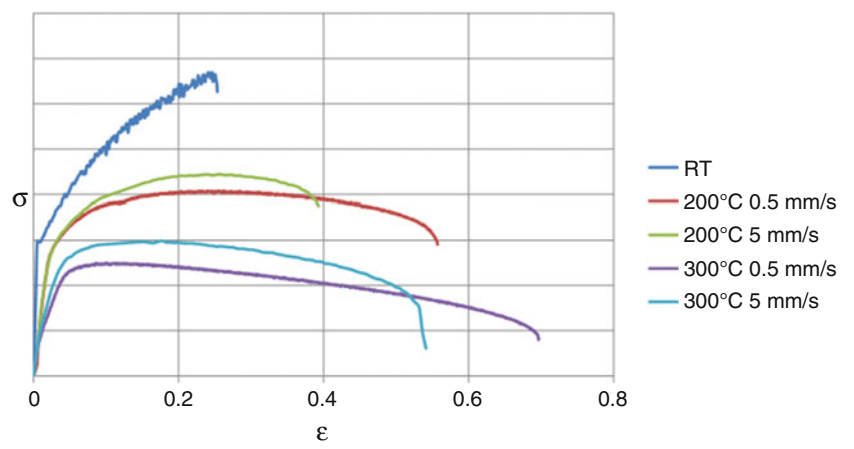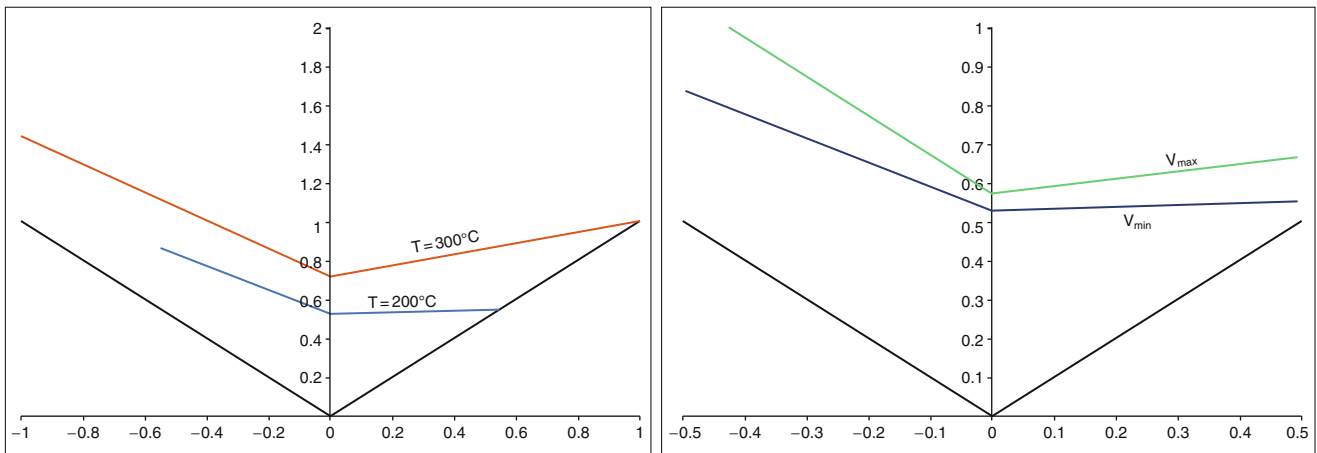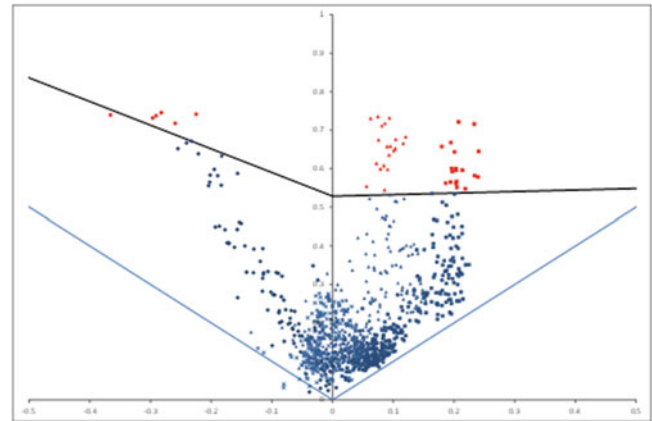**Fig. 31.9** Tensile test

Fig. 31.10 FLD 200° v$_{max}$

Fig. 31.11 FLC comparison between different temperatures and different speeds

The forming limit curves (FLC) have been obtained through the interpolation of the maximum major strain values of all the different tests. Fig. 31.11 shows a comparison between the FLCs obtained at different temperatures and different speeds.

Experimental data are input into a Matlab® optimization procedure where material parameters of the theoretical plastic model are iteratively changed in order to minimize the force error between test and numerical data obtained from a tensile test FEM simulation (Fig. 31.12). The resulting calibrated model is able to describe the material response in a general deformation process.

In Fig. 31.13, the experimental curve and the numerical one obtained by the Matlab® optimization are shown.

Starting from the inverse FEM results, a different FEM model for the Nakazima test has been realized. Fig. 31.14 shows a screen of the FEM model, a principal tensile map in a section view and with a full axisymmetric view. Results are consistent with the experimental ones and can be adopted, varying the specimen size ratio, to complete the material FLD curves.

31.5   Conclusions

The present article has shown the job made to analyze the hot formability process of a 5000 series aluminium alloy, obtaining the FLD and stress-strain curves.

Strain measure has been made trough an optical technique for the strain measure based on the grid method. In the last years, most of the measure performed to obtain the stain levels of a material have been made manually, trough plenty tools like calibers, callipers, Mylar tape, microscopes etc. able to measure the length change in the grid elements printed on the specimen.
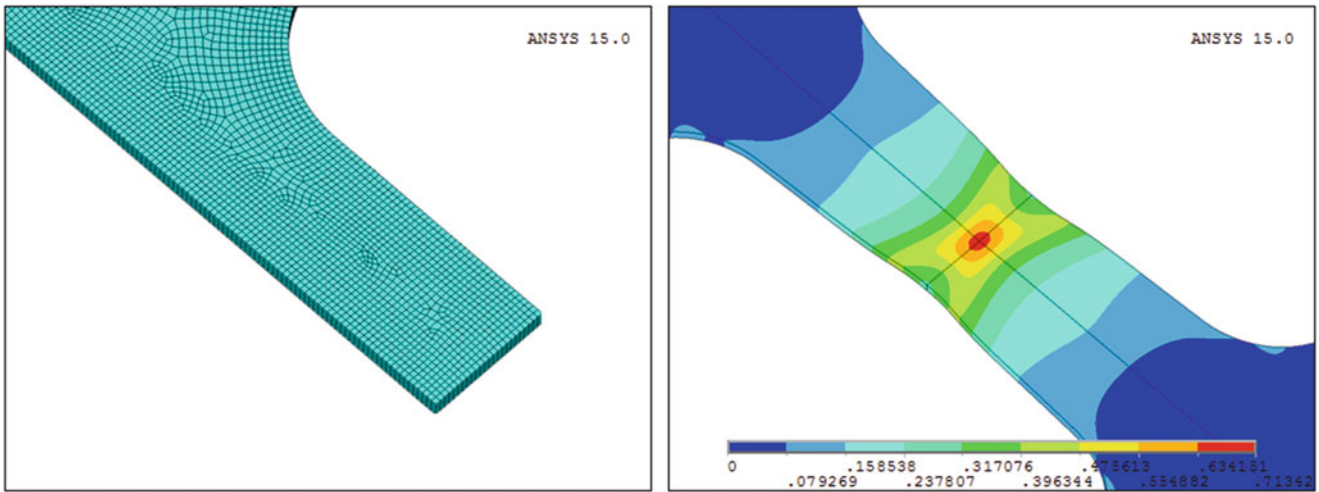
Fig. 31.12 Tensile test FEM model

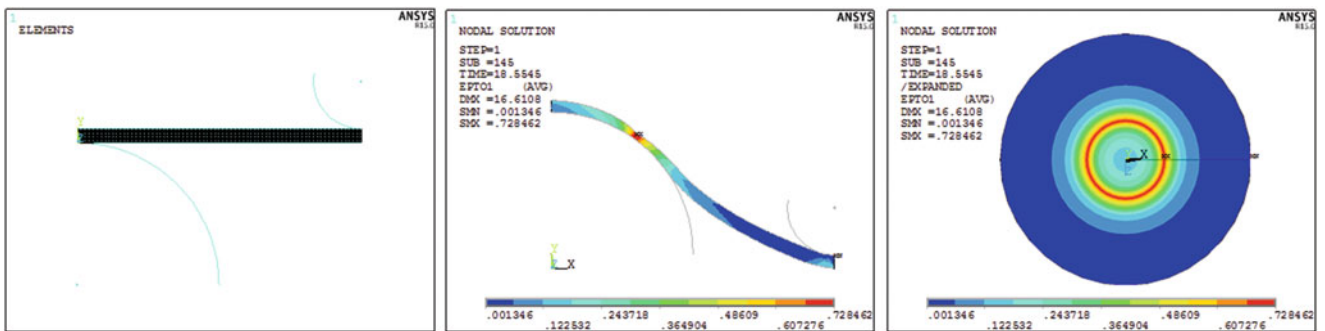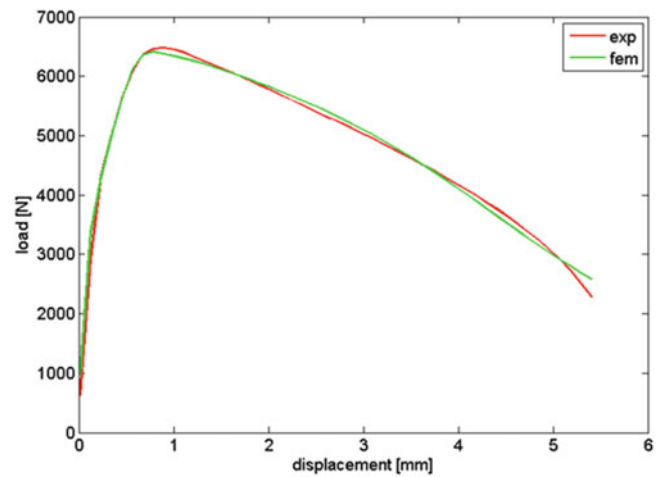**Fig. 31.13** Experimental and numerical "load-displacement" curves

Fig. 31.14 Nakazima test FEM model

Manually measures requires an expensive experimental work and most of all are commonly affected by errors due to the operator interpretation, the automatic method instead allows to obtain the deformation reliably and directly; furthermore the result has been represent as a full field coloured map with a spatial resolution higher than the manual methods one.

Trough an inverse-FEM procedure (ANSYS) optimized with Matlab®, all the material parameters of the theoretical plastic model have been obtained and have been verified trough a FEM simulation of the Nakazima test, having the same

results of the sperimental test. Future possible developments could be the utilization of the numerical methods for the strain calculation based on the XFEM theory (eXtended Finite Element Method), in order to get the strain value from the grid deformation even on the clique edge and then obtain more accurate forming limit diagrams.

References

1. Makinouchi, A.: Sheet metal forming simulation in industry. J. Mater. Process. Technol. **60**, 19–26 (1996)
2. Goodwin, G.M.: Application of strain analysis to sheet metal forming problem in the press shop, society of automotive engineers, no. 680093, pp. 380–387 (1968)
3. Ricci, P., El Mehtedi, M., Barone, L., Spigarelli, S.: Effects of temperature and sheet thickness on formability of AZ31 magnesium alloy. Mater. Sci. Forum **604–605**, 147–152 (2009)
4. Banabic, D., Bunge, H.-J., Pöhlandt, K., Tekkaya, A.E.: Formability of Metallic Materials. Springer, Berlin (2000)
5. ASTM E2218-2: Standard test method for determining forming limit curves
6. Knockaert, R., Chastel, Y., Massoni, E.: Experimental and numerical determination of texture evolution during deep drawing tests. J. Mater. Process. Technol. **110**, 300–311 (2001)
7. Sasso, M., Chiappini, G., Rossi, M., Amodio, D.: Strain assessment in cracked sheet metals by optical grid method. Conf. proc. of SEM series, Advancement of Optical Methods in Experimental Mechanics, Volume 3, pp 39–46 (2015)

Chapter 32
Accurate Strain Distribution Measurement Based on the Sampling Moiré Method

S. Ri, Y. Fukami, Q. Wang, and S. Ogihara

Abstract To obtain accurate measurement of non-uniform strains over the entire surface of materials or structures, in this study, the sampling moiré method is applied to two-dimensional measurement of in-plane displacement and strain distributions. The two-dimensional displacement distribution is obtained by detecting the phase difference of the moiré fringes, and the strain distribution is determined by measuring the change of grating pitches on the specimen in vertical and horizontal directions before and after deformations. A compensation technique of fringe order is proposed to eliminate the pitch error of fabricated grating. In addition, a spatial filtering procedure in phase distribution is suggested to reduce the random measurement error. The deformations of an aluminum specimen with a through hole under different tensile loads were measured by the proposed method. Experimental results indicated that the measurement accuracy of strain distribution can be dramatically improved by combination the above-mentioned two techniques. This method is useful to evaluate mechanical properties of various materials under tension/compression or heating/cooling testing.

Keywords Sampling moiré method • Optical method • Strain measurement • Elastic-plastic deformation • Material evaluation

32.1 Introduction

To evaluate the mechanical properties and understand the instability behaviors of various structures, it is necessary to measure the strain distribution with high accuracy [1, 2]. Optical methods, such as digital image correlation (DIC) method [3], electronic speckle pattern interferometers (ESPI) [4], shearography [5], digital holography [6], are effective and widely applied experimental techniques for displacement and strain determinations due to the advantages of non-contact, full-field, and fast measurement. Moiré technique is one of the optical methods for measuring the displacement and strain distributions using grids [7] or diffraction gratings [8]. The moiré method is suitable to measure complex strain fields of various composite materials.

Recently, a sampling moiré method [9, 10] has been developed to measure the small displacement by using a repeated pattern. By using the sampling moiré method, the grating pitch can also be measured with high accuracy [11]. Then, the strain can be directly determined from the change of grating pitches on the specimen before and after deformations according to the tensile loading [12].

In this study, an accurate strain distribution measurement technique based on the sampling moiré method is proposed. A tensile test of an aluminum specimen with a 0.5 mm-pitch grating was performed. The deformations of the specimen under different tensile loads were measured by the proposed method. Experimental results demonstrated that full-field strain measurement can be performed accurately in the elastic-plastic region for small strain. It is expected that our proposed method can be applied to deformation problems in solid mechanics for a complex strain field phenomenon.

S. Ri (✉) • Q. Wang

Research Institute for Measurement and Analytical Instrumentation, National Institute of Advanced Industrial Science and Technology, Tsukuba, Ibaraki 305-8568, Japan
e-mail: ri-shien@aist.go.jp

Y. Fukami

National Institute of Advanced Industrial Science and Technology (AIST), Tsukuba, Japan

Department of Mechanical Engineering, Tokyo University of Science, Chiba 278-8510, Japan

S. Ogihara

Department of Mechanical Engineering, Tokyo University of Science, Chiba 278-8510, Japan

32.2 Principle

32.2.1 Principle of the Sampling Moiré Method

Figure 32.1 shows the basic principle of the sampling moiré method [9, 10] based on the down-sampling and intensity-interpolation image processing. First, when an original grating of pitch p is captured by a CCD camera as shown in Fig. 32.1a, the recorded intensity of the grating [Fig. 32.1b] with an initial phase φ_0 can be presented in Eq. (32.1).

$$I(i) = I_a(i) \cos \left(2\pi i/P + \varphi_0\right) + I_b(i) = I_a(i) \cos \left[\varphi(i)\right] + I_b(i) \tag{32.1}$$

where $I_a(i)$ represents the amplitude of the grating intensity and are sensitive to the phase change of the grating; $I_b(i)$ represents background intensity in the image, which are insensitive to the change in phase; P is the captured grating pitch as pixel unit in the digital image, and $\varphi(i)$ can be regarded as the phase value of the original grating at pixel i in the CCD plane.

In the sampling moiré method, multiple phase-shifted moiré fringe can be obtained by down-sampling the captured single grating image. In Fig. 32.1b, the sampling pitch T is 4-pixel. When every T pixel (sampling pitch) from the first sampling point is picked up, a moiré fringe with pitch $P \cdot T/|T - P|$ can be obtained. If the second, third, and fourth sampling points are selected as the first sampling point, multiple phase-shifted moiré fringes can be obtained, as shown in Fig. 32.1c. This process corresponds to the phase shifting. By performing an image interpolation using neighboring sampled intensity data, smooth phase-shifted moiré fringes of the same size as the original grating image can be reconstructed. The kth phase-shifted moiré fringe image, shown in Fig. 32.1d, can be expressed as follows:

$$I_m(i; k) = I_a(i) \cos \left[2\pi \left(\frac{1}{P} - \frac{1}{T}\right) i + \varphi_0\right] + I_b(i) = I_a(i) \cos \left[\varphi_m(i) + 2\pi \frac{k}{T}\right] + I_b(i) \tag{32.2}$$

Then, the phase value of the moiré fringe can be calculated by phase shifting method using discrete Fourier transform (DFT) algorithm, as presented in Eq. (32.3).

Fig. 32.1 Principle and image processing procedure of the sampling moiré method for phase analysis of a single fringe pattern. (**a**) relation between an original grating with pitch P and pixel array of a charge-coupled device (CCD), (**b**) the recorded intensity of the grating, (**c**) down-sampling process by changing the start point with a sampling pitch T, and (**d**) intensity interpolation process to generate multiple phase-shifted moire fringe
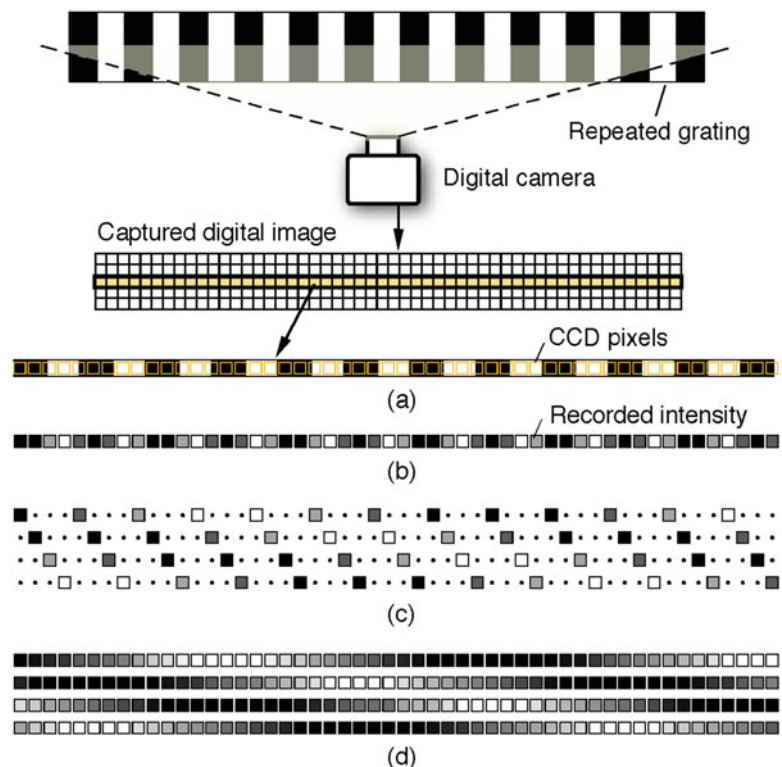
$$\varphi_m(i) = -\tan\frac{\sum_{k=0}^{T-1} I_k(i;k) \sin\left(2\pi\frac{k}{T}\right)}{\sum_{k=0}^{T-1} I_k(i;k) \cos\left(2\pi\frac{k}{T}\right)} \tag{32.3}$$

The phase distribution of the moiré fringe after deformation can be obtained in the same manner. The displacement can be obtained from the phase difference of the moiré fringe $\Delta\varphi_m(i) = \varphi'_m(i) - \varphi_m(i)$ before and after deformation. The displacement is directly proportional to the phase difference of the moiré fringe as follows.

$$u(i) = -\frac{P}{2\pi}\Delta\varphi_m(i) \tag{32.4}$$

If a 2D grating is used, 2D distributions of deformation can be obtained. In this case, a low-pass filter is applied to extract the x or y directional grating in advanced. The pitch of the grid can be obtained from the phase of the moiré fringe by following equation:

$$P(i) = \frac{2\pi T}{2\pi + \nabla\varphi_m(i)T} \tag{32.5}$$

where $\nabla\varphi_m(i)$ is the phase gradient of the moiré fringes, and can be calculated by Eq. (32.6).

$$\nabla\varphi_m(i) = [\varphi_m(i+1) - \varphi_m(i-1)]/2 \tag{32.6}$$

Finally, the strain (in x-direction) is simply obtained as the change of grating pitches before and after deformations.

$$\varepsilon(i) = \frac{P'(i) - P(i)}{P(i)} \times 10^6 \tag{32.7}$$

Figure 32.2 shows an example of the strain distribution measurement based on the sampling moiré method by simulation. Figure 32.2a shows the captured gratings before and after deformations. Figure 32.2b shows the phase-shifted moiré fringes after down-sampling and 2-order (B-spline) intensity interpolation. Figure 32.2c shows the phase distributions of the moiré fringes using the phase-shifting method. Figure 32.2d shows the grating pitches determined by Eqs. (32.5) and (32.6).
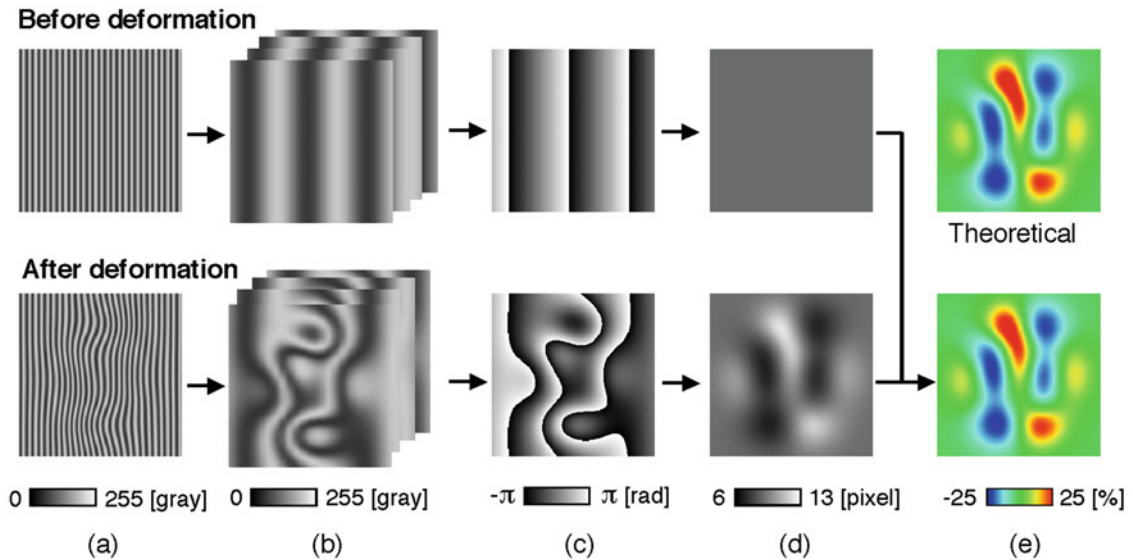

Fig. 32.2 Principle and the procedure of image processing to determine strain filed based on the sampling moiré method. (**a**) grating, (**b**) sampling moire, (**c**) moire phase, (**d**) grating pitch, (**e**) strain (x-dir)

Fig. 32.3 Principle of compensation of fringe order by using the measured displacement results
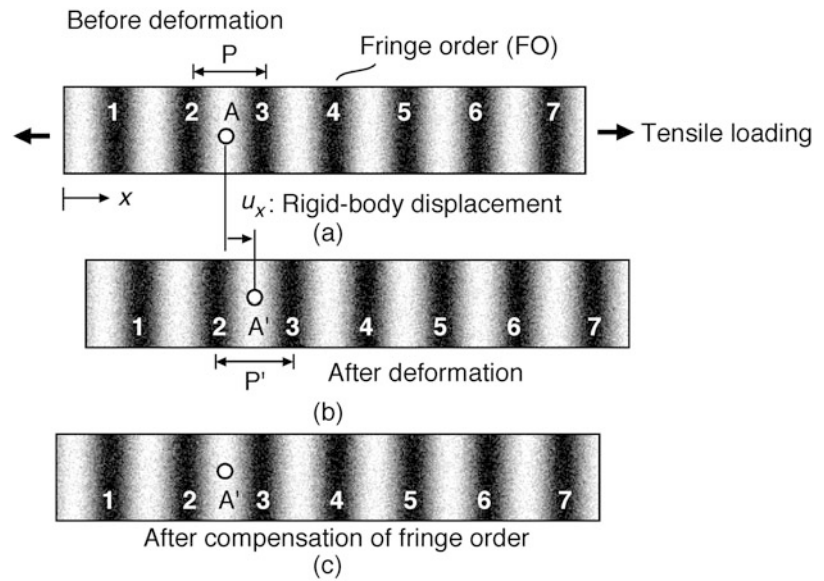

Figure 32.2e shows the *x*-direction strain by calculating the change of grating pitches before and after deformations. As shown in Fig. 32.2e, the measured strain is in agreement with the theoretical result.

32.2.2 Compensation of Fringe Order to Improve Strain Measurement Accuracy

For the strain measurement in elastic deformation, generally, the strain is lower than 0.2 % (i.e., 2000 με). For this reason, to fabricate a fine grid with high accuracy is not an easy task. Here, we proposed a compensation method of fringe order to improve the strain measurement accuracy.

Figure 32.3 shows the principle of compensation of fringe order by using the measured displacement results. Figure 32.3a, b show the captured grating before and after deformation by tensile loading. The number 1, 2, and 3, etc. indicated the fringe order (FO). After tensile loading, the grating pitch could be changed from P to P'. At the same time, a rigid-body displacement also could be occurred in most cases. If we directly calculate the strain from the pitch change at each pixel, the imperfect fabrication of grid will bring a large strain error. Therefore, we first measure the displacement amount of point A using Eq. (32.4), then we move the deformed image by u_x pixel so that the fringe order be the same for point A′, as shown Fig. 32.3c. Because the strain is directly measured from the change of grating pitch, the strain measurement accuracy could be improved after we compensate the fringe order as the same. In this case, the fabrication accuracy of grating is not longer important.

32.2.3 Adaption of Spatial Filtering (Sine/Cosine Average Filter) to Reduce Random Noise

To reduce the strain error due to random noise of the camera, we use the sine/cosine average filter [13] in the phase calculation procedure step. The sine/cosine average filter is a simple image processing and excellent in automatically remove the random noise in phase distribution of the fringe pattern. By performing the sine/cosine filtering, the strain error according to the random noise of the camera can be reduced. In this study, we suggested an improve method to use the combination of the fringe order compensation and sine/cosine average filter for reducing both the grating fabrication error and random noise of the camera.

32.3 Experiment

32.3.1 Specimen and Grid Fabrication

Figure 32.4 shows the specimen and optical setup for measuring tensile strain. The tested specimen is made of aluminum alloy (A7075P-T6) with a through hole, as shown in Fig. 32.4a. The width and thickness of the specimen are 12.5 and 2 mm, respectively. A through hole is introduced in the center position of the specimen. The diameter of the hole is 5 mm. To measure the strain distribution by the moiré method, after careful polishing (Step-1) and black anodic oxidation coatings (Step-2) were completed, a 3-axis YVO4 Laser marker (KEYENCE; MD-V9900A) was used to fabricate a fine cross grid with a 0.5-mm-pitch onto the surface of specimen (Step-3). The advantage of the laser marking technique is that the grid can be directly patterned on the surface, and the problem of this technique is that the fabricated grid pitch will be slightly different due to the surface roughness of the specimen.

32.3.2 Experimental Setup and Analysis Condition

Figure 32.4b shows the experimental setup for measuring tensile strain. We used a USB3.0 CMOS camera (Lumenera; Lt425C) to capture the image. The pixel size of the CMOS camera is 5.5 μm and the captured image is an 8-bit gray-scale with 2048 by 2048 pixels size. In order to eliminate the effect of out-of-plane displacement, we used a telecentric lens (EDMUND; TS Silver series, $\times 0.16$). The distance between the CMOS camera and the specimen was 180 mm. In this case, the imaging size is 34.375 μm/pixel. To keep a bright condition during recording, we used two LED lightings (NIKON; LD-1000) on the left and right sides of the camera. The specimen was loaded by a tensile machine (SHIMAZU; EZ-L 5kN). After applied 260 N pre-load, we captured one initial image as 0 με condition, and then we applied the strain from 0 με (260 N) to 2500 με (4640 N) at a 500 με (880 N) incremental step.

In this experiment, for a 0.5-mm-pitch grating, one period of the grating corresponds to 14.5 pixels. Therefore, in the strain analysis, we used the down-sampling pitch as 15 pixels. In this case, the spatial resolution was $2T - 1 = 29$ pixels. The 1D binary grating in y-direction was obtained by performed a low-pass filter (LPF) to the recorded 2D grating. Then, the phase shifted moiré fringes were generated by down-sampling with 15 pixels and intensity interpolation. Finally, the displacement distribution was calculated from the phase distribution of the moiré fringe before and after deformations. For the step of sine/cosine average filter, we used 29 by 29 pixels filter size because the down-sampling pitch was 15 pixels and the spatial resolution was 29 pixels.
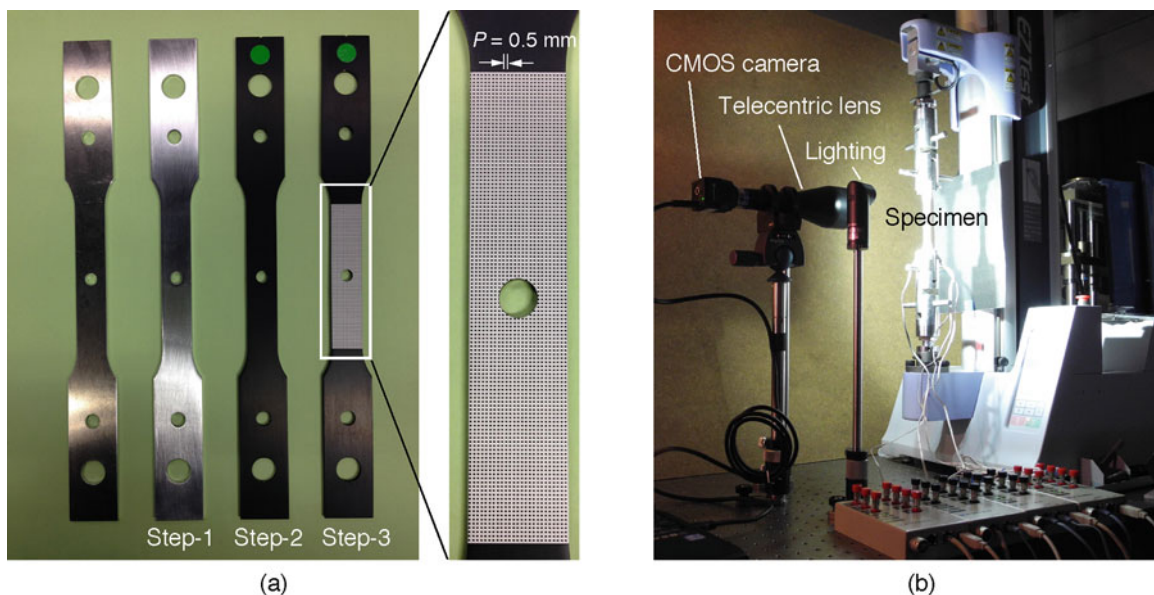

Fig. 32.4 Non-uniform strain field measurement experiment: (**a**) specimen, (**b**) optical setup using a single digital camera

32.3.3 Experimental Results

Figure 32.5a shows the captured grid image before deformation. Figure 32.5b shows the measured strain distribution in case of loading force is 4640 N (the average strain is 2500 με) obtained by the previous direct method [12]. Figure 32.5c shows the measured strain distribution obtained only using spatial filtering (sine/cosine average filter; filter size is 29 by 29 pixels) method. Obviously, the random noise is suppressed but the strain concentration near the hole cannot be observed. Figure 32.5d shows the strain distribution after compensation of fringe order (FO). In this case, we can observe the strain concentration near the hole but is not clear because the fluctuation due to the random noise is still large. Figure 32.5e shows the strain distribution after performing the compensation of fringe order and sine/cosine average filter (i.e., the combination of Fig. 32.5c, d). In this case, we can clearly see the strain concentration near the hole of the specimen. It demonstrated that our proposed method is effective to measure the strain distribution in the elastic deformation or elastic-plastic deformation. Figure 32.6a shows the captured grid image before deformation. Figure 32.6b shows the measured strain distributions from 0 με to 2500 με at a 500 με incremental step by the proposed method using both compensation of fringe order and spatial filtering. According to the increase of loading force, the strain near the hole could be larger and non-uniform strain fields were successfully obtained.
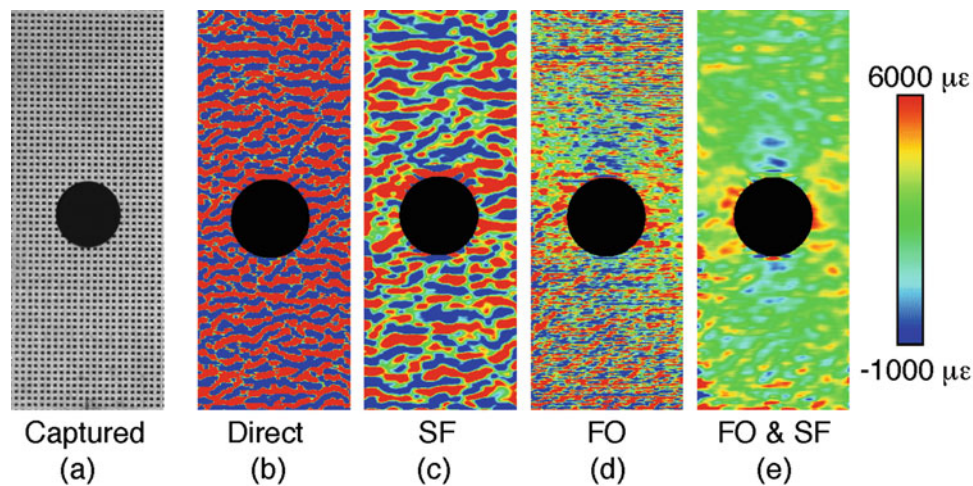

Fig. 32.5 Experimental results: (**a**) captured image before deformation; measured strain distributions obtained four different methods: (**b**) direct (conventional) method, (**c**) only using spatial filtering (SF) method, (**d**) only using compensation of fringe order (FO), and (**e**) both using compensation of fringe order and spatial filtering (FO & SF)
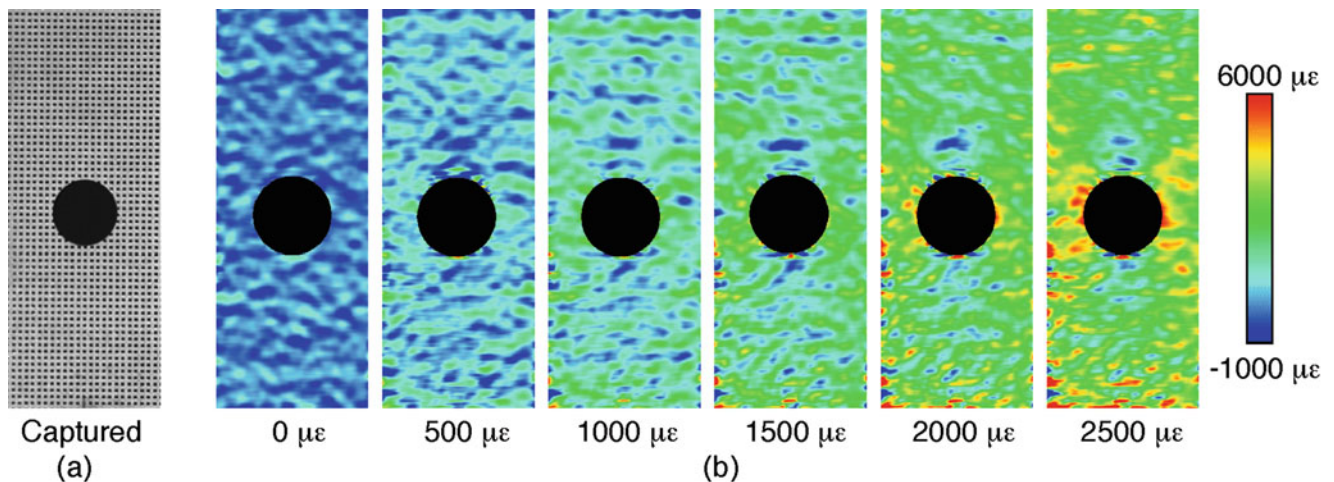

Fig. 32.6 Experimental results: (**a**) captured image before deformation, (**b**) measured strain distributions from 0 με to 2500 με at 500 με step by the proposed method using both compensation of fringe order and spatial filtering

32.4   Conclusions

We proposed an accurate strain distribution measurement technique, which can measure the non-uniform strain field in the region of elastic deformation or elastic-plastic deformation, based on the sampling moiré method. A tensile loading test for an aluminum specimen with a hole was carried out. Experimental results demonstrated that our proposed method is effective not only to suppress the noise by performing the sine/cosine average filter in phase map of the moiré fringe, but also to reduce the fixed noise by compensating the fringe order. As the result, strain concentration near the hole of the specimen can be clearly observed. This method is useful to evaluate mechanical properties of various materials under tension/compression or heating/cooling testing.

References

1. Dally, J.W., Riley, W.F.: Experimental Stress Analysis, 3rd edn. McGraw-Hill, New York (1991)
2. Kobayashi, A.S.: Handbook on Experimental Mechanics, 2nd edn. VCH Publishers, New York (1993)
3. Sutton, M.A., Cheng, M., Peters, W.H., Chao, Y.J., McNeil, S.R.: Application of an optimized digital correlation method to planar deformation analysis. Image Vis. Comput. **43**, 143–150 (1986)
4. Martinez, A., Rayas, J.A., Rodriguez-Vera, R., Puga, H.J.: Three-dimensional deformation measurement from the combination of in-plane and out-of-plane electronic speckle pattern interferometers. Appl. Opt. **43**(24), 4652–4658 (2004)
5. Hung, Y.: Shearography for non-destructive evaluation of composite structures. Opt. Lasers Eng. **24**, 161–182 (1996)
6. Morimoto, Y., Nomura, T., Fujigaki, M., Yoneyama, S., Takahashi, I.: Deformation measurement by phase-shifting digital holography. Exp. Mech. **45**(1), 65–70 (2005)
7. Goldrein, H.T., Palmer, S.J.P., Huntely, J.M.: Automated fine grid technique for measurement of large-strain deformation maps. Opt. Lasers Eng. **23**, 305–318 (1995)
8. Ifju, P., Masters, J.: The use of moiré interferometry as an aid to standard test-method development for textile composite materials. Compos. Sci. Technol. **53**, 155–163 (1995)
9. Ri, S., Fujigaki, M., Morimoto, Y.: Sampling moiré method for accurate small deformation distribution measurement. Exp. Mech. **50**(4), 501–508 (2010)
10. Ri, S., Muramatsu, M., Saka, M., Nanbara, K., Kobayashi, D.: Accuracy of the sampling moiré method and its application to deflection measurements of large-scale structures. Exp. Mech. **52**(4), 331–340 (2012)
11. Ri, S., Saka, M., Nanbara, D., Kobayashi, D.: Dynamic thermal deformation measurement of large-scale, high-temperature piping in thermal power plants utilizing the sampling moiré method and grating magnets. Exp. Mech. **53**, 1635–1646 (2013)
12. Ri, S., Wang, Q., Tsuda, H., Iida, I., Sato, H., Nakajima, T.: Strain measurement of structural materials using the sampling moiré method (in Japanese). J Jpn. Soc. Non-Destr. Inspect. **64**(4), 160–165 (2015)
13. Aebischer, H., Waldner, S.: A simple and effective method for filtering speckle-interferometric phase fringe patterns. Opt. Commun. **162**, 205–210 (1999)

Chapter 33
Full-Field Measurements of Principal Strains and Orientations Using Moiré Fringes

Q. Wang, S. Ri, Y. Takashita, and S. Ogihara

Abstract The principal strains at the microscale are the key parameters for evaluating the instability behaviors of materials. In this study, we developed a technique to acquire the full-field distributions of the principal strains and their orientations by integrating the scanning moiré method and the theoretical analysis of strain status. The normal strains in two perpendicular directions were first measured using the SEM scanning moiré fringes. The principal strains with orientations were then determined based on the analysis of strain status for plane stress problems. In this study, the maximum and the minimum principal strains and their orientations of carbon fiber reinforced plastics under a three-point bending test were measured. The maximum principal strain is greatest in the bottom-left region and the absolute value of the minimum principal strain is greatest in the upper-right region of this specimen. This technique is independent of the specimen grating direction and is useful to detect the potential failure characteristics of various composite materials.

33.1 Introduction

Due to the advantages of high strength and lightweight, carbon fiber reinforced plastics (CFRPs) have been extensively used in the fields of aerospace, automobiles, motorcycles, computers, etc. [1]. Their mechanical properties and instability behaviors have received significant research interests in both academia and industries for toughening and strengthening of materials and structures. Since deformation distributions play an important role in evaluations of mechanical properties and failure behaviors, it is essential to measure the full-field deformations especially the strains of CFRPs. Furthermore, because the crack initiation and growth are closely related to the maximum microscale deformation, the microscale principal strain distributions are indispensable factors to understand the failure mechanisms of materials.

The microscale full-field deformations are nondestructively measurable by optical methods. The commonly used microscale optical methods include the grid-based methods such as the moiré methods [2–5], the grid method [6] and the geometric phase analysis [7, 8], and the speckle-based methods such as the digital image correlation method [9] and the speckle interferometry [10]. Although the speckle-based methods are simple and have a large field of view, the measurement repeatability is low because the speckle is easily affected by noise. Fortunately, the grid or grating is robust in confronting the influence of noise. Among the grid-based methods, the sampling moiré method [3, 11], the digital moiré method [12], the grid method and the geometric phase analysis are limited by their fields of view because the specimen grid or grating has to be observed during experiments. The scanning moiré method needs not observe the specimen grating, and thus has a large field of view. In the last decades, the scanning electron microscope (SEM) moiré method [13–17], the transmission electron microscopy moiré method [18], and the laser scanning microscope moiré method [19] have been developed. The normal strains and the shear strain in a large field of view are obtainable from the scanning moiré method.

In this study, we will combine the scanning moiré method and the theoretical analysis of strain status for measurements of the principal strains and their orientations of a CFRP specimen under a three-point bending test. The normal strains and the shear strain will be measured by the SEM scanning moiré method. The principal strains and their orientations will be determined by the theoretical analysis. The deformation features of this specimen will be discussed. The combination of the

Q. Wang (✉) • S. Ri
Research Institute for Measurement and Analytical Instrumentation, National Institute of Advanced Industrial Science and Technology, Tsukuba, Ibaraki 305-8568, Japan
e-mail: wang.qinghua@aist.go.jp; ri-shien@aist.go.jp

Y. Takashita • S. Ogihara
Department of Mechanical Engineering, Tokyo University of Science, Chiba 278-8510, Japan

scanning moiré method and the theoretical analysis of strain status is effective in determining the strain distributions, even if the specimen grating is not parallel to the axial direction of the specimen.

33.2 Strain Measurement Methods

33.2.1 Normal and Shear Strains from Scanning Moiré Method

The normal strains and the shear strain of the specimen in this work will be measured from the microscopic scanning moiré method. The scanning moiré fringes are generated from the interference between the specimen grating and the microscope scanning lines (reference grating), as seen in Fig. 33.1. The displacement of the specimen grating after deformation relative to the scanning lines [13] can be determined by

$$u_{i\_rela} = m_i T \quad (i = x, \; y) \tag{33.1}$$

where T is the scanning spacing and m_i indicates the moiré fringe order ($m_i = \ldots, -1, 0, 1, 2, \ldots$) in the i direction. Usually, the moiré fringes in the y direction is first recorded. The scanning lines or the specimen stage is then rotated by 90°, and the moiré fringes in the x direction will emerge and be recorded.

The first-order differentials of the relative displacements will give us the normal and the shear strains of the specimen relative to the scanning lines

$$\varepsilon_{i\_rela} = \frac{\partial u_{i\_rela}}{\partial i} \quad (i = x, \; y) \tag{33.2}$$

$$\gamma_{xy\_rela} = \frac{\partial u_{x\_rela}}{\partial y} + \frac{\partial u_{y\_rela}}{\partial x} \tag{33.3}$$

The actual normal strains of the specimen due to deformation can be measured from the geometric relationship (Fig. 33.2) among the specimen grating pitch, the scanning spacing and the relative strains

$$\varepsilon_i = (1 + \varepsilon_{i\_rela})\frac{T}{p_i} - 1 \quad (i = x, \; y) \tag{33.4}$$

where p_i represents the specimen grating pitch in the i direction. From the positional relationship (Fig. 33.2) among the specimen gratings before and after deformation as well as the scanning lines, the actual shear strain of the specimen is equivalent to the relative shear strain

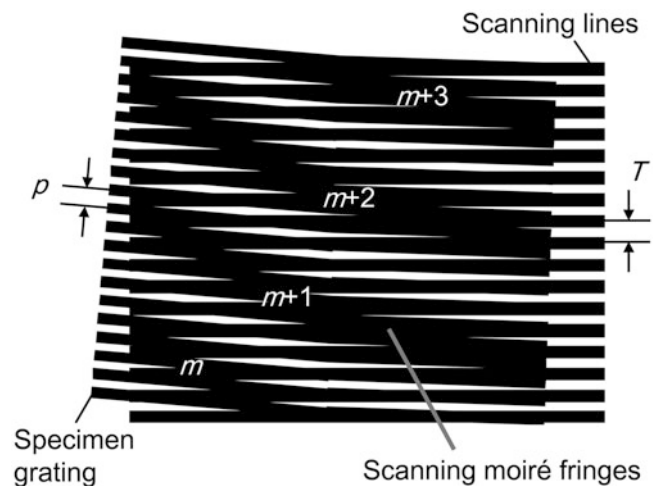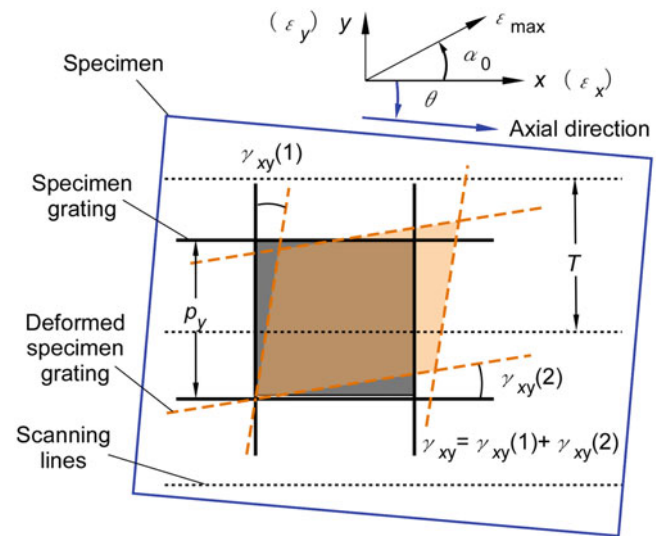**Fig. 33.1** Formation of the microscope scanning moiré fringes

Fig. 33.2 Geometric and positional relationships between the specimen grating and the scanning lines

$$\gamma_{xy} = \gamma_{xy\_rela} \tag{33.5}$$

33.2.2 Principal Strains from Analysis of Strain Status

Since the principal strains are more essential to characterize the strain status and the potential failure modes, the maximum and the minimum principal strains will be further measured from the theoretical analysis of strain status. For the plane stress problems, the maximum and the minimum principal strains [20] can be expressed by

$$\varepsilon_{\max} = \frac{\varepsilon_x + \varepsilon_y}{2} + \sqrt{\left(\frac{\varepsilon_x - \varepsilon_y}{2}\right)^2 + \frac{\gamma_{xy}^2}{4}} \tag{33.6}$$

$$\varepsilon_{\min} = \frac{\varepsilon_x + \varepsilon_y}{2} - \sqrt{\left(\frac{\varepsilon_x - \varepsilon_y}{2}\right)^2 + \frac{\gamma_{xy}^2}{4}} \tag{33.7}$$

The orientation of the maximum principal strain is obtainable from

$$\tan 2\alpha_0 = \frac{\gamma_{xy}}{\varepsilon_x - \varepsilon_y} \tag{33.8}$$

The orientation of the minimum principal strain is perpendicular to that of the maximum principal strain.

33.3 Materials and Loading Experiments

33.3.1 Specimen Preparation and Mechanical Properties

Two CFRP specimens were mixed with 5-μm-diameter IM600 carbon fibers, 10~11-μm-diameter K13D carbon fibers and epoxy resins. The IM600 layer with thickness of approximately 110 μm and the K13D layer with thickness of approximately 300 μm were arranged alternately. These two specimens were cut to the size of 1 mm × 5 mm × 30 mm using an abrasive wheel cutting machine. All the carbon fibers were perpendicular to the 1 mm × 30 mm surface.

One specimen was loaded under an electronic universal testing machine (SHIMADZU, AG-100kND), as shown in Fig. 33.3a. It should be noted that, because of the machining error, the specimen size varied a little. The three-point bending support span was $L = 16$ mm, 16 times the specimen thickness (1 mm), meeting the standards of American Society for
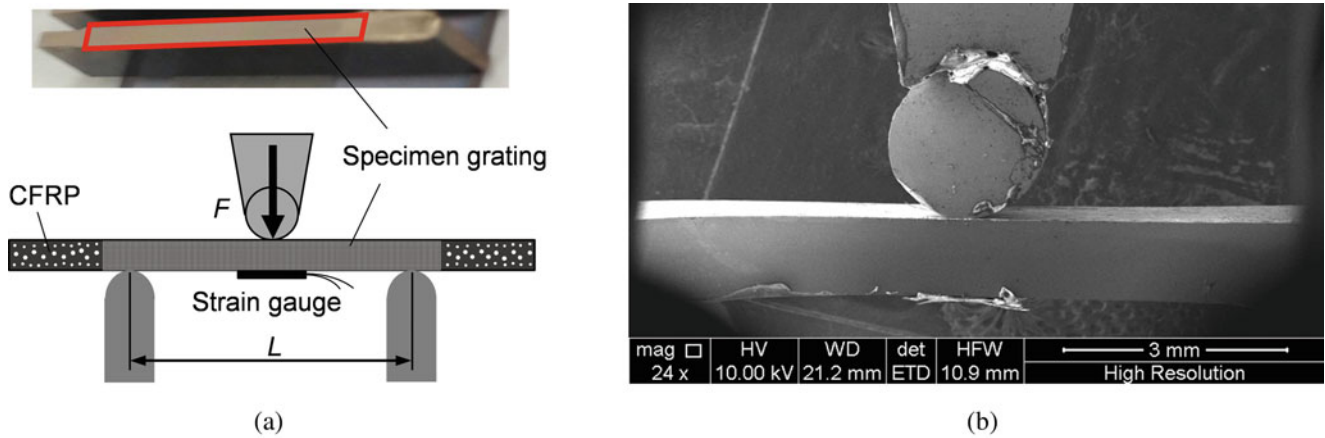
Fig. 33.3 (**a**) Schematic diagram and (**b**) SEM image of the three-point bending test to the CFRP specimen
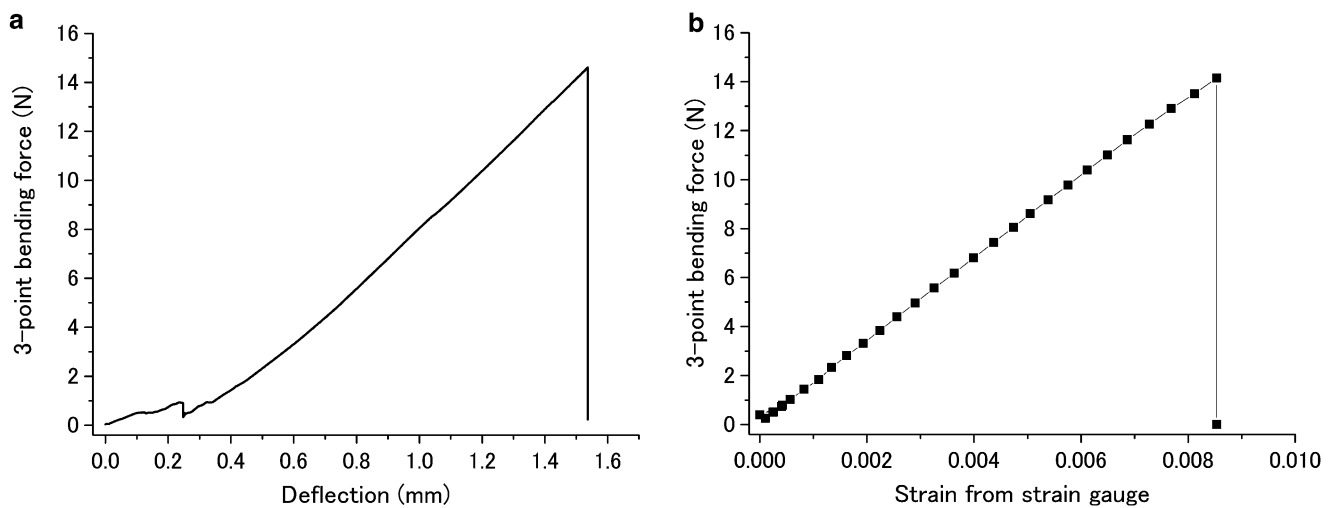

Fig. 33.4 (**a**) Three-point bending force-deflection curve and (**b**) three-point bending force-strain curve of CFRP, where the strain was measured by a strain gauge on the bottom surface

Testing and Materials (ASTM, No. D 790-03). A strain gauge was pasted on the bottom surface (5 mm × 30 mm) to measure the maximum tensile strain. The loading speed was 0.1 mm/min. The three-point bending force-deflection curve and the force-strain curve of this CFRP specimen were plotted in Fig. 33.4. These two curves show the mechanical properties and the global deformation behavior of this CFRP specimen under the three-point bending test. The fracture (maximum bending) force was 14.61 N, the maximum deflection was 1.54 mm, and the maximum tensile strain on the bottom surface was 0.009.

33.3.2 Grating Fabrication and Loading Test in SEM

To measure the deformation distribution, the front surface (1 mm × 30 mm) of the other CFRP specimen was first polished with sandpapers and polishing solutions. Next, a micron cross grating with pitch of $p = 3.72$ μm was produced on the front surface by UV nanoimprint lithography (Fig. 33.5). The resist was PAK01 and the UV exposure time was 30 s in the used UV nanoimprint device (EUN-4200 device). The grating area was about 1 mm × 20 mm. Then, the grating surface was coated with a thin layer of gold to improve the surface conductivity. The SEM image of the micron grating is displayed in Fig. 33.6.

Fig. 33.5 Grating fabrication process of nanoimprint lithography
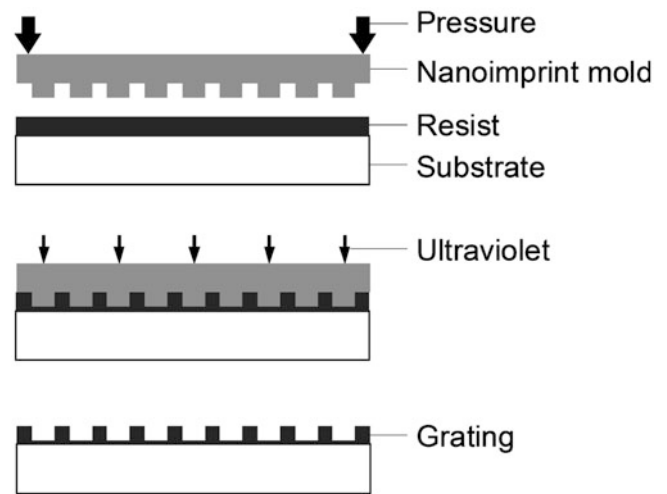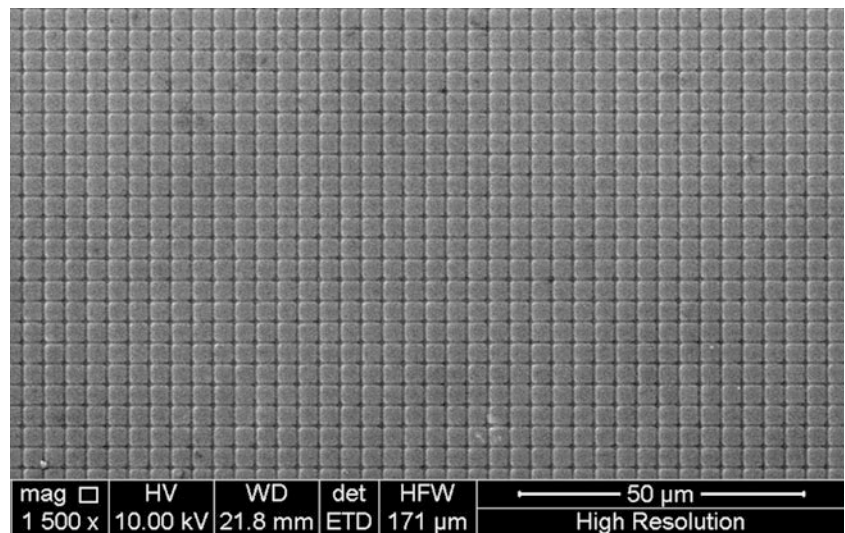

Fig. 33.6 SEM image of the micron cross grating on CFRP

This CFRP specimen was loaded under a simple loading jig in a SEM (FEI Quanta 200FEG). The three-point bending support span was also 16 mm, as seen in Fig. 33.3a. Another strain gauge was also affixed on the bottom surface (5 mm × 30 mm) to measure the maximum tensile strain. The loading configuration inside the SEM is illustrated in Fig. 33.3b. The case when the strain gauge value was 0.006 was selected as an example to be used to investigate the deformation distributions of this CFRP specimen. Based on Fig. 33.4, when the maximum tensile strain was 0.006, the three-point bending force was 10.2 N, and the corresponding deflection was 1.18 mm. Under this circumstance, the specimen grating and the SEM moiré fringes will be observed for the full-field strain measurement using the methods introduced in Sect. 33.2.

33.4 Strain Distributions and Discussion

33.4.1 SEM Moiré Fringes and Displacement Distributions

It is found that, when the SEM magnification is ×140, the scanning spacing is $T = 3.60$ μm, close to the specimen grating pitch (3.72 μm). In this case, SEM scanning moiré fringes can be clearly observed. However, because the grating direction is not parallel to the axial direction of the CFRP specimen owing to the positioning error in the grating fabrication process, the SEM moiré fringes are too dense when the scanning direction is parallel to the axial direction. In order to avoid the potential
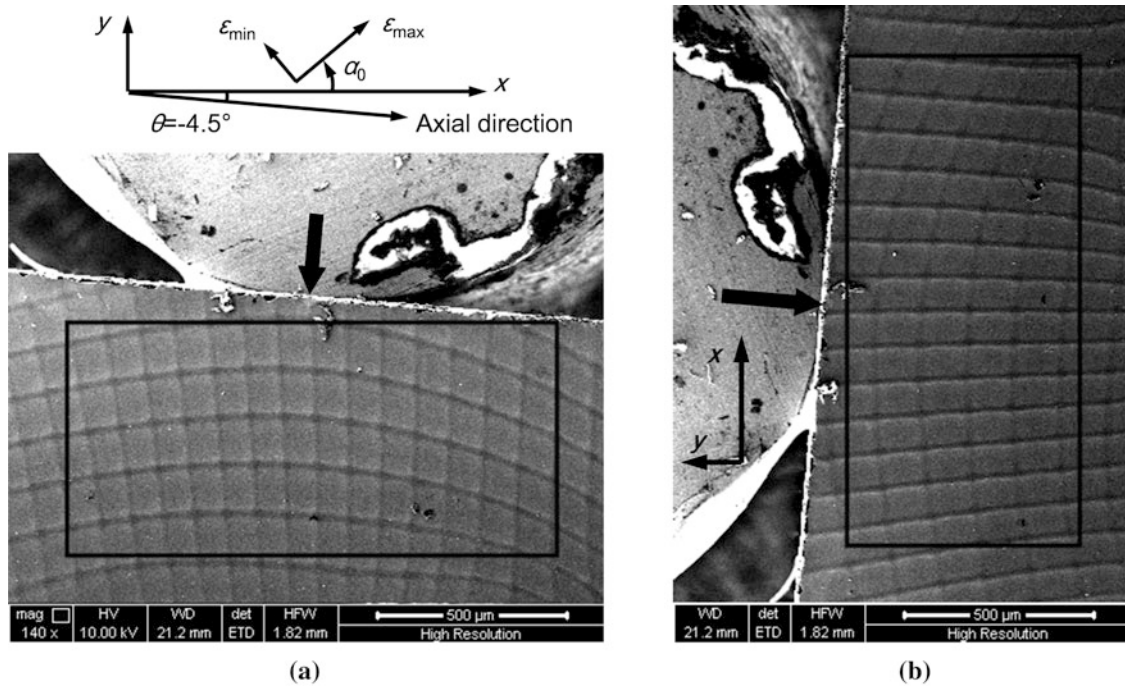
Fig. 33.7 SEM moiré fringes on CFRP under three-point bending when the scanning direction anticlockwise deviates (**a**) 4.5° and (**b**) 94.5° from the axial direction, where the former and the latter show the moiré fringes in the y and the x directions, respectively

error in deformation measurement caused by the dense moiré fringes, we will find a better moiré pattern by rotating the scanning lines. If the scanning direction is rotated, the normal strains and the shear strain will vary, however, the principal strains and their directions will not be influenced by the rotation angle theoretically. As the principal strains are independent of the scanning direction, the directions x and y are flexible with respect to the axial direction of the specimen. Therefore, we can chose any direction as the scanning direction to calculate the principal strains.

From our experiments, when we anticlockwise rotated the scanning lines by 4.5°, the scanning lines were almost parallel to one of the grating directions. In this case, the scanning moiré fringes were distinct and visually reflected the displacement distribution because moiré fringes were displacement contours. For two-dimensional deformation measurement, we further rotated the scanning lines by 90° to get the SEM scanning moiré fringes in the other direction. Figure 33.7 presents the SEM scanning moiré fringes in the y direction when the scanning direction anticlockwise deviates 4.5° from the axial direction (Fig. 33.7a) and the moiré fringes in the x direction when the scanning direction anticlockwise deviates 94.5° from the axial direction (Fig. 33.7b).

The displacement distributions were measured using the SEM scanning moiré method. To avoid the influence of the contaminated site near the bottom edge caused by the strain gauge adhesive blue, a same square region with size of 1300 μm × 620 μm in the upper area was chosen as the region of interest, labeled in Fig. 33.7. The relative displacement distributions in the x and the y directions were calculated using Eq. (33.1), as illustrated in Fig. 33.8a, b, respectively. The relative displacement vector distribution is presented in Fig. 33.8c. It can be seen that, the specimen has bottom-leftward displacement in the left region and bottom-rightward displacement in the right region below the three-point bending loading head.

33.4.2 Distributions of Normal and Shear Strains

The first-order differentials of the relative displacements in Fig. 33.8 were used to calculate the relative normal and shear strains using Eqs. (33.2) and (33.3). The relative strains were then used to measure the actual normal strains and the shear strain based on Eqs. (33.4) and (33.5). The measured distributions of the actual normal strains of this CFRP specimen in the x and the y directions and the actual shear strain are exhibited in Fig. 33.9.
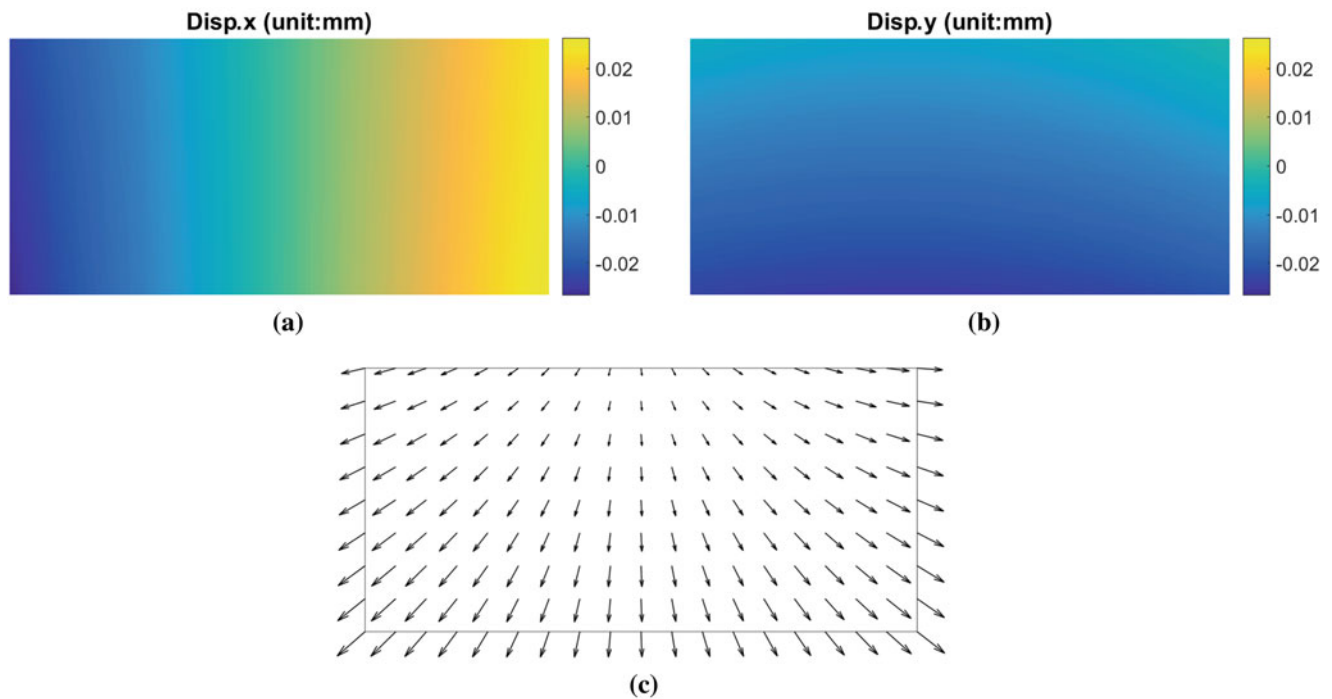
Fig. 33.8 Displacement distributions of CFRP (**a**) in the *x* direction, (**b**) in the *y* direction and (**c**) the displacement vector relative to the scanning lines (1300 μm × 620 μm)
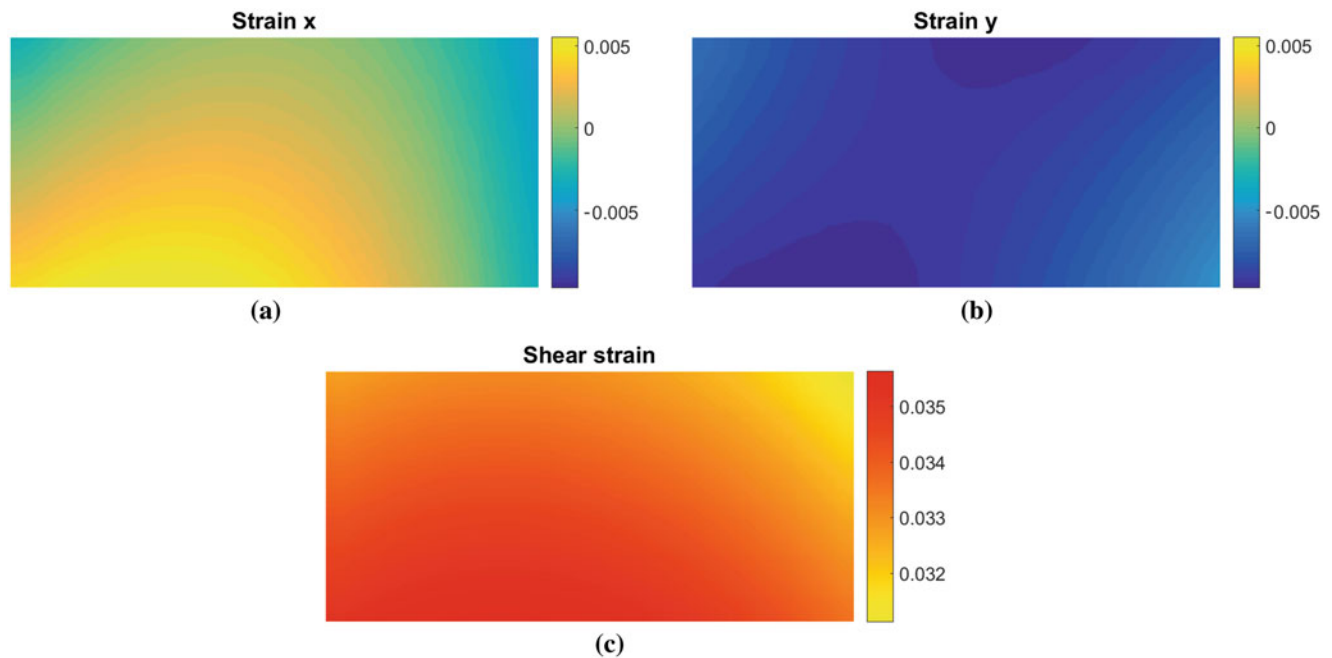
Fig. 33.9 Strain distributions of CFRP (**a**) in the *x* direction, (**b**) in the *y* direction and (**c**) the shear strain (1300 μm × 620 μm)

The normal strain in the *x* direction is tensile in the bottom area, and is compressive in the upper area. The normal strain in the *y* direction is compressive in the whole area, and the absolute value gradually decreases from middle to the left and right sides. These phenomena are basically consistent with the strain characteristics of solid materials under a three-point bending test. Because the *y* direction is not perpendicular to the axial direction of the specimen (the angle is 94.5°), the maximum absolute values of the compressive strain in the *y* direction are not in the vertical direction, but along the bottom-left to

upper-right direction. The unique deformation features of CFRP as a composite material include the following aspects. The normal strain in the x direction is maximal in the bottom-left area, gradually decreases towards the upper-left and upper-right directions, and is compressive in the right area. The normal strain in the y direction has a higher decreasing speed from middle to the left and right sides than the conventional materials. The shear strain is positive in the whole area, and the value is much higher than the normal strain values. The shear strain has a similar distribution feature as the normal strain in the x direction, i.e., the maximum shear strain is in the bottom-left area and gradually decreases towards the upper-right and upper-left areas.

33.4.3 Distributions of Principal Strains and Orientations

From the distributions of the normal strains and the shear strain in Fig. 33.9, the maximum and the minimum principal strains and their orientations were calculated using Eqs. (33.6)−(33.8). The distributions of the maximum and the minimum principal strains of this CFRP specimen under the three-point bending load are illustrated in Fig. 33.10. Their orientations are shown in Fig. 33.11.

The maximum principal strain is positive, and the distribution feature is almost the same to that of the shear strain and that of the normal strain in the x direction. The maximum principal strain is greatest in the bottom-left region and gradually decreases towards the upper and right regions. As the shear strain has much greater value than the normal strains, the shear strain contributes the most to the maximum principal strain. The minimum principal strain is compressive, and the distribution feature is slightly similar to that of the normal strain in the y direction. The absolute value of the minimum principal strain is greater than the maximum principal strain, and the greatest absolute value appears in the upper-right area. The maximum and the minimum principal strains are more likely to cause instability of this specimen, and the damage is more likely originated in the bottom-left and upper-right regions. The orientations of the principal strains in Fig. 33.11 reveal the potential damage direction. The principal strains and their orientations are valuable for understanding the potential instability behaviors of materials.
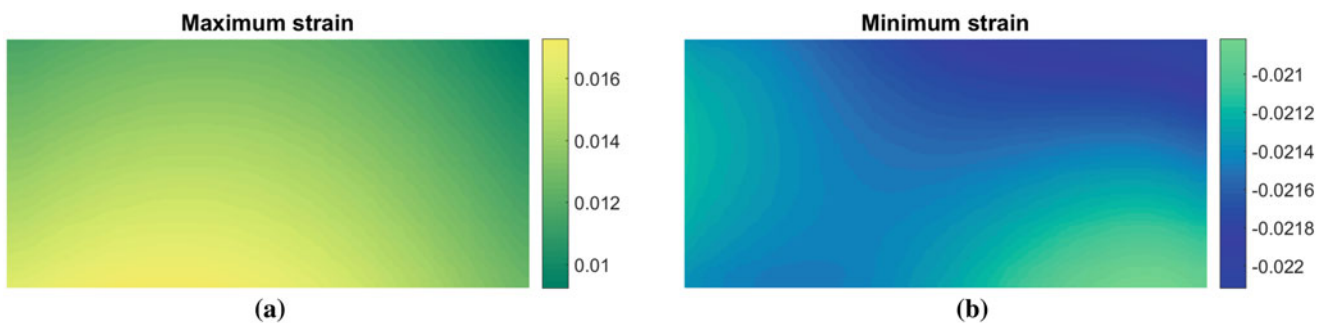

Fig. 33.10 (**a**) Maximum and (**b**) minimum principal strain distributions of CFRP (1300 μm × 620 μm)
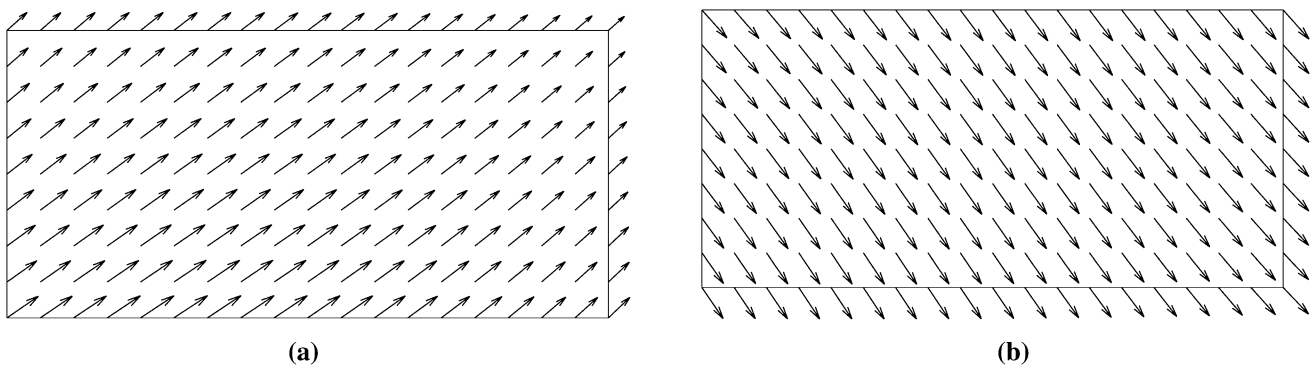
Fig. 33.11 Orientation distributions of (**a**) maximum and (**b**) minimum principal strains of CFRP (1300 μm × 620 μm)

33.5   Conclusions

The microscale distributions of the normal strains, the shear strain, the principal strains and their orientations of a CFRP specimen under a three-point bending test were investigated. The maximum principal strain has a similar distribution feature as the shear strain and the normal strain in the x direction except the values. The minimum principal strain has a slightly similar distribution feature as the normal strain in the y direction. The maximum and the minimum principal strains are more likely to induce instability, and the bottom-left and upper-right regions are the most unstable regions. The orientations of the principal strains show the potential instability direction. The combination of the scanning moiré method and the theoretical analysis of strain status is independent of the specimen grating direction, and useful in evaluating the microscale principal strain distributions of various materials.

References

1. Naito, K., Yang, J.M., Kagawa, Y.: Tensile properties of high strength polyacrylonitrile (PAN)-based and high modulus pitch-based hybrid carbon fibers-reinforced epoxy matrix composite. J. Mater. Sci. **47**(6), 2743–2751 (2012)
2. Kishimoto, S., Egashira, M., Shinya, N.: Microcreep deformation measurements by a moiré method using electron beam lithography and electron beam scan. Opt. Eng. **32**(3), 522–526 (1993)
3. Ri, S., Muramatsu, T., Saka, M., Nanbara, K., Kobayashi, D.: Accuracy of the sampling moiré method and its application to deflection measurements of large-scale structures. Exp. Mech. **52**(4), 331–340 (2012)
4. Wang, Q.H., Tsuda, H., Xie, H.M.: Developments and applications of moiré techniques for deformation measurement, structure characterization. Recent Pat. Mater. Sci. **8**(3), 188–207 (2015)
5. Post, A., Han, B., Ifju, P.: [High Sensitivity Moiré: Experimental Analysis for Mechanics and Materials]. Springer, New York (2012)
6. Jin, H., Haldar, S., Bruck, H.A., Lu, W.Y.: Grid method for microscale discontinuous deformation measurement. Exp. Mech. **51**(4), 565–574 (2011)
7. Liu, Z.W., Xie, H.M., Gu, C.Z., Meng, Y.G.: Digital geometric phase technique applied to deformation evaluation of MEMS devices. J. Micromech. Microeng. **19**(1), 015012 (2009)
8. Wang, Q.H., Kishimoto, S., Xie, H.M., Liu, Z.W., Lou, X.H.: In situ high temperature creep deformation of micro-structure with metal film wire on flexible membrane using geometric phase analysis. Microelectron. Reliab. **53**(4), 652–657 (2013)
9. Hu, Z.X., Xie, H.M., Lu, J., Hua, T., Zhu, J.G.: Study of the performance of different subpixel image correlation methods in 3D digital image correlation. Appl. Opt. **49**(21), 4044–4051 (2010)
10. Erf, R. (ed.) Speckle Metrology. Elsevier, London (2012)
11. Ri, S., Muramatsu, T.: Theoretical error analysis of the sampling moiré method and phase compensation methodology for single-shot phase analysis. Appl. Opt. **51**(16), 3214–3223 (2012)
12. Wang, Q.H., Kishimoto, S., Yamauchi, Y.: Three-directional structural characterization of hexagonal packed nanoparticles by hexagonal digital Moiré method. Opt. Lett. **37**(4), 548–550 (2012)
13. Wang, Q.H., Kishimoto, S.: Simultaneous analysis of residual stress and stress intensity factor in a resist after UV-nanoimprint lithography based on electron moiré fringes. J Micromech. Microeng. **22**(10), 105021 (2012)
14. Kishimoto, S.: Electron moiré method. Theor. Appl. Mech. Lett. **2**(1), 011001 (2012)
15. Wang, Q.H., Kishimoto, S., Jiang, X.F., Yamauchi, Y.: Formation of secondary moiré patterns for characterization of nanoporous alumina structures in multiple domains with different orientations. Nanoscale **5**(6), 2285–2289 (2013)
16. Li, C.W., Liu, Z.W., Xie, H.M., Wu, D.: Statistics-based electron moiré technique: a novel method applied to the characterization of mesoporous structures. Nanoscale **6**(22), 13409–13415 (2014)
17. Wang, Q.H., Ri, S., Tsuda, H., Kishimoto, S., Tanaka, Y., Kagawa, Y.: Deformation measurement of carbon fiber reinforced plastics using phase-shifting scanning electron microscope moiré method after Fourier transform. In: Proc. SPIE icOPEN 2015, 9524-43 (2015)
18. Kondo, Y., Okunishi, E.: Magnified pseudo-elemental map of atomic column obtained by Moiré method in scanning transmission electron microscopy. Microscopy **63**(5), 391–395 (2014)
19. Xie, H.M., Wang, Q.H., Kishimoto, S., Dai, F.L.: Characterization of planar periodic structure using inverse laser scanning confocal microscopy moiré method and its application in the structure of butterfly wing. J. Appl. Phys. **101**(10), 103511 (2007)
20. Hibbeler, R.C.: Statics and Mechanics of Materials. Pearson Higher Ed. (2013)

Chapter 34
A Self-Recalibrated 3D Vision System for Accurate 3D Tracking in Hypersonic Wind Tunnel

Ran Chen, Meng Liu, Kai Zhong, Zhongwei Li, and Yusheng Shi

Abstract 3D vision system becomes a critical tool in wind tunnel experiment. However, in hypersonic wind tunnel vibration is unavoidable, it will disturb the pose of cameras in vision system and heavily decrease the measurement accuracy. Aiming at solving this problem, an accurate and stable two-step self-calibration method is proposed. Firstly, a stable and fast non-iterative method is adopted to calculate the initial value of camera pose. Then, a globally convergent orthogonal iterative algorithm is used to obtain an accurate solution. According to the experiment results, the 3D vision system with self-calibration method can get accurate measurement results in hypersonic wind tunnel. And we applied the 3D vision system to measure the deformation of an aircraft wing model in hypersonic wind tunnel of China Aerodynamics Research and Development Center successfully.

Keywords 3D vision system • Wind tunnel • Vibration • Self-calibration • Pose estimation

34.1 Introduction

3D vision system becomes a critical tool in wind tunnel experiment [1–3]. For instance, vision system is the most widely used technique for deformation measurements in wind tunnel, which can provide data that can be compared with computational fluid dynamics (CFD) predictions to help validate design geometries [4]. However, it's hard to get high precision measurement results in hypersonic wind tunnel. The main reason is that in hypersonic wind tunnel vibration is unavoidable, it will move the vision system and change the camera pose. Generally, the world coordinate system is set on one of the cameras. Once the vision system moves, the world coordinate will move, too. These will heavily decrease the measurement accuracy of vision system. This problem can be solved by setting the world coordinate system on a still object. On the other hand, changing the camera pose will case the extrinsic parameter altering and lead to the measurement results becoming inaccurate.

In order to get high precision measurement results in hypersonic wind tunnel, the pose of camera must be estimated accurately to rectify the extrinsic parameters, which also called self-calibration or pose estimation. The aim of self-calibration is to obtain the position and orientation of a camera given its intrinsic parameters and a set of correspondences between 3D points and 2D points [5]. The methods to solve the self-calibration problem can be classified as iterative methods and non-iterative methods. In order to get accurate results, the iterative method is a good choice which is more precise than the non-iterative method. But the iterative method is unstable under the influence of image noise and the number of reference points. Oberkampf [6] and Schweighofer [7] proposed that there are two reasons to cause the instability of iterative self-calibration method. Firstly, the initial value of many iterative methods are arbitrary value or based on an assumption. Secondly, most of the iterative algorithm are the general algorithm to solve the common problem, which may lead the self-calibration problem cannot convergence or fall into local optimum. Aiming at solve the second problem, Lu [8] proposed an orthogonal iterative algorithm that formulated the self-calibration problem as that of minimizing an error metric based on collinearity in object space, which is globally convergent and computationally efficient. It has proved that Lu's method is more accurate and stable than other self-calibration methods [9]. However, Lu's method relies on an initial estimation of the camera pose based on a weak-perspective assumption, which can lead to instabilities when the assumption is not satisfied. This happens when the points of the object are projected onto a small region on the side of the image. This problem can be solved by using an accurate non-iterative solution to initialize the orthogonal iterative method. Due to the

R. Chen • M. Liu • K. Zhong • Z. Li (✉) • Y. Shi
State Key Laboratory of Material Processing and Die & Mould Technology, Huazhong University of Science and Technology,
1037 Luoyu Road, Wuhan, China
e-mail: chenran@hust.edu.cn; zwl@hust.edu.cn

limitation of space and measuring range, there are few number of reference points in hypersonic wind tunnel, the non-iterative method must insensitive to the number of reference points. An accurate non-iterative method is adopted, which is faster and more stable than other non-iterative methods [10].

In this paper, a two-step self-calibration method was proposed to estimate the camera pose, which using an accurate and stable non-iterative method to calculate the initial value and then using the orthogonal iterative method to get the precise solution. According to the experiment results, the 3D vision system with self-calibration method can get accurate measurement results in hypersonic wind tunnel. And we applied our 3D vision system with self-calibration to measure the deformation of an aircraft wing model in hypersonic wind tunnel of China Aerodynamics Research and Development Center (CARDC).

34.2 Theory

34.2.1 The Non-iterative Method

Let us assume the intrinsic parameters is given, and a set of reference points whose 3D coordinates are known in the world coordinate system and whose 2D image projections are also known. Each the 3D reference point can be expressed as a weighted sum of the four visual control points.

$$\mathbf{p}_i^w = \sum_{j=1}^{4} \alpha_{ij} \mathbf{c}_j^w, \quad \text{with} \quad \sum_{j=1}^{4} \alpha_{ij} = 1, \; i = 1, \ldots n, \; j = 1, \ldots, 4, \tag{34.1}$$

Where the $\mathbf{p}_i^w$ are the points whose 3D coordinates are known in the world coordinate system, the $\mathbf{c}_j^w$ are the four visual control points. And the α_{ij} are homogeneous barycentric coordinates, they are uniquely defined and can easily be estimated. When necessary, we will specify that the point coordinates are expressed in the world coordinate system by using the ^{w} superscript, and in the camera coordinate system by using the ^{c} superscript. The same relation holds in the camera coordinate system and we can also write

$$\mathbf{p_i^c} = \sum_{j=1}^{4} \alpha_{ij} c_j^c. \tag{34.2}$$

According to the pinhole image model, we have:

$$\omega_i \begin{bmatrix} u_i \\ v_i \\ 1 \end{bmatrix} = \begin{bmatrix} f_u & 0 & u_c \\ 0 & f_v & v_c \\ 0 & 0 & 1 \end{bmatrix} \sum_{j=1}^{4} \alpha_{ij} c_j^w. \tag{34.3}$$

Where the ω_i are scalar projective parameters, the f_u and f_v are focal length coefficients, the (u_c, v_c) are principal point, and the $[u_i, v_i]^T$ are 2D coordinates points.

We expand this expression by the specific 3D coordinates $[x_j^c, y_j^c, z_j^c]^T$ of each $\mathbf{c}_j^c$ control point. Substituting the last row of Eq. (34.3) in the first two rows yields two linear equations for each reference point:

$$\sum_{j=1}^{4} \alpha_{ij} f_u x_j^c + \alpha_{ij}(u_c - u_i) z_j^c = 0, \tag{34.4}$$

$$\sum_{j=1}^{4} \alpha_{ij} f_v y_j^c + \alpha_{ij}(v_c - v_i) z_j^c = 0. \tag{34.5}$$

By concatenating them for all reference points, we generate a linear system of form

$$\mathbf{Mx} = 0 \tag{34.6}$$

Where $\mathbf{x} = \left[c_1^{c\mathrm{T}}, c_2^{c\mathrm{T}}, c_3^{c\mathrm{T}}, c_4^{c\mathrm{T}}\right]^{\mathrm{T}}$ is a 12-vector made of the unknowns, and $\mathbf{M}$ is a 2n × 12 matrix, generated by arranging the coefficients of Eqs. (34.4) and (34.5) for each reference point. The solution therefore belongs to the null space or kernel of M that can be found efficiently. The pose of camera can be calculated when the control point coordinates in the camera coordinate system and the world coordinate system are known.

34.2.2 The Orthogonal Iterative Method

Lu's iterative method formulate the self-calibration problem as that of minimizing an object-space collinearity error. From this new objective function, an algorithm is derived that operates by successively improving an estimate of the rotation portion of the pose and then estimates an associated translation. The intermediate rotation estimates are always the best "orthogonal" solution for each iteration. And the orthogonality constraint is enforced by using singular value decomposition.

The mapping from 3D reference points $\mathbf{P}_i = (x_i, y_i, z_i)^{\mathrm{T}}, i = 1, \ldots, n$ to 2D image coordinates $\mathbf{u}_i = (u_i, v_i)^{\mathrm{T}}$ can be formalized as follows:

$$\mathbf{Rp}_i + \mathbf{t} = \mathbf{U}_i(\mathbf{Rp}_i + \mathbf{t}), \tag{34.7}$$

where

$$\mathbf{U}_i = \frac{\mathbf{u}_i \mathbf{u}_i^T}{\mathbf{u}_i^T \mathbf{u}_i}, \tag{34.8}$$

is the line-of-sight projection matrix. $\mathbf{R}$ and $\mathbf{t}$ are the rotation matrix and the translation vector, respectively.

Then the self-calibration problem is formulated as the problem of optimizing the following objective function:

$$e_i = \left\| \left(\mathbf{RP}_i^w + \mathbf{t}\right) - \mathbf{U}_i\left(\mathbf{RP}_i^w + \mathbf{t}\right) \right\|. \tag{34.9}$$

We seek to minimize the sum of the squared error

$$E(\mathbf{R}, \mathbf{t}) = \sum_{i=1}^{n} e_i^2 = \sum_{i=1}^{n} \left\| (\mathbf{I} - \mathbf{U}_i)\left(\mathbf{RP}_i^w + \mathbf{t}\right) \right\|^2 \tag{34.10}$$

over $\mathbf{R}$ and $\mathbf{t}$. Note that all the information contained in the set of the observed image points $\{\mathbf{u}_i\}$ is now completely encoded in the set of projection matrices $\{\mathbf{U}_i\}$. Since this objective function is quadratic in $\mathbf{t}$, given a fixed rotation $\mathbf{R}$, the optimal value for $\mathbf{t}$ can be computed in closed form as:

$$\mathbf{t}(\mathbf{R}) = \frac{1}{n}\left(\mathbf{I} - \frac{1}{n}\sum_i \mathbf{U}_i\right)^{-1} \sum_i (\mathbf{U}_i - \mathbf{I})\mathbf{RP}_i^w. \tag{34.11}$$

Given the optimal translation as a function of $\mathbf{R}$ and defining

$$\mathbf{P}_i^c(\mathbf{R}) = \mathbf{U}_i\left(\mathbf{RP}_i^w + \mathbf{t}(\mathbf{R})\right), \tag{34.12}$$

Equation (34.10) can be rewritten as:

$$E(\mathbf{R}) = \sum_{i=1}^{n} \left\| \mathbf{R}\mathbf{M}_i^w + \mathbf{t}(\mathbf{R}) - \mathbf{M}_i^c(\mathbf{R}) \right\|^2 \tag{34.13}$$

$\mathbf{R}$ can be computed iteratively, and $\mathbf{t}$ will be calculated according to Eq. (34.11). The pose of camera now is obtained accurately.

34.3 Experiments

34.3.1 Synthetic Experiments

Considering that the Gaussian-Newton iterative method and the Levenberg-Marquardt method is easier to fall into local optimum than that of the gradient descent iterative method. We compare the accuracy and stability of our method against that of Lu's method and the gradient descent iterative method though simulated experiment. Lu's method and the gradient descent iterative method are initialized with a weak perspective assumption and the non-iterative solution, respectively.

We produced synthetic 3D-to-2D correspondences in a 1280×1024 image acquired using a visual calibrated camera with an effective focal length of $f_u = f_v = 2400$ and a principal point at $(u_c, v_c) = (639.5, 511.5)$. We generated different sets for the input data, and added Gaussian image noise to the corresponding 2D point coordinates, for which the 2D coordinate was randomly selected within the whole image.

Given the true camera rotation $\mathbf{R_t}$ and translation $\mathbf{t_t}$, we computed the relative error of the estimated rotation $\mathbf{R}$ by $E_r = \|\mathbf{q_t} - \mathbf{q}\| / \|\mathbf{q}\|$, where $\mathbf{q}$ and $\mathbf{q_t}$ are the normalized quaternions corresponding to the rotation matrices. Similarly, the relative error of the estimated translation $\mathbf{t}$ is determined by $E_t = \|\mathbf{t_t} - \mathbf{t}\| / \|\mathbf{t}\|$.

To compare the accuracy of all the method against noise, we plot the rotational and translational errors produced by the three methods as a function of noise when point number is fixed to 6. On Fig. 34.1, we show the mean error of rotation and translation. According to the figures, our method is consistently more accurate and stable than the other methods, especially for large amounts noise. All the plots discussed in this section were created by running 1000 independent MATLAB simulations (Fig. 34.1)
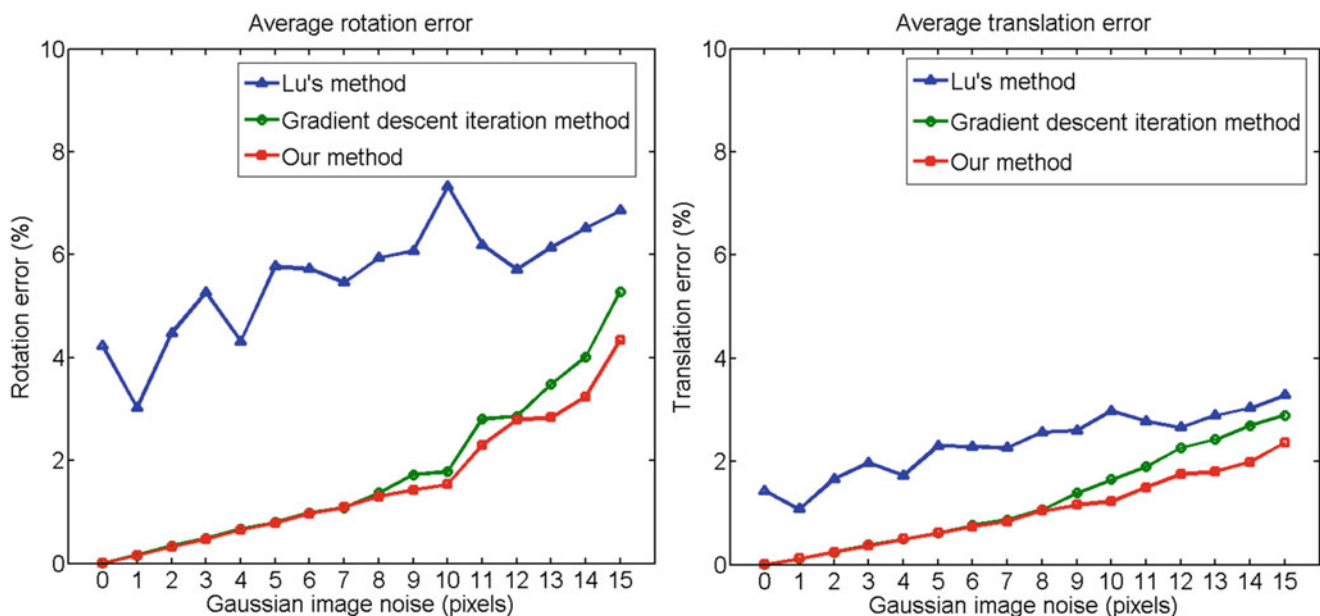

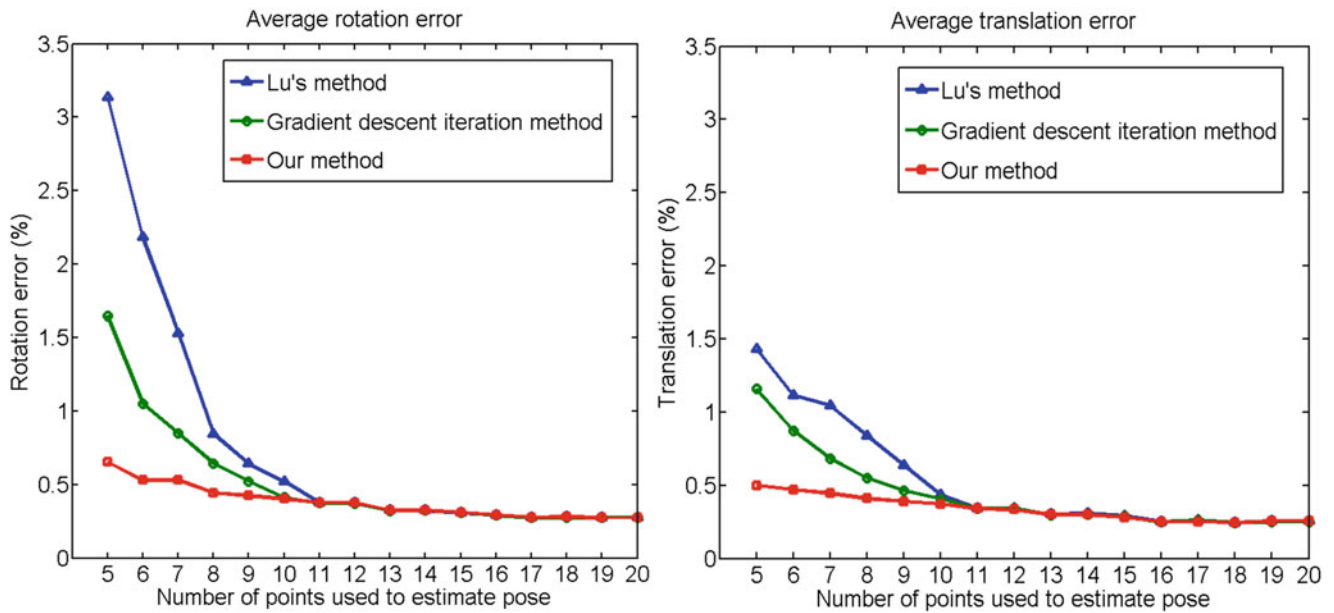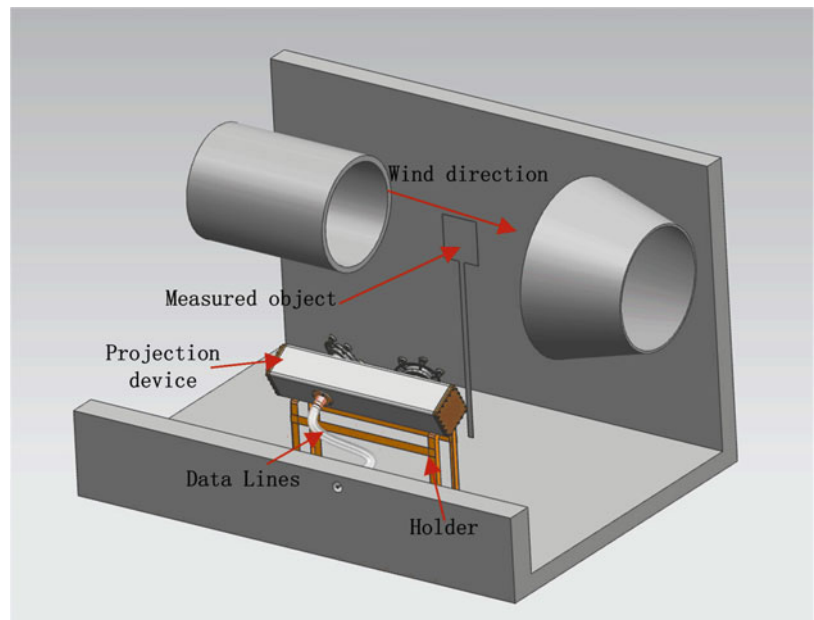**Fig. 34.1** Average rotational and translational errors for defferent gaussian image noise

Fig. 34.2 Average rotational and translational errors for defferent point number

Fig. 34.3 The structure
diagram of wind tunnel

In order to analysis the influence of the number reference points to the accuracy of all the methods, we plot the rotational and translational errors as a function of point number when noise is fixed to five. As shown in Fig. 34.2, our method performs better than the other methods, especially when the number of reference points is less than 10. All the plots discussed in this section were created by running 300 independent MATLAB simulations.

34.3.2 Experiments and Applications in Hypersonic Wind Tunnel

Flutter is one of the most important issues in dynamic aeroelasticity. And flutter of aircraft may lead to disastrously structure damaging of aircraft. Deformation data of flutter test in wind tunnel can help engineer analyzing the critical conditions of aircraft flutter. In this paper, we applied a 3D vision system to measure the deformation of an aircraft wing model in

hypersonic wind tunnel of CARDC. And a protection device was designed to protect the 3D vision system from the damage of high-speed air flow and reduce the influence of vibration. As shown in Fig. 34.3, the 3D vision system was installed in the protection device, the protection device was fixed in wind tunnel and connected to the atmosphere, which can protect the 3D vision system from the damage of high-speed air flow and the varying air pressure in hypersonic wind tunnel. In Fig. 34.4, we show the structure diagram of the protection device and the 3D vision system. The protection device was consist of hoder, glass, matal tube and damping device. And the damping device was used to reduce the vibration of vision system. In the 3D vision system two cameras with 1280 × 1024 pixels resolution were employed to capture images, and the measuring range was 1.2 m × 1 m × 1 m. In the experiment, the wind speed in hypersonic wind tunnel was 5 Mach, and the frame rate of
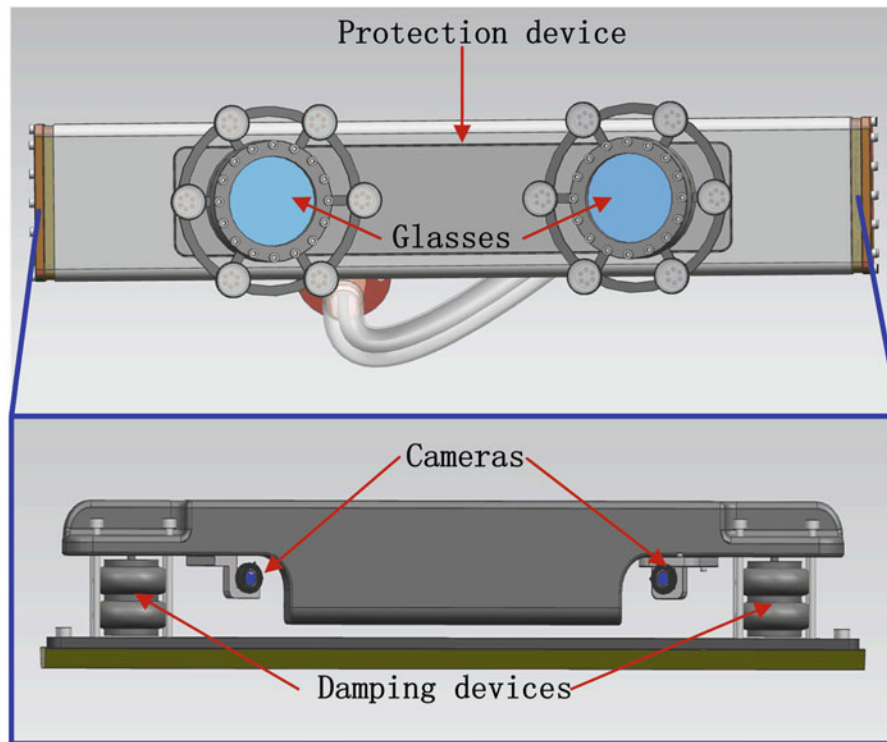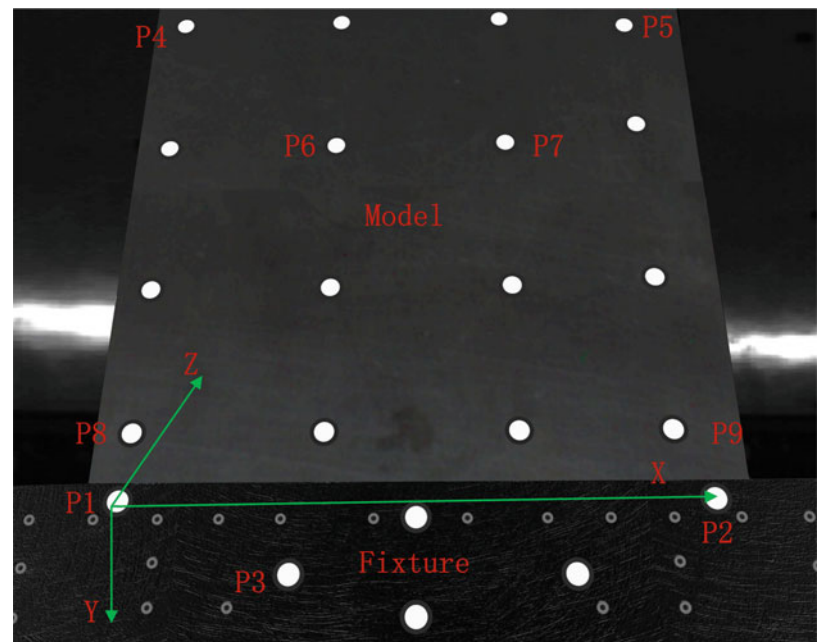

Fig. 34.4 The structure diagram of the protection device and 3D vision system
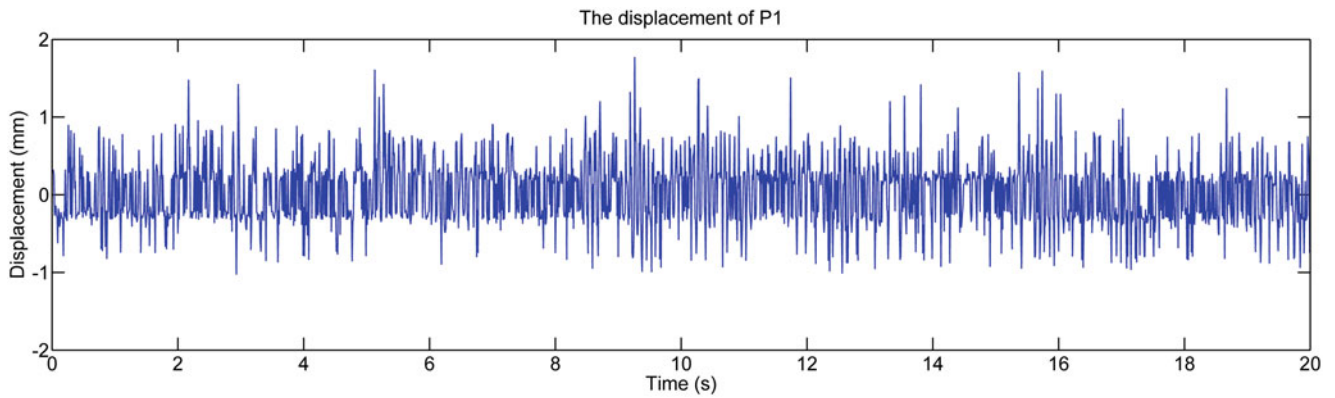
Fig. 34.5 The measuring model

Fig. 34.6 The displacement of P_1 when the world coordinate system was set on the camera

Table 34.1 Standard deviation of distance between P_1 and P_2 (mm)

Experiments	1	2	3	4	5	6	7	8
Without self-calibration	0.478	0.489	0.495	0486	0.508	0493	0.501	0.516
With self-calibration	0.034	0.044	0.029	0.017	0.023	0.028	0.013	0.020

camera was 150 HZ. During each experiment, 3000 images of each camera were captured. As shown in Fig. 34.5, in hypersonic wind tunnel the model was fixed on the fixture, a number of target points were set on it to measure the model's deformation, and six reference points which were relative static were distributed on the fixture to rectify the camera pose. Near P_6 and P_7, two acceleration transducers were installed in the model, we can contrast our measurement results with that of the acceleration transducers. And P_4, P_5, P_8, P_9 were on the corner of the model, the deformation data of these points is important to analyze the critical conditions of aircraft flutter. So in this paper, we measured the deformation of P_4, P_5, P_6, P_7, P_8 and P_9.

In hypersonic wind tunnel, the 3D vision system may move by the influence of vibration. If the world coordinate system was set on one of the cameras, the world coordinate system will move with the camera. To analyze the movement of vision system, we plot the displacement of P_1 which should be still while the camera don't move when the world coordinate system was set on the camera. As shown in Fig. 34.6, the displacement of P_1 is varying during the experiment, and the maximum displacement is more than 1.5 mm. It proves that during the experiment the vision system was moving, and the measurement results when the world coordinate system was set on the camera were incredible. As the model was fixed on the fixture tightly, we can set a dynamic world coordinate system which can be defined by three points on the fixture to get precise measurement results. As shown in Fig. 34.5, we define P_1 as the origin of the world coordinate system, X orientation define by P_1P_2, and P_1, P_2, P_3 is on the XOY plane. Then, during the measurement the coordinates of P_1 is always (0, 0, 0).

In this paper, the standard deviation of distance between P_1 and P_2 was measured during the experiments to verify that the self-calibration method can improve the measurement accuracy of vision system in hypersonic wind tunnel. The experiment run eight times. As shown in Table 34.1, by using the self-calibration method, the standard deviation of distance between P_1 and P_2 was less than 0.05 mm. While without using the self-calibration method the standard deviation of distance between P_1 and P_2 was no less than 0.4 mm. It proves that the self-calibration method can rectify the camera pose accurately and improve the measurement accuracy in hypersonic wind tunnel. The deformation of P_4, P_5, P_6, P_7, P_8 and P_9 were measured (Fig. 34.7 shows the coordinates of P_4 during the measurement). And we drew the spectrogram of these points in Fig. 34.8 to analyze the vibration of model. As shown in Fig. 34.8 the inherent frequency of model was 30.8 HZ, which was equal to the measurement results of the acceleration transducer. It proves that the 3D vision system can measure the deformation of model in hypersonic wind tunnel accurately.
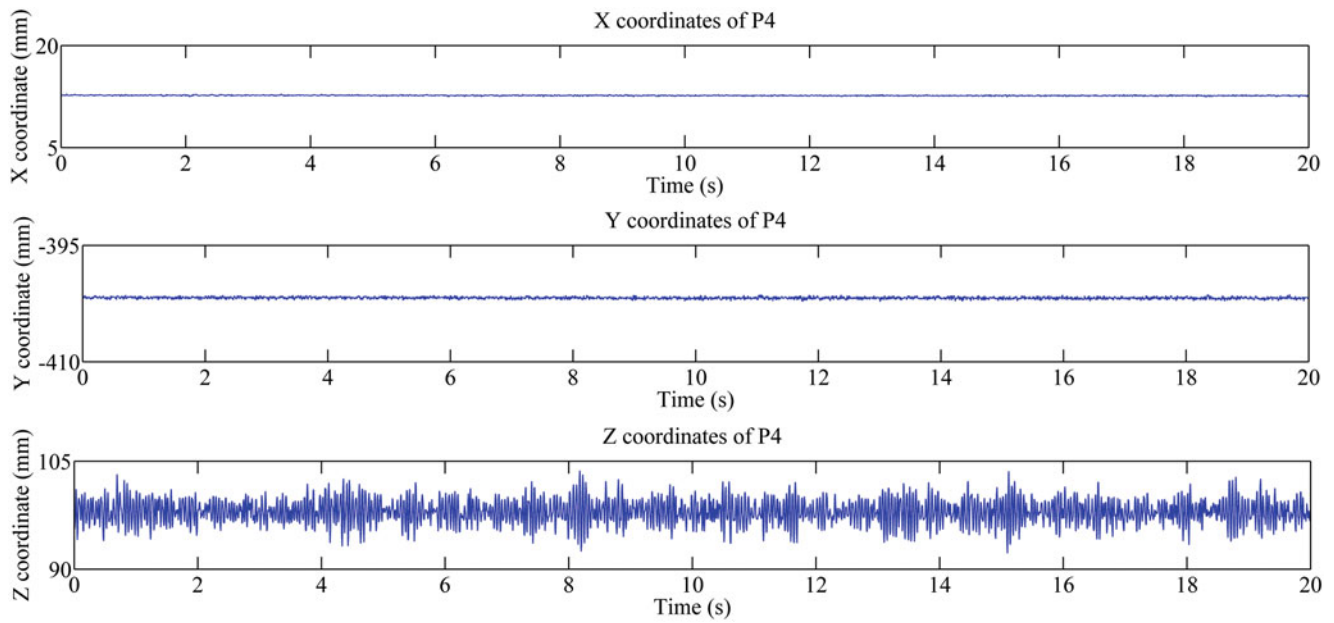
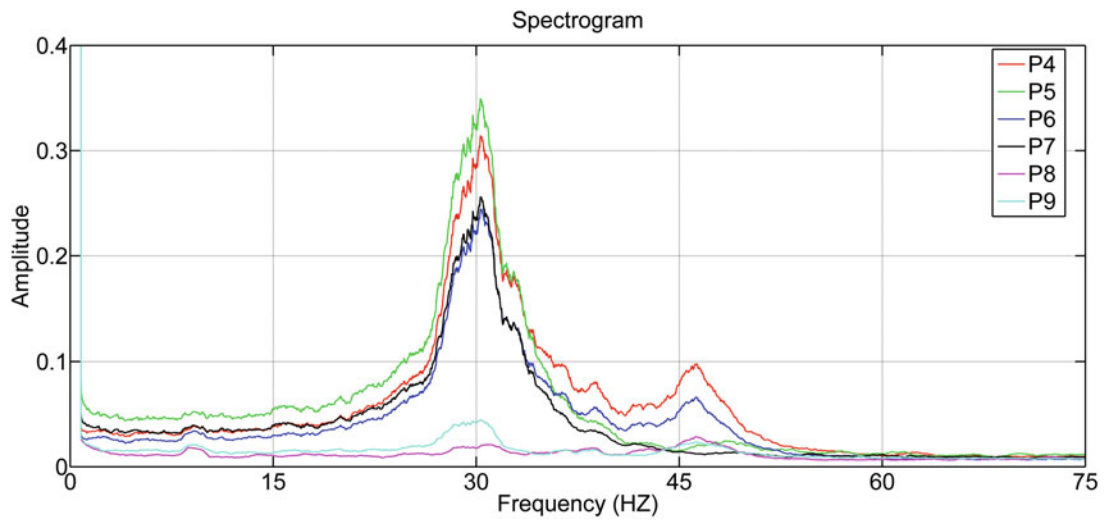**Fig. 34.7** The coordinates of P$_4$ during the measurement

Fig. 34.8 The Spectrogram of P$_4$, P$_5$, P$_6$, P$_7$, P$_8$ and P$_9$

34.4 Conclusions

To apply the 3D vision system in hypersonic wind tunnel, a two-step self-calibration method was proposed in this paper which uses a non-iterative solution to initial the orthogonal iterative method. The synthetic experimental results shows that our self-calibration method is more accurate and stable than other iterative method. And the 3D vision system with self-calibration method was applied to measure to deformation of an aircraft wing model in hypersonic wind tunnel of CARDC. According to the experiment results, the 3D vision system can get accurate measuring results in hypersonic wind tunnel.

References

1. Barrows, D.A.: Videogrammetric model deformation measurement technique for wind tunnel applications. AIAA paper 2007-1163 (2007)
2. Liu, T., Cattafesta, L., Radezsky, R., Burner, A.W.: Photogrammetry applied to wind tunnel testing. AIAA J. **38**(6), 964–971 (2000)
3. Zhang, Z., Wang, S., Sun, Y.: Videogrammetric measurement for model displacement in wind tunnel. Appl. Mech. Mater. **130–134**, 103–107 (2012)
4. Silva, J., Marques da Silva, F., Couto, A., Estanqueeiro, A.: A method to correct the flow distortion of offshore wind data using CFD simulation and experimental wind tests. J. Wind Eng. Ind. Aerodyn., **140**, 87–94 (2015)
5. Sun, P., Sun, C., Li, W., Wang, P.: A new pose estimation algorithm using a perspective-ray-based scaled orthographic projection with iteration. PLoS One **10**(7), e0134029 (2015)
6. Oberkampf, D., Dementhon, D.F., Davis, L.S.: Iterative pose estimation using coplanar feature points. Comput. Vis. Image Underst. **63**(3), 495–511 (1996)
7. Schweighofer, G., Pinz, A.: Robust pose estimation from a planar target. IEEE Trans. Pattern Anal. Mach. Intell. **28**(12), 2024–2030 (2006)
8. Lu, C.-P., Hager, G.D.: Fast and globally convergent pose estimation from video images. IEEE Trans. Pattern Anal. Mach. Intell. **22**(6), 610–622 (2000)
9. Moreno-Noguer, F., Lepetit, V., Fua, P.: Accurate noniterative o(n) solution to the pnp problem. In: IEEE International Conference on Computer Vision, Rio de Janeiro (2007)
10. Lepetit, V., Moreno-Noguer, F., Fua, P.: EPnP: an accurate O(n) solution to the PnP problem. Int. J. Comput. Vis. **81**(2), 155–166 (2009)

Chapter 35
Evaluating Stress Triaxiality and Fracture Strain of Steel Sheet Using Stereovision

D. Kanazawa, Satoru Yoneyama, K. Ushijima, J. Naito, and S. Chinzei

Abstract This paper studies a method for evaluating the stress triaxiality and the fracture strains of thin steel plates which are used for an automobile body frame. Three-dimensional displacements and strains on the surface of the thin steel plates are measured using a stereovision. In particular, to measure the through-thickness deformation of the steel plates, the measurements are performed from the both sides of the steel plates. Based on the strain incremental theory, the stress triaxiality is evaluated from the measured strains considering the variation of the thickness of the steel plates. The effectiveness of the proposed procedure is validated by applying it to the evaluation of the stress triaxiality of high strength steel plates. Results show that the stress triaxiality and the fracture strains can be evaluated by the proposed method.

Keywords Digital image correlation • Stress triaxiality • Stress-strain curve • Tensile strength • Stereo vision • Fracture stress • Fracture strain

35.1 Introduction

Recently, metal materials for an automobile body frame are advanced to be high strength and thinner. Accordingly, predictions of deformation and fracture phenomenon of the thin steel at the time of collision have become important. It is known that the fracture strains depend on the hydrostatic stress strongly. Therefore, the evaluation and the modeling of the fracture strains as well as the stress triaxiality have become essential.

Effelsberg et al. [1] have revealed that the stress triaxiality changes as the deformation of the materials. Therefore, the stress triaxiality needs to be evaluated considering the deformation of the materials. Bai and Wierzbicki [2, 3] revealed that the fracture strains depend on the stress triaxiality strongly, and proposed a method for evaluating the stress triaxiality from the increments of principal plastic strains. Also, they revealed the relationship between the fracture strains and the stress triaxiality. They did not use the through-thickness deformation for evaluating the stress triaxiality but used the in-plane strains. However, the thickness of the thin plate reduces significantly with progress of the plastic deformation. Therefore, not only the in-plane strains but also the through-thickness strains should be used for evaluating the stress triaxiality.

In this study, therefore, a method is developed for evaluating the stress triaxiality and the fracture strains accurately considering the deformation of thin steel plates. Here, three-dimensional displacements are measured using digital image correlation (DIC) [4], and the strain are calculated from measured displacements [5]. Then, the variation of the stress triaxiality is evaluated from the measured strains. In the evaluated method of stress triaxiality currently being considered, there are a method that the stress triaxiality is calculated from the strains and a method that the stress triaxiality is calculated from the stresses. For the stress triaxiality calculated from the strain, the stress triaxiality is calculated based on the strain incremental theory. In particular, to measure the through-thickness strains, the measurement is performed from the both sides of the steel plates. For the stress triaxiality calculated from the stresses, the stresses are obtained from the measured strains using the total strain theory. Also, in each evaluation method, the evaluation of the stress triaxiality is performed with and without considering the through-thickness deformation.

D. Kanazawa (✉) • S. Yoneyama
Department of Mechanical Engineering, Aoyama Gakuin University, 5-10-1 Fuchinobe, Sagamihara, Kanagawa 252-5258, Japan
e-mail: c5615102@aoyama.jp

K. Ushijima
Department of Mechanical Engineering, Tokyo University of Science, 6-3-1 Niijyuku, Katsushika-ku, Tokyo 125-8585, Japan

J. Naito • S. Chinzei
Kobe Steel, LTD, 1-5-5 Takatsukadai, Nishi-ku, Kobe, Hyogo 651-2271, Japan

35.2 Evaluation Methods of the Stress Triaxiality

In the method for the calculation of the stress triaxiality proposed by Bai and Wierzbicki [2], the stress triaxiality η is represented by the following equation.

$$\eta = \frac{d\varepsilon_1^P + d\varepsilon_2^P}{\sqrt{3\left(\left(d\varepsilon_1^P\right)^2 + d\varepsilon_1^P d\varepsilon_2^P + \left(d\varepsilon_2^P\right)^2\right)}} \tag{35.1}$$

Here, $d\varepsilon_1^P$ and $d\varepsilon_2^P$ are the increments of the principal plastic strains. In Eq. (35.1), the through-thickness deformation is not considered. On the other hand, the following equation is proposed for calculating the stress triaxiality in this study.

$$\eta = \frac{d\varepsilon_1^P + d\varepsilon_2^P - 2d\varepsilon_3^P}{3\sqrt{\left(d\varepsilon_1^P\right)^2 + \left(d\varepsilon_2^P\right)^2 + \left(d\varepsilon_3^P\right)^2 - d\varepsilon_1^P d\varepsilon_2^P - d\varepsilon_2^P d\varepsilon_3^P - d\varepsilon_3^P d\varepsilon_1^P}} \tag{35.2}$$

Here, in Eq. (35.2), $d\varepsilon_3^P$ is the third component of the principal plastic strains. That is, the through-thickness deformation is considered. Here, in the above methods, the stress triaxiality can be evaluated from the measured strains using DIC [5]. However, in this method, it is difficult to separate the elastic strains and the plastic strains. Therefore, the stress triaxialities evaluated by Eqs. (35.1) and (35.2) are influenced by the elastic strain increments.

Next, the stress triaxiality is evaluated from the principal stresses that are calculated from the strains. In the total strain theory, the stress-strain relationships of the elastic-plastic material are represented by the following equation.

$$\varepsilon_1 = \left(\varphi + \frac{1}{2G}\right)\left(\frac{2\sigma_1 - \sigma_2}{3}\right) + \frac{1}{3K}\sigma_m$$
$$\varepsilon_2 = \left(\varphi + \frac{1}{2G}\right)\left(\frac{2\sigma_2 - \sigma_1}{3}\right) + \frac{1}{3K}\sigma_m \tag{35.3}$$

Here, G is the shear modulus, K is the bulk modulus, σ_1 and σ_2 are the principal stresses, and σ_m is the mean stress. The symbol ϕ in Eq. (35.3) is represented by the following equation.

$$\varphi = \frac{3}{2}\frac{\varepsilon_e^p}{\sigma_e} \tag{35.4}$$

Here, ε_e^P is the equivalent plastic strain and σ_e is the equivalent stress. The principal stresses are calculated from the strains using the numerical calculation. The stress triaxiality expressed with the in-plane principal stresses are represented by the following equation.

$$\eta = \frac{\sigma_1 + \sigma_2}{3\sqrt{\left(\sigma_1\right)^2 - \sigma_1\sigma_2 + \left(\sigma_2\right)^2}} \tag{35.5}$$

On the other hand, by considering the through-thickness deformation, the following equation is used with Eq. (35.3).

$$\varepsilon_3 = \left(\varphi + \frac{1}{2G}\right)\left(-\frac{\sigma_1 + \sigma_2}{3}\right) + \frac{1}{3K}\sigma_m \tag{35.6}$$

From Eqs. (35.3) and (35.6), the principal stresses are calculated and substituted into Eq. (35.5). Then, the stress triaxiality is calculated from the stresses considering the through-thickness deformation.

35.3 Experimental Method

The shape and the size of the specimen used in this study are shown in Fig. 35.1. The specimens have three type of the tensile strength of more than 1500 MPa, more than 980 MPa and more than 590 MPa, each specimen has two type of the notch radius of 2 and 5 mm. In this study, the experimental results of the specimen whose tensile strength is more than 1500 MPa with the notch radius of 5 mm are shown. The experimental device is shown in Fig. 35.2. In the experiment, the tensile machine is used, and the cameras whose resolution of 2048 × 2048 pixels, whose pixel size of 5.5 × 5.5 μm and whose frame rate is 90 fps are used. The cameras are placed at a distance of 300 mm from each other and at a distance of 500 mm from the specimen. Two light sources are installed in the back of the cameras in order to clarify the brightness of the images. Also, the function generator is introduced in order to synchronize the timing of the shooting of the cameras which are placed by two on the both side of the specimen and the timing of the load measurement. The tensile speed of the tensile machine is set at 0.5 mm/min, and the tensile test is done until the specimen is broken.
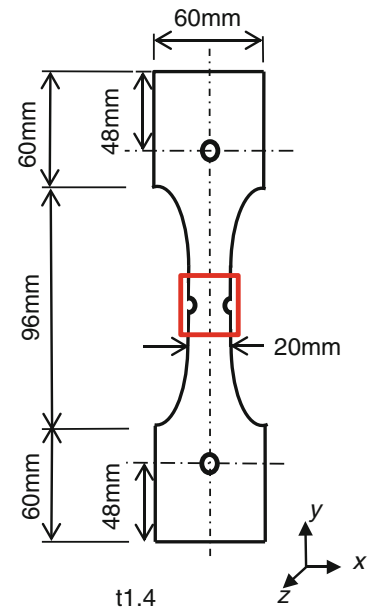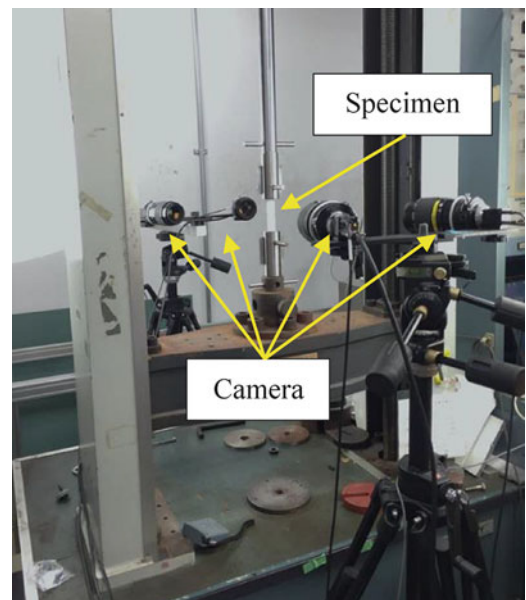

Fig. 35.1 Shape of the specimen

Fig. 35.2 Experimental device

The load applied to the specimen is measured using the load cell, and the three-dimensional displacements and the strains are measured using DIC. The measurement area on the specimen is indicated by a frame in Fig. 35.1. In this study, the measurement area is set to 20 mm in width and 20 mm in height, and the evaluation point of the stress triaxiality is the center of the notch bottom. The reference value of the stress triaxiality of the specimen with the notch radius of 5 mm, which is obtained with the assumption of elastic small deformation, is calculated as $\eta = 1/\sqrt{3} \fallingdotseq 0.577$ with the conditions of the plane stress ($\sigma_3 = 0$) and $\sigma_1 = 2\sigma_2$ [6]. This value and the stress triaxialities which are obtained by the each method are compared.

35.4 Experimental Results

The load-displacement curve of the specimen whose tensile strength is more than 1500 MPa with the notch radius of 5 mm is shown in Fig. 35.3. The three-dimensional displacement distributions of the front surface of the specimen after 278 s are shown in Fig. 35.4 and the back surface of those are shown in Fig. 35.5. The three-dimensional strain distributions of the front surface of the specimen are shown in Fig. 35.6 and the back surface of those are shown in Fig. 35.7. Here, the displacements and the strains of the back surface are seen from the front surface because the coordinate systems are unified into the front surface coordinate systems. The stress triaxiality and the equivalent plastic strain distributions calculated using Eqs. (35.1), (35.2) and (35.5) are shown in Fig. 35.8. The equivalent plastic strains are calculated by the following equation.
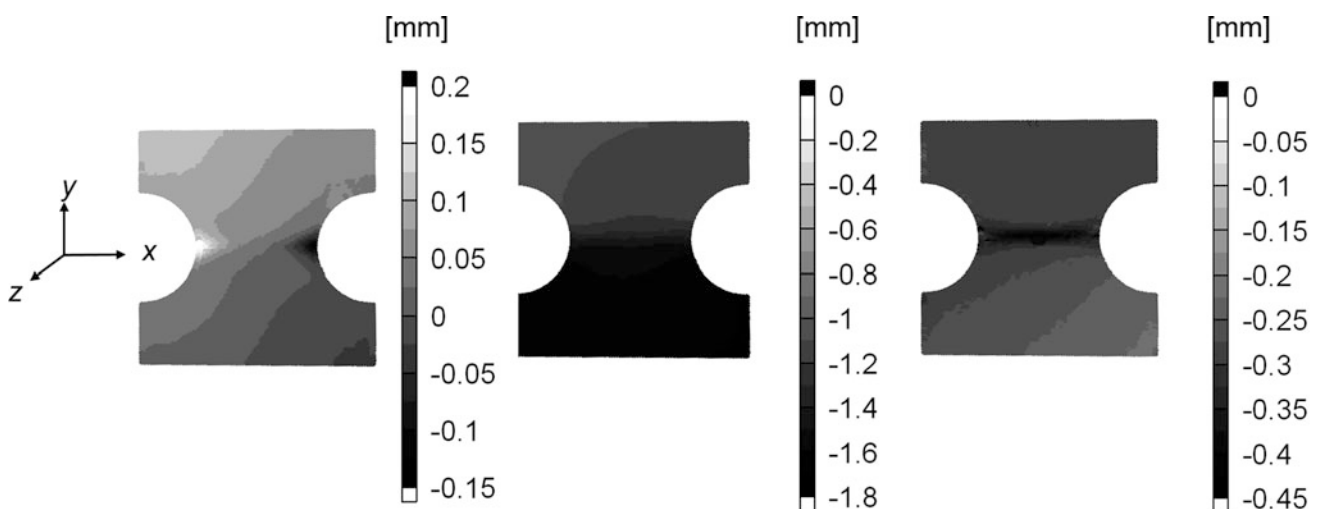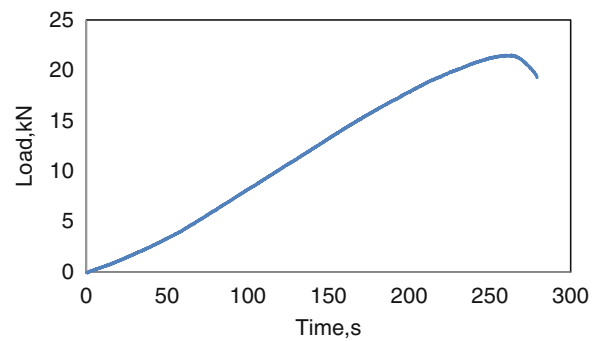
Fig. 35.3 Load-time diagram

Fig. 35.4 Displacement distribution of the front surface after 278 s: (**a**) x direction; (**b**) y direction; (**c**) z direction

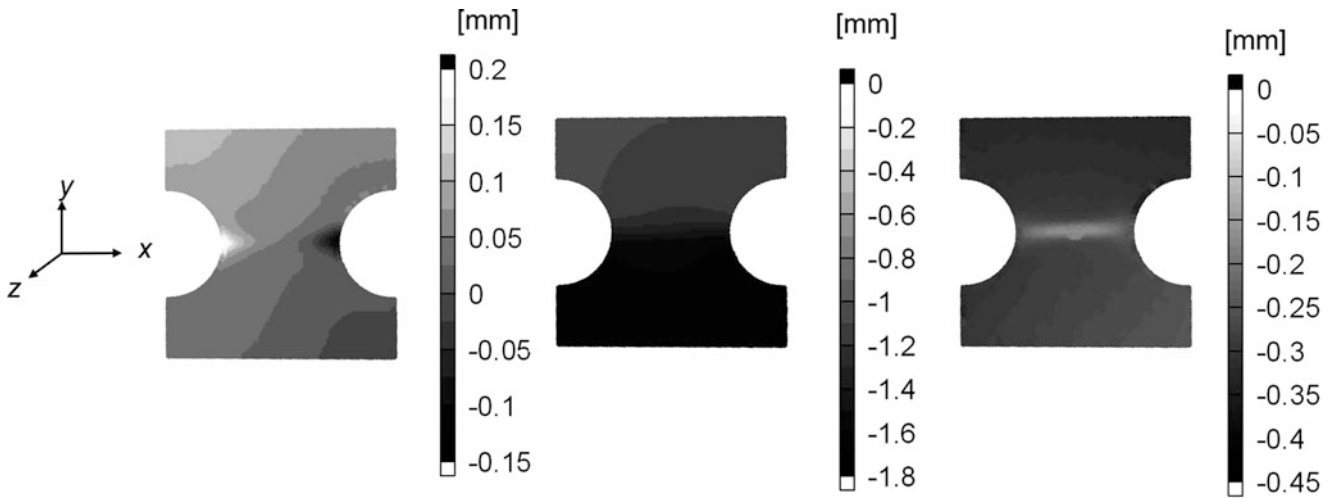**Fig. 35.5** Displacement distribution of the back surface after 278 s: (**a**) *x* direction; (**b**) *y* direction; (**c**) *z* direction

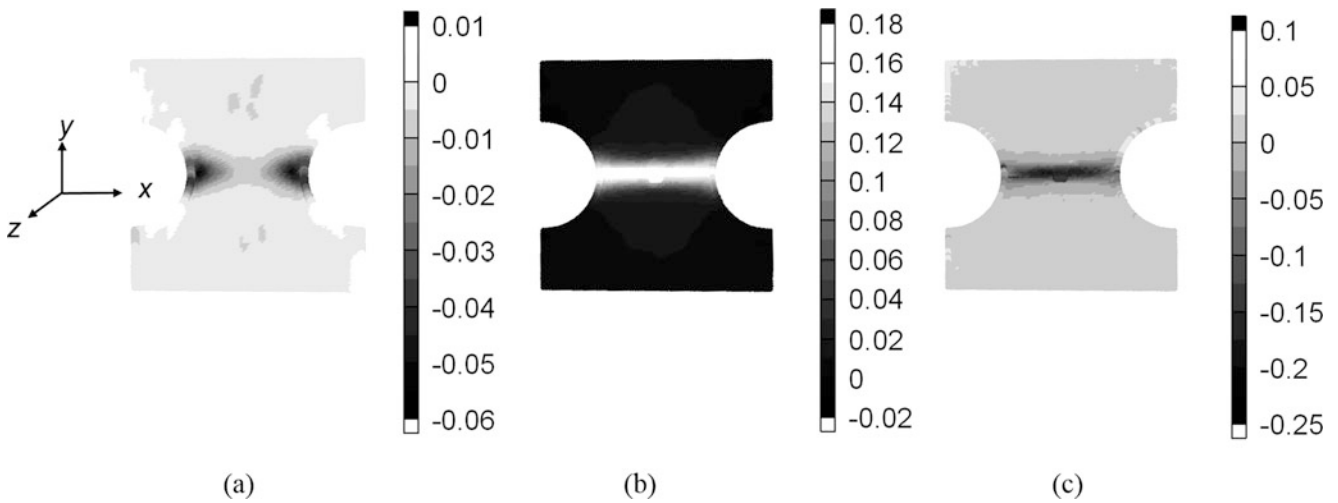(a)   (b)   (c)

Fig. 35.6 Strain distribution of the front surface after 278 s: (**a**) *x* strain; (**b**) *y* strain; (**c**) *z* strain
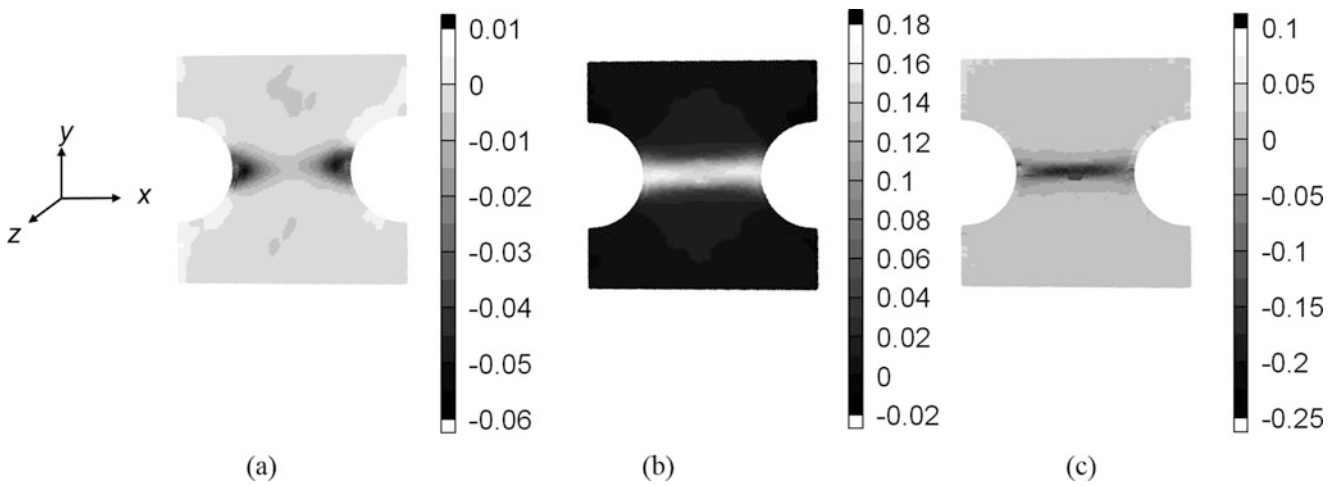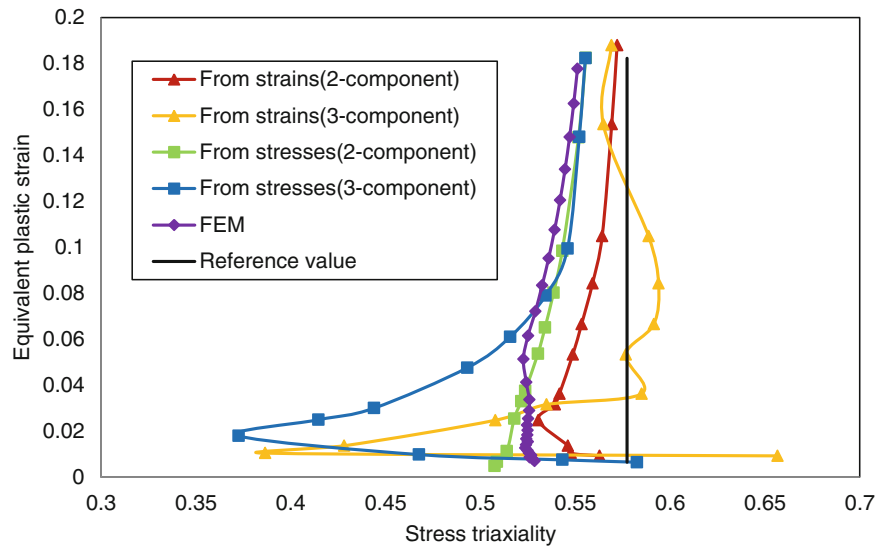

(a)   (b)   (c)

Fig. 35.7 Strain distribution of the back surface after 278 s: (**a**) *x* strain; (**b**) *y* strain; (**c**) *z* strain

Fig. 35.8 Stress triaxiality-equivalent plastic strain distribution

$$\varepsilon_e^P = \sqrt{\frac{2}{3}\left\{\left(\varepsilon_1^P\right)^2 + \left(\varepsilon_2^P\right)^2 + \left(\varepsilon_3^P\right)^2\right\}} \tag{35.7}$$

Here, ε_1^P, ε_2^P, and ε_3^P are the principal plastic strains. In this study, the elastic strains are regarded to be sufficiently small. Therefore, the strain measured using DIC are regarded to be the plastic strains.

35.5 Discussion

From Fig. 35.8, the values of the stress triaxiality calculated in all methods increase as the value of the equivalent plastic strains increases. It is thought that the stress triaxialities are changed by the deformation of the specimen. When the value of the equivalent strain is lower than 0.05, the stress triaxialities which are calculated in all methods are far from the reference value. When the value of the equivalent plastic strain is larger than 0.15, the stress triaxialities become the close value as the reference value. It can be considered that the stress states of the evaluation point substantially equal to that one of the reference value. The values of the stress triaxialitiy evaluated from the strain increments using Eqs. (35.1) and (35.2) agree well with the value obtained using FEM. When the through-thickness strains are taken into account for evaluating the stress triaxiality, the values of the stress triaxiality deviate from the values obtained by other methods in the early stage of the test. In the latter stage, these values agree well with the values obtained without the through-thickness strains. Further discussion is required for the evaluation method of the stress triaxiality.

35.6 Conclusions

A method for evaluating the stress triaxiality and the fracture strains of thin steel plates is studied in this paper. Three-dimensional displacements and strains on both sides of the thin steel plates are measured using a stereovision. The stress triaxiality is evaluated from the measured strains considering the variation of the thickness of the steel plates. The effectiveness of the proposed procedure is validated by applying it to the evaluation of the stress triaxiality of high strength steel plates. Results show that the stress triaxiality and the fracture strains can be evaluated by the proposed method.

References

1. Effelsberg, J., Haufe, A., Feucht, M., Neukamn, F., Du Bois, P.: On parameter identification for the GISSMO damage model. In: International LS-DYNA, Metal Forming 3, pp. 1–12 (2012)
2. Bai, Y., Wierzbicki, T.: Forming severity concept for predicting sheet necking under complex loading histories. Int. J. Mech. Sci. **50**, 1012–1022 (2008)
3. Bai, Y., Wierzbicki, T.: Application of extended Mohr-Coulomb criterion to ductile fracture. Int. J. Fract. **161**, 1–20 (2010)
4. Orteu, J.: 3-D computer vision in experimental mechanics. Opt. Lasers Eng. **47**, 282–291 (2009)
5. Yoneyama, S.: Computing strain distributions from measured displacement on a three-dimensional surface. J. JSEM **10**, 113–118 (2010)
6. Till, E., Hackl, B., Schauser, H.: Crash simulating of roll formed parts by damage modelling taking into account preforming effects. In: AIP Conference Proceedings, pp. 267–274 (2011)

Chapter 36
Shadowgraph Optical Technique for Measuring the Shock Hugoniot from Standard Electric Detonators

Vilem Petr, Erika Nieczkoski, and Eduardo Lozano

Abstract This research paper overviews the detonation characteristics of the liquid-desensitized function detonator used for the oil and gas industry. The liquid-desensitized function is designed to protect perforating tools from any liquid that penetrates inside the tool during operation. Additionally, the number 8 standard electric detonator is analyzed using the same technique. The measurement of the energy release from these types of initiation systems becomes critical for the evaluation of their initiation ability of the firing sequence, as well as from the standardization point of view.

The Advanced Explosive Research Processing Group (AXPRO) presents a new method for experimentally measuring air shock properties and energy fluence from detonators by the using a single indoor experiment. The retro-reflective shadowgraph technique was used for measuring shock wave expansion rate. The method was effectively improved by replacing the continuous light with a strobe light. This new technique allows us to obtain much higher image quality than the one obtained by the Schlieren method. The shock Hugoniot and conservation equations provided a full characterization of the released energy from the high explosive base charge contained within the detonator. This technique produces data in general agreement with published data for the detonation and air shock properties from high explosives. This new method could constitute a practical and simplified experimental tool for industry use due to its relatively low cost, high data accuracy, and reduced data-analysis time.

Keywords High-speed imaging • Retro-reflective • shock wave • Detonation • Initiation system

36.1 Introduction

In order to initiate high explosives and the blasting agents, strong shock or detonation is required. A capsule of sensitive explosive material termed a detonator can accomplish this. Figure 36.1 shows two different designs of electric detonators that are generally used throughout the world. One is a standard mining and construction detonator Electric SP Number 8 and the other is a fluid desensitized oil and gas detonator Number 6.

High-speed imaging technologies are constantly being improved for the study of detonation properties of explosive materials [1–9]. The goal of this research was to develop a "relatively simple" experimental method that validates the explosive energy inside of a detonator. The challenge of this endeavor emerges from the nature of manufacturing; detonator designs are always unique and the composition, as well as the combination, of explosive materials used is variable and depends on the manufacturer.

The first detonator was developed in 1890s, and had a single explosive base. Since then, there have been significant improvements in initiation system technology. Presently, detonators frequently have two different explosive base materials: a sensitive primary explosive (primer charge), and a less sensitive, but more high-powered (brisance) secondary explosive (base charge), as is shown in Fig. 36.1.

Detonator technology has developed significantly since the first initiation system was created. In general, a detonator consists of a metal capsule, tube or shell. The first detonator shells were constructed from paper, and then later advanced to copper, bronze, aluminum, and finally, plastic in the pursuit of the mitigation of fragments. There have also been advancements to universal detonator requirements. The United Nations' specifications for electric detonators generally require a 7.00–8.00 mm diameter and a varying length depending upon whether the detonator is an instantaneous or delay type.

V. Petr (✉) • E. Nieczkoski • E. Lozano

Colorado School of Mines, 1600 Illinois Street, Golden, CO 80401, USA

e-mail: vpetr@mines.edu

Fig. 36.1 Two main electric detonators types used in mining and construction and oil and gas industries. Units are in millimeters
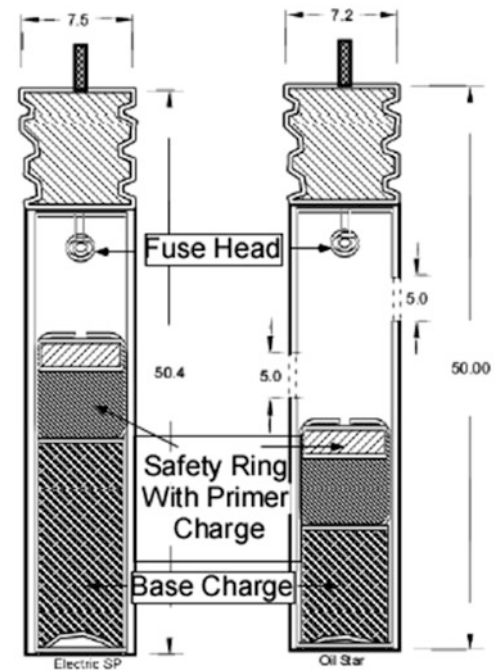
When manufactured, the detonator base charge is placed at the bottom of the metal shell. Both the primer charge and the base charge are compacted together under adequate pressure to ensure the desired strength. Strength of detonator is based upon the quantity of base charge and primary charge; detonators are typically numbered from their strength. Traditionally, detonator strength is characterized through manual indirect measurement techniques. These techniques require detonating an initiation system into a soft medium (Sand Test, 1916), or in some cases, next to a lead or/and metal witness plate (plate test), are time consuming and imprecise. On other hand high-speed imaging systems, which were previously unfeasible for research and development use due to their high-expense, are now an obvious replacement for these methods.

36.2 Theory Background

A high explosive material is characterized by a detonation process where the front of the chemical reaction moves faster through the material than its speed of sound. This sudden release of energy is usually accompanied by the creation of a propagating disturbance in the surrounding medium known as shock or blast wave. By knowing the medium and the rate of expansion of this shock wave, one is able to characterize not only the shock effects on the medium, but also the energy source.

The shock front of a blast wave is in many ways a determining factor in its behavior. The goal of this paper is to characterize detonator initiation strength from its performance in air, which for present purposes may be considered as an ideal gas. Using a Lagrangian coordinate system one can describe the five basic parameters in the air before and after the pass of the shock front. Three first relationships can be derived from the fact that we must conserve mass, momentum, and energy across the shock front. At this point, an equation describing the equilibrium states in which a material can exist in expressed by the Equation of State (EOS). This equation was empirically determined by many experiments in the past, and it was found that the shock velocity was linearly related to the particle velocity for most materials [10]. This empirical relationship is called Hugoniot and it is expressed as follows:

$$U = C_0 + su$$

Where U represents shock velocity, u is particle velocity, C_0 is bulk sound speed, and s is a dimensionless term. For air, Deal [11] measured Hugoniot coefficient C to be 2375 m/s and s to be 1.0575 for measured shock wave velocities up to 4500 m/s. As reported by Biss [12], using these equations, it is possible to calculate the transmitted shock wave properties in air through the sole measurement of the air shock wave expansion rate. From the measure of the detonator shock wave

expansion rate in air, the incident air shock wave properties are determined: shock wave velocity U_s, shock wave Mach number M_s, particle velocity u_s, and incident shock wave pressure P_s. Additionally, the energy per unit area or energy fluence transferred from the detonator to an another possible energetic material can be calculated from the values of shock wave pressure P_s, and time duration t_d if the properties (Hugoniot) of the material are known.

36.2.1 Air Shock Characterization

The present paper reports the shock wave expansion from two types of electric detonators corresponding to two different values of strength: number 6 and number 8. The expansion is measured in two coordinates X and Y, corresponding with the longitudinal and transversal axes of the detonator. This is due to the initial elliptical expansion of the shock wave in the 2D plane produced by the charge geometry. As the shock wave expands, it decays in strength, lengthens in duration, and slows down, both because of the spatial divergence and because of the medium attenuation.

Most of the sources of compiled data for air blast waves from high explosives are limited to bare, spherical charges in free air. However, different experiments conducted with alternative charge geometries show how explosive materials tens to drive their energy to the larger area of their outer surface. Esparza [13] presented a spherical equivalency of cylindrical charges in free air where a higher explosive yield is reached at 90° from the longitudinal charge axis. The difference in the shock wave magnitude in the different directions will decrease as the shock expands through the air adopting a final spherical shape. This data is in agreement with the experimental observations presented in this paper where the two detonator studied are cylindrical in shape. This shape will produce an initially ellipsoidal expanding shock wave creating higher overpressure in the plane normal to the charge axis. As the shock wave moves outward, the initial ellipsoid will degenerate into an expanding sphere.

The shock wave expansion rate in atmospheric air is experimentally measured by using a retro-reflective shadowgraph technique. This expansion is measured along the longitudinal and transversal axes of the detonator providing two set of data. The measured shock wave expansion rate is then fitted to an empirical equation developed by Dewey [14] and reported by Hargather et al. [15] and Biss (2009). This empirical correlation is as follows:

$$R_s(t_a) = A + Ba_0t_a + Cln(1 + a_0t_a) + D\sqrt{ln(1 + a_0t_a)} \tag{36.1}$$

Where R_s represents distance from the center of the blast, t_a represents time of arrival of the shock wave, a_0 is the local speed of sound, and A, B, C, and D are the yielding coefficients. For curve fits to data close to the charge center, B should be set to 1 to guarantee an asymptote to the speed of sound for large time [14]. The calculation of the parameters A, B, C, and D was performed by least-squares curve-fit through a computational code written in MATLAB [15].

Next, a relationship between shock velocities versus time can be obtained by simple derivation of the Eq. (36.1) for longitudinal and transversal directions:

$$\frac{dR_s(t_s)}{dt_s} = Ba_0 + \frac{Ca_0}{1 + a_0t_s} + \frac{Da_0}{2(1 + a_0t_s)\sqrt{ln(1 + a_0t_s)}} \tag{36.2}$$

An explosive shock moving with a certain velocity U_s into an atmosphere where the sonic or acoustic speed is C_a will produce an associated pressure jump known as overpressure of the explosive shock front. Assuming a constant heat capacity ratio for air of 1.4, Kinney and Graham [17] defined the following equation describing the blast overpressure as a function of the shock Mach number $M_s = U_s/C_a$ and the atmospheric pressure P_a.

$$P_s = \frac{7(M_s^2 - 1)}{6} \cdot P_a \tag{36.3}$$

As can be deduced from Eq. (36.3), for shock waves generated in an explosion, where intensity of shock diminishes with distance from the center of the explosion, shock overpressure approached zero and shock velocity approached sonic as distance increases. That is, any explosive shock wave ultimately degenerates into a sound wave. Equation (36.3) and some alternative forms presented in [17] have been widely used for indirect computation of overpressures from shock velocity measurements.

In order to fully characterize the explosive energy release, the duration of the overpressure must be calculated. Kinney and Graham [17] proposed a theoretical method for the calculation of the positive phase duration upon knowing the speed of the shock wave as a function of the radius and assuming that the point marking the end of the positive pressure phase travels at the speed of sound of the gas right behind the shock wave. This blast overpressure duration can be calculated from the shock Mach number versus the distance by the Rankine-Hugoniot theory where each point is assumed to have a static temperature caused by a shock wave passing at a given Mach number [17].

Ultimately, in order to validate overpressure-duration values indirectly calculated from the optical methods presented in this paper, pressure sensors recorded direct measurements of blast overpressure from the passage of the shock wave.

36.2.2 Initiation Strength: Energy Fluence

A detonator is a device used to trigger by shock an explosive device. The energy released by this shock becomes essential while determining the strength of such detonator. Experiments have been conducted in the last decades using different initiators such a flyer plates, where the shock pressure was varied by changing the impact velocity. Each explosive was found to have a unique range of energy fluence above which prompt detonation was always obtained, and below which it was not. The average of this range is called the "critical energy fluence" [10]. For this reason, the energy provided by the detonator must be accurately calculated in order to evaluate its initiation ability assuming not only a direct contact charge-detonator, but also in the case of a certain standoff distance (Gap Test). The term energy per unit area or energy fluence is then expressed as follows:

$$E = \int P u_p dt \approx \frac{P^2 t_d}{2\rho_0 U} = \frac{P^2 t_d}{2Z_{material}} \tag{36.4}$$

Where the P is the shock pressure, t_d is the shock duration, ρ_0 is the density of the material and U is the shock velocity on the material (detonation velocity for high explosives). The denominator is often called the shock impedance of a material and for the range of overpressure involved in shock initiation, it can be considered to be nearly constant for each explosive [10]. It should be noted, that the energy fluence will be dependent on the energy source and the matter where the energy is transferred. Equation (36.4) represents a rough approximation of the integral because the profile of the blast overpressure versus time will change with the time producing different wave form factors. For the purpose of this paper and in order to provide a simple solution, the shock wave profile is assumed triangular which adds a factor of 2 in the divider.

Different approaches have been unsuccessfully addressed for the measure of the energy release from optical methods. The classical similarity solution for a point energy release and strong shock wave formation by Taylor predicts the motion of the shock wave and the resulting physical property distributions and using the dimensional analysis [18]. This ideal prediction however cannot be directly applied to typical explosions where the energy is released over a finite time. These real explosions are better analyzed experimentally by measuring shock propagation or property variations then applying scaling laws [15]. Here, the shock propagation is measured from the center of the explosive as a function of time and becomes the primary data for developing an explosive characterization.

36.3 Experimental Procedure

36.3.1 Number #6: Detonator with Fluid-Desensitizing Function and Number #8: Electric SP

Based upon the quantity of base and A.S.A charge, detonators are designated from No. 1 to No. 10, with the standard detonator being the Number 8 detonator. From design alone, we should expect to see the Number 8 detonator produce a much stronger pressure pulse than a Number 6 detonator, as the Number 8 contains 0.35 g of A.S.A mixture and 0.25 g of base charge.

Table 36.1, below, showing the first detonators specifications for only the base charge (mercury fulminate), was the first classification for blasting cups according the blasting strength, and still used today. In general, a Number 8 classic detonator can be described as a metal shell that contains a secondary base charge (typically PETN, RDX, HMX) which is capped with a primary charge (typically mercury fulminate, lead azide, or silver fulminate), positioned on one end of the shell.

Table 36.1 Different amount of lead azide explosives to characterize the strength of detonator

Detonator standard no.	1	2	3	4	5	6	7	8	9	10
Mercury fulminate (g)	0.3	0.4	0.54	0.65	0.8	1	1.5	2	2.5	3

Adjacent to this, but a sufficient distance away, is a fuse head, a low donor explosive, embedded with a bridge wire, which connects two leg wires, thus forming a means of electrical ignition. If a firing current is applied to the leg wires, the bridge wire becomes incandescent, and the fuse head is initiated. This initiation has enough force to initiate the very sensitive primary charge, and subsequently the secondary charge.

The Number 6 fluid-desensitized detonator is quite similar to the Number 8 detonator. However, as it is used in the oil and gas industry for perforating guns, it operates in a very specific manner. Because the detonator is often exposed to a wet environment, RDX, which is water-resistant, is the strictly used secondary explosive. To prevent industrial accidents and expenses from the accidental leakage of water into a perforator, the Number 6 fluid desensitized detonator is manufactured with two holes between the fuse head and the primary and secondary explosive cap. Should any liquid fill the space between fuse head and the charges, then the initiation of the fuse head charge should not have enough force to initiate the explosives (at a sufficient amount of pressure due to depth in the liquid).

36.3.2 Shadowgraph Technique

Shadowgraphy was invented as a visualization method in 1672, where the Sun was used to cast a shadow on a white surface. "Modern" shadowgraphy differs from this more rustic method in its use of specialized screens, light sources, and high-speed imaging systems.

The direct shadowgraph technique is simple and robust, requiring only a light source, a camera, and a screen on which to cast a shadow. In general, a light source is placed at an optimum distance, L, from the screen, and from refractive disturbances in the Schlieren object, a shadow is projected at a certain height, h, onto the screen. Edgerton retro-reflective shadowgraphy, specifically, requires the use of a retro-reflective screen and a rod mirror, which is aligned with the camera axis, illuminating the retro-reflective screen with a significant amount of light, and thus providing a high quality image. This technique is useful for the characterization of explosive energy, as it is able to measure blast wave parameters in the air, while also "de-emphasizing other, less abrupt flow features" [1]. According to United Nations' specifications, a detonator must have a reaction within 25 μs, and must deliver a detonation velocity of 8000 m/s—undoubtedly, the Edgerton retro-reflective shadowgraph technique would be very useful for manufacturers or explosive users who are looking to control and understand the specifications of their product or purchase. In order to explore the shockwaves generated by laboratory-scale explosions from the two categories of detonator, a combination of modern high-speed videography and Edgerton shadowgraph was used.

36.3.2.1 Retro-Reflective Shadowgraphy Experimental Methods

The experimental setup used during the experiments is shown in the image below. High speed camera, collimated strop lighting system, lens with rod mirror, and a retro-reflective screen are required instrumentation for the execution of Edgerton shadowgraph.

Our Edgerton shadowgraph setup, shown in Fig. 36.2, is elegant in its simplicity, robustness, and ease of use. The system is most appealing for small-scale blast chamber applications, as it consists only of a retro-reflective screen, a rod mirror, a high-speed imaging system, and a light source.

The retro-reflective screen is made of 3 M Scotchlite TM 7610, a high gain, industrial grade, exposed-lens, plastic-based material pre-coated with a pressure-sensitive adhesive. An industrial supplier can provide screens made of this material. Our currently used screen is a 2.4 m^2 and costs about 4000 USD.
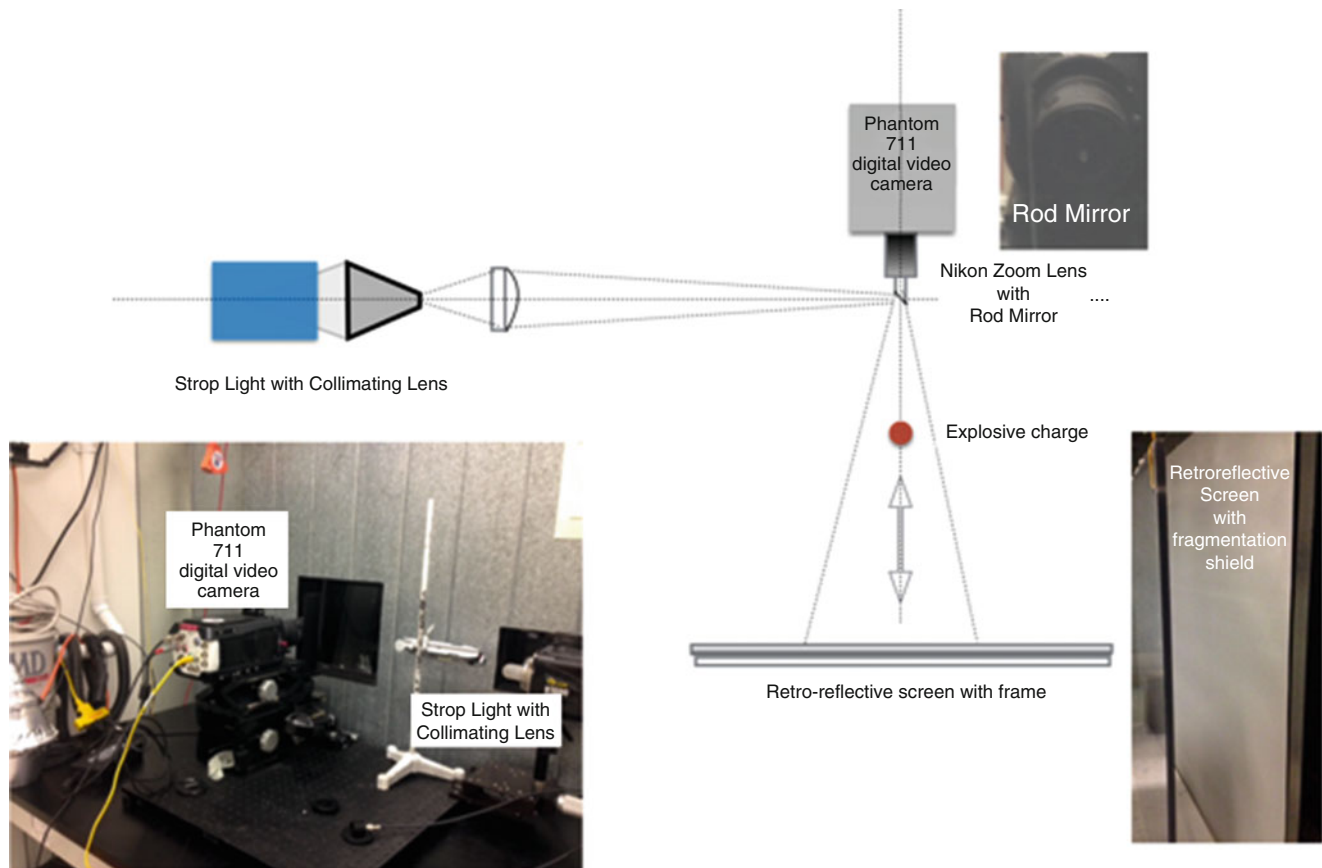
Fig. 36.2 Edgerton retro-reflective shadowgraph system, *top view*

36.3.3 Pressure Gauges

Two PCB Piezotronics model 137A23 pressure gauges are placed in the camera plane for the validation of the shock wave incident pressure and positive time duration. Both sensors were mounted in a steel rod pointing in an axial direction to the detonator. Standoff distances from the energy source varied from 325 to 430 mm. At that range, and considering the explosive yield within the detonator, the sensitivity of the pressure sensors seems reasonable (100 mV/psi). The diaphragm was insulated using common black vinyl electrical tape to minimize possible signals generated by flash temperatures due to the passing of the shock front. Additionally, the bodies of the gauges were isolated from the ground by placing common black vinyl electrical tape in the contact surface with the steel rod.

The two pressure sensors were connected by coaxial cable to a PCB sensor signal conditioner model 482C05. Both outputs were also connected to channel 1 and channel 2 of a Tektronix DP 3014 Oscilloscope where the signal provided by each gauge was recorded. Triggering was implemented from the firing machine and a signal differentiator which provides with a 2 V output to the lighting system, high-speed camera, and Oscilloscope.

36.4 Results and Discussion

36.4.1 Camera Results

The events were captured by using a Phantom High Speed Camera v.711. Resolution of the image was set to 912 × 848 with a sample rate of 9100 fps, and 0.294 us exposure (Fig. 36.3). Frame sequences for Number 6 and Number 8 detonators are shown in Fig. 36.4. The shock wave front traveling outwards has been highlighted with a white contour. As it is shown, the initial blast wave presents a sharp elliptical shape due to charge geometry. As the shock expands, the spatial divergence and

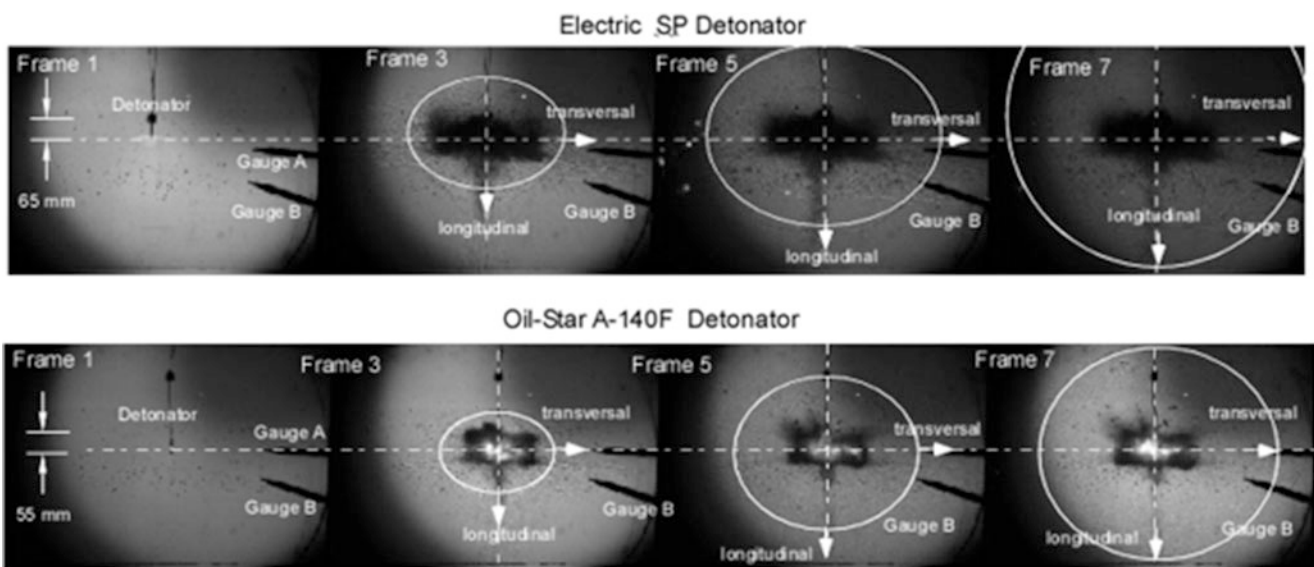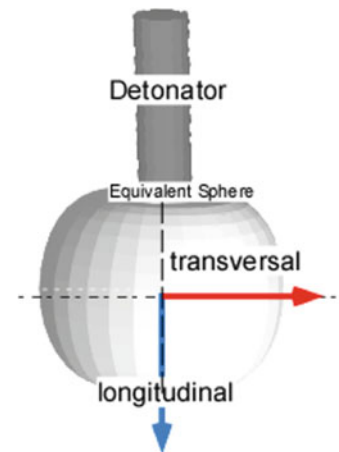**Fig. 36.3** Axis position with respect to the detonator's body and base charge's location

Fig. 36.4 Frame sequence for electric detonator #8 (*top*) and #6 (*bottom*)

medium attenuation cause a gradual change in shape ending as a spherical shock wave (frame 7). Thirty Number 6 electric detonators and 50 Number 8 detonators were tested by the use of this technique. This technical paper only reports the results obtained for one test per detonator as demonstration of the technique.

The ellipsoidal shock generated by the explosive charge produces higher shock velocity values in the transversal plane of the charge versus those recorded in the longitudinal axis. For this reason, the explosive energy delivered by the detonator will be different for each direction with respect its body. This difference will decrease as one moves away from the center of the explosion as it will show in the following sections. The next diagram illustrate the two dimensional position of each axis with respect to the body of the detonator.

Additionally, the symmetry axis of a cylindrical detonator corresponds with its longitudinal axis and therefore seems reasonable to assume that the shock expansion in the normal plane of the camera view will be equal to the one recorded along the transversal direction. In order to accurately measure this third dimension, a second high speed camera would be required.

36.4.2 Gauge Measurements

For the Number 8 electric detonator, gauges A and B were placed in the plane of the camera and at a distance of 325 and 345 mm from the center of the explosion. Gauge A was place approximately aligned with the transversal axis of the detonator ($-4°$ from the transversal axis) and Gauge B at $-20°$ from the transversal axis.

A triggering delay was measured from the actual triggering to the instant of initiation in the detonator. This triggering delay was calculated using the frames of the camera because of its almost instant response and the very short length of the cables employed. From t_0 to the actual instant of the detonation, a triggering delay of 400 us was measured and subtracted in the oscilloscope triggering signal during the experiment by using a delay generator. The sample length was 10,000 with a sample rate set to 500 KS/s. The next two Figures show the signal recorded from Gauges A and B from the initiation of the detonation. P_s represents peak incident overpressure, t_a is the time of arrival of the shock, and t_d is the measured positive phase duration.

As it is shown in Figs. 36.5 and 36.6, the gauge located in the transversal axis recorded a higher peak incident overpressure. This fact corresponds with the images obtained by the shadowgraph where the higher shock velocities are produced throughout this axis.

The gauge lectures are also noised during a certain period of time before the shock arrival. By observing the images provided by the high speed camera, the experimentalist can deduce that the peaks generated are due to the Mach waves produced by the primary fragments from the detonator aluminum casing during their supersonic flight.
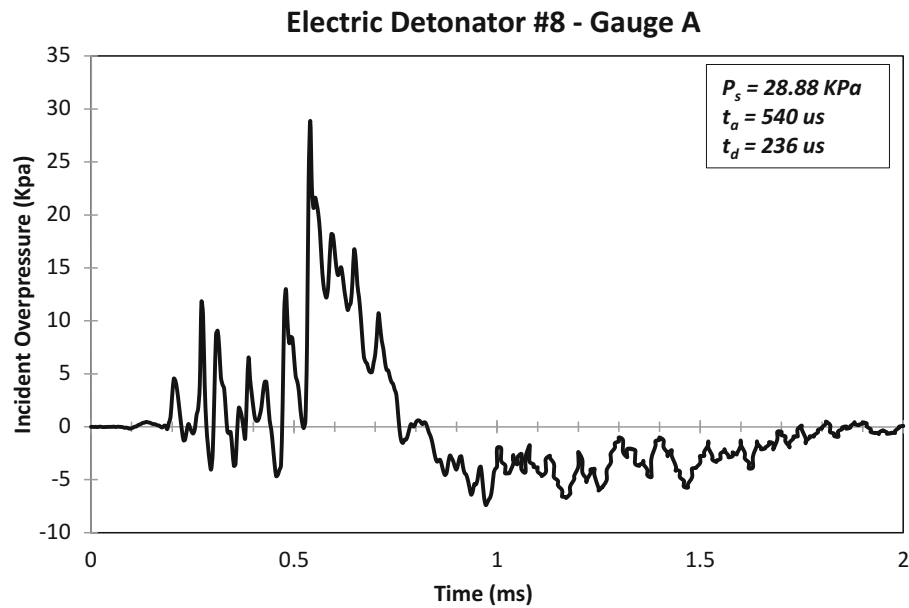

Fig. 36.5 Incident overpressure versus time. Detonator #8 Gauge A. Standoff: 325 mm. Angle: $-4°$
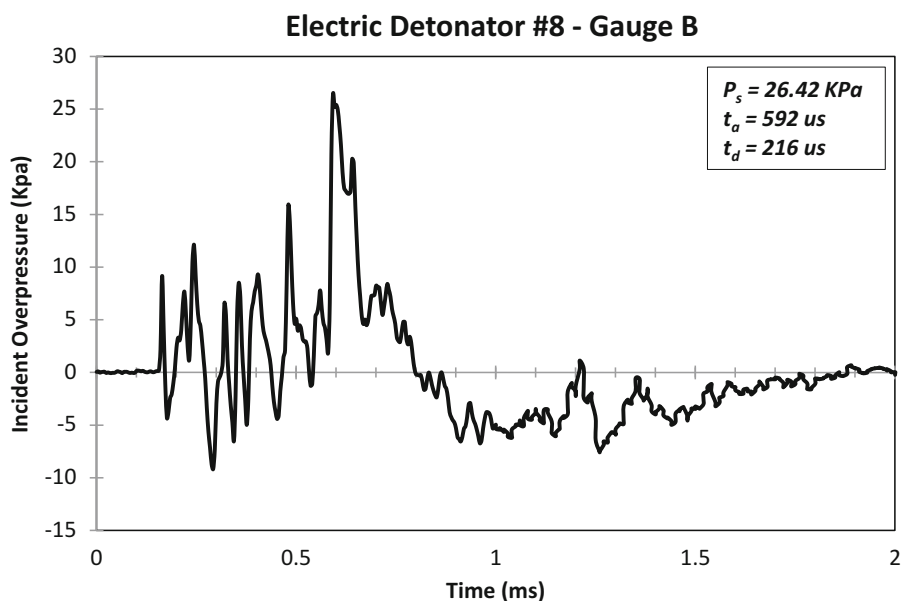

Fig. 36.6 Incident overpressure versus time. Detonator #6. Standoff: 345 mm. Angle: $-20°$

A similar analysis is performed for the number 6 electric detonator. Gauges A and B were placed in the plane of the camera and at a distance of 410 and 430 mm from the center of the explosion. Gauge A was place approximately aligned with the transversal axis of the detonator (+2° from the transversal axis) and Gauge B at −15° from the transversal axis.

The same triggering delay of 400 us was measured and subtracted in the oscilloscope triggering signal during the experiment by using a delay generator. In this case the sample length was 100,000 with a sample rate set to 5 MS/s. The next two Figures show the signal recorded from Gauges A and B from the initiation of the detonation. P_s represents peak incident overpressure, t_a is the time of arrival of the shock, and t_d is the measured positive phase duration.

As it is shown in Figs. 36.7 and 36.8, the gauge located in the transversal axis recorded in this case a lower value of overpressure. One possible explanation is the unintentional error induced in the pencil gauge tilting producing a lower value than expected because of the oblique shock interaction. For this detonator, the gauge lectures are also noised during a certain
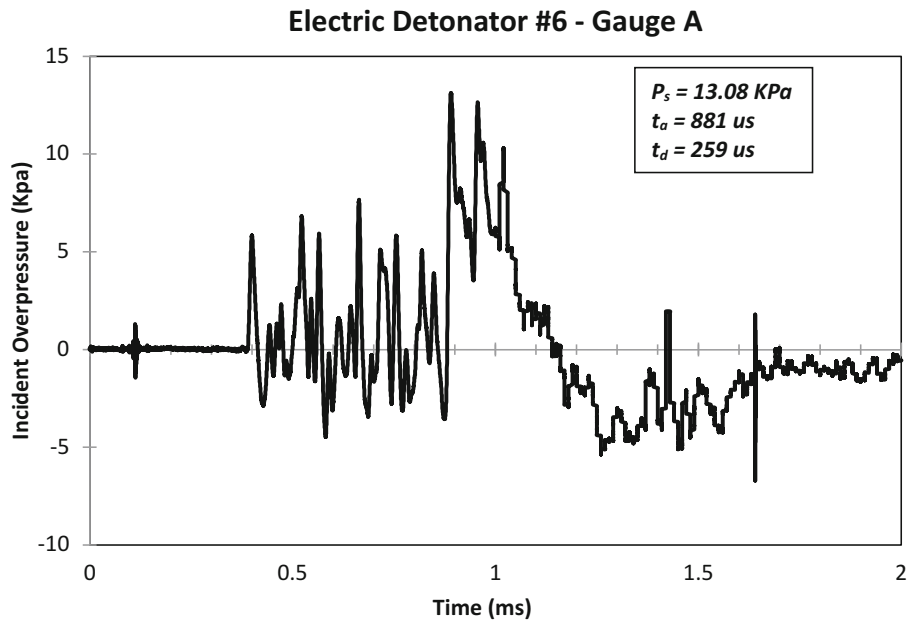

Fig. 36.7   Incident overpressure versus time. Detonator #6 Gauge A. Standoff: 410 mm. Angle: +2°
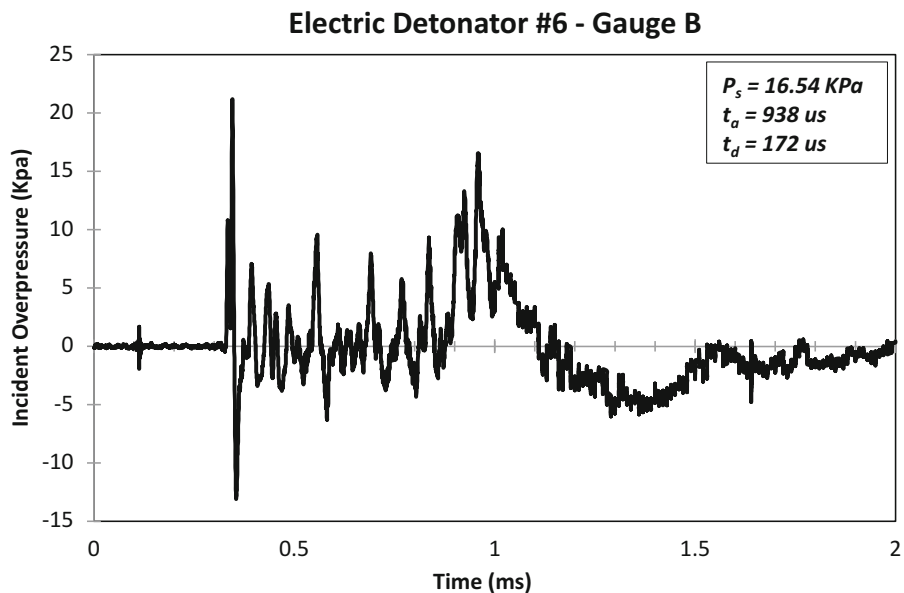

Fig. 36.8   Incident overpressure versus time. Detonator #6 Gauge A. Standoff: 430 mm. Angle: −15°

period of time before the shock arrival due to the Mach waves generated by the supersonic fragments initially traveling at a higher speed than the blast shock front.

Two verifications are recommended in order to check a good data collection while using pressure sensors. First, a rising time less than 10 us from the zero line to 2/3 of the maximum incident overpressure pulse is recommended in order to validate a proper sensor's response. Second, adequate pressure sensor sensitivity can be confirmed by a signal to noise ratio less than 10. In other words, when dividing the maximum peak overpressure (voltage) recorded by the peak to peak noise value, the result must be always less than 10. A lower ratio value would be symptom of too low gauge sensitivity for the desired experiment. In this case, for each of the four measurements performed by the pressure gauges, these two conditions are ample satisfied.

Relating to data interpretation, two other considerations are recommended to take into account. The maximum value recorded by the oscilloscope will not exactly match with the peak incident overpressure because of the resolution of the oscilloscope. Oscilloscopes with low resolution (low number of bits) will approximate to a larger voltage level during the measurements. For our purposes, we can consider the difference negligible. If a higher accuracy is desired, a good method for obtaining a closer value to the real peak overpressure is by the fitting of the waveform. A second consideration in data analysis is that pressure sensors tend to keep a higher temperature after the passing of the positive blast pulse, ending with larger "P zero" values than in the real experiment. This fact might imply relatively low impulse measurements.

36.4.3 Air Shock Properties and Energy Fluence

Three different tests are reported in this technical paper. Due to camera resolution and sample rate, 8–9 points are recorded from the instant of the detonation, each of them corresponding with a camera frame. From the images, the shock wave expansion in each direction within a 2D plane is successfully measured. For the purpose of this document, two directions are recorded corresponding with the longitudinal and transversal axis of the detonator. The same behavior observed for the transversal direction is assumed for the third dimension due to charge symmetry. Therefore two measurements are implemented from the high-speed images provided by the camera: shock wave expansion rate in the transversal direction and shock wave expansion rate in the longitudinal direction. Additionally, by assuming than the volume of air being compressed by the ellipsoidal shock wave is the same than the one compressed by an equivalent sphere of radius R, one can provide an estimation of the expansion rate for an equivalent spherical shock wave. For explosive yield determination, this assumption seems convenient since most of the data from high explosives is expressed for spherical blast waves. It must be remarked than this initial ellipsoidal blast wave will end up adopting a spherical shape due to geometrical expansion and medium attenuation.

From the camera frames, the shock wave distance versus time from the center of the charge is collected for the two models of electric detonators. By applying least-squares regression, coefficients A, B, C and **D** are determined for the use of the Dewey's Equation. The coefficients are determined six different times, one for each shock wave propagation direction (transversal, longitudinal, and spherical equivalent) and per detonator (Number #8 and Number #6). The next table summarizes the calculated parameters values along with the coefficient of determination per curve (Table 36.2).

The next two figures represent the shock wave expansion rates (data points and fitting curves) for Number 6 and Number 8 detonators in transversal and longitudinal directions (Figs. 36.9 and 36.10). Additionally, the expansion rate of an equivalent spherical wave is plotted.

Although an empirical correlation, Eq. (36.1) does satisfy the appropriate physical condition as the time tends to infinity, ensuring that the shock wave velocity approaches the atmospheric speed of the sound [16]. Next, by simply deriving Eq. (36.1), an expression for the shock velocity versus time is obtained. From there, Mach number versus time can be

Table 36.2 Curve fitting coefficients for Dewey's equation

Detonator	Direction	A	B	C	D	R^2 (%)
#6	Transversal	3.3606	1	28.8071	−20.8846	99.90
	Longitudinal	3.4813	1	38.9471	−62.4522	99.99
	Spherical equ.	3.4017	1	34.0745	−39.4129	99.95
#8	Transversal	3.5594	1	25.4924	2.0478	99.95
	Longitudinal	3.737	1	43.593	−56.1228	99.88
	Spherical equ.	3.6229	1	33.0109	−21.0115	99.99

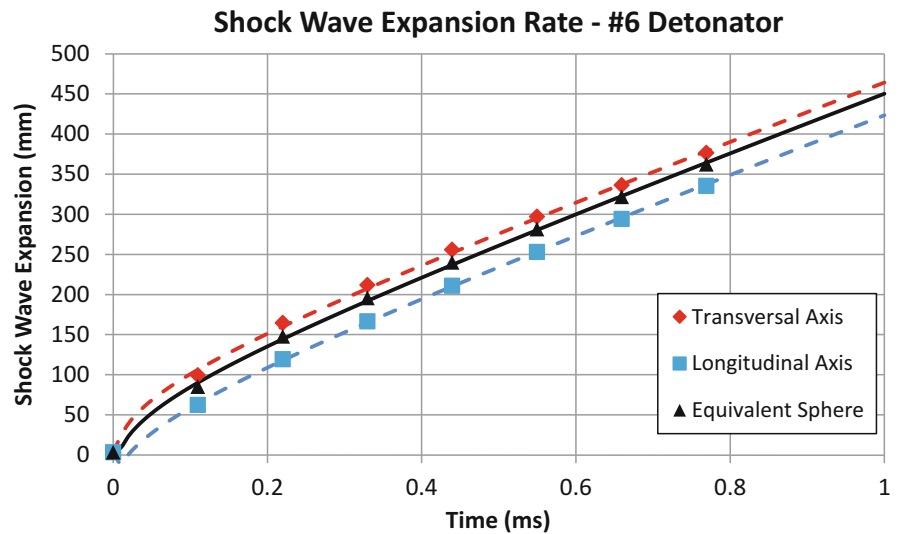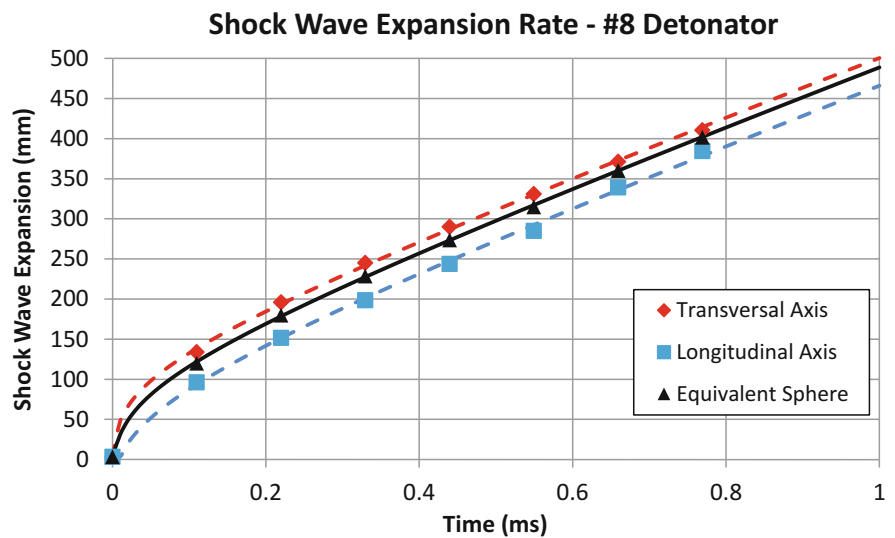**Fig. 36.9** Shock wave expansion rate for number #6 electric detonator

Fig. 36.10 Shock wave expansion rate for number #8 electric detonator

determined, and consequently the blast incident overpressure by using Eq. (36.3). The following figures represent the value of the peak incident overpressure versus distance from the center of the explosion in logarithmic scale for detonators number 6 and 8 (Figs. 36.11 and 36.12). Such graphs can be used for the calculation of the explosive yield. In addition, Edgerton shadowgraph allows calculating the blast in a specific direction from the charge.

In order to validate the level of accuracy provided by the Edgerton shadowgraph method for detonator characterization, the values of overpressure recorded by optical techniques and from the pressure gauges are compared. This information is summarized in the following table where the percent difference between each pair of values is calculated:

Table 36.3 shows good correlation between the experimental pressure recorded from the retro-reflective shadowgraph and the pressure gauges. Pressure A recorded an unusual low value of blast overpressure during the experiment with the detonator number #6. One possible explanation is the error in the pencil orientation producing a lower value than expected because of the oblique shock interaction.

By comparing the values of peak incident overpressure calculated at different distance from each detonator, one can estimate the percent difference between number 6 and number 8 detonators. The next table shows a summary of the peak incident overpressure generated by each detonator at 200 and 400 mm from the center of the explosion and for each axis (Table 36.4).

Finally, the positive phase duration is measured and an approximation of the energy fluence from the detonator to the ambient air is performed. Calculation of the positive phase duration from the shock Mach number versus distance was initially proposed by Kinney and Graham [17] and successfully reported by other researchers [15, 16, 18]. From the instant

Fig. 36.11 Incident
Overpressure vs Distance for
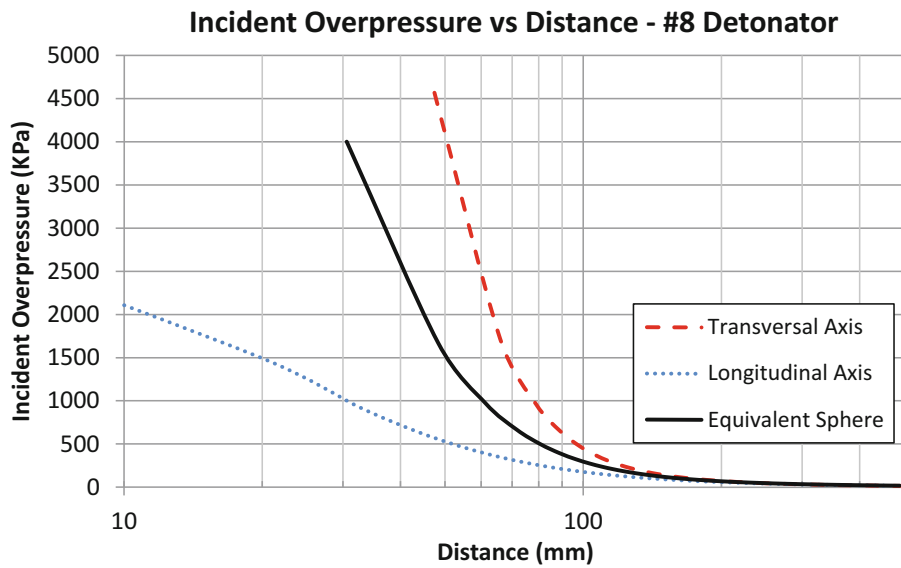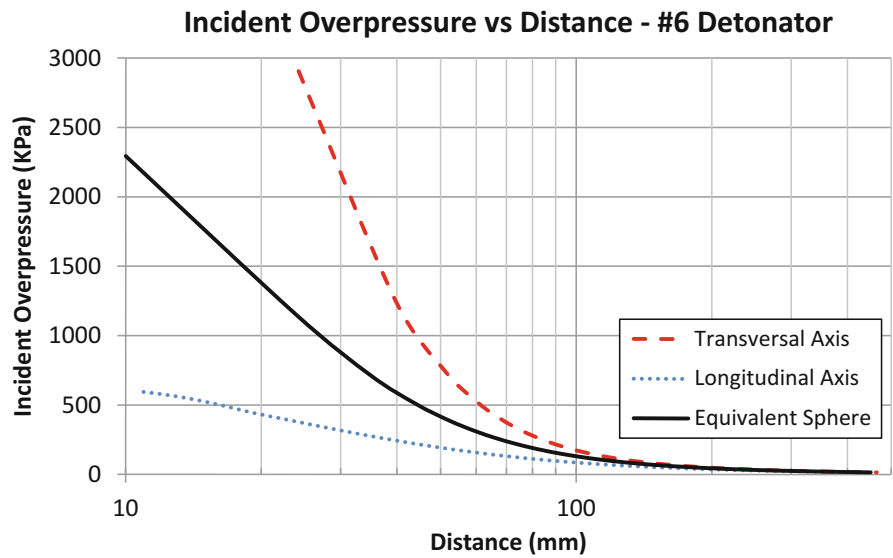number #6 electric detonator

Incident Overpressure vs Distance - #6 Detonator

Fig. 36.12 Incident Overpressure vs Distance for number #8 electric detonator

Table 36.3 Blast overpressure gauge readings and values calculated from shadowgraph

Detonator	Direction	Gauge reading (KPa)	Shadowgraph (KPa)	%Difference
#8	Gauge A	28.88	28.84	0.14 %
	Gauge B	26.42	26.26	0.61 %
#6	Gauge A	13.08	16.63	23.89 %
	Gauge B	16.54	15.70	5.21 %

Table 36.4 Blast overpressure comparison for detonators number 6 and number 8

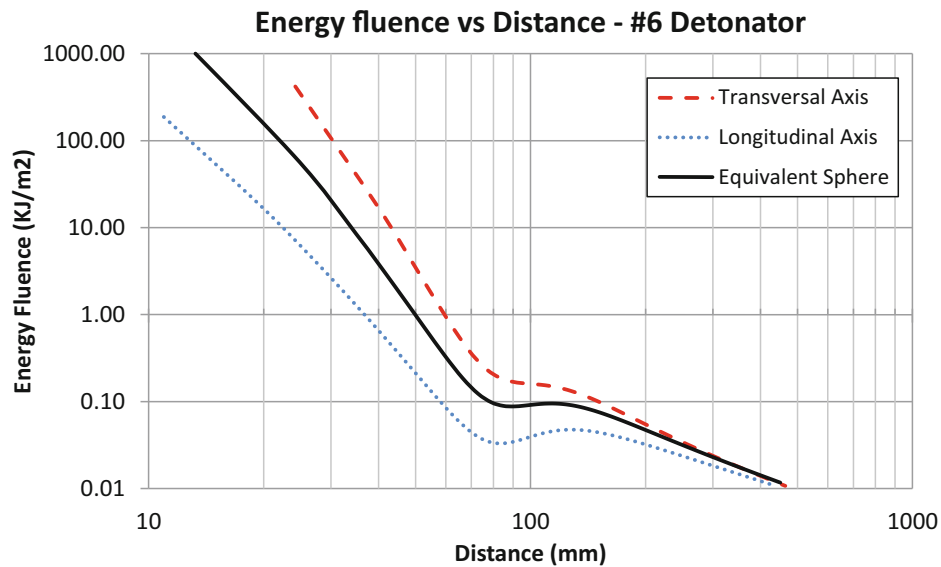| Distance	Direction	#6 Detonator (KPa)	#8 Detonator (KPa)	%Difference
200 mm	Transversal	47.80	72.02	40.43 %
	Longitudinal	36.63	59.65	47.81 %
400 mm	Transversal	17.33	20.98	19.06 %
	Longitudinal	16.21	22.86	34.04 %

Fig. 36.13 Energy fluence vs. distance in air for electric #6 detonator
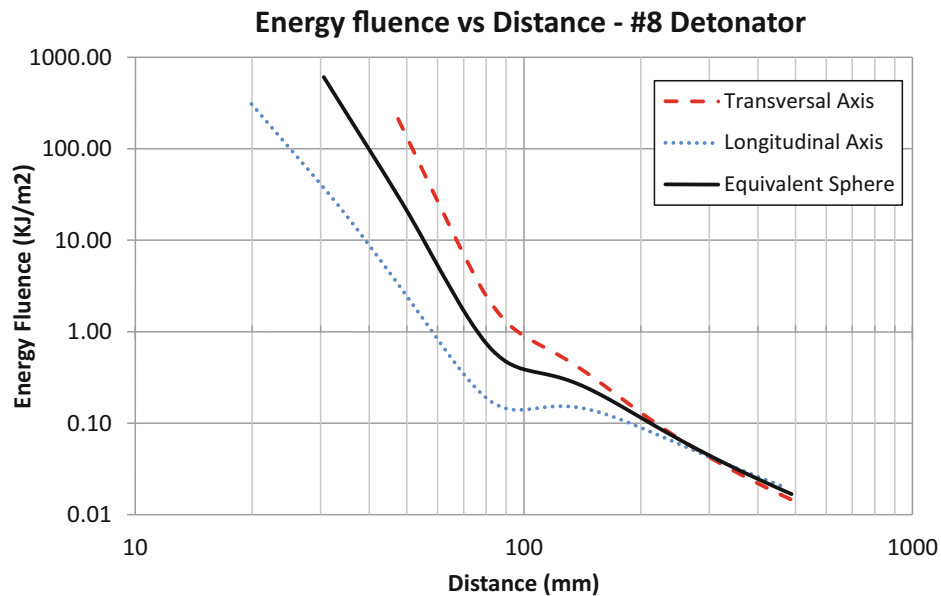

Fig. 36.14 Energy fluence vs. distance in air for electric #8 detonator

value of the blast incident overpressure, the positive time duration, and the acoustic impedance of the air, a value of the energy (KJ) per unit area (m^2) can be obtained for different distances from the detonator by using the simplified expression in Eq. (36.4). The results obtained for Number 6 and Number 8 electric detonators are presented in the following graphs with horizontal and vertical logarithmic scales:

As shown in Figs. 36.13 and 36.14, the energy fluence has a decreasing tendency with the distance for both detonators. Even though, the duration of the positive shock increases with the distance from the explosion as it propagates through a medium, the energy fluence is also function of the square pressure which decays exponentially. Higher values of energy fluence are also observed for the number 8 detonator due to a higher net explosive content. For both experiments, the value of the acoustic impedance was obtained from the air density (1.2 kg/m^3) and the speed of sound (343.21 m/s).

Each high explosive was found to have a unique range of energy fluence above which prompt detonation was always obtained, and below it was not. The average of this range is called the "critical energy fluence" and it represents the amount of energy per unit area (KJ/m^2) that the explosive needs in order to be initiated by shock. Reference values for different types

of explosives material can be found in the literature [10]. The characterization of a detonator is based on its ability as initiation system and therefore a measure of the shock energy per unit area seems appropriate. For the purpose of this paper, only the energy from the chemical reaction is accounted. Primary fragmentation from the casing also carries a certain amount of kinetic energy that may take part in the initiation of a firing sequence. Additionally, it must be recalled that the term energy fluence is a measure of the energy transferred and therefore it is dependent not only on the energy source but also on the material o medium receiver. This receiver is characterized by its acoustic impedance. Therefore by the use of the Hugoniot curves for both, initiator and acceptor; the amount of energy transferred can be predicted. Future work should aim to the characterization of such detonators in alternative mediums.

36.5 Conclusion

The retro-reflective shadowgraph technique for measuring shock from high explosives has proven to be a fast and accurate tool for charactering the strength of detonators and blast waves in general. This paper provides a full description of the methodology for and validation for the study of explosive energy from standard Number 6 and Number 8 detonators. By measuring the shock wave expansion rate from each initiation system, a complete characterization of the blast is performed with a high level of accuracy. Shock wave velocity, incident shock Mach number, peak incident overpressure, and time duration are successfully calculated versus distance and time scales. Optical measurements are additionally validated with piezoelectric pressure gauges that recorded overpressure vs. time histories at specific locations.

Because of their geometry, standard detonators show an initial ellipsoidal shock expansion that degenerates in a final spherical wave. This non-uniform shape of the shock derives in different blast overpressure values in the different directions. For this reason, transversal and longitudinal directions from the body detonator are studied along with an equivalent spherical blast for convenience purposes. Finally, an approximation of the energy fluence from each detonator in ambient air is performed. The results can be extrapolated to other fluids and materials by using the Hugoniot curves and therefore the shock initiation performance of each detonator can be established under different conditions.

References

1. Edgerton, H.E.: Shockwave photography of large subjects in daylight. Rev. Sci. Instrum. **29**(2), 171–172 (1958)
2. Settles, G.S., Grumstrup, T.P., Miller, J.D., Hargather, M.J., Dodson, L.J., Gatto, J.A.: Full-scale high-speed 'Edgerton' retro-reflective shadowgraphy of explosions and gunshots. In: Proceedings 5th Pacific Symposium on Flow Visualisation and Image Processing, PSFVIP5, paper 251 (Australia, 27-29 September 2005)
3. Biele, J.K.: Point-source spark shadowgraphy at the historic birthplace of supersonic transportation—a historical note. Shock Waves **13**(3), 167–177 (2003)
4. Parthasarathy, S.P., Cho, Y.I., Back, L.H.: Wide-field shadowgraphy of tip vortices from a helicopter rotor. AIAA J. **25**(1), 64–70 (1987)
5. Settles, G.S.: High-speed imaging of shock waves, explosions and gunshots. Am. Sci. **94**(1), 22–31 (2006)
6. Hargather, M.J., Settles, G.S., Gatto, J.A., Grumstrup, T.P., Miller, J. D.: Full-scale optical experiments on the explosive failure of a ULD-3 air cargo container. In: Proceedings of the 4th International Aviation Security Technology Symposium (Washington DC, Nov. 2006)
7. Virtual Backgrounds, 101 Uhland Road, Ste. 106, San Marcos, TX 78666 (USA), 1-800-831-0474. www.virtualbackgrounds.net
8. Hargather, M.J., Settles, G.S., Gatto, J.A.: Gram-range explosive blast scaling and associated materials response. In: Proceedings ISSW26, paper 3131 (July 2007)
9. Settles, G.S.: Schlieren and Shadowgraph Techniques: Visualizing Phenomena in Transparent Media. Springer, Berlin (2001). ISBN 978-3-642-63034-7
10. Cooper, P.W.: Explosives Engineering. Wiley-VCH, New York (1966). ISBN 0-471-18636-8
11. Deal, W.E.: Shock hugoniot of air. J. Appl. Phys. **28**(7), 782–784 (1957)
12. Biss, M.M.: Energetic material detonation characterization: a laboratory-scale approach. Propell. Explos.Pyrotech. **38**, 477–485 (2013)
13. Esparza, E.D. Spherical equivalency of cylindrical charges in free-air. Southwest Research Institute, 25th Department of Defense Explosives Safety Seminar (1992)
14. Dewey, J.M.: Air velocity in blast waves from TNT explosions. R. Soc. Lond. Proc. Ser. A **279**, 366–385 (1964)
15. Hargather, M.J.: Scaling, characterization, and application of gram-range explosive charges to blast testing of materials. Pennsylvania State University (2008)

16. Biss, M.M.: Characterization of blast from laboratory-scale composite explosive charges. Pennsylvania State University (2009)
17. Kinney, G.F., Graham, K.J.: Explosive Shocks in Air, 2nd edn. Springer, Berlin (1985)
18. Taylor, G.I.: The formation of a blast wave by a very intense explosion. 1. Theoretical discussion. Proc. R. Soc. Lond. Ser. A Math. Phys. Sci. **201**(1065), 159–174 (1950)

Chapter 37
Assessment of Fringe Pattern Normalisation for Twelve Fringe Photoelasticity

Phani Madhavi Ch, Vivek Ramakrishnan, and Ramesh Krishnamurthi

Abstract Single colour image based photoelastic techniques have gained importance in the recent years. In twelve fringe photoelasticity (TFP) technique, the whole field fringe order (N) data is obtained by comparing RGB intensities of all the pixels in the image with that in the calibration table. This technique is suitable for problems where multiple acquisitions of the model are difficult. Initially, the methods were proposed to demodulate a maximum fringe order of 3 since the colours tend to merge after this. There have been efforts to push this limit by using advanced imaging hardware and fluorescent light sources. Recent research in this field explored the use of fringe pattern normalisation in conjunction with the use of theoretically generated calibration table for isochromatics modulation. However, the method was demonstrated using models having almost uniform fringe gradients. This work assesses the performance of fringe pattern normalisation for twelve fringe photoelasticity in problems having different fringe gradients. Studies are carried out in the benchmark problem of a circular disc under diametral compression. The isochromatic results obtained are compared with the corresponding values obtained analytically.

Keywords Twelve fringe photoelasticity • Fringe pattern normalisation • Image processing • RGB photoelasticity • Isochromatics

37.1   Introduction

Photoelasticity is a whole field technique which gives direct information about principal stress difference and their orientations. Over the years, several digital methods have been proposed for whole field determination of isochromatic data [1]. Among these, Twelve Fringe Photoelasticity (TFP) has gained importance as they require only a single colour image for whole field isochromatics demodulation [2–4]. In this technique, the fringe orders are estimated based on the colour components in the isochromatic image. The modelling of the intensity variation of the output image depends on many parameters such as transmission response of the components in the polariscope, spectral composition of the light source, quarter-wave plate error, dispersion of the stress-optic coefficient and the spectral response of the camera [2]. Since accurate consideration of all these parameters is difficult, in practise, a method based on calibration table and color matching is followed [1–4]. The technique is useful especially in problems involving time-varying phenomena and industrial problems where one does not have the luxury to acquire multiple images.

Determination of isochromatic data using TFP is performed in three steps i.e., calibration, fringe order estimation by colour difference formula and its refinement by invoking fringe order continuity. The total fringe order at a point of interest in the model is obtained by comparing the colour components at the point of interest with that in the calibration table. Several investigators [5–7] identified that noise present in the results obtained by color difference formula could be removed by taking into account the fringe order of the neighbouring resolved pixel. Quiroga et al. [5] proposed a window search method to refine the fringe order data and demonstrated it experimentally along a line in a loaded C-shaped specimen. Madhu and Ramesh [6] brought out that noise in TFP is due to the repetition of colours and proposed a noise immune colour difference formula which ensures a smooth variation of fringe orders. This approach was christened as Refined Three Fringe Photoelasticity (RTFP). Ajovalasit et al. [7] improved the work of Quiroga et al. [5] and arrived at a criterion for selecting the size of the window in the window search method. The scanning scheme adopted should be such that it is able to refine the entire domain of models having any complex shapes. In 2013, Kale and Ramesh [8] proposed a scanning scheme, called advancing front scanning in conjunction with multiple seed points to solve models of complex geometry.

P.M. Ch (✉) • V. Ramakrishnan • R. Krishnamurthi

Department of Applied Mechanics, Indian Institute of Technology Madras, Chennai 600 036, India

e-mail: am14m010@smail.iitm.ac.in

Ideally, calibration and application experiments should follow the same experimental conditions e.g. polariscope set up, ambient illumination and the camera settings in order to get accurate results. However in practice, there can be variations in the experimental conditions which can lead to false estimation of fringe orders. To eliminate this, the concept of colour adaptation was first introduced by Madhu and Ramesh [9] who proposed a single-point colour adaptation scheme using no-load bright field images of the calibration and application specimens. Later, Neethi Simon and Ramesh [10] proposed a two-point colour adaptation scheme, which only needs the isochromatic image of the model for adaptation.

The calibration table is generated using a beam under four point bending [1, 6], C-shaped specimen under tension [7] or an eccentrically loaded tensile specimen [11]. In 2015, Swain et al. [12] have proposed the use of theoretically generated calibration table which eliminates the need for separate calibration experiments provided the material stress fringe values (F_σ) are accurately known. The use of theoretically generated calibration table in conjunction with the normalisation of the isochromatic images will minimise the influence of experimental conditions as brought out in [13].

37.2 Normalisation of Isochromatic Image

Normalisation in image processing is a process that alters the range of pixel intensity values. Normalization transforms an image with intensity values in the range (*Min*, *Max*), into a new image with intensity values in the range (*newMin*, *newMax*). Several normalisation techniques have been proposed over the years. Fringe pattern normalisation generally involves two steps—background suppression and modulation normalisation [isotropic ndimension]. In 2001, Larkin et al. [14] proposed a method for fringe pattern normalisation using a two-dimensional quadrature which has connections with the Riesz transform in harmonic analysis. In the same year, Quiroga et al. [15] proposed an algorithm for fringe pattern normalization which uses two orthogonal band pass filters. The efficiency of the method is reduced in images with very low modulation regions or stepped contrast changes [16]. Later, Quiroga et al. [17] proposed another method of normalization using n-dimensional quadrature transform. However, the method needs pre-processing the fringe pattern to remove the bias term [16]. Guerrero et al. [18] proposed an iterative procedure based on the construction of an adaptive filter as a linear combination of isotropic bandpass filters. Ochoa and Silva-Moreno [19] introduced a method to formulate cosine profile of the fringe pattern which is based on the use of directional derivatives.

Swain et al. [13] have used the normalisation technique proposed in [14] for normalisation of the isochromatic fringe image TFP analysis. Following this work, in this paper, the normalisation scheme involving a high band pass filter for background suppression followed by the use of Hilbert transform is adopted. The calibration table is theoretically generated using the material stress fringe (F_σ) values corresponding to red, green and blue channels respectively. Though the method of normalisation has been successfully applied, an assessment of the performance of the method in relation to the fringe gradients in the model is lacking in the literature. This paper investigates the suitability of the method to solve problems having different fringe gradients.

37.3 Isochromatic Demodulation by Image Normalisation

Consider a problem of a circular disc made up of epoxy subjected to diametral compression (Load = 492 N, Diameter = 60 mm). The isochromatic data is obtained by TFP using a theoretically generated table in conjunction with image normalisation. The material stress fringe value of the model is measured as 13.52, 12.10 and 9.66 N/mm/fringe for red ($\lambda = 619$ nm), green ($\lambda = 546$ nm) and blue ($\lambda = 430$ nm) channels respectively. The theoretical generation of the calibration table is performed as detailed in [12]. The isochromatic image is first filtered to remove the low frequency background noise. A radius value (R) of 3 pixels is used for the high band pass filter. For comparison of the fringe order results, analytical obtained values are considered.

Figure 37.1 shows the plot showing the variation of the fringe orders along the horizontal diameter of the disc. It can be seen that the use of theoretical calibration approach yield results that closely follow the analytical values. The mean error in the fringe order was found to be less than 0.06. Hence, the simulated calibration table in conjunction with image normalisation is found to work well for this case. The subsequent sections discuss the performance of the method applied to problems involving high and low fringe gradient zones.

Fig. 37.1 Variation of fringe order values along the horizontal diameter of a disc under diametral compression (Load = 492 N) obtained experimentally using the theoretically generated table. Corresponding values obtained analytically are taken as the reference for comparison
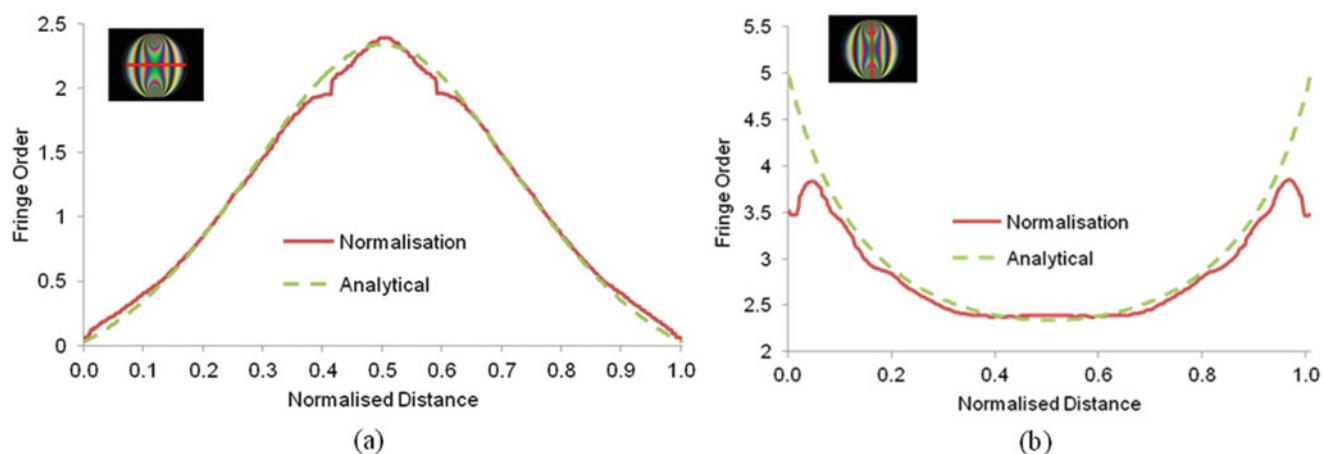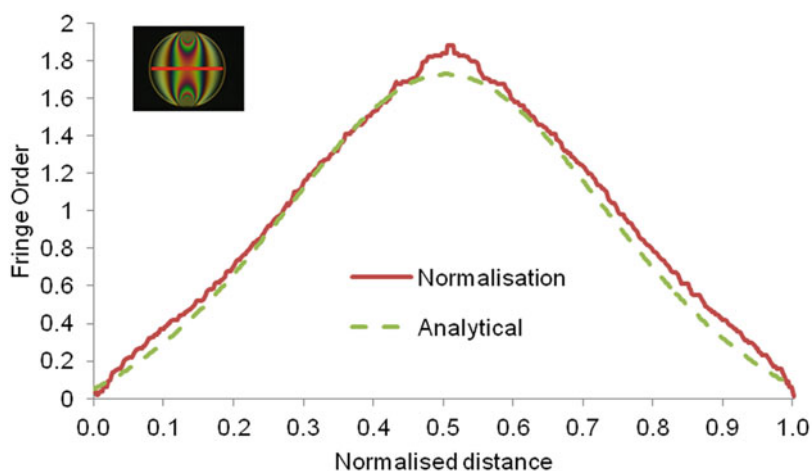

Fig. 37.2 Variation of fringe order values in a circular disc under diametral compression subjected to a higher load of 574 N obtained using normalisation along the (**a**) horizontal diameter, (**b**) vertical diameter. Values obtained analytically are taken as reference for comparison

37.3.1 High Fringe Gradient Zones

Next another circular disc specimen subjected to a higher load of 574 N is considered. The material stress fringe values of this disc are 12.01, 10.42 and 9.00 N/mm/fringe for red, green and blue channels respectively. The isochromatic image is normalised by the similar procedure adopted in the previous problem using $R = 3$. A line along the horizontal diameter gives consistent results with the analytical values (Fig. 37.2a) and the mean errors are found to be less than 0.04. When the fringe order values along the vertical diameter were analysed, it is found that isochromatics demodulation only till a fringe order of 3.7 is possible. However, the maximum perceivable fringe order in the model is close to 5 near the loading points of the disc. Hence, the method adopted is unable to correctly demodulate near the high fringe gradient zones.

It is found that the radius (R) of the high pass filter used for background suppression during normalisation affects the isochromatics demodulation in the high gradient zones. To study the influence of the radius of the high band pass filter, the isochromatic image of the disc is normalised using different values of R. Radius values of 2, 3, 7 and 12 pixels are considered for normalisation and Fig. 37.3 shows the variation of the fringe order values obtained after applying colour difference formula followed by refining each of them. It is seen that the isochromatic image normalised using higher radius filter gives better results in the high fringe gradient zones. Isochromatic demodulation of fringe orders upto 3.1 and 3.7 are obtained using radii 2 and 3 pixels respectively. The radii of 7 pixels and more are found to give a maximum fringe order of 4.7. Hence the use of higher radius value is recommended in problems involving a high fringe gradient.

Fig. 37.3 Variation of fringe order values obtained in the circular disc subjected to a higher load of 574 N along the vertical diameter using difference radius values for background suppression. Values obtained analytically are taken as reference for comparison
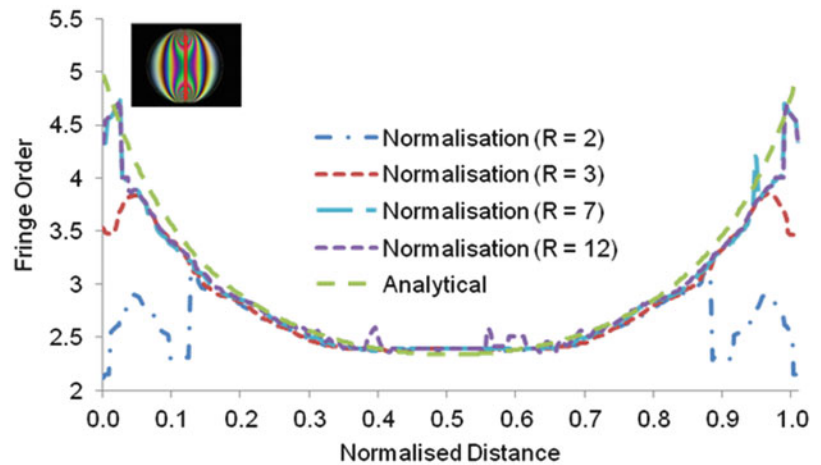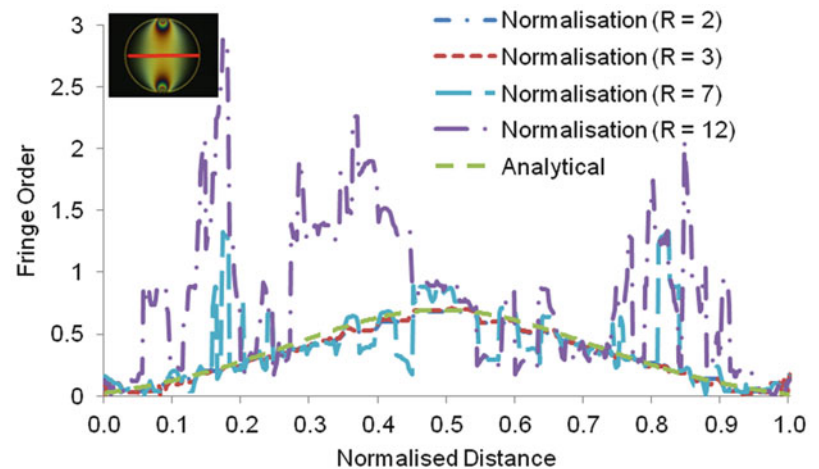

Fig. 37.4 Variation of fringe order values obtained in the circular disc under diametral compression subjected to a load of 174 N along the horizontal diameter using difference radii values for background suppression. Values obtained analytically are taken as reference for comparison

37.3.2 Low Fringe Gradient Zones

To assess the performance of the method in the low gradient zones, a circular disc subjected to a small load of 174 N is considered. The calibration table is theoretically generated using the material stress fringe values of 11.19, 10.01 and 7.9 N/mm/fringe for red, green and blue channels respectively. The dark field isochromatic image is normalised using different radii of the high band pass filter and demodulation is carried out using TFP.

Figure 37.4 shows the variation of the fringe orders along the horizontal diameter for radii values of 2, 3, 7 and 12. The fringe order values are compared with analytical results. It is found that the fringe order values obtained using a lower radius value ($R = 2$ and 3) gives good results and closely follow the analytical values. The use of higher R values makes normalisation sensitive to slight intensity variations in the model and amplifies them. It can be seen that the use of higher radii ($R = 7$ and $R = 12$) leads to false estimation of fringe orders. The absolute mean errors obtained are 0.031, 0.033, 0.129 and 0.500 fringe orders using radii of 2, 3, 7 and 12 pixels respectively. Hence, the use of low radii for the high pass filter are recommended for problems where the fringe gradient is small.

37.4 Conclusions

The performance of single colour image based twelve fringe photoelasticity using theoretically generated calibration table in conjunction with isochromatic image normalisation is studied for problems having a variety of fringe gradients. The use of normalisation has an advantage that it eliminates the need for experimental calibration provided the material stress fringe

values of the photoelastic material is accurately known. However, in the present work, it is found that the radius of high pass filter used for background suppression during image normalisation affects the fringe order results. A lower value of radius is found to work well in the zones of low fringe gradient and a higher value of radius is required to demodulate isochromatics in the high fringe gradient zones.

For problems in which fringe gradients are uniform a single value of R for background suppression followed by normalisation is sufficient for isochromatics demodulation using TFP. However, in case of problems with varied fringe gradients, image normalisation using a single radius value throughout the model is insufficient to demodulate different zones of the model. Work on the development of appropriate normalisation scheme to solve such problems is currently underway.

References

1. Ramesh, K.: Digital photoelasticity (Chap. 8). In: Rastogi, P. (ed.) Digital Optical Measurement Techniques and Applications, pp. 289–344. Artech House, London (2015)
2. Ajovalasit, A., Petrucci, G., Scafidi, M.: Review of RGB photoelasticity. Opt. Lasers Eng. **68**, 58–73 (2015)
3. Ramesh, K., Kasimayan, T., Neethi Simon, B.: Digital photoelasticity—a comprehensive review. J Strain Anal. Eng. Des. **46**(4), 245–266 (2011)
4. Ramesh, K., Vivek, R., Ramya, C.: New initiatives in single colour image fringe order estimation in digital photoelasticity. J Strain Anal. Eng. Des. **50**(7), 488–504 (2015)
5. Quiroga, J.A., Garcia Boetella, A., Gomez Pedero, J.A.: Improved method for isochromatics demodulation by RGB calibration. Appl. Optics **41**, 3461–3468 (2002)
6. Madhu, K.R., Ramesh, K.: Noise removal in three fringe photoelasticity by adaptive colour difference estimation. Opt. Lasers Eng. **45**, 175–182 (2007)
7. Ajovalasit, A., Petrucci, G., Scafidi, M.: RGB photoelasticity: review and improvements. Strain **46**, 137–147 (2010)
8. Kale, S., Ramesh, K.: Advancing front scanning approach for three-fringe photoelasticity. Opt. Lasers Eng. **51**, 592–599 (2013)
9. Madhu, K.R., Prasath, R.G.R., Ramesh, K.: Colour adaptation in three fringe photoelasticity. Exp. Mech. **47**, 271–276 (2007)
10. Neethi Simon, B., Ramesh, K.: Colour adaptation in three fringe photoelasticity using a single image. Exp. Tech. **35**, 59–65 (2011)
11. Swain, D., Philip, J., Pillai, S.A.: A modified regularized scheme for isochromatic demodulation in RGB photoelasticity. Opt. Lasers Eng. **61**, 39–51 (2014)
12. Swain, D., Thomas, B.P., Philip, J., Pillai, S.A.: Novel calibration and colour adaptation schemes in three-fringe RGB photoelasticity. Opt. Lasers Eng. **66**, 320–359 (2015)
13. Swain, D., Thomas, B.P., Philip, J., Pillai, S.A.: Non-uniqueness of the color adaptation techniques in RGB photoelasticity. Exp. Mech. **55**, 1031–1045 (2015)
14. Larkin, K.G., Bone, D.J., Oldfield, M.A.: Natural demodulation of two-dimensional fringe patterns. I. General background of the spiral phase quadrature transform. J. Opt. Soc. Am. A **18**(8), 1862–1870 (2011)
15. Quiroga, J.A., Gomez Pedrero, J.A., Garcia Botella, A.: Algorithm for fringe pattern normalization. Opt. Commun. **197**, 43–51 (2001)
16. Bernini, M.B., Federico, A., Kaufmann, G.H.: Normalization of fringe patterns using the bidimensional empirical mode decomposition and the Hilbert transform. Appl. Optics **48**(36), 6862–6869 (2009)
17. Quiroga, J.A., Servin, M.: Isotropic n-dimensional fringe pattern normalization. Opt. Commun. **224**, 221–227 (2003)
18. Guerrero, J.A., Marroquin, J.L., Rivera, M., Quiroga, J.A.: Adaptive monogenic filtering and normalization of ESPI fringe patterns. Opt. Lett. **30**, 3018–3020 (2005)
19. Ochoa, N.A., Silva-Moreno, A.A.: Normalization and noise-reduction algorithm for fringe patterns. Opt. Commun. **270**, 161–168 (2007)

Chapter 38
Novel Scanning Scheme for White Light Photoelasticity

Vivek Ramakrishnan and Ramesh Krishnamurthi

Abstract The use of white light based Twelve Fringe Photoelasticity/RGB Photoelasticity has gained popularity in the recent years. The main advantage of this technique is that it requires only a single image recorded under white light for isochromatic demodulation. This makes it suitable for problems where multiple acquisitions are difficult. Accuracy of fringe order estimation using Twelve Fringe Photoelasticity is dependent on the spatial resolution of the isochromatic fringe pattern. The existing scanning schemes for refining the fringe order data do not take this into account and leads to the propagation of noise from the low resolution zones. In this work, a novel scanning scheme is proposed whose progression is guided by the spatial resolution of the isochromatic fringe pattern. Initially, a method based on the intensity gradients is developed to create a whole field map resembling the resolution of the fringe pattern. This map is used to guide the scanning scheme for refining the fringe order data. The proposed scanning scheme encapsulates the noise within the zones of low spatial resolution and eliminates their propagation. The working of the scanning scheme is demonstrated using the benchmark problem of a circular disc subjected to diameter compression.

Keywords Digital photoelasticity • Image processing • RGB photoelasticity • Twelve fringe photoelasticity • Isochromatics

38.1 Introduction

Recent developments in white light photoelasticity make it possible to determine whole field isochromatic data from a single colour image with high accuracy [1–3]. Twelve Fringe Photoelasticity (TFP) has been used for a variety of applications ranging from residual stress analysis in glass [4, 5] to analysis of civil structures [6]. Use of photoelasticity for inter-disciplinary research demands that even personnel with a limited background in photoelasticity are able to conveniently perform post processing of the isochromatic fringe patterns. Further, the use of TFP/RGB photoelasticity to solve new problems requires it to be robust in order to handle models of complex geometry and accommodate fringe patterns of varied shapes and gradients.

Mathematical modelling of intensity variation in the isochromatic image requires accurate consideration of various factors including spectral composition of the light source used, transmission response of the optical elements, quarter-wave plate error, dispersion of birefringence and spectral response of the camera. Hence, in practise an approach based on the use of a calibration table is generally followed. In RGB Photoelasticity (RGBP) or Twelve Fringe Photoelasticity (TFP), the isochromatic parameter is determined by comparing the colour components at a point on the model with that in the calibration table. Calibration table is generated using specimens of known fringe order variation such as beam under four point bending. Initially, the fringe orders are estimated by the colour difference formula. The fringe order results obtained using the colour difference formula are prone to errors owing to the repetition of colours after every fringe [1]. These errors are eliminated by incorporating fringe order continuity by taking into account the fringe order value of the neighbouring resolved pixel. This is achieved by a modified colour difference formula [7] or window search method [8]. It is to be noted that the fringe order value at a pixel estimated initially using the colour difference formula is independent of the surrounding pixels, whereas after refining the fringe order data values are influenced by the fringe order of the neighbouring pixel locations. Though the incorporation of fringe order continuity has helped to improve the quality of results in general, this has also made the method vulnerable to the scanning scheme adopted for refining.

Several scanning schemes have been proposed in the literature to refine the fringe order data. They are horizontal/vertical scanning [9], combined horizontal and vertical scanning [9], flood fill scanning [10], four sub-image scanning [8] and

V. Ramakrishnan (✉) • R. Krishnamurthi
Department of Applied Mechanics, Indian Institute of Technology Madras, Chennai 600 036, India
e-mail: vivekrk1990@gmail.com

advancing front scanning scheme [11]. The accuracy of the fringe order obtained using TFP is dependent on the spatial resolution of the isochromatics fringe patterns. It is reported that a spatial resolution of atleast 10 pixels per fringe order is necessary for accurate results [8]. The existing scanning schemes do not take this into account, which leads to the origin and propagation of noise from the low spatial resolution zones. Among the proposed scanning schemes, the advancing front scanning scheme can minimise this noise propagation by using multiple seed points to scan the model domain. However, this requires careful selection of seed points by analysing the fringe order results as well as the progression of the scanning scheme interactively.

In this work, a novel scanning scheme which accounts for the spatial resolution of the fringe pattern in the recorded isochromatic image is proposed. Initially, a method is proposed to generate a map which resembles the gradient of the fringe pattern in the model. This map is then used to guide the scanning scheme for refining. The working of the proposed scanning scheme is demonstrated using the benchmark problem of a circular disc subjected to diametral compression.

38.2   Fringe Resolution Guided Scanning Scheme

38.2.1   Creation of Resolution Map

The first step is to develop a method to create a whole field map of the spatial resolution of the fringe patterns in the isochromatic image. Till date, there is no standard method reported for quantifying the spatial resolution/gradient of photoelastic fringe patterns. In this work, a method based on the intensity gradients of the isochromatic image is used to create a map that is representative of the fringe gradient in the model. The method is first illustrated using theoretically obtained dark field fringe pattern in a circular disc under compression and later applied on the experimental image recorded using white light.

Figure 38.1a shows theoretically generated fringe pattern in a disc (compressive load $= 492$ N, diameter $= 60$ mm). The objective is to generate a map which is representative of the fringe gradient in the model with values increasing towards the load application points.

First, the intensity gradients are computed in the horizontal direction as follows,

$$Grad_x = \frac{I(i, j+1) - I(i, j-1)}{2} \tag{38.1}$$

where I represents the intensity and (i, j) represent the coordinates of the pixel under consideration. Similarly, the gradient along the vertical direction is given by,
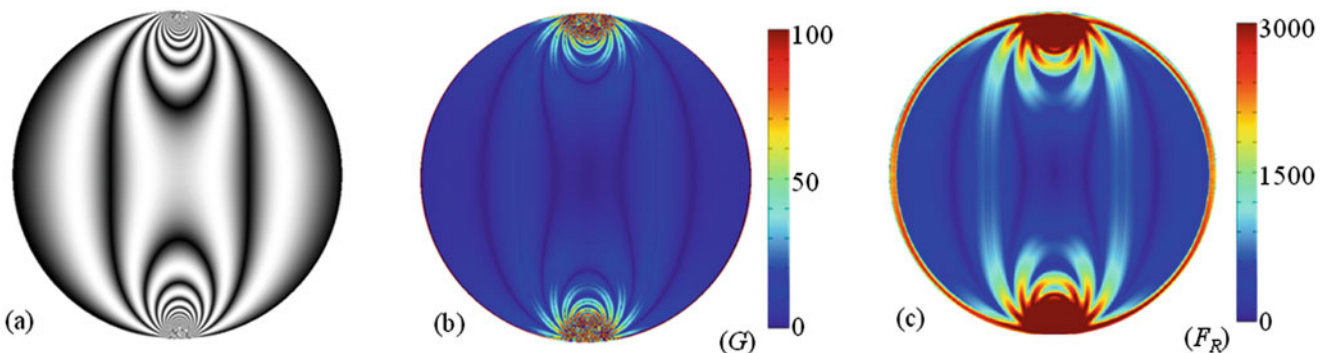
$$Grad_y = \frac{I(i+1, j) - I(i-1, j)}{2} \tag{38.2}$$

Fig. 38.1 (**a**) Theoretically simulated fringe pattern in a circular disc under diametral compression. (**b**) The intensity gradient map G. (**c**) Whole field map resembling the fringe gradient (F_R_map)

Next, the absolute gradient is calculated for each pixel in the image by the following relation,

$$G = \sqrt{Grad_x^2 + Grad_y^2} \tag{38.3}$$

Figure 38.1b shows the contour map of absolute gradient G corresponding to the fringe pattern shown in Fig. 38.1a. It is found that the value of G is high in most of the zones near loading points. However, on close observation, it can be found that some pixels in the high gradient zones have comparatively low values of G (appears as blue). These pixels correspond to the fringe skeleton points where the intensity variation is small. Ideally, all the pixels at the high fringe gradient zones should have higher values and hence, the quantity G alone is not adequate to represent of the fringe gradient of the model.

The whole field map that completely captures the fringe gradient in the model is obtained by taking the sum of the absolute intensity gradients G over a $k \times k$ pixel window. This quantity F_R is given by,

$$F_R(i,j) = \sum_{m=i-p}^{m=i+p} \sum_{n=j-p}^{n=j+p} G(m,n) \ \ \text{where} \ \ p = \frac{1}{2}(k-1) \tag{38.4}$$

where (i, j) are the global coordinates of a pixel in the image and (m, n) are the local coordinate in the $k \times k$ window. A window size of 11 pixels was found to be sufficient for the problem studied in this work. The value of F_R is evaluated at each pixel in the model domain and the whole field map thus obtained is labelled as F_R_map. Figure 38.1c shows the F_R_map for the circular disc and it can be seen that all the pixels in the high fringe gradient have high values compared to the low gradient zones away from the loading points. A low value in the F_R indicates higher spatial resolution and low fringe gradient whereas a higher value of F_R indicates low spatial resolution and a high fringe gradient.

38.2.2 Experimental Isochromatic Colour Images

Figure 38.2a shows the dark field isochromatics in a circular disc under diametral compression recorded under white light (Load = 492 N, Diameter = 60 mm). The spatial resolution of the fringe pattern is very less near the loading points (<10 pixels per fringe order). The methodology discussed in the previous section is extended for colour images obtained using white light. The absolute intensity gradient G is computed using Eq. (38.3) for red, green and blue colour planes separately. Figure 38.2b–d show the contour map of the absolute intensity gradients obtained for red, green and blue colour planes respectively. The maps of G obtained from each colour component is added together to obtain the total intensity gradient (G_t) map (Fig. 38.2e). Finally, the F_R_map is created from G_t by using Eq. (38.4).

The F_R_map obtained for the isochromatic image of the disc under diametral compression is shown in Fig. 38.2f. It can be seen that the values increase towards the loading points and the model edges where the gradients are high. The values in the F_R_map for the circular disc problem are in the range of 20 to more than 2000. It is to be noted that though the magnitude of the values in the map is problem dependent, the proposed scanning scheme is independent of the absolute values and progresses towards the high gradient zones in a comparative manner.

38.2.3 Scanning Scheme

The new scanning scheme is designed to resolve zones of low gradients having a higher spatial resolution first before refining the zones having low spatial resolutions. The flowchart of the proposed Fringe Resolution Guided Scanning in Twelve Fringe Photoelasticity (FRSTFP) is shown in Fig. 38.3. The generation of the resolution map and the scanning scheme is implemented using Matlab. Once the image, boundary mask and the calibration table are loaded, the fringe orders are first estimated by the least squares method using the colour difference formula. The F_R_map for the isochromatics image is obtained using Eqs. (38.1)–(38.4) as discussed in the previous section. The refining process is started from a point that is correctly resolved by the least squared method (usually known as the seed point). The method of refining may be RTFP [7] or window search method [8]. From the initial seed point, the scanning scheme progresses such that the next point considered for refining is the one having a minimum value of F_R in a 3×3 window centered around the current pixel. Hence, all the zones in the image corresponding to low fringe gradients and higher spatial resolution are refined first. Subsequently, the scan proceeds to the high gradient zones where the spatial resolution is very less. Thus, the proposed scanning scheme refines
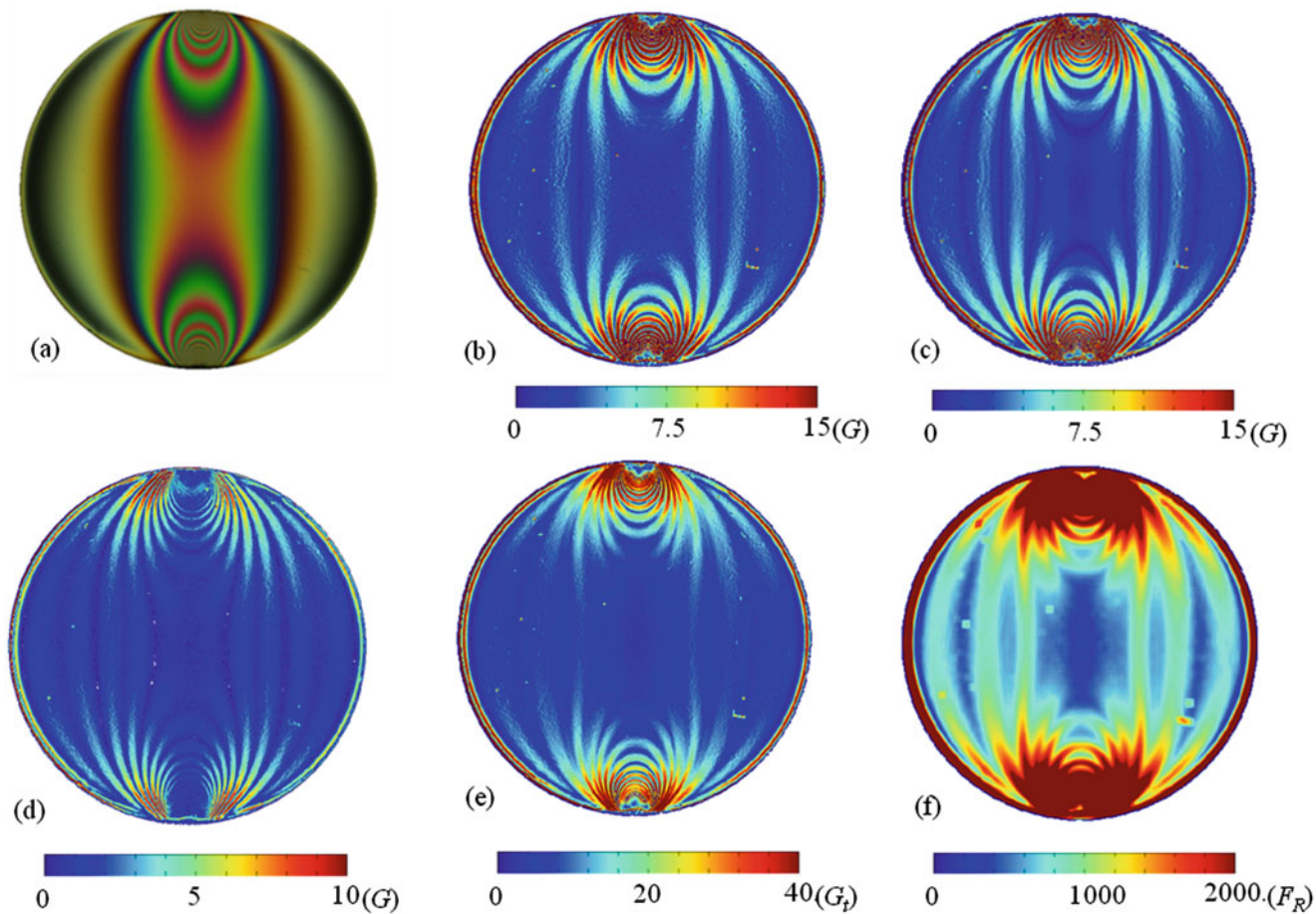
Fig. 38.2 (**a**) Dark field isochromatics in the circular disc under diametral compression. Absolute gradient for different colour planes of the image (**b**) red, (**c**) green, (**d**) blue. (**e**) Sum of the absolute gradients (G_t). (**f**) Contour plot of the F_R map
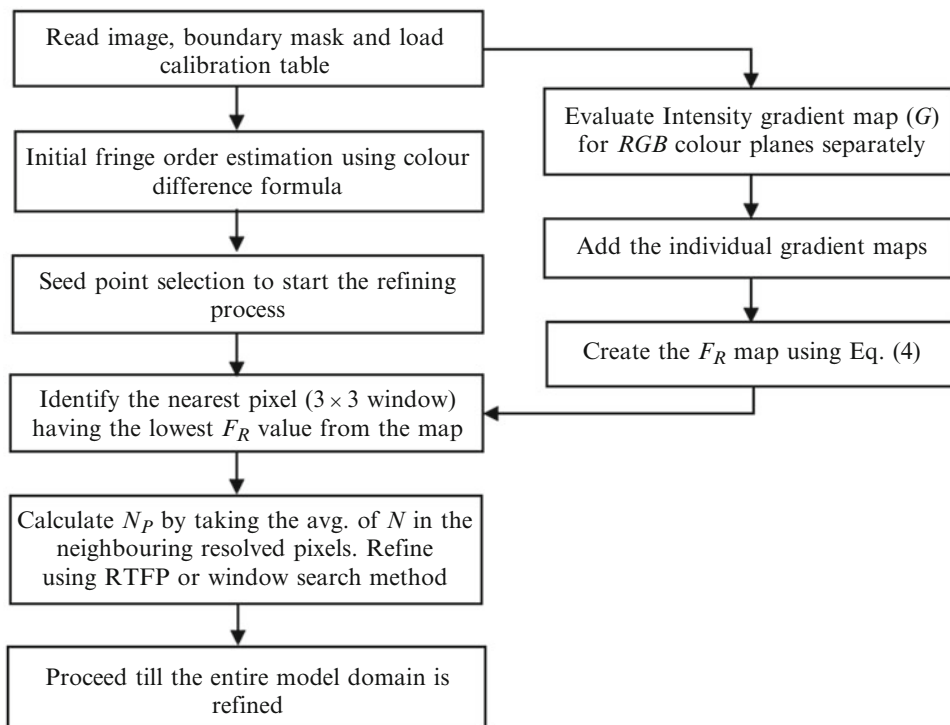

Fig. 38.3 Flowchart of the fringe resolution guided scanning scheme in TFP

the fringe order data in the low spatial resolution zones in the image only at the end and hence, encapsulating the noise within these zones and preventing their propagation to other zones of the model.

As the scan proceeds, if the pixel under consideration has more than one neighbouring resolved pixel, an average value of the fringe order is considered thereby maximising the use of neighbouring resolved pixel data. This average value is used in the noise immune colour difference formula in case of RTFP [7] or is used to select the appropriate window in window search method [8]. Hence, the proposed scanning scheme retains the advantage of the advancing front scanning method while addressing the issue of varying spatial resolution of the isochromatic image.

38.3   Results and Discussions

The proposed fringe resolution guided scanning scheme is used to determine the whole field isochromatic data in the circular disc shown in Fig. 38.2a. The fringe orders estimated by the colour difference formula have abrupt jumps in some zones owing to colour repetition (Fig. 38.4a). The seed point selected for refining the fringe order data is shown as red dot in Fig. 38.4a. Figure 38.4b shows the greyscale representation of the fringe order results obtained after refining using the proposed scanning scheme. It can be observed from the surface plot in Fig. 38.4c that the fringe order variation is smooth and all the jumps are removed. Figure 38.4d–i show the progression of the scanning scheme at an interval of every 3000 pixels scanned. It can be observed from the progression that the scanning scheme first scans the central region of the disc where the spatial resolution of the fringe pattern is high. Once all these high resolution zones are refined, the scanning scheme proceeds towards the high gradient zones near the loading points.

The proposed scanning scheme has applications in problems having stress concentration zones where the spatial resolution of the recorded fringe pattern is generally less. The application of the existing scanning schemes leads to the propagation of noise that originates from the pixels having low spatial resolution to other zones of the model. This pollutes even the points where least squares method has yielded correct results. The fringe resolution guided scanning scheme proposed in this work eliminates this. The spatial resolution guided progression of the scanning scheme makes it an ideal choice for solving fracture problems using TFP. It is also found that the scanning scheme is useful in problems having noise randomly scattered throughout the model domain. In such cases, the proposed scheme first refines all the zones surrounding the noise points and encapsulates them.
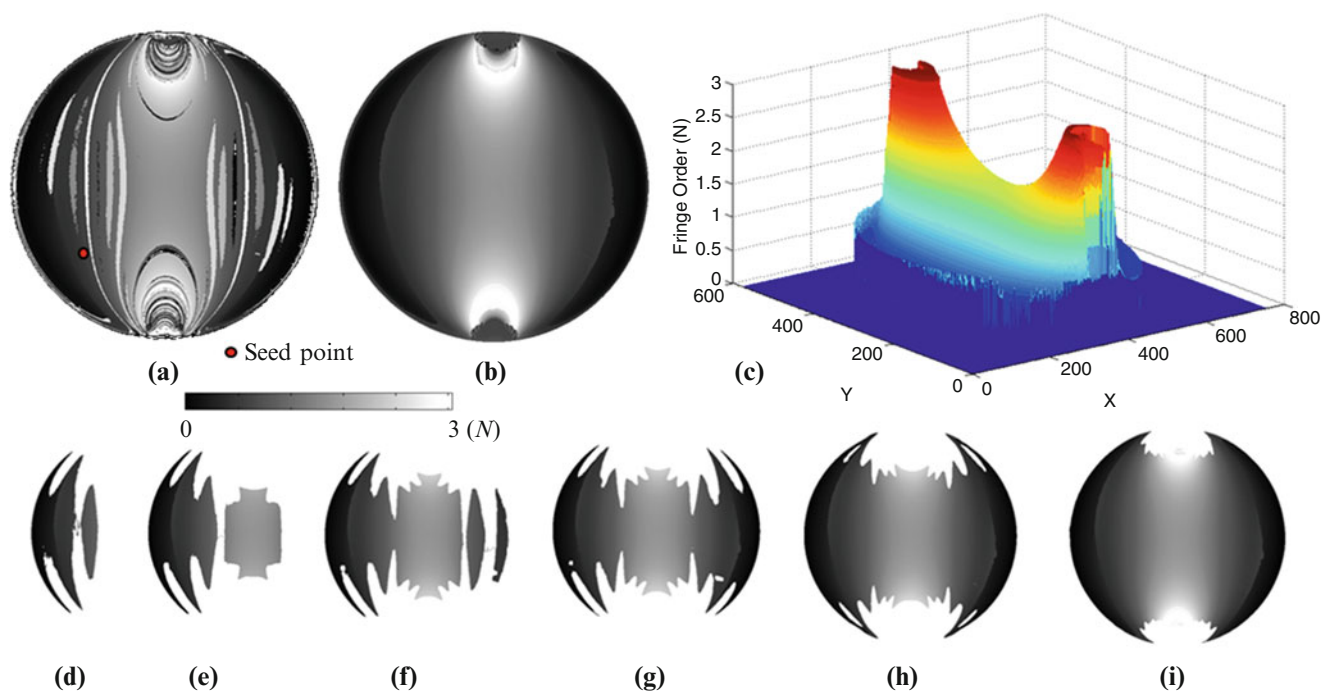

Fig. 38.4 (**a**) Greyscale representation of the fringe order values obtained using the colour difference formula. Abrupt jumps show inaccurate estimation due to colour repetition. Fringe order results obtained after refining using the proposed scanning scheme in (**b**) greyscale representation, (**c**) surface plot. (**d–i**) Progression of the proposed fringe resolution guided scanning scheme

38.4 Conclusions

A novel fringe resolution guided scanning scheme for refining in twelve fringe photoelasticity is proposed which takes into account the spatial resolution of the isochromatic fringe patterns. Initially, a method for creating a whole field map based on intensity gradients which is representative of the fringe gradient in the model is proposed. The procedure for generating the map is discussed using a theoretically generated fringe pattern in the benchmark problem of a circular disc under diametral compression and later extended to experimental colour image. The progression of the proposed scanning scheme is demonstrated using an experimental isochromatic image of a circular disc under diametral compression. The proposed scanning scheme has a variety of applications especially in problems involving stress concentration zones. Application of the proposed scanning scheme to solve problems having varying fringe gradients across the domain is currently underway.

References

1. Ajovalasit, A., Petrucci, G., Scafidi, M.: Review of RGB photoelasticity. Opt. Lasers Eng. **68**, 58–73 (2015)
2. Ramesh, K.: Digital photoelasticity, Chap. 8. In: Rastogi, P. (ed) Digital Optical Measurement Techniques and Applications, pp. 289–344. Artech House, London (2015)
3. Ramesh, K., Kasimayan, T., Neethi Simon, B.: Digital photoelasticity—a comprehensive review. J. Strain Anal. Eng. Des. **46**(4), 245–266 (2011)
4. Scafidi, M., Toscano, A., Petrucci, G., Alessi, S., Ajovalasit, A.: Review of photoelastic image analysis applied to structural birefringent materials: glass and polymers. Opt. Eng. **54**(8), 081206 (2015)
5. Ajovalasit, A., Petrucci, G., Scafidi, M.: RGB photoelasticity applied to the analysis of membrane residual stress in glass. Meas. Sci. Technol. **23**, 025601 (2012)
6. Baig, I., Ramesh, K., Hariprasad, M.P.: Analysis of stress distribution in dry masonry walls using three fringe photoelasticity. In: Proc. SPIE 9302, International Conference on Experimental Mechanics, 93022P (2014)
7. Madhu, K.R., Ramesh, K.: Noise removal in three fringe photoelasticity by adaptive colour difference estimation. Opt. Lasers Eng. **45**, 175–182 (2007)
8. Ajovalasit, A., Petrucci, G., Scafidi, M.: RGB photoelasticity: review and improvements. Strain **46**, 137–147 (2010)
9. Swain, D., Philip, J., Pillai, S.A.: A modified regularized scheme for isochromatic demodulation in RGB photoelasticity. Opt. Lasers Eng. **61**, 39–51 (2014)
10. Madhu, K.R., Ramesh, K.: New boundary information encoding and autoseeding for effective phase unwrapping of specimens with cut-outs. Strain **43**, 54–57 (2007)
11. Kale, S., Ramesh, K.: Advancing front scanning approach for three-fringe photoelasticity. Opt. Lasers Eng. **51**, 592–599 (2013)

Chapter 39
Investigation of Non-equibiaxial Thin Film Stress by Using Stoney Formula

Wei-Chung Wang, Po-Yu Chen, and Yen-Ting Wu

Abstract Since the use of the Stoney formula only requires the measurement of the radii of curvature of specimens before and after coating the thin film, the formula has been widely used in the measurement and calculation of thin film stress. However, many assumptions were adopted in the derivation of the original Stoney formula. In particular, the state of thin film stress must be equibiaxial. In the literatures, even the thin film stress may be non-equibiaxial in some cases, the original Stoney formula was still employed to determine the thin film stress. In the past, several improvements on the assumptions of the original Stoney formula have been attempted so that the corrected formula can be applicable to both equibiaxial and non-equibiaxial states of thin film stresses. However, those improvements have not been verified experimentally. In this paper, the stress and the radii of curvature of circular disks made of PSM-1 photoelastic material and coated with the silicon dioxide (SiO_2) thin film of different thicknesses were measured by photoelasticity and Fizeau interferometer, respectively. The thin film stresses determined by the two methods were then compared to assess the accuracy of the Stoney formula.

39.1 Introduction

To enhance effectiveness or reduce size of optical and electronic components, various thin films are coated on those components. Sometimes, the number of layers of thin film even attains to the dozens [1–4]. Stresses are unavoidably produced in the thin film after coating. The yield rate, stability and reliability of components are affected by the presence of the thin film stress. To the worst, those components are damaged due to the large thin film stress [5]. Therefore, accurate determination of thin film stress is essential. To implement the Stoney formula [6], only the measurement of the radii of curvature of specimens before and after coating the thin film is needed. However, the correctness and accuracy of the formula have not been experimentally verified. Because of its simplicity, the formula has been widely used in the measurement and calculation of thin film stress. During the derivation of the Stoney formula, many assumptions were used. Especially, the thin film stress must be equibiaxial. In the literatures [7–10], several efforts were attempted to remove some restrictions of the original Stoney formula for various applications, however, no experimental verification was performed either. By considering the non-uniform shear traction at the film/film and film/substrate interfaces, Feng et al. [11] extended Stoney formula for a multilayer thin film/substrate system subjected to arbitrary temperature distribution. However, their improved Stoney formula was not verified by experiment either. Dong, et al. [12] employed coherent gradient sensing technique to measure the full-field topography and curvature at high temperature and used the improved Stoney formula derived by Feng et al. [11] to determine the thin film stress.

Owing to advantages of optical method are real-time, whole-field, non-contact and non-destructive etc., the radius of curvature of a specimen is generally measured by optical methods such as coherent gradient sensing technique [12], Fizeau interferometry [13], Twyman-Green interferometry [14] and shadow moiré method [15], etc. In this paper, Fizeau interferometry was used to measure the radii of curvature of specimens.

In this paper, the state of stress of three specimens made of photoelastic material PSM-1 [16] before and after coating the thin film was measured by photoelasticity. Each PSM-1 specimen was coated by one layer silicon dioxide (SiO_2) film. Three different thicknesses of SiO_2 layer, 200, 400 and 600 nm, were adopted. The radii of curvature of the PSM-1 specimen before and after coating the thin film were measured by a Fizeau interferometer. The thin film stress was then calculated by

W.-C. Wang (✉) • P.-Y. Chen • Y.-T. Wu
Department of Power Mechanical Engineering, National Tsing Hua University, Hsinchu 30013, Taiwan, Republic of China
e-mail: wcwang@pme.nthu.edu.tw

substituting the measured radii of curvature to the Stoney formula. By comparing the results obtained from photoelasticity and Stoney formula, the accuracy of Stoney formula can be assessed.

39.2 Theory

39.2.1 Stoney Formula [6]

In 1909, Stoney investigated the deformation of a structure composed of a thin film coated on a relatively thick substrate (Fig. 39.1). By analyzing the radii of curvature of the structure before and after deformation, the thin film stress σ_f can be obtained as follows

$$\sigma_f = \frac{E_s t_s^2}{6(1 - \nu_s)t_f} \frac{1}{(R - R_0)} \tag{39.1}$$

where E_s and ν_s are Young's modulus and Poisson's ratio of the substrate, respectively; t_s and t_f are the thicknesses of the substrate and thin film, respectively; R_0 and R are radii of curvature before and after coating, respectively. Equation (39.1) was derived based on several assumptions such as both thin film and substrate are homogeneous, isotropic and linearly elastic; $t_s \gg t_f$; the thin film stress states are equibiaxial, etc.

39.2.2 Four-Step Phase Shifting in Photoelasticity

To avoid the error produced by the quarter wave plane, plane polariscope was adopted in the photoelastic setup. The light intensity I_i transmitted from the plane polariscope can be expressed as [17]

$$I_i = I_b + I_a \left[\cos^2\frac{\delta}{2}\cos^2(\beta_i - \alpha_i) + \sin^2\frac{\delta}{2}\cos^2(\beta_i + \alpha_i - 2\theta) \right] \tag{39.2}$$

where I_b and I_a are the stray light/background illumination and the amplitude of light; β_i and α_i refer to the angles between the axis of polarization of the analyzer and the polarizer with the horizontal, respectively; δ and θ are relative retardation and principal direction, respectively. There are four unknowns in Eq. (39.2), i.e. I_b, I_a, δ and θ. They can be obtained by four-step phase shifting through rotating the analyzer and polarizer. The relative angles of analyzer and polarizer as well as the corresponding light intensity can be expressed as

Fig. 39.1 Schematic diagram of the deformation of the structure after coating the thin film
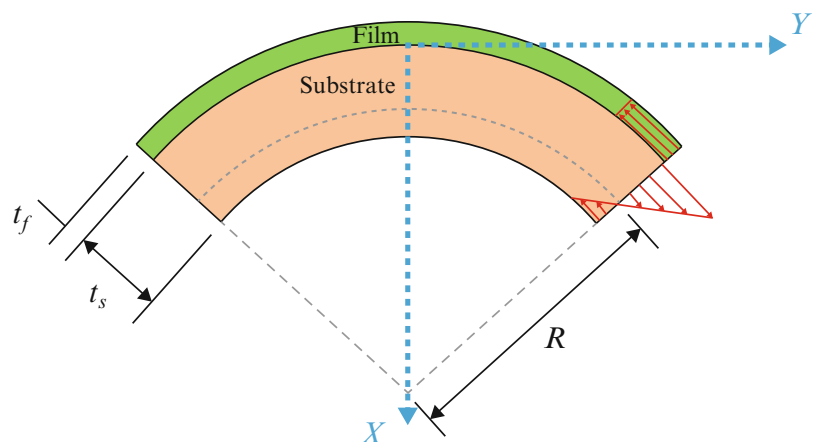
$$I_1 = I_b + I_a \left[\frac{1}{2} + \frac{1}{2} \sin^2 \frac{\delta}{2} \sin 4\theta \right] \quad (\alpha_i = 0°, \beta_i = 45°) \tag{39.3}$$

$$I_2 = I_b + I_a \left[\frac{1}{2} \sin^2 \frac{\delta}{2} (1 - \cos 4\theta) \right] \quad (\alpha_i = 0°, \beta_i = 90°) \tag{39.4}$$

$$I_3 = I_b + I_a \left[\frac{1}{2} - \frac{1}{2} \sin^2 \frac{\delta}{2} \sin 4\theta \right] \quad (\alpha_i = 0°, \beta_i = 135°) \tag{39.5}$$

$$I_4 = I_b + I_a \left[\frac{1}{2} \sin^2 \frac{\delta}{2} (1 + \cos 4\theta) \right] \quad (\alpha_i = 45°, \beta_i = 135°) \tag{39.6}$$

By simultaneously solving Eqs. (39.3)–(39.6), the relative retardation can be obtained as

$$\delta = 2 \tan^{-1} \sqrt{\frac{\sqrt{(I_4 - I_2)^2 + (I_1 - I_3)^2}}{I_1 + I_3 - I_4 - I_2}} \tag{39.7}$$

Finally, the stress of the specimen can be obtained by substituting the relative retardation into the stress-optical law.

39.3 Experimental Setup

The test specimen is made of transparent photoelastic material PSM-1 [16]. The original shape of PSM-1 material is rectangle as shown in Fig. 39.2a. As shown in Fig. 39.2b, the PSM-1 material was cut into a circular disk by CNC lathe. The diameter of the PSM-1 disk is 25.4 mm.

The material of the thin film used in this paper is the transparent SiO_2 which has been widely employed for the antireflection film of optical lens. Before coating, the stress and the radii of curvature of PSM-1 disks were measured by photoelasticity and Fizeau interferometer, respectively. And then SiO_2 film was deposited on PSM-1 disks by electron-beam gun evaporation method with ion-assisted deposition. The coating of the SiO_2 film was manufactured by Instrument Technology Research Center, National Applied Research Laboratories, Taiwan, Republic of China [18]. Three coating thicknesses of SiO_2 film were adopted, i.e. 200, 400 and 600 nm. For each thickness of SiO_2 film, two PSM-1 disks were prepared. A1 and A2, B1 and B2 as well as C1 and C2 were named for the two PSM-1 disks for each thickness of SiO_2 film, i.e. 200, 400 and 600 nm, respectively.
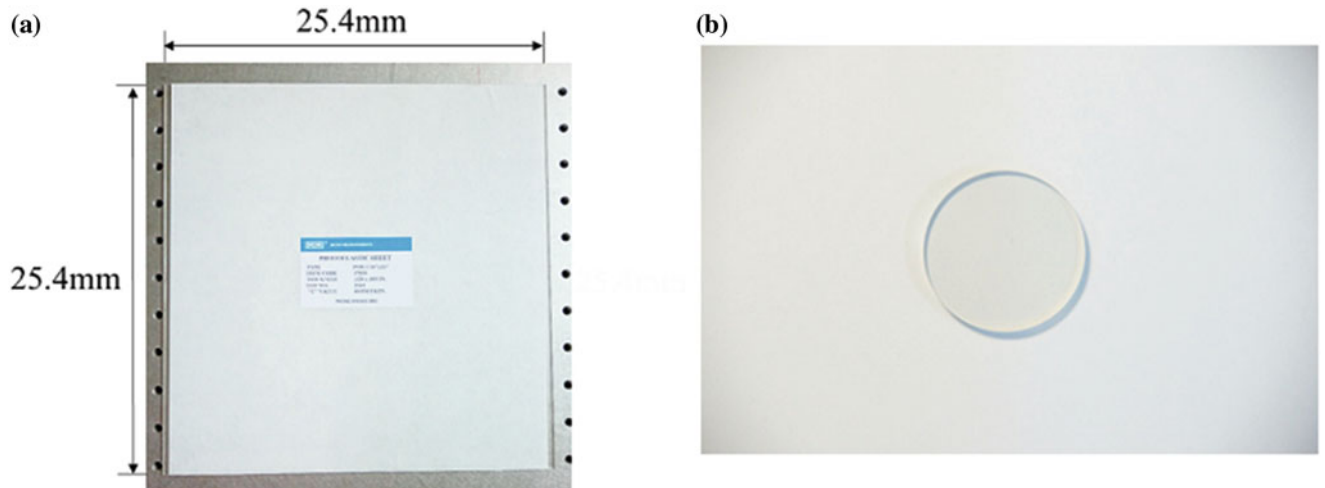

Fig. 39.2 Photographs of PSM-1 material and specimen. (a) Original size of the PSM-1 material, (b) circular disk specimen
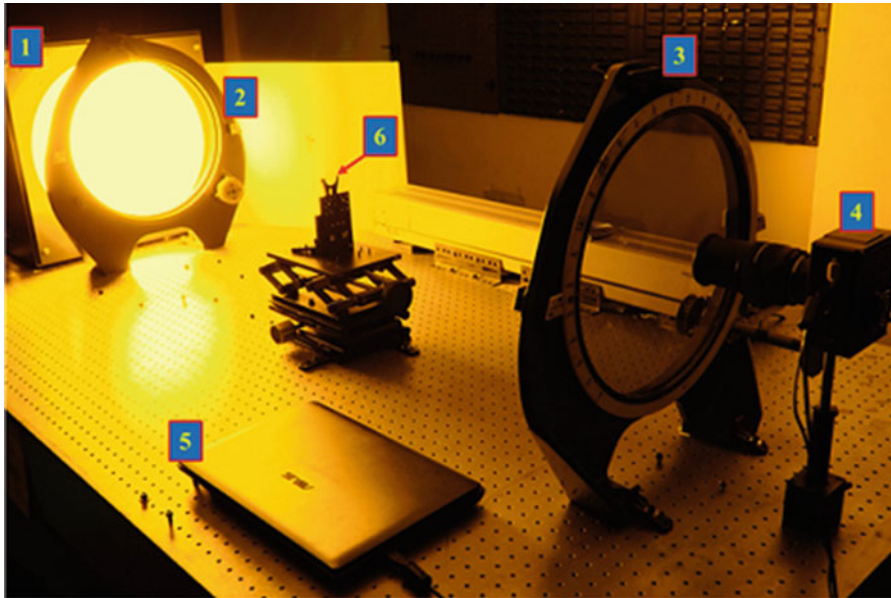
Fig. 39.3 The experimental setup of photoelastic system. *1* light source, *2* polarizer, *3* analyzer, *4* CCD camera, *5* laptop, *6* specimen

The experimental setup of photoelastic system is shown in Fig. 39.3. The light source used is a sodium lamp with wavelength 589.3 nm. The A/D converter of the CCD Camera is 16 bit. A mechanical shutter was used with the CCD camera to correct the dark current so that the electronic noise in captured images can be reduced.

The radii of curvature of PSM-1 disks were measured by Fizeau interferometer (Model AK-100, Hsintek Optical Instrument Co. [19]). The commercially available software Intelliwave [20] was used in conjunction with the interferometer. The experimental setup of the Fizeau interferometer is shown in Fig. 39.4. He-Ne laser of wavelength 632.8 nm was used as the light source.

39.4 Results and Discussions

Topographies of all six PSM-1 disks obtained by Fizeau interferometer before and after coating are shown in Figs. 39.5 and 39.6, respectively. It is obvious that all topographies are not uniform. After the SiO_2 thin film is coated on a non-uniform PSM-1 disk, most likely the state of thin film stress cannot be equibiaxial. This is a direct violation of one of the essential assumptions of the Stoney formula. In addition, in almost all literatures, a single radius of curvature was used in the Stoney formula. In other words, a parabolic curve (a second order polynomial function) was adopted to fit the topography. The second order polynomial fitting results of the topography of PSM-1 disk A2 are shown in Fig. 39.7. It is obvious that both positive and negative curvatures appear in Fig. 39.7. Therefore, significant deviations of the topography from the second order polynomial curve can be observed. In fact, as depicted in Fig. 39.7, a cubic spline function can be used to fit the topography quite well. Since the major purpose of this paper is to experimentally assess the correctness and accuracy of the original Stoney formula, a single radius of curvature was used. For both before and after coating, clockwise every 36° from the diametral top point of the PSM-1 disk to 144°, second order polynomial function fitting curvatures along five lines were obtained from topographies measured by the Fizeau interferometer. Three out of five best curvatures were adopted and substituted into the Stoney formula to calculate the thin film stress. Based on those three values of thin film stress, principal stress difference of the PSM-1 disk was determined and the photoelastic fringe patterns can be plotted.

Photoelastic fringe patterns of PSM-1 disk A1 before coating are shown in Fig. 39.8. It is clear that the level of stress is very low so that almost no visible photoelastic fringe pattern can be observed. As shown in Fig. 39.9, the relative retardation can then be calculated by using Eq. (39.7). It is obvious that the level of relative retardation of the disk is very close to the

Fig. 39.4 The Fizeau interferometer
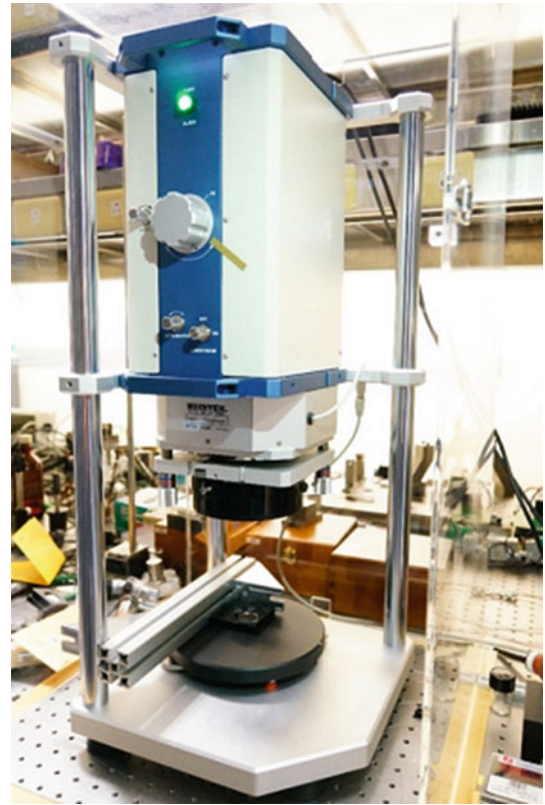
lowest level of relative retardation of the background. Significant error is therefore produced. To analyze this low level relative retardation, a new photoelastic method named enhanced exposure theory of photoelasticity (EETP) [21] was proposed. EETP is a whole-field method to measure very low level stress (<0.05 MPa). The stress results of PSM-1 disks obtained by the proposed EETP before coating are shown in Fig. 39.10.

The stress of each PSM-1 disk after coating was also measured by photoelasticity and is shown in Fig. 39.11. Based on the equilibrium conditions, the relationship between thin film stress and substrate stress can be expressed as

$$\sigma_f = -\sigma_s \times \frac{t_s}{t_f} = -\left(\sigma_{s\_after} - \sigma_{s\_before}\right) \times \frac{t_s}{t_f} \tag{39.8}$$

where σ_{s_before} and σ_{s_after} are the stresses of PSM-1 disks before and after coating, respectively.

The stress results obtained from photoelasticity and Stoney formula are shown in Fig. 39.12. The maximum and minimum differences between the two results are 87.1 % and 5.8 %, respectively. This significant stress difference shows the importance of the measurement of topography and whole-field determination of radius of curvature. In 2014, Ardigo et al. [22] used an optical profilometer to measure the radii of curvature along two orthogonal directions of a silicon substrate deposited with a 2.2 μm titanium nitride coating before and after coating. They pointed out the fact that no clear description of which radius of curvature (maximum, minimum or mean value, with or without initial curvature correction) was used in the literatures when Stoney formula was used. They reported that the maximum difference of radius of curvatures among different directions can be up to 80 %. However, they didn't report any stress results. With the help of the EETP proposed in this paper, the low level thin film stress of PSM-1 disks can be obtained and compared with that obtained from Stoney formula.

39.5 Conclusions

The two fundamental conditions to maintain the validity of the Stoney formula, i.e. equibiaxial state of thin film stress and uniform curvature of the structure before and after coating the thin film, were found that not sustaining in most practical applications. Nevertheless, because of its simplicity, Stoney formula has been widely used. In the literatures, many efforts
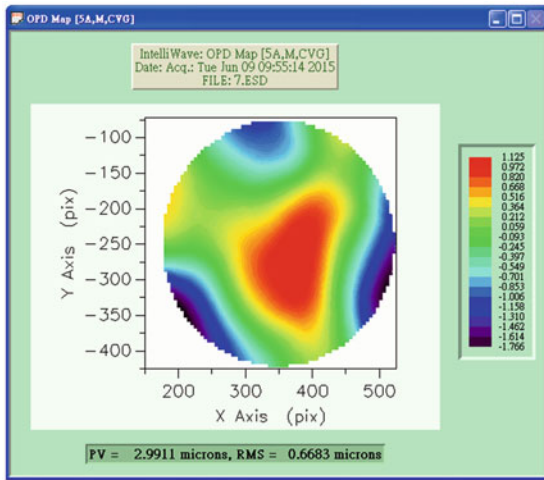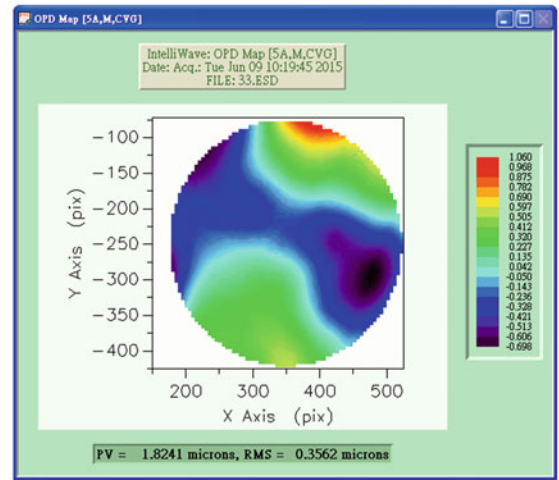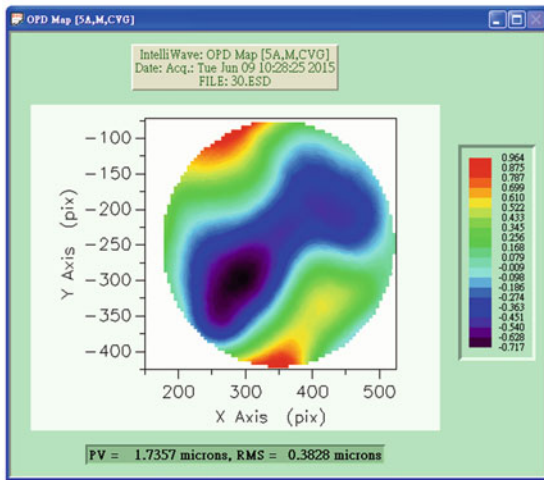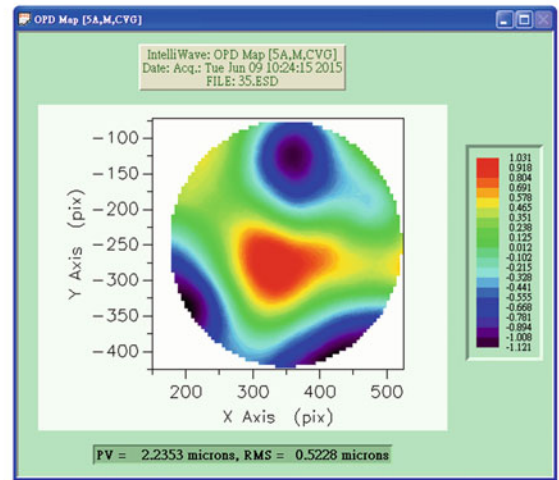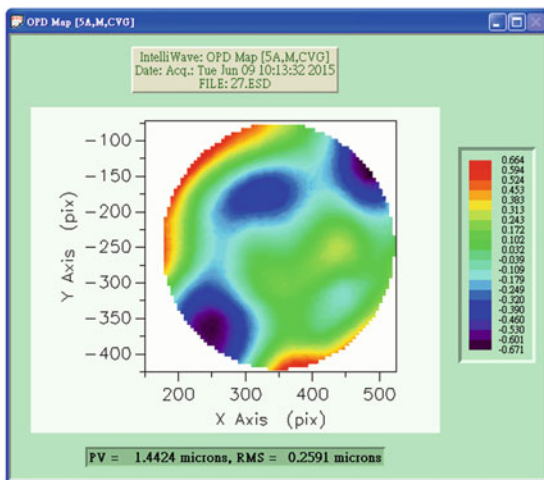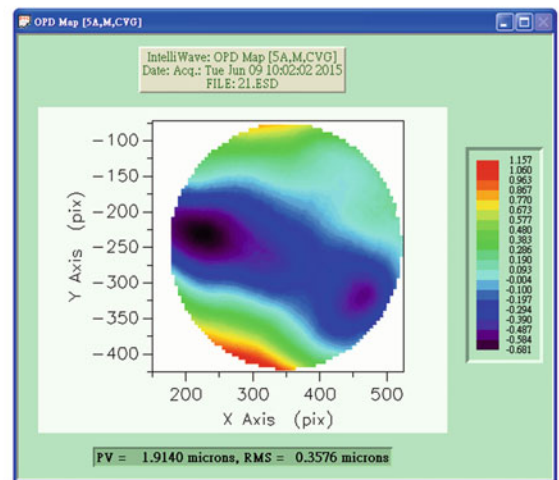
Fig. 39.5 Topographies of PSM-1 disks before coating. (**a**) A1, (**b**) A2, (**c**) B1, (**d**) B2, (**e**) C1, (**f**) C2
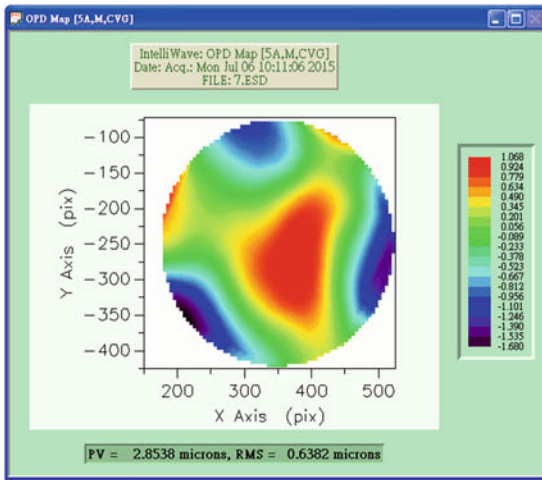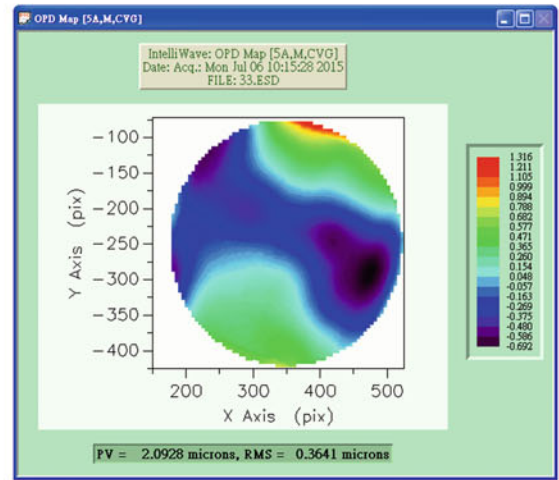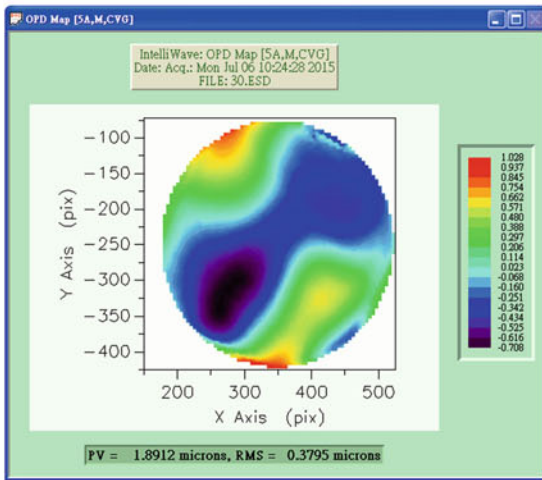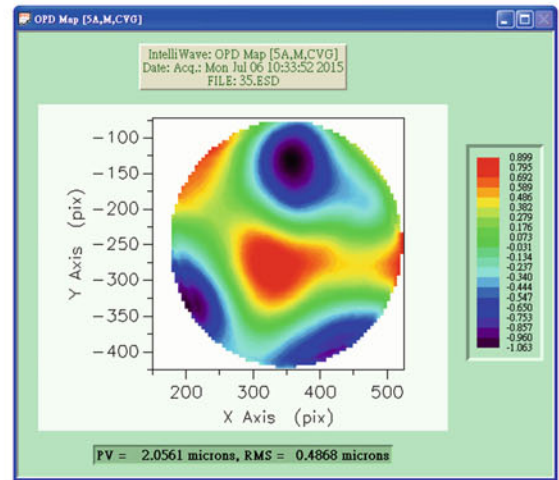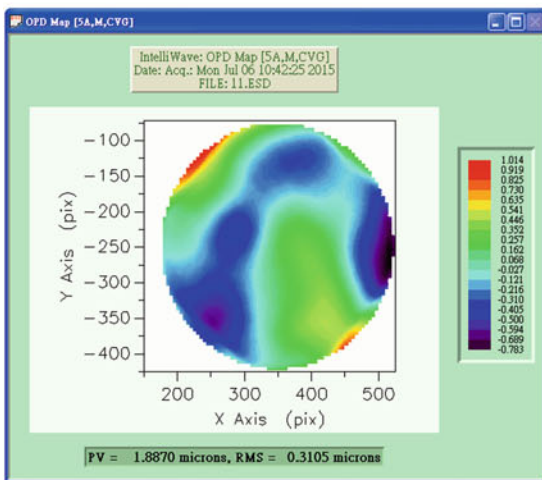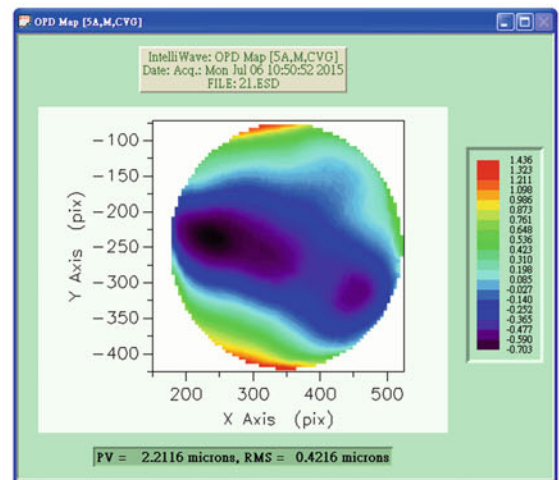
Fig. 39.6 Topographies of PSM-1 disks after coating. (**a**) A1, (**b**) A2, (**c**) B1, (**d**) B2, (**e**) C1, (**f**) C2
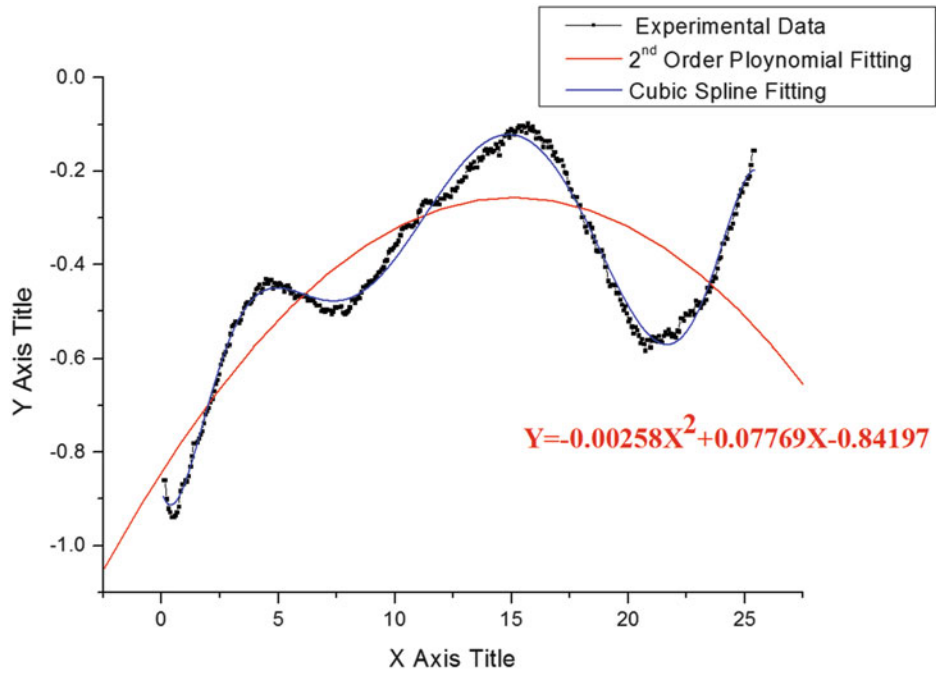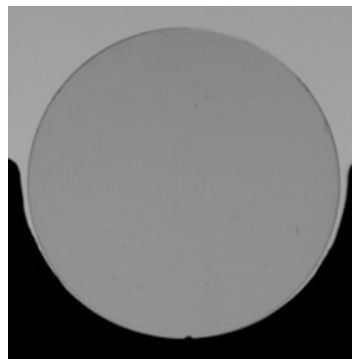
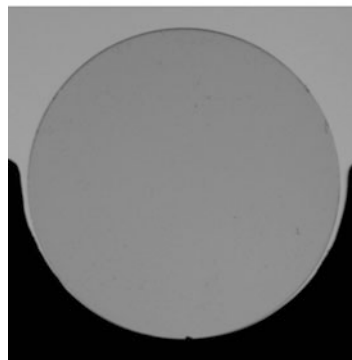**Fig. 39.7** The polynomial fit results of the topography of PSM-1 disk A2 before coating

Fig. 39.8 Photoelastic fringe patterns of PSM-1 disk A1 of different phases before coating. (**a**) $\alpha_1 = 0°, \beta_1 = 45°$, (**b**) $\alpha_2 = 0°, \beta_2 = 90°$, (**c**) $\alpha_3 = 0°, \beta_3 = 135°$, (**d**) $\alpha_4 = 45°, \beta_4 = 135°$
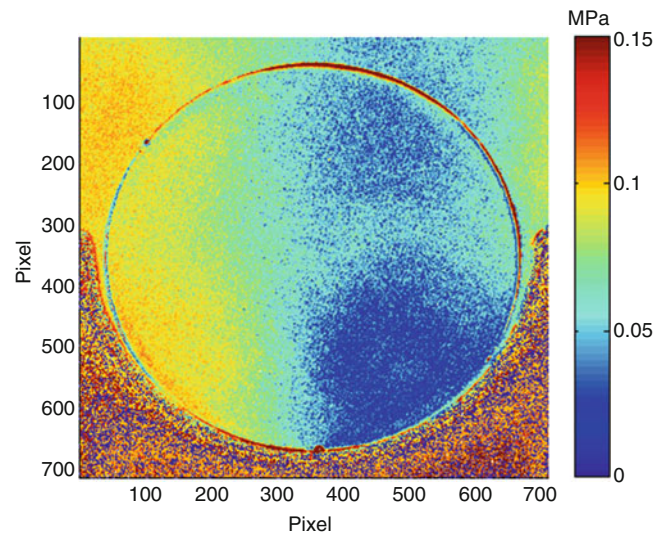
Fig. 39.9 The relative retardation results of PSM-1 disk A1

were devoted to extend the Stoney formula for various applications. Several improved or modified Stoney formulae were reported without experimental verification.

In this paper, both the Fizeau interferometry and photoelasticity were used to obtain the whole-field distribution of curvature and stress before and after the thin film was coated on the PSM-1 disk. Not surprisingly, the distribution of the curvature is not uniform due to the uneven surface of the PSM-1 disk. A single radius of curvature as only required by the Stoney formula was found too much over-simplified. A cubic spline fit was found to provide the best fit of the curvature distribution. However, an improved Stoney formula by using whole-field radii of curvature may need to be developed. With the fact that the level of thin film stress is very low, new methodology of photoelasticity must be introduced to overcome the measurement difficulty. In this paper, the EETP was introduced and the thin film stress produced by the coating was successfully obtained. Significant difference was found between the stress values determined from photoelasticity and Stoney formula.
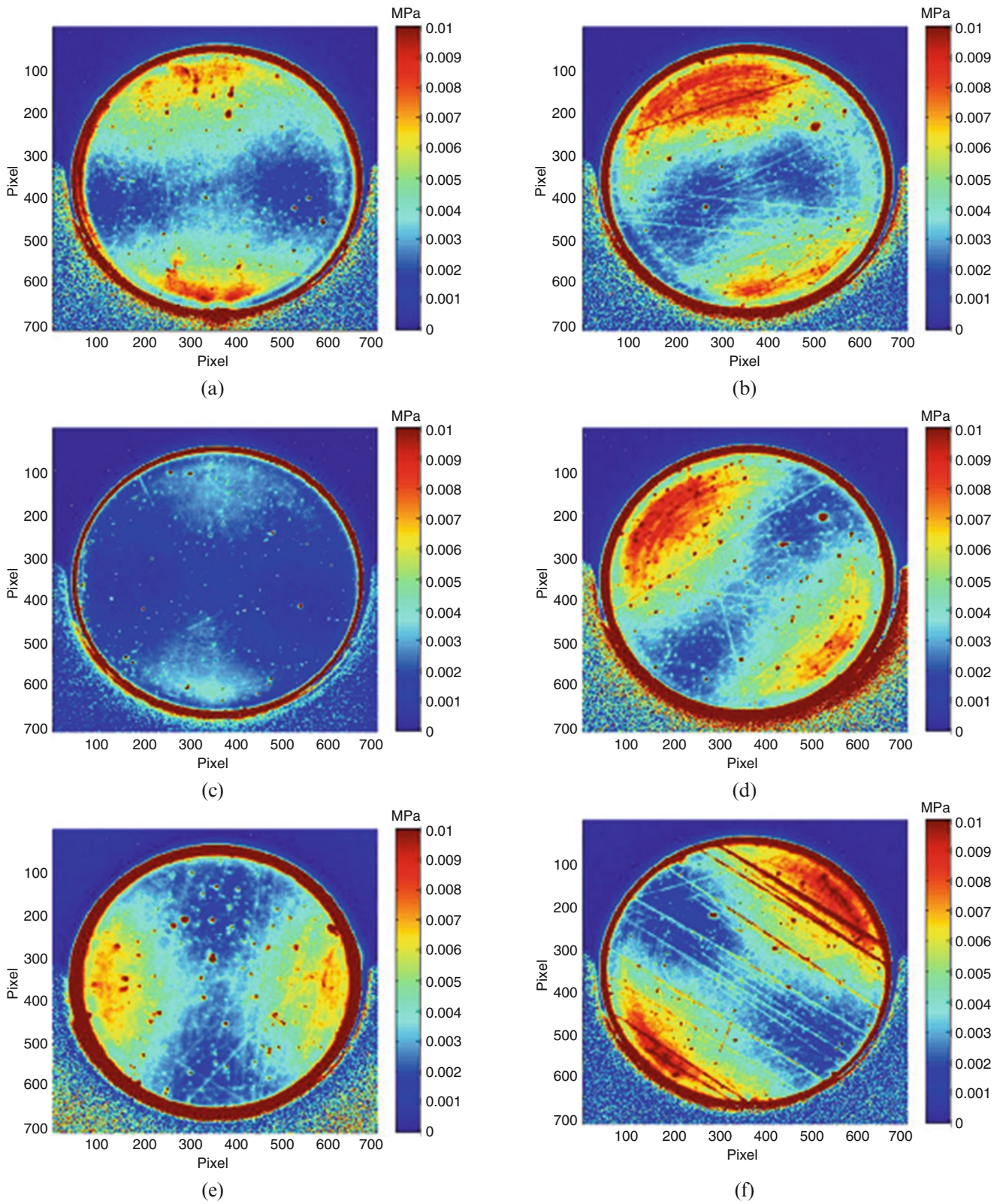
Fig. 39.10 Stress results of PSM-1 disks obtained by the proposed EETP before coating. (**a**) A1, (**b**) A2, (**c**) B1, (**d**) B2, (**e**) C1, (**f**) C2

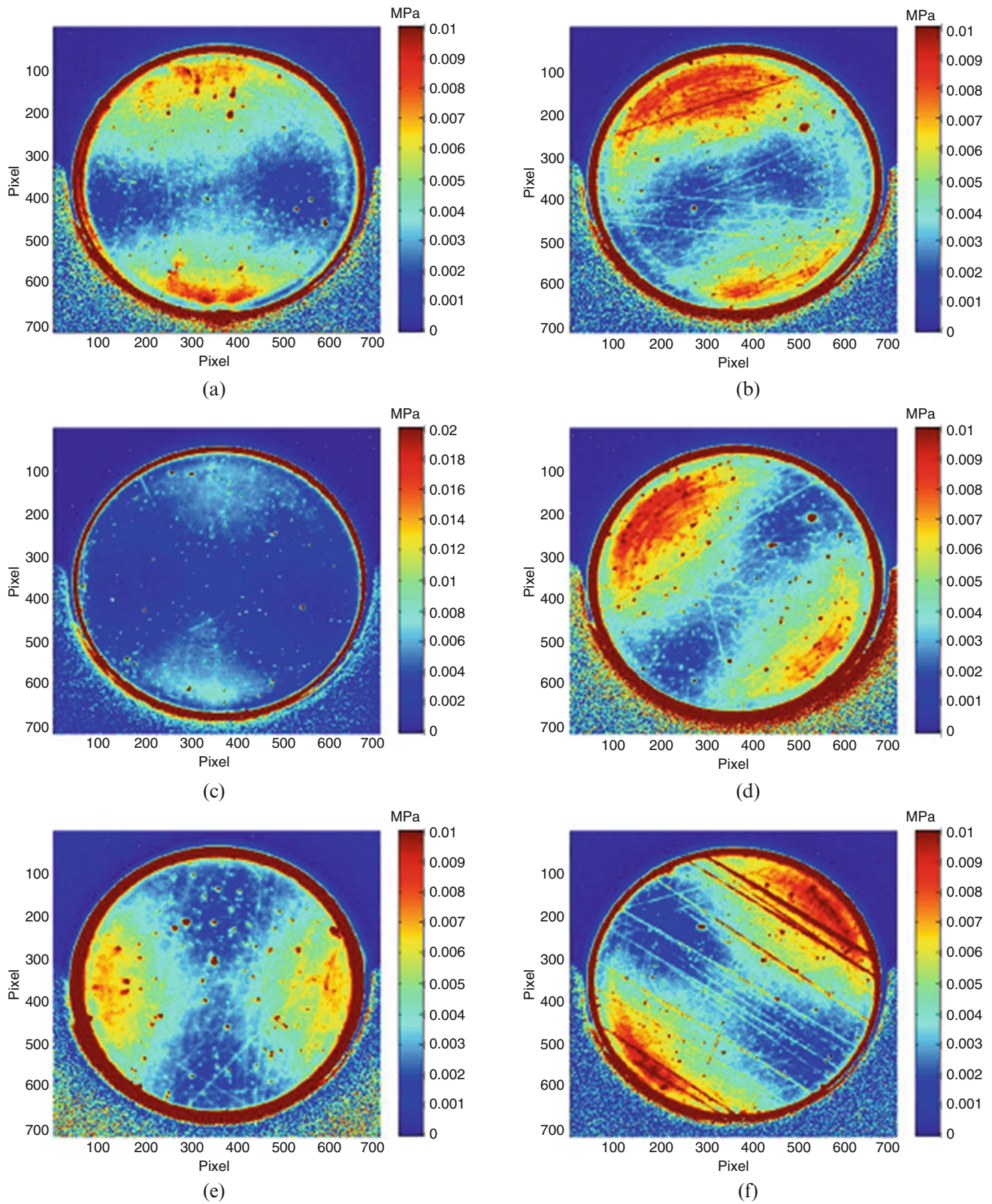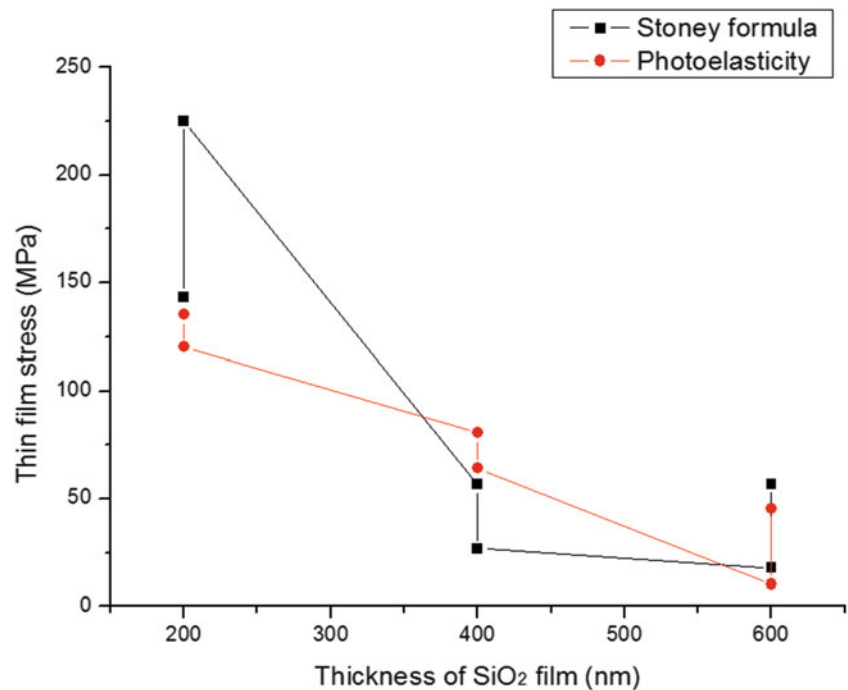**Fig. 39.11** Stress results of PSM-1 disks obtained by the proposed EETP after coating. (**a**) A1, (**b**) A2, (**c**) B1, (**d**) B2, (**e**) C1, (**f**) C2

Fig. 39.12 Comparison between the results of photoelasticity and Stoney formula

References

1. Chao, C.C., Scholz, K.D., Leibovitz, J., Cobarruviaz, M., Chang, C.C.: Multi-layer thin-film substrates for multi-chip packaging. IEEE Trans. Compon. Hybrids Manuf. Technol. **12**, 180–184 (1989)
2. Akedo, K., Miura, A., Fujikawa, H., Taga, Y.: Flexible OLEDs for automobiles using SiNx/CNx:H multi-layer barrier films and epoxy substrates. J. Photopolym. Sci. Technol. **19**, 203–208 (2006)
3. Fadhillah, F., Zaidi, S.M.J., Khan, Z., Khaled, M.M., Rahman, F., Hammond, P.T.: Development of polyelectrolyte multilayer thin film composite membrane for water desalination application. Desalination **318**, 19–24 (2013)
4. Hajimirza, S., Howell, J.R.: Computational and experimental study of a multi-layer absorptivity enhanced thin film silicon solar cell. J. Quant. Spectrosc. Radiat. Transf. **143**, 56–62 (2014)
5. Smith, D.L.: Thin-Film Deposition: Principles and Practice. McGraw-Hill, New York (1995)
6. Stoney, G.G.: The tension of metallic films deposited by electrolysis. Proc. R. Soc. Lond. **82**, 172–175 (1909)
7. Chu, S.N.G.: Elastic bending of semiconductor wafer revisited and comments on Stoney's equation. J. Electrochem. Soc. **145**, 3621–3627 (1998)
8. Klein, C.A.: How accurate are Stoney's equation and recent modifications. J. Appl. Phys. **88**, 5487–5489 (2000)
9. Blech, I.A., Blech, I., Finot, M.: Determination of thin-film stresses on round substrates. J. Appl. Phys. **97**, 113525-1–113525-7 (2005)
10. Pureza, J.M., Lacerda, M.M., Oliveira, A.L.D., Fragalli, J.F., Zanon, R.A.S.: Enhancing accuracy to Stoney equation. Appl. Surf. Sci. **255**, 6426–6428 (2009)
11. Feng, X., Huang, Y., Rosakis, A.J.: Stresses in a multilayer thin film/substrate system subjected to nonuniform temperature. J. Appl. Mech. **75**, 021022-1-7 (2008)
12. Dong, X., Zhang, C., Feng, X., Hwang, K.C.: Full-field measurement of topography and curvature by coherent gradient sensing method at high temperature. Exp. Mech. **53**, 959–963 (2013)
13. Rezadad, I., Boroumand, J., Smith, E., Figueiredo, P., Peale, R.E.: Stress analysis of free-standing silicon oxide films using optical interference. In: Proceedings of Materials Research Society Spring Meeting, vol. 1536, pp. 155–160 (2013)
14. Jozwik, M., Gorecki, C., Sabac, A., Delobelle, P., Kujawinska, M.: Evaluation of micromechanical properties of buckled SiO$_x$N$_y$-loaded membranes by combining the Twyman-Green interferometry with nanoindentation and point-wise deflection technique. Opt. Lasers Eng. **41**, 703–716 (2004)
15. Chen, K.S., Chen, T.Y.F., Chuang, C.C., Lin, I.K.: Full-field wafer level thin film stress measurement by phase-stepping shadow Moiré. IEEE Trans. Compon. Packag. Technol. **27**, 594–601 (2004)
16. http://www.vishaypg.com/micro-measurements/
17. Ramesh, K.: Digital Photoelasticity: Advanced Techniques and Applications. Springer, Berlin (2000)
18. https://www.itrc.narl.org.tw/

19. http://hsintekoptics.com/
20. www.intelliwave.com
21. Apparatus and method thereof for quantifying stress of a material, to be filed for submission for a USA patent
22. Ardigo, M.R., Ahmed, M., Besnard, A.: Stoney formula: investigation of curvature measurements by optical profilometer. Adv. Mater. Res. **996**, 361–366 (2014)

Chapter 40
ESPI Analysis of Thermo-Mechanical Behavior of Electronic Components

C. Casavola, G. Pappalettera, and C. Pappalettere

Abstract Thermo-mechanical aspects must be conveniently taken into account when designing electronic components and devices. Reliability issues can in fact arise due to stress induced by thermal field acting on materials with different coefficients of thermal expansion. In this paper an optical system based upon Phase Shifting Electronic Speckle Interferometry (PS-ESPI) was developed; it allows analyzing the in-plane displacement map experienced by the tested component during its working operation as a consequence of the Joule's effect. The adoption of an optical technique allowed to get the measurement without contact with the component that is to say without altering the capability of thermal dissipation of the component. The system was demonstrated to be effective in analyzing asymmetries in the displacements along the component and in evaluating how different kinds of constraints can drastically affect the thermo-mechanical behavior of a given component. Furthermore the system was used to compare the thermo-mechanical response of the same component in presence or in absence of a critical defect. It was verified the ability of the set up designed to detect the very different thermo-mechanical response of a damaged electronic component with respect to an undamaged one.

Keywords ESPI • Electronics components • Thermal field • Defect detection

40.1 Introduction

Electronics has deeply contributed to the great development of modern technological systems and is now used almost everywhere. Designing new electronics components or also new electronics packages is a complex task entailing issues about materials and processing, electrical performances and thermo-mechanical behavior [1]. This last aspect is also strictly connected with reliability performances of the component itself. In fact an electronic component is a complex object made by the superposition of different layers with different coefficients of thermal expansion; the presence of a thermal field can then result in a stress field that can cause delamination of the structure and, as a consequence, the mechanical breaking of the components [2, 3]. Nowadays the continuous push towards reduction in size and weight of electronics device leads to the use of high-density packaging where thermo-mechanical issues are even higher due to limited volume for thermal dissipation [4]. Quite recently interferometric optical techniques (OT) have been introduced in the analysis of electronic devices [5]. Generally speaking, OT are based on the modulation of a light wave front that interacts with the specimen surface. The modulation leads to the formation of a pattern of fringes encoding full-field information on the displacement field experienced by the specimen surface. Strains can be either obtained optically or through differentiation of displacement fields. OT were successfully applied in a variety of fields in experimental mechanics [6–10] and in view of their capability to get the full-field map of deformations with high sensitivity, no contact and in a non-destructive way [11–15] they appear to be of great interest for characterizing the thermo-mechanical response of an electronic component [16–19]. High sensitivity, in fact, has to be a basic requirement of the measuring system because of the magnitude of the deformations involved. The absence of contact, moreover, warrants that no alteration occur in the thermal dissipation of the elements examined and avoid errors related to the physical interaction between object and measuring instrument. This paper presents a PS-ESPI set up for the transient analysis of thermo-mechanical response of electronic components under different structural and constraint configurations. To that purpose, the mechanical behaviour of a fixed positive voltage regulator was analyzed to verify how its response and its deformation behavior can be affected by the adopted constraint configuration. It was also verified the ability of the system to detect the different mechanical response of an electronic component in presence or absence of defects; ESPI analysis were performed on the voltage regulator in its intact and, subsequently, damaged configuration.

C. Casavola (✉) • G. Pappalettera • C. Pappalettere
Dipartimento di Meccanica, Matematica e Management, Politecnico di Bari, Viale Japigia 182, Bari 70126, Italy
e-mail: casavola@poliba.it; katia.casavola@poliba.it

40.2 Materials and Methods

A phase-shifting ESPI set-up based upon the Lendeertz interferometer configuration was built. A schematic of the set-up is presented in Fig. 40.1. The coherent light output from a DPSS laser source (50 mW, $\lambda = 488$ nm) is reflected and directed along the optical axis of the system by the mirror 1. Laser output from the adopted source had a diameter d = 0.7 mm; therefore, a beam expander was required to get beam size comparable with the dimensions of the component. It was also necessary to filter the beam in order to improve its quality. In order to accomplish both tasks the beam was filtered by a spatial filter made up by a microscope objective M 20× and a pinhole having a 10 µm diameter. The microscopic lens focuses the laser beam into pinhole which acts like a passband optical filter. A plano-convex lens was also placed having the focal plane coincident with the pinhole plane in order to obtain a collimating beam. Before illuminating the test object, about half of the collimated laser beam is intercepted by the mirror 2 (Fig. 40.1): in this way a portion of the beam directly illuminates the measurement area of the electronic board while the remaining part irradiates the same area after being reflected thus realizing the typical configuration of Leendertz which allows detection of the u displacement component in the plane of the board.

The mirror 2 was installed on a translator actuated by a PZT crystal allowing to implement the technique of the temporal phase shifting [20, 21]. Five phases algorithm was used and final phase was obtained by spanning tree unwrapping algorithm [22, 23]. A CCD camera IRF AVT Marlin F146C was installed perpendicularly to the electronic board (Fig. 40.2) analyzed and over a horizontal and vertical translation which will enable the spatial positioning relatively to the board under test. The camera was equipped with an objective lens having a field of view FOV = 21 mm.

The ESPI thermo-mechanical analysis was carried out on a fixed positive voltage regulator. The component was mounted on a PCB board and powered at 12 V by a DC power supply following the technical specifications of the component. A loading resistance was inserted to close the electrical circuit (Fig. 40.3). The surface of the component was coated with a layer of gray spray to improve the contrast of the fringes. Two configurations of the component were prepared, namely the so called fully constrained and the partially constrained configurations. In the first configuration the body and the pins of the component are fixed to the PCB. In the second case only the body of the component is attached to the board while the pin are

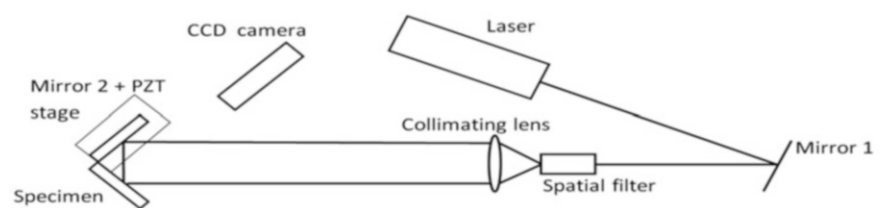**Fig. 40.1** Lendeertz interferometer configuration

Fig. 40.2 Detail of the ESPI set-up for the measurement of map displacement on electronic components
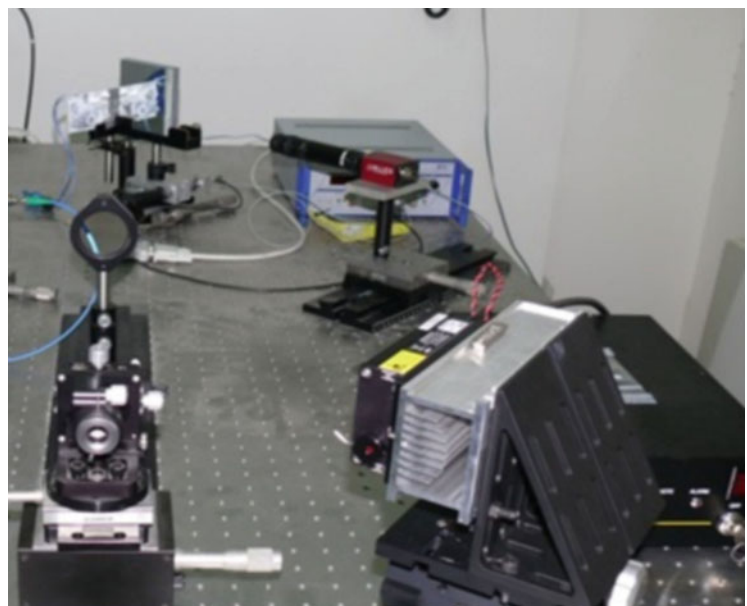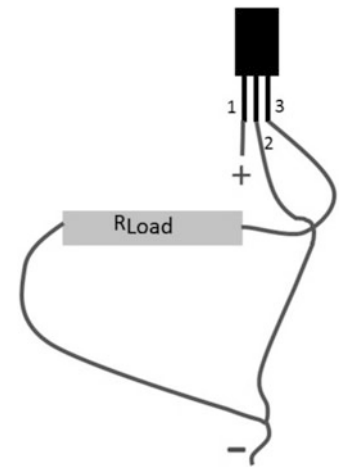
Fig. 40.3 Schematic of the circuit adopted for the measurement. *1* input, *2* GND, *3* output

directly connected to the wires without being attached to the board. ESPI analysis of the electronic component in the two described configurations was performed.

After acquiring five reference images without powering the chip, the component was powered for a total time of 7 s. During this stage a series of images were recorded respectively at 2, 5 and 7 s from the application of the load. The thermo-mechanical response of the component was then analyzed to evaluate the influence that the two different configurations constraint can have on the overall deformation behavior. A second ESPI set of measurements was performed to evaluate differences in thermo-mechanical response if a severe defect is introduced in the component. In order to perform this kind of measurement a crack was artificially introduced on the input pin and the time evolution of the thermo-mechanical response was investigated following the same procedure as described before. This kind of failure it is to be intended as a functional failure; in other words the component is not broken in absolute sense but it does not perform properly the function for which it was designed [24].

40.3   Results and Discussion

Results of the ESPI analysis performed on the positive voltage regulator are here presented. Figures 40.4 and 40.5 show the ESPI correlation fringes recorded in the case of both fully constrained and partially constrained configuration. Reported speckle images were acquired after 2 s of powering of the component and show the cross sections taken for the assessment of the relative strains whose results are reported in Table 40.1.

It is possible to clearly observe a substantial difference in the thermo-mechanical behavior of the fully constrained component between the left and the right part of its body, as can be seen from the values in Table 40.1. This appears evident just by examining the different fringe pattern in the two examined situations. In particular, the ε_{XX} strain identified in correspondence of the input power pins are of considerable magnitude, with an average value of 990 µstr in the case of fully constrained configuration. The component in partially bound configuration shows, on the contrary, a rather uniform distribution of displacements and strains as can be seen from the results shown in Table 40.1. This is a clear evidence that constraints greatly influences the strain behavior: the electronic component tends, in the free pins and bound body condition (partially constrained configuration) to exhibit a predominant component of shear ε_{XY}, as witnessed by the pattern of predominantly horizontal fringes recorded. The presence of constraints on the pins tends, instead, to alter this strain behavior: the fringes, in fact, show a shear behavior to which is superimposed to a strain component along x direction. Their combination produces inclined fringes especially identifiable close to the power pins as it can be seen in Fig. 40.4. Data about the different thermo-mechanical response of the component in presence of a crack-like defect are presented as in Tables 40.2 and 40.3. Results reported show a significant difference in terms of thermo-mechanical behavior of the electronic device in the presence or absence of a fault. The component in its damaged configuration displays strains of considerably less magnitude if compared with those highlighted in the intact configuration. In particular, it can be easily seen that the difference in terms of ε_{XY} strain is of two orders of magnitude higher in the intact device than in the damaged one. This behavior is largely justified by the type of damage introduced in the electronic component (i.e. the crack of the input pin); this caused an increase in the input resistance and a consequent reduction in the intensity of the input current.

Fig. 40.4 ESPI correlation fringes of the component in its fully constrained configuration after 2 s of powering; line 1 and 2 correspond to the cross sections along which are extrapolated the strain values reported in the Table 40.1
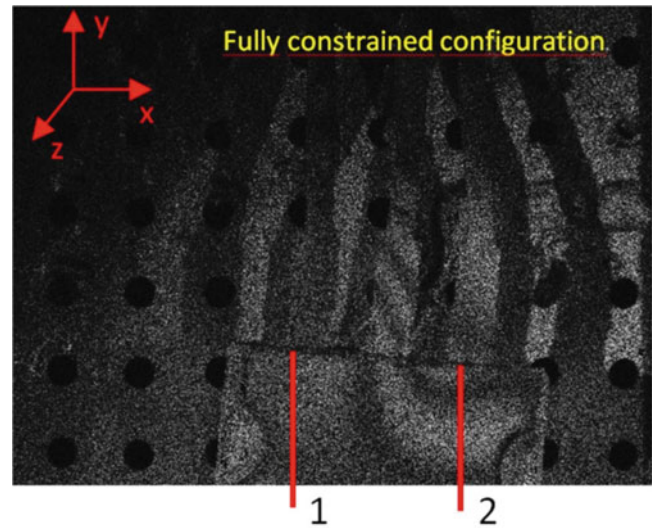
Fig. 40.5 ESPI correlation fringes of the component in its partially constrained configuration after 2 s of powering; line 1* and 2* correspond to the cross sections along which are extrapolated the strain values reported in Table 40.3
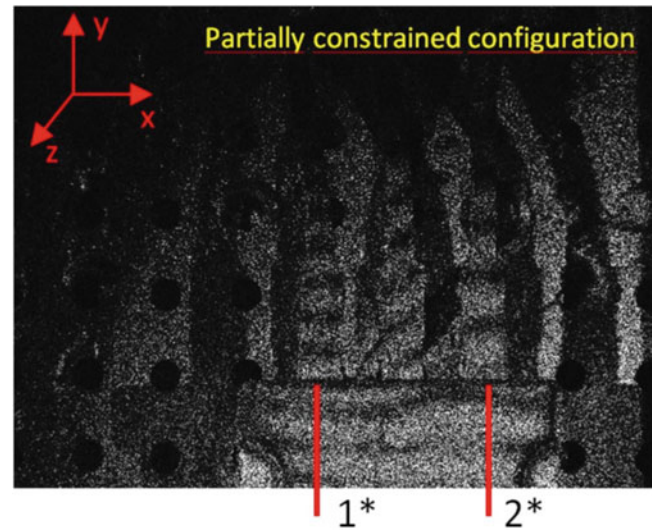
Table 40.1 Comparison of the ε_{XY} strain values of the component in its fully and partially constrained configuration; strain values are referred to the lines specified in Figs. 40.4 and 40.5

Fully constrained component			Partially constrained component	
ε_{XX} (µstr) line 1	ε_{XX} (µstr) line 2	ε_{XX} (µstr) power supply pin	ε_{XX} (µstr) line 1*	ε_{XX} (µstr) line 2*
58	181	990	14	11

Table 40.2 ε_{XY} strain values of LM7812 component in intact configuration

Intact configuration	
Time (s)	ε_{XY} (µstr)
0	2
2	−423
5	−501
7	−585

The overall joule effect results, therefore, clearly reduced resulting in a consequent reduction of the overall strain of the component, easily detectable from the data reported in Table 40.3.

Table 40.3 ε_{XY} strain values of the component in damaged configuration

Damaged configuration	
Time (s)	ε_{XY} (μstr)
0	8
2	4
5	6
7	2

40.4 Conclusions

In this work an ESPI setup was built up and employed in order to verify how the thermo-mechanical behaviour of an electronic component can be drastically influenced by its specific constraint configuration. In particular, it was analysed a fixed positive voltage regulator. Two different constraint configurations, namely called fully constrained and partially constrained, were made and then analysed. The system demonstrated itself to be able to assess the presence of asymmetries in the strain field of the component and to detect the most stressed areas and to detect substantial differences in the deformation modes depending on the constraints configurations. Also the ability of the ESPI set-up to detect the effects of the presence of a defect in terms of thermo-mechanical response of the device was tested. For the analyzed component great difference in the shear component was observed allowing to detect the presence of a function defect. It worth observing that it was sufficient to power the component just for a few seconds in order to observe very different responses in the thermos-mechanical behavior of the component. This is an interesting aspect from a practical point of view because it introduces the possibility to adopt this kind of approach as a fast monitoring tool about the malfunctioning of a component on a board. This could be done by recording some references displacement maps as exhibited by the component properly operating that could be compared, quite rapidly, with those recorded in real time on the component under exercise.

References

1. Haque, S., Siddabattula, K., Craven, M., Wen, S., Liu, X., Boroyevich, D., Lu, G.-Q.: Design issues of a three-dimensional packaging scheme for power modules. Microelectron. Reliab. **41**, 295–305 (2011)
2. Haque, S., Stinnett, W.A., Nelson, D.J., Lu, G.-Q.: Thermal management of power electronics modules packaged by a stacked-plate technique. Microelectron. Reliab. **39**, 1343–1349 (1999)
3. Shkarayev, S., Madenci, E., Ibnabdeljalil, M., Savruk, M.P.: Analytical stress singularities for a crack at a Bi- or triple junction of dissimilar materials with bilinear behaviour. Eng. Fract. Mech. **68**, 475–486 (2001)
4. Massénat, M.R., Val, A.: High density modular packaging for space electronics. Int. J. Microcircuits Electron Packag. **23**(3), 265–271 (2000)
5. Casavola, C., Lamberti, L., Moramarco, V., Pappalettera, G., Pappalettere, C.: Experimental analysis of thermo-mechanical behaviour of electronic components with speckle interferometry. Strain **48**(6), 497–506 (2013)
6. Barile, C., Casavola, C., Pappalettera, G., Pappalettere, C.: Mechanical characterization of SLM specimens with speckle interferometry and numerical optimization. In: Conference Proceedings of the Society for Experimental Mechanics Series, vol. 6, pp. 837–843 (2011)
7. Barile, C., Casavola, C., Pappalettera, G., Pappalettere, C.: Residual stress measurement by electronic speckle pattern interferometry: a study of the influence of analysis parameters Struct. Integr. Life **12**(3), 159–163 (2012)
8. Casavola, C., Lamberti, L., Pappalettera, G., Pappalettere, C.: Application of contouring to dental reconstruction. In: Conference Proceedings of the Society for Experimental Mechanics Series, vol. 3, pp. 183–191 (2015)
9. Barile, C., Casavola, C., Pappalettera, G., Pappalettere, C.: Hybrid characterization of laminated wood with ESPI and optimization methods. In: Conference Proceedings of the Society for Experimental Mechanics Series, vol. 3, pp. 75–83 (2013)
10. Barile, C., Casavola, C., Pappalettera, G., Pappalettere, C.: Analysis of the effects of process parameters in residual stresses measurements on titanium plates by HDM/ESPI. Measurement **40**, 220–227 (2014)
11. Barile, C., Casavola, C., Pappalettera, G., Pappalettere, C.: Residual stress measurement by electronic speckle pattern interferometry: a study of the influence of geometrical parameters. Struct. Integr. Life **11**(3), 159–163 (2012)
12. Barile, C., Casavola, C., Pappalettera, G., Pappalettere, C., Tursi, F.: Drilling speed effects on accuracy of HD residual stress measurements. Residual Stress, Thermomechanics & Infrared Imaging, Hybrid Techniques and Inverse Problems, vol. 8, pp. 119–125. Springer, New York (2014)
13. Barile, C., Casavola, C., Pappalettera, G., Pappalettere, C.: Considerations on the choice of experimental parameters in residual stress measurements by hole-drilling and ESPI. Frat. Integr. Strut. **30**, 211–216 (2014)
14. Barile, C., Casavola, C., Pappalettera, G., Pappalettere, C.: Remarks on residual stress measurement by hole-drilling and electronic speckle pattern interferometry. Sci. World J. **2014**, 7 (2014)
15. Casavola, C., Pappalettera, G., Pappalettere, C.: Design of a double-illumination ESPI system for the measurement of very slow motions. Adv. Opt. Methods Exp. Mech. **3**, 97–102 (2015)

16. Dilhaire, S., Jorez, S., Cornet, A., Schaub, E., Claeys, W.: Optical method for the measurement of the thermomechanical behaviour of electronic devices. Microelectron. Reliab. **39**, 981–985 (1999)
17. Salbut, L., Kujawinska, M.: The optical measurement station for complex testing of microelements. Opt. Lasers Eng. **36**, 225–240 (2001)
18. Nassim, K., Joannes, L., Cornet, A., Dilhaire, S., Schaub, E., Claeys, A.: Thermomechanical deformation imaging of power devices by electronic speckle pattern interferometry (ESPI). Microelectron. Reliab. **38**, 1341–1345 (1998)
19. Guo, Y., Lim, C.K., Chen, W.T., Woychik, C.G.: Solder ball connect (SBC) assemblies under thermal loading: I. Deformation measurement via moire interferometry and its interpretation. IBM J. Res. Dev. **37**, 635–647 (1993)
20. Kujawinska, M.: Interferogram Analysis. Institute of Physics Publishing, Philadelphia (1993)
21. SmartTech Ltd. Fringe Application 2001 Version 1.0, Warsaw (Poland). www.smarttech.pl (2001)
22. Ghiglia, D.C., Pritt, M.D.: Two-Dimensional Phase Unwrapping Theory, Algorithms and Software. Wiley Interscience, New York (1998)
23. Ching, N.H., Rosenfeld, D., Braun, M.: Two-dimensional phase unwrapping using a minimum spanning tree algorithm. IEEE Trans. Image Process. **1**, 355–365 (1992)
24. Abdérafi, C.R., Laronde, F., Bigaud, F.: Robustness Evaluation Using Highly Accelerated Life Testing, 2nd edn. Springer, London (2011)

Chapter 41
Shear Banding Observed in Real-Time with a Laser Speckle Method

Pasi Karppinen, Antti Forsström, Kimmo Mustonen, and Sven Bossuyt

Abstract In many high-strength materials, such as in metallic glasses, localized deformations can lead to quasi-brittle behavior where the amount of energy dissipated by mechanical deformation prior to material failure is small, as only a small volume fraction of the material deforms inelastically. Thus, techniques that allow observations of localized deformations at relevant length and time scales are instrumental in order to engineer such materials. Here, a real-time optical system based on high-speed imaging of laser speckle is applied to the propagation of shear bands in metallic glass. The quality and accuracy of information obtainable by this technique as well as its applicability to study important aspects of shear banding in metallic glasses are discussed and a comparison with more conventional approaches are presented.

Keywords Metallic glass • Shear band • Real-time • Laser speckle • High-speed imaging

41.1 Introduction

Metallic glasses can be thought of as the extreme limit of solid crystalline metals with reduced grain size, or the extreme limit of liquid metals with reduced fluidity. Their amorphous atomic structure confers them with a set of unique properties, some of which highlight that important aspects of the behavior of liquids are not yet properly understood, and that useful properties of crystalline metals become increasingly precarious when their mechanical properties are pushed to extremes, and some of which make them interesting for practical applications. In particular, whereas metallic glasses are extremely ductile on a microscopic scale, embodying ideal elastic-plastic behavior, many of them are quasi-brittle macroscopically [1]. The origin of this mismatch between micro- and macro-mechanics is strain localization: the deformation becomes highly dynamic as well as highly localized when it is concentrated in a shear band that is typically on the order of 100 nm wide. Interest in these materials has been fueled by the discovery of bulk metallic glass (BMG) forming compositions in the 1980s [2, 3], and the more recent discoveries of ultra-hard [4] and ultra-tough BMG compositions [5].

Recent reviews testify to the widespread interest in BMG both from a fundamental science perspective and for practical applications [6–8]. Metallic glasses are metals that have been solidified by cooling from the molten state to below the glass transition temperature, without crystallizing. They have the amorphous structure of the metallic liquid, but they are solids. Completely homogeneous above the level of the atomic-scale randomness of their amorphous structure, they are ideal model materials. BMG are also technologically relevant. Ordinary metals need to be cooled at extremely high cooling rates, $>10^6$ K/s, to avoid crystallization and form a glass, but cooling at 0.1 K/s suffices for the very best BMG alloys. As a result, BMG's can be formed much like plastics by injection molding or by thermoplastic forming, with excellent surface finish and precise tolerances. Without cold working or heat treatment, complex shapes can be produced with excellent mechanical properties: purely elastic deformation up to a yield strain of typically 2 %, resulting in tensile strength from 1500 to 6000 MPa, with Young's modulus from 70 to 275 GPa, depending on alloy composition. However, this ultra-high strength would be more useful if the materials also had high toughness.

P. Karppinen
ProtoRhino, Salomonkatu 17A, Helsinki 00100, Finland

A. Forsström • S. Bossuyt (✉)
Department of Mechanical Engineering, Aalto University, PO Box 14200, Aalto 00076, Finland
e-mail: sven.bossuyt@aalto.fi

K. Mustonen
ProtoRhino, Salomonkatu 17A, Helsinki 00100, Finland

Department of Physics, University of Vienna, Boltzmanngasse 5, Vienna 1090, Austria

Thus, there has been much research into characterizing and understanding the shear banding phenomena that are responsible for macroscopically quasi-brittle behavior, as well as ways to mitigate their effect [1]. This poses particular challenges, due to the spatial [9] and temporal [10] localization of the deformation in shear bands. There has been limited success with high-speed video of shear bands in metallic glass [11, 12] to analyze the images *a posteriori*. Here, we present a method to detect localized deformation in metallic glasses with millisecond-scale temporal resolution and micrometer-scale spatial resolution, in real time.

41.2 Method Description

41.2.1 Optical Detection of Shear Bands by DynaMat Laser Speckle Measurement System

A non-contact method for detection of shear band activity can be realized by optically tracking the specimen surface at sufficiently high magnification to resolve events at micrometer scale. The analysis of conventional images, however, when the location of the shear bands is not *a priori* known, is time-consuming. To overcome this barrier, we have used a commercially available, standalone FlexRHINO DynaMat laser speckle measurement system (ProtoRhino Ltd, Finland). The system consists of a high-speed camera equipped with a telescopic zoom lens (visible in Fig. 41.1a), a coherent laser source (638 nm laser diode, power 200 mW) for specimen illumination, and a FlexRHINO processing unit with a field programmable gate array (FPGA) chip for data acquisition and storage.

The formation of shear bands was detected by utilizing the speckle effect: a scattered coherent light results in a 2-dimensional interference pattern, due to surface roughness and resulting varying path lengths (Fig. 41.1b) [13]. The observed interference pattern (i.e. speckle pattern) is extremely sensitive for changes in the surface roughness and thus, to appearance of small-scale damage such as voids, cracks, and slip bands [14]. With the aid of a high speed monitoring system, the intention was to detect *in-situ the* shear band formation in metallic glass.

The system acquired 500 fps (8-bit gray scale) at a resolution of 120×200 pixels (pixel size 7.9 μm), corresponding to a total imaging area of 0.95 mm $\times$ 1.58 mm, from which an arbitrary region of interest (ROI) could be cropped out. The frame rate was limited to 500 fps due to low reflectivity of the sample, which resulted in low photon flux. The image data was transferred and stored on the FlexRHINO unit through a camera link connection for later analysis. Every 500th frame was refreshed on the operator monitor to follow the shear band formation.

41.2.2 The Reference Method: Scanning Electron Microscopy

For quantitative comparison, the samples were imaged with scanning electron microscopy (SEM). A Zeiss Ultra 55 field-emission scanning electron microscope (FEG-SEM) was used with acceleration voltage of 10 kV and by utilizing an in-lens detector. Imaging was done before the tensile test to verify the pristine condition of the specimen and after straining the specimen to verify the cause of observed events in the laser speckle pattern. Therefore, the tensile test had to be halted and the sample removed for SEM observations whenever interesting events appeared.

Fig. 41.1 The measurement setup and principle of operation: (**a**) the test setup. The illuminated specimen is visible through the round window in the enclosed tensile testing chamber. (**b**) The specimen is monitored perpendicularly through a zoom lens with a high-speed camera and illuminated with a laser from the side. A low angle of incidence results in scattered light to reach the camera and form a speckle pattern
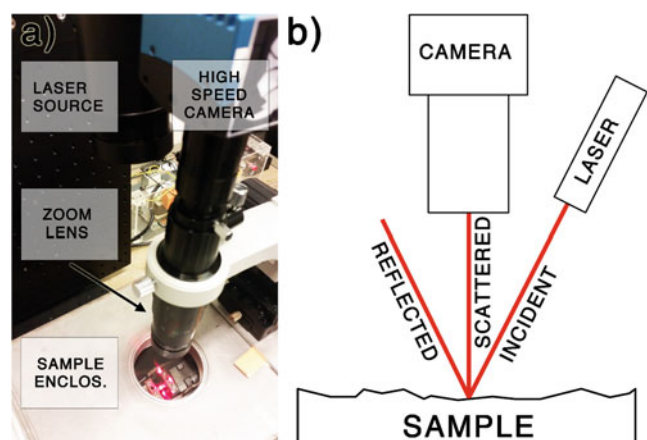
41.2.3 The Specimen Preparation

A metallic glass ingot with composition $Zr_{55}Cu_{10}Ni_{30}Al_5$ was produced by melting together the pure elements (>99.9 % purity), under a purified argon atmosphere, and casting into a copper mold, using a tilt-casting arc-melting furnace [15]. The maximum thickness of the ingot was 5 mm. The tensile test specimens were cut from the cast ingot by electro discharge machining (EDM). The specimen geometry is presented in Fig. 41.2a. Notches were included in the middle of the gauge length to localize the maximum stress, and therefore, to make sure that shear bands formed in the monitored area. The notches were sharpened with a diamond file, because in the preliminary tests the rough EDM cut surface caused over exposure in the laser speckle pattern near the edge of the notch. After filing the notches, the sample surfaces were polished to roughness of 1 μm with conventional wet grinding and diamond paste polishing. The final specimen thickness was then 0.2–0.3 mm depending on the specimen.

41.2.4 The Measurements

For mechanical testing, the specimens were placed into a purpose built chamber with the possibility of using a gas atmosphere/vacuum, hydrogen charging, and temperature control of the specimen. However, these were not used for the tests presented in this paper. A Deben 2 kN tensile test machine was placed inside the chamber so that the specimen could be monitored through a transparent borosilicate window glass (c.f. Fig. 41.1a). To improve reproducibility of the measurement, the camera focus distance was set manually under normal white light illumination conditions (Fig. 41.2b).

The specimens were subjected to a steadily increasing stress at strain rate of 0.033 mm/min until changes in the speckle pattern were visually observed by the DynaMat operator. The tensile test was then halted and the specimens were removed from the tensile testing machine, so that the shear band formation could be imaged in SEM. After imaging, the specimen was inserted back to the tensile testing machine so that straining could be continued. After seeing more events the test was halted again and more imaging was done in SEM.

41.3 Results

The SEM observations reveal a clear emergence of shear bands from the area of highest stress at the bottom of the notches (Fig. 41.3). In pristine condition the sample surface is smooth, but after the first loading cycle (first CYCLE) roughly 100 μm long shear bands emerge from the sharpest features perpendicular to the edge of the notch. The shear bands become more
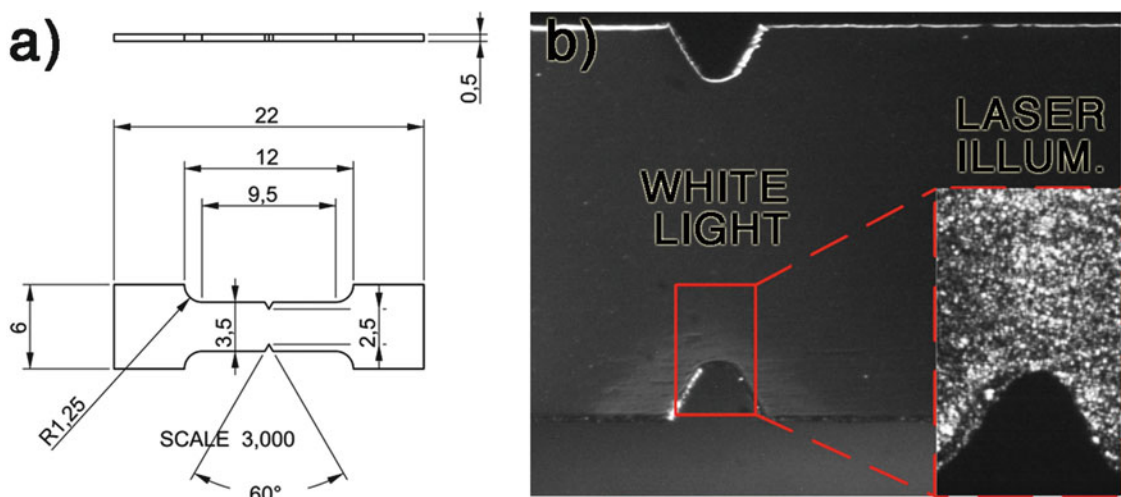

Fig. 41.2 (**a**) The specimen geometry. (**b**) The specimen imaged with white light illumination, and the speckle pattern as seen by FlexRHINO DynaMat with laser illumination (*insert*)
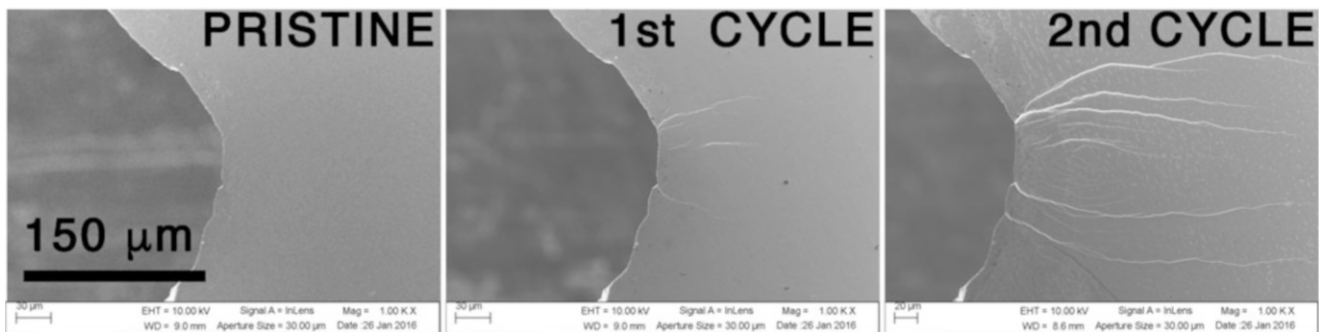
Fig. 41.3 SEM observations of the specimen at different loading stages: pristine, after the first loading cycle, and after the second loading cycle

pronounced after the second stress cycle (second CYCLE) extending to 200–300 μm. It is possible to see that the same shear bands continue growing, as at the same time new shear bands form.

To extract spatial and temporal occurrence of slip band formation from the image stream data, a dynamic window of successive images were bandpass filtered (pixel-by-pixel) at 40–60 Hz. This frequency range was optimized iteratively, since the rate at which the interesting events occurred was unknown. An occurrence was interpreted as an event only if after the filtration, the pixel amplitude surpassed a given trigger value. The events were overlaid on the initial DynaMat image data, of which a few examples are shown in Figs. 41.4 (after the first loading cycle) and 41.5 (after the second loading cycle).

In order to correlate the thus extracted speckle pattern events with real events on the specimens, the optical data was overlaid with SEM images, also shown in Figs. 41.4 and 41.5. This was possible since the actual magnification of both speckle pattern and SEM images were known and hence, the images could easily be scaled and overlaid at a precision of a single pixel (~7.9 μm). The events plotted in both, Figs. 41.4 and 41.5 are extracted from the image stream at different positions 5–20 s prior to stopping the tensile test at both first and second loading cycle. As evident, the events overlap with the emergence of shear bands as observed with the SEM. However, this overlap is not perfect, which we suspect is an artefact caused by both plastic and elastic deformations in the sample material: the SEM images were acquired exclusively after each loading cycle and thus, not in the same moment as during the loading. This discrepancy cannot easily be compensated for, when overlaying the optical events on the SEM images.

Initially, the events are concentrated where the maximum stress is situated, i.e. at the tip of the notch (Fig. 41.4 left column). They then proceed deeper into the material as the stress increases (Fig. 41.4 middle column and right column). This corresponds to the well-established mechanism of shear banding at a blunt notch in metallic glasses [1].

During the second loading cycle the events continue to progress deeper into the material. Again, the position and size of these events correlate well with what is seen in SEM, as shown in Fig. 41.5. The frequency and area of occurrence of the events become greater as the shear bands become longer.

41.4 Discussion

The laser speckle method was capable of detecting the emergence of shear bands in glassy metals in real-time. The appearance of the shear bands was also observed in the SEM after the loading cycles. To our knowledge, this is the first demonstration of such capability and we will shortly discuss prospects of these findings.

The speckle pattern, being an intensity pattern produced by mutual interference of wave fronts, is extremely sensitive for changes in surface roughness when formed from a diffracted wave bundle [13]. Hence, by tracking the speckle pattern by adequate optical means, the appearance of surface features larger than half of the wavelength of the light source ($\sim \frac{1}{2} \lambda =$ ~300 nm for a typical 633 nm laser). The temporal and spatial resolution of such a system is set by a combination of pixel resolution, optical magnification, and the frame rate at which the speckle patterns are acquired. In this contribution we observed events at frequency of 40–60 Hz caused by shear band formation. This frequency suggests that when considering the Nyquist theorem, a frame rate of as low as ~200 fps would satisfy the image acquisition demand. With modern high-speed cameras and data links, image size of several megapixels could easily be recorded at satisfying frame rate. This opens up possibilities to acquire fairly large image area of even several square centimeters, while still reaching a pixel resolution of 7.9 μm or smaller.
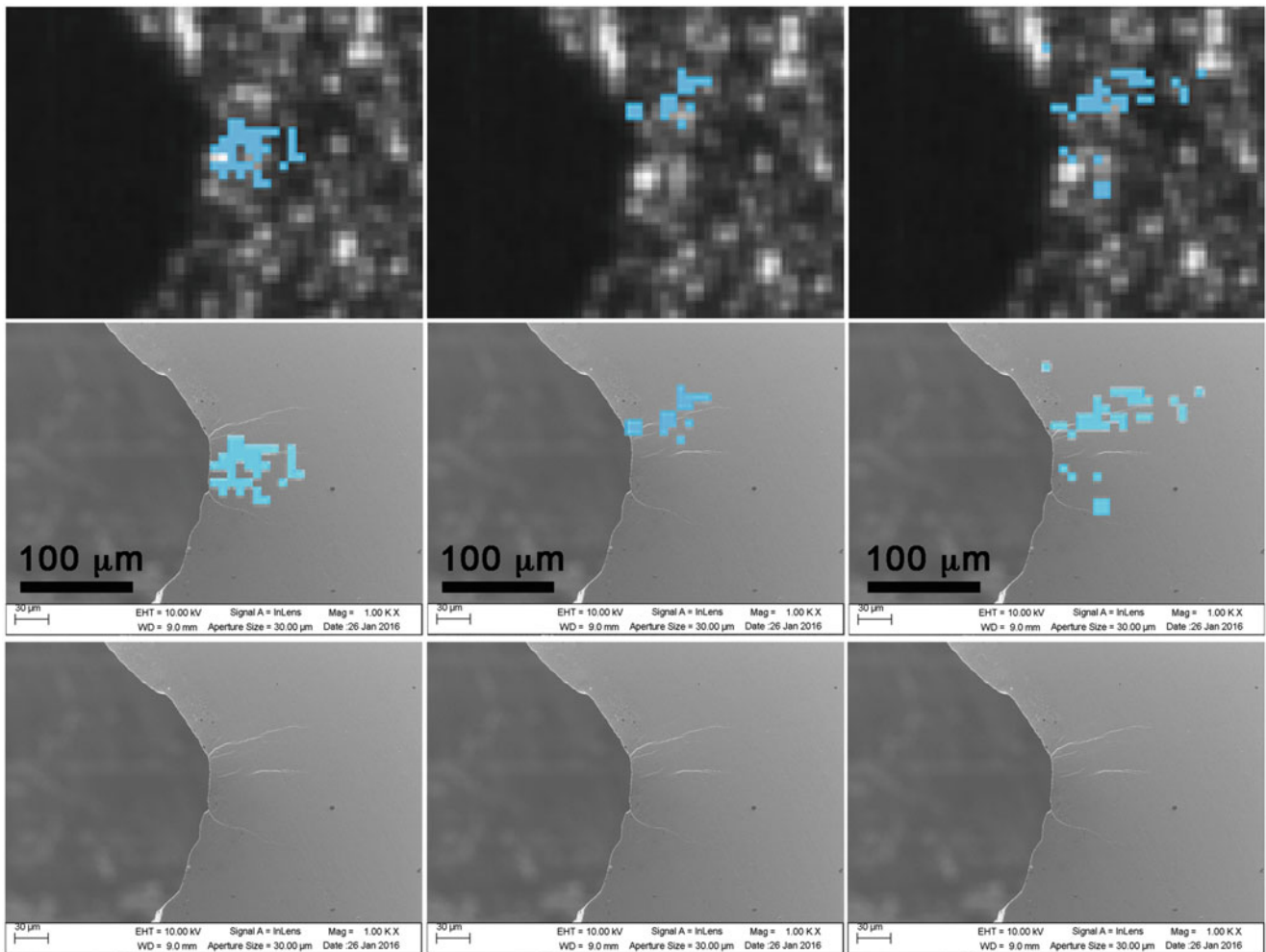
Fig. 41.4 Shear bands as seen by the laser speckle method during the first loading cycle and SEM after the loading cycle. The *upmost row* shows events taking place at frequency of 40–60 Hz in the image data, overlaid on top of the speckle pattern recorded by the DynaMat 5–20 s before stopping the tensile test. In the *middle row*, the same events are overlaid on the SEM image taken after the first loading cycle. For comparison, the *bottom row* repeats the SEM image to show clearly the actual position of the shear bands

Even more interesting horizons are provided by the FPGA technology. The processing power of FPGA allows running the image processing algorithms in real-time, which would greatly reduce the data storage requirements, as only interesting events would need to be stored for later analysis. This would also enable an automatic stopping of stress ramping when interesting events occur, thus providing a possibility to observe damage propagation in step-wise manner by other means, such as electron microscopy.

As for future work, our measurements were conducted in temperature-controlled enclosure with a transparent viewport for optical measurements, allowing measurements also in lower temperature. Under such conditions the propagation velocity of shear bands is lower and the localization of deformation in shear bands no longer manifests as serrated flow [1, 10]. The ability to observe the dynamics of localized flow using the method presented here would therefore be especially useful for such experiments.

41.5 Conclusion

In this contribution, we have successfully demonstrated the first real-time optical detection of shear band formation in glassy metals by using a laser speckle based method. The detection was verified by observations using a scanning electron microscope. These complementary methods suggest that slip bands emerge from the point of maximum stress at the sample
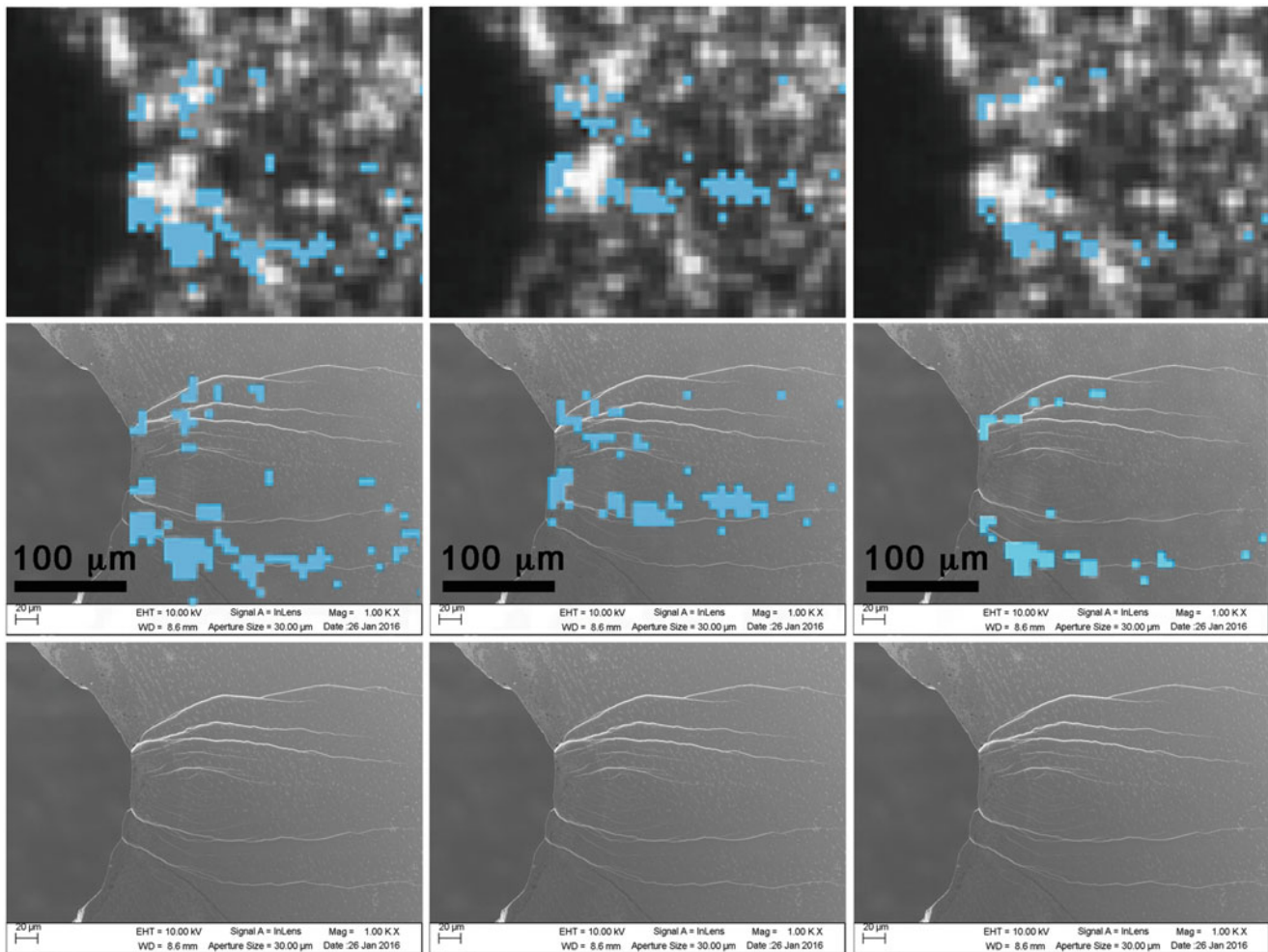
Fig. 41.5 Shear bands as seen by the laser speckle method during the second loading cycle and SEM after the loading cycle. The *upmost row* shows events taking place at frequency of 40–60 Hz in the image data, overlaid on top of the speckle patterns recorded by the DynaMat 5–20 s before stopping the tensile test. In the *middle row*, the events are overlaid on the SEM image taken after the second loading cycle. For comparison, the *bottom row* repeats the SEM image to show clearly the actual position of the shear bands

edge and proceed towards the center. According to observations presented, the events related to shear band propagation were detected at pixel resolution of ~7.9 μm and at frequency of 40–60 Hz, setting the minimum frame rate of ~200 fps for their reliable detection. Although smaller pixel size and higher frame rates would increase both temporal and spatial resolutions, this would be achieved at inflated overall expenses both in computing power and money. Yet, even at current configuration, the method demonstrated opens up a new avenue for a cost efficient, real-time detection of micro-scale deformations in glassy metals and possibly in materials thereof.

References

1. Greer, A.L., Cheng, Y.Q., Ma, E.: Shear bands in metallic glasses. Mater. Sci. Eng. R **74**, 71–132 (2013)
2. Inoue, A., Zhang, T., Masumoto, T.: Zr-Al-Ni amorphous alloys with high glass transition temperature and significant supercooled liquid region. Mater. Trans. JIM **31**(3), 177–183 (1990)
3. Peker, A., Johnson, W.L.: A highly processable metallic glass—$Zr_{41.2}Ti_{13.8}Cu_{12.5}Ni_{10.0}Be_{22.5}$. Appl. Phys. Lett. **63**(17), 2342–2344 (1993)
4. Wang, J., Li, R., Hua, N., Zhang, T.: Co-based ternary bulk metallic glass with ultrahigh strength and plasticity. J. Mater. Res. **26**(16), 2072 (2011).
5. Demetriou, M., Floyd, M., Crewdson, C., et al.: Liquid-like platinum-rich glasses. Scr. Mater. **65**, 799–802 (2011)
6. Inoue, A., Takeuchi, A.: Recent development and application products of bulk glassy alloys. Acta Mater. **59**, 2243–2267 (2011)

7. Chen, M.: Mechanical behavior of metallic glasses: microscopic understanding of strength and ductility. Annu. Rev. Mater. Res. **38**, 445–469 (2008)
8. Schuh, C., Hufnagel, T., Ramamurty, U.: Mechanical behavior of amorphous alloys. Acta Mater. **55**, 4067–4109 (2007)
9. Zhang, J., Aimedieu, P., Hild, F., Roux, S., Zhang, T.: Complexity of shear localization in a Zr-based bulk metallic glass. Scr. Mater. **61**(12), 1145–1148 (2009)
10. Klaumünzer, D., Maaß, R., Dalla Torre, F.H., Löffler, J.F.: Temperature-dependent shear band dynamics in a Zr-based bulk metallic glass. Appl. Phys. Lett. **96**, 061901 (2010)
11. Song, S.X., Wang, X.-L., Nieh, T.G.: Capturing shear band propagation in a Zr-based metallic glass using a high-speed camera. Scr. Mater. **62**(11), 847–850 (2010)
12. Yokoyama, Y., Tokunaga, H., Yavari, A., et al.: Viscous flow in sliding shear band formed during tensile deformation of hypoeutectic Zr-based metallic glass. Intermetallics **19**, 1683 (2011)
13. Dainty, C. (ed): Laser Speckle and Related Phenomena. Springer, Berlin (1984). ISBN 0-387-13169-8
14. Jones, R., Wykes, C.: Holographic and Speckle Interferometry. Cambridge University Press, Cambridge (1983)
15. Soinila, E., Pihlajamäki, T., Bossuyt, S., Hänninen, H.: A combined arc-melting and tilt-casting furnace for the manufacture of high-purity bulk metallic glass materials. Rev. Sci. Instrum. **82**, 073901 (2011)

Chapter 42
Numerical and Experimental Eigenmode Analysis of Low Porosity Auxetic Structures

L. Francesconi, M. Taylor, K. Bertoldi, and A. Baldi

Abstract This study presents an evaluation of the mechanical behaviour of low porosity, ductile auxetic structures.

Using time-averaged speckle interferometry and a specific experimental set-up, the eigenmodes and displacement fields of three low-porosity metallic auxetic samples were assessed and compared with the numerical simulations obtained using the commercial software Abaqus/Standard (Simulia Providence, RI).

Guided by the finite element predictions, the eigenmode analysis was carried out by vibrating the specimens—each characterized by a different pore geometry—from 100 Hz to about 10 kHz analysing the structural response. A good agreement between the numerical calculations and the experimental results was found. This study not only validates the numerical-experimental approach used to analyse materials, but also to open a way to test and validate the performances of negative Poisson's ratio structures and meta-materials in general applications.

Furthermore, the findings of this work provides a new convincing and reliable experimental data, enlarge the knowledge about the elastic instabilities in metallic auxetic structures, supporting their use in critical applications.

Keywords Auxetic material • Digital image correlation • Low porosity • Negative Poisson's ratio • Speckle interferometry

42.1   Introduction

A structure can be defined "auxetic" if, when stretched along a direction, not only it becomes longer in the direction of the stretch but, it shows a lateral expansion when the normal experience should suggest a contraction to happen [1, 2].

The ratio between the deformation along the direction of the stretch and the transverse expansion (or contraction) is a scalar quantity called Poisson's ratio (often indicated with the Greek letter "ν"). This is a fundamental parameter to describe the mechanical behaviour of materials. Most common engineering materials have a positive Poisson's ratio—they contract laterally when extended. However, the possibility of having negative values of ν, i.e. auxetic behaviour, is thermodynamically admissible [2]. Despite this counterintuitive behaviour, auxetic materials are not so uncommon; several auxetic materials have been discovered and designed at different scales [2, 3], and used in different applications and fields [2–5].

It is important to underline that, for the vast majority of the cases here cited, auxetic behaviour is not an innate property of the materials but it's something provided by the structure, usually through a periodic bi-dimensional or tri-dimensional patterns of voids or inclusions that, during the deformation processes, allow the systems to perform particular changes in shape and in pores' volume.

Although most of the existing applications use rubber-like elastic materials, recent studies have focused on low (2–10 % of through-thickness porosity) and ultralow (below 2 %) porosity ductile materials [4–6] in order to increase some essential properties as fracture toughness, indentation resistance, thermo-mechanical properties and vibration/acoustic damping capability.

Focusing on perforated structures with a reduced porosity is a crucial point for the researchers working in this field since large porosity macro-structures have a very limited structural applications while low porosity (from 2 to 10 %) ones—especially in critical sector such as aerospace or aeronautic engineering [–] and protection devices [–] for sport, civil and

L. Francesconi (✉) • A. Baldi
Dipartimento di Ingegneria Meccanica, Chimica e dei Materiali, Università degli Studi di Cagliari, Via Marengo, 2, Cagliari 09123, Italy
e-mail: lucafrancesconi@unica.it

M. Taylor
Department of Mechanical Engineering, Santa Clara University, Santa Clara, CA 95053, USA

K. Bertoldi
School of Engineering and Applied Science, Harvard University, Cambridge, MA 02138, USA

335

army—could have a remarkable impact combining qualities of ductile materials with the additional features typical of these smart structures.

While utilizing ductile materials for the bulk structure has many positives, there are some drawbacks such as, stress concentrations at void interfaces, manufacturing limits, strain-hardening processes, and plasticity. This is particularly true when low porous structures are taken into account since the fabrication processes and the experimental testing have to deal with very small features, thus requiring non-trivial techniques and analysis.

Optical methods for deformation measurements, such as Digital Image Correlation (DIC), speckle and moiré interferometry, have been used in the last decades in different fields [7] and they represent a mature and very suitable non-contact experimental way to assess the behaviour of auxetic structures in both static and dynamical range.

Recently Taylor et al. [8] tested finite-size low porosity auxetic samples using DIC, showing good agreement between experimental and numerical simulations.

Although some recent numerical, analytical and experimental studies [5, 6, 8] demonstrated that auxetic behaviour could be induced in finite size structures cutting voids shapes from thin sheets of metals, no known experimental work has been carried out to characterize the dynamic or vibration behaviour. In particular, there has been no numerical or experimental characterization of the eigenmode behaviour of this class of structures yet.

This work aims to make a significant step in that direction, providing a modal analysis and analyzing the dynamic structural response of three low porosity auxetic metal samples characterized by different geometry of the pores.

The eigenmodes analysis of the samples was carried out both numerically through finite element simulations using the commercial software Abaqus/Standard (Simulia Providence, RI), and experimentally, spanning a vast range of frequencies and extracting the in-plane and the out-of-plane eigenmodes using a piezoelectric-excited loading fixtures in union with speckle interferometry. The full displacement fields were recorded using "time-averaged speckle interferometry" while the samples are excited close to their natural frequencies.

A detailed description of the experimental setup and the methods used along all the investigation will be presented in the next sections.

42.2 Fabrication of the Samples

Four different rectangular samples (Fig. 42.1) of 300 × 50 mm by 1 mm made of stainless steel were cut using an electrical discharge machine (EDM). The choice of using an EDM was indispensable due to the disposition and to the small size of the voids' geometry. The samples are characterized by having the same porosity (i.e. the total volume of the voids divided by the total volume of the material), of about 4.55 %, so that they are considered low porosity structures.

The base cells (reported in right side of Fig. 42.1) of the samples follow a square array; the geometrical centre of each void is placed 6.25 mm distant from the next one both in the horizontal and in the vertical direction. Different geometries
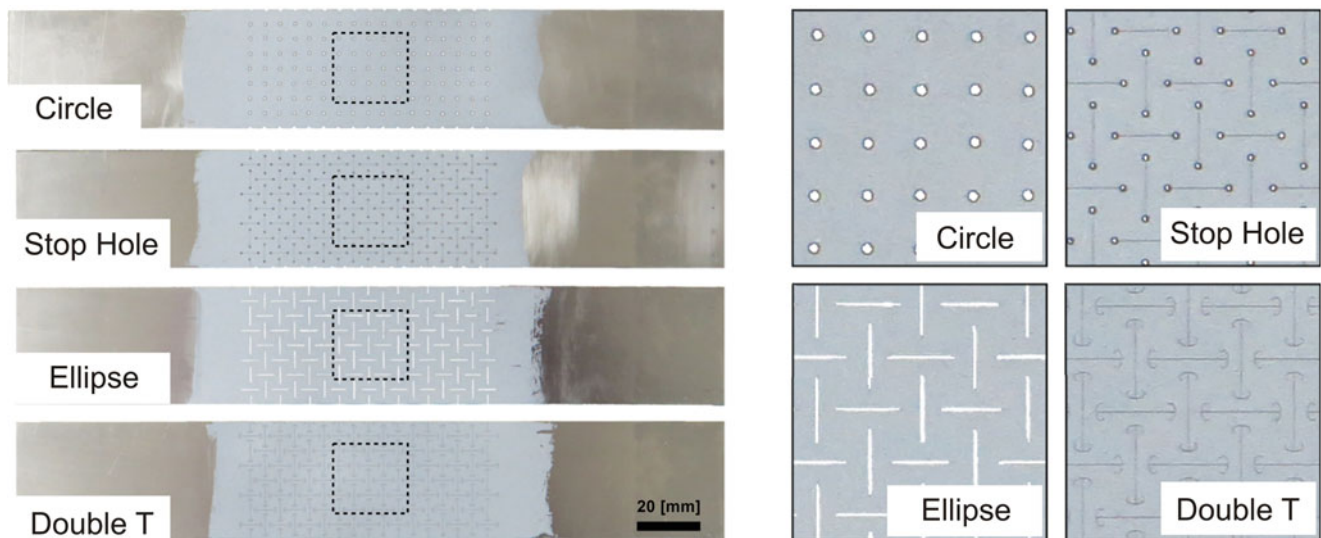

Fig. 42.1 Samples fabricated and tested in this study (*left*) and a magnification of the pattern and of the different features of the specimens (*right*)

Table 42.1 Effective Poisson's ratio of the tested samples

Poisson's ratio	Base material (stainless steel)	Circular (b)	Stop hole (c)	Ellipsis (d)	Double T (e)
	+0.30	+0.281	−0.671	−0.605	−0.832

were selected basing on the authors' experience and by numerically exploring several solutions; neither parametric studies nor optimization analyses have been performed.

The names "Stop Hole", "Ellipse", "Double T" and "Circle" refer to the geometry of the pores as visible in Fig. 42.1, but different considerations were made on the selection of the shapes:

The "Ellipse" was chosen since, based on the previous work of Bertoldi, Taylor et al. [6, 8], it was demonstrated that it's possible to tune the Poisson' ratio by the variation of the aspect ratio (the ratio between the two major axis) of a regular patterns of ellipsis. However, the modification of the aspect ratio of the ellipsis introduces in the structures very sharp tips leading to high stress concentration factors and allowing the samples to be easily prone to plasticity and failures. The other two proposed solutions, the "Stop Hole" and the "Double T", were then designed in order to limit this detrimental effect. The "circle" sample was fabricated and included in the study to provide a non-auxetic benchmark during the investigation. The first part of the investigation was to characterize the structure by calculating numerically the effective Poisson's ratio from the finite element simulations. The results are reported in Table 42.1:

42.3 Experimental Procedures and Methods

To accomplish the eigenmode analysis, the specimens need to be clamped and to be excited close to their natural frequencies. This goal was attained by designing a customized loading fixture modifying one of the two clamps of an Hemo fix-point vice (Fig. 42.2) to include a Thor Labs, PZS001 piezo actuator driven by an E-500 High Power (80 W) amplifier and a piezo-controller system manufactured by Physik Instrumente.

The additional support was made by aluminium and designed in order to load the samples along the longitudinal dimension of the sample, thus limiting the out-of-plane components of the displacement. Both the designing and the fabrication processes were supported and verified by means of finite element simulations.

During the testing operation, two different speckle interferometers were utilized to catch the intensity images of the speckle produced on the sample surfaces; among all the different possibilities, we used one optical set-up sensitive to the in-plane displacement and a second one partly sensitive to the out-of-plane component of the displacement [6, 9, 10].

The optical set-up, shown in the left and in the central part of Fig. 42.3, is relatively simple: the laser beam generated by a NdYg laser (Cobolt Samba, wavelength = 532 nm, power = 300 mW) is halved by a cubic beam splitter and then expanded and driven along the two branches by using other standard optical equipment; in particular, one of the two beams is reflected by a mirror moved by a piezo-actuator in order to perform the phase-shifting.

This is a fundamental step to quantitative measuring the displacement of the samples since at least three images are required to calculate the phase. Among all the possible available solutions, we favored the 5-image Hariharan phase-shifting algorithm [11] due to its superior performance in error compensation and precision, compared to other classical methods. The speckle field was recorded using a CCD digital mono camera (Allied Vision Pike F421, resolution = 2048 × 2048, pixel size 7.4 μm) using time-averaged speckle interferometry.

The "time-averaged method" [12, 13], is a particular way to perform the numerical integration of the speckle fields directly using the camera CCD; if the frequency of the object recorded is higher than the shutter, during a single acquisition the sensor of the camera "physically" integrates the speckle patterns (having a varying light intensity during the acquisition period) and straight provides the Bessel fringes connected with the displacement of the object.

In the right side of Fig. 42.3, a basic scheme of the optical setup is presented for the interferometer sensitive to the in-plane displacement but the second configuration is also very similar since the two set-ups only differ in the orientation of the diffusing surface (the NPR sample) while no other changes are required in the remaining optical equipment.

By rotating the specimen with respect to a vertical axis, the sensitivity vector becomes a simultaneous function of the in-plane and the out-of-plane components of the displacement. In the case the sample is perfectly parallel to the CCD camera (as showed in the three frames of Fig. 42.3), only the planar component of the displacement vector is obtained.

The main advantage of using an interferometer partly sensible to the out-of-plane displacement is that, since the transverse motion of the samples is large, a normal interferometer sensitive to the out-of-plane displacement could easily run into de-correlation problems due to their high sensitivity.

Fig. 42.2 The modified
support of the Hemo fix-point
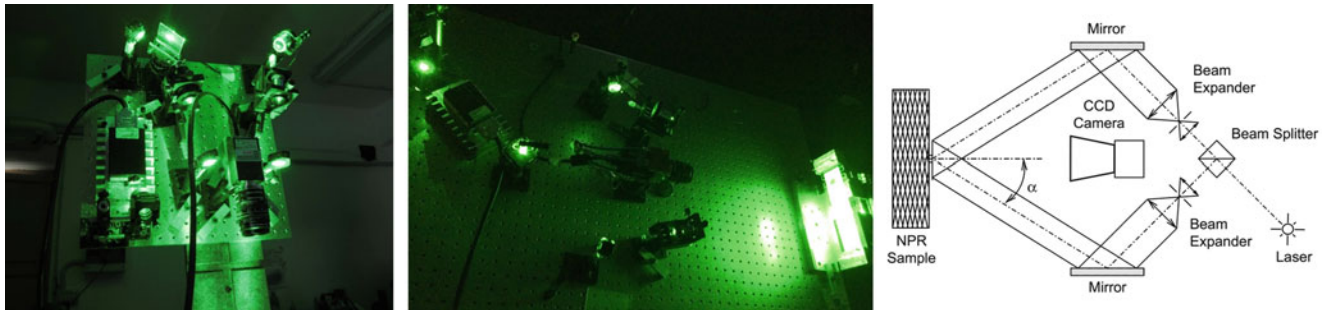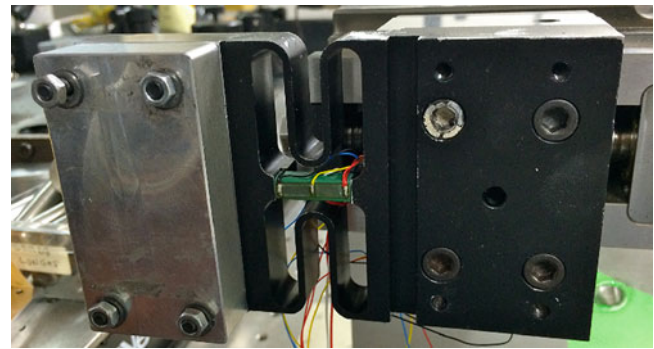vice with the piezo-electric
actuator

Fig. 42.3 Interferometers sensitive to the in-plane displacement used in this study (*left* and *centre*) and a schematic view of the optical set-up (*right*)

That's the reason why this device is often referred as "desensitized interferometer". Furthermore, the same set-up offers great advantages while working "in-plane" because simply modifying the angle between the two illuminating directions it's possible to change the sensitivity of the measurements, a particular useful aspect analysing stiffer samples and in-plane modes where very small displacements have to be detected.

42.4 Results and Discussions

The commercial finite element code ABAQUS/Standard was used to model the samples, run the modal analysis and predict the structural response of the samples. The specimens of Fig. 42.1 were modeled using a single layer of about 200,000 ten-node, quadratic tetrahedral solid elements (Abaqus element type C3D10).

The eigenmode and the eigenfrequencies have been obtained with a single step dynamic stress/displacement analysis for natural frequency extraction using the Lanczos eigenvalue extraction methods.

Two different constraint conditions were considered: the boundary conditions were first implemented to reproduce the real constraint conditions used during the experimental testing stage while, in the second case the out-of-plane motion was neglected for all the nodes of the model to focus exclusively on the in-plane modes calculations.

The results of the numerical simulation are reported in Fig. 42.4: on the left part of the figure it is possible to visualize the first 15 eigenmodes (plotted together with the experimental data) for the four samples, while on the other side of the same image only the in-plane modes are reported for frequencies ranging from 0 to 35,000 kHz.

From the examination of Fig. 42.4, it appears that for the out-of-plane modes the agreement between the numerical simulations and the experimental results is excellent. The relative errors between the predictions and the experimental data were found to be in the order of 10–30 Hz leading also to an easy experimental determination of the eigenmodes. Through spanning a small range of frequencies using the numerical prediction as a starting point, the modes were differentiated by detecting the modification in the acoustic emissions. This detection was done through the use of a professional microphone connected to a PC with audio analyser software.

The out-of-plane chart plotted in the left side of Fig. 42.4 shows one more evidence of certain interest for several applications: since the sequence of the natural frequencies of the specimens is a function of the Poissons' ratio and the stiffness, it's possible to modify the dynamical behaviour of the samples by only modifying the voids' geometry (acting on
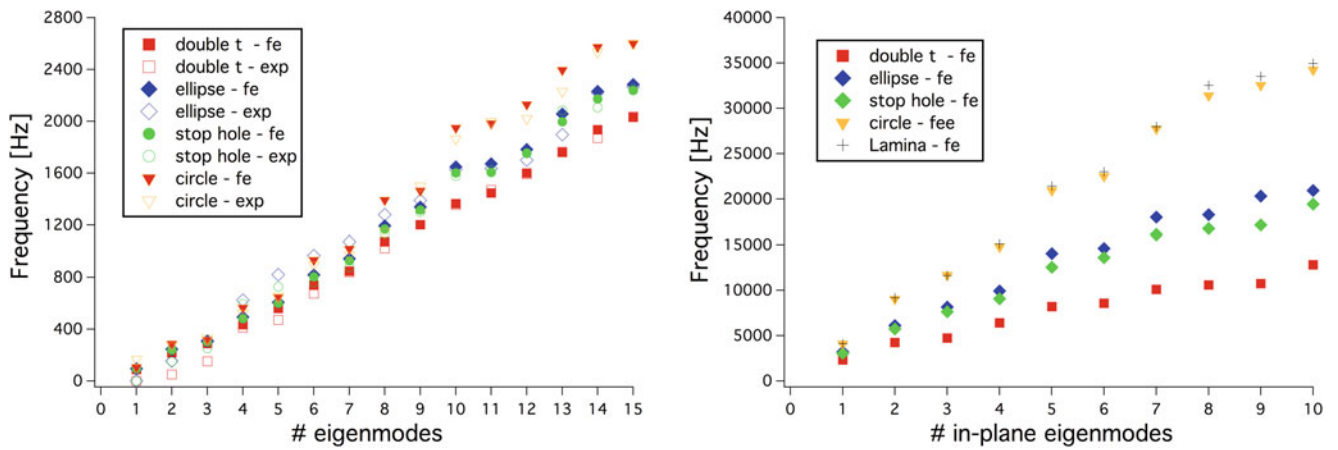
Fig. 42.4 Finite element simulation and experimental data for the out-of-plane (*left*) and the in-plane (*right*) eigenmodes of the four specimens tested in this study
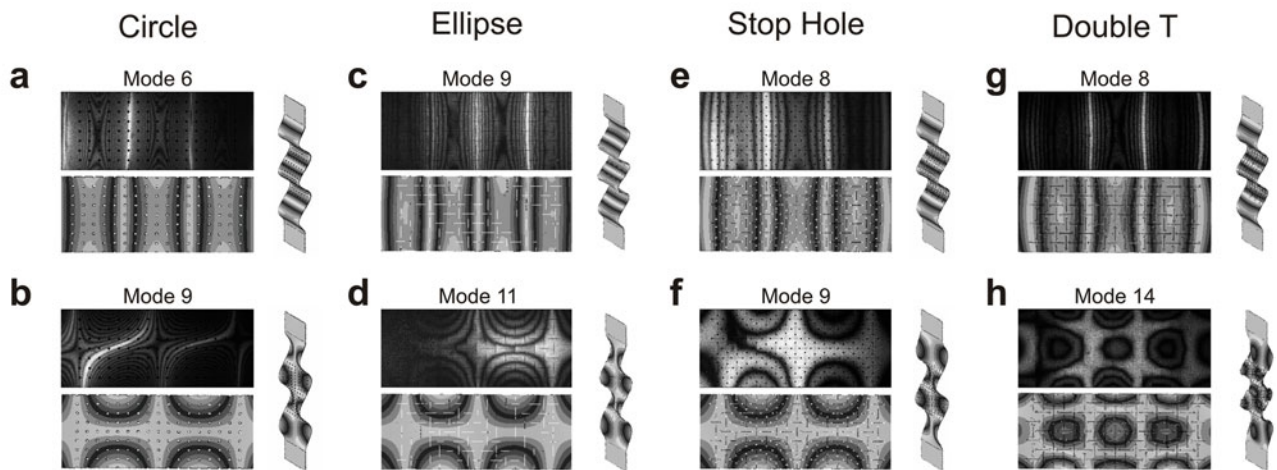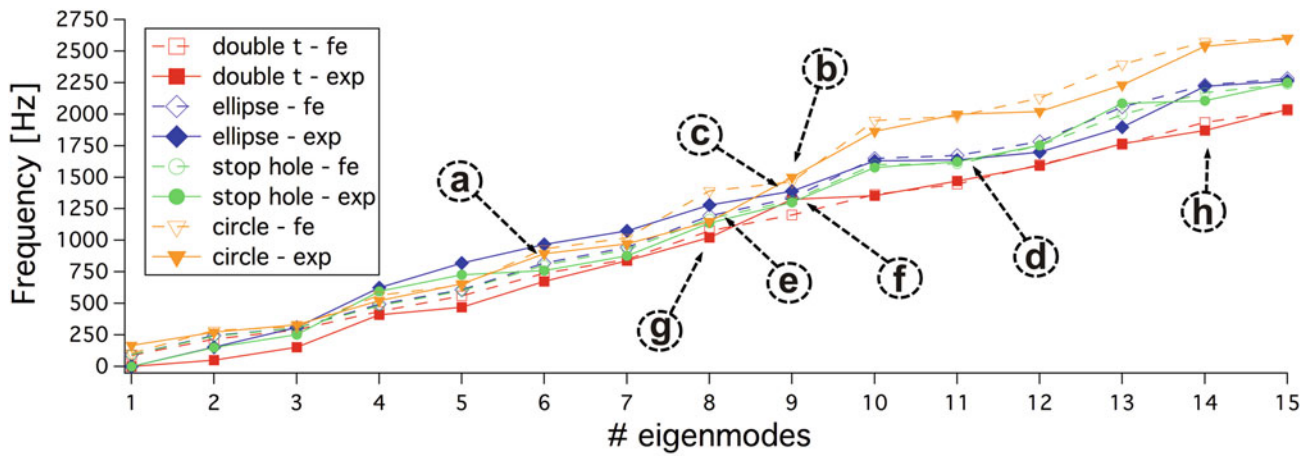

Fig. 42.5 Finite element simulation and horizontal and vertical displacement maps

the porosity and the stiffness of the samples), tuning the auxetic properties to obtain the desired effect and response of the materials.

To better understand the evolution of the out-of-plane modes, in Fig. 42.5 eight different eigenmodes were plotted spanning a range of frequencies between 0 and 3000 Hz. The pictures report the numerical vs. experimental curves of the

natural frequencies of the four samples and eight different spot (Fig. 42.5a–h) have been highlighted to show different behaviours of the samples by comparing the experimental and the finite element displacement maps.

In Fig. 42.5a–h, the displacement maps provided by Abaqus and by the speckle interferometry have been reported for flexural (top pictures: Fig. 42.5a, c, e, g) and torsional (Fig. 42.5b, d, f, h) eigenmodes; only the longitudinal component of the displacement (the one directed along the longer side of the specimens) was considered in the numerical simulation to correctly compare them with the experimental results obtained by speckle interferometry.

For each specimen a flexural and a torsional mode were selected, and as an additional clarification, an isometric view was placed on the right side of each displacement map to give a more general view on the overall motion of the excited samples.

The displacement maps were obtained using the two interferometers described in the previous sections: the need of using different set-ups is due to the fact that the character of the deformations is highly variable from one mode to one other: the out-of-plane components of the displacement were very large compared to the in-plane counterparts thus a desensitised interferometer was needed to avoid decorrelation problems.

This was really helpful also for the last part of the investigation when we tried to demonstrate the auxetic behaviour analysing in-plane eigenmodes that usually occur at higher energy level and frequencies than the out-of-plane counterparts and are characterized by smaller displacement.

In Fig. 42.6, a detailed plot of the in-plane eigenmodes vs. frequency is reported. One comparison between the numerical and the experimental data has been made in terms of displacement map and, similarly to the previous plots, an isometric view was added on the side of the horizontal displacement map of the fourth in-plane mode of the double-t sample.

The eigenmodes showed in Fig. 42.6 was chosen since it was the one we could excite most easily experimentally. The previous ones, even if characterized by lower natural frequencies, were in proximity of other out-of-plane modes complicating the measure processes.

The double-t was preferred among the others since it was the least stiff structure analysed and, hence, the easiest to vibrate close to an eigenfrequency (of about 6000 Hz) connected to an in-plane mode as suggested by the simulations.

In the upper part of Fig. 42.6 we show the displacement contours generated from both numerical simulation (top) and experiment (bottom) for one particular in-plane mode. The comparison shows again a very good agreement demonstrating the ability of correctly simulate the considered phenomena.

The in-plane modes are appropriate to highlight the auxetic behaviour of the sample since for thin structures the auxetic properties are more evident considering the in-plane deformations.

In the displacement maps of Fig. 42.6 the overall motion of the sample is reported: a contraction when a compression is present and a dilatation when a tensile stress state is present indicate that the specimen is characterized by a negative value of the Poisson's ratio and from a more detailed analysis of the displacement fields it's possible to notice that the deformation
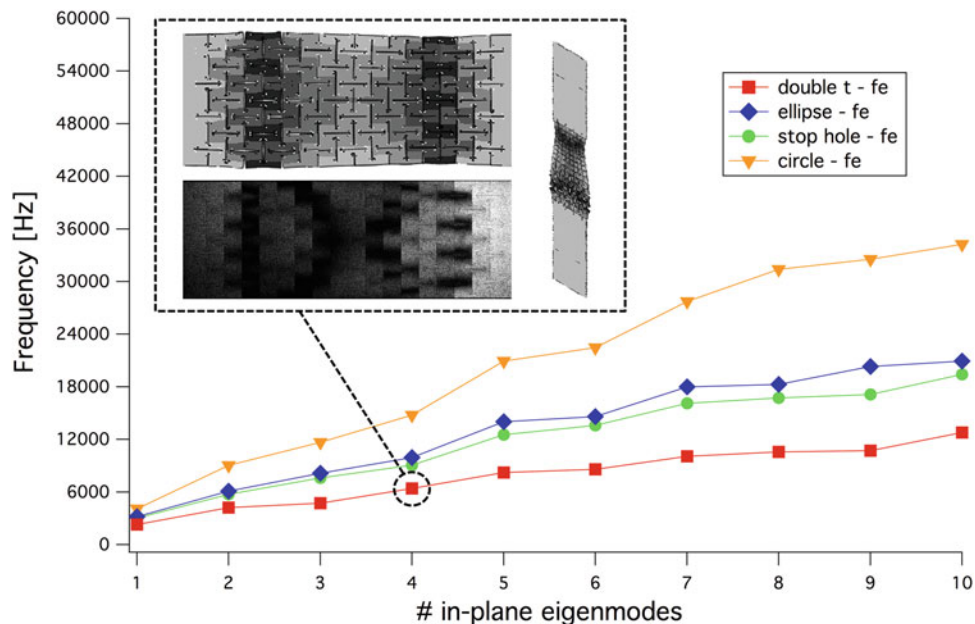

Fig. 42.6 Finite element simulation and horizontal and vertical displacement maps

mechanism that leads to a negative Poisson's ratio in the double-T sample is mostly due to rotation of the single base cells and not connected with the material by itself validating all the assumption and observation made along the paper.

An interesting application would be focusing on in-plane modes at higher frequencies to demonstrate the auxetic behaviour in a more critical dynamical stage and for different stiffness and geometry that was not possible during this investigation since this investigation was limited by the maximum frequency, of about 10,000 Hz, allowed by the piezo-actuators the amplifier and the controller.

42.5 Conclusions

Three different thin low porosity metal negative Poisson's ratio structures were tested numerically and experimentally with speckle interferometry to assess their auxetic behavior and their eigenmodes.

Different interferometers sensitive to the in-plane displacements were used during this investigation to obtain the displacement maps along the whole surface of the samples and the results were compared with the numerical calculation of the modal analysis performed with the finite element software Abaqus/Standard and an excellent agreement was found.

Torsional, flexural and in-plane modes were observed and the experimental natural frequencies were found to be very close to the ones provided experimentally, thus obtaining a very good prediction of the real resonance frequencies of the structures.

The results validate the numerical approaches used to predict the overall response opening a way to design more complex and advanced auxetic structures.

This investigation validates the utilization of this type of meta-structure using ductile materials, and demonstrates that by varying the pore's geometry and the stiffness, it's possible to modify the dynamical behavior of the samples tuning the auxetic properties in function of the requirement of the design.

In addition, the findings of this study provide a basis for future researches to address some of the problems related to using ductile materials to create more advanced metallic auxetic structures, such as optimizing the geometry, the fabrication processes and minimize the stress concentration for different scenarios.

References

1. Evans, K.E., Alderson, A.: Auxetic materials: functional materials and structures from lateral thinking. Adv. Mater. 12(9), 617–628 (2000)
2. Alderson, A., Alderson, K.L.: Auxetic materials. Proc. Inst. Mech. Eng. Part G J. Aerosp. Eng. 221(4), 565–575 (2007)
3. Lakes, R.: Advances in negative Poisson's ratio materials. Adv. Mater. 5, 293–296 (1993)
4. Prawoto, Y.: Seeing auxetic materials from the mechanics point of view: a structural review on the negative Poisson's ratio. Comput. Mater. Sci. 58, 140–153 (2012)
5. Sanami, M., Ravirala, N., Alderson, K., Alderson, A.: Auxetic materials for sports applications. Procedia Eng. 72, 453–458 (2014)
6. Bertoldi, K., Reis, P.M., Willshaw, S., Mullin, T.: Negative Poisson's ratio behaviour induced by an elastic instability. Adv. Mater. 22, 361–366 (2010)
7. Lehmann, M.: Statistical theory of two-wave speckle interferometry and its application to the optimization of deformation measurements. PhD Thesis, Ecole Polytechnique Federal de Lausanne (1998)
8. Taylor, M., Francesconi, L., Gerendas, M., Shanian, A., Carson, C., Bertoldi, K.: Low porosity metallic periodic structures with negative Poisson's ratio. Adv. Mater. 26(15), 2365–2370 (2014)
9. Jacquot, P.: Speckle interferometry: a review of the principal methods in use for experimental mechanics applications. Strain 44, 57–69 (2008)
10. Baldi, A., Jacquot, P.: Data analysis of speckle interferometry measurements for residual stress determination in composite specimen. In: Proceedings of ICEM12—12th International Conference on Experimental Mechanics (2012)
11. Hariharan, P., Oreb, B.F., Eiju, T.: Digital phase-shifting interferometry: a simple error-compensating phase calculation algorithm. Appl. Optics 26(13), 2504–2506 (1987)
12. Tiziani, H.J., Klenk, J.: Vibration analysis by speckle techniques in real time. Appl. Optics 20(8), 1467–1470 (1981)
13. Romero, G., Alvarez, L., Alanis, E., Nallim, L., Grossi, R.: Study of a vibrating plate: comparison between experimental (ESPI) and analytical results. Opt. Lasers Eng. 40, 81–90 (2003)